Examining the mechanistic regulation of starvation-induced autophagy via the identification and characterisation of novel ULK kinase substrates

Thomas John Mercer

University College London

and

The Francis Crick Institute

PhD Supervisor: Sharon A. Tooze

A thesis submitted for the degree of

Doctor of Philosophy

University College London

September 2019

Declaration

I, Thomas John Mercer confirm that the work presented in this thesis is my own. Where information has been derived from other sources, I confirm that this has been indicated in the thesis.

Abstract

Autophagy involves the formation of an endoplasmic reticulum-derived membrane termed a phagophore which expands to engulf cytoplasmic cargo before sealing to form an autophagosome. Amino acid starvation is amongst the most potent autophagic stimuli, however whilst the key signalling complexes involved in starvation-induced autophagy are known, the precise regulatory mechanisms remain poorly understood. The serine/threonine kinase ULK1 and close homolog ULK2 assume the most upstream position in the autophagic signalling cascade and play a crucial yet enigmatic role in coordinating the autophagic machinery.

To further understand the mechanisms of starvation-induced autophagy, I performed a number of unbiased phosphoproteomic screens to identify ULK substrates before classifying their roles in starvation-induced autophagy. Analysis of these datasets has revealed that loss of ULK results in significant changes to the phosphoproteome and has yielded a high confidence list of potential substrates whilst also offering interesting insights into the veracity of the published ULK consensus signature. Amongst the novel phosphorylation targets are components of the retromer and AMPK complexes along with multiple components of the class III PI3K VPS34 complex. The pseudokinase p150, scaffolding component of the VPS34 complex, is phosphorylated by ULK1 *in vitro* and *in vivo* at serine 861. CRISPR-based knockout of p150 results in inhibition of autophagy and endosomal trafficking, whilst mutating the phosphorylated residue in p150 alters both omegasome establishment and autophagic flux. Furthermore, incorporation of phosphomutant p150 into the VPS34 complex modulates its lipid kinase activity in vitro. These data identify a novel ULK-dependent signalling axis and help illuminate the complexities of signal transduction in autophagy.

Impact Statement

Autophagy is a catabolic process of quality control for both proteins and organelles. It is a major mechanism by which homeostasis is maintained and the requisite protein/lipid machinery are essentially conserved across all Eukarya. The rapidly broadening implication of autophagy in both physiology and pathophysiology has garnered much interest in recent years with the importance of autophagy research signified by the awarding of the 2016 Nobel Prize in Medicine or Physiology to Yoshinori Oshumi, the researcher responsible for the discovery of many of the core autophagy-regulatory genes in *Saccharomyces cerevisiae*.

Autophagy requires the activity of ULK1 and homolog ULK2, the only serine/threonine kinases in the autophagic signalling cascade, however the exact mechanism by which they function is unclear. Their importance is exemplified by the increasing identification of autophagy-dependent and -independent pathological phenotypes associated with loss of ULK. More pertinently, as kinases they are considered druggable targets and a number of small-molecule ULK1 agonists/antagonists have recently been developed, some with the proven capacity to drive cancer cell death in both cultured cells and in murine tumour xenografts. These insights highlight the potential importance of ULK activity modulation in human therapeutics and in turn emphasise the requirement for a comprehensive understanding of how the kinases elicit their downstream functions.

Via the identification and validation of novel ULK substrates, I have illuminated new facets of ULK-dependent signalling with potential implications both in academia and in human health. By unpicking the signalling network within which ULK1 and ULK2 are integrated and by studying how this system is perturbed upon their loss, I have provided tangible evidence as to how to the kinases function. Each of the novel substrates could serve as therapeutic biomarkers for ULK activity. Importantly, amongst them are components of well conserved and lipid and protein kinase complexes that are implicated in crucial cellular processes from membrane trafficking to energy homeostasis. The findings described in this thesis therefore provide ample scope for future discoveries with relevance across disciplines.

Acknowledgements

I would like to thank my PhD supervisor Sharon Tooze for giving me the opportunity to work in her laboratory. The support and freedom I have been given during my PhD have been invaluable to my development thus far and I am lucky to have been mentored by such an excellent scientist.

Thank you to my examiners, Ian Ganley and Robin Ketteler for taking the time to read my thesis so quickly, I look forward to our conversation.

The Science Technology Platforms have been essential to the progress of my project. I thank the Genomics Equipment Park and Proteomics teams for their considerable input and offer special thanks to Stefan Boeing from the Bioinformatics team for the contribution of his time and expertise during analysis of my phosphoproteomic datasets.

I thank my Thesis Committee members – Jeremy Carlton, Chris Stefan and Peter Parker for their helpful advice throughout my PhD. Particular thanks go to Peter Parker who provided the concept for the *in vivo* crosslinking screen.

I thank our collaborator Roger Williams and his team for their time and expert advice, as well as for the provision of materials and data, all of which have been essential to the furtherance of the p150 project. Yohei Ohashi has been outstanding in this regard and I am especially grateful for his input.

The past and present members of the MCBA laboratory have shaped my experience here like no other and it has been brilliant to work with such enthusiastic and intelligent colleagues and friends. I particularly thank Martina Wirth for her creative and insightful ideas and for always being available for a chat whatever the time or topic. I thank Harold for his work on the SILAC screen and Justin for helping me settle in back in Lincoln's Inn Fields. Thanks go to Alex, Minoo, George and Tim for the funny and interesting conversations which have so often been the highlight of my day.

Thank you to my friends for making the past 4 years so memorable as well as to my hugely supportive family. Particular thanks go to Mum and Grandad for being such steadfast role models, providing me with love and advice always, to Grandma and my brother Sam for their love and encouragement and to my sister Kaite for her wisdom and for always being my biggest fan.

Finally, I would like to thank Aimee for her constant support, for being so loving and for making life so much fun.

Table of Contents

Table of Figures

List of Tables

Abbreviations

AbKRS – AbK tRNA synthetase

Aff Pur/AP – Affinity Purification

ALPS – Amphipathic Lipid Packing Sensor

Atg – Autophagy-Related

AU – Arbitrary Units

Avg – Average

BARA – β-α repeated autophagy

BATS – Barkor/ATG14(L) autophagosome-targeting sequence

Bl6 – Black 6

BSA – Bovine Serum Albumin

CI – VPS34 Complex I

CII – VPS34 Complex II

CBS – Cystathionine β-Synthase

CMA – Chaperone-Mediated Autophagy

CMV – Cytomegalovirus

CoIP – Coimmunoprecipitation

COP – Coatomer protein

Corcoeff – Correlation Coefficient

CRISPR – Clustered Regularly Interspaced Short Palindromic Repeats

cryoEM – Cryogenic Electron Microscopy

CTD – C-Terminal Protein Interaction Domain (or) C-Terminal Domain

DMEM – Dulbecco's Modified Eagle Medium – High Glucose

DNA –Deoxyribose Nucleic Acid

EBSS – Earle's Balanced Salt Solution

Endo – Endogenous

ER – Endoplasmic Reticulum

ERGIC – Endoplasmic Reticulum-Golgi Intermediate Compartment

ESCRT – Endosomal Sorting Complexes for Transport

Exo – Exogenous

F – Fed

F.S. – Frame Shift

FACS – Fluorescence Activated Cell Sorting

FB – Fed + Bafilomycin A1

FBS – Foetal Bovine Serum

FM – Full Medium

Fwd – Forward

FYVE – Fab1p, YOTB, Vac1p and EEA1

GAP – GTP-Activating Protein

GCE – Genetic Code Expansion

GEF – Guanine-Nucleotide Exchange Factor

GUV – Giant Unilamellar Vesicle

H/L – - Heavy/Light

HA – Human Influenza Hemagglutinin

HEK293A – Human Embryonic Kidney 293

HeLa – Henrietta Lacks

HOPS – Homotypic Fusion and Protein Sorting

HORMA – Hop1, Rev7, Mad2

HRP – Horseradish Peroxidase

IF – Immunofluorescence

Indel – Insertion/Deletion

Inh – Inhibitor

IP – Immunoprecipitation

IP-Re – Immunoprecipitation-Recapture

iTRAQ – Isobaric Tags for Relative and Absolute Quantitation

IVKA – *In vitro* Kinase Assay

KD – Kinase Domain

KI – Kinase Inactive

KLD – Kinase-Ligase-Dpn1

KRB – Kinase Reaction Buffer

Lipo – Lipofectamine 2000

LFa – Leucine-Phenylalanine-Acidic

LIR – LC3-Interacting Region

MAM – Mitochondria-Associated ER Membrane

MGI – Mouse Genome Informatics

MS1 – First stage of tandem mass spectrometry

MS2 – Second stage of tandem mass spectrometry

Mt – Mutant

mTORC1 – Mammalian Target of Rapamycin Complex 1

mTORC2 – Mammalian Target of Rapamycin Complex 2

N.S. – Not Significant

NEB – New England Biolabs

NES – Nuclear Export Signal

NESAbKRS – Nuclear Export Signal-tagged AbK tRNA synthetase

NGF – Nerve Growth Factor

NTKD – N-terminal kinase domain

PAGE – Polyacrylamide Gel Electrophoresis

PAS – Phagophore Assembly Site

PBS – Phosphate Buffered Saline

PBST – Phosphate Buffered Saline 0.1% Tween 20 (v/v)

PC – Peptide Competition

PCR – Polymerase Chain Reaction

PH – Pleckstrin-Homology

$PI(3,4,5)P_3$ – Phosphoinsositide-3,5-Trisphosphate

$PI(3,4)P_2$ – Phosphoinsositide-3,4-Bisphosphate

$PI(3,5)P_2$ – Phosphoinsositide-3,5-Bisphosphate

$PI(4,5)P_2$ – Phosphoinsositide-4,5-Bisphosphate

PI3P – Phosphoinsositide-3-Phosphate

PIP_2 – Phosphoinsositide-3,5-Bisphosphate/Phosphoinsositide-3,4-Bisphosphate/Phosphoinsositide-4,5-Bisphosphate

PI3KCI – Phosphatidylinositol 3-Kinase Complex 1

PI3KCII – Phosphatidylinositol 3-Kinase Complex 2

pKD – Pseudokinase Domain,

Ponc – Ponceau

PROPPIN – β-Propellers that bind Polyphosphoinositides

PS – Phosphatidylserine

PSSM - position-specific scoring matrix

PTM – Post-Translational Modification

PVDF – Polyvinylidene Fluoride

PX – Phox-Homologous

PylRS – Pyrrolysine tRNA Synthetase

RF – RISC-Free (or) Refed

Rev – Reverse

RNAi – RNA interference

SDM – Site Directed Mutagenesis

SDS – Sodium Dodecyl Sulphate

SFM – Serum-Free Medium

SILAC – Stable isotope labelling by amino acids in cell culture

sgRNA – Single Guide RNA

siRNA – Small Interfering RNA

SNARE – Soluble NSF Attachment Protein Receptor

SPRD – Serine-/Proline-Rich Domain

St – Starved

StB – Starved + Bafilmoycin A1

STP – Science Technology Platform

SUV – Small Unilamellar Vesicle

Ta – Annealing Temperature

TBST – Tris-Buffered Saline

TEV – Tobacco Etch Virus

Tfn – Transferrin

TGN – Trans Golgi Network

TMT – Tandem Mass Tag

TORC1 – Target of Rapamycin Complex 1

UPS – Ubiquitin Proteasome System

V-ATPase – Vacuolar-Type H+ -ATPase

Ve – Vehicle

Vps – Vacuolar Protein Sorting

WB – Western Blot

WC – Whole Cell

WIPI – WD40 Repeat Protein Interacting with Phosphoinositides

WT –Wild Type

Chapter 1. Introduction

1.1 Proteostasis

1.1.1 What is proteostasis

The mechanism by which protein synthesis and protein degradation are balanced is termed proteostasis. It is required to maintain sufficient protein activity and is therefore crucial for cell viability. Bulk synthesis, as well as that of specific proteins, is controlled at transcriptional and translational levels. However, due a multitude of factors including chaperone availability, the presence of environmental stresses as well as a protein's intrinsic stability, proteins become damaged or misfolded over time. Improperly structured proteins (i.e. proteins in a sub optimal thermodynamic conformation) can be highly toxic due to pathological gain of functions (M Dong et al., 1994, Chen et al., 2011) or due to their tendency to form aggregates with the latter implicated in many neurodegenerative disorders (Ross and Poirier, 2004). It is therefore crucial that damaged proteins are recognised and cleared efficiently.

There have evolved two systems to facilitate protein degradation, the activities of which are highly interconnected (Ji and Kwon, 2017): lysosomal degradation and the ubiquitin-proteasome system (UPS) (Figure 1.1).

1.1.2 Lysosomal degradation: autophagy

Lysosomes are membranous organelles specialised in the catabolism of proteins, lipids and glycans. They are enriched in hydrolytic enzymes and maintain an acidic pH (~pH5) via the activity of the surface localised vacuolar-type H+ -ATPase (V-ATPase). Cargo destined for degradation is delivered to the lysosomal lumen by a variety of methods. After internalisation, extracellular cargo are trafficked to lysosomes either directly (as with phagocytic vesicles) or indirectly through the endosomal system (as with surface receptors). The products of degradation access the cytoplasm for reassimilation via membrane-localised lysosomal permeases.

Degradation of surface receptors requires the multiprotein ESCRT (endosomal sorting complexes required for transport) complexes. Four such complexes exist (ESCRT-0, ESCRT-1, ESCRT-2 and ESCRT-3) all of which are conserved from yeast to metazoans. After internalisation and trafficking to early endosomes, ubiquitinated cargo is bound by ESCRT 0, which localises to endomembranes via association with the phospholipid signalling intermediate PI3P (phosphoinsositide-3-phosphate). ESCRT-1 and ESCRT-2 promote inward budding of the membrane, with ESCRT-2 also able to bind both ubiquitin and PI3P. Membrane scission is achieved by ESCRT-3, which dynamically polymerises around the neck of the intralumenal vesicles (ILVs). ESCRT-3 is disassembled in a ATP-dependent manner via the activity of the AAA ATPase VPS4A/VPS4B (Hurley and Hanson, 2010). Endosomes accrue ILVs and gradually acidify before mature late endosomes terminally fuse with lysosomes to facilitate degradation of ILV-associated cargo. These are the mechanisms by which extracellular cargo are degraded. Intracellular cargo follows a similar but distinct route which also terminates at the lysosome, with the sequestration and lysosomal turnover of intracellular cargoes, themselves targeted in a non-selective or ubiquitin-mediated manner, termed autophagy (Figure 1.1A). Three sub-classifications of autophagy exist, chaperone-mediated autophagy, microautophagy and macroautophagy, each of which are described below.

CMA (chaperone-mediated autophagy) involves the engagement of cytosolic proteins destined for degradation by the heat shock family chaperone HSC70 alongside cochaperones, before association with the lysosomal membrane-spanning glycoprotein LAMP2A. Cargo unfolding by the chaperone complex and association with LAMP2A allows translocation of proteins across the membrane whereupon they are degraded by resident proteases (Kaushik and Cuervo, 2018). LAMP2A multimerisation promotes cargo recognition and unfolding (Bandyopadhyay et al., 2010, Bandyopadhyay et al., 2008, Rout et al., 2014), with stability of the translocation complex increased by association of GFAP at the cytosolic face of the lysosome (Bandyopadhyay et al., 2010).

CMA, which has been observed in mammalian and avian cells only (Kaushik and Cuervo, 2018), is stimulated by cellular stresses such as reactive oxygen species, long term nutrient starvation and hypoxia (Valdor et al., 2014, Cuervo et al., 1995, Ferreira et al., 2015). Alongside modulation via control of *Lamp2a* transcription (Valdor et al., 2014), CMA can be regulated via AKT1-dependent phosphorylation of GFAP at the lysosomal surface leading to its self-

association and the consequent destabilisation of the translocation complex. Activation of AKT1 by mTORC2 inhibits CMA basally, with translocation PH domain leucine-rich repeat-containing protein phosphatase 1 (PHLPP1) relieving this repression via AKT1 dephosphorylation (Arias et al., 2015).

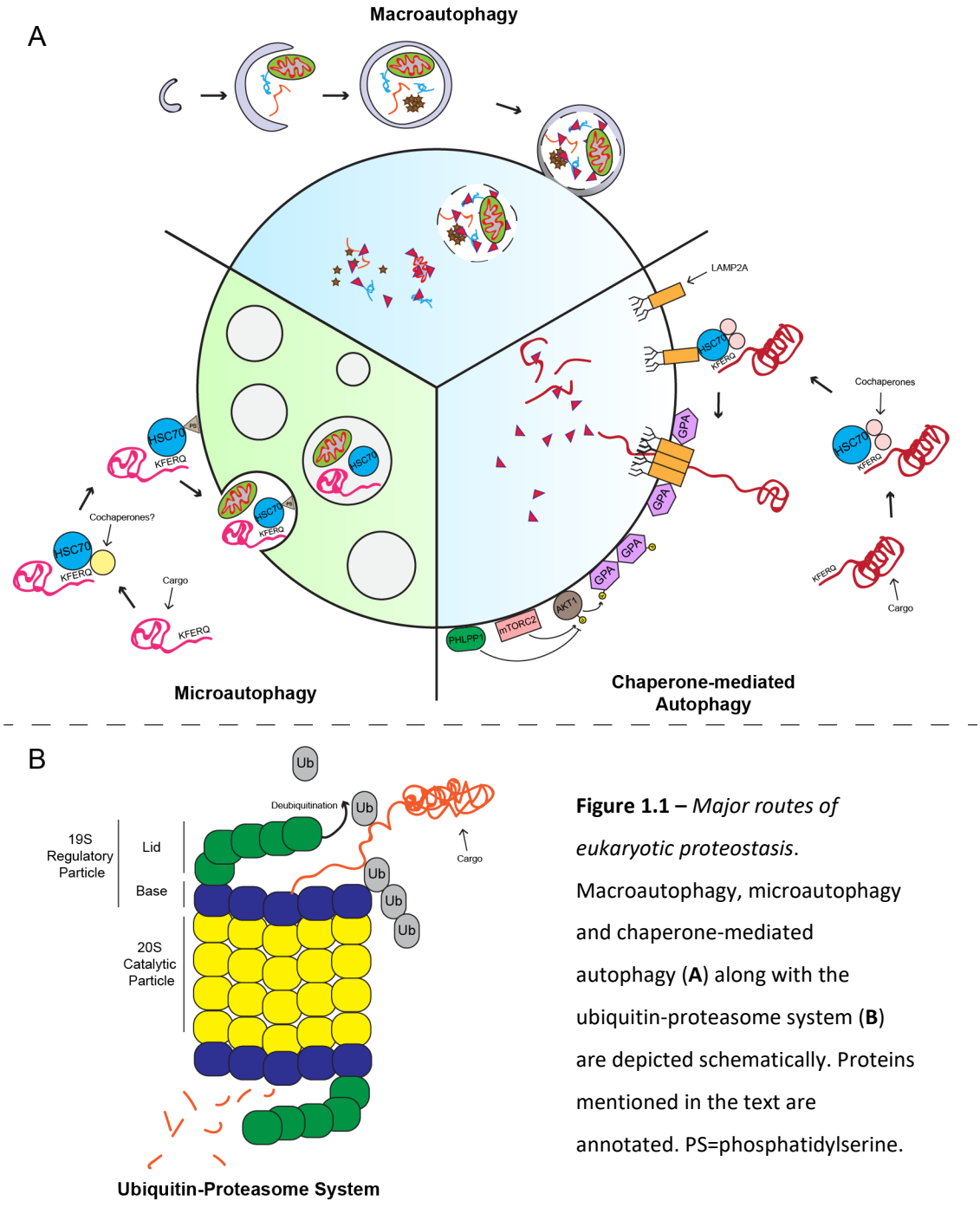

Figure 1.1 – *Major routes of eukaryotic proteostasis*. Macroautophagy, microautophagy and chaperone-mediated autophagy (**A**) along with the ubiquitin-proteasome system (**B**) are depicted schematically. Proteins mentioned in the text are annotated. PS=phosphatidylserine.

The necessary selection of cargo via association of HSC70 means that CMA is an obligatorily selective procedure that only targets proteins. HSC70 binds with KFERQ-like motifs in cargo proteins, which are necessary and sufficient to direct substrates for CMA, and this can be driven by post translational modification revealing or concealing the motifs as observed with HIF1α and MST1 degradation respectively (Ferreira et al., 2015, Li et al., 2015b).

Microautophagy is best understood as the sequestration of cytoplasmic cargoes via the invagination of endolysosomal membranes leading to their turnover at the lysosome. It was first described as a bulk degradation process; however, the selective uptake of many substrates has now been well established including mitochondria, lipid droplets, peroxisomes, portions of the nucleus and ER in yeast (Schuck et al., 2014, Tekirdag and Cuervo, 2018). Whilst uptake of bulk and specific cargoes via invagination of vacuolar membranes is readily apparent in yeast, it has been suggested that that the process is facilitated by late endosomes in mammalian cells (Tekirdag and Cuervo, 2018, Sahu et al., 2011). Additionally, microautophagy via the extension and wrapping of lysosomal/vacuolar tubules around portions of the cytoplasm, protein aggregates and organelles has been reported (Oku and Sakai, 2018). However, this process is relatively poorly described and is better established in yeast and plant species than in mammals (Guan et al., 2001, Oku et al., 2006, Chanoca et al., 2015).

Membrane invagination in mammalian microautophagy is ESCRT-dependent (Sahu et al., 2011). Cargo can be sequestered in a bulk or selective manner, with HSC70 again implicated in the latter, resulting in many substrates being shared with CMA (Sahu et al., 2011). However, as the presence of a KFERQ-like motif is not sufficient to promote microautophagic degradation (Koga et al., 2011) and as microautophagy can target proteins than cannot be unfolded or those in complexes, their substrates repertoires differ. HSC70 targets associated cargo to endolysosomal membranes where it directly binds phosphatidylserine in the cytoplasmic leaflet, with this interaction required for cargo internalisation (Sahu et al., 2011, Morozova et al., 2016). Notably, mammalian microautophagy bears parallels with the ESCRT-dependent turnover of plasma membrane-transmembrane proteins via endocytosis.

Of note, the turnover of mitochondrial proteins by autophagy is achieved by a number of methods. One such process involves the formation of mitochondria-derived vesicles which are enriched in proteins damaged via oxidation. They can be engulfed into late endosomes/

multivesicular bodies when targeted by microautophagy (known as Type 3 Micromitophagy) (Lemasters, 2014), with the direct fusion of mitochondria-derived vesicles with lysosomes also observed (McLelland et al., 2016). Whole mitochondria can be sequestered and degraded by the final autophagic sub-classification to be introduced, macroautophagy.

Like microautophagy, macroautophagy facilitates the degradation of a wide array of biomolecules and is well conserved from yeast to humans. Macroautophagy is the process by which cytoplasmic cargos are sequestered in double-membraned vesicles termed autophagosomes before delivery to the lysosome resulting in the degradation of contents. Autophagosomes form *de novo* at specialised regions of the endoplasmic reticulum (ER) and expand to engulf portions of the cytosol in non-specific/bulk macroautophagy, or specific cargo in selective macroautophagy.

First to be discovered, non-selective/bulk macroautophagy affords the turnover of long-lived proteins. It occurs constitutively but can be stimulated by cellular stressors such as amino acid starvation (nitrogen starvation in yeast), growth factor restriction and hypoxia (Mauvezin et al., 2015, Li et al., 2013a, Daskalaki et al., 2018). Additionally, in yeast as well as mammals, a wide array of often cytotoxic substrates are targeted by selective macroautophagy, ranging from protein aggregates (aggrephagy), to mitochondria (mitophagy) and portions of the ER (ERphagy/reticulophagy), as well as invading pathogens (xenophagy) in metazoans (Zaffagnini and Martens, 2016). The mechanisms of macroautophagy will be discussed in sections 1.2-1.3.

1.1.3 The ubiquitin proteasome system

In the UPS (ubiquitin proteasome system), both cytosolic and nuclear cargo destined for degradation are targeted to the proteasome, a ~2.5MDa barrel shaped complex with a protease-lined pore (Figure 1.1B). Made up of a core 20S catalytic particle and one or two 19S regulatory particles, the 26S proteasome facilitates degradation of client proteins (Tanaka, 2009). Whereas long-lived proteins, or those in large aggregates or damaged organelles are targeted by autophagy, short-lived proteins tend to be degraded by the proteasome. The 700kDa 19S regulatory particle promotes catalytic activation of the core subcomplex. It is composed of lid and base subcomplexes, with the former implicated in substrate deubiquitination (see below) and the latter in substrate recognition, ATP-dependent substrate

unfolding and translocation into the 750kDa 20S catalytic particle. Threading of unfolded polypeptides into the 20S subcomplex, the opening pore of which is too narrow to allow polypeptides to pass in the absence of the 19S sub complex, results in their processive degradation, yielding 3-15 residue oligopeptides. See Figure 1.1 for a schematic depiction of the main routes of eukaryotic proteostasis.

1.1.4 Regulation of proteostasis through ubiquitination

Substrate selectivity of the UPS is maintained via the post translational covalent attachment of the 8.6kDa protein ubiquitin proteins to be targeted for degradation. Termed ubiquitination, this can serve as a degradation signal that is recognised by proteasomal ubiquitin binding proteins, such as the 19S proteasomal subunits RPN10 and RNP13 (Collins and Goldberg, 2017). Alongside marking proteins for degradation, ubiquitination can also modulate their biological functionality, with a protein's fate depending on the number of ubiquitin modules conjugated (either mono-, multiple mono- or poly-ubiquitin chains, with the latter either linear or branched), to the lysine on ubiquitin by which it is conjugated or even by the presence of post-translational modifications on conjugated ubiquitin (Kazlauskaite et al., 2014b).

Ubiquitin conjugation is facilitated by three families of enzymes. Most upstream are ubiquitin-activating enzymes (E1), which covalently binds ubiquitin via a catalytic cysteine, expending ATP in the process. Ubiquitin is then transferred onto a ubiquitin carrier protein (E2), again via attachment to a catalytic cysteine (Komander and Rape, 2012). Finally, both the E2 enzyme and the protein substrate bind to an E3 enzyme which catalyses the transfer of cysteine onto an accessible lysine on the substrate. This process is repeated to generate polyubiquitin chains (Hershko and Ciechanover, 1998). The relative numbers of ubiquitin-processing enzymes reflect the manner in which substrate selectivity is maintained. Whilst only 2 E1 proteins and ~30-50 E2 proteins have been identified, the substrate-binding E3 enzymes represent ~5% of the human genome with around 600-700 different species estimated to exist. Unsurprisingly, E3 enzymes display the most diversity in their catalytic domains with three main families identified (Zheng and Shabek, 2017).

The most prominent ubiquitin linkage identified in the cell and also the major driver of proteasomal degradation is lysine 48-linked ubiquitin (Ji and Kwon, 2017). Interestingly,

ubiquitin-independent proteasomal degradation has been reported for some cargo, with these requiring alternative activators in place of the 19S subcomplex such as REGγ or PA200/Blm10 (Sadre-Bazzaz et al., 2010, Chen et al., 2007). Whilst the majority of autophagic cargo do not require ubiquitination before targeting, lysine 63-linked ubiquitin chains have been implicated in around half of the 20 types of selective macroautophagy identified (Deng et al., 2017, Grumati and Dikic, 2018, Ji and Kwon, 2017) and the autophagic adaptor p62 preferentially binds ubiquitin linked in this manner (Kirkin et al., 2009). However, K6, K11, K46 and M1 have minor and potentially substrate-specific roles in autophagic targeting (Cunningham et al., 2015, Dwane et al., 2017, Ji and Kwon, 2017, Riley et al., 2010, van Wijk et al., 2017).

For the remainder of this thesis, I will be mainly discussing canonical bulk macroautophagy (herein referred to as autophagy) in mammalian systems, which is the chief focus of my work. However, I will refer to insights from model organisms as well as those from selective autophagy where appropriate.

1.2 Autophagy

1.2.1 The importance of autophagy research

Based on its central role in the turnover of cytoplasmic material and the freeing of metabolic substrates for reuse, autophagy regulates cellular homeostasis at multiple levels. Amongst other roles, it is crucial for the maintenance of genomic stability through controlling redox, iron and lipid homeostasis, as well as mitochondrial function and survival during nutrient starvation. Unsurprisingly therefore, autophagy is implicated in a wide array of physiological and pathophysiological processes (Levine and Kroemer, 2019).

Autophagy has been implicated in adaptive immunity via the delivery of antigens for MHC class II presentation (Crotzer and Blum, 2009) and in innate immunity via xenophagy and control of interferon signalling (Ravenhill et al., 2019, Konno et al., 2013). It has also been implicated in both the promotion and the suppression of cancer depending on the tissue, stage and present genetic mutations. Whilst the autophagic program is often upregulated in cancer cells to survive the metabolic stress experienced in the tumour environment (Tooze et al., 2019), it has also been shown to promote anti-cancer immune surveillance via both cancer-cell intrinsic and

systematic means (Michaud et al., 2011, Crotzer and Blum, 2009, Ma et al., 2013). The autophagy protein BECN1 (see section 1.3.4), which is frequently monoallelically deleted in murine and human cancers, controls levels of the tumour suppressor protein p53 by stabilising the deubiquitinases USP13 and thus USP10, with the latter directly targeting p53 (Liu et al., 2011). Intriguingly, the tumour suppressor p53 also promotes autophagy suggesting that its upregulation is part of its anti-oncogenic program, however p53 is also degraded by autophagy despite BECN1's role in proteasomal protection and thus autophagy may facilitate tumour promotion (White, 2016). Confusing this scenario, autophagy deficient mice were found to generate benign hepatic tumours only (Takamura et al., 2011). The role of autophagy in cancer therefore evades a simple description; generally, it is seen as being tumour suppressive in healthy cells whilst favouring tumour progression after oncogenesis (Galluzzi et al., 2015).

Autophagy has been shown to promote longevity. There is a strong correlation between advanced age and the suppression of autophagy and it has been well established that dietary restriction without malnutrition (which stimulates autophagy) extends lifespan, with both observations made in several model organisms (Hansen et al., 2018). Whilst ubiquitous overexpression of the autophagy gene *Atg5* (see section 1.3.6) was shown to extend lifespan in mice (Pyo et al., 2013) and despite the increase in longevity demonstrated after upregulating autophagy in intestine-, muscle- and immune system-tissue, the link between neuronal autophagy with both extension of lifespan and age-related pathologies has garnered the most attention in recent years (Hansen et al., 2018).

Neurones are highly metabolically active and post-mitotic and therefore rely on high levels of basal autophagy to clear damaged proteins and organelles that cannot be diluted upon cell division. Misregulated autophagy is implicated in various neurodegenerative disorders such as Alzheimer's disease, Parkinson's disease, amyotrophic lateral sclerosis and polyglutamine (PolyQ) disorders, all of which are characterised by the build-up of neuronal aggregates (Metaxakis et al., 2018, Fujikake et al., 2018, Ashkenazi et al., 2017, Hara et al., 2006, Komatsu et al., 2006). Autophagy is therefore an attractive therapeutic target for the treatment of neurodegenerative diseases.

These and other discoveries underscore the importance of autophagy research. Work in baker's yeast (*S. cerevisiae*) has led to the identification of 41 *ATG* (autophagy-related) genes,

less than half of which are conserved in humans (Tsukada and Ohsumi, 1993, Thumm et al., 1994, Harding et al., 1995, Wen and Klionsky, 2016). The identification of a suite of genes and proteins that regulate autophagy has allowed us to greatly increase our understanding of its molecular mechanisms. Whilst not all of the *ATG* genes are conserved in humans, the main signalling complexes are found across Eukaryota (see section 1.3). In the next section the main morphological stages of autophagy as well as molecular machinery that facilitate them will be discussed.

1.2.2 Stages of Autophagy

Shortly after their discovery in rat liver homogenates, lysosomes were shown to contain intracellular material (Clark, 1957, Novikoff, 1959, De Duve et al., 1955). Based on these and other observations, they were soon implicated in the turnover of cytoplasmic components, with Christian De Duve christening the process autophagy, Greek for 'self-eating' (De Duve, 1963, Ohsumi, 2014). Whilst partially degraded cytoplasmic and organellar material were observed on multiple occasions within lysosomes or in lysosome-like bodies, the identification of double-membraned organelles loaded with cytoplasmic material in the absence of hydrolytic enzymes, known today as autophagosomes, came some years later (Arstila, 1968, Smith and Farquhar, 1966).

All of these observations were made by electron microscopy, the only way to study autophagy prior to the identification of specific protein markers. Today this technique is still instrumental in studying the morphological stages of autophagy at an ultrastructural level (Eskelinen et al., 2011). However confocal microscopy alongside more sophisticated techniques such as correlative cryo-fluorescence and cryo-soft X-ray microscopy have greatly increased our understanding as to the morphological stages of autophagy (Duke et al., 2014).

The first stage in the autophagic program is autophagosome initiation/nucleation. This takes place at specialised regions of the ER termed omegasomes due to the unique omega-shaped morphology of the nascent autophagosomal membrane (Axe et al., 2008). As autophagosome biogenesis proceeds, a cup-shaped membrane termed the phagophore detaches from the ER to enclose the material destined for degradation. The phagophore is supported on either side by neighbouring ER cisternae (Hayashi-Nishino et al., 2009, Yla-Anttila et al., 2009) and is

shaped by localised F-actin polymerisation (Mi et al., 2015). Phagophore closure results in the formation of a double membraned autophagosome of around 0.5-2µm in diameter (0.3-0.9µm in yeast), which is then trafficked along the microtubule network towards the perinuclear region of the cell (Fass et al., 2006). In metazoans, autophagosomes mature by fusing with late endocytic compartments (Tooze et al., 1990), with the resultant organelle termed an amphisome. Amphisomes or autophagosomes then fuse with lysosomes to form an autolysosome. In yeast no equivalent to amphisomes exist, with autophagosomes fusing directly with the vacuole (yeast equivalent to the lysosome). Within autolysosomes the inner membrane along with associated cargo is destroyed by resident hydrolases. Lysosomes are regenerated via autophagic-lysosome reformation (Figure 1.2) (Munson et al., 2015, Yu et al., 2010).

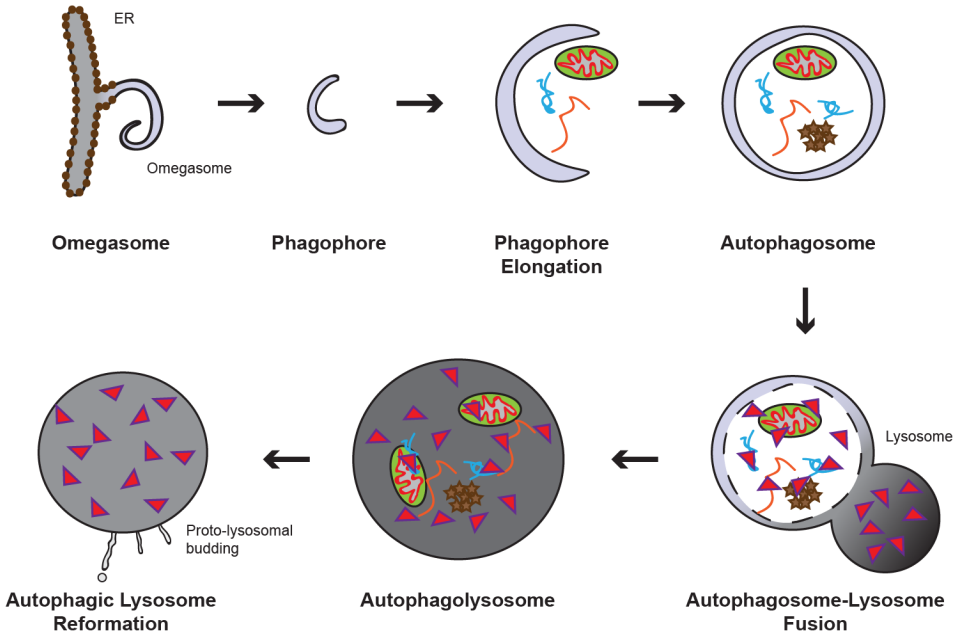

Figure 1.2 – *Schematic depiction of the stages of autophagy*. The main morphological stages of autophagy from autophagosome biogenesis through to termination are shown. The brown ER-localised dots represent ribosomes, which are absent on omegasomes. Magenta triangles represent lysosomal hydrolases. Dashed line represents the degrading inner autophagosomal membrane.

1.2.3 Membrane trafficking in autophagy

A schematic depicting the sources of autophagosomal membranes and associated protein machinery discussed in this section is shown in Figure 1.3.

1.2.3.1 Initiation

It is widely accepted that autophagosomes nucleate from specialised ER-regions termed omegasomes (Lamb et al., 2013). However, it has also been suggested that autophagosomes form at recycling endosomes (Puri et al., 2018, Knævelsrud et al., 2013), mitochondria (Hailey et al., 2010), the Golgi (Ohashi and Munro, 2010, Geng et al., 2010, Nishida et al., 2009) and the plasma membrane (Nascimbeni et al., 2017, Ravikumar et al., 2010). The apposition of ER cisternae with many intracellular membranes (Marsh et al., 2001, Fernández-Busnadiego et al., 2015, Phillips and Voeltz, 2015) may have confounded accurate identification of the autophagosome nucleation site and could therefore explain the wide-ranging attributions that exist in the literature. Whilst it is possible that autophagosomes nucleate from several organelles independently, the weight of existing data supports the ER as the site of autophagosomal biogenesis and will be considered thus herein (Lamb et al., 2013).

The hierarchy of Atg protein recruitment to the ER upon autophagy initiation is largely conserved from yeast to humans, with autophagy initiation complexes such as the protein kinase ULK complex, the lipid kinase VPS34 complex and the autophagy-specific transmembrane protein ATG9A (which associates transiently) the first to be recruited (Suzuki et al., 2007, Nakatogawa et al., 2009, Karanasios et al., 2016). Localisation of these complexes to omegasomes is crucial for downstream effector recruitment and consequently for the significant membrane reorganisation associated with autophagosome biogenesis (see section 1.3) (Suzuki et al., 2007, Mercer et al., 2018).

In yeast autophagosomes emanate from a single area juxtaposed to the ER – the PAS (phagophore assembly site). In metazoans however, omegasomes form at several sites across the ER simultaneously, at regions coincident with ERES (ER-exit sites) and the ERGIC (ER-Golgi intermediate compartment) (Karanasios et al., 2016). The majority of ER to Golgi transport proceeds via the formation of vesicotubular trafficking intermediates from ERES, which fuse to form the ERGIC before cargo is trafficked on to the Golgi. ER-Golgi anterograde traffic utilises COPII (coatomer protein) machinery, with COPI proteins regulating retrograde traffic between the Golgi cisternae and the ER.

Whilst earlier data suggested COPI-dependent traffic was not implicated in autophagosome biogenesis (Carlos Martín Zoppino et al., 2010) and instead regulated autophagosome maturation via control of early endosome functionality (Razi et al., 2009), it was recently shown that dual inhibition of bidirectional ER-Golgi trafficking via inhibition of COPI/II activity was required to abolish the formation of autophagosomes upon starvation (Karanasios et al., 2016). Furthermore, it was demonstrated using super resolution microscopy that starvation induces omegasomal formation at specialised ERES/ERGIC regions in close proximity with vesicles enriched in ATG9A (Karanasios et al., 2016). Supporting this notion is the established roles of COPII coat in the promotion of autophagosome biogenesis in both yeast and mammals (Shima et al., 2019, Ge et al., 2014, Davis et al., 2016, Tan et al., 2013, Graef et al., 2013, Webster et al., 2016), as well as the capacity of ERGIC membranes to promote *in vitro* and *in vivo* LC3 lipidation (a crucial step in autophagosome formation covered below) and to recruit the autophagy markers ATG14 and DFCP1 *in vivo* (Karanasios et al., 2016, Ge et al., 2013). Furthermore RAB1, whose isoforms regulate COPI and COPII activity to control ER-Golgi and intra-Golgi traffic (García et al., 2011), has also been implicated in the establishment of omegasomes (Webster et al., 2016, Tan et al., 2013) with knockdown of RAB1B or overexpression of a dominant-negative mutant resulting in the reduction of autophagosome number likely due to the disruption of COPII-dependent ERES formation (Carlos Martín Zoppino et al., 2010).

ER-mitochondria contact sites or MAMs (mitochondria-associated ER membrane) have also been identified as the region of autophagosome biogenesis (Garofalo et al., 2016, Hamasaki et al., 2013, Tang et al., 2019). The SNARE (soluble NSF attachment protein receptor) protein STX17 was shown to relocalise to MAMs upon starvation and recruit ATG14. Disruption of MAM formation via knockdown of key structural proteins resulted in the inhibition of ATG14 recruitment to mitochondria and inhibited autophagic flux (Hamasaki et al., 2013). The identification of starvation-induced lipid rafts at MAMs provided further mechanistic insight into the role of ER-mitochondria contact sites in autophagy induction. MAM-localised lipid rafts recruit the autophagy regulators WIPI1 and the VPS34 complex (via AMBRA1) upon starvation (Garofalo et al., 2016). Finally, ER-plasma membrane (ER-PM) contact sites have also been identified as platforms of starvation-induced autophagosome biogenesis (Nascimbeni et al., 2017).

1.2.3.2 Elongation

Each of the membrane sources previously mooted as sites of autophagosome initiation may provide lipids to growing phagophores. Lipid transfer may occur via membrane bridges, vesicular traffic or lipid transport proteins (Biazik et al., 2015), with the ATG9A-positive membrane trafficking potentially implicated in the latter two forms of transfer (see below and section 1.3.7). Furthermore, lipid delivery may occur via the *de novo* production of lipids on the surface of autophagosomes, however little evidence exists to support this model.

ATG9A is mainly localised at the Golgi in basal conditions and disperses to peripheral vesicles upon starvation which are believed to supply lipids to growing phagophores in both yeast and humans (see section 1.3.7). A population of ATG9A localises to endosomal compartments and the early endosomal pool of ATG9A pool exists in close proximity with ANXA2, a positive regulator of actin polymerisation that regulates early to late endosomal maturation (Moreau et al., 2015, Morel et al., 2009). ANXA2 is upregulated on starvation in a c-Jun/JNK-dependent manner and it colocalises with ATG9A at early endosomes. Here, ANXA2 positively regulates autophagy by regulating ATG9A trafficking to recycling endosomes via its effectors ARP2 and SPIRE1 (Moreau et al., 2015). The PX-BAR protein SNX18 was shown to drive the formation of recycling endosome tubules enriched with ATG9A and ATG16L1 (see section 1.3.6) which promoted their trafficking to sites of autophagosome formation upon starvation (Søreng et al., 2018b, Knævelsrud et al., 2013, Søreng et al., 2018a). Interestingly, the phospholipase D1 inhibitor HS1BP3 was identified in recycling endosome-derived vesicles along with ATG9A and ATG16L1, with these structures observed to fuse with early autophagosomal membranes. HS1BP3 decreases phosphatidic acid levels in the autophagic precursors which corresponds with a decrease in autophagosome number, likely due to inhibition of membrane delivery to forming autophagosomes (Holland et al., 2016). Additionally, recycling endosomes contribute to autophagosomal biogenesis via ATG9A-independent mechanisms. Longatti et al., showed that an ULK1-positive but ATG9A-negative recycling endosome-derived vesicles contribute to forming autophagosomes in a RAB11-dependent manner (Longatti et al., 2012).

Aside from the Golgi and endosomes, various distinct membrane compartments are believed to contribute lipids to growing autophagosomes. ATG9A-mediated trafficking is implicated in lipid transfer to autophagosomes from the plasma membrane (Zhou et al., 2017).

Furthermore, ATG16L1-positive vesicles, which form at the plasma membrane via clathrin-mediated endocytosis upon ATG16L1 overexpression (Ravikumar et al., 2010), were shown to undergo homotypic fusion, possibly demonstrating the direct generation of early autophagosomal precursors from the plasma membrane (Moreau et al., 2011). ANXA2 positively regulates the recruitment of phosphatidylinositol and phosphatidylserine to ATG16L1-positive vesicles, as well as their fusion (Morozova et al., 2015). Finally, recent data suggest that COPII vesicles fuse with autophagic membranes in budding yeast (Shima et al., 2019, Tan et al., 2013, Graef et al., 2013). However, as with other vesicular-fusion dependent mechanisms, it remains unknown how resident membrane proteins would be excluded to prevent their autophagosomal degradation.

In *S. cerevisiae*, Atg2p tethers the tips of growing phagophores to ER membranes (Suzuki et al., 2013, Gómez-Sánchez et al., 2018, Obara et al., 2008) and 98% of PAS-localised Atg2p-GFP puncta were shown to colocalise with the ubiquitin-like key autophagic effector Atg8p by immunofluorescence (see below and section 1.3.6), similarly supporting a role in expansion (Graef et al., 2013). In *S. pombe*, a sporulating yeast more closely related to metazoans than *S. cerevisiae*, the membrane-associated autophagy regulator Atg2p in complex with Atg18p was shown to link highly curved liposomes and promote direct lipid transfer via a conserved Vps13p-like domain (Osawa et al., 2019). Importantly, the human homologs ATG2A and ATG2B were shown contain membrane-binding domains at both N and C termini which, cooperatively with the PI3P-binding Atg18p homologs WIPI1 or WIPI4, tether ER- and phagophore- like liposomes (Chowdhury et al., 2018, Maeda et al., 2019). Moreover, ATG2A was also shown to possess the capacity to transfer lipids such as phosphatidylserine and/or phosphatidyl-ethanolamine between such liposomes *in vitro* (Valverde et al., 2019, Maeda et al., 2019), indicating that ATG2-dependent tethering and lipid transfer between ER and autophagic membranes to provide lipids to the growing phagophore might be conserved between humans and yeast. Very recently, the integral outer mitochondrial membrane proteins TOM40 and TOM70 were shown to recruit ATG2A to MAMs upon starvation to facilitate phagophore elongation in an ATG9A-dependent but WIPI4-independent manner. Deletion of ATG2A's ATG9A-binding region prevented elongation and led to an accumulation of ATG9 vesicles at autophagosome-assembly sites. This indicates that ATG2 facilitates the contribution of membranes from ATG9 vesicles to the expanding phagophore, however the mechanism of lipid transfer from ATG9 vesicles to the phagophore was not elucidated (Tang et al., 2019).

Finally, direct connections between ER and autophagosomal membranes have been observed by electron tomography (Uemura et al., 2014, Yla-Anttila et al., 2009) raising the possibility that diffusion of lipids might contribute to phagophore extension. Taken together, despite recent and valuable insights, the mechanisms by which disparate membranes, especially those from non-ER compartments, supply lipids to expanding phagophores remain unclear and warrant further study.

Conjugation of yeast Atg8p with phosphatidylethanolamine (referred to as lipidation) and its consequent association with autophagosomal membranes was reported to promote phagophore elongation (Nakatogawa et al., 2007) and evidence exists suggesting that this function is somewhat conserved for its mammalian homologs (Weidberg et al., 2011, Tsuboyama et al., 2016, Nguyen et al., 2016, Sou et al., 2008). They are grouped into two families based on sequence similarity: the LC3 subfamily (LC3A, LC3B, LC3B2, LC3C) and the GABARAP subfamily (GABARAP, GABARAPL1, GABARAPL2), collectively referred to herein as the LC3/GABARAPs. The identification of homolog-specific functionalities has garnered much attention in recent years. An early knockdown study suggested that the LC3s were crucial for phagophore elongation, with GABARAPs functioning later on (potentially in autophagosome closure) (Weidberg et al., 2010). In a later paper from the same group, both LC3 and GABARAP proteins (LC3B and GABARAPL2) were shown to possess intrinsic fusogenic properties, promoting membrane tethering and fusion *in vitro*. Mutation of the responsible N-terminal motifs resulted in an accumulation of early autophagosomal structures suggesting a role in elongation *in vivo* (Weidberg et al., 2011). Interestingly, a later study found that GABARAP and GABARAPL2 (Landajuela et al., 2016), in concert with curvature-modifying lipids, promoted *in vitro* vesicle fusion, thought to be crucial for phagophore elongation, with much increased efficiency compared to LC3s.

Alongside ANXA2, a host of actin polymerisation regulators of have been implicated autophagosomal biogenesis (Knorr et al., 2015, Zhen et al., 2019). In particular, membrane deformation during phagophore elongation is facilitated by the recruitment of the heterodimeric actin capping complex CAPZ, which binds PI3P at forming autophagosomes and produces branched actin scaffolds detectable as phalloidin-positive puncta within nascent phagophores (Mi et al., 2015).

1.2.3.3 Closure

Autophagosome closure is perhaps the least understood stage of the autophagic process. It is mediated by membrane fission with membrane topologies matching those observed in ESCRT-dependent ILV budding (Knorr et al., 2015). Current data suggests all 4 ESCRT complexes are implicated in yeast and metazoan autophagy (Rusten and Stenmark, 2009), with perturbation of complex members associated with inhibited autophagic flux and the accumulation of p62-/ubiquitin-positive aggregates (Oshima et al., 2016, Filimonenko et al., 2007, Rusten et al., 2007). Intriguingly, it was recently demonstrated in both yeast and mammals that the ESCRT machinery is recruited to phagophores to promote closure by driving membrane fission (Takahashi et al., 2018, Zhen et al., 2019, Zhou et al., 2019). In an ESCRT knockdown screen, removal of CHMP2A (an ESCRT-3 component) resulted in the pronounced accumulation of unclosed autophagosomes. The authors showed that CHMP2A translocation to phagophores is required for basal and starvation-induced autophagy in a VPS4-dependent manner (Takahashi et al., 2018). Furthermore, a second ESCRT-3 component CHMP4B was shown to recruit transiently to forming autophagosomes upon starvation and in the presence of the mitophagy inducer deferiprone whereupon it promotes autophagosome closure only in the presence of CHMP2A (Allen et al., 2013, Zhen et al., 2019). The mechanism of ESCRT recruitment has been illuminated by recent work in yeast. Zhou and colleagues showed that ESCRT recruitment is stabilised by interaction between the Atg1p complex component Atg17p and Snf7p (homologous to CHMP4 in humans), which occurred in a Rab5p-dependendent manner (Zhou et al., 2019).

ATG2 homologs have been implicated in autophagosome closure. RNAi-mediated double knockdown of ATG2A and ATG2B results in the stalling of autophagy and the build-up of unclosed autophagosomal structures (Velikkakath et al., 2012). Further mechanistic insight was provided by Bozic et al., who report that ATG2A/ATG2B double knockout cells along with those expressing ATG2A deficient for GABARAP but not WIPI4 binding displayed a large reduction in LC3 and GFP-STX17 colocalisation (which succeeds closure, see below) along with a decrease in membrane-encapsulated (i.e. protease-protected) p62. This phenotype indicates that mammalian ATG2 is required for early stages of autophagy, with the authors suggesting that they facilitate autophagosomal closure (Bozic et al., 2019). An accumulation of

ATG16L1/p62 double-positive structures was observed after CRISPR-mediated deletion of ATG2A/ATG2B in THP-1 cells, similarly indicating that closure is ATG2-dependent (Tang et al., 2017b), however the formation and maturation of small autophagosomes was permitted in an independent ATG2A/ATG2B CRISPR KO U2OS line suggesting that defective closure might be caused by insufficient membrane expansion (Tang et al., 2019).

Finally, the LC3/GABARAPs are implicated in autophagosome closure. Prevention of LC3/GABARAP lipidation in HeLa (Kishi-Itakura et al., 2014), HEK293A (Fujita et al., 2008a) and in MEF cells (Sou et al., 2008, Tsuboyama et al., 2016, Kishi-Itakura et al., 2014) leads to an accumulation of unclosed autophagic structures. These findings were supported by Tsuboyama and colleagues, who showed that abolishing lipidation in MEFs leads to 70% of nascent autophagosomes failing to close (compared to 7% in WT MEFs) (Tsuboyama et al., 2016). Furthermore, an accumulation of unclosed, ER-apposed phagophores is noted in ATG5 knockout HeLa and Atg5 knockout MEF cells (see section 1.3.6) (Kishi-Itakura et al., 2014). In yeast, outer autophagosomal membrane-localised Atg8p is delipidated after autophagosome formation, a process understood to be crucial to allow dissociation of autophagic machinery for reuse (Nair et al., 2012, Kirisako et al., 2000). Interestingly, prevention of Atg8p delipidation by knocking out the Atg8p protease Atg4p whilst expressing pre-primed/lipidation sufficient Atg8p (see section 1.3.6) decreased autophagosome size and number whilst also inhibiting autophagosomal closure (Nair et al., 2012). In humans however, LC3/GABARAP delipidation does not appear to be necessary for autophagy as expression of pre-primed LC3B in HeLa lacking of 4 human Atg4p homologs (ATG4A, ATG4B, ATG4C, ATG4D) is sufficient to rescue basal autophagy and delivery of LC3B to LAMP1-positive lysosomes upon pharmacological induction of autophagy (Agrotis et al., 2019a).

1.2.3.4 Maturation

As previously noted, autophagosome maturation proceeds via the fusion of fully-formed autophagosomes or amphisomes with lysosomes. Terminal fusion with lysosomes is crucial for cargo degradation, with this stage commonly targeted using Chloroquine or its derivatives (Mauthe et al., 2018). It has been reported that prolonged treatment with Bafilomycin A1, which binds the $V0_C$ subunit of the V-ATPase to inhibit H^+ influx, also prevents autophagosome-lysosome fusion after extended treatment times via the inhibition of

lysosomal acidification (itself sufficient to prevent lysosomal function) (Klionsky et al., 2008). Intriguingly, by comparing Drosophila larvae fat body cells in which V-ATPase components were knocked down with those treated with Bafilomycin A1, it was shown that drug treatment actually prevents autophagosome-lysosome fusion by binding and inhibiting the ER calcium pump Ca-P60A/SERCA, with SERCA speculated to regulate fusion by depressing cytoplasmic calcium levels or by allowing localised influx of calcium near sites of autolysosome formation (Mauvezin et al., 2015).

In yeast autophagosomes are physically tethered to both ER and vacuolar membranes during biogenesis (Graef et al., 2013). In mammals however, tethering of autophagosomes to the ER prevents lysosomal fusion (Wijdeven et al., 2016), with fully formed autophagosomes trafficked towards the perinuclear region in an amino acid- and serum starvation-dependent manner (Li et al., 2016b, Kimura et al., 2008). The role of SERCA in late-stage autophagy regulation resembles that of the mTOR-regulated endolysosomal calcium channel TRPML1, pharmacological inhibition of which prevents the centripetal redistribution of lysosomes in starved HeLa, Cos1 and MEF cells thus preventing fusion with autophagosomes (Li et al., 2016b). Removal of the Drosophila homolog of TRPML1 also prevented lysosomal fusion with late endosomes/amphisomes, suggesting that this role is evolutionarily conserved (Wong et al., 2012).

The actin cytoskeleton has been implicated in autophagosome trafficking. For example, upon starvation the RAB12 guanine nucleotide exchange factor (GEF) DENND3 is phosphorylated and activated by ULK1, leading to its association with LC3 at recycling endosomes and autophagosomes to promote the trafficking of the latter towards lysosomes (Xu et al., 2015). Recently, DENND3 was shown to associate with myosin IIA, implicating the actin motor in autophagosomal trafficking (Xu et al., 2015, Xu et al., 2018). Furthermore, ARP2/3-dependent comet tails have been linked to autophagosome motility (Kast and Dominguez, 2017).

Alongside contributions from the actin cytoskeleton, traffic of autophagosomes is largely mediated by the recruitment of microtubule motors via adaptor proteins such as JIP1, RILP and FYCO1 (Fu et al., 2014, Pankiv et al., 2010, Wijdeven et al., 2016). Binding of autophagosomes is mediated by LC3 for JIP1 and FYCO1 (which also binds PI3P) and by RAB7 (which localises to autophagosomes prior to fusion with lysosomes (Gutierrez et al., 2004)) for RILP and FYCO1.

RILP also interacts with the hexameric HOPS (homotypic fusion and protein sorting) complex, another RAB7 effector and the master effector of lysosomal fusion, that interacts with endosomes, autophagosomes and lysosomes to promote tethering as well as fusion both directly and via *trans*SNARE complex stabilisation (see below) (Balderhaar and Ungermann, 2013, Baker and Hughson, 2016). Of note, RILP is also implicated in the centripetal trafficking of lysosomes (Jordens et al., 2001), downstream of both amino acid-starvation and cholesterol accumulation (Starling et al., 2016, Li et al., 2016b). Interestingly, dephosphorylation of threonine 50 in LC3B's cargo-binding pocket by the Hippo kinase/innate immunity pathway regulators STK3 and STK4 prevents the perinuclear transport of autophagosomes without affecting cargo binding (see section 1.3.6) (Wilkinson et al., 2015), with potential implications in the mechanisms described in this section.

As well as regulating autophagosome trafficking, the LC3/GABARAP proteins promote autophagosome-lysosome tethering and fusion. Atg8p and its mammalian homologs were shown to possess intrinsic fusogenic properties *in vitro* (Weidberg et al., 2010, Landajuela et al., 2016, Nakatogawa et al., 2007) as discussed in section 1.2.3.2, although these properties may only become apparent when incorporated into membranes containing non-physiological levels of phosphatidylinositol (Nair et al., 2011). *In vivo*, LC3/GABARAPs promote HOPS recruitment to autophagosomes via the recruitment of fusion adaptors such as the RAB7 effector PLEKHM1 (McEwan et al., 2015) – a role shown to be largely GABARAP-specific (Nguyen et al., 2016). GABARAP also recruits the lipid kinase PI4K2A to autophagosomes which similarly promotes autolysosome formation (Wang et al., 2015). At the autophagosomal membrane, PI4K2A is speculated to recruit the RAB7, HOPS complex and PLEKHM1 fusogenic machinery either directly or through production of the signalling lipid PI4P (Wang et al., 2015, Albanesi et al., 2015). The *C. elegans* Atg8p homolog Lgg-2 can recruit the HOPS complex via association with the Vps39 subunit to promote autophagosome-lysosome tethering (Manil-Ségalen et al., 2014). An additional HOPS-independent putative tether, TECPR1, was shown to localise to lysosomal and autophagosomal membranes via association with both LC3/GABARAP lipidation machinery (the ATG5-ATG12 conjugate, see section 1.3.6) and PI3P. Its depletion leads to an accumulation of both lipidated LC3 and unfused autophagosomes due to inhibition of autophagic flux, suggesting that TECPR1 facilitates autophagosome-lysosome fusion (Chen et al., 2012).

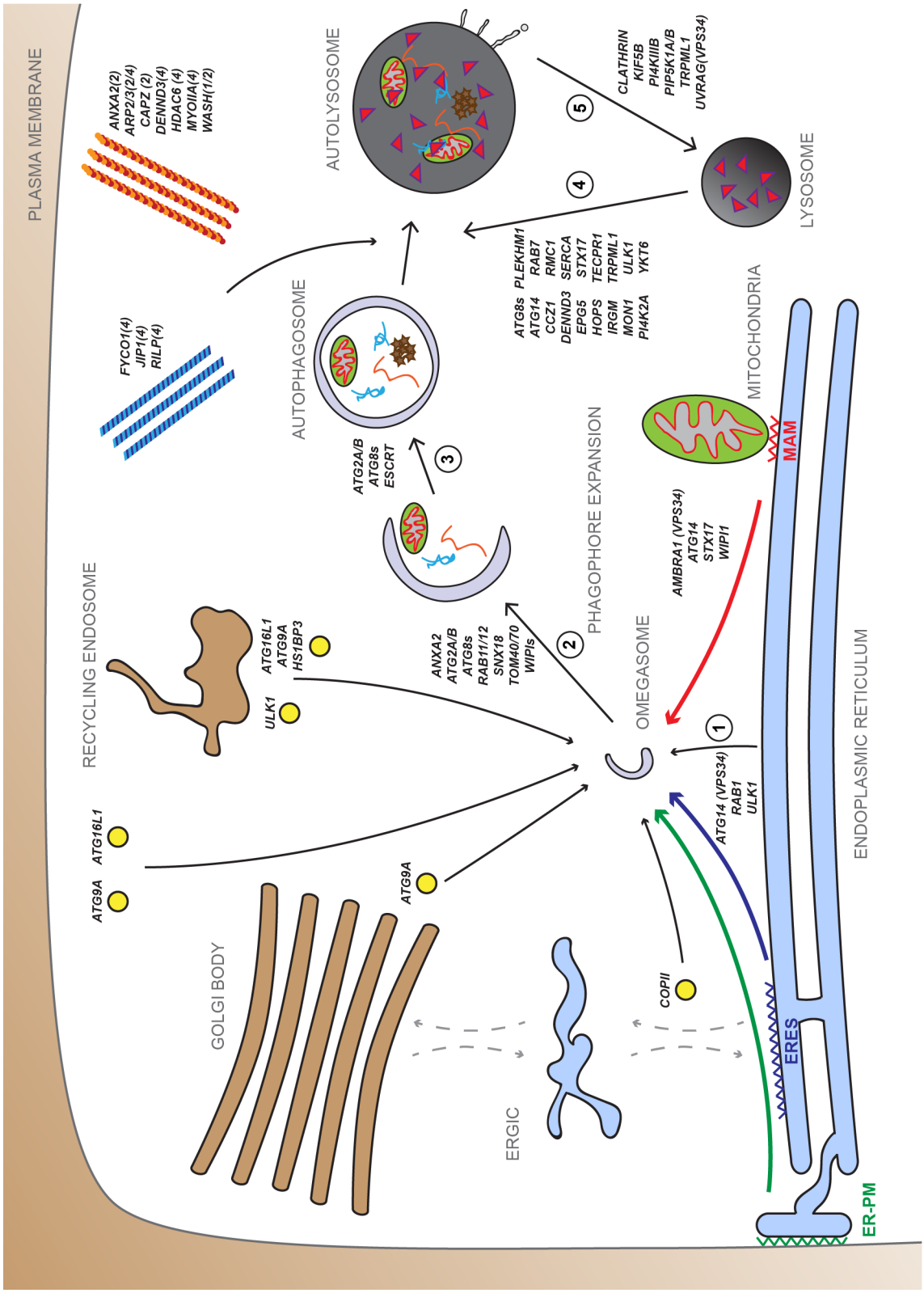
PLASMA MEMBRANE
ANXA2(2)
ARP2/3(2/4)
CAPZ (2)
DENND3(4)
HDAC6 (4)
MYOIIA(4)
WASH(1/2)
AUTOLYSOSOME
CLATHRIN
KIF5B
PI4KIIIB
PIP5K1A/B
TRPML1
UVRAG(VPS34)
5
4
LYSOSOME
FYCO1(4)
JIP1(4)
RILP(4)
AUTOPHAGOSOME
ATG8s PLEKHM1
ATG14 RAB7
CCZ1 RMC1
DENND3 SERCA
EPG5 STX17
HOPS TECPR1
IRGM TRPML1
MON1 ULK1
PI4K2A YKT6
MITOCHONDRIA
ATG2A/B
ATG8s
ESCRT
3
MAM
PHAGOPHORE EXPANSION
AMBRA1 (VPS34)
ATG14
STX17
WIPI1
RECYCLING ENDOSOME
ATG16L1
ATG9A
HS1BP3
ULK1
ANXA2
ATG2A/B
ATG8s
RAB11/12
SNX18
TOM40/70
WIPIs
2
OMEGASOME
1
ATG14 (VPS34)
RAB1
ULK1
ATG16L1
ATG9A
ATG9A
GOLGI BODY
ENDOPLASMIC RETICULUM
COPII
ERGIC
ERES
ER-PM

Figure 1.3 – *Membrane trafficking in autophagy*. Each of the main stages of autophagy are depicted and numbered: 1 – Initiation, 2 – Elongation, 3 – Closure, 4 – Maturation/Fusion with Lysosomes and 5 – Autophagic-Lysosome Reformation. Directionality is indicated by thin black arrows. The protein machinery discussed in the text are listed next to each stage. Organelles contributing membranes to autophagosomes are depicted in brown, organelles from which autophagosomes are believed to originate are depicted in blue. Vesicles contributing lipids to autophagosomes are depicted in yellow with associated protein constituents listed alongside. ER contact sites (acronyms defined in text) that have been identified as sites of omegasome formation are depicted as coloured zigzags apposed to the ER with thick coloured lines directed towards the omegasome. Orange/red lines represent actin and light/dark blue lines represent microtubules. Cytoskeleton-associated proteins are listed next to each, with the stage at which they are implicated in brackets after the protein name.

The generation of cell lines in which LC3/GABARAPs or their associated lipidation machinery has been knocked out has helped clarify the roles of Atg8p homologs in autophagy. Building on the work of Sou and colleagues (Sou et al., 2008), it was recently shown that preventing Atg8p homolog membrane incorporation via removal of lipidation machinery in MEFs decreased but did not abolish autophagosomal closure (as discussed in section 1.2.3.3) and, whilst permitting autolysosomal fusion, prevented degradation of autophagosomal cargo (Tsuboyama et al., 2016). However, as these cells retained the unlipidated proteins, the role of LC3/GABARAPs in autophagosome maturation is perhaps best demonstrated by the generation of HeLa cell lines lacking either LC3 homologs (LC3A, LC3B, LC3C; LC3B2 was not removed), GABARAP homologs (GABARAP, GABARAPL1, GABARAPL2) or all 6 proteins (hexaKOs) (Nguyen et al., 2016). Autophagosomes persisted in hexaKOs, although they were smaller and fewer in number. However, fusion with lysosomes was inhibited, suggesting that the Atg8p homologs are necessary for lysosomal fusion. Interestingly, comparison of LC3 and GAPARAP KO cells lines revealed that the GABARAPs alone are necessary and sufficient for both starvation-induced autophagy and mitophagy, with LC3s potentially playing roles in later stages of autophagy, basal autophagy and/or other subtypes of selective autophagy (Grunwald et al., 2019, Nguyen et al., 2016). Similar results were observed in independently-generated LC3 and GABARAP triple knockout HeLa cell lines (Vaites et al., 2017). Considering the previously discussed observation that expression of pre-primed LC3B rescues autophagy in ATG4-deficient HeLa (Agrotis et al., 2019a), these data potentially corroborate previous reports suggesting that LC3/GABARAPs possess lipidation-independent functions in autophagy (Joachim et al., 2015).

As fusion of unclosed autophagosomes with lysosomes cannot result in cargo degradation, it follows that there are likely signalling mechanisms by which fully-formed autophagosomes become fusion-competent. In yeast, outer membrane Atg8p delipidation (Yu et al., 2012) and removal of the lipid signalling intermediate PI3P are potentially required before fusion can occur (Cebollero et al., 2012). However, these mechanisms are likely not conserved in metazoans (Agrotis et al., 2019a, Søreng et al., 2018b, Cheng et al., 2014). Furthermore, recent data suggest Mon1p-Cczp, the GEF complex for Ypt7p (the yeast homolog of RAB7) binds Atg8p on autophagic membranes to promote HOPS-dependent fusion with the vacuole (Gao et al., 2018), indicating that some lipidated Atg8p persists. Interestingly, recruitment of MON1-CCZ1 to autophagosomes was recently shown to promote fusion with lysosomes in metazoans Vaites et al., 2017). Proteomics analysis on autophagosomes for which fusion with lysosomes was blocked revealed enrichment of a novel MON1 -CCZ1 activating protein, RMC1. This is necessary for loading of RAB7A onto autophagosomal/endosomal membranes and is required for both basal and starvation-induced autophagic flux (Vaites et al., 2017).

Another such fusion-promoting signal appears to be the translocation of the SNARE protein STX17 to autophagosomes, which only occurs after closure is complete. SNARE proteins function by tightly associating with complementary SNARE proteins on target membranes via formation of the *trans*SNARE complex, which in turn pulls membranes within close proximity to drive fusion. While amphisomes fuse with lysosomes using the well characterised late endocytic fusion machinery (Pryor et al., 2004), STX17 was the first autophagosome-specific SNARE identified in mammals (Itakura et al., 2012) and its role is conserved in Drosophila (Mauvezin et al., 2015). STX17 drives fusion with lysosomes by forming a *trans*SNARE complex with SNAP29 and VAMP8 in a HOPS-dependent manner (Jiang et al., 2014).

Recently it was shown that this is facilitated by association with IRGM (immunity-related GTPase M), which itself interacts with LC3/GABARAP proteins and the HOPS complex. STX17 is transferred from IRGM to autophagic membranes upon starvation and is stabilised by LC3/GABARAPs in both membrane- and IRGM-bound states (Kumar et al., 2018). Furthermore, the RAB7 effector EPG5 stabilises STX17-SNAP29-VAMP7/8 *trans*SNARE complexes in an LC3-dependent manner (Wang et al., 2016), and the VPS34 component ATG14 undergoes homooligomerisation before binding STX17 and SNAP29 at mature autophagosomes to

promote fusion with endolysosomes *in vitro* and *in vivo* (Diao et al., 2015). Finally, a direct interaction between the STX17 and the autophagy initiating kinase ULK1 is implicated in autophagosome-lysosome fusion (see section 1.3.3.1)(Wang et al., 2018b).

STX17 has been identified on mitochondria-derived vesicles and to facilitate their fusion with endosomes (McLelland et al., 2016), however it is not required for PINK/Parkin-dependent mitophagy (Nguyen et al., 2016), indicating that further autophagosome-lysosome fusion mechanisms exist. Supporting this notion, recently another autophagosome-specific SNARE protein was identified, YKT6. This was shown to promote autophagosome-lysosome fusion along with SNAP29 and STX7 but independently of STX17 and its functionality is conserved in yeast (Matsui et al., 2018, Kriegenburg et al., 2019).

Alongside implications in autophagosome motility, actin polymerisation has also been implicated in autophagosome-lysosome fusion. The ubiquitin-binding aggresomal marker deacetylase HDAC6 recruits cortactin to autophagosomes to stabilise polymerised actin thus promoting fusion with lysosomes and is implicated in basal autophagy, mitophagy and the selective autophagy of protein aggregates, but not starvation-induced autophagy (Lee et al., 2010a).

1.2.3.5 Autophagic-lysosome reformation

To regenerate lysosomes and thus sustain proteostasis, autolysosomes undergo autophagic lysosome reformation (ALR) (Søreng et al., 2018b). During ALR, small pH-neutral tubules containing lysosomal membrane proteins extrude vesicles termed proto-lysosomes which acidify as they accrue lysosome lumenal proteins, eventually forming mature lysosomes. This occurs in an mTORC1-dependent manner, which is reactivated during prolonged periods of starvation sustained by the products of autophagic degradation (Yu et al., 2010, Munson et al., 2015). ALR is accompanied by the dissociation of RAB7 (Yu et al., 2010, Zhang et al., 2016b), with STX17 detachment also observed after successful cargo degradation (Tsuboyama et al., 2016).

To drive ALR, the double phosphorylated phosphoinositide PI(4,5)P_2 is produced by on the autolysosomal surface by PIP5K1B. This leads to the recruitment of clathrin (Rong et al., 2012)

which generates clustered PI(4,5)P_2-enriched microdomains, which in turn recruit the microtubule motor KIF5B (Du et al., 2016). KIF5B then promotes tubulation via physical pulling of the membrane. Tubule scission, which is promoted by PIP5K1A activity (Rong et al., 2012), requires mTORC1-dependent phosphorylation of the VPS34 complex component UVRAG. Reconstitution of U2OS cells expressing siRNAs against UVRAG with an unphosphorylatable form of the protein resulted in the accumulation of elongated tubules compared to wild type UVRAG and was associated with decreased VPS34 lipid kinase activity *in vitro* and *in vivo*, implicating another phosphoinositide, PI3P in the regulation of ALR (Munson et al., 2015). Additionally, PI4P produced downstream of PI4KIIIB has also been implicated in vesicular scission (Sridhar et al., 2013). Finally, PI(3,5)P_2 is also implicated in ALR by activating calcium channel TRPML1. By facilitating retrograde traffic of lysosomes along microtubules, TRPML1 additionally promotes ALR alongside perinuclear clustering as discussed previously (Li et al., 2016b).

A schematic depicting the sources of autophagic membrane and associated protein machinery discussed in this section is shown in Figure 1.3.

A defining feature of autophagosomes is that their lumenal content matches that of the surrounding cytoplasm. However, the exact lipid composition of the autophagosomal membrane remains unknown. It is possible that the lipid composition of the autophagosome varies depending on which organellar membrane sources were available during biogenesis. However, whilst roles for a wide variety of specific bioactive lipids continue to be identified (Wijdeven et al., 2016, Landajuela et al., 2016, de la Ballina et al., 2019), the indispensable roles of phosphoinositide signalling have been long established. PI3P signalling will be the focus of this thesis, with reference made to pertinent recent findings regarding PI4P.

In the next section, the key conserved signalling complexes in starvation-induced bulk autophagy will be discussed. In recent years, a number of autophagy pathways have been mapped out that don't require some of these proteins/complexes ('non canonical' autophagy is reviewed in (Dupont et al., 2017)), however these will not be discussed in this thesis, the focus of which is ULK-dependent, canonical autophagy.

1.3 Autophagic signalling complexes

1.3.1 mTORC1

The canonical signal for autophagy, amino acid starvation, is detected by mammalian target of rapamycin complex 1 (mTORC1). The serine/threonine kinase complex mTORC is an evolutionarily conserved regulator of protein, lipid and mitochondrial homeostasis and thus controls both cell proliferation and response to stress (Laplante and Sabatini, 2013). It is found in distinct complexes and its interaction partners designate its cellular function. mTORC1 and mTORC2 share common components, however a third complex, named mTORC3, was recently identified and is defined by the unique component ETV7, previously characterised as a transcription factor (Harwood et al., 2018). Of the three, mTORC1 is the most studied. It consists of the mTOR catalytic subunit along with the positive regulators RAPTOR (which associates with substrates directly to maintain target specificity) and mLST8 (which stabilises the interaction with RAPTOR), and the negative regulators DEPTOR and PRAS40 (Laplante and Sabatini, 2009). Both growth factor and amino acid signals converge on mTOR to regulate its activity. As starvation media utilised to induce autophagy in cells is typically devoid of serum as well as amino acids, both mTOR stimuli will be discussed here.

Depending on the growth factor, receptor binding results in the activation of class I PI3K-AKT or ERK1/2-RPS6K pathways, with both converging on the TSC1-TSC2-TBC1D7 complex. This binds the lysosome-anchored small GTPase RHEB. In the presence of growth factors, TSC2 is phosphorylated by AKT (Paquette et al., 2018, Menon et al., 2014), resulting in its dissociation from TSC1 and its consequent redistribution from the lysosome. TSC2 is a RHEB GTPase-activating protein (GAP), therefore its dissociation promotes RHEB activity. GTP-bound RHEB binds both mTOR's catalytic domain and mLST8 (Long et al., 2005), resulting in the activation of mTORC1 and its recruitment to the lysosomal membrane.

The presence of amino acids (specifically leucine, arginine and glutamine (Carroll and Dunlop, 2017, Nwadike et al., 2018)) further drives the recruitment of mTORC1 to lysosomal membranes. This requires a second set of small GTPases, the RAG proteins. The 4 RAG proteins exist in heterodimers; RAGA or RAGB associates with RAGC or RAGD with proteins within each pair believed to be functionally redundant. In amino acid replete conditions, RAGA/B binds GTP and RAGC/D binds GDP, with this configuration promoting direct association between the

RAG proteins and mTORC1 via RAPTOR, thus promoting RHEB-dependent activation of mTORC1 (Sancak et al., 2010, Sancak et al., 2008). RAG proteins are not post-translationally prenylated like most small GTPases, however they are anchored to the lysosome via the heteropentameric Ragulator complex, which possesses GEF activity towards RAGA/B (Bar-Peled et al., 2012, Sancak et al., 2010). The GEF activity towards the RAG proteins requires physical association of Ragulator with the lysosomal V-ATPase and only occurs in the presence of amino acids, however the exact mechanism of V-ATPase signalling to Ragulator is unclear (Bar-Peled et al., 2012). Alongside GEFs, a number of RAG GAPs have been identified, including GATOR1 (which targets RAGA/B in the absence of leucine and arginine), the FLCN-FNIP1/2 complex (which binds RAGA/B-GDP and targets RAGC/D-GTP) and potentially leucyl tRNA synthetase (which targets RAGD in the presence of leucine) (Kim et al., 2017, Meng and Ferguson, 2018, Tsun et al., 2013, Bar-Peled et al., 2013, Carroll and Dunlop, 2017).

In starvation conditions, the activity and localisation of a host of GAPs and GEFs are modulated to promote loading of RAGA/B with GDP and RAGC/D with GTP. This releases mTORC1 into the cytoplasm and prevents its activation by RHEB. When amino acids are replenished either directly or because of autophagic activity after long periods of starvation (Yu et al., 2010), the RAG heterodimer GTP-binding state is switched, leading to the recruitment of mTOR to the lysosomal surface and its activation via association with RHEB.

1.3.2 AMPK

Alongside nutrient status, autophagy is also regulated by ATP availability. Cellular energy homeostasis is maintained by AMPK (adenosine monophosphate-activated kinase) a heterotrimeric serine/threonine kinase complex comprised of a catalytic α subunit (PRKAA), a scaffolding β subunit (PRKAB) and a regulatory γ subunit (PRKAG). The γ subunit binds adenosine phosphates via 4 tandem cystathionine beta-synthase domains that detect ratios of ATP with ADP or AMP. When an excess of ATP is metabolised and relative amounts of ADP and AMP increase, the catalytic PRKAA subunit is allosterically activated. AMPK activity is further augmented by phosphorylation at threonine 172 in PRKAA2 (threonine 183 in PRKAA1), as well as by the concomitant protection from phosphatases such as PP2Cα (Gowans et al., 2013). Generally, AMPK activates ATP-generating pathways whilst downregulating ATP-consuming pathways.

Two PRKAA isoforms exist alongside two PRKAB isoforms and three PRKAG isoforms. AMPK complex composition varies between tissues (Cheung et al., 2000), however, all possible isoform combinations can form *in vivo*, yielding a total of 12 possible complexes that vary in subcellular localisation, kinase activity and sensitivity to adenosine phosphates/small molecule agonists (Cheung et al., 2000, Cao et al., 2017, Rajamohan et al., 2016, Willows et al., 2017, Ross et al., 2016). In HEK293A, the main cell line employed in this thesis, PRKAA1/PRKAB1/ PRKAB2/PRKAG1 isoforms account for the majority of AMPK activity (Hawley et al., 2010). Based on the constituent isoforms and the prevailing signalling environment, AMPK can localise to the cytoplasm as well as a variety of subcellular compartments such as the nucleus (Cao et al., 2017), Z-discs/T-tubules (in cardiomyocytes) (Pinter et al., 2013) or glycogen particles (McBride et al., 2009).

The major kinase implicated in threonine 172 phosphorylation during energy stress is LKB1, which exists in complex with STRAD and MO25 (Hawley et al., 2003). This is constitutively active, however upon energy stress (typically induced by glucose deprivation) it is recruited to the lysosome where it phosphorylates and activates AMPK. Both translocation to lysosomes and colocalisation with AMPK are facilitated by the scaffolding protein AXIN to which binding of both LKB1 and AMPK increases upon glucose starvation (Zhang et al., 2013b). Interestingly, glucose starvation promotes the concurrent association of LBK1-AXIN with V-ATPase, which promotes AMPK activation whilst also inhibiting Ragulator GEF activity to inactivate mTORC1 (Zhang et al., 2014). There is further crosstalk between the AMPK and mTORC1 signalling networks (Carroll and Dunlop, 2017). AMPK phosphorylates and activates TSC2 resulting in RHEB GTP hydrolysis (Inoki et al., 2003) and also RAPTOR to inhibit mTOR kinase activity whilst promoting 14-3-3 association (Gwinn et al., 2008). Therefore, the switch from mTORC1 to AMPK signalling is associated with a binary shift from anabolic to catabolic processes.

Both mTORC1 and AMPK converge on the ULK complex, the first autophagy-specific signalling complex discussed thus far.

1.3.3 ULK Complex

The ULK (Unc51-like kinase) kinases were initially identified as the mammalian homologs of *C. elegans* protein Unc51, named due to the 'unc'oordinated movement phenotype displayed by mutant animals. In early genetic screens, mutation of Unc51 yielded short, fat worms with generalised paralysis and egg laying defects (Brenner, 1974). Later studies demonstrated that Unc51 is enriched in the nervous system and is expressed in almost all neurones, with the uncoordinated phenotype in mutants ascribed to aberrant formation and guidance of a variety of neuronal subtypes (Kuroyanagi et al., 1998, McIntire et al., 1992, Desai et al., 1988, Hedgecock et al., 1985, Siddiqui, 1990). Cloning of the *Unc51* gene allowed its identification as a serine/threonine kinase whose activity was crucial for its role in axonal elongation and guidance (Ogura et al., 1994b).

Whilst *S. cerevisiae* Atg1p was identified as early as 1993 (Tsukada and Ohsumi, 1993), it was first shown to be a serine/threonine kinase and homolog of *C. elegans* Unc51 in 1997 (Matsuura et al., 1997). This was followed shortly by the identification of the mammalian homologs, with murine Ulk1 discovered shortly before its human counterpart (Yan et al., 1998, Kuroyanagi et al., 1998). Whilst the link between yeast Atg1p and Unc51/ULK1 was known, their similarities in function were initially thought to extend to control of membrane dynamics. Indeed, guided by the previously described Unc51 phenotype in *C. elegans*, ULK1 and close homolog ULK2 were first characterised as regulators of neuronal outgrowth in mice (Tomoda et al., 1999). However, roles in autophagy were soon identified for *C. elegans* Unc51, as well as for Atg1p homologs in Dictyostelium (Otto et al., 2004) and Drosophila (reviewed in (Chan et al., 2009)). Whilst human ULK1 was earlier shown to direct intracellular trafficking of ATG9A upon starvation in 2006 (Young et al., 2006), its formal implication in autophagy came a year later when it was shown to prevent formation of starvation-induced GFP-LC3 lipidation in a kinome-wide siRNA screen for autophagy regulators (Chan et al., 2007).

Atg1p has 5 homologs in mammals (ULK1, ULK2, ULK3, ULK4 and STK36), with ULK1 and ULK2 most closely related and serving conserved and largely redundant roles in autophagy (Chan et al., 2009). ULK1 and ULK2 (collectively known as ULK1/2) occupy the most upstream position in the autophagy pathway, which they regulate via a wide array of catalytic and non-catalytic functions. They are crucial in translating nutrient-dependent signals to the autophagic

machinery to drive autophagosome formation from nucleation to autophagy (Anwar et al., 2019, Wang et al., 2018b, Löffler et al., 2011, Petherick et al., 2015, Chan et al., 2009). Overexpression of kinase-deficient ULK1 results in the dominant negative inhibition of autophagy, with the remaining autophagic flux corresponding to the level of kinase activity remaining (Chan et al., 2009, Hara et al., 2008). Similar results are observed in yeast (Suzuki et al., 2013), indicating that the key upstream functions of the ULK proteins in autophagic signalling are evolutionarily conserved.

ULK1/2 display wide and overlapping patterns of expression in mammals (Yan et al., 1998, Yan et al., 1999). Due to functional redundancy, removal of ULK1 or ULK2 alone yields viable, fertile mice that are autophagy-sufficient (Kundu et al., 2008, McAlpine et al., 2013, Lee and Tournier, 2011). Removal of both ULK1 and ULK2 *in vivo* results in the abolition of autophagy upon amino acid deprivation, an increase in early embryonic mortality alongside defective axon guidance (Wang et al., 2018a), either perinatal or neonatal mortality (Lechauve et al., 2019, McAlpine et al., 2013, Cheong et al., 2014), lung structural abnormalities (Cheong et al., 2014), reduced neutralisation of ROS in erythrocytes (Li et al., 2016a) and misregulation of the unfolded protein response (Joo et al., 2016). Whilst distinct roles for both homologs have been identified in cells and tissues (Ro et al., 2013, Kundu et al., 2008, Lee and Tournier, 2011), ULK1 is expressed most highly and is by far the best characterised.

ULK1 and Atg1p possess a conserved domain structure, comprising an N-terminal serine/threonine kinase domain followed by the intrinsically disordered serine/proline-rich domain and culminating in the CTD (C-terminal protein interaction domain). Murine and human ULK1 are 93% similar, and whilst mammalian ULK1 has a relatively low degree of amino acid identity with *S. cerevisiae* Atg1p, conservation is increased in the N and C-terminal domains (Figure 1.4A).

Both the ULK and Atg1p associate with non-catalytic regulatory components, with complex association crucial for regulation, stability and function. The Atg1p complex contains 4 other proteins: Atg13p, Atg17p, Atg29p and Atg31p. Atg1p constitutively associates with Atg13p, via two tandem microtubule interacting domains in Atg1p's CTD (otherwise known as early autophagy targeting domain) and Atg13p's dual MIM (microtubule interacting and transport interacting motifs) domains (Stjepanovic et al., 2014, Fujioka et al., 2014). Upon autophagy

induction, the Atg1p-Atg13p subcomplex is recruited to the PAS by the Atg17p-Atg29p-Atg31p subcomplex via direct interaction between Atg13p and Atg17p (Stjepanovic et al., 2014, Yamamoto et al., 2016). The crescent-shaped Atg17p subunit is capable of homodimerisation to form an elongated rod which scaffolds the early autophagic machinery at the PAS (Ragusa et al., 2012, Stjepanovic et al., 2014, Yamamoto et al., 2016, Rao et al., 2016). The binding affinity between the Atg1p-Atg13p and Atg17p-Atg29p-Atg31p subcomplexes is relatively weak (2 orders of magnitude lower than that shared between Atg1p and Atg13p (Stjepanovic et al., 2014)), so must be stabilised upon induction of autophagy. Atg17p recruits the GEF for Ypt1p (yeast homolog of RAB1) which in turn promotes the stabilisation of Atg1p at the PAS (Wang et al., 2013). Furthermore, pentameric complex formation is observed only after dephosphorylation of Atg13p. Inhibiting phosphorylation of three sites in particular, serine 379, serine 428 and serine 429 reveals two Atg17p binding sites on Atg13p allowing its association with two Atg17p dimers and promoting the formation of higher-order initiation complexes at the PAS (Yamamoto et al., 2016).

The ULK complex consists of either ULK1 or ULK2 (~150kDa), the Atg13p homolog ATG13 (~60kDa) (Chan et al., 2009), the structural homolog of both Atg17p (and also the partially redundant Atg11p) FIP200 (220KDa) and ATG101 (25KDa), which has no homolog in *S. cerevisiae* yet is present in fission yeast (Figure 1.4B). ULK's CTD binds the final 134 amino acids of ATG13 (Jung et al., 2009) and FIP200 interacts with ULK1 directly in *in vitro* binding assays (Ganley et al., 2009). However, abolishing the interaction between FIP200 and ATG13 is sufficient to inhibit autophagy in cells and in animals (Chen et al., 2016) potentially indicating the primacy of the FIP200-ATG13 interaction. Of note, blocking interaction with ATG13 via deletion of the ULK1 CTD blocked association between ULK1-FIP200, suggesting that this region is implicated in the association with FIP200 either directly or through ATG13 (Hara et al., 2008). Both ATG13 and ATG101 contain a HORMA domain (Hop1, Rev7, Mad2) through which they stably interact (Suzuki et al., 2015, Qi et al., 2015). ATG13 and FIP200 promote ULK1 stability, kinase activity and translocation from the cytoplasm to the omegasome (Jung et al., 2009, Ganley et al., 2009, Hosokawa et al., 2009a). ATG101 promotes the basal phosphorylation of ULK1 as well as the stability of both ULK1 and ATG13 (Hosokawa et al., 2009b, Mercer et al., 2009).

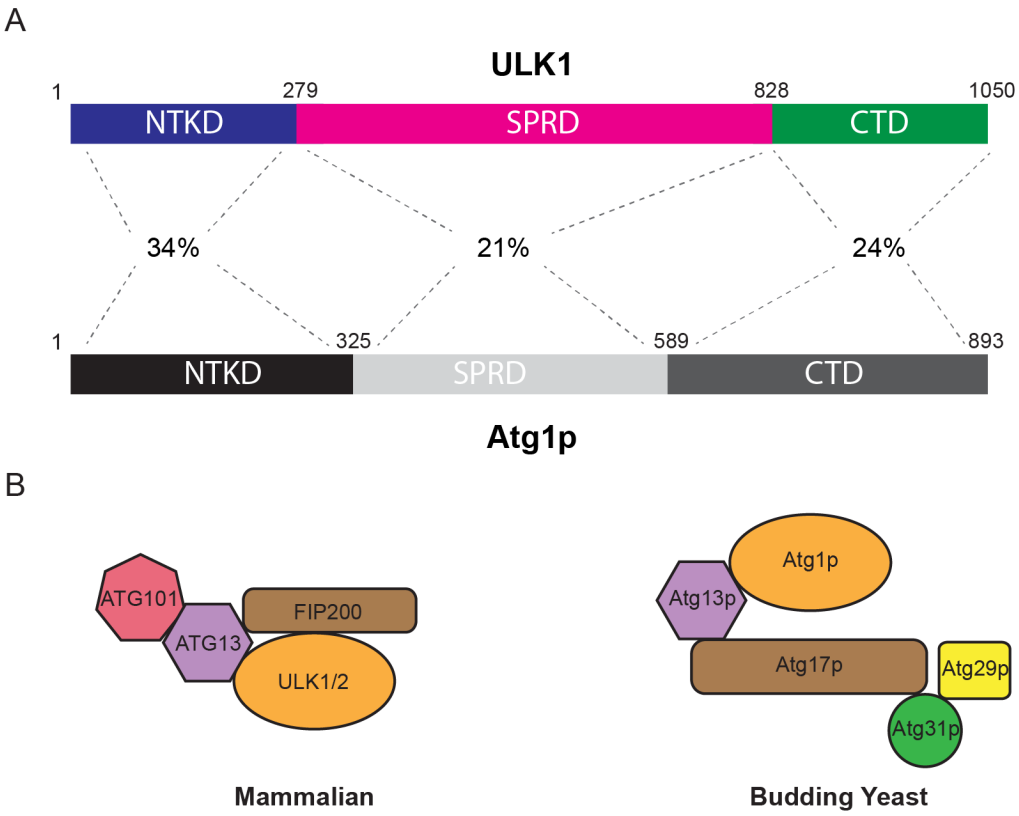

Figure 1.4 – *Conservation of ULK1 in yeast*. **A** – Human ULK1 and S. cerevisiae Atg1p are depicted in 2D with amino acid boundaries between domains listed. NTKD (N-terminal kinase domain), SPRD (serine/proline-rich domain) and CTD (C-terminal protein interaction domain). The amino acid identity percentage reflects the degree to which each domain is conserved. Protein sequence identities calculated at https://www.ebi.ac.uk/Tools/msa/clustalo/. **B** – Schematic depiction of ULK/Atg1p complexes from mammalian and budding yeast respectively. Identically coloured proteins reflect sequence/structural conservation.

The ULK/Atg1p complex has resisted crystallisation, likely due to the high occurrence of intrinsically disordered regions, however structures for some of the subcomplexes have been solved. Notable examples include the Atg17p-Atg29p-Atg31p subcomplex. This was shown to form 2:2:2 complex dimers via homodimerisation of Atg17p, which possessed an extended rod structure (Ragusa et al., 2012). This conformation was later shown to reveal the second binding site for Atg13p discussed above (Yamamoto et al., 2016). The ATG13-ATG101 subcomplex was crystallised first in *S. pombe* (Suzuki et al., 2015) before the human structure was solved (Qi et al., 2015), revealing that both subcomplexes possess similar gross structures. Qi and colleagues

identified a novel functional unit in ATG101, the WF finger, which is likely subject to regulation. Finally, the human ULK1 kinase domain was crystallised with a range of inhibitors in 2015, revealing a standard kinase fold with a large and flexible interlobe linker (which is conserved from Atg1p but is least conserved region in the kinase domain between human ULK homologs) and confirming the existence of the autophosphorylated threonine 180 in the activation loop (Bach et al., 2011, Lazarus et al., 2015). Acquiring insights into ULK complex structure allows hypothesis-driven research and could prove instructive when designing pharmacological activators/inhibitors.

1.3.3.1 Regulation by post-translational modification

Regulation by phosphorylation

Unlike the Atg1p complex, the tetrameric ULK complex is believed to remain associated regardless of nutrient status (Hosokawa et al., 2009a, Jung et al., 2009). However, complex independent functions for ULK1, ULK2, ATG101, ATG13 and FIP200 components have been identified (Hieke et al., 2015, Joo et al., 2016, Yang et al., 2016a, Shin et al., 2015, Alers et al., 2011, Joo et al., 2011, Chen et al., 2016). It is therefore possible that ULK complex formation is actively regulated. For example, ULK1 binds and is phosphorylated by the oncokinase TOPK at serine 469, serine 495 and serine 533 in the serine/proline-rich domain, which decreases complex association, stability and kinase activity (Lu et al., 2019). Furthermore, upon lipopolysaccharide stimulation, p38MAPK phosphorylates murine Ulk1 at serine 504 and serine 757 (serine 505/758 in human ULK1), which similarly prevents interaction with Atg13 and decreases kinase activity (He et al., 2018).

Alongside TOPK and p38MAPK, the ULK kinases are subject to phosphorylation by a host of regulatory kinases including PKA (Shin et al., 2015, Stephan et al., 2009), AKT (Bach et al., 2011) and PKCα (Wang et al., 2018b). However, the aforementioned nutrient sensing kinase complex mTORC1 is the chief regulator of ULK-dependent autophagy. When amino acids are replete, the mTORC1 subunit RAPTOR directly associates with ULK1, with binding occurring independently of ULK1 kinase activity (Hosokawa et al., 2009a, Lee et al., 2010b, Dunlop et al., 2011). mTORC1 inhibits ULK complex activity by phosphorylating ULK1 at serine 638 and serine 758, and ATG13 at serine 259 (serine 258 in murine Atg13) (Puente et al., 2016, Kim et al., 2011, Shang et al., 2011). Alignment of the phosphorylation sites in the serine/proline-rich

domain, which is extensively phosphorylated, yields a proline-directed motif bearing close resemblance to that of mTORC1. Exocyst, a tethering complex that usually resides at the plasma membrane, was shown to facilitate mTORC1-dependent regulation of ULK activity. It binds the mTORC1 and ULK complexes in basal conditions, as well as the lipid kinase VPS34, maintaining the latter two kinase complexes in an inactive state. Upon starvation, the small GTPase RALB becomes loaded with GTP, which promotes reorganisation of Exocyst leading to the dissociation of mTORC1 and activation of the ULK and VPS34 complexes (see section 1.3.5) (Bodemann et al., 2011). (Dunlop et al., 2011). The key role of mTORC1 in autophagy regulation is further emphasised by its evolutionary conservation. In yeast, phosphorylation of Atg13p by TORC1 prevents formation of the pentameric Atg1p complex and is therefore a key handbrake preventing signalling in basal conditions (Kamada et al., 2010).

As alluded to earlier, the energy-sensing kinase complex AMPK is also implicated in autophagy regulation. AMPK directly associates with ULK1 (Kim et al., 2011, Mack et al., 2012, Shang et al., 2011), phosphorylating it at serine 317, serine 467, serine 556, threonine 574, serine 638, threonine 660 and threonine 778 which promotes autophagic flux upon glucose starvation, ULK1 recruitment to damaged mitochondria, recruitment of 14-3-3 family proteins to ULK1 and proper trafficking of ATG9A amongst other mechanisms (Shang et al., 2011, Tian et al., 2015, Kim et al., 2011, Mack et al., 2012, Egan et al., 2011). AMPK is therefore believed to promote ULK-dependent autophagy, indeed, phosphorylation of serine 758 in ULK1 by mTORC1, which is facilitated by serine 638 phosphorylation, is believed to inhibit autophagy by disrupting the AMPK-ULK1 association (Kim et al., 2011, Shang et al., 2011). However, AMPK also phosphorylates ATG13 at serine 224 (Puente et al., 2016) and Atg13 KO MEFs rescued with Atg13 S224A/S258A (the AMPK and mTOR target sites) display increased autophagic flux and ULK1 *in vitro* kinase activity (Puente et al., 2016). Furthermore, both mTOR and AMPK share a target site in ULK1 – serine 638. Therefore, the roles for AMPK in autophagy are complex. Recently, Nwadike et al. closely examined the induction of autophagy by AMPK in HEK293A cells. It was observed that translocation of ULK1 to nascent autophagosomes and lysosomal acidification only occurred upon amino acid starvation, with AMPK activation via glucose starvation or treatment with agonists resulting in the inhibition of autophagic flux and lysosomal activity (Nwadike et al., 2018). These data suggest that a threshold energy level is required to successfully mount the autophagic program. Confusingly however, knockout of the AMPK catalytic subunit PRKAA1 was recently shown to inhibit starvation-induced autophagy

by abrogating autophagosome-lysosome fusion (Jang et al., 2018), and Ampk activity was shown to be required for Ulk1 activation and metabolic adaption in mouse skeletal muscle (Laker et al., 2017). Furthermore, ULK- and VPS34-independent autophagy has been reported upon glucose starvation (McAlpine et al., 2013). It is possible that the outcome of AMPK-dependent ULK1 phosphorylation differs depending on the cell type or stimulus - the role of AMPK in autophagy demands further study.

PKCα was recently shown to regulate both the stability and localisation of ULK1 by targeting a single phosphoacceptor residue. Whilst leaving complex member association and kinase activity unaffected, phosphorylation of ULK1 by PKCα at serine 423 potentiates downregulation of ULK1 via CMA by promoting association of ULK1's KFERQ-like motif (amino acids 227-231) with HSC70 and LAMP2A, with phosphorylation blocked when cells were cultured in the absence of serum and upon fasting in mice (Wang et al., 2018b). As noted in section 1.2.3.4, STX17 recruits ULK1 to promote autophagosome-lysosome fusion. Intriguingly, STX17 was shown to directly associate with the N-terminal half of ULK1's serine/proline-rich domain *in vitro* and *in vivo* with binding inhibited by PKCα-dependent phosphorylation of ULK1 at serine 423 (Wang et al., 2018b).

As well as kinases, ULK1 is also the target of a number of phosphatases including the PP2A–B55α complex (Wong et al., 2015) and PPM1D (Torii et al., 2016), both of which target the shared AMPK/mTOR site serine 638 upon starvation- and genotoxic stress-induced autophagy respectively. Additionally, serine 758 is dephosphorylated by PP1, which binds and targets ULK1 upon glucose starvation (Pyo et al., 2018). A 2D schematic depicting the protein-protein interaction and phosphorylation events discussed herein is shown in Figure 1.5.

Regulation by other post-translational modifications

Alongside phosphorylation, ULK1 stability and activity is regulated by a number of other post-translational modifications. ULK1 is acetylated at 2 sites, lysine 162 and lysine 607 by the acetyltransferase TIP60. This occurs in a GSK3-dependent manner upon serum-starvation and increases ULK1 kinase activity which is required to stimulate LC3-positive autophagosome accumulation and LC3 lipidation (Lin et al., 2012). GSK3-TIP60-dependent ULK1 acetylation is also implicated in the promotion of autophagy and consequent protection against apoptosis during ER-stress (Nie et al., 2016).

O-GlcNAcylation refers to the cytoplasmic post-translational conjugation of the mono saccharide O-linked N-acetylglucosamine to serine or threonine residues and is facilitated by a single enzyme - OGT. O-GlcNAcylation rates and substrate specificity corresponds to with saccharide availability (Taylor et al., 2008), itself a proxy for cellular energy level. Therefore, OGT often competes with kinases for substrates and allows cellular energy status to directly impinge on phosphorylation-dependent signalling. OGT binds ULK1, and both ULK1 and ULK2 are O-GlcNAcylated upon nutrient starvation and glucagon treatment (Ruan et al., 2017). OGT targets threonines 635 and 754 in murine Ulk1 and threonines 613 and 727 in murine Ulk2 (636/755 in ULK1, 613/726 in ULK2), mutation of which reduces O-GlcNAcylation and kinase activity (Ruan et al., 2017). The authors speculate that this inhibition is caused by the reduced binding of/phosphorylation by AMPK, leaving mTORC1 signalling unaffected. However, a later study demonstrated that ULK1 is O-GlcNAcylated upon glucose starvation at threonine 754 (755 in ULK1), dependent on dephosphorylation of the adjacent mTORC1 site serine 757 (758 in ULK1) and occurring after AMPK phosphorylation at serine 317 and serine 555 (317 and 556 in human ULK1) (Pyo et al., 2018). Blocking O-GlcNAcylation at threonine 754 does not affect kinase activity or complex association (measured by the ability to phosphorylate or bind ATG13), however it is required for ATG14 interaction, and the increase of *in vitro* VPS34 lipid kinase activity observed in cells overexpressing Ulk1 is blocked by mutating this residue to asparigine (Pyo et al., 2018).

Ubiquitination is increasingly understood to regulate multiple facets of ULK1 bioactivity. Conjugation with lysine 63-linked ubiquitin chains in an AMBRA1-TRAF6-dependent manner drives ULK1 dimerisation and consequent activation (Nazio et al., 2013). This pathway is inhibited by mTORC1-dependent phosphorylation of AMBRA1 and is implicated in development of resistance to chemotherapeutic agents in leukaemia (Han et al., 2019, Nazio et al., 2013). AMBRA1 is also implicated in the targeting of ULK1 by another E3 ligase, TRIM32. In muscle tissue, AMBRA1-TRIM32 bind and activate ULK1 via unanchored lysine 63-linked polyubiquitin chain attachment, with mutations inhibiting the ULK1-TRIM32 interaction associated with pathogenic muscle atrophy (Di Rienzo et al., 2019). Finally, the molecular chaperone p32 directly associates with ULK1 to inhibit lysine 48-linked ubiquitination and

promote lysine 63-linked ubiquitination via an unknown E3 ligase, with p32-dependent modulation crucial for both autophagy and mitophagy (Jiao et al., 2015).

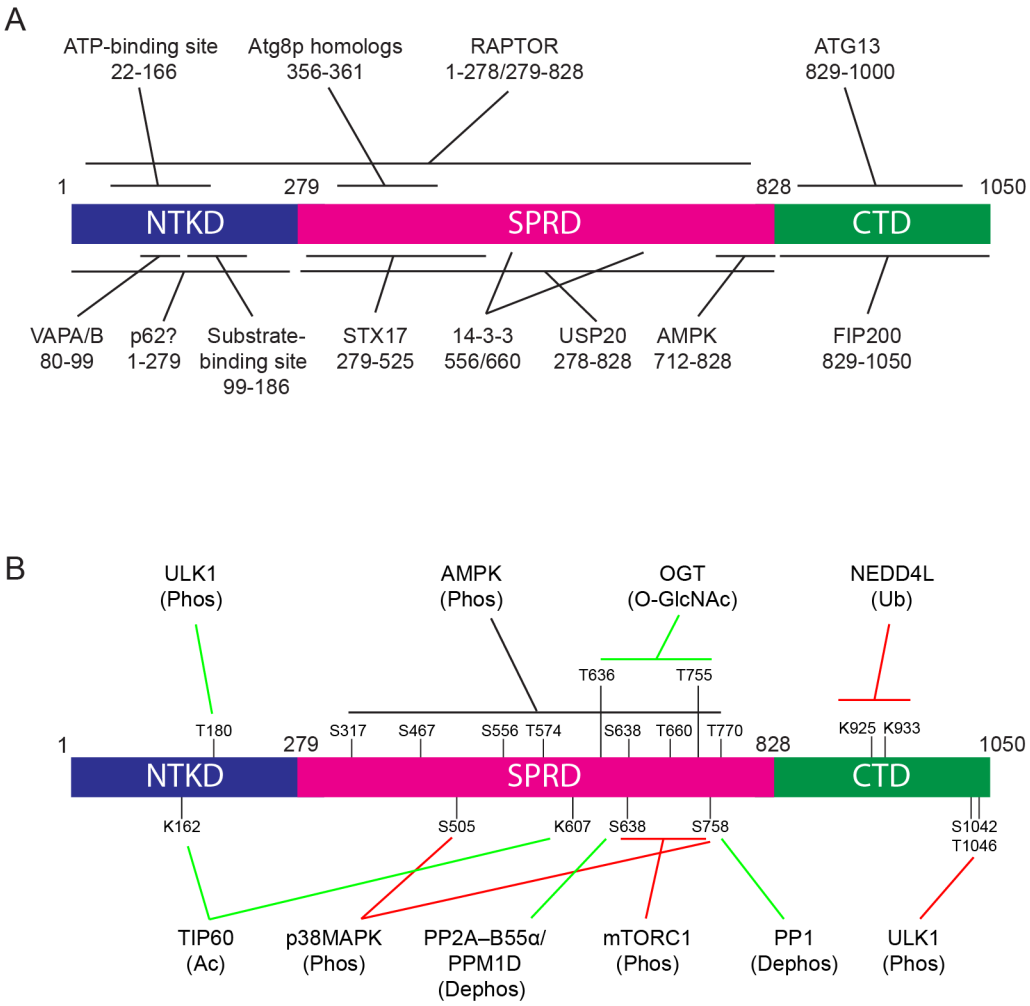

Figure 1.5 – *ULK1 is a signalling hub*. **A** – Human ULK1 is depicted in 2D format as previously. All protein interaction events discussed in section 1.3.3.1 for which binding sites were mapped are annotated. **B** – The PTM (post-translational modification) events discussed in section 1.3.3.1 that have been accurately mapped are annotated and the responsible enzymes included. The type of modification included in brackets. Line colour indicates whether the PTM promotes (green) or inhibits (red) kinase activity/autophagy. AMPK is black indicating its controversial role in ULK regulation. For both Figures 1.5A and 1.5B human residue numbers given despite some interaction regions/PTM sites being mapped in murine Ulk1.

As previously noted, ULK1 is basally turned over by CMA (Wang et al., 2018b). However, ULK1 is also targeted by proteasomal degradation (Kim et al., 2018b, Li et al., 2015a, Liu et al., 2016, Nazio et al., 2016, Allavena et al., 2016). ULK1 protein levels are progressively downregulated during prolonged starvation in multiple cell types (Liu et al., 2016, Nazio et al., 2016, Allavena

et al., 2016, Kim et al., 2018b). Starvation drives ULK1 autophosphorylation at serine 1042 and threonine 1046, which in turn promotes recruitment of CULLIN3-KLHL20 (an E3 ligase-adaptor complex), lysine 48-linked ubiquitination and thus ULK1 degradation (Liu et al., 2016). Finally, the E3 ligase NEDD4L conjugates lysine 27 and lysine 29-linked ubiquitin to ULK1's CTD at positions 925 and 933, ultimately culminating in proteasomal degradation (Nazio et al., 2016).

The deubiquitination of ULK1 is also dynamically regulated. The deubiquitinase USP20, which is required for ULK1 activation and starvation-induced autophagy, binds ULK1's serine/proline-rich domain. Direct deubiquitination of ULK1's CTD prevents proteolytic destruction, thus maintaining basal expression of ULK1. Intriguingly however, USP20 was shown to dissociate from ULK1 in prolonged periods of starvation, resulting in increased lysosomal turnover. This process was shown to be implicated in the switch from autophagic to apoptotic signalling during protracted nutrient starvation (Kim et al., 2018b). Furthermore, removal of the deubiquitinase USP1 leads to increased lysine 63-linked ubiquitination of ULK1, and consequently its aggregation and the inhibition of canonical autophagy (Raimondi et al., 2019). Similar results were observed upon treatment with the deubiquitinase inhibitor WP1130 (Drießen et al., 2015). Where specific target residues have been mapped, the acetylation, O-GlcNAcylation and ubiquitination sites in ULK1 are depicted schematically in Figure 1.5B.

Further complexity is introduced by the transcriptional regulation of *ULK1* upon induction of autophagy. *ULK1* mRNA levels increase upon starvation or treatment with the mitophagy inducers Oligomycin or Antimycin A (Allavena et al., 2016, Nazio et al., 2016). Upon mitophagy induction, increased *ULK1* transcription was AMPK-dependent and led to higher protein expression, however upon starvation *ULK1* mRNA translation was blocked (Allavena et al., 2016). Altogether, the careful, dynamic and differential regulation of ULK1 expression controls the duration and amplitude of autophagy in response to varying stimuli, supporting its identification as the master regulator of autophagy.

1.3.3.2 Regulation via ULK complex relocalisation

The ULK complex largely exists in the cytoplasm, however populations localise to mitochondria (Tian et al., 2015, Wu et al., 2014), recycling endosomes (Longatti et al., 2012)and the ER. In contrast with yeast, in which the Atg17p-Atg29p-Atg31p subcomplex is the first to be recruited

at the PAS with Atg1p-Atg13p recruited upon autophagy induction as previously discussed, amino acid deprivation leads to ER recruitment of the fully formed ULK complex. This results in omegasome formation and is a necessary step in canonical autophagosome biogenesis.

Previous experimental insights suggested that ULK remains associated until autophagosome closure, at which point it is recycled to the cytoplasm (Karanasios et al., 2013). However, these insights were made by studying the dynamics of fluorescently-tagged ATG13 as a proxy for the tetrameric ULK complex and are challenged by recent reports describing a role for ULK1 in autophagosome-lysosome fusion as discussed previously (Wang et al., 2018b). This perseverance of ULK beyond the omegasome formation has precedence in yeast. Atg1p persists at the PAS during phagophore expansion, which is believed to occur independently of the other complex members and to require Atg8p (Lin et al., 2018, Suzuki et al., 2013). Evidencing complex-independent roles of Atg1p, it was shown to be recruited to the PAS at roughly twice the stoichiometry of Atg13p and Atg17p, with inhibition of Atg1p-Atg13p dissociation blocking phagophore elongation (Lin et al., 2018).

These data bear parallels with those of Kraft and colleagues, who observed that Atg1p-Atg13p is retained on later autophagosomal membranes through interaction with Atg8p, eventually being delivered for destruction at the vacuole (Kraft et al., 2012). The interaction between Atg1p and Atg8p is conserved in mammals (Kraft et al., 2012) and it was later reported that ULK1, ULK2, ATG13 and FIP200 all interact preferentially with GABARAP subfamily proteins via LIRs (LC3-interacting regions) promoting colocalisation with the phagophore markers, importantly however autophagic-degradation of complex members does not appear to be conserved (Alemu et al., 2012). Recent data support this initial insight. The existence of functional GABARAP subfamily-specific LIRs in ULK1 and ATG13 was corroborated, however no LIR-dependent LC3/GABARAP binding by FIP200 could be detected (Grunwald et al., 2019). These data were supported by disabling the LIRs in ULK1 or ATG13 via CRISPR-based genome editing which greatly reduced ULK activity and autophagy initiation. Importantly, examination of ULK activity in LC3 and GABARAP subfamily knockout cell lines (described previously (Nguyen et al., 2016)) revealed that ablation of GABARAPs significantly dampened *in vivo* ULK signalling (as measured by accumulation of phosphorylated substrates), inhibited its activation upon starvation, decreased protein levels and prevented starvation-dependent puncta formation. This was rescued by re-expression of GABARAP and to a lesser extent GABARAPL1.

Intriguingly, removal of LC3 family proteins led to an increase in ULK activity, which was shown to be dependent on LC3B and LC3C, indicating that the LC3 and GABARAP subfamily proteins play opposite roles in regulating ULK activity. Potentially contrasting with Joachim et al, who showed that a pool of GABARAP residing at the Golgi transits to sites of autophagosomal biogenesis via the microtubule organising centre and promotes activation of ULK1 in a lipidation-independent but LIR-dependent manner (Joachim et al., 2015), GABARAP/ GABARAPL1 lipidation was required to both stabilise association with and increase the activity of ULK1 (Grunwald et al., 2019). Together, it is tempting to speculate that GABARAP subfamily proteins scaffold the ULK complex to promote its activation at phagophores.

Alongside the potential role of the LC3/GABARAPs, a number of other proteins have been implicated in the translocation of ULK1 to omegasomes. Intriguingly, the ANXA2 binding partner S100A10 was recently shown to bind the ULK complex and promote its recruitment to MAMs upon interferon gamma treatment (Chen et al., 2017). Whether this is indicative of stimulus-specific spatial regulation of ULK complex recruitment to the ER is unclear at this stage. Similarly to the role of Ypt1p in Atg1p recruitment to the PAS as discussed above (Wang et al., 2013), RAB1 promotes ULK1 recruitment and activation via its effector C9orf72 (Webster et al., 2016, Jung et al., 2017). Along with its binding partner SMCR8, C9orf72 binds with the ULK complex and stabilises ULK1 which is required for autophagy in neurones (Yang et al., 2016a, Ho et al., 2019). The C9orf72-SMCR8 complex has additional implications in autophagy. It is known to colocalise with a host of autophagic RABs (RAB1, 5, 7 and 11) (Farg et al., 2014) and is implicated in the positive and negative regulation of the mTORC1 signalling axis (Jung et al., 2017, Ugolino et al., 2016) as well as the modulation of autophagosome maturation (Yang et al., 2016a) and selective autophagy of RNA-protein granules (Sellier et al., 2016).

Alongside its previously described roles in autophagosome biogenesis and maturation, the SNARE protein STX17 binds ULK complex components to regulate their intracellular trafficking upon starvation (Kumar et al., 2019). Constitutive phosphorylation of STX17 at serine 202 by the immunoregulatory kinase TBK1 is required for relocalisation of STX17 from the Golgi to peripheral membrane compartments upon starvation and blocking phosphorylation prevents omegasome formation. STX17 binds FIP200 basally and STX17-ATG13 binding is increased upon starvation. The discovery that STX17 associates with ULK complex members and regulates their intracellular trafficking to govern autophagy initiation suggests that it might

govern ULK complex formation. However, it is unknown whether ATG13 and FIP200 are trafficked alone, and if so at which point they become incorporated into the complex (Kumar et al., 2019).

Integral ER-membrane proteins are implicated in the recruitment and stabilisation of early autophagy proteins at the ER. One such protein, VMP1, transiently localises to omegasomes (Itakura and Mizushima, 2010) and recruits the VPS34 complex (Molejon et al., 2013). However, VMP1 is unlikely to function as a tether for ULK complex components as cells lacking VMP1 display defective phagophore elongation whilst establishment of PI3P-enriched omegasomes is unaffected (Zhao et al., 2017, Kishi-Itakura et al., 2014). Recently it was demonstrated that VMP1 depletion strengthens the association of the ER with other organelles including phagophores, leading to the inhibition of elongation. This was driven by an increase in cytosolic calcium concentration after inactivation of the ER-localised calcium channel SERCA (Zhao et al., 2017). The proteins VAPA and VAPB (VAPA/B) are better candidates for ER-resident ULK binding proteins. They associate with tethering proteins to establish multiple membrane contact sites, and their depletion reduces both LC3 lipidation and puncta formation upon starvation. VAPA/B translocate to omegasomes in a PI3P-dependent manner upon starvation and bind ULK1 and FIP200 via conserved FFAT motifs (consisting of two phenylalanine residues in an acidic tract). Intriguingly, VAPA/B depletion weakened the interaction between ULK1 and FIP200 (whilst leaving interaction with ATG13 unaffected) and blocked starvation-induced ULK1 puncta formation whilst leaving FIP200 puncta unaffected. These data suggest that FIP200 is recruited upstream of ULK1 and that VAPA/B recruit ULK1 to pre-existing FIP200 puncta (Zhao et al., 2018).

The recruitment of the ULK complex to sites of autophagosomal biogenesis may be promoted by the direct engagement of its components with membranes and lipids. The ULK1 CTD binds membranes (Chan et al., 2009) and a basic patch located in the N-terminus of ATG13 binds acidic phospholipids with its mutation reducing ULK1 puncta formation upon starvation by ~50% (Karanasios et al., 2013). Direct membrane recruitment is also observed in yeast. In the absence of Atg13p, the Atg1p CTD is highly dynamic and can physically associate with membranes (Ragusa et al., 2012, Stjepanovic et al., 2014).

An emerging theme in ULK complex regulation is the coupling of ULK1 physical relocalisation and its activation. Current data appear to indicate that increasing the local concentration of ULK1 is instrumental in its activation, possibly through autophosphorylation (a common theme amongst serine/threonine kinases (Endicott et al., 2012)). Atg1p self-associates in autophagy-inducing conditions in a Atg13p-dependent manner and is required for (trans) autophosphorylation at threonine 226 (threonine 180 in ULK1, as discussed above) (Yeh et al., 2011), and a somewhat similar mechanism is speculated to exist in mammals (Nazio et al., 2013). Furthermore, the Atg13p-dependent formation of oligomeric 'supramolecular' assemblies in yeast (noted above) may be crucial to maintain the local Atg1p concentration above the threshold required for its activation (Yamamoto et al., 2016). Interestingly, a major portion of ULK1- and almost all of ULK2-contining complexes migrate at ~1.2MDa on native PAGE gels (Chan et al., 2009) and Ulk1 complex members were shown to enter a 3MDa complex by gel filtration (Hosokawa et al., 2009a), supporting the persistence of some degree of ULK complex oligomerisation humans. These data indicate that membrane recruitment might precede kinase activation, with autophagic membranes therefore serving as scaffolds to promote ULK complex activation. Supporting this notion, ULK1 kinase activity is dispensable for membrane recruitment (Chan et al., 2009).

The direct recruitment of the ULK complex to autophagic cargo is implicated in some forms of selective autophagy. Via interaction between the cargo adaptor NDP52 (an autophagy adaptor that simultaneously interacts with LC3/GABARAPs and polyubiquitinated cargo to facilitate their selective sequestration) and FIP200, the ULK complex is directly recruited to intracellular *S. typhimurium* followed by the raft of downstream autophagic machinery to promote autophagosome biogenesis during xenophagy (Ravenhill et al., 2019). A similar NDP52/FIP200-dependent mechanism occurs in mitophagy, which is driven by ULK independently of mTORC1 and AMPK signalling and can be promoted by ectopic localisation of ULK1 to mitochondria (Vargas et al., 2019).

Huntingtin (a protein implicated in the pathogenesis of Huntington's disease) was shown to be required for proteostasis in Drosophila and mammals via the control of various types of selective autophagy. It independently binds the cargo adaptor p62 and ULK1 and promotes the recognition of lysine 63-ubiquitinated cargo and LC3 by p62. Huntingtin facilitates the activation of autophagy upon proteotoxic stress by displacing mTORC1 from ULK1, thus

providing a physical scaffold and a conducive signalling milieu to allow ULK activation in the presence of nutrients (Rui et al., 2015). Interestingly, it was reported that polyQ expanded Huntingtin is itself becomes a substrate of ULK1-dependent selective autophagy via p62 (Lim et al., 2015). The presence of either polyQ Huntingtin or polyubiquitinated protein aggregates promotes association between p62 and ULK1 with the interaction abolished upon removal of ULK1's kinase domain or mutation of p62's ubiquitin binding domain. The presence of polyQ proteins results in the phosphorylation of p62 by ULK1 which promoted its affinity for lysine 63-linked ubiquitin forming a positive feedback loop to promote recruitment of autophagic machinery and therefore cargo clearance (Lim et al., 2015).

As alluded to earlier, this cargo-centric/localisation-dependent mechanism of ULK activation appears to be conserved in yeast. Torggler et al., demonstrated that exogenous targeting of Atg1p to the spindle pole bodies (chosen as a non-specific scaffold) in cells lacking Atg13p and Atg19p (a cargo receptor required for selective autophagy) was sufficient for Atg1p activation. Furthermore, they show that cargo clustering at the vacuolar membrane causes local Atg1p activation to promote cytoplasm-to-vacuole targeting (related to selective autophagy in metazoans) in the absence of other autophagic stimuli. However, whilst cargo clustering at the vacuolar surface is required to drive Atg1p activation, Atg1p recruitment to the vacuole was independent of cargo but required Atg13p, suggesting the existence of sophisticated mechanisms regulating the spatiotemporal control of Atg1p activation (Torggler et al., 2016).

Together, these data indicate that clustering of ULK1/Atg1p likely precedes kinase activation in selective (and likely bulk) autophagy. As described, induction of selective autophagy is often driven by recruitment of cargo adaptors such as p62 and NDP52. Due to the wide array of cargoes and cargo adaptors present, a number of parallel mechanisms likely exist to promote ULK complex recruitment to autophagic cargoes (Kimura et al., 2015, Mandell et al., 2014, Turco et al., 2019a, Turco et al., 2019b, Murakawa et al., 2019). A particularly elegant example was described recently by Turco and colleagues (Turco et al., 2019b). They identified a C-terminal domain of FIP200, termed the 'claw', which possesses homology with the yeast Atg11p and was crucial for clearance of ubiquitin positive aggregates. This domain competes with LC3B for binding to p62. Direct binding of p62 by FIP200 therefore facilitates ULK1 clustering on autophagic cargo, with the consequent production of lipidated LC3 leading to ULK complex displacement to prevent its lysosomal degradation.

1.3.3.3 ULK substrates

Despite the crucial upstream role of the ULK complex in the autophagy, surprisingly few direct substrates have been verified, with the functional significance unknown in large proportion cases. Consensus motifs derived for both ULK1 and Atg1p have been instructive in the identification of novel ULK substrates (Papinski et al., 2014, Egan et al., 2015). Both kinases display similar substrate biases based on primary sequence alone, preferring aliphatic or aromatic hydrophobics at positions -3, +1 and +2 relative to the phosphoserine. Compared to Atg1p however, ULK1 prefers methionine over leucine at position -3, aromatics at position +1 and tolerates serine at position +2. Importantly however, a large number of direct ULK1 substrates do not match the reported motif (Sellier et al., 2016, Egan et al., 2015, Park et al., 2016, Li et al., 2017, Xu et al., 2015, Dite et al., 2017, Alers et al., 2011, Gan et al., 2017, Dunlop et al., 2014, Löffler et al., 2011, Li et al., 2016a, Dunlop et al., 2011, Dorsey et al., 2009, Liu et al., 2016, Wang et al., 2019, Saito et al., 2019), demonstrating that our understanding as to what drives phosphorylation by ULK1 *in vivo* remains incomplete. A catalogue of direct ULK1 substrates identified in the literature thus far is listed in Table 1.1.

Protein Name	Residue	Human Isoform 1	Function	Ref
ULK1	T180	-	Positively regulates ULK1 activity	(Lazarus et al., 2015, Bach et al., 2011)
	S341	S341	May regulate Atg8 homolog binding	(Dorsey et al., 2009)
	S1042	-	Positively regulates recruitment of CULLIN3	(Dorsey et al., 2009, Liu et al., 2016)
	T1046	-		
AMBRA1	S465	-	May regulate translocation of PI3K Complex to omegasome	(Egan et al., 2015, Di Bartolomeo et al., 2010)
	S635	-		
ATG101	S11	-	Unknown	(Egan et al., 2015)

	S203	-		
ATG13	S48	-	Unknown	(Alers et al., 2011)
	T170	-	Unknown	(Alers et al., 2011)
	S318	S355	Promotes mitophagy	(Joo et al., 2011)
	T331	T368	Unknown	(Alers et al., 2011)
	S389	-	Unknown	(Egan et al., 2015)
	T428	T465	Unknown	(Alers et al., 2011)
	T478	T515	Unknown	(Alers et al., 2011)
ATG14	S29	-	Positively regulates VPS34 activity	(Park et al., 2016)
	T48	-	Unknown	
	S61	-		
	S232	-		
ATG16L1	S278	-	Promotes xenophagy via ATG16L1 recruitment to internalised bacteria. Promotes ATG16L1 T300A caspase cleavage	(Alsaadi et al., 2019)
ATG4B	S316	-	Decreases affinity of ATG4B for LC3	(Pengo et al., 2017)
ATG9A	S14	-	Regulates ATG9A endocytic trafficking	(Zhou et al., 2017)
	?	-	Unknown	(Weerasekara et al., 2014)
BECN1	S15	-	Positively regulates VPS34 activity	(Russell et al., 2013)
	S30	-	Positively regulates VPS34 activity	(Egan et al., 2015) (Park et al., 2018)
	S96	-	May stimulate Atg8p homolog binding	(Egan et al., 2015)
	S279	-	Unknown	(Egan et al., 2015)
	S337	-		
CDC37	S339	-	Reduces HSP90-CDC37 client stability	(Li et al., 2017)

DAPK3	?	-	Regulates ATG9A trafficking	(Tang et al., 2011)
DENND3	S554	S472	Activates Rab12	(Xu et al., 2015)
	S572	S490		
DVL1	S266	S265	Negatively regulates WNT signalling by blocking TCF/ β-catenin interaction	(Hwang et al., 2019)
ENO1	S115	-	Promotes glycolytic flux	(Li et al., 2016a)
	S282	-		
FBP1	S63	-	Promotes glycolytic flux	(Li et al., 2016a)
	S88	-		
FIP200	S943	-	Unknown	(Egan et al., 2015)
	S986	-		
	S1323	-		
FLCN1	S316	-	Unknown	(Dunlop et al., 2014)
	T317	-		
	S406	-	Promotes dissociation of FLCN from GABARAP and autophagic flux	
	S537	-		
	S542	-		
FUNDC1	S17	-	Promotes mitophagy	(Wu et al., 2014)
HK1	S124	-	Promotes glycolytic flux	(Li et al., 2016a)
	S364	-		
MAD1	S546	-	Promotes recruitment to kinetochore during mitosis	(Yuan et al., 2019)
MKK4	?	-	Promotes phosphorylation/activation of JNK	(Sun et al., 2018)
MKK7	S35	-	Promotes phosphorylation/activation of JNK	(Sun et al., 2018)
	S378	-		
	S392	-		
	S403	-		
NR3C2	S843	-	Inhibits transcriptional factor activity by blocking aldosterone binding	(Shibata et al., 2018)

NRBF2	?	-	Unknown	(Ma et al., 2017b)
P62	S405	S403	Promotes selective autophagy	(Ro et al., 2014, Lim et al., 2015)
	S409	S407		
PFK1	S74	-	Promotes glycolytic flux	(Li et al., 2016a)
	S762	-		
PRKAA1	S287	S296	Unknown	(Dite et al., 2017)
	S360/ T368	S360/ T368	Negatively regulates AMPK activity	(Löffler et al., 2011, Dite et al., 2017)
	S397	S397		
	S486/ T488	S486/ T488		
	S489	S498	Unknown	(Dite et al., 2017)
PRKAB1	S49	-	Unknown	(Dite et al., 2017)
	S96	-		
	S108	-	Sensitizes AMPK to ADaM site ligands	(Dite et al., 2017)
	S170		Unknown	(Dite et al., 2017)
PRKAB2	S38	S39	Negatively regulates AMPK activity	(Löffler et al., 2011)
	T39	T40		
	S68	S69		
	S173	S174		
PRKAG1	S260/ T262	S261/ T263	Negatively regulates AMPK activity	(Löffler et al., 2011, Dite et al., 2017)
	S269	S270		
RAB9A	S179	S179	Induces Parkin-independent and Rip1-/Drp1-dependent mitophagy	(Saito et al., 2019)
RAPTOR	S792	-	Negatively regulates mTORC1 substrate binding	(Dunlop et al., 2011)
	S855	-		
	S859	-		
	S863	-		
	S877	-		
SDCBP	S6	-	Inhibits interaction with ubiquitin	(Rajesh et al., 2011)

	S61	-	Unknown	(Egan et al., 2015)
SEC16A	S846	S668	Regulates ERES formation/ER-Golgi traffic	(Joo et al., 2016)
SEC23A	S207	-	Regulates ERES formation/ER-Golgi traffic	(Gan et al., 2017)
	T405	-		
	S312	-	Unknown	
SEC23B	S186	-	Promotes COPII transport by increasing SEC23B stability	(Jeong et al., 2018)
SESN2	?	-	Unknown	(Ro et al., 2014)
SMCR8	S400	-	Unknown	(Sellier et al., 2016)
	S492	-		
	S562	-		
	T666/ S667	-		
STING	S366	-	Negatively regulates IRF3 activity	(Konno et al., 2013)
VCP	S13	-	Increases ATPase activity to promotes resolution of stress granules	(Wang et al., 2019)
	S282	-		
	T761	-		
VPS34	S249	-	Stimulates Atg8p homolog binding	(Egan et al., 2015, Birgisdottir et al., 2019)

Table 1.1 – *Previously identified ULK1 substrates*. ULK substrates currently identified in the literature are listed, those not known to physically interact with the ULK complex are highlighted in grey. The residue identified and the corresponding amino acid in the Uniprot designated human isoform 1 are listed, followed by the proposed function of each phosphorylation event where known. Where the phosphoacceptor residue is not known, potential residues are listed separated by a stroke. Notably, the function of many of the phosphorylation events listed is uncertain. Adapted from (Mercer et al., 2018).

The routes ULK-dependent regulation of autophagy by phosphorylation covered in Table 1.1 are summarised in Figure 1.6. Some characteristics of ULK signalling can be gleamed from this data. For example, a clear preference for serine over threonine is observed. Additionally, the vast majority of substrates physically interact with the ULK complex (either directly or indirectly). For example, alongside the previously described activating phosphorylation of p62

(Lim et al., 2015), ULK1 inhibits mTORC1 via multisite phosphorylation of RAPTOR (Dunlop et al., 2011) and AMPK via phosphorylation of α, β and γ subunits (Löffler et al., 2011, Dite et al., 2017). Furthermore, as well as substrates implicated in both early and late stage autophagy, a number of phosphorylation events function in autophagy independent processes.

1.3.3.4 Non-canonical ULK-signalling

The ULK kinases have been implicated in the negative regulation of Wnt signalling (Hwang et al., 2019), angiotensin II-mediated transcriptional regulation (Shibata et al., 2018), maintenance of glucose catabolism and redox homeostasis (Li et al., 2016a), facilitation of spindle assembly checkpoint (Yuan et al., 2019), activation of JNK-dependent necroptotic cell death during acetaminophen-induced liver injury and dampening of IRF3-dependent innate immune signalling (Konno et al., 2013) amongst other roles.

In both *C. elegans* and Drosophila, the ULK homologs play well established roles in axon guidance by regulating the trafficking of crucial guidance molecules (Toda et al., 2008, Ogura et al., 1994a, Ogura and Goshima, 2006, Mochizuki et al., 2011). Current data suggest this function is conserved in mice as previously noted (Wang et al., 2018a, Zhou et al., 2007). Ulk1 and Ulk2 localise to the growing tips of cultured dorsal root ganglion neurones with their removal singly or doubly preventing axonal growth and increasing branching. They promote TrkA receptor-mediated NGF (nerve growth factor) endocytosis, with NGF stimulation promoting Ulk1 lysine 63-linked polyubiquitination and physical association with TrkA and p62 (Zhou et al., 2007). More recent insights from germline and central nervous system-specific $Ulk1^{-/-}Ulk2^{-/-}$ mouse models reveal that loss of ULK results in a severe axon guidance defect. This phenotype is believed to be partially autophagy-independent as, whilst neurodegeneration was detected, the mutant mice lack the excessive cell death and accumulation of p62-/ubiquitin positive bodies observed upon knockout of other key autophagy proteins (Wang et al., 2018a). Interestingly, the *C. elegans* homolog of PP2A, Let-92, was shown to control the amplitude of Unc51 signalling by binding the kinase and dephosphorylating its substrates, such that reducing Let-92 signalling partially rescued axonal guidance defects observed upon reduction of Unc51 signalling (Ogura et al., 2010). As PP2A is implicated in regulation of ULK signalling in mammals, it is tempting to consider that the potential implication in neuronal signalling is evolutionarily conserved (Wong et al., 2015).

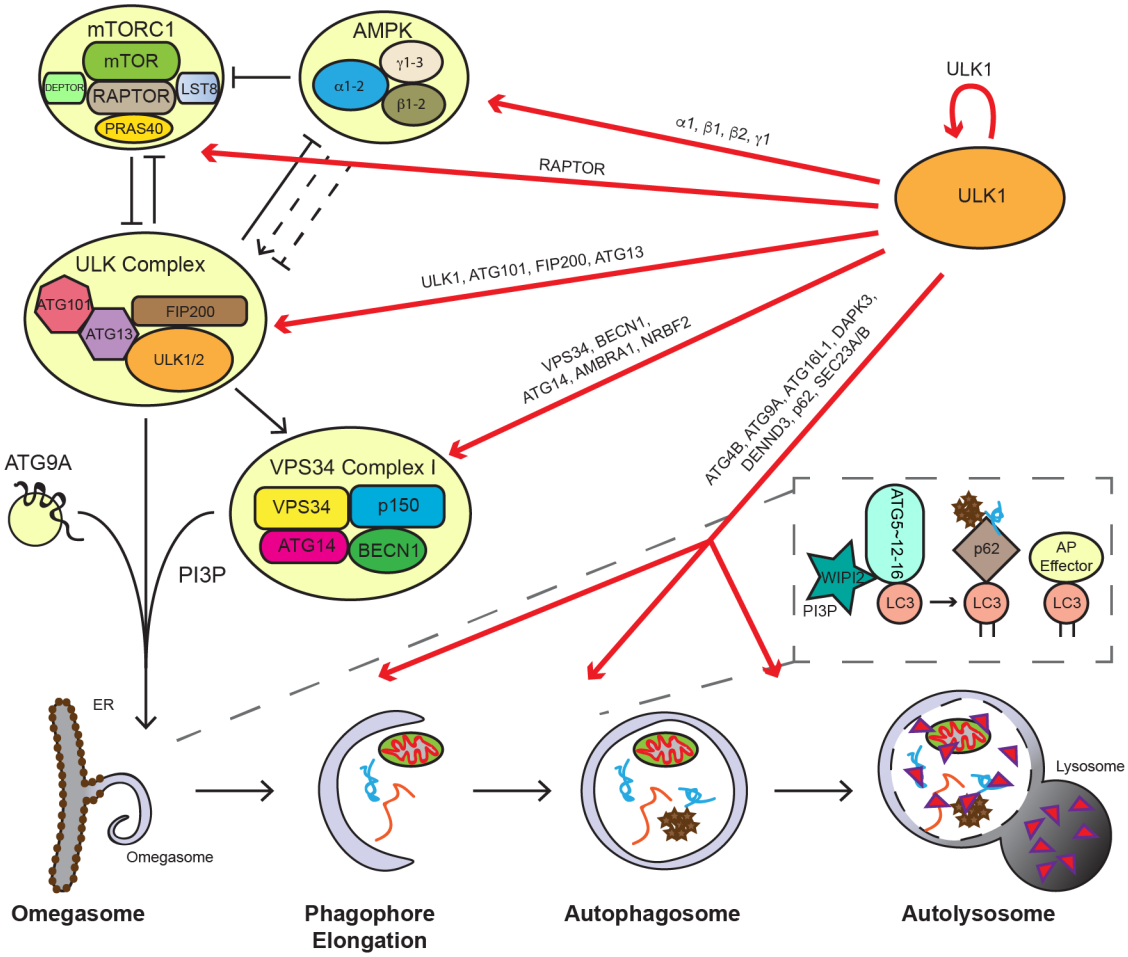

Figure 1.6 – *Regulation of autophagy by ULK1*. Clusters of autophagic signalling components are depicted in yellow ovals. Left - mTOR and AMPK regulate the activity of the ULK complex, which upon stimulation localises with the VPS34 complex and ATG9A-containing vesicles at the omegasome, which is enriched in PI3P. Dashed arrows convey conflicting data on the regulation of ULK activity by AMPK. Right - ULK substrates discussed and featured in Table 1.1 that regulate autophagy are annotated. The dashed inset box shows a key function of PI3P – the recruitment of WIPI2, which in turn binds the lipid conjugation machinery to promote LC3/GABARAP lipidation and membrane insertion. LC3/GABARAPs bind cargo adaptors such as p62 as well as autophagy effectors to promote progression of the autophagic program.

Alongside TrkA receptor-mediated NGF endocytosis, a further example of ULK-dependent non-autophagic membrane trafficking was identified by Joo and colleagues. They discovered that the ULK kinases regulate ER-Golgi traffic in multiple cell types by promoting COPII-dependent transport of specialised cargo (including the serotonin receptor SLC6A4) to the synapse in neurones. The formation of SEC24C containing ERES is promoted by direct SEC16A

phosphorylation by ULK1, which occurs in the absence of ATG13 (Joo et al., 2016). Further aspects of ULK-dependent ERES regulation were discovered by Gan et al., who show that ULK1 interacts with the COPII protein SEC23A only in the presence of nutrients. ULK1 overexpression promotes ERES clustering which occurs in the absence of ATG13. This is caused by phosphorylation of SEC23 by ULK1 which inhibits interaction with outer coat component SEC31 and thus prevents ER-Golgi traffic (Gan et al., 2017).

Finally, the ULK kinases have been implicated in the disassembly of ribonucleoprotein stress granules (Wang et al., 2019). An ULK hypomorph mouse line in which mice expressed no Ulk1 and significantly reduced levels of Ulk2 had shortened lifespan and stunted growth, displaying pathological malformations in brain, spinal cord, kidney, muscle and liver tissues. The muscle phenotype, which was also observed muscle specific Ulk1/2 (but not Atg7) mutants, was found to resemble that observed in inclusion body myopathy which features the accumulation of large ribonucleolar stress granules. Ulk1 was shown to bind stress granule components and promote their dissolution independently of Atg7, Atg14, Atg13 or Fip200. Inclusion disassembly in multiple cell lines was promoted by interaction of ULK1 with the AAA ATPase VCP, which led to direct VCP phosphorylation and activation. Interestingly, recruitment of ULK1 to stress granules was shown to be cell type specific, revealing the complexity of ULK-dependent signalling on an organismal level and cautioning against inferring the ubiquity of cell line-derived insights (Wang et al., 2019).

Whilst many ULK substrates have been identified in autophagy-dependent/independent pathways, a primary function of the ULK kinases at autophagosomal membranes is the targeting and activation of the VPS34 complex at the ER. Supporting this notion, exogenous targeting of BECN1 to the ER drove LC3 lipidation and autophagosome formation in ULK1/2 double knockout (DKO) MEFs maintained in both basal and starvation conditions. However, autophagic flux was not rescued in these cells, evidencing roles of the ULK kinases in later stages of autophagy (Anwar et al., 2019). The regulation and function of the VPS34 complex in autophagy will be discussed in the next section.

1.3.4 VPS34 Complex

Immediately downstream of the ULK complex is the class III PI3K (phosphatidylinositol-3 kinase) VPS34 (Itakura and Mizushima, 2010). Whilst ULK complex translocation to omegasomes occurs in a VPS34-independent manner both *in vitro* and in cells (Brier et al., 2019), the recruitment and activation of VPS34 is required to prevent its rapid dissociation. The stabilisation of both ULK and VPS34 complexes at the omegasome drives a positive feedback loop and creates the required conditions for autophagosome biogenesis via the production of the signalling lipid PI3P (Karanasios et al., 2013). Inhibition of VPS34 signalling via treatment with pharmacological inhibitors (e.g. Wortmannin) or via deletion of VPS34 greatly reduces starvation-induced and basal autophagy, although some forms of non-canonical autophagy are permitted depending on the stimuli present (Zhou et al., 2010, McAlpine et al., 2013).

Three classes of PI3K enzymes exist in mammals, all of which phosphorylate the 3' hydroxyl moiety of the D-myo-inositol head group (Jean and Kiger, 2014). The key phosphoinositide in autophagic signalling is the singly phosphorylated PI3P, which is largely produced by the class III PI3K, VPS34. However, class II PI3Ks have been implicated in autophagy-dependent PI3P production (Devereaux et al., 2013) and, whilst their implication in autophagy regulation is poorly supported currently, PIP_2 phosphatases could theoretically contribute to the autophagic pool of PI3P (Vergne and Deretic, 2010, Bharadwaj et al., 2016, Bago et al., 2014). Supporting this notion, the phosphatase INPP5E, which hydrolyses $PI(3,5)P_2$ to PI3P and is mutated in Joubert syndrome, was recently shown to positively regulate autophagosome-lysosome fusion in neurones, with disease-causing missense mutations impairing autophagy in cultured cells (Hasegawa et al., 2016). The *S. cerevisiae* genome encodes only one PI3K, the homolog of VPS34, Vps34p (Schu et al., 1993). Therefore, due to the relatively simplified source of PI3P and the high degree of conservation with mammals, yeast have provided an excellent model for the study of VPS34-dependent autophagy.

The Vps (vacuolar protein sorting) genes were identified by the inability of mutant yeast to target carboxypeptidase Y to the vacuole. Vps34p was cloned and characterised in the laboratory of Scott Emr (Herman and Emr, 1990), with the first implication in autophagy coming some years later (Kiel et al., 1999). In both yeast and mammals, the majority of cellular

VPS34/Vps34p is incorporated into a heterodimer with p150/Vps15p or into a heterotrimer with p150/Vps15p and BECN1/Atg6p (Kim et al., 2013, Yuan et al., 2013, Russell et al., 2013, Rostislavleva et al., 2015). It further incorporates into two tetrameric protein complexes, named VPS34 complex I (CI) and complex II (CII) (Itakura et al., 2008, Kihara et al., 2001). Whilst VPS34 CII is generally implicated in later stages of autophagy, the initiation of autophagosome biogenesis requires the omegasomal translocation and activation of VPS34 CI. Both are comprised of the lipid kinase VPS34/Vps34p, the pseudokinase scaffold p150/Vps15p and the regulatory subunit BECN1/Atg6p, along with either ATG14/Atg14p or UVRAG/Vps38p defining CI and CII respectively.

VPS34 probably never works alone (Backer, 2016). Monomeric VPS34 is inactive *in vitro* and overexpression of p150 leads to a significant increase in VPS34 specific activity (Yan et al., 2009). Tetrameric complex incorporation further augments activity, likely by improving VPS34 stability and substrate access (Yan et al., 2009, Rostislavleva et al., 2015). Full complex association also promotes a binary switch in the regulation of VPS34 activity in response to nutrients, with glucose starvation promoting CI/CII activity and amino acid starvation promoting CI activity, whilst both conditions inhibit heterodimeric/trimeric subcomplex activity (Kim et al., 2013, Yuan et al., 2013, Russell et al., 2013). This insight makes sense of the observation that, whilst bulk VPS34 specific activity is decreased upon starvation, the levels of autophagic PI3P increase (Byfield et al., 2005).

Whilst structures had been elucidated for a number of isolated VPS34 complex component domains, recent cryoEM structures for human CI and CII with resolutions ranging from 28Å to 6.8Å have provided an invaluable insight into the primordial kinase complexes at an atomic scale (Stjepanovic et al., 2017, Baskaran et al., 2014, Ma et al., 2017a, Chang et al., 2019). Arguably however the 4.4Å crystal structure of yeast CII, which was published relatively early on, has proved the most instructive in the study of VPS34 complex structure/function (Rostislavleva et al., 2015). All VPS34 complex structures elucidated to date reveal the same gross architecture, adopting a 'Y' shape. Referring to the human proteins alone, the VPS34-p150 subcomplex comprises the catalytic right arm of the 'Y', with ATG14/UVRAG-BECN1 subcomplex dominating the regulatory left arm (Ohashi et al., 2019). At 1358 amino acids, the scaffolding component p150 is the largest in the complex and the only component to span both arms.

The tip of each arm contains membrane-interacting regions that promote targeting of the complex to membranes. These include the catalytic right arm which harbours p150's conserved N-terminal myristoylation motif (Herman et al., 1991b, Panaretou et al., 1997) and the activation loop and kα12 helix in VPS34's lipid kinase domain (Rostislavleva et al., 2015). Furthermore the regulatory left arm contains the membrane binding aromatic finger in BECN1's C-terminal BARA (β-α repeated autophagy) region (Rostislavleva et al., 2015, Chang et al., 2019) and the BATS (Barkor/ATG14(L) autophagosome-targeting sequence) domain in the C-terminus of ATG14 that binds both $PI(4,5)P_2$ and PI3P promoting complex stability and recruitment to highly curved membranes respectively (Fan et al., 2011, Tan et al., 2016). The base of the complex is constituted by the N termini of both ATG14/UVRAG and BECN1, and by p150's HEAT domain. Tandem N-terminal CXXC domains in ATG14 provide further constitutive anchoring to ER membranes (Matsunaga et al., 2010) (Figure 1.7).

Whilst yeast and mammalian PI3K complexes are highly conserved, some key differences exist. For example, the yeast Vps34p complex is resistant to the pharmacological inhibitors Wortmannin and LY294002 and, whereas yeast express 3-fold more Vps34p than Vps15p (Stack et al., 1993), p150 is more highly enriched than VPS34 in HeLa cells (Murray et al., 2002, Itzhak et al., 2016). Furthermore, in yeast no difference in *in vitro* lipid kinase activity on highly curved (omegasome-like) membranes between CI and CII is observed, and CII alone is active on larger, less curved (endolysosome-/plasma membrane-like) membranes (Rostislavleva et al., 2015). When human VPS34 complexes are compared however, CI activity on highly curved membranes is roughly twice that of CII, with CI and CII activity decreasing to comparative levels as curvature decreased (Brier et al., 2019). This is due to the presence of the BATS domain in mammalian ATG14, which is absent in Atg14p. The BATS domain facilitates tight membrane anchoring of VPS34 CI *in vitro* and *in vivo* (Ma et al., 2017a). Sophisticated reconstitution experiments revealed that an ALPS (amphipathic lipid packing sensor) motif, situated within the BATS domain, significantly augments VPS34 kinase activity *in vitro*. Intriguingly, whilst CII can generate PI3P *in vitro* (albeit with 50% reduction in efficiency compared to reconstituted CI), the presence of the ALPS motif was required for downstream LC3 lipidation suggesting that CI promotes omegasome establishment via ALPS-dependent yet kinase-independent mechanisms (Brier et al., 2019). These differences in the yeast and mammalian VPS34 complexes may be reflected in the contrasting distribution of PI3P on

autophagic membranes between the two (PI3P is more abundant in the lumenal leaflet of yeast autophagosomes, however in mammals it is exclusively present on the cytoplasmic leaflet (Cheng et al., 2014)), which in turn indicates non-conserved roles for the signalling lipid in autophagy between the model systems. Therefore, despite close similarities, care should be taken when extrapolating hypotheses from the Vps34p CII crystal structure.

Generally, CII is implicated in VPS34's endosomal functions (Backer, 2016). The VPS34 complex is recruited and activated at target membranes via direct association of p150 with RAB5 and RAB7 (Stein et al., 2003, Christoforidis et al., 1999, Murray et al., 2002). Interestingly, it was recently established that VPS34 promotes endolysosomal maturation by driving recruitment of the PI3P-biniding RAB7 GAP ARMUS and thus negatively regulating RAB7 activity (Jaber et al., 2016), a function that appears to be somewhat conserved in *C. elegans* (Law et al., 2017). Intriguingly, ARMUS was shown to interact with autophagosomal membranes in an LC3-dependent manner to regulate RAB7-dependent fusion with lysosomes (Carroll et al., 2013), however the role of PI3P in this mechanism was not investigated.

CII has also been directly implicated in autophagy, via the promotion of autophagosome maturation (Kim et al., 2015, Sun et al., 2011) and ALR (Munson et al., 2015). Autophagy is inhibited by the specific VPS34 CII antagonist RUBICON which binds UVRAG, VPS34 and BECN1 and decreases both membrane association (by obscuring BECN1's aromatic finger motif) and VPS34 lipid kinase activity (Zhong et al., 2009, Kim et al., 2015, Sun et al., 2011, Chang et al., 2019). RUBICON binding is promoted by mTORC1-dependent phosphorylation of UVRAG at serine 498 (Kim et al., 2015), and is prevented by sequestration of RUBICON by RAB7 (Sun et al., 2010). Interestingly, RUBICON also inhibits fusion of autophagosomes and endosomes with lysosomes in a VPS34-independent manner by blocking the VPS34-independent association of UVRAG with the HOPS tethering complex (Sun et al., 2010, Liang et al., 2008, Kim et al., 2015), although conversely HOPS-dependent autophagosome-lysosome fusion was reported to be unaffected by knockdown of UVRAG, bringing this model into question (Jiang et al., 2014). Finally, UVRAG is implicated in ER-Golgi traffic. By binding PI3P via its C2 domain, UVRAG is recruited to the ER where it facilitates COPI-dependent retrograde traffic via incorporation into the RINT1 tethering complex (He et al., 2013). Upon induction of autophagy, UVRAG disengages from RINT1 to promote VPS34 CII-dependent ATG9A trafficking from the Golgi – a function that also requires direct PI3P binding (He et al., 2013).

1.3.4.1 Localisation of VPS34 CI to autophagic membranes

Current data indicate that whilst the total level of VPS34 CI localised to the ER remains stable, autophagy induction drives a redistribution to punctate omegasomes requiring both ATG14 membrane targeting domains and the ULK complex (Itakura and Mizushima, 2010, Matsunaga et al., 2010). Challenging this view, after examining the colocalisation of BECN1 with the organelle markers via immunofluorescence it was reported that that BECN1 recruitment to the ER increases upon starvation. In these experiments, the pool of endogenous BECN1 shown to reside constitutively at the ER was depleted by ~50% after deletion of ULK1 and ULK2 in MEFs in keeping with the upstream role of ULK in autophagy, however starvation promoted its recruitment in an ULK-independent manner (Anwar et al., 2019).

The mechanisms of VPS34 recruitment to membranes by accessory proteins association discussed in this section are summarised in Figure 1.7. Alongside direct recruitment of ATG14 by STX17 at MAMs (Hamasaki et al., 2013), colocalisation of the ULK and VPS34 complexes is promoted by direct interaction between the ATG13 HORMA domain and ATG14, which is also observed in yeast (Jao et al., 2013, Park et al., 2016). Strikingly however, whilst targeting of Vps34p to the PAS requires Atg14p, Vps15p translocation occurs independently of this subunit (Obara et al., 2006). A novel C-terminal region of ATG101, a protein absent in *S. cerevisiae*, was recently shown to mediate interaction between the ULK complex with both VPS34 CI and CII components and was required for LC3 puncta formation upon starvation (Kim et al., 2018a). VPS34, ATG14 and BECN1 were all recently shown to bind Atg8p homologs with a preference for GABARAP and GABARAPL1. ATG14's LIR lies adjacent to the ALPS motif and its mutation prevents both localisation with LC3B and mitophagy (Birgisdottir et al., 2019). These data suggest that, similarly to the ULK complex (Alemu et al., 2012), the VPS34 complex might be recruited to sites of autophagosome biogenesis in a LIR-dependent manner. VMP1 transiently localises to omegasomes, where it binds BECN1 preventing association with antagonist BCL2 (Molejon et al., 2013). Another transmembrane ER protein, EMC6, positively regulates autophagy by interacting with BECN1-containg VPS34 complexes and RAB5A, with knockdown resulting in the enlargement of omegasomes and reduced LC3 lipidation (Li et al., 2013b). Additionally, VPS34 can be sequestered at sites away from the ER. In basal conditions, VPS34/BECN1-positive complexes are sequestered on microtubules, with starvation resulting

in their release and allowing translocation to omegasomes (Di Bartolomeo et al., 2010). Finally, as previously described, the co-association of both ULK and VPS34 complexes with Exocyst and the relocalisation of this regulatory complex to sites of autophagosome biogenesis helps coordinate their activation upon induction of autophagy (Bodemann et al., 2011). Together, these data indicate that localisation of VPS34 to the omegasome is highly-regimented and reinforced via parallel redundant mechanisms, some of which display conservation from yeast to mammals.

1.3.4.2 Regulation of VPS34 CI activity via accessory protein association and post-translational modification

As well as promoting translocation to omegasomes, accessory protein binding is also implicated in the regulation of VPS34 complex stability and activity (see Figure 1.8). For example, many regulatory pathways modulate VPS34 activity by regulating the association of BECN1 with its antagonist BCL2 (Backer, 2016, Molejon et al., 2013). Moreover, RACK1 (Zhao et al., 2015), Dapper1 (Ma et al., 2014), PAQR3 (Xu et al., 2016) and NRBF2 (Ohashi et al., 2016, Young et al., 2016, Lu et al., 2014) associate with ATG14-containing complexes to promote autophagy. Both PAQR3 and NRBF2 constitutively interact with VPS34 CI, and have been proposed as a 5th components of VPS34 CI. NRBF2 was also identified as an ULK1 interactor (Behrends et al., 2010), and its association with VPS34 CI is conserved in yeast (Ohashi et al., 2016). It occupies the same area as UVRAG's C2 domain in VPS34 CII and promotes VPS34 CI dimerization whilst potently increasing lipid kinase activity via independent mechanisms (Young et al., 2016). Interestingly, it can both positively (Young et al., 2016, Lu et al., 2014) or negatively (Zhong et al., 2014) regulate PI3K signalling depending on the signalling environment (Ma et al., 2017b).

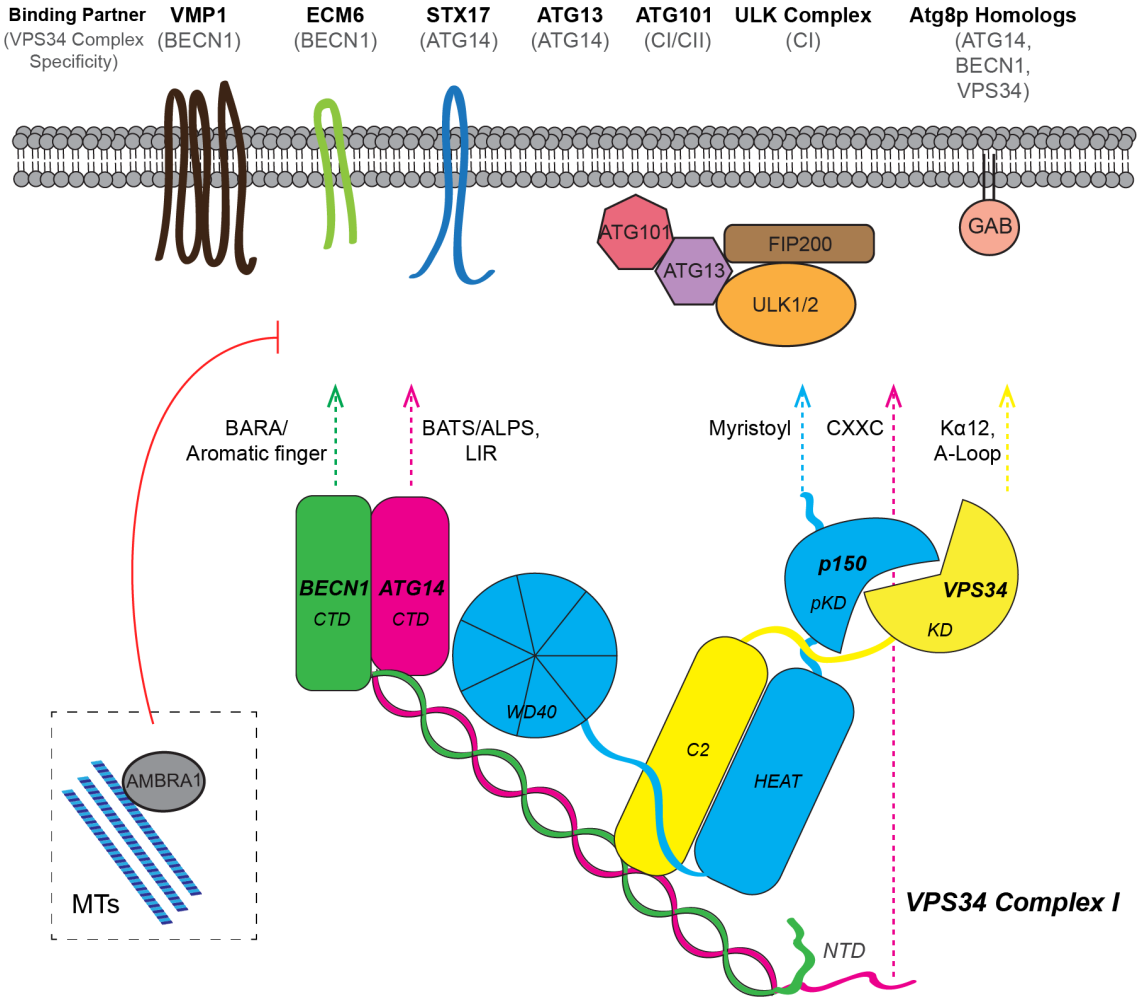

Figure 1.7 – *Recruitment of VPS34 complex I to membranes.* Proteins implicated in recruitment of VPS34 CI to membranes are annotated with the VPS34 complex-specificity or specific binding partner where known listed in brackets below protein name (top). Domains of VPS34 CI components implicated in direct membrane interaction are annotated with dashed lines (bottom). Inset box shows microtubule-associated AMBRA1, which sequesters VPS34-/BECN1-containing complexes away from autophagic membranes. Schematic approximately conveys relative positioning of assembled VPS34 complex components (reviewed by (Ohashi et al., 2019)). KD = kinase domain; pKD = pseudokinase domain, CTD = C-terminal domain, A-loop = Activation Loop, MTs = Microtubules.

The VPS34 CI core components and accessory proteins, particularly BECN1, are the target of a number of regulatory phosphorylation events (Hill et al., 2019). The N-termini of ATG14 (serine 29) and BECN1 (serine 15/30) are directly phosphorylated by ULK1 (Table 1.1). These sites localise to the base of CI and their phosphorylation is required for lipid kinase activation in cells and *in vitro* (Park et al., 2018, Park et al., 2016, Russell et al., 2013). Interestingly, ATG14's

C-terminal LIR was necessary for phosphorylation at S29, and ULK1 phosphorylation of VPS34 at serine 249 broadened its Atg8p homolog specificity whilst greatly increasing binding strength. Phosphorylation of BECN1 at serine 90, serine 93 and serine 96 also facilitated GABARAP/GABARAPL1 binding (Birgisdottir et al., 2019), with serine 90 and serine 93 substrates of AMPK (see below) and serine 96 a predicted substrate of ULK1 (Egan et al., 2015). The aforementioned starvation-dependent release of VPS34 from microtubules required ULK-dependent phosphorylation of AMBRA1, an accessory component of the VPS34 complex (Di Bartolomeo et al., 2010). Phosphorylation of AMBRA1 by ULK1 was also shown to promote its dissociation from the E3 ligase CULLIN4, thus promoting AMBRA1 stabilisation and autophagy initiation (Antonioli et al., 2014). ULK1 also phosphorylates NRBF2 *in vitro*, however the specific substrate residues and functional consequence remain unknown (Ma et al., 2017b) (Table 1.1).

As well as ULK1, several kinases are implicated in the augmentation of VPS34 activity upon cell stress. For example, upon amino acid sufficiency, mTORC1 phosphorylates several VPS34 complex components. ATG14 undergoes multisite phosphorylation by mTORC1 at serine 3, serine 223, threonine 233, serine 383 and serine 440 resulting in the inhibition of autophagy in basal conditions by inhibiting VPS34 activity on autophagic membranes without affecting total cellular levels of PI3P (Yuan et al., 2013). Phosphorylation of NRBF2 by mTORC1 (at serine 113 and serine 120) switches if from positive to a negative regulator of VPS34 CI activity, with dephosphorylation facilitating VPS34-p150 subcomplex association with both ATG14-BECN1 and ULK complex components (Ma et al., 2017b). Furthermore, AMBRA1 is phosphorylated at serine 52, which regulates autophagy in a VPS34-independent fashion by preventing TRAF6-dependent polyubiquitination and stabilisation of ULK1 as described previously (Nazio et al., 2013).

AMPK is a crucial regulator of VPS34 complex activity. Upon glucose starvation AMPK phosphorylates VPS34 directly at threonine 163 and serine 165 to inhibit its lipid kinase activity (Kim et al., 2013). However, incorporation into CI/CII prevents phosphorylation at these residues. In this instance, AMPK phosphorylates BECN1 at serine 90 and serine 93 (91 and 94 in murine Becn1) to promote PI3P formation *in vivo* (Kim et al., 2013) and at threonine 388 which promotes autophagy by specifically stabilising VPS34 CI (Zhang et al., 2016a). Serine 90 is modified in a starvation-dependent manner by three further phosphoregulatory enzymes:

the kinases MAPKAPK2 and DAPK3, and the phosphatase complex PP2A-B55α (Fujiwara et al., 2016, Wei et al., 2015). The previously mentioned scaffolding components RACK1 and PAQR3 are also regulated by AMPK. RACK1, the removal of which was shown inhibit both basal and amino acid starvation-induced autophagy, is phosphorylated by AMPK at threonine 50 to allow association with p150, ATG14 and BECN1 (Zhao et al., 2015). Whilst PAQR3 deletion dampens basal/stress-induced autophagic flux generally, indicating that it might promote VPS34 activity constitutively, AMPK-dependent phosphorylation of CI-associated PAQR3 at threonine 32 is specifically required to activate VPS34 activity on glucose starvation, possibly via promotion of BECN1 phosphorylation at serine 93 (Figure 1.8) (Xu et al., 2016).

Alongside phosphorylation, VPS34 CI components are the target of a wide range of post-translational modifications. The acetyltransferase p300 targets BECN1 at lysine 430 and lysine 437 to inhibit autophagosome maturation by promoting RUBICON association (Sun et al., 2015). p300 also acetylates VPS34 at three residues (lysine 29, lysine 771 and lysine 781) which blocks both BECN1 association and phosphatidylinositol binding, with deacetylation required for starvation-induced autophagy (Su et al., 2017).

Ubiquitination is also implicated in both positive and negative regulation of VPS34 complex activity depending on the cellular context. For example, TRAF6-dependent lysine 63-linked ubiquitination of BECN1 is implicated in autophagy induction in macrophages (Shi and Kehrl, 2010). Furthermore, the actin polymerising protein WASH binds BECN1 in basal conditions excluding it from association with AMBRA1. This interaction is disrupted upon starvation allowing AMBRA1-dependent lysine 63-linked polyubiquitination of BECN1 at lysine 437, thus activating autophagic VPS34 signalling (Xia et al., 2013). Conversely, ubiquitination also negatively regulates VPS34 signalling. CULLIN3-KLHL20 (an E3 ligase-adaptor complex that also targets ULK1) binds BECN1 and VPS34 and promotes their degradation upon starvation via lysine 48-linked polyubiquitination (Liu et al., 2016). Competitive displacement of the deubiquitinase ATXN3 from BECN1 (shown to occur via overexpression of the expanded polyQ region from Huntingtin) results in increased lysine 48-linked polyubiquitination at lysine 402 and consequently decreased BECN1 stability, VPS34 activity and autophagic flux (Ashkenazi et al., 2017). Finally, BECN1 associates with the deubiquitinases USP13 and more transiently with USP10 which protects it from proteasomal degradation (Liu et al., 2011).

In the absence of autophagic stimuli, PI3P is virtually absent in the cytosolic leaflet of the ER (Gillooly et al., 2000). Via mechanisms discussed in this section, VPS34 is activated and recruited to omegasomes, where it drives the formation of PI3P-enriched subdomains with the capacity to recruit downstream autophagy effectors, eventually resulting in the morphological changes associated with autophagosome biogenesis.

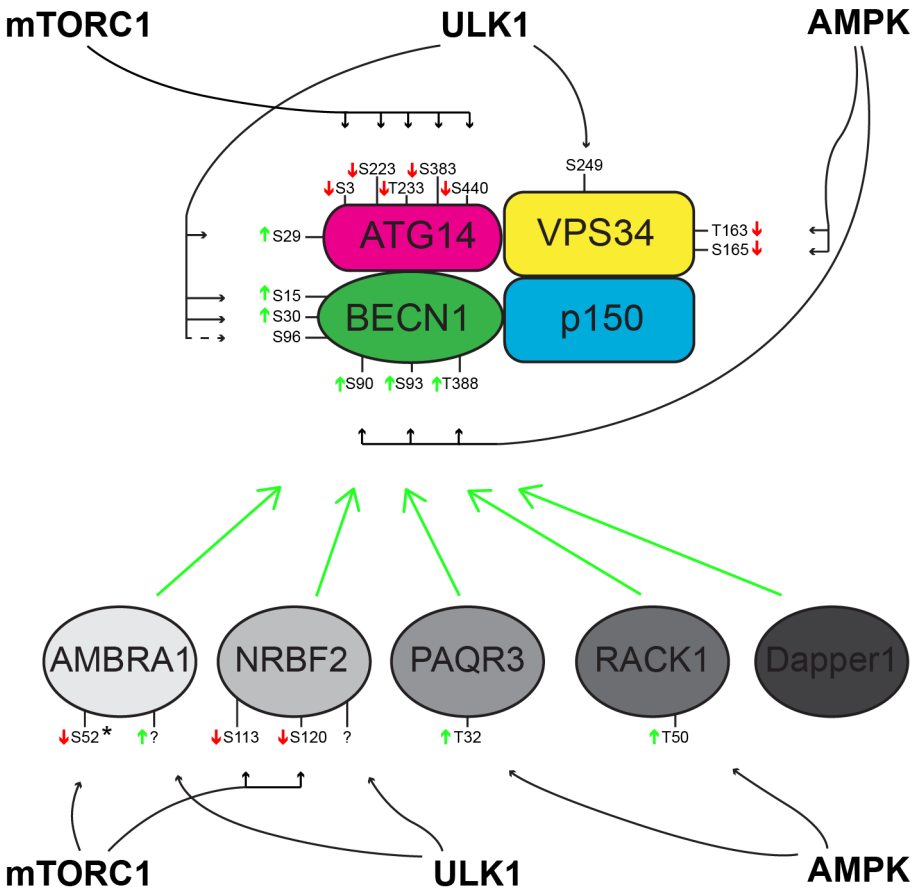

Figure 1.8 – *Regulation of VPS34 complex I by nutrient and energy status-regulated phosphorylation and accessory protein association.* Direct phosphorylation events on VPS34 complex components or accessory proteins by the mTORC1, ULK1 and AMPK are depicted. The dashed arrow indicates that the phosphorylation of BECN1 at serine 96 is validated less thoroughly than serine 15 or serine 30. Where the effect on VPS34 activity is known it is depicted with an arrow with activating phosphorylation events in green and inactivating events in red. The 5 accessory proteins discussed in the text are shown below, all of which bind ATG14-containing complexes to promote VPS34 activity. '?' represents that phosphoacceptor sites have not been mapped. * Phosphorylation of AMBRA1 serine 52 is implicated in the VPS34-independent negative regulation of ULK1 stability.

1.3.5 PI3P effectors

Numerous components of the early autophagic machinery are recruited to autophagic membranes via PI3P-binding domains. Several PI3P binding domains exist, some with the capacity to distinguish autophagic and endosomal pools of PI3P. The FYVE (Fab1p, YOTB, Vac1p and EEA1) finger domain is perhaps the best characterised. The isolated FYVE domain from the ESCRT-0 protein HGS labels global pools of PI3P *in vivo*. As already covered, UVRAG binds PI3P via its C2 domain (He et al., 2013). PX (Phox homologous) domains were first identified in p40phox (gene name *NCF4*), but have since been identified in a range of other proteins including the negative regulator of autophagy HS1BP3 (Holland et al., 2016). The PX domain from p40phox binds global pools of PI3P with high specificity and can be used to probe for PI3P *in vitro* (Munson et al., 2015, Munson and Ganley, 2016). PH (Pleckstrin homology) domains, the 11th most common domain in the human proteome, typically bind phosphoinositides with at least two adjacent phosphates in their inositol head group (i.e. PI(3,4)P_2, PI(4,5)P_2 and PI(3,4,5)P_3) (Lemmon, 2007). However, PI3P-specific PH domains have been identified, such as that in the putative autophagosome-lysosome tether TECPR1 (Chen et al., 2012). Finally, the PROPPIN (β-propellers that bind polyphosphoinositides) family proteins bind PI3P and PI(3,5)P_2 in a curvature-dependent fashion (Busse et al., 2015).

The earliest identified PI3P-binding protein to be recruited to autophagosomes is the double-FYVE containing protein DFCP1. This protein resides at the ER and Golgi in basal conditions and translocates to omegasomes upon starvation, however as depleting DFCP1 leaves LC3 lipidation unaffected its function in autophagy is unknown (Itakura and Mizushima, 2010, Axe et al., 2008). WIPI1-4 (WD40 repeat protein interacting with phosphoinositides) are PROPPIN family proteins which are also recruited to omegasomes at early time points. They are homologous to yeast Atg18p and performing somewhat conserved roles in autophagy with both WIPI4 and Atg18p binding to ATG2A/ATG2B and Atg2p implicated in autophagosome membrane formation (Rieter et al., 2013). In mammalian autophagy, WIPI2b (one of the five WIPI2 isoforms) binds ATG16L1 to drive the lipidation of Atg8p homologs at PI3P-enriched phagophores and thus the progression of autophagosome biogenesis (Dooley et al., 2014) (Figure 1.6).

1.3.6 Ubiquitin-like conjugation systems

The lipidation of LC3/GABARAP proteins requires two ubiquitin-like conjugation systems that are highly conserved from yeast to mammals. Among the requisite protein machinery are two structural homologs of ubiquitin, ATG12 and the LC3/GABARAP proteins (Noda et al., 2009). These are conjugated in a coordinated series of stages that bear close resemblance to those implicated in ubiquitination (reviewed in (Nakatogawa, 2013)). ATG12 is activated at the expense of ATP by the E1-like ATG7 via the formation of a thioester bond between ATG12's C-terminal glycine and ATG7's catalytic cysteine. Activated ATG12 is then attached to the catalytic cysteine in the E2-like ATG10, before being transferred to ATG5 via a glycine-lysine isopeptide bond, thus forming the ATG5~ATG12 conjugate (Mizushima et al., 1998). There is no E3-like enzyme in the ATG12 system, instead the constitutively-formed ATG5~ATG12 conjugate acts as an E3-like enzyme in the LC3/GABARAP ubiquitin-like conjugation system. ATG5~ATG12 conjugate localisation is regulated by ATG16L1 which directly associates with ATG5 to form the ATG5~ATG12-ATG16L1 subcomplex (Mizushima et al., 2003).

As noted in section 1.2, the 7 LC3/GABARAP proteins (LC3A, LC3B, LC3B2, LC3C, GABARAP, GABARAPL1, GABARAPL2) are homologs of yeast Atg8p. They are synthesised bearing a C-terminal extension that must be cleaved by the cysteine protease ATG4, to expose a glycine and thus prime the proteins for lipid conjugation (Agrotis et al., 2019a). ATG7, which functions as an E1-like enzyme in both pathways, activates primed LC3/GABARAPs whereupon they are transferred to the E2-like ATG3. The LC3/GABARAPs are then transferred directly onto phosphatidylethanolamine via an amide linkage. Using LC3B as an example, typically the unlipidated form is referred to as LC3B-I and the lipidated form LC3B-II. The E2-like ATG3 possesses the capacity to directly recognise and conjugate LC3/GABARAPS to phosphatidylethanolamine (and also phosphatidylserine) *in vitro* (Sou et al., 2006). However, its activity is greatly increased by association with ATG5~ATG12 subcomplex, which was shown in yeast to impose an optimal orientation of key residues in ATG3's catalytic centre (Sakoh-Nakatogawa et al., 2013). Delipidation of LC3/GABARAPs by ATG4 frees them from the membrane to be recycled in another round of conjugation, however this process occurs at a much slower rate compared to priming/propeptidase cleavage (Kauffman et al., 2018).

The conjugation systems possess various features that ensure the spatial accuracy of LC3/GABARAP lipidation. ATG3 has an N-terminal amphipathic helix that promotes *in vitro* LC3 lipidation on highly curved membranes and is probably required to recognise phosphatidylethanolamine. This is required for ATG3 activity *in vivo*, leading the authors to speculate that it allows ATG3 to target the tips of growing phagophores/omegasomes (Nath et al., 2014). ATG16L1 regulates the localisation of the ATG5~ATG12-ATG16L1 subcomplex, which in turn regulates ATG3 localisation via direct interaction with ATG12 (Metlagel et al., 2013). Whilst LC3/GABARAP are present in both inner and outer autophagosomal membranes, the ATG5~ATG12-ATG16L1 complex resides largely on the outer surface of mammalian phagophores (Mizushima et al., 2001), similar to the outer membrane localisation of PI3P (Cheng et al., 2014). Exogenous targeting of ATG16L1 to the plasma membrane results in aberrant lipidation at that site (Fujita et al., 2008b) and abolishing the interaction between ATG16L1 and WIPI2b results in the inhibition of LC3 puncta formation upon starvation and LC3-II accumulation upon starvation in the presence of Bafilomycin A1 (Dooley et al., 2014). Alongside WIPI2b, ATG16L1 also binds the ULK complex component FIP200, and this interaction is necessary for its translocation to ubiquitin-decorated endosomes to enhance bacterial clearance during xenophagy (Fujita et al., 2013). Direct FIP200 binding was also reported to recruit ATG16L1 to omegasomes upon starvation (Gammoh et al., 2013, Nishimura et al., 2013), however it was later shown that the relocalisation observed is WIPI2b-dependent and that FIP200 binding is dispensable (Dooley et al., 2014).

Intriguingly, ATG16L1 was recently demonstrated to directly associate with membranes via two functionally independent binding domains. A C-terminal motif is present in its β isoform facilitates non-canonical LC3-lipidation on low curvature membranes such as artificially neutralised endosomes, being unnecessary for starvation-induced autophagy. By comparison, a small N-terminal domain comprising a highly conserved amphipathic helix present in both α and β isoforms is indispensable for all forms of LC3B lipidation. It is not required for localisation to omegasomes, but is speculated to facilitate close association of ATG3 with target membranes (Lystad et al., 2019). These data are in line with those of Brier et al, who observed in *in vitro* experiments that whilst the membrane recruitment of WIPI2 and consequently LC3 lipidation required the presence of VPS34 C1, this was dispensable for ATG16L1 and ATG3 (Brier et al., 2019).

Accurate LC3/GABARAP targetting is further maintained by the ATG4 cysteine proteases. As described in section 1.2, whereas yeast possess only one ATG4 homolog (Atg4p), humans possess four ATG4 (ATG4A-D). They are largely redundant as removal of all four is required to block priming and delipidation of all LC3/GABARAP homologs (Agrotis et al., 2019a). However, ATG4B has the broadest specificity and the highest activity both *in vitro* and *in vivo*, with it recently proposed that LC3/GABARAP priming by ATG4B is uniquely efficient, whilst the delipidation activity of all four homologs was roughly similar and dependent on a C-terminal LIR (Agrotis et al., 2019a, Kauffman et al., 2018). ULK1 phosphorylates ATG4B at serine 316 to inhibit interaction with LC3 (Table 1.1), suggesting that LC3/GABARAP delipidation may be inhibited in the presence of active ULK1 thus maintaining high local concentrations of LC3/GABARAP-II at nascent autophagic membranes (Pengo et al., 2017). Mutation of the equivalent serine to alanine or aspartate in S. cerevisiae Atg4p does not affect autophagy progression as measured by Pho8Δ60 assay, however yeast Atg1p was shown to bind Atg4p at autophagosomal membranes and also phosphorylates it at serine 307 which similarly blocks interaction with Atg8p (Sánchez-Wandelmer et al., 2017). Therefore, whilst the implicated sites differ, the ULK-ATG4 signalling axis appears to be conserved throughout evolutionary history.

In yeast, it has been suggested that Atg4p-dependent delipidation prevents ectopic targeting of Atg8p-II (Nakatogawa et al., 2012), however as removal of ATG4A-D does not affect the localisation of exogenous pre-primed LC3B or GABARAP, this function is probably not conserved in humans (Agrotis et al., 2019a). Intriguingly however, expression of pre-primed and deconjugation-deficient form of LC3B in HeLa leads to the accumulation of LC3/GABARAP-protein conjugates, with similar results obtained upon expression of pre-primed LC3 family proteins in ATG4B knockout cells, and GABARAP family proteins upon the coincident removal of ATG4A and ATG4B. The covalent conjugation of multiple LC3/GABARAP units (termed ‘LC3ylation’) to ATG3 was demonstrated, with multiple protein targets speculated (Agrotis et al., 2019b). Therefore, ATG4 proteolysis is implicated in the reversal of erroneous targeting of LC3/GABARAP to proteins.

As discussed in previous sections, recruitment of LC3/GABARAPs to autophagosomal membranes serves multiple purposes in autophagy. They can be grouped into three main functions - LC3/GABARAP incorporation promotes progression of autophagy by: modulating of

biophysical properties of membranes (i.e. promoting elongation/fusion etc), recruiting autophagy effectors (e.g. ULK/VPS34 complex components) or by sequestering cargo via adaptor proteins in selective autophagy (e.g. p62 and NRBF2) (Figure 1.6). As it is upregulated upon the induction of autophagy, the lipidation of LC3/GABARAP is commonly used to measure autophagy in cell/animal models. Whereas autophagy effectors are typically not turned over in the lysosome during autophagy, cargo adaptors (along with lumenal LC3/GABARAP-II) are, therefore autophagy adaptor degradation is also used to track autophagic flux. Of note, the recruitment of autophagy effectors and cargo adaptors occurs through linear LIR motifs on target proteins, which discern between LC3/GABARAP proteins depending on their amino acid sequence (recently characterised rigorously by Wirth et al. (2019)). It likely that the varied roles of Atg8p homologs described throughout the introduction are dictated by their varied binding repertoires, which in turn are dictated by subtle differences in LIR motifs encoded in client proteins.

1.3.7 ATG9

Along with the ULK complex, the VPS34 complex, the WIPI proteins and the ubiquitin-like conjugation systems, the final autophagy-specific effector is ATG9. Hierarchical analyses in yeast showed that Atg9p is one of the first ATG proteins to localise to the PAS and is required for expansion of nascent autophagosomal membranes (Suzuki et al., 2007). This property is conserved in mammals (Karanasios et al., 2016, Orsi et al., 2012) in which knockdown ATG9 greatly reduces autophagosome numbers (Saitoh et al., 2009). ATG9 is the only transmembrane Atg protein in both yeast and mammalian systems. It contains 6 conserved transmembrane domains with cytosolic N and C terminal regions which show no conservation between yeast and mammals (He et al., 2006, Young et al., 2006). Two isoforms are expressed in mammals, ATG9A and ATG9B. Of the two, ATG9A is the most widely expressed and the best characterised.

After translation into the ER, N-glycosylated ATG9A resides in the Golgi from where it emanates to form the ‘ATG9 compartment’. This distinct entity is comprised of vesicotubular structures radiating from vacuolar bodies, similar to the bundles of vesicles and tubules observed in yeast (Mari et al., 2010, Orsi et al., 2012). In mammals, the ATG9A compartment exists mostly at the TGN (trans-Golgi network) in basal conditions, although pools have been

identified in the early, late and recycling endosomes as well as the plasma membrane (see section 1.2) (Ravikumar et al., 2010, Young et al., 2006, Orsi et al., 2012). Upon starvation, ATG9A disperses to peripheral regions of the cell in an ULK- and ATG13-dependent manner (Chan et al., 2009, Mack et al., 2012, Young et al., 2006). A pool of ATG9A-containing vesicles associates with omegasomes (Karanasios et al., 2016) and it has been speculated that ATG9A-mediated lipid transport provides a mechanism by which diverse organelles can contribute lipids/regulators to growing membranes (see section 1.2). Furthermore, ATG9A positive vesicles were recently shown to facilitate the delivery of the lipid modifying kinase PI4KIIIβ and its enzymatic product PI4P to omegasomes, which is speculated to facilitate ULK complex recruitment via ATG13's N-terminal lipid-binding domain (Judith et al., 2019).

Despite gross similarities in the autophagic function of yeast and mammalian ATG9 in autophagy, key differences exist. Upon starvation in yeast, Atg9p-containing vesicles assemble at the PAS where they integrate with the forming autophagosomal outer membrane to fulfil the lipid-requirement for rapid elongation (Yamamoto et al., 2012), after which Atg9p is removed from autophagosomal membranes either before or after delivery to the vacuole (Reggiori et al., 2004, Yamamoto et al., 2012). Neither process has yet been substantiated in mammals. Furthermore, whereas knockdown of ULK1 prevents the escape of ATG9A from the TGN (Young et al., 2006), kinase inactivation of Atg1p (coupled with removal of the selective autophagy-specific Atg1p complex component Atg11p) results in Atg9p accumulation at the PAS (Yamamoto et al., 2012).

The mechanisms controlling recruitment of ATG9 to early autophagosomal structures has been carefully dissected in yeast. Atg9p-containing vesicles directly associate with Atg2p (Gómez-Sánchez et al., 2018) and COPII component Sec24p (Davis et al., 2016), as well as the Atg1p complex components Atg13p (Suzuki et al., 2015), Atg17p (Rao et al., 2016), cargo-bound Atg11p (He et al., 2006, Matscheko et al., 2019) and potentially Atg1p itself via its CTD, although only in its Atg13p-free form (Ragusa et al., 2012). Due to poor conservation, the relevance of these interactions in mammalian systems is often questionable, however some similarities are observed. For example, ATG9A directly binds ATG2A to be recruited to nascent autophagosomes as described in section 1.2.3.2 (Tang et al., 2019) and as the CTD of ULK also binds membranes, it could equally be speculated that it is implicated in ATG9A vesicle association (Chan et al., 2009).

Mammalian ATG9A cycling is regulated by direct post-translational modification. Mutating Ampk target sites in murine Ulk1 (serine 555, serine 637 and threonine 659) to alanine prevents the accumulation of Atg9a at perinuclear clusters (likely representing the TGN) in basal conditions (Mack et al., 2012). Interestingly, AMPK also directly phosphorylates ATG9A. Serine 761 phosphorylation is maintained at low levels in an AMPK- and ULK1-dependent manner in basal conditions, however in hypoxia AMPK-dependent phosphorylation at this residue is upregulated which is necessary for both ATG9A dispersal and LC3 puncta formation (Weerasekara et al., 2014).

More recently, ULK1 has been implicated in the direct phosphorylation of ATG9A to regulate its autophagic trafficking. Upon starvation, ULK1 phosphorylates ATG9A at serine 14 which acts synergistically with a phosphotyrosine at position 8 (which is phosphorylated constitutively to maintain retrograde trafficking of ATG9A from the plasma membrane) to promote starvation-dependent ATG9A export from the TGN and plasma membrane in an AP1/2 complex-dependent manner (Zhou et al., 2017). Furthermore, ULK1 phosphorylates the multifunctional kinase DAPK3, which in turn activates myosin II which physically interacts with ATG9A upon starvation to promote its dispersal from the TGN in mammalian cells (a model which is likely conserved in Drosophila) (Tang et al., 2011). Downstream of trafficking to the PAS, Atg1p associates with Atg9p via its C-terminal cytosolic region and phosphorylates Atg9p at 6 serine residues in the poorly conserved cytosolic regions (1 in the N-terminus, 1 in an inter-transmembrane-domain loop and 4 in the C-terminus) which is crucial for Atg18p and Atg8p recruitment and therefore the progression of starvation-induced autophagy (Papinski et al., 2014).

Additional ULK-independent ATG9A trafficking effectors have been identified, including ANXA2 and SNX18 which mediate cycling from early and recycling endosomes discussed in section 1.2 (Søreng et al., 2018a, Moreau et al., 2015). Further examples include RAB1 and RAB11, which mediate the constitutive cycling of ATG9A to the Golgi from endosomes (Lamb et al., 2016), AP4, which facilitates dispersal of ATG9A from the TGN upon starvation (Davies et al., 2018, Ivankovic et al., 2017, Mattera et al., 2017) and p38IP (gene name *SUPT20H*), which promotes ATG9A cycling by binding its C terminal region, a process likely augmented by the starvation-dependent inactivation of p38 MAPK (Webber and Tooze, 2010).

1.4 Aims

The ULK kinase complex is the master regulator and sole serine/threonine kinase in the canonical autophagy pathway. It is amongst the most upstream signalling components in both starvation-induced and basal autophagy, regulating the processes from initiation through to termination. Furthermore, ULK signalling is implicated in a broadening array of autophagy-independent activities. The scientific interest surrounding ULK kinase biology is demonstrated by the exponentially increasing volume of related articles published in past years, as well as the range of agonists and antagonists that have been developed recently (some of which have shown promise as anti-cancer agents) (Tang et al., 2017a, Ouyang et al., 2018, Zhang et al., 2017, Egan et al., 2015, Lazarus et al., 2015, Martin et al., 2018, Petherick et al., 2015). Despite such wide-ranging implications however, the specific mechanisms by which ULK1 and ULK2 orchestrate their cellular functions remain elusive.

The generation of $Ulk1^{-/-}$ /$Ulk2^{-/-}$ MEFs has proved instrumental in the characterisation of ULK-dependent phenotypes at a cellular level (McAlpine et al., 2013). Furthermore, recent crystallographic and biochemical analyses have provided a molecular insight into the structure and substrate specificity of the ULK1 kinase domain (Lazarus et al., 2015, Egan et al., 2015). I aim to use this knowledge to illuminate novel facets of ULK biology via the identification and characterisation of novel kinase substrates. I intend to employ a range of phosphoproteomic screening techniques to examine how removal of ULK affects the phosphoproteome, before interrogating these data to identify ULK phosphotargets. Promising candidates will be validated and their role in autophagy and other processes will be characterised.

Chapter 2. Materials and Methods

2.1 Cell culture and Transfection

2.1.1 Cell Culture

Dulbecco's Modified Eagle Medium-High Glucose (DMEM) and 0.25% trypsin-EDTA solution were purchased from Sigma and all cell culture vessels were from Corning. Earle's Balanced Salt Solution (EBSS) (5.56mM D-glucose, 123.08mM NaCl, 5.37mM KCl, 1.82mM CaCl2, 0.81mM $MgSO_4$, 0.99mMNa_2PO_4, 13.1mM $NaHCO_3$), phosphate buffered saline (PBS) (137mM NaCl, 3.4mM KCl, 10mM Na_2HPO_4, 1.8mM KH_2PO_4, pH7.2) and versene (0.02% (w/v) EDTA, 11mg/L phenol red in PBS) were produced by the Media Preparation Service, Francis Crick Institute.

MEFs, HEK293A and HEK293T were procured from Cell Services, Francis Crick Institute. $Ulk1^{-/-}$ $Ulk2^{-/-}$ MEFs used in the SILAC screen were described in (McAlpine et al., 2013). The $Ulk1^{-/-}$ $Ulk2^{-/-}$ MEF line used in the TMT screen, as well as the p150 knockout cells and their stably rescued counterparts were generated by myself (see section 2.1.3). All cell lines were maintained at 10% CO_2 and cultured in DMEM with the addition of 10% foetal bovine serum (FBS, Sigma), 500U/ml Penicillin + 100µg/ml Streptomycin (Pen-Strep, Sigma) and 4.8mM L-glutamine (full medium). The identity of every cell line utilised in this thesis was confirmed via short tandem repeat analysis (performed by Cell Services).

Cells were grown to ~90% confluency before passaging, which entailed washing once with versene before incubation for 2 minutes at 37˚C with 0.25% trypsin-EDTA solution. After detachment, full media was used to inactivate trypsin and to harvest cells from the culture vessel. For maintenance, a new vessel was seeded such that the cell confluency would reach 50% confluency the next day. This process was repeated until cells reached a passage number of 22, at which point they were discarded. For long-term storage, cells from a 90% confluent T75 flask were pelleted after trypsinisation (1000rcf, 3mins), before resuspension in 2ml ice-cold media (90% FBS, 10% DMSO). 0.5ml aliquots were frozen at -80C before delivery to the Cell Services facility for storage in liquid nitrogen. Upon retrieval, these aliquots were used to reseed a T75 flask.

Before seeding cells for treatment, coverslips, multi-well plates and 6, 10 or 15cm dishes were coated with poly-D-lysine (0.1mg/ml). Cells were grown for at least 16 hours before treatment. 'Fed' or 'basal' cells were cultured in full medium, and cells were incubated in EBSS to trigger amino acid starvation-induced autophagy. Prior to starvation, cells were washed 3x in EBSS before incubation for 1 hour unless otherwise stated. The following treatments were applied for specified times, diluted in either EBSS or full medium: SBI-0206965 (1μM, Sigma), MRT68921 (1μM, Sigma), Torin 1 (100nM, Cayman Chemical), Bafilomycin A1 (100nM, Calbiochem), Wortmannin (100nM or 10μM, Calbiochem), IN-1 (1μM, Cayman Chemical), Epoxomycin (10μM, Sigma) or AbK (0.1-1mM, Tocris).

To stain acidic endolysosomal compartments for immunofluorescence analysis (see section 2.3.12), media was supplemented with Lysotracker Red DND99 (1nM, Sigma) for 2 hours prior to fixation. To assess epidermal growth factor (EGF) and transferrin (Tfn) distribution by immunofluorescence, cells were washed three times and then pre-incubated for 60 minutes in serum-free medium (SFM). Cells were treated with SFM supplemented with fluorophore-conjugated ligands for 60 minutes prior to fixation. These were EGF-555 (2μg/ml, Thermo) and Tfn-647 (25μg/ml, Thermo).

2.1.2 Plasmid/siRNA transfection

When using plasmids, cells were grown to 70-80% confluency on the day of transfection. The standard transfection protocol in 12 well format follows. $1.2x10^5$ cells were plated on day 1 and on day 2 DNA and transfection reagent (Lipofectamine 2000 (Life Technologies)) were each diluted in separate tubes containing in 250μl OptiMEM per well and mixed gently. Unless otherwise specified, 0.5μg DNA and 1.2μl lipofectamine 2000 (lipo) per well were used. After incubating the lipo solution for 5 minutes at room temperature, it was mixed with the DNA solution at a 1:1 ratio. This was well mixed by inversion and incubated for 20 minutes at room temperature before drop-wise addition to cells. Cells were incubated with the DNA-lipo mixture for 4 hours before aspirating and replenishing with full media. 18-48 hours after transfection, cells were harvested.

siRNA stock was made up in siRNA dilution buffer (Dharmacon) to 20μM and was 'forward' or 'reverse' transfected at 50nM final concentration. For forward transfection in 6cm dish format,

cells were seeded to 50% confluency on Day 1. On Day 2, 5µl siRNA and 5µl lipo were each diluted separately in 500µl OptiMEM. After mixing and room temperature incubation for 5 minutes as previously described, the solutions were mixed 1:1 and incubated for a further 20 minutes at room temperature. The 1ml transfection mixture was added to the cells and incubated for 4 hours, at which time full media was replenished. For reverse transfection in 6cm dish format, siRNA and lipo mixtures were diluted in OptiMEM. Per dish, 5µl siRNA stock and 5µl lipo were diluted in to 200µl OptiMEM in separate mixtures. After mixing by inversion, the lipo mix was incubated at room temperature for 5 minutes before mixing at a 1:1 ratio, inverting and leaving to stand at room temperature for 20 minutes. This mixture (400µl) was added to a 6cm dish before addition of HEK293A cell suspension (1.6ml, ~$4.5x10^5$ cells total). One or two rounds of siRNA knockdown were utilised as indicated. Cells were analysed 72 hours after the first transfection.

For both plasmid and siRNA transfections, the volumes used in the transfection mixtures were scaled up or down relative to the surface area of the culture vessel used.

Table 2.1 siRNAs used in this thesis

Target Gene	siRNA	Target Sequence	Supplier
RISC-free	D-001220-01	N/A	Dharmacon
CAPZB (SMARTpool)	D-011990-01 D-011990-02	GAAGUACGCUGAACGAGAU GGAGUGAUCCUCAUAAAGA	Dharmacon
PIK3R4	D-005025-05	CAGCUGAUGUCUACUGUAA	Dharmacon
PI4K2A	(custom)	UGAAGCAGAACCUCUUCCUGAUU	Dharmacon

2.1.3 Lentiviral/retroviral transduction

$Ulk1^{-/-}$ $Ulk2^{-/-}$ (ULK1/2 DKO) MEFs derived by Harold Jefferies PhD were retrovirally immortalised by stable integration of SV40 large T antigen. 3rd generation lentiviral transfer vectors encoding wild type, S861A, S861E, ΔV50, 6SA or 6SE p150-HA_IRES_EGFP (see Table 2.7 and section 5.13 for details) were used to stably rescue p150 effective KO CRISPR clones (see section 2.2 for details). Pen-Strep was excluded from full media during all stages of viral transduction and was replenished after successful transduction.

HEK293T cells were used to produce both lentiviruses and retroviruses, with the former used for stable expression and the later for primary cell immortalisation. In both cases, a 10cm dish was seeded with $2x10^6$ HEK293T for each virus generated. To make lentiviruses, lentiviral transfer plasmids (pLV-CMV-MCS-SV40-Puro) along with plasmids encoding psPAX2 gag-pol packaging proteins and VSVG were transfected as previously described at a 4:3:1 ratio. Retroviruses were generated by transfecting plasmids encoding pBABE SV40T Puro, MMLVgag-pol and VSVG were transfected as described previously at a 3:2:1 ratio. In both cases, the cells were replenished with 6ml full medium after transfection. After 24 hours, the virus-containing media was collected and the dishes replenished with 6ml full medium. Polybrene (Sigma) was added to the virus-containing medium to a final concentration of 8µg/ml, before centrifugation at 4000rcf for 5 minutes and filtration through a 0.45µM Millex HV filter (Millipore).

When transducing with retroviruses, the target cell populations ($Ulk1^{-/-}$ $Ulk2^{-/-}$ primary MEFs derived from two independent embryos) were exposed to virus-containing media when already adherent. Before transduction, the MEFs were cultured in DMEM supplemented with 20% FBS. For lentiviral transduction, 5ml virus-containing medium was mixed with 5ml cell suspension ($1x10^5$ cells/ml) with this mixture used to seed a 10cm dish.

If lentiviral transduction efficiency was poor, viral media was again harvested from the HEK293T and Polybrene added before filtration as previously (i.e. 48hr virus-containing medium). The target cell population was then replenished with the new virus-containing medium. This process was repeated up to three times total. After 72 hours post-transfection the HEK293T cells were discarded. All lentivirus-transfected cells were selected by fluorescence activated cell sorting (FACS) 5-7 days after transduction. Cells expressing low levels of EGFP were pooled and retained for future experiments. Retrovirally-immortalised MEFs and p150 6SA/6SE-rescued sgA-D6 (p150 effective knockouts) were replenished with full medium supplemented with Puromycin (1µg/ml, Sigma) and maintained in selection media for a further 7 days resulting in a population in which all cells had been transduced.

2.2 CRISPR Clones

2.2.1 Generation of CRISPR/Cas9 knock out cell lines

p150 CRISPR knockout (KO) HEK293A were generated according to the Zhang laboratory protocol (Ran et al., 2013). Single guide RNAs (sgRNAs) targeting p150 (gene name *PIK3R4*) exon 2 were generated using an online design tool from the same group (now offline, previously available at https://zlab.bio/guide-design-resources), and were cloned into the pX458 vector – itself encoding EGFP-tagged spCas9. Three sgRNAs were designed to target different regions of exon 2 and after cloning the resulting three vectors were transfected into passage 4 HEK293A in 6 well dish format. After 24 hours, the cells were trypsinised and EGFP expressing cells were single cell FACS sorted into 96 well dishes. The cells were allowed to divide and media was refreshed as needed. When clonal cell populations reached 100% confluence, they were trypsinised and transferred into larger culture vessels for expansion and phenotypic/genotypic assessment.

Table 2.2 Guide RNAs used in this thesis

Primer Name	Primer Sequence (5'-3')
PIK3R4 Guide A Fwd	CACCGCAAAAACCTTCACAACGACCGTTT
PIK3R4 Guide A Rev	AAACGGTCGTTGTGAAGGTTTTTGCGGTG
PIK3R4 Guide B Fwd	CACCGAAGTCTACAAGCGGAGTTGAGTTT
PIK3R4 Guide B Rev	AAACTCAACTCCGCTTGTAGACTTCGGTG
PIK3R4 Guide C Fwd	CACCGACAAATCTGGAGTTCGTCATGTTT
PIK3R4 Guide C Rev	AAACATGACGAACTCCAGATTTGTCGGTG

2.2.2 Genotyping CRISPR Clones

$0.5x10^6$-$1x10^6$ cells of each CRISPR clone were trypsinised and pelleted. Each pellet was resuspended in 20µl PCR Yolk Buffer (Viagen Biotech) supplemented with RNAase (10µg total, Thermo) and incubated at room temperature for 10 minutes. An additional 20µl of PCR Yolk Buffer supplemented with 4µg Proteinase K (Life Technologies) was then added and the mix incubated with shaking for 60 minutes at 55˚C. To terminate the reaction, samples were heat inactivated at 85˚C for 60 minutes. 2µl of the resultant mixture was used as a template for PCR

amplification. Primers were designed to amplify a ~200 base pair region centred on the targeted protospacer adjacent motif, which varied depending on which sgRNA was used. The PCR reaction was performed using MegaMix Blue (Microzone):

PCR Reaction Mix:

46µl MegaMix Blue
2µl Genomic DNA mixture
1µl Forward primer (10µM)
1µl Reverse primer (10µM)

PCR Program:

Step	Cycles	Temperature (°C)	Time (Secs)
1	1	95	180
2	30	95	30
		51.5	60
		72	60
3	1	8	∞

TOPO TA cloning was used to ligate the fragment into a pCR 4 vector for sequencing.

TOPO Cloning mix:

4µl PCR product
1µl Salt Solution (200mM NaCl, 10mM $MgCl_2$)
1µl Linearised Vector

The mixture was incubated at room temperature for 4.5 hours then transformed (see section 2.4.6) into 40µl Stellar *E. coli* (strain HST08, Takara Bio). Bacteria were grown on LB-agar plates containing ampicillin, IPTG and X-Gal to facilitate drug resistance and blue/white screening. Colonies lacking a blue hue were expanded and the mini prepped plasmid was sequenced with

M13 Forward primers to reveal the sequence of the genomic PCR product. See section 2.4.6 for further details of the bacterial transformation and plasmid sequencing protocols.

2.3 Biochemistry

2.3.1 Antibodies

Table 2.3 List of primary antibodies

Antigen	Species	Antibody	Supplier	Dilution	Notes
ACTIN	Mouse	ab11003	Abcam	WB 1:1000	
ATG101	Rabbit	SAB4200175	Sigma	WB 1:1000	
ATG13	Rabbit	STO281	Tooze Laboratory	WB 1:1000	
ATG13 p318	Rabbit	600-401-C49	Rockland	WB 1:500	Dilute in TBST 5% milk
ATG14	Mouse	M184-3	MBL	WB 1:1000	
ATG2A	Rabbit	23226	Protein Tech	WB 1:1000	
BECN1	Rabbit	3738	Cell Signalling	WB 1:1000	
Beta Tubulin	Rabbit	6046	Abcam	WB 1:8000	
CapZB	Mouse	sc-136502	Santa Cruz	WB 1:1000	
EEA1	Rabbit	243	M. Claque PhD	IF 1:200	Triton X-100 permeabilisation
EGRF	Rabbit	4267	Cell Signalling	WB 1:1000	
ERK1/2	Mouse	6496	Cell Signalling	WB 1:2000	Dilute in TBST 5% BSA
ERK1/2 pT202/Y204	Rabbit	4370	Cell Signalling	WB 1:2000	Dilute in TBST 5% BSA
FAM21	Rabbit	sc-137995	Santa Cruz	WB 1:500	
FIP200	Rabbit	A301-536A-1	Bethyl Labs	WB 1:2000	
FLAG M2	Mouse	F3165	Sigma	WB 1:2000 IF 1:4000	Methanol permeabilisation
GAPDH	Mouse	MAB374	Millipore	WB 1:1000	
GFP	Mouse	3 E1	CRUK	WB 1:2000	

GST	Goat	RPN1236	GE Healthcare	Peptide Array 1:5000	HRP-Conjugates
HA	Mouse	901513	Biolegend	WB 1:1000	
HA	Rat	11 867 423 001	Roche	IF 1:1000	Methanol permeabilisation
LAMP1	Mouse	CD107a	BD	IF 1:250	
LC3B	Rabbit	ab48394	Abcam	WB 1:1000 IF 1:2000	Methanol permeabilisation
Myc	Mouse	9E10	CRUK	WB 1:1000 IF 1:400	
NRBF2	Mouse	TA803856	Origene	WB 1:1000	
p150	Rabbit	NBP1-30463	Novus	WB 1:2000 IF 1:100	Triton X-100 permeabilisation
p150 S861	Rabbit	STO343	Tooze Laboratory	WB 1:100	Neat sera, non-specific
p150 S861	Rabbit	STO344	Tooze Laboratory	WB 1:100	Neat Sera
p150 S861	Rabbit	STO344	Tooze Laboratory	WB 1:1800 (AP)	PBST 5%BSA, 440ng/µl, use with peptide competition
p150 S861	Rabbit	STO345	Tooze Laboratory	WB 1:100	Neat sera, non-specific
p150 S861	Rabbit	STO345	Tooze Laboratory	WB 1:900(AP)	246ng/µl, non-specific
p62	Guinea Pig	GP62-C	Progen Biotechnik	IF 1:300	Methanol permeabilisation
p62	Mouse	610833	BD	WB 1:500	
PI4K2A	Mouse	sc-390026	Santa Cruz	WB 1:500	
PRKAG2 p124	Rabbit	Rabbit 29	Tooze Laboratory	WB 1:100	
PRKAG2 p124	Rabbit	Rabbit 32	Tooze Laboratory	WB 1:100	

RPS6	Rabbit	2217	Cell Signalling	WB 1:1000	TBST 5% BSA, block without Tween 20
S6 p240/244	Rabbit	2215	Cell Signalling	WB 1:1000	TBST 5% BSA, block without Tween 20
TIM23	Mouse	611223	BD	WB 1:1000	
ULK1	Rabbit	sc-33182	Santa Cruz	WB 1:250	
ULK1 p757	Rabbit	6888	Cell Signalling	WB 1:1000	
UVRAG	Mouse	M160-3	MBL	WB 1:1000	
Vinculin	Mouse	V9264	Sigma	WB 1:30,000	
VPS34	Rabbit	3811	Cell Signalling	WB 1:250	
VPS34 p249	Rabbit	13857	Cell Signalling	WB 1:200	
WIPI2	Mouse	2A2	Dundee Cell Products	IF 1:250	Affinity purified. Methanol or triton X-100

(AP) = Affinity Purified

Table 2.4 List of secondary antibodies

Antigen	Conjugated to	Supplier	Dilution
Rabbit IgG	HRP	GE Healthcare	WB 1:5000
Mouse IgG	HRP	GE Healthcare	WB 1:5000
Rabbit IgG	Alexa Fluor 488	Life Technologies	IF 1:1000
Rabbit IgG	Alexa Fluor 555	Life Technologies	IF 1:1000
Rabbit IgG	Alexa Fluor 647	Life Technologies	IF 1:1000
Mouse IgG	Alexa Fluor 488	Life Technologies	IF 1:1000
Mouse IgG	Alexa Fluor 555	Life Technologies	IF 1:1000
Mouse IgG	Alexa Fluor 647	Life Technologies	IF 1:1000
Guinea Pig IgG	Alexa Fluor 555	Life Technologies	IF 1:1000
Rat IgG	Alexa Fluor 555	Life Technologies	IF 1:1000

2.3.2 Cell lysis for Western blot

For analysis of autophagic flux, protein expression or knockdown/knockout efficiency, adherent cells were washed 2x in PBS before lysis on ice in TNTE buffer (20mM Tris pH6.8, 150mM NaCl, 5mM EDTA, 1% w/v Triton X-100) containing 1X PhosSTOP (Roche) and 1X EDTA-Free Complete Protease Inhibitor cocktail (Roche). HEK293A that were starved in EBSS before lysis were not washed to minimise cell detachment. Single wells from a 12 well plate were lysed in 150µl lysis buffer, with volumes scaled up according to the surface area of the cell culture dish. Cells were pipetted up and down whilst scraping thoroughly with the pipette tip. Lysates were transferred to 1.5ml Eppendorfs before centrifugation for 5 minutes at 13,200rcf in a cooled centrifuge. Post-nuclear supernatants were transferred to fresh 1.5ml Eppendorfs before mixing with 5X sample buffer (213.5mM Tris-HCl pH6.8, 50% w/v glycerol, 16% β-mercaptoethanol, 15% w/v SDS, bromophenol blue) to a final concentration of 1X. At this stage, samples that were not analysed immediately were stored at -20˚C. For Western blot analysis, lysates in sample buffer were incubated at 100˚C for 5 minutes and briefly centrifuged. Lysates were then analysed by SDS PAGE.

2.3.3 Laemmli-SDS PAGE and Western blot protein transfer

Samples were loaded onto mini/midi NuPAGE 4-12% Bis-Tris precast gels (Life Technologies), before electrophoresis in MES (50mM MES, 50mM Tris Base, 0.1% SDS, 1mM EDTA, pH 7.3; Novex) or MOPS (50mM MOPS, 50mM Tris Base, 0.1% SDS, 1mM EDTA, pH 7.7; Novex) running buffer at 200V until the dye front reached the bottom of the gel. MES was used to improve separation of lower molecular weight proteins (e.g. LC3-I and LC3-II), however MOPS was used when analysing higher molecular weight proteins. For analysis of phosphorylation-dependent band shifts, SDS PAGE was performed using hand-poured 8% agarose gels comprising a running gel (for 9ml: 2.25ml 4X Running Buffer (1.5M Tris-HCl, 0.4% w/v SDS, pH8.8; Nat. Diag.), 2.408ml PAA/Bis (30% w/v Acrylamide, 0.8% w/v Bis-Acrylamide; Nat. Diag.), 4.5µl TEMED (Sigma), 45µl 10% w/v Ammonium Persulphate (Sigma), 4.293ml dH_2O) and a stacking gel ([or 4ml: 4X Stacking Buffer (0.5M Tris HCl, 0.4% w/v SDS, pH 6.8; Nat. Diag.), 0.6ml PAA/Bis (Nat. Diag.), 4µl TEMED (Sigma), 40µl 10% w/v Ammonium Persulphate (Sigma), 2.356ml dH_2O]. When using hand-poured gels, samples were electrophoresed in Tris-

Glycine running buffer (Glycine 190mM, 25mM Tris-HCl pH8.8, 1% w/v SDS,) until the 31KDa marker (Full-Range Rainbow Marker, GE Healthcare) reached the bottom of the gel.

Proteins were transferred onto polyvinylidene fluoride (PVDF) membrane using Genie Blotter (Idea Scientific Company). PVDF membrane was activated by wetting in methanol followed by rinsing in distilled water and soaking in transfer buffer (20% methanol, 150mM glycine, 20mM Tris base). Whatman 3mm Chromatography paper (GE Healthcare), transfer sponges and SDS PAGE gels were also soaked in transfer buffer prior to use. Proteins were transferred at 27V for approximately 90 minutes, with the transfer apparatus maintained in a 4˚C cold room. To assess transfer efficiency, membranes were incubated in Ponceau S (Sigma) for ~ 5 minutes before washing thoroughly in distilled water to remove excess unbound stain. Membranes were scanned before further processing.

2.3.4 Detection

Membranes were blocked in PBST (PBS 0.1% Tween 20 (Sigma)) plus 5% milk (Sigma) by rocking at room temperature for 20-60 minutes. Membranes were then incubated in primary antibodies diluted in the appropriate buffer, rocking overnight at 4˚C or 2-4 hours at room temperature. After primary antibody removal, membranes were washed 3x5minutes in PBST, discarding wash buffer each time. Membranes were then incubated in HRP-conjugated secondary antibodies, diluted in PBST 5% milk as indicated in Table 2.4, rocking at room temperature for 1 hour. Membranes were then rinsed 3 times with PBST before 3 further 5 minute washes with fresh PBST. Depending on the primary antibody used, in some cases either PBST 5% bovine serum albumin (BSA; Roche), TBST (Tris-Buffered Saline 0.1% Tween 20) 5% milk or TBST 5% BSA was used in place of PBST 5% milk during blocking as well as primary and secondary antibody incubation stages (see Table 2.3). In the latter two scenarios, TBST was used in place of PBST during washing stages.

Washed membranes were laid out on a clean glass plate before application of ECL reagent (Amersham ECL Prime Western Blotting Detection Reagent, GE) and incubation for 1 minute. Blots were drained, covered with cling film and exposed to chemiluminescence detection film (Amersham Hyperfilm ECL, GE). Immobilon Crescendo Western HRP Substrate (Merck Millipore) was utilised instead of ECL reagent to amplify signals that were particularly weak.

For instances where membranes were re-probed with additional primary antibodies, membranes were incubated with stripping buffer (200mM Glycine, 1% w/v SDS, pH2.5) for 12 minutes rocking at room temperature and then washed thoroughly (rinsed 6x with PBST and washed 3x5minute with PBST rocking at room temperature) before repeating the antibody staining process from the blocking stage.

2.3.5 Immunoprecipitation

For immunoprecipitation (IP) or coimmunoprecipitation experiments, $1.5x10^6$ cells were seeded in 10cm dishes on day 1 for transfection of plasmids for tagged bait proteins on day 2 as described in section 2.1.2. On day 3, cells were washed with cold PBS twice before addition of ice cold 500µl lysis buffer, and the dishes were scraped thoroughly to maximise lysate recovery. As indicated cells were incubated in EBSS for 30-60 minutes prior to lysis. Post-nuclear supernatants were prepared as in section 2.3.2. A sample of PNS was retained and mixed with sample buffer comprising the loading control/input sample.

The majority of IP experiments included in this thesis utilised antibodies covalently-conjugated to resins. The antibody-conjugate used along with the volume of 50% slurry utilised per 10cm dish is as follows: Anti-HA Affinity Matrix (Roche) – 30µl, Pierce™ Anti-HA Magnetic Beads (Thermo) – 25µl, FLAG M2 Affinity Gel (Sigma) – 30µl, Flow affinity resin (GE Healthcare) – 50µl, myc-Trap_A (ChromoTek) – 50µl and GFP-Trap_A (ChromoTek) – 10µl. When using pre-conjugated resins, beads were washed by adding 1ml PBS, briefly vortexing followed by pelleting beads via centrifugation (1 minute, 7000rcf) before removal of the buffer. This wash step was repeated once more with PBS and twice with lysis buffer before beads were resuspended in lysis buffer to reconstitute the 50% slurry. When using Pierce™ Anti-HA Magnetic Beads, all centrifugation steps were replaced with clearance using a magnetic stand.

To purify myc-Ulk1 1-427 for use in the peptide array-based *in vitro* kinase assay (see section 4.9), murine anti-myc 9E10 was bound to protein G sepharose beads (Sigma) as follows. To bind antibodies to beads, 50µl protein G sepharose slurry per 10cm dish was transferred to a 1.5ml Eppendorf and washed four times in PBS as described earlier. The beads were then resuspended in 700µl PBST and incubated with 15µg antibody, turning end over end at 4˚C for

60 minutes. The beads were then washed twice PBS. After the final aspiration, an equal volume of PBS was added to the volume of beads restore the 50% slurry.

IPs were performed by adding washed beads to the PNS before rotating end over end at 4˚C from 2-4 hours. 1.5ml Eppendorfs containing the lysate-resin mixture were centrifuged at 7000rcf to pellet the beads; a sample of the supernatant was retained and mixed with sample buffer in fresh tubes to constitute the unbound sample. The supernatant was then aspirated and the pelleted beads washed 3-5x1ml in TNTE containing 0.1% Triton X-100. Depending on the experiment, the beads were either processed further or fully aspirated and boiled in 30µl 2X sample buffer before SDS-PAGE and Western blot analysis.

When ULK kinases were immunopurified, to improve sample purity the NaCl concentration in the TNTE 0.1% Triton X-100 wash buffer was increased from 150mM to 300mM. To further decrease coimmunoprecipitation of non-specific proteins, HEK293A expressing ULK1-mutants (see Figure 4.2C) were lysed in TNTE supplemented with 10% w/v glycerol. When PRKAG2 and its fragments were immunoprecipitated (see section 4.10) for use in *in vitro* kinase assays (see below), RIPA (50mM Tris HCl, 150mM NaCl, 50mM NaF, 1mM EDTA, 1mM EGTA, 0.05% w/v SDS, 1% w/v Triton X-100, 0.5% w/v sodium deoxycholate) was used in place of TNTE to lyse cells to prevent the coimmunoprecipitation of active AMPK isoforms. In these experiments, both kinase and substrate immunoprecipitates were washed in TNTE 0.1% Triton X-100 wash buffer containing 500mM NaCl.

In some instances where expression levels of proteins differed, immunoprecipitates had to be normalised prior to Western analysis to allow proper comparison. For example, in the crosslinking screen optimisation experiments detailed in section 4.2, ULK1 WT expression levels were much greater than those of ULK1 TAG mutants, which also displayed expression differences between each other. In this case, the amount of ULK1 WT plasmid used for transfection was reduced empirically until the expression levels were within the same range. The total amount of DNA used for transfection was maintained by the proportionate addition of pcDNA3.1 (+) empty vector. In this case, to control for remaining variation samples were immediately frozen at -80˚C after lysis and loading control samples analysed by Western blot to test overexpression levels. Lysates were then thawed and volumes were altered accordingly before incubation with beads.

2.3.6 *In vivo* crosslinking

To express ULK mutants for use in crosslinking screen experiments (see sections 4.1-4.4), HA-ULK1_TAG mutants were coexpressed in HEK293A in 6 or 10cm dish format as described in section 2.1.2. Single plasmids encoding $tRNA^{Pyl}$ and either pyrrolysyl-tRNA synthetase (PylRS) or AbK-tRNA synthetase (AbKRS) were cotransfected with ULK1_TAG at a 1:1 ratio (or 2:2:1 [ULK1:AbKRS:ATG13] where ATG13-FLAG was included) and cells were cultured in medium containing 1mM 3'-azibutyl-*N*-carbamoyl-lysine (AbK, Tocris) or 1mM N(epsilon)-Boc-L-Lysine (Boc-Lysine, Alfa Aesar) as indicated. After 18 hours overexpression, HEK293A expressing mutant kinases/WT controls were starved for 60 minutes to activate autophagy. Immediately afterwards, starvation media was replaced with PBS and dishes with their lids removed were placed on ice for UV irradiation. This was achieved using a Blak-Ray (Fisher) lamp with a 365nm 100W bulb, placed 8cm from the dish surface. Cells were continuously irradiated for 10 minutes, a time shown to be sufficient to drive almost complete photolysis of AbK in solution in optimisation experiments. Cells were then lysed and kinase-substrate conjugation was assessed by Western blot (see section 2.3.4) or by mass spectrometry.

To generate crosslinking screen samples for mass spectrometry analysis (see sections 2.3.14 and 4.4), differentially SILAC-labelled control (ULK1 WT) and experimental (ULK1_TAG) sample protein levels were assessed by Bradford Assay (using Protein Assay Dye Reagent Concentrate (Biorad)) during which lysates were kept on ice. Based on the Bradford Assay results, equal levels of protein were mixed before HA-tagged kinases were immunoprecipitated using Pierce™ Anti-HA Magnetic Beads (Thermo) as described in section 2.3.5.

2.3.7 Immunoprecipitation-Recapture

Immunoprecipitation-Recapture (IP-Re) was performed to increase the purity of crosslinking screen samples (see above and section 4.4). Immediately after pull down and washing, beads were incubated in 50µl denaturing elution buffer (0.1M Tris HCl pH7.5, 1% w/v SDS, 10mM dithiothreitol) for 5 minutes at room temperature and 5 minutes at 95°C before being allowed to cool to room temperature. 10µl 10% (w/v) BSA was added and the solution mixed gently before the addition of 1ml non-denaturing lysis buffer (50mM Tris HCl pH7.5, 1% w/v Triton X-

100, 300mM NaCl, 5mM EDTA, 0.02% w/v NaN_3, 10mM iodacetimide, 1X EDTA-free Complete Protease Inhibitor cocktail (Roche)). A second round of immunoprecipitation was then performed using Pierce™ Anti-HA Magnetic Beads (Thermo) as described in section 2.3.5 and the resulting IP sample was prepared for mass spectrometry analysis (see section 2.3.14).

2.3.8 Elution

In section 4.9, peptide competition was utilised to elute immunoprecipitated myc-Ulk1 from beads for use in *in vitro* kinase assays in peptide array format (see below). Before lysis and immunoprecipitation, all kinase-expressing cells were incubated in EBSS for 1 hour to activate Ulk1. Where wild type vs kinase inactive Ulk1 were compared, 2x10cm HEK293A dishes overexpressing myc-Ulk1 WT and 8x10cm dishes overexpressing myc-Ulk1 KI were generated. When Ulk1 WT +/- inhibitor were compared, 6x10cm dishes were transfected with myc-Ulk1 WT, 3 of which were treated with EBSS supplemented with the small molecule ULK1 inhibitor MRT68921 prior to lysis. In both cases, 500µl lysis buffer was used per 10cm dish. Like lysates were pooled and myc-Ulk1 was then immunoprecipitated from 1ml aliquots using anti-myc 9E10-coated beads as described in section 2.3.5. After washing, the supernatant was aspirated before the beads were shaken at room temperature for 20 minutes in 100µl kinase reaction buffer per 10cm dish (KRB - 20mM HEPES pH7.4, 20mM $MgCl_2$, 25mM beta-glycerophosphate, 2mM dithiothreitol, 100µM sodium orthovanadate) supplemented with 0.5mg/ml myc peptide (see Table 2.5). Ulk1 KI eluates were combined and aliquots were taken to assess protein expression level. For Ulk1 WT + inhibitor samples, MRT68921 was added to the elution buffer, such that the final concentration in the *in vitro* kinase assay reaction mixture was 1µM (see below).

2.3.9 *In vitro* kinase assay

To test the phosphorylation of putative substrates by ULK *in vitro*, both kinase and substrate were immunoprecipitated as described in section 2.3.5. Before lysis, myc-Ulk1 WT/KI expressing cells were incubated in EBSS for 30-60 minutes and in all cases other than the kinase assay in peptide array format (see below), both kinase and substrate were bead-bound during *in vitro* phosphorylation. After immunoprecipitation and washing, beads were subject to an additional wash step with KRB before aliquots of kinase- or substrate-bound resin were

mixed in specified combinations. Samples of substrate or kinase were also analysed alone as negative controls. Each sample was fully aspirated before addition of 32µl KRB supplemented with 100µM ATP and 2µCi ATP[γ-^{32}P] (Easy Tide Lead, Perkin Elmer) was added to the beads, before incubation at 30˚C for 30 minutes. Reactions were ended via addition of 5X sample buffer to a final concentration of 1X and samples were electrophoresed by SDS PAGE. The gels were fixed using Instant Blue Coomassie staining (Expedeon) and then destained using dH_2O. Stained gels were dried before being used to expose autoradiography/chemiluminescence film (Amersham Hyperfilm ECL, GE).

Where *in vitro* phosphorylation was detected by band shift or utilised to enrich for phosphorylated epitopes when testing phosphoantibodies (i.e. where maximal substrate phosphorylation was desirable) the kinase assay reaction mixture consisted of KRB with 1.8mM ATP without radioactive ATP. 'Cold' ATP *in vitro* kinase assay samples were analysed by Western blot (see section 2.3.4).

As discussed above, Ulk1 was eluted to assess phosphorylation of arrayed peptides *in vitro* (see section 4.9). Peptide arrays were produced by the Peptide Chemistry STP, Francis Crick Institute. For each experiment, two identical array membranes were incubated in methanol for 2 minutes for activation, before rinsing thoroughly with wash buffer (20mM HEPES pH7.4, 0.02% Triton X-100). Complete removal of methanol was achieved by 4x10 minute further washes with wash buffer. Membranes were rocked overnight at 4˚C in blocking buffer (20mM HEPES pH7.4, 0.02%Triton X-100, 0.2mg/ml BSA). The next day, Ulk1 WT/KI or WT+/- inhibitor kinase eluates were generated before diluting to 5ml in protein dilution buffer (KRB 0.05mg/ml BSA). Kinase samples were diluted 1:1 with ATP solution (KRB + 200µM ATP, 200µCi ATP[γ-^{32}P]) to generate the reaction mixtures. For each experiment, the two 10ml reaction mixtures were added to the peptide array membranes and incubated with gentle rocking at room temperature for 15 minutes. The membranes were rinsed well in PBS before washing extensively as follows (each stage involved gently rocking for 10 minutes at room temperature): 2x PBS, 3x 30% Glacial Acetic Acid (Fisher), 2x dH_2O, 1x 0.1N NaOH, 2x dH_2O, 2x 30% Glacial Acetic Acid. Following this, membranes were soaked in methanol before air drying. Peptide phosphorylation was visualised via exposure of dried membranes to autoradiography/ chemiluminescence film (Amersham Hyperfilm ECL, GE).

2.3.10 λ phosphatase assay

For cell lysates intended for dephosphorylation the cells were lysed in TNTE lacking both EDTA and phosphatase inhibitor (PhosSTOP, Roche), before PNS samples were generated as described in section 2.3.2. IP samples intended for dephosphorylation were generated as described in section 2.3.5 until the washing stage, during which the samples were washed in TNTE 0.1% Triton X-100 lacking EDTA and phosphatase inhibitor (PhosSTOP, Roche). After 3x 1ml washes, IP samples were reconstituted with wash buffer to facilitate phosphatase treatment.

Typically, 79µl of sample intended for dephosphorylation was transferred into 1.5ml Eppendorfs. To this was added 10µl of 10mM $MnCl_2$ (New England Biolabs), 10µl 10X PMP buffer (0.5M HEPES, 0.1M NaCl, 20mM dithiothreitol, 0.1% Brij 35 - New England Biolabs) and 1µl λ phosphatase. Where negative controls were included, λ phosphatase was replaced in the reaction mixture with 100µM sodium orthovanadate. These volumes were scaled up accordingly when larger sample volumes were dephosphorylated. The samples were mixed well and incubated for 30 minutes at 30˚C before stopping the reaction with the addition of 5X sample buffer to a final concentration of 1X. Reaction efficiency was assessed by Western blot analysis.

2.3.11 Phosphoantibody generation

To generate phosphoantibodies, 15mer peptides spanning the target phosphosites were generated by Dhira Joshi in the Peptide Chemistry STP, Francis Crick Institute (p150 phosphoS861) or by Covalab, UK (PRKAG2, phosphoS124). In each case, both phosphorylated and non-phosphorylated peptides were made with the former used for inoculation; peptides were made with an end cysteine to allow carrier protein conjugation. Between 2 and 3 rabbits were immunised per epitope. Control sera were taken on day 0 and rabbits were immunised several times over a 77-day procedure. Two p150 S861 sera derived after exsanguination (STO344 and STO345) were purified based on their affinity for the phosphoS861 peptide (see Table 2.3)

Table 2.5 List of peptides

Name	Amino Acid Sequence	Application
Myc	EQKLISEEDL	Elution of mUlk1 1-427
PRKAG2 S124	CRSPRRMSFSGIFRS	Generation of PRKAG2 S124 phosphoantibodies
PRKAG2 phospho-S124	CRSPRRMSF(pS)GIFRS	Generation of PRKAG2 S124 phosphoantibodies
p150 S861	NVNEEWKSMFGSLDC	Generation of p150 S861 phosphoantibodies. Removal of non-specific antibodies during STO344 affinity purification
p150 phospho-S861	NVNEEWK(pS)MFGSLDC	Generation of p150 S861 phosphoantibodies

* pS=phosphorylated serine. See Appendix Table B and Appendix Table D for details of peptides synthesised in array format

2.3.12 Peptide array overlays

To assess binding of Atg8 homologs to predicted p150 LIRs, WT and phosphomutant peptides spanning each of the selected LIRs were immobilised on peptide arrays (see section 5.16 and a Appendix Table D). 7 duplicate arrays were activated by brief incubation with methanol, which was removed by rinsing thoroughly with TBST followed by 3x5minute washes with TBST rocking at room temperature. Arrays were blocked via rocking at room temperature in TBST 5% milk for 60 minutes, after which residual milk was removed via rinsing and washing as before. GST constructs were purified from *E. coli* by Martina Wirth PhD. 20µg aliquots of each GST construct (GST-LC3A, GST-LC3B, GST-LC3C, GST-GABARAP, GST-GABARAPL1, GST-GABARAPL2 and GST alone) were diluted to 20ml in TBST to a final protein concentration of 1µg/ml and incubated with the peptide arrays for 2 hours with gentle rocking at room temperature. The arrays were rinsed with TBST followed by 3x5minute TBST washes. Arrays were then incubated for 60 minutes at room temperature with rocking in TBST 5% milk containing HRP-conjugated anti-GST-specific antibodies (see Table 2.3). The binding of Atg8 homologs was assessed by exposing membranes to autoradiography/chemiluminescence detection film (Amersham Hyperfilm ECL, GE).

2.3.13 Immunofluorescence labelling and confocal microscopy

For immunofluorescence (IF), $1.2x10^5$ cells were plated on coverslips coated with poly-D-lysine in 12 well plates the day before fixation. If cells were to be transfected on day 2, no fewer than $1.0x10^5$ cells were plated on day 1 due to toxicity associated with Lipofectamine 2000 transfection. All fixation and subsequent permeabilisation and staining steps were performed at room temperature. Coverslips were fixed by incubation with 3% paraformaldehyde (Agar Scientific) in PBS supplemented with 0.01mM $CaCl_2$ and 0.01mM $MgCl_2$ for 20 minutes followed by washing once in PBS. Cells were then permeabilised by one of 2 methods, either with incubation in room temperature methanol for 5 minutes or with 0.2% Triton X-100 (w/v) in PBS (see Table 2.3). The cells were then washed twice in PBS to remove residual permeabilisation agent, then PBS 5% BSA was used to block fixed cells for 30 minutes before the coverslips were inverted onto 50µl drops of primary antibody solution and incubated for 60 minutes. Coverslips were then washed four times with PBS and then incubated with fluorophore-conjugated secondary antibodies in the same manner. Primary and secondary antibodies were diluted in PBS 5% BSA as indicated in Tables 2.3 and 2.4. When specified, secondary antibody solutions were supplemented with Hoechst (Sigma) to a final concentration of 5µg/ml. After incubation with secondary antibodies, coverslips were washed four times in PBS then a further four times in dH_2O and mounted onto glass microscope slides (Thermo) with 4µl Moiwol 4-88 (Calbiochem) used as the mounting medium.

Coverslips were imaged using a Zeiss LSM 710 Axioplan 2 laser-scanning microscope with a 63X, 1.4NA oil immersion objective (Carl Zeiss MicroImaging, Inc). Slice thickness was 1µm and laser settings kept constant between images and conditions.

2.3.14 Preparation of samples for mass spectrometry analysis

SILAC phosphoproteomic screen samples (see Chapter 3) were generated by Harold Jefferies PhD in collaboration with the Proteomics STP, Francis Crick Institute. Before generating crosslinking screen samples (see section 4.4), low passage HEK293A were cultured in DMEM for SILAC (Thermo) supplemented with either light- (R0, K0) or heavy- (K8, R10) isotopically labelled lysine and arginine along with 10% FBS (Sigma) and Pen-Strep (Sigma). Cells were cultured for >3 weeks and full label incorporation confirmed by mass spectrometry before use.

Cells were transfected and processed as described in section 2.3.6. Mixed lysate as well as samples after the first and second immunoprecipitation stages were separated by SDS PAGE on a precast 4-12% mini gel (NuPAGE) until the dye front was ~2/3 to the bottom. The gel was fixed and stained (Instant Blue, Expedeon) and destained in dH_2O. The fixed gel was cut as depicted in Figure 4.4D. Protein extraction via in-gel digestion and data generation was performed by the Proteomics STP.

To generate starvation time course samples for TMT analysis, 5x15cm dishes were seeded with $2.8x10^6$ WT MEFs or $3x10^6$ ULK1/2 DKO MEFs (10 dishes total). Slightly more DKO MEFs were plated to account for differences in growth rate between cell lines. The next day paired WT/DKO dishes, which were ~80% confluent, were subject to EBSS starvation over a time course as indicated in section 4.5. Cells were then trypsinised as described in section 2.1.1, washed in 10ml PBS 0.1% (w/v) BSA to inactivate trypsin, pelleted via centrifugation at 3000rcf for 1 minute, washed in 20ml ice cold PBS to remove BSA, pelleted via centrifugation at 3000rcf for 1 minute then lysed in 200µl 8M Urea lysis buffer (8M Urea, 50mM HEPES pH8.2, 75mM NaCl, 1X PhosStop (Roche), 1X Complete EDTA-Free Protease Inhibitor). Lysates were sonicated ([10 second pulse, 10 second rest]x6) then frozen at -80˚C for storage. Lysates were thawed and protein concentration was assessed by using the Coomassie Plus (Bradford) Assay Kit (Thermo). For each sample, 129µl 1.7µg/µl aliquots were made (~220µg protein per aliquot), which were subject to full trypsin/rLysC (Promega) digestion and processed for TMT analysis via manufacturer's instructions (TMT 10plex™, #90110, Thermo). Phosphopeptides were enriched using the High-Select SMOAC Protocol, with half the peptide pool subject to TiO2 Phosphopeptide Enrichment (#A32993, Thermo) and the remaining half subject to Fe-NTA Phosphopeptide Enrichment (#A32992, Thermo) as per manufacturer's instructions. The enriched TMT-labelled phosphopeptides were pooled before high pH fractionation Pierce High pH Reverse-Phase Peptide Fractionation Kit (#84868, Thermo). Mass spectrometry data were generated by the Proteomics STP, Francis Crick Institute.

To examine p150 phosphorylation by overexpressed Ulk1 *in vivo* (see Figure 5.1A), HEK293A in 10cm dish format were transfected with VPS34 complex 1 components (see Table 2.7) alone or with myc-Ulk1WT or myc-Ulk1KI. Cell lysis was followed by VPS34 complex 1 immunoprecipitation via ATG14-ZZ using IgG Sepharose 6 Fast Flow affinity resin as described in section 2.3.5. The resulting IP samples were electrophoresed on a precast 4-12% mini gel

(NuPAGE) before fixation and staining (Instant Blue, Expedeon) and destaining using dH_2O. The bands corresponding to p150 were excised. Protein extraction, mass spectrometry and data analysis were performed by the Proteomics STP, Francis Crick Institute. Phospho-serine/threonine residues specifically enriched in myc-Ulk1 WT-expressing cells were considered potential direct substrates. For notes on mass spectrometry data analysis, see section 2.5.4.

2.3.15 Assessing VPS34 complex characteristics in vitro

In vitro reconstitution of VPS34 complexes was performed by Yohei Ohashi PhD in the laboratory of Roger Williams. Wild type, 6SA or ΔV50 p150-ZZ (mutant constructs provided by myself, see Table 2.7) were coexpressed with VPS34 complex members before cell lysis, coimmunoprecipitation, ZZ tag cleavage and size exclusion chromatography. Thermal stability assays as well as GUV and SUV *in vitro* lipid kinase assays were performed by Yohei, and SUV liposome floatation assays were performed by Shirley Tremel.

2.4 Molecular Biology

2.4.1 PCR

PCR (polymerase chain reaction) was performed using a PTC-200 thermal cycler (MJ research). With the exception of CRISPR clone genotyping (see section 2.2.2) PCR was performed using AccuPrime™ *Pfx* DNA Polymerase (Thermo).

PCR Reaction Mix:

10X AccuPrime™ *Pfx* Reaction Mix	5µl
Template DNA mixture (100µg/µl)	1µl
Forward primer (10µM)	1µl
Reverse primer (10µM)	1µl
AccuPrime™ *Pfx* DNA Polymerase (2.5 U/µL)	1µl
dH_2O	41µl

PCR Program:

Step	Cycles	Temperature (°C)	Time (Secs)
1	1	95	120
2	30	95	30
		Ta (55–64)	30
		68	60/kb
3	1	8	∞

Ta = Primer-specific annealing temp

Typically, the full PCR product was either directly assessed by agarose gel electrophoresis (see below) or purified for digestion with restriction enzymes (see section 2.4.3). The Nucleospin column purification kit (#740609, Macherey Nagel) was utilised to purify the PCR reaction as per manufacturer's instructions, with DNA eluted by passing 2x20µl TE (Tris-EDTA) buffer (Macherey Nagel) through the column with 2 minute incubations at 65°C prior to centrifugation.

2.4.2 DNA agarose gel electrophoresis

Depending on the sizes of DNA fragments to be analysed, gels were made containing 0.7%-2% (w/v) agarose in 1X Tris-borate-EDTA (TBE) buffer (Media Preparation Service, Francis Crick Institute). Agarose was melted using a microwave and poured into a gel mould. Immediately after pouring the gel, ~10µl GelRed (Biotium) per 100ml molten agarose was added and stirred well before the gel was allowed to set at room temperature. 6X Gel Loading Dye (New England Biolabs) was added to DNA solutions to a final concentration of 1X before loading into the gel along with molecular weight markers (HyperLadder™ 1kb, Bioline). Samples were electrophoresed at 150V (120V for smaller gels to prevent melting) after which DNA was imaged using a BioDoc-It®2 imaging system (UVP). Where appropriate, bands were excised and gel slices transferred to a fresh 1.5ml Eppendorf. During excision, DNA was visualised using a benchtop UV transilluminator (UVP) with exposure time to UV minimised. Gel slices were purified using the Nucleospin column purification kit (Macherey Nagel) as per manufacturer's instructions with DNA eluted in 2x20µl TE buffer with 2 minute incubations at 65°C as before.

2.4.3 DNA digestion with restriction enzymes

All restriction enzymes and associated buffers were purchased from New England Biolabs. PCR fragments and plasmid DNA were digested as per the manufacturer's instructions.

Restriction Digest Reaction Mix:

10X Reaction buffer (CutSMART, 2.1 or 3.1)	5µl
DNA	Xµg
Restriction enzyme (maximum 2 used)	1µl per enzyme
dH_2O	to 50µl

Restriction digests were performed at 37°C for 60 minutes and enzymes were heat inactivated (20 minutes at 65°C or 80°C) if possible. If plasmid DNA was singly digested for use in DNA ligation, 5´ and 3´ ends were dephosphorylated using Antarctic Phosphatase (New England Biolabs). In this case, the restriction digest reaction mix was supplemented prior to digestion with 5µl Antarctic Phosphatase Reaction Buffer (10X) and 10 units Antarctic Phosphatase.

2.4.4 DNA ligation

Ligation of linearised DNA fragments was performed using T4 DNA Ligase (New England Biolabs) as per the manufacturer's instructions.

Ligation Reaction Mix (volumes specified by manufacturer are halved):

10X T4 DNA Ligase Buffer	1µl
Vector DNA	50ng
Insert DNA	5:1 molar ratio
Nuclease-free dH_2O	to 10µl

The following formula was used to calculate insert DNA amount [5(insert length bp/vector length bp) x vector amount ng = insert amount ng]. If ligations were unsuccessful, insert:vector ratios were increased or elution buffer (see section 2.4.2) was changed from TE to nuclease-

free dH_2O. T4 ligase was heat inactivated for 10 minutes at 65°C and the resultant ligation product was used to transform One Shot™ TOP10 (see section 2.4.6).

2.4.5 Site-directed mutagenesis

Both QuikChange Multi Site-Directed Mutagenesis (Agilent Technologies) and Q5 Site-Directed Mutagenesis (New England Biolabs) kits were utilised to facilitate site-directed mutagenesis (SDM). In both cases, primers were designed to incorporate single or multiple nucleotide mismatches as per the manufacturer's instructions. The primers used in this thesis are listed in Table 2.6.

In the Quikchange mutagenesis protocol, single-stranded mutagenized products were generated by the replication of template DNA with single mutagenic primers in a *PfuTurbo* DNA Polymerase-dependent manner. Single-stranded products were ligated by nickases in the proprietary enzyme mix. In the second stage of the protocol, parental/unmodified DNA strands were destroyed by Dpn1 endonuclease treatment (75 minutes at 37°C followed by 20 minutes at 80°C to heat inactivate) and the single-stranded mutagenized product was used to transform XL-10 Gold ultracompetent cells (see below).

When using the Q5 Site-Directed Mutagenesis kit, pairs of mutagenic primers were used to generate double stranded mutagenized plasmids using Q5 Hot Start High-Fidelity DNA Polymerase. Termed the KLD (Kinase-Ligase-Dpn1) reaction, the second step involved Dpn1-dependent template strand degradation and 5' end phosphorylation/ligation of the mutagenized product. The KLD reaction was perforemd at room temperature for 10 minutes before being used to transform NEB 5-alpha *E. coli* (New England Biolabs) (see below). The Q5 SDM protocol was faster and more efficient than the QuikChange SDM protocol so was used preferentially.

In both instances, colonies obtained after plating transformed bacteria (see below) were selected for mini-prep plasmid purification and verification by sequencing.

QuikChange SDM PCR reaction mixture (volumes specified by manufacturer are halved):

10X QuikChange Multi reaction buffer	1.25µl
QuikSolution	0.25µl
Template DNA (100ng/µl)	0.5µl
Mutagenic primer (100ng/µl)	0.5µl
dNTP mix	0.5µl
QuikChange Multi enzyme blend	0.5µl
dH_2O	9µl

QuikChange SDM PCR Program:

Step	Cycles	Temperature (°C)	Time (Secs)
1	1	95	60
2	30	95	60
		55	60
		65	120/kb
3	1	8	∞

Q5 SDM PCR reaction mixture (volumes specified by manufacturer are halved):

Q5 Hot Start High-Fidelity 2X Master Mix	6.25µl
Template DNA (25ng/µl)	0.5µl
Forward mutagenic primer (10µM)	0.625µl
Reverse mutagenic primer (10µM)	0.625µl
dH_2O	4.5µl

Q5 SDM PCR Program

Step	Cycles	Temperature (°C)	Time (Secs)
1	1	98	30
2	25	98	10
		Ta (50–72)	30
		72	30/kb
3	1	8	∞

Ta = Primer-specific annealing temp

Q5 SDM KLD reaction mixture (volumes specified by manufacturer are halved):

2X KLD reaction buffer	2.5µl
PCR Product	0.5µl
10X KLD enzyme mix	0.5µl
dH_2O	1.5µl

2.4.6 Bacterial transformation

Chemically competent *E. coli* (DH5α – Life Technologies, NEB 5-alpha – New England Biolabs, Stellar – Takara Bio, One Shot™ TOP10 – Life Technologies, XL10-Gold – Agilent) were stored at -80°C. Bacteria were thawed on ice and 25µl aliquots were used for transformation. When transforming ligation or SDM products, 5µl of the final DNA reaction mixtures were added to bacteria and when maxi-prepped DNA was transformed 500ng was used. When transforming QuikChange SDM products into XL10-Gold, 1µl β-mercaptoethanol (provided with the kit) was gently mixed with the bacteria which were then incubated on ice for 10 minutes before introduction of DNA. Bacteria and DNA were gently mixed and incubated on ice for 30 minutes before being heat shocked at 42°C for 30 seconds. After a further incubation on ice for 5 minutes, 950µl LB (1% w/v Bacto-Tryptone, 0.5% w/v yeast extract, 170mM NaCl – Francis Crick Institute) or 250µl SOC (2% w/v tryptone, 0.5% w/v yeast extract, 10mM NaCl, 27mM KCl, 21mM $MgCl_2$, 20.8mM $MgSO_4$, 20mM D-glucose – Francis Crick Institute) were added to the mixtures (LB to DH5α, NEB 5-alpha and Stellar, SOC to One Shot™ TOP10 and XL10-Gold,) and the bacteria were recovered shaking at 37°C in an Eppendorf Thermomixer for 1 hour. Bacteria were then spread onto LB-agar plates (1% w/v Bacto-Tryptone, 0.5% w/v yeast extract, 170mM NaCl, 1.5% agar – Francis Crick Institute) containing either ampicillin (100mg/ml) or kanamycin (50mg/ml). When ligation or QuikChange SDM products were transformed (into One Shot™ TOP10 and XL10-Gold respectively), the whole ~275µl volume was plated. When TOPO cloning products, Q5 SDM products or maxi prepped DNA was transformed (into Stellar, NEB 5-alpha and DH5α respectively), 100µl was plated. Overnight incubation at 37°C allowed formation of bacterial colonies.

2.4.7 Purification of plasmid DNA

When selecting clones for sequencing, bacterial colonies were used to inoculate 5ml starter cultures of LB containing the appropriate antibiotic at the same concentration as given above. Cultures were incubated shaking at 37°C overnight before pelleting at 4122rcf for 8 minutes. The pellets (typically 8-16 per plasmid when sequencing ligation or SDM products) were processed by the Genomics Equipment Park STP, Francis Crick Institute.

When larger quantities of plasmid DNA were required, colonies were picked as before and used to inoculate 200ml LB containing the appropriate antibiotic. Bacterial cultures were grown in a shaking incubator at 37°C for 24 hours before pelleting at 4122rcf for 8 minutes. Plasmid DNA maxi-prep purifications were performed using Nucleobond Xtra Midi Plus kit (Macherey Nagel) as per manufacturer's instructions. The resulting DNA was precipitated and washed before dissolving in TE buffer. DNA concentration was measured using a Nanodrop spectrophotometer (Thermo). DNA was then diluted in TE to a final concentration of 1µg/µl and stored at -20°C.

2.4.8 Primers

All primers were purchased from Sigma.

Table 2.6 Primers used in this thesis

Primer Name	Primer Sequence (5'-3')	Used for	To make
SORBS2_S239A	TGTATCAGTCCTCTATAGAC GGAGCCCTGGAAAGACCCA	SDM (QC)	FLAG-SORBS2 S239A
SORBS2_S298A	CAAAGTCTTTCACTAGCGCT TCTCCTTCTTCCCCA	SDM (QC)	FLAG-SORBS2 S298A
SORBS2_S299A	TGATGGGGAAGAAGGAGCA GAGCTAGTGAAAGACT	SDM (QC)	FLAG-SORBS2 S299A
SORBS2_S301A	GCTCTTGATGGGGAAGCAG GAGAAGAGCTAGTG	SDM (QC)	FLAG-SORBS2 S301A
SORBS2_S302A	CTCTTGATGGGGCAGAAGG AGAAGAGCTAGTGAAAG	SDM (QC)	FLAG-SORBS2 S302A

ULK1_TAG_H105	GCGTGCGCATGGCCTACAG GTAGTCGGCC	SDM (QC)	HA-ULK1_TAG_H105
ULK1_TAG_R108	CTACCTGCACGCCATGTAGA CGCTGAGCGAGGACA	SDM (QC)	HA-ULK1_TAG_R108
ULK1_TAG_Q142	CGCGACCTGAAACCGTAGA ACATCCTGCTGT	SDM (QC)	HA-ULK1_TAG_Q142
ULK1_TAG_M186	CTGCGGCTCCCCCTAGTACA TGGCCCCC	SDM (QC)	HA-ULK1_TAG_M186
ULK1_TAG_K218	GCCTGACGGGGTAGGCGCC CTTC	SDM (QC)	HA-ULK1_TAG_K218
ULK1_TAG_Q222	AAGGCGCCCTTCTAGGCCA GCAGCC	SDM (QC)	HA-ULK1_TAG_Q222
AbKRS_QF_NES	CCGCCGCTGGAACGCCTGA CCCTGGATGGGGATAAAAA ACCATTAGATGTTTTAATAT CTGC	SDM (Q5)	NES-AbKRS
AbKRS_QR_NES	CAGCTGCAGCGGCACCGGG CACGCCATGGTGGCAAGCTT CCGTGC	SDM (Q5)	NES-AbKRS
ULK1_D165N	CATCCGCGTCAAGATCGCTA ACTTCGGCTTCG	SDM (QC)	ULK1 D165N crosslinking mutants
ATG13_S355/356A	AGGATACTGAAACCGTATCA AACGCCGCTGAGGGACGGG CCTCC	SDM (QC)	ATG13-FLAG S355/356A
RUBCN_QF_S350A	TCGCTCCCATGCGGATACCA G	SDM (Q5)	Rubicon-GFP S351A
RUBCN_QR_S350A	ATGTGGCTTTTCTTTGCCC	SDM (Q5)	Rubicon-GFP S351A
RUBCN_QF_S350D	TCGCTCCCATGATGATACCA GCATTG	SDM (Q5)	Rubicon-GFP S351D
RUBCN_QR_S350D	ATGTGGCTTTTCTTTGCC	SDM (Q5)	Rubicon-GFP S351D
ATG2A_QF_S1268A	GAGTCCTGCCGCTCTGCCCT C	SDM (Q5)	HA-ATG2A S1266A

ATG2A_QR_S1268A	TCCGAGAGCTGTACCTTCTG	SDM (Q5)	HA-ATG2A S1266A
ATG2A_QF_S1268D	GAGTCCTGCCGATCTGCCCTCG	SDM (Q5)	HA-ATG2A S1266D
ATG2A_QR_S1268D	TCCGAGAGCTGTACCTTC	SDM (Q5)	HA-ATG2A S1266D
PI4K2A_QF_ST462/6AA	CCTACGCACAGAGCTTTCAGAGCCG	SDM (Q5)	GFP-PI4K2A STAA siR
PI4K2A_QR_ST462/6AA	ACTCGGCAGAAGACCGCTGGTGGGA	SDM (Q5)	GFP-PI4K2A STAA siR
PI4K2A_QF_ST462/6DD	CTACGACCAGAGCTTTCAGAGCCGG	SDM (Q5)	GFP-PI4K2A STDD siR
PI4K2A_QR_ST462/6DD	GACTCGTCAGAAGACCGCTGGTGGGA	SDM (Q5)	GFP-PI4K2A STDD siR
PI4K2A_QF_insCA	CACCTGTGATTGTCGAGACGG	SDM (Q5)	GFP-PI4K2A siR
PI4K2A_QR_insCA	GCATCTGGACGAGGTGCA	SDM (Q5)	GFP-PI4K2A siR
PI4K2A_QF_siR	CCGCTGCCTGAGAACACTAACCGGC	SDM (Q5)	GFP-PI4K2A siR
PI4K2A_QR_siR	CTCCGCCTCAAAACGCCGCAGCCAA	SDM (Q5)	GFP-PI4K2A siR
ANXA2_QF_S127A	CGACGAGGACGCTCTCATTGAG	SDM (Q5)	HA-ANXA2 S127A
ANXA2_QR_S127A	GTTCCCAGCCCCTTCATG	SDM (Q5)	HA-ANXA2 S127A
mULK1_QF_K46I	GTGGCCGTCATTTGCATTAACAAGAAGAAC	SDM (Q5)	myc-Ulk1 KI 1-427
mULK1_QR_K46I	CTCCAGGTCGTGCTTCTC	SDM (Q5)	myc-Ulk1 KI 1-427
PRKAG2_QF_122/124del	GGGATCTTCCGCTCCTCC	SDM (Q5)	FLAG-PRKAG2 ΔS
PRKAG2_QR_122/124del	CATGCGTCGAGGGGAGCG	SDM (Q5)	FLAG-PRKAG2 ΔS
PRKAG2_F(1-242)_HindIII	AGCAAAGCTTATGGGAAGCGCGGTTATGGACA	Ligation cloning	GFP-PRKAG2 WT/ΔS (1-242)

PRKAG2_R(1-242+2)_Bamh1	CTTAGGATCCCCCTCCAGCATGCCGGCTT	Ligation cloning	GFP-PRKAG2 WT/ΔS (1-242)
PRKAG2_F(1-136)_HindIII	AGCAAAGCTTATGGATTACAAGGATGAT	Ligation cloning	GFP-PRKAG2 WT/ΔS (1-136)
PRKAG2_R(1-136+2)_Bamh1	CTTAGGATCCCCGGGGGAAGACTCTTT	Ligation cloning	GFP-PRKAG2 WT/ΔS (1-136)
p150_QF_S813A	TCTTCATGATGCTAGTCAGAAAGGTGTAATTGAC	SDM (Q5)	p150-ZZ S813A (donor mutated before ligation)
p150_QR_S813A	TGGCTCTGGTCCACTATA	SDM (Q5)	p150-ZZ S813A (donor mutated before ligation)
p150_QF_S861A	AGAATGGAAAGCCATGTTTGGGTCAC	SDM (Q5)	p150-ZZ S861A (donor mutated before ligation)
p150_QR_S861A	TCATTTACATTTGAGTCTTGTTTTAC	SDM (Q5)	p150-ZZ S861A (donor mutated before ligation)
p150_QF_S865A	CATGTTTGGGGCACTGGACCC	SDM (Q5)	p150-ZZ S865A (donor mutated before ligation)
p150_QR_S865A	CTTTTCCATTCTTCATTTACATTTGAGTCTTG	SDM (Q5)	p150-ZZ S865A (donor mutated before ligation)
p150_QF_S861/865A	TTGGGGCACTGGACCCACCAAACA	SDM (Q5)	p150-ZZ S861/865A (donor mutated before ligation)
p150_QR_S861/865A	ACATGGCTTTCCATTCTTCATTTACATTTGAGTC	SDM (Q5)	p150-ZZ S861/865A (donor mutated before ligation)
p150_QF_S861E	AGAATGGAAAGAGATGTTTGGGTCACTG	SDM (Q5)	p150-ZZ S861E (donor mutated before ligation)
p150_QR_S861E	TCATTTACATTTGAGTCTTGTTTTAC	SDM (Q5)	p150-ZZ S861E (donor mutated before ligation)
p150_QF_S879A	ACCTAAAGGGGCTGATCAGGAGGTGATTCAGAC	SDM (Q5)	p150-ZZ S879A (donor mutated before ligation)
p150_QR_S879A	AGGGCCTGTGGCATGTTT	SDM (Q5)	p150-ZZ S879A (donor mutated before ligation)
p150_QF_S1039A	TCTTACATACGCCCGAATTGGAGG	SDM (Q5)	p150-ZZ S1039A (donor mutated before ligation)

p150_QR_S1039A	ATAGATCTGGTAGTGGTG	SDM (Q5)	p150-ZZ S1039A (donor mutated before ligation)
p150_QF_S1289A	CCCATCTGTGGCCTACTACAG	SDM (Q5)	p150-ZZ S1289A (donor mutated before ligation)
p150_QR_S1289A	GAACTAGTACTTCCTGCAAC	SDM (Q5)	p150-ZZ S1289A (donor mutated before ligation)
PIK3R4_QF_05(RPE)	TATTGCAAACTGATGCCTTATCTTG	SDM (Q5)	p150-HA siR
PIK3R4_QR_05(RPE)	TACGTCGGCTGTACTTATTTGACGAG	SDM (Q5)	p150-HA siR
p150siRC1_HA_F	CCAGATTACGCTTGAAGTCGAGTCTAGAGGGCC	SDM (Q5)	p150-HA siR
p150siRC1_HA_R	TACGTCGTATGGGTATTTCCACACCTTCACAATCC	SDM (Q5)	p150-HA siR
p150_QF_V50del	TGTGAAGGTTTTTGCAATTCAGGATCC	SDM (Q5)	p150-HA ΔV50 siR
p150_QR_V50del	ACCAGGCCTTCTCGGTGC	SDM (Q5)	p150-HA ΔV50 siR
PIK3R4_dV50_F1	GCAGATCGATAAGCTTATGGGAAATCAGC	Ligation cloning	p150-ZZ ΔV50 (donor mutated before ligation)
PIK3R4_dV50_R1	GCTTATTCTGAATTTCCTGGAC	Ligation cloning	p150-ZZ ΔV50 (donor mutated before ligation)

*QC = QuikChange (Agilent); Q5 = Q5 Site-Directed Mutagenesis (New England Biolabs)

2.4.9 Plasmids

Table 2.7 Plasmids used in this thesis

Name	Insert	Vector	Resistance	Source
myc-Ulk1 WT	Murine Ulk1 WT	pRK5 Myc	Ampicillin	T. Tomoda
myc-Ulk1 KI	Murine Ulk1 K46I	pRK5 Myc	Ampicillin	E. Chan
myc-Ulk2 WT	Murine Ulk2 WT	MYC-Sal pRK5	Ampicillin	E. Chan

myc-Ulk2 KI	Murine Ulk2 K39I	MYC-Sal pRK5	Ampicillin	
FLAG-SORBS2	Human SORBS2	pFLAG-CMV2	Ampicillin	P. Soubyeran
FLAG-SORBS2 S239A	Human SORBS2 bearing alanine at position 239	pFLAG-CMV2	Ampicillin	T. Mercer
FLAG-SORBS2 S298A	Human SORBS2 bearing alanine at position 298	pFLAG-CMV2	Ampicillin	T. Mercer
FLAG-SORBS2 S299A	Human SORBS2 bearing alanine at position 299	pFLAG-CMV2	Ampicillin	T. Mercer
FLAG-SORBS2 S301A	Human SORBS2 bearing alanine at position 301	pFLAG-CMV2	Ampicillin	T. Mercer
FLAG-SORBS2 S302A	Human SORBS2 bearing alanine at position 302	pFLAG-CMV2	Ampicillin	T. Mercer
LSR-GFP	Human LSR isoform = AAH04381.2	pEGFP N1	Kanamycin	P. Papatheodorou
CapZB-myc	Murine CapZB	pCMV	Ampicillin	L. Yu
FAM21A-GFP	Human FAM21A	pEGFP	Kanamycin	M. Seaman
GFP-FAM21A tail	Human FAM21A residues 228-1341	pEGFP	Kanamycin	M. Seaman
HA-ULK1 WT	Human Ulk1 WT	pcDNA3.1+	Ampicillin	A. Longatti
HA-ULK1 KI	Human Ulk1 K46I	pcDNA3.1+	Ampicillin	A. Gubas
PylRS	*M. barkeri* PylRS (CMV) and pyltRNA (U6)	pCMV	Ampicillin	P. Schultz
AbKRS	AbKRS (CMV) and tRNAPyl (U6)	pCMV	Ampicillin	P. Schultz
NES-AbKRS	AbkRS (CMV) with 54bp insertion encoding NES, initiator M->G. And tRNAPyl (U6)	pCMV	Ampicillin	T. Mercer
HA-ULK1_TAG_H105	Human ULK1 bearing TAG mutation at position 105	pcDNA3.1+	Ampicillin	T. Mercer

HA-ULK1_TAG_R108	Human ULK1 bearing TAG mutation at position 108	pcDNA3.1+	Ampicillin	T. Mercer
HA-ULK1_TAG_Q142	Human ULK1 bearing TAG mutation at position 142	pcDNA3.1+	Ampicillin	T. Mercer
HA-ULK1_TAG_M186	Human ULK1 bearing TAG mutation at position 186	pcDNA3.1+	Ampicillin	T. Mercer
HA-ULK1_TAG_K218	Human ULK1 bearing TAG mutation at position 218	pcDNA3.1+	Ampicillin	T. Mercer
HA-ULK1_TAG_Q222	Human ULK1 bearing TAG mutation at position 222	pcDNA3.1+	Ampicillin	T. Mercer
HA-ULK1_D165N	Human ULK1 bearing asparagine at position 165	pcDNA3.1+	Ampicillin	T. Mercer
HA-ULK1_TAG_H105_D165N	ULK1_TAG_H105 bearing asparagine at position 165	pcDNA3.1+	Ampicillin	T. Mercer
HA-ULK1_TAG_R108_D165N	ULK1_TAG_R108 bearing asparagine at position 165	pcDNA3.1+	Ampicillin	T. Mercer
HA-ULK1_TAG_Q142_D165N	ULK1_TAG_Q142 bearing asparagine at position 165	pcDNA3.1+	Ampicillin	T. Mercer
HA-ULK1_TAG_M186_D165N	ULK1_TAG_M186 bearing asparagine at position 165	pcDNA3.1+	Ampicillin	T. Mercer
HA-ULK1_TAG_K218_D165N	ULK1_TAG_K218 bearing asparagine at position 165	pcDNA3.1+	Ampicillin	T. Mercer
HA-ULK1_TAG_Q222_D165N	ULK1_TAG_Q222 bearing asparagine at position 165	pcDNA3.1+	Ampicillin	T. Mercer
ATG13-FLAG WT	Human ATG13	pcDNA3.1-	Kanamycin	N. McKnight

ATG13-FLAG S355/356A	Human ATG13 bearing alanine at positions 355 and 356	pcDNA3.1-	Kanamycin	T. Mercer
Rubicon-GFP WT	Human Rubicon	pCMV5D	Ampicillin	I. Ganley
Rubicon-GFP S351A	Human Rubicon bearing alanine at position 351	pCMV5D	Ampicillin	T. Mercer
Rubicon-GFP S351D	Human Rubicon bearing alanine at position 351	pCMV5D	Ampicillin	T. Mercer
HA-ATG2A	Human ATG2A	pHAGE-eGFP	Ampicillin	D. McEwan
HA-ATG2A S1266A	Human ATG2A bearing alanine at position 1266	pHAGE-eGFP	Ampicillin	T. Mercer
HA-ATG2A S1266D	Human ATG2A bearing aspartate at position 1266	pHAGE-eGFP	Ampicillin	T. Mercer
EGFP	EGFP	EGFP N1	Kanamycin	Clontech
GFP-PI4K2A siR	Human PI4K2A with synonymous mutations conferring resistance to siRNA (see table 2.1)	pEGFP C1	Kanamycin	T. Mercer (initially S. Minogue)
GFP-PI4K2A STAA siR	Human PI4K2A bearing alanine at positions 462 and 466 (si-resistant)	pEGFP C1	Kanamycin	T. Mercer
GFP-PI4K2A STDD siR	Human PI4K2A bearing aspartate at positions 462 and 466 (si-resistant)	pEGFP C1	Kanamycin	T. Mercer
GFP-PI4K2A KD siR	Kinase dead human PI4K2A PI4K2A bearing T465^G466insAAT (aa N155^E156insN), and K152A (si-resistant)	pEGFP C1	Kanamycin	T. Mercer (initially S. Minogue)
myc-Ulk1 WT 1-427	Murine Ulk1 WT residues 1-427	pRK5 Myc modified to	Ampicillin	E. Chan

		insert 3’ Xba I site		
myc-Ulk1 KI 1-427	Murine Ulk1 K46I residues 1-427	pRK5 Myc modified to insert 3’ Xba I site	Ampicillin	T. Mercer
VPS34 Complex 1	Human VPS34 complex 1: ZZATG14L+EGFP+BECN1+VPS34+p150	pcDNA4TO	Ampicillin	R. Williams
VPS34 Complex 2	Human VPS34 complex 2: UVRAG-2xstrep-ZZ+EGFP+BECN1+VPS34+p150	pcDNA4TO	Ampicillin	R. Williams
HA-ANXA2	Human Annexin A2	pCMV5	Ampicillin	K. Moreau
HA-ANXA2 S127A	Human Annexin A2 bearing alanine at position 127	pCMV5	Ampicillin	K. Moreau
FLAG-PRKAG2	Human PRKAG2 isoform A	pcDNA 3.1	Ampicillin	G. Hardie
FLAG-PRKAG2 ΔS	Human PRKAG2 isoform A with residues 122-124 deleted	pcDNA 3.1	Ampicillin	T. Mercer
GFP-PRKAG2 WT (1-136)	Human PRKAG2 isoform A 1-136	pEGFP N1	Kanamycin	T. Mercer
GFP-PRKAG2 ΔS (1-136)	Human PRKAG2 isoform A 1-136 with residues 122-124 deleted	pEGFP N1	Kanamycin	T. Mercer
GFP-FLAG-PRKAG2 WT (1-242)	Human PRKAG2 isoform A 1-242	pEGFP N1	Kanamycin	T. Mercer
GFP-FLAG-PRKAG2 ΔS (1-242)	Human PRKAG2 isoform A 1-242 with residues 122-124 deleted	pEGFP N1	Kanamycin	T. Mercer
p150-ZZ	Human p150	pCAG	Ampicillin	R. Williams

p150-ZZ 6SA	Human p150 bearing alanine at positions 813, 861, 865, 879, 1039 and 1289	pCAG	Ampicillin	T. Mercer
p150-ZZ 2SA	Human p150 bearing alanine at positions 861 and 865	pCAG	Ampicillin	T. Mercer
p150-ZZ S813A	Human p150 bearing alanine at positions 813	pCAG	Ampicillin	T. Mercer
p150-ZZ S861A	Human p150 bearing alanine at positions 861	pCAG	Ampicillin	T. Mercer
p150-ZZ S865A	Human p150 bearing alanine at positions 865	pCAG	Ampicillin	T. Mercer
p150-ZZ S879A	Human p150 bearing alanine at positions 879	pCAG	Ampicillin	T. Mercer
p150-ZZ S1039A	Human p150 bearing alanine at positions 1039	pCAG	Ampicillin	T. Mercer
p150-ZZ S1289A	Human p150 bearing alanine at positions 1289	pCAG	Ampicillin	T. Mercer
p150-ZZ S861E	Human p150 bearing glutamate at positions 861	pCAG	Ampicillin	T. Mercer
p150-ZZ ΔV50	Human p150 with residue 50 deleted	pCAG	Ampicillin	T. Mercer
p150-HA siR	Human p150 with synonymous mutations conferring resitiance to siRNA (see table 2.1)	pcDNA4TO	Ampicillin	T. Mercer
p150-HA 6SA siR	Human p150 bearing alanine at positions 813, 861, 865, 879, 1039 and 1289 (si-resistant)	pcDNA4TO	Ampicillin	T. Mercer
p150-HA ΔV50 siR	Human p150 with residue 50 deleted (si-resistant)	pcDNA4TO	Ampicillin	T. Mercer

GFP-2xFYVE	Tandem FYVE domain from human Hrs	pEGFP C2	Kanamycin	G. Banting
p150 WT-HA_IRES EGFP (lenti)	Human p150_IRES_GFP	pLV[Exp]-Puro-CMV	Ampicillin + Puromycin	VectorBuilder
p150 S861A-HA_IRES EGFP (lenti)	Human p150_IRES_GFP bearing alanine at position 861	pLV[Exp]-Puro-CMV	Ampicillin + Puromycin	T. Mercer
p150 S861E-HA_IRES EGFP (lenti)	Human p150_IRES_GFP bearing glutamate at position 861	pLV[Exp]-Puro-CMV	Ampicillin + Puromycin	T. Mercer
p150 ΔV50-HA_IRES EGFP (lenti)	Human p150_IRES_GFP with residue 50 deleted	pLV[Exp]-Puro-CMV	Ampicillin + Puromycin	T. Mercer
p150 6SA-HA_IRES EGFP (lenti)	Human p150_IRES_GFP bearing alanine at positions 813, 861, 865, 879, 1039 and 1289	pLV[Exp]-Puro-CMV	Ampicillin + Puromycin	T. Mercer
p150 6SE-HA_IRES EGFP (lenti)	Human p150_IRES_GFP bearing glutamate at positions 813, 861, 865, 879, 1039 and 1289	pLV[Exp]-Puro-CMV	Ampicillin + Puromycin	T. Mercer
EGFP (lenti)	EGFP	pLV[Exp]-Puro-CMV	Ampicillin + Puromycin	T. Mercer
SV40 T	SV40 large T antigen	pBABE puro	Ampicillin + Puromycin	A. Cameron
pMDLgp	gag-pol for MMLV amphotropic virus	pMD	Ampicillin	F. Randow
pMD g	VSVG protein for MMLV amphotropic virus	pMD	Ampicillin	F. Randow
psPAX2	gag-pol pax2	psPAX2	Ampicilin	S. Giradin
GFP-Rab5 wt	Human Rab5	pEGFP C2	Kanamycin	T. Jeffries
GFP-Rab5 Q79L	Human Rab5 bearing leucine at position 79	pEGFP C2	Kanamycin	K. Deinhardt

GFP-Rab7 wt	Human Rab7	pEGFP C2	Kanamycin	T. Jeffries
GFP-Rab7 Q67L	Human Rab7 bearing leucine at position 67	pEGFP C2	Kanamycin	K. Deinhardt

2.5 Data Analysis

2.5.1 Imaris image analysis software

LC3 and WIPI2 puncta number were quantified using Imaris 8x64 software (Bitplane). Detection thresholds based on puncta size and intensity were established manually by comparing starved versus fed conditions. Within each experiment, thresholds were kept constant between analysed images. Cell number was calculated manually.

2.5.2 ImageJ densitometry

ImageJ (National Institute of Health) was used to quantify signal intensities from Western blots, autoradiograms and Coomassie gels. Data were imported into excel for analysis. Band intensities were calculated by subtracting background noise from total isolated band intensity. This was typically normalised by dividing by these intensities with that of a housekeeping protein, for example Actin, which was visualised in parallel to control for protein levels. Normalised intensities were divided by a common sample in the dataset with relative intensity values (in arbitrary units) plotted in figures and used to quantify statistical changes.

2.5.3 DNA/protein sequence analysis

DNASTAR (Lasergene) programs were used to align, display and otherwise manipulate nucleotide/amino acid sequence files. Model organism amino acid sequence alignments for p150 were generated at http://www.proviz.ucd.ie/ (Jehl et al., 2016), with residues annotated following the default ClustalX colour scheme (Larkin et al., 2007).

2.5.4 Mass spectrometry data analysis

Mass spectrometry data was quantified using MaxQuant, and prepared for analysis using Perseus (SILAC and TMT) and Skyline (p150 band ID) frameworks by the Proteomics STP, Francis Crick Institute. Phosphoproteomic data processing and analysis was performed with the help of Stefan Boeing PhD (Bioinformatics STP, Francis Crick Institute). Graphics were generated using Perseus (*in vivo* crosslinking - section 4.2; p150 interactome - section 5.6.2) or using software developed by Stefan Boeing (SILAC/TMT Phopshoproteomics – sections 3.2, 3.4 and 4.3).

2.5.5 Statistical analysis

All experiments were repeated ≥ 2 times unless otherwise stated and ≥ 3 times when quantifications are shown. Where quantified immunofluorescence is shown, 8 images (~100 cells) were imaged per condition per experimental repeat. Exceptions include experiments involving mass spectrometry analysis and those performed in peptide array format which were performed once. When utilising peptide array, each peptide was spotted in triplicate to improve result reliability. Statistics were calculated using GraphPad Prism 7.0b. One-tailed ANOVAs were performed in all cases other than in Figures 5.18 and 5.19, in which students T tests were employed.

2.6 Comment on nomenclature

All gene names in the body of the text are given in italics. Human protein/gene names are represented in uppercase, whilst for non-human homologs (typically murine unless otherwise stated) only the first letter is capitalised. Yeast protein names are comprised of the gene name followed by a lowercase letter ‘p’ (e.g. *Vps34* and Vps34p). Rare exceptions to these rules are indicated in the text, e.g. ‘Huntingtin’, for which the first letter alone is capitalised in keeping with trends in the literature. Furthermore, the human proteins p150 and p62 are spelled with a lowercase p to correspond with the prevalent naming convention. Finally, ‘ULK’ (as opposed to ULK1 or Ulk2) is employed when referring to ULK homologs generally.

Chapter 3. Identification of novel ULK substrates using SILAC-based phosphoproteomics

3.1 Introduction and aims

Post translational modification (PTM) is the term given to the array of covalent alterations that occur to a polypeptide after synthesis. Depending on the position, nature and combination of the PTMs a protein acquires, its functional characteristics can be significantly altered. Phosphorylation makes up the majority of experimentally-verified PTMs by far, with a 2011 study noting that of the 87,309 PTM events experimentally verified at the time, 57,191 were phosphorylation events with phosphoserine accounting for ~75% (43,125), phosphothreonine ~17% (9481) and phosphotyrosine ~8% (3849) (Khoury et al., 2011). In total, over 90% of the proteins in the human proteome are thought to be phosphorylated, with the primacy of phosphorylation-dependent signalling is reflected by the observation that genes encoding kinases represent ~2% of the human genome, the largest of any PTM-catalysing enzymatic family (Rubin et al., 2000). Unsurprisingly, aberrant kinase/phosphatase signalling is commonly implicated in human disease. Elucidating specific kinase-substrate relationships is therefore key to the understanding of signalling networks.

A number of different approaches exist to identify kinase substrates. The traditional gold standard for substrate validation is the *in vitro* kinase assay, in which high concentrations of both kinase and suspected substrate are incubated together in the presence of ATP before phosphorylation is measured. However, this is a biased and relatively low-throughput approach requiring semi-purified samples of both kinase and substrate and is therefore unsuitable for large scale and unbiased screens. Amongst the unbiased approaches, knockout/knockdown screens for genes that functionally interact with a given kinase have been employed, but as this approach suffers from a high false positive rate and lacks site-specific resolution it has largely been subsumed by phosphoproteomic profiling techniques (Xue and Tao, 2013).

The phosphoproteome is the total complement of phosphorylated proteins/residues in an organism, tissue or cell. H. *sapiens* have ~20,000 protein-coding genes however, the number of unique protein species is amplified exponentially by presence of the around 960,000 unique

phosphorylation events predicted to constitute the human phosphoproteome (~180,000 of which are experimentally verified) (see Kinexus PhosphoNET (www.phosphonet.ca)) (Wirbel et al., 2018, Ponomarenko et al., 2016). Accordingly, the generation and analysis of phosphoproteomic data is complex and has relied heavily on advancements made first in mass spectrometry-based proteomics.

Mass spectrometry-based proteomics allows for the unbiased assessment of the protein constituents in a sample, providing a qualitative (what proteins are present), as well as quantitative (in what amounts) insight depending on which technique is chosen. Whereas workflows exist for the analysis of intact proteins, 'bottom up' techniques, in which proteins of interest are reduced to peptides via proteolytic digestion preceding analysis, are the most common.

Briefly, a common workflow for bottom up proteomics follows: First, the proteinaceous sample is isolated before being fully digested with proteinases. Techniques such as liquid chromatography are then used to physically separate peptides in the sample based on a chemical characteristic (e.g. their hydrophobicity), thereby reducing sample complexity and improving sensitivity and specificity of detection, before transfer into the mass spectrometer. Electrospray ionisation is commonly used to facilitate this transfer step, in which peptides are rapidly evaporated and ionised before separation based on mass to charge ration (m/z) via electromagnetic deflection in the first mass spectrometry stage (MS1). Termed precursor ions, specific peptides isolated after MS1 are then fragmented, usually via collision-induced dissociation, in the second stage of mass spectrometry (MS2). A second round of m/z-based separation allows for the identification of the constitutive polypeptide fragments upon data analysis, and eventual alignment with the source protein.

The techniques adapted for proteomics can be applied in phosphoproteomics. This is often facilitated via the inclusion of an additional phosphopeptide enrichment stage during sample preparation. Immobilised metal affinity chromatography and metal oxide affinity chromatography are often used in used in tandem to maximise phosphopeptide retrieval. Whilst they have subtly different binding specificities, both rely on electrostatic attraction between positively charged metal ions and negatively charged phosphate groups.

Notably, some peptides have intrinsically poor ionisation efficiency at the electrospray ionisation stage, reducing their detection rate at MS1 and thereby reducing global proteome coverage to preclude direct assessment of absolute peptide quantity based on signal intensity alone (Jarnuczak et al., 2016). To combat this phenomenon, relative quantification techniques are frequently employed which largely fit into two categories, label-free and stable isotope labelling. Of the two, stable isotope labelling is the most reliable. Four major stable isotope labelling techniques exist, differing largely in labelling chemistry and the stage at which peptide quantity is assessed (MS1 vs MS2). These are SILAC (stable isotope labelling by amino acids in culture), dimethyl labelling, iTRAQ (isobaric tags for relative and absolute quantitation) and TMT (tandem mass tag). SILAC- (covered below) and TMT- (covered in Chapter 4) based labelling techniques are used in this thesis.

First published in 2002, the Mann laboratory pioneered the use of SILAC in quantitative proteomics (Ong et al., 2002). This procedure involves the full incorporation of isotopically-labelled amino acids (typically lysine and arginine) in a metabolically active cell population by culturing cells in media containing serum that had been dialysed before replacement with 'heavy' or 'light' amino acids, and allowing time for complete isotope incorporation (typically >10 cell divisions). Differentially-labelled samples are then mixed at a 1:1 ratio before or immediately after cell lysis, removing inter-sample variance introduced during sample preparation for mass spectrometry. Peptides derived from each labelling condition are identified at MS1 based on predicable variations in mass introduced by the labelled amino acids, allowing for peptide-by-peptide calculation of the relative contribution from each sample.

Aims:

- Utilise SILAC coupled with mass spectrometry to quantitatively assess how removal of Ulk1 and Ulk2 affects the phosphoproteome
- Use these data to compile a shortlist of putative ULK substrates

3.2 SILAC-Based phosphoproteomics to identify ULK substrates

3.2.1 SILAC screen design

The identification of novel ULK substrates is crucial if we are to gain a mechanistic understanding of autophagy. Ulk1 and Ulk2 double knockout (DKO) MEFs were generated to use as tools in the identification of kinase substrates (McAlpine et al., 2013). To study the ULK phosphoproteome, wild type (WT) and DKO MEFs were cultured in SILAC media in preparation for SILAC-based phosphoproteomics. Fully labelled cells were cultured in autophagy-inducing conditions before harvesting, tryptic digestion, phosphopeptide enrichment and mass spectrometry analysis; phosphopeptides specifically depleted in Ulk DKO cells were considered potential kinase substrates (Figure 3.1A). Both spontaneously and SV40-immortalised MEFs were utilised and two autophagy-inducing conditions were tested (2hrs starvation and 2hrs Torin 1, 100nM). Forward, reverse and control labelling conditions were tested to exclude variance introduced by labelling and focus on reproducible results (Figure 3.1B).

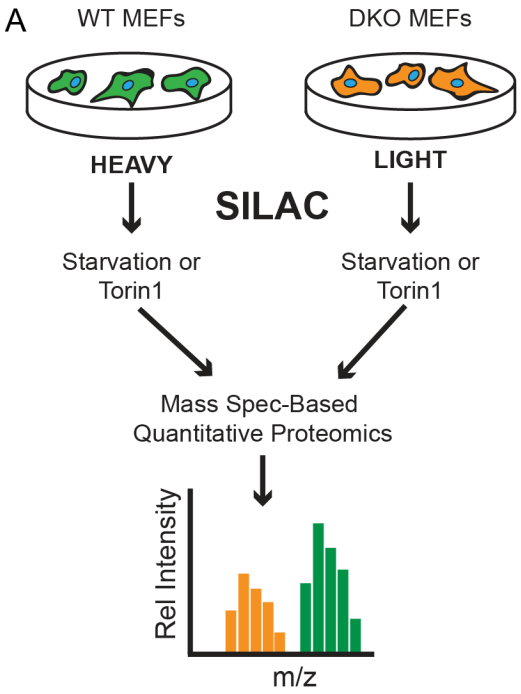

B

	Experiment 1	2	3
MEF Type	SV40	SV40	SI
Treatment	Torin 1	Starved	Starved

FWD: DKO(Heavy)/WT(Light)
REV: WT(Heavy)/DKO(Light)
CTRL: WT(Heavy)/WT(Light)

Figure 3.1 – *SILAC-Based phosphoproteomics to identify ULK substrates.* **A** – Schematic representation of SILAC screen design, SILAC screen samples were produced by Harold Jefferies PhD. **B** – Cell type and treatment combinations utilised in SILAC experiments 1, 2 and 3. Whilst same primary MEF stocks were used in each experiment, 'MEF Type' indicates the method of immortalisation employed. SI = spontaneously immortalised. Thee same forward (FWD), reverse (REV) and control (CTRL) mixes were utilised in each instance.

3.2.2 Loss of Ulk1 and Ulk2 results in large scale alterations to phosphoproteome

Focussing only on sites detected in both forward and reverse experiments, the resulting dataset contained 17940 unique phosphorylation events (in total: 16308 in experiment 1, 7774 in experiment 2 and 4193 in experiment 3). 513 phosphorylation sites were highly depleted in DKO cells (with a $\log_2$(DKO/WT) of less than -1.5 when forward (Fwd) and reverse (Rev) ratios were averaged in at least one experiment whilst scoring between 0.5 and -0.5 in all control scenarios) and there was a high degree of reproducibility within experiments (Fwd vs Rev samples). Importantly, reproducibility between experiments was also observed (Figure 3.2A). Notably, more data was collected in experiment 1 than in 2 or 3, and many sites were detected in only one or two of the experiments with very few identified in all three.

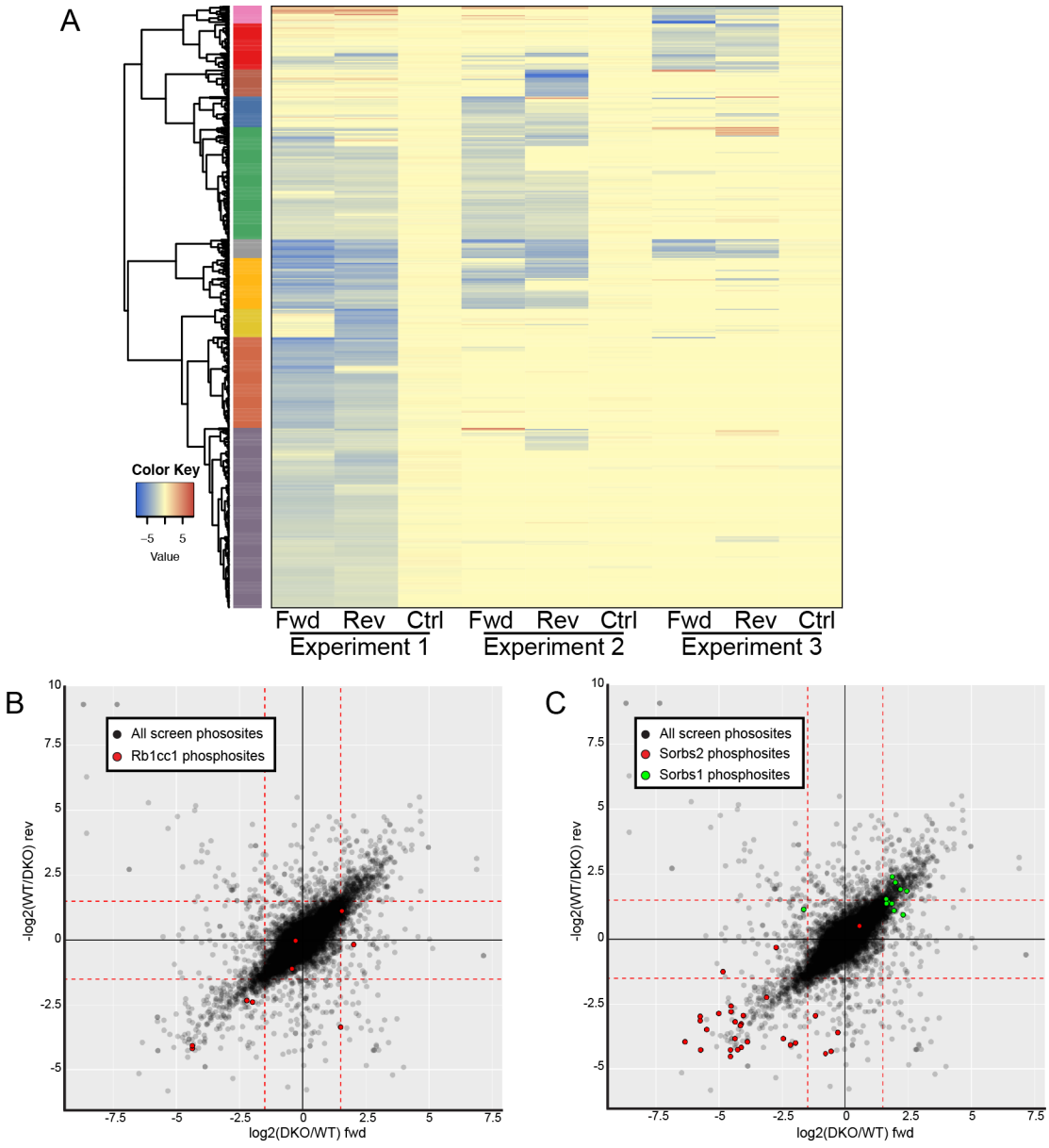

Figure 3.2 – *Loss of Ulk1 and Ulk2 results in significant alterations to phosphoproteome.* **A** – Heat map displaying SILAC ratios for the most depleted phosphopeptides in Ulk1$^{-/-}$/Ulk2$^{-/-}$ MEFs. Displayed are sites with an average log_2(DKO/WT) value of <-1.5 in forward and reverse labelling permutations from at least one experiment. Sites that displayed label-dependent enrichment in any of the three control conditions were removed. In a given labelling condition (column), phosphopeptides (row) depleted in DKOs were coloured in blue and those enriched in red, whilst sites that were neither enriched nor depleted were coloured yellow. Yellow was also used to indicate sites that were not detected in a given mix. Colour intensity indicates log_2 enrichment level as described in colour key. Data from three independent experiments (1, 2 and 3) are displayed. Peptides were grouped by global correlation cluster analysis - the 10 most common clusters are annotated on the left. **B** – Scatterplot showing relative phosphopeptide levels in Ulk1/2 double knockout (DKO) and wild-type (WT) MEFs detected in experiment 1. Log_2 SILAC ratios from both forward (X axis) and reverse (Y axis) labelling conditions were plotted. In reverse scenarios, reciprocal ratios were plotted. Phosphopeptides scoring <-1.5 in both forward and reverse experiments (bottom left box, enclosed by red dashed line) were considered to be robustly depleted in DKOs. Phosphosites are depicted in black, with those assigned to Rb1cc1 highlighted in red. Of the 9 such phosphopeptides detected, 4 were reproducibly depleted. **C** – All detected phosphopeptides for Sorbs2 (red) and Sorbs1 (green) are highlighted in the scatterplot described in 3.2B. Peptides from each protein displays opposite patterns of enrichment in each cell type. For plots B and C only phosphopeptides detected in both forward or reverse repeats are depicted. The analyses in Figure 3.2 were performed with the help of Stefan Boeing from the Bioinformatics STP.

Plotted in Figure 3.2B are the SILAC ratios for phosphopeptides detected in of experiment 1, chosen for display due to the relatively high number of unique phophosites detected. Interestingly, 4 of the 9 sites detected in Fip200 (gene name *Rb1cc1*), a known ULK substrate phosphorylated at yet unknown residues, were reproducibly depleted in Ulk1/2 DKO cells (Figure 3.2B), suggesting that the experiment had worked successfully. The first stage of analysis involved focussing on phosphopeptides that were reproducibly depleted to the greatest extent (Appendix Table A). Phosphopeptides mapping to the Sorbin and SH3 domain-containing protein (SORBS)-family protein Sorbs2 were highly overrepresented in this selection. However, almost all peptides assigned to this protein were depleted in Ulk1/2 DKOs and interestingly the opposite trend was noted for all detected peptides assigned to another SORBS family protein, c-Cbl associated protein (gene name *Sorbs1*) which were comparatively enriched in DKO cells (Figure 3.2C). These trends are potentially indicative of protein level

differences, however, without further confirmatory experiments this cannot be confidently inferred. These examples were selected to convey the impact that 'non-specific' protein level differences between WT and DKO cell lines could have on the data set, revealing an additional layer of complexity to be considered during analysis.

As previously noted, at first the most depleted phosphopeptides were brought forward for further analysis. From these hits, candidates were selected for validation based either on extent of depletion in Ulk1/2 DKO MEFs or conceivable roles in autophagy (e.g. proximity to the autophagic machinery). The following section covers validation of three such proteins: SORBS2, FAM21 and CAPZB.

3.3 Validating most depleted phosphopeptides as direct ULK substrates

3.3.1 SORBS2 is an in vivo substrate of ULK

The multidomain signalling adaptor SORBS2 localises to focal adhesions and stress fibres (Anekal et al., 2015) where it associates with a host of signalling proteins such as ABL1, CBL and ARG Kinase (hence the alternative name Arg Kinase Binding Protein 2) (Cestra et al., 2005). SORBS2 has been implicated in the control of cell migration and has no identified role in autophagy. However, the targeted downregulation of focal adhesions via autophagic removal of PAXILLIN is associated with increased cell motility after metastasis (Sharifi et al., 2016) and Paxillin is a substrate of Atg1 in Drosophila (Chen et al., 2008), suggesting feasible links between SORBS2 and autophagy.

Supporting the notion that SORBS2 might regulate autophagy, overexpression in HEK293A reduced LC3 puncta upon 1hr starvation + Bafilomycin (Figure 3.3A). Interestingly, starvation resulted in the translocation of SORBS2 from filamentous structures to plasma membrane-associated foci. SORBS2 underwent an electrophoretic mobility shift after coexpression with WT Ulk1 and Ulk2 but not with forms of Ulk1/Ulk2 bearing kinase-inactivating (KI) mutations (Ulk1-K46I or Ulk2-K39I), indicating *in vivo* phosphorylation by both kianses (Figure 3.3B). To identify which SORBS2 residue(s) were phosphorylated by ULK, the relative enrichment data from the SILAC screen together with the recently published ULK1 consensus sequence, was used to select 5 residues for serine-to-alanine site-directed mutagenesis (SDM). After

coexpressing of 5 single serine to alanine (SA) mutants with Ulk1 or Ulk2, none exhibited clear variations in electrophoretic mobility compared to WT (Figure 3.3C).

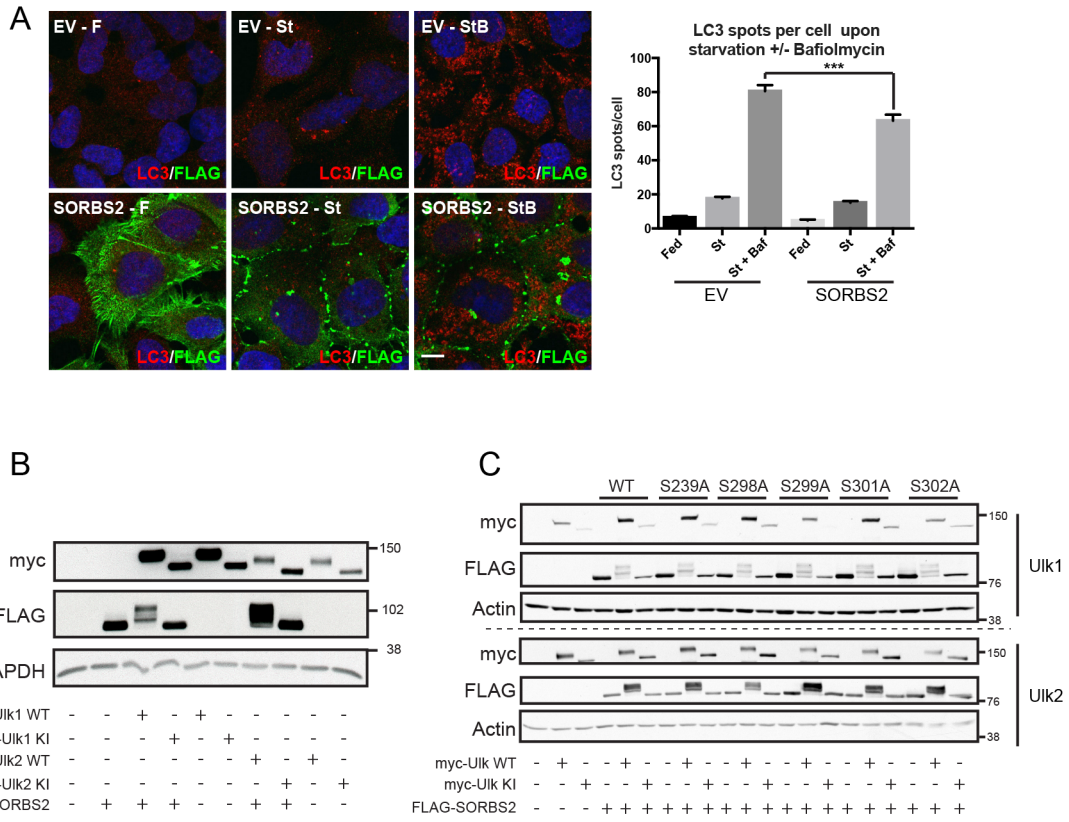

Figure 3.3 – *SORBS2 is an in vivo substrate of ULK.* **A** – Exogenous expression of FLAG-SORBS2 leads to a reduction of LC3 puncta following starvation. HEK293A cells were transfected with empty vector (EV) or FLAG-SORBS2, before culturing for 1hr in full media (F) or EBSS in the presence (StB) or absence (St) of 100nM Bafilomycin A1. The distribution of SORBS2 (green), LC3 (red) and DAPI were revealed by immunofluorescence. Quantification of LC3 puncta from three independent experiments revealed a significant decrease in spot count in cells overexpressing SORBS2. Scale bar = 10µm. Data represents mean +/- SEM, n=3, ***<p0.001 (ANOVA). **B** – HEK293A were transiently transfected with FLAG-SORBS2 and wild-type (WT)/kinase-inactive (KI) myc-Ulk1/2 as indicated. SDS PAGE separation followed by Western blot analysis revealed electrophoretic mobility shifts in SORBS2 when expressed with Ulk1 or Ulk2 wild-type (WT). **C** – SORBS2 is phosphorylated by Ulk1 (top) and Ulk2 (bottom) at an unknown residue. HEK293A cells were transiently transfected with constructs encoding FLAG-tagged WT, S239A, S298A, S299A, S301A or S302A SORBS2. Cells were cotransfected with myc-tagged WT/kinase inactive (KI) myc-Ulk1/2 as specified. Gel mobility shifts reveal the phosphorylation of SORBS2 increases upon overexpression of both WT kinases. However, of the mutated residues, none appear to be solely responsible for phosphorylation of SORBS2.

3.3.2 LSR is not phosphorylated by Ulk1 in vitro

Lipolysis-stimulated lipoprotein receptor (gene name *LSR*) is a plasma membrane-associated transmembrane protein involved in the formation of tricellular tight junctions (Furuse et al., 2012). 6 phosphoserines arrayed along the cytoplasmic C-terminus were greatly depleted in Ulk1/2 DKO MEFs. An *in vitro* kinase assay was performed with Ulk1 and GFP-LSR. Whilst ULK1 was capable of efficient autophosphorylation, no LSR phosphorylation was noted suggesting that in these conditions LSR is not phosphorylated by ULK1.

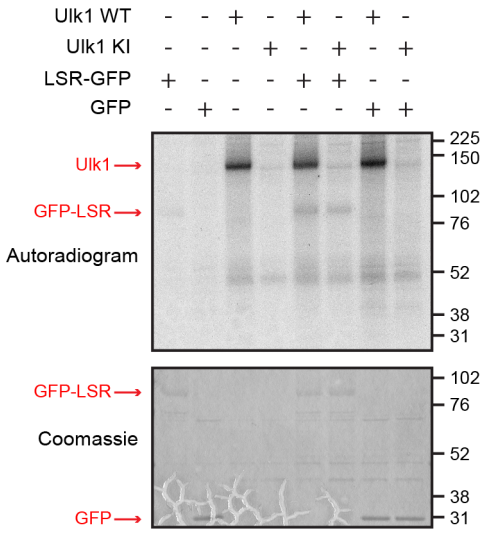

Figure 3.4 – *LSR is not phosphorylated by ULK1 in vitro.* A kinase assay was performed to test the phosphorylation of LSR by Ulk1 *in vitro*. Substrates (LSR-GFP or GFP) and kinases (myc-Ulk1 WT/wild type or myc-Ulk1 KI/kinase inactive were immunopurified before mixing as indicated. After *in vitro* phosphorylation, the samples were separated by SDS PAGE. The autoradiogram (top) shows that in these conditions LSR is not phosphorylated by Ulk1. The Coomassie-stained gel (bottom) shows that relative protein levels of LSR and GFP used in the assay were even. Experiment performed once (n=1).

3.3.3 Capzb and FAM21 are phosphorylated by ULK1 *in vivo*

The next putative ULK substrate brought forward for validation was CAPZB, part of the F actin capping CAPZ complex which binds to the growing end of F actin filaments to block polymerisation. In the SILAC screen, Capzb phosphorylation at serine 263 was reproducibly depleted in Ulk1/2 DKO MEFs. This was particularly interesting, as knockdown of CAPZB was reported to reduce LC3-II accumulation upon starvation in the presence of Bafilomycin A1 by 50% (Pavel et al., 2018) and it has been implicated in the formation of actin scaffolds within nascent autophagosomes (Mi et al., 2015). The CAPZB transcript is alternatively spliced, yielding proteins with distinct C terminal coding regions. Serine 263 resides at the C-terminal end of the muscle-specific CAPZB isoform 2 (Schafer et al., 1994).

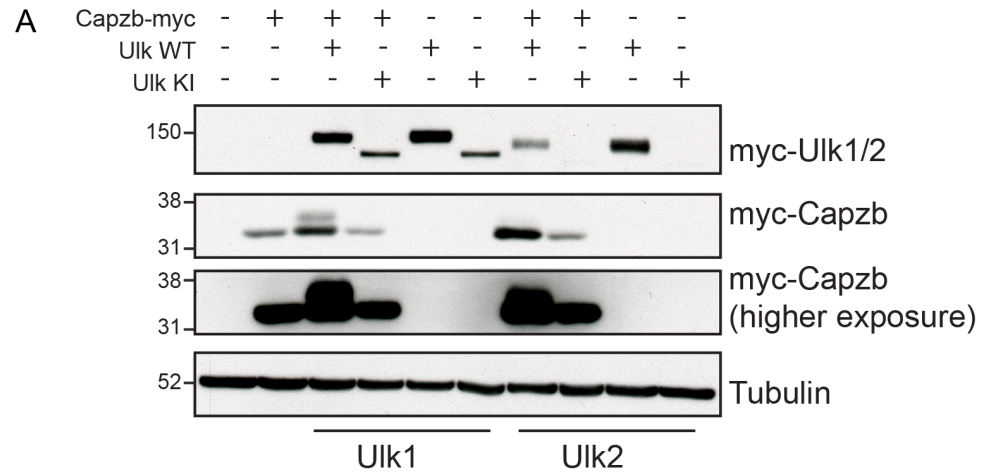
A
Capzb-myc
Ulk WT
Ulk KI
150
myc-Ulk1/2
38
31
myc-Capzb
38
31
myc-Capzb
(higher exposure)
52
Tubulin
Ulk1
Ulk2

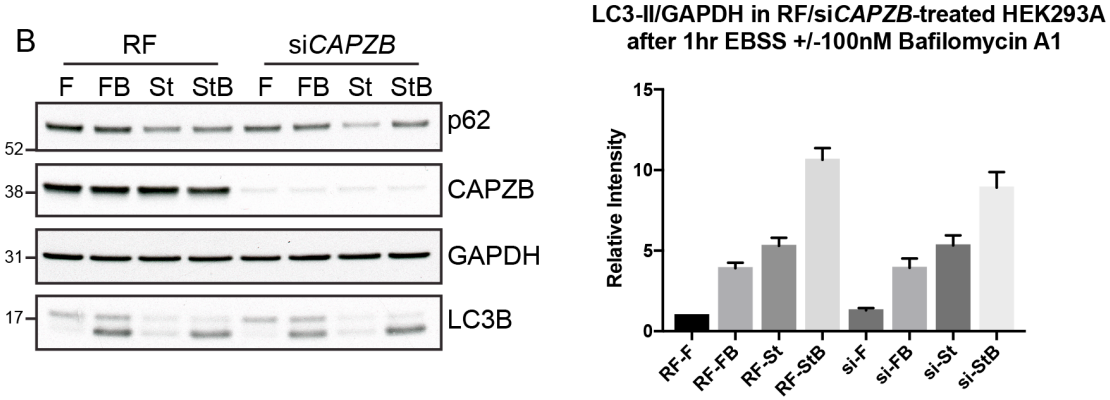
B
RF
siCAPZB
F FB St StB F FB St StB
52
p62
38
CAPZB
31
GAPDH
17
LC3B
LC3-II/GAPDH in RF/siCAPZB-treated HEK293A
after 1hr EBSS +/-100nM Bafilomycin A1
Relative Intensity
15
10
5
0
RF-F
RF-FB
RF-St
RF-StB
si-F
si-FB
si-St
si-StB

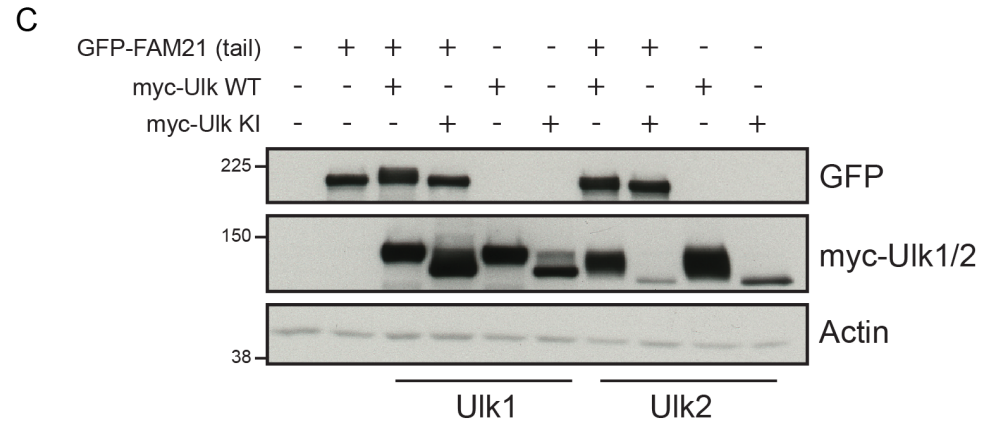
C
GFP-FAM21 (tail)
myc-Ulk WT
myc-Ulk KI
225
GFP
150
myc-Ulk1/2
Actin
38
Ulk1
Ulk2

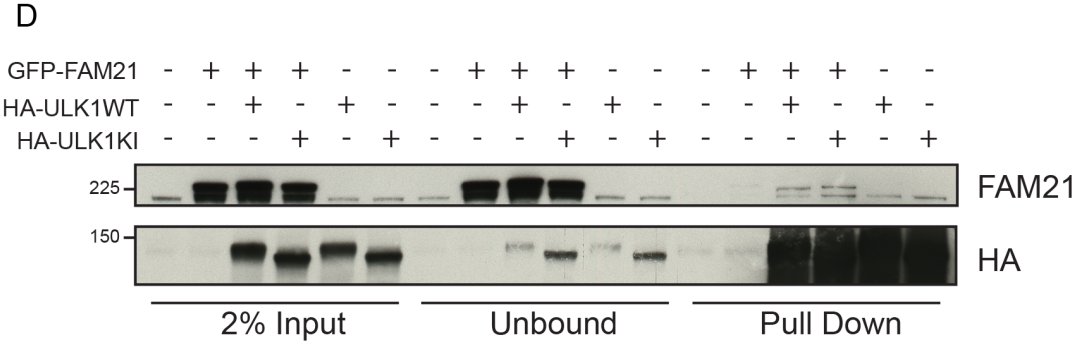
D
GFP-FAM21
HA-ULK1WT
HA-ULK1KI
225
FAM21
150
HA
2% Input
Unbound
Pull Down

Figure 3.5 – *Capzb and FAM21 are phosphorylated by ULK1 in vivo.* **A** – HEK293A were transiently transfected with Capzb-myc and wild-type (WT)/kinase-inactive (KI) myc-Ulk1/2 as indicated. SDS PAGE separation followed by Western analysis revealed electrophoretic mobility shifts in Capzb when expressed along with Ulk1 and Ulk2 WT. **B** – Knockdown of CAPZB in HEK293A did not modulate autophagic flux as measured by accumulation of LC3-II upon 1hr starvation in the presence of Bafilomycin A1 (100nM). F = Fed, FB = Fed + Bafilomycin A1, St = Starved, StB = Starved + Bafilomycin A1. **C** – FAM21A's C-terminal tail fused to GFP was expressed along with Ulk1/2 WT and KI as described for Capzb in Figure 3.5A. Electrophoretic mobility shifts indicated that the FAM21A C-terminus is phosphorylated by both kinases. **D** – GFP-FAM21A was coexpressed along with HA-ULK1 WT or KI before immunoprecipitation with anti-HA resin. Endogenous and exogenous FAM21 were detected in ULK1 WT and KI immunoprecipitates.

Due to an inability to acquire a construct encoding isoform 2, CapZB isoform 1, which does not encode S263, was coexpressed with Ulk1 and Ulk2 and underwent a phosphorylation-dependent band shift (Figure 3.5A). However, knockdown of CAPZB did not affect autophagic flux upon (Figure 3.5B), suggesting that it is not required for starvation-induced autophagy.

Interestingly, Fam21 (gene name *Washc2*), the 1341aa core component of the WASH complex that interacts directly with Capzb was also identified in the screen. The WASH complex harnesses actin polymerisation via ARP2/3 activation (implicated in nearly all membrane remodelling events (Rotty et al., 2012) to affect endosomal tubulation during retromer cargo sorting. It has been implicated in the positive (Zavodszky et al., 2014) and negative (Xia et al., 2013) regulation of autophagy. Furthermore, the WASH complex colocalises with ATG5, p62 and LC3 (Xia et al., 2013) and its perturbation leads to accumulation of ATG9A at the Golgi (Zavodszky et al., 2014). FAM21 contains a ~220aa globular head domain, which is sufficient for interaction with the remaining 4 WASH complex members, followed a long, highly repetitive and disordered tail constituting 21 LFa (Leucine-Phenylalanine-acidic) repeats which bind amongst other proteins the CAPZ and Retromer complexes (Jia et al., 2010). Two sites of interest were detected in FAM21 – serine 539 and 728 (533 and 723 in mouse protein), residing within LFa-5 and LFa-10 respectively. Promisingly, an indirect interaction between ULK1 and FAM21 through CCDC53 was previously reported (Huttlin et al., 2017, Stark et al., 2006).

Coexpression of a fragment encoding the tail alone with Ulk1 and Ulk2 similarly resulted in an electrophoretic band shift, supporting the ULK-dependent phosphorylation of FAM21's C-terminal tail (Figure 3.5C). As ULK1 is known to interact with many of its substrates (Mercer et al., 2018) (Table 1.1), the interaction between FAM21 and ULK1 was analysed. GFP-FAM21 was coexpressed with either HA-ULK1 WT or HA-ULK1 KI, before immunoprecipitation with anti HA resin. Both ULK1 WT and ULK1 KI were able to co-immunoprecipitate endogenous (lower band) and exogenous (upper band) FAM21 (Figure 3.5D). However, whilst a small band shift was apparent with overexpressed FAM21, no band shift was observed with the endogenous protein. FAM21 remains an attractive potential ULK substrate and both residues identified in the screen remain untested. However as both potential ULK sites were localised within the highly repetitive and serine/threonine-rich LFa repeats, and due to the lack of observable phosphorylation of endogenous FAM21, a more tractable novel substrate was sought.

These data indicate that SORBS2, Capzb and FAM21 are likely ULK kinase substrates. However, the specific target residues and relevance to autophagy remain in question. Returning to the SILAC dataset, it is likely that the potential prevalence of non-specific hits (Figure 3.2C) precludes 'simple' analysis, necessitating a more sophisticated approach to dataset interrogation.

3.4 Bioinformatics analysis of phosphoproteomic dataset

3.4.1 Detecting ULK's signature in the SILAC dataset

To attempt to isolate ULK-dependent phosphorylation events and to exclude false positives, the ULK1 consensus signature (Egan et al., 2015) was used to annotate the dataset (Figure 3.6A). The distribution of peptides matching this motif displayed no significant enrichment in either cell type. Consensus sequence enrichment, which can be used to identify the responsible kinase(s) from given set of substrates by describing the 'average' motif, revealed a sequence that was strikingly dissimilar from the ULK1 motif in all three SILAC experimental datasets when focussing on sites depleted in Ulk1/2 DKOs (Figure 3.6B). Proline was overrepresented at every position examined excluding the phosphoacceptor – this was particularly striking as the presence of proline at any position from -3 to +2 relative to the phosphoacceptor was found to strongly hamper phosphorylation by ULK1 in vitro (Egan et al.,

2015). Furthermore, a bias for basic residues N terminal and acidic residues C terminal to the phosphoacceptor was detected. Focussing only on peptides with a proline in the +1 position removed the charge bias, potentially indicating the modulation of more than one kinase in the DKO MEFs. Notably removal of proline-directed sites did not clearly reveal the predicted ULK1 signature. Taken together, these data indicate that much of the variation in the dataset might not stem directly from loss of ULK activity.

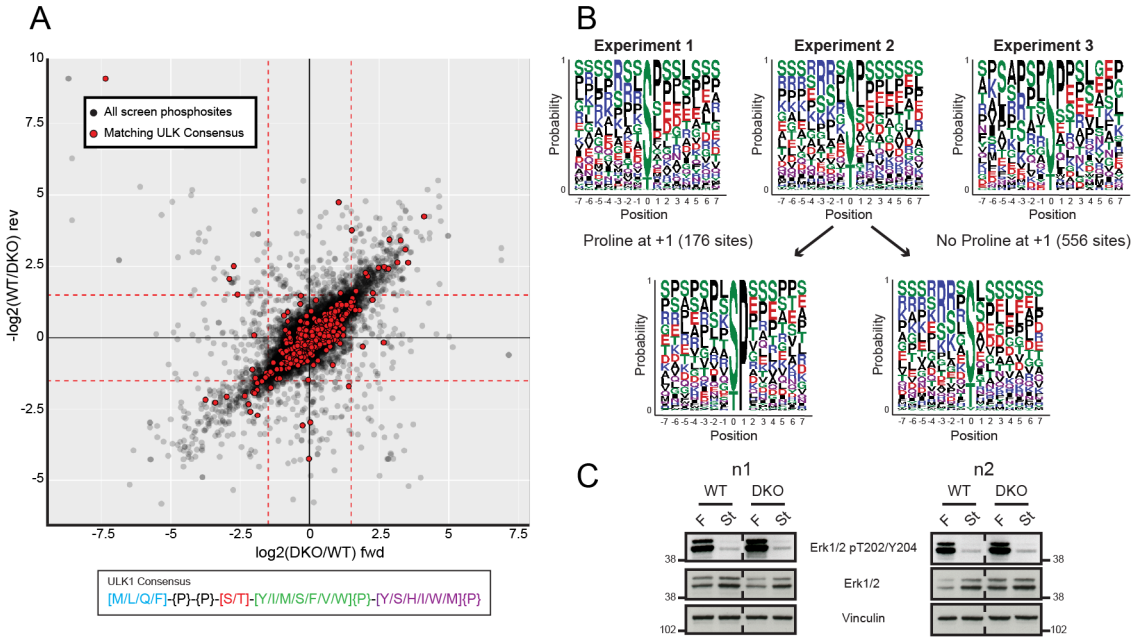

Figure 3.6 – *Detecting the ULK's signature in the SILAC dataset.* **A** – Forward and reverse SILAC ratios from phosphopeptides detected in experiment 1 were plotted as in Figure 3.2B/C. Phosphopeptides matching the ULK1 consensus motif are shown in red (560 phosphosites) whilst mismatches are shown in black (15,748 phosphosites). Phosphopeptides scoring <-1.5 in both forward and reverse experiments (bottom left box, enclosed by red dashed line) were considered to be robustly depleted in DKOs. **B** – Consensus logos showing the relative enrichment of amino acids surrounding phospho-sites depleted in Ulk1/2 DKO MEFs (scoring $\log_2$(DKO/WT)<-1.5 in either forward or reverse conditions). Data from experiments 1, 2 and 3 are shown separately. For experiment 2, separate logos display average motifs for peptide subsets with and without proline at position +1. **C** – Wild type (WT) and Ulk1/2 double knockout (DKO) MEFs were starved of amino acids for 2hrs before lysis and Western blot analysis. In two independent experiments, Erk1/2 phospho-T202/Y204 staining revealed no clear reduction in Erk1/2 activity in DKO MEFs. For plots 3.6A and 3.6B only phosphopeptides detected in both forward and reverse repeats are depicted and analyses were performed with the help of Stefan Boeing (Bioinformatics STP).

The consensus signatures revealed in Figure 3.6B bore a noticeable resemblance to kinases in the mitogen-activated kinase pathway, specifically ERK1 (gene name *MAPK3*) and ERK2 (gene name *MAPK1*), herein known as ERK1/2, and p90RSK (gene name *RPS6KA1*). This branch of the MAPK signalling cascade is active in the presence of growth factors and drive cell proliferation. ERK1/2 are 'proline-directed' kinases. They target serine and threonine residues immediately preceding a proline residue, and proline is highly overrepresented at almost every position N- and C-terminal to the phosphoacceptor in the ERK1 and ERK2 consensus signature. On the other hand, the ERK1/2 effector p90RSK displays a specificity for serine preceded by basic residues and followed by acidic residues (Hornbeck et al., 2015).

MGI Symbol	Uniprot ID	Target Site	-3	-2	-1	0	1	2	Mean Expt 1	Mean Expt 2	Mean Expt 3	Loose	Stringent
Adgre5	E9QJS7	S799	F	N	S	S	T	T	-1.261	0	-1.7085	+	
Aim1	E9PVP1	T20	Q	K	S	T	D	S	-0.9805	-2.035	0	+	+
Akap5	H3BIV5	S249	Q	R	A	S	L	L	-3.344	-0.7035	0	+	
Cgn	D3YUW7	S130	L	I	R	S	Q	S	-2.523	0	0	+	+
Cgn	D3YUW7	S444	L	K	H	S	Q	S	-2.832	0	0	+	+
Cgn	D3YUW7	S269	V	L	Q	S	F	E	-2.2625	0	0	+	
D8Ertd82e	E9QLH9	S704	M	N	K	S	S	S	-1.6845	0	0	+	+
Dennd5b	A2RSQ0	S690	L	R	Q	S	S	E	-1.9725	0.345	0.0555	+	+
Efnb1	P52795	S282	L	S	L	S	T	L	-3.484	-0.2955	0	+	
Eif6	O55135	S239	M	R	D	S	L	I	-0.7535	-1.6305	-0.381	+	+
Ezr	P26040	T533	Q	L	L	T	L	S	-1.8615	0	0	+	+
Fzd6	Q542J1	S519	I	S	E	S	R	R	-2.7855	0	0	+	
Gpr126	Q6F3F9	S1134	L	S	S	S	S	I	-2.1855	0	0	+	+
Kiaa1671	Q8BRV5	S166	I	S	H	S	L	R	-1.726	0	0	+	
Lmtk2	Q3TYD6	S656	L	S	S	S	L	D	-1.8535	0	0.112	+	
Lsr	Q99KG5	S588	L	A	L	S	R	E	-4.166	-2.7475	0	+	
Mapkbp1	Q921Q9	S411	L	A	R	S	I	S	4.1855	0	-1.953	+	+
Nedd4l	Q3TQK9	T287	V	T	D	T	V	A	-1.657	-0.6595	0.4465	+	
Nes	Q6P5H2	S977	M	V	R	S	L	E	-2.303	-2.825	0	+	
Nhsl1	E0CYL9	S189	L	R	R	S	L	I	-1.59	0	0	+	+
Pak3	A3KGC0	S4	M	S	D	S	L	D	-1.5535	0	-0.5285	+	
Pik3r4	Q8VD65	S865	M	F	G	S	L	E	-3.109	0	0	+	
Ppl	Q9R269	S1656	L	R	R	S	I	V	-1.5745	-0.908	0	+	+
Prkab2	Q6PAM0	S38	M	V	G	S	T	D	-3.3515	-1.788	1.5325	+	
Rab38	Q5FW76	S187	L	L	E	S	I	E	-2.96	0	0	+	+
Rab3b	A2A7Z6	S199	M	S	D	S	M	D	-2.302	-2.562	0	+	+
Rb1cc1	Q9ESK9	S257	L	V	T	S	F	H	-2.2625	0	-2.3545	+	+
Rb1cc1	Q9ESK9	S237	M	K	R	S	T	E	-4.278	-3.551	-3.29	+	
Rb1cc1	Q9ESK9	S643	V	S	T	S	Q	A	-2.1815	0	0	+	
Rps9	Q6ZWN5	S160	I	D	F	S	L	R	-1.5225	0	0	+	
Rrm1	P07742	S780	M	V	C	S	L	E	-1.771	0	0	+	
Scd2	P13011	S37	F	E	K	S	S	H	-1.6255	0	0	+	+
Slc12a6	A2AGJ6	T977	L	R	L	T	S	I	-1.9605	0	0	+	+
Slk	O54988	S645	V	S	E	S	N	S	-0.0515	0	-1.877	+	
Sorbs2	B2RXQ9	S239	I	D	R	S	L	E	-3.4975	-2.923	0	+	
Strn	O55106	S227	L	T	D	S	A	S	-2.364	0	0	+	+
Ulk1	Q3UFT4	S465	I	R	R	S	G	S	-4.0505	0	0	+	
Vamp5	Q5M9K2	S48	L	D	M	S	S	A	-1.74	0	0	+	+
Prkag2	Q91WG5	S122	R	R	M	S	F	S	-3.0315	0	0		
Prkag2	Q91WG5	S124	M	S	F	S	G	I	0	0	0	+	+

Table 3.1 – *Phosphopeptides depleted in Ulk1/2 DKOs matching the ULK1 consensus sequence*. Phosphopeptides with $\log_2$(DKO/WT)< -1.5 when forward and reverse SILAC ratios were averaged in at least one experiment that also matched the ULK1 consensus motif are listed. The loose and stringent renderings of the ULK1 consensus motif are described in Figure 3.7A. Rows 4-10 contain amino acid identities at each position relative to the phosphoacceptor at position 0. Prkag2, separated by an empty row at the bottom, was included as whilst serine 122 was highly depleted in the absence of ULK, the neighbouring serine 124 closely matches the consensus sequence suggesting that either or both could be targeted by ULK. The analysis in Table 3.1 was performed with the help of Stefan Boeing (Bioinformatics STP).

To test whether aberrant MAPK regulation might be partially responsible for the differences noted in the Ulk1/2 DKO MEF phosphoproteome, Erk1/2 activity, measured by assessment of phospho-T202/Y204 levels, was assessed in WT and DKO MEFs in both basal and starvation conditions. No difference in Erk1/2 activity was detected in either condition.

3.4.2 Fine-grained analysis of SILAC dataset yields high confidence ULK substrate shortlist

With the low representation of phosphopeptides matching the ULK consensus motif in mind, the dataset was pared down further to increase the likelihood of identifying direct ULK1 substrates (Figure 3.7A). To focus on reliably depleted sites, phosphosites that had an assigned SILAC ratio in both forward and reverse scenarios in at least one experiment and no variation in any control scenario were again brought forward (Appendix Table A). To isolate putative direct substrates, the ULK1 motif from (Egan et al., 2015) was utilised to annotate the dataset as before. Loose and stringent renderings of the consensus sequence were employed, resulting a list of phosphopeptides depleted upon ablation of ULK that matched the ULK1 consensus signature (Table 3.1). To further increase the confidence with which ULK substrates were identified, a conservative protein-protein interaction network was generated (Türei et al., 2015, Stark et al., 2006, Giurgiu et al., 2019) (Figure 3.7B). By annotating the network with phosphopeptides reproducibly depleted in DKOs, it was discovered that a number of proteins within 2 nodes of ULK1 and ULK2 bear differentially regulated phosphorylation sites. In the AMPK complex, two serine residues (one each of the beta and gamma subunits) were depleted for phosphorylation in Ulk1/2 DKO MEFs. Promisingly, ULK-regulated phosphorylation at one of these sites, serine 38 in 5'-AMP-activated protein kinase subunit beta-2 (gene name *Prkab2*) has been reported previously (Table 1.1).

Phosphorylation of Atg14 at serine 9 was reduced in Ulk1/2 DKO MEFs. This is in the same region as serine 29, a known ULK1 substrate (Table 1.1). These sit in Atg14's N terminus, a region that mediates docking to ER sites during the formation of the phagophore (Park et al., 2016, Baskaran et al., 2014). Interestingly, two phosphorylation sites within the pseudokinase p150 (gene name *Pik3r4*) were depleted in absence of Ulk1/2 with one of these sites (Serine 865) bearing close similarity to the ULK consensus signature. Instructed by the protein-protein

interaction network and ULK1 consensus motif, as well as by previously-published studies in which potential autophagy regulators were identified, a shortlist of putative ULK substrates was compiled (Figure 3.7C).

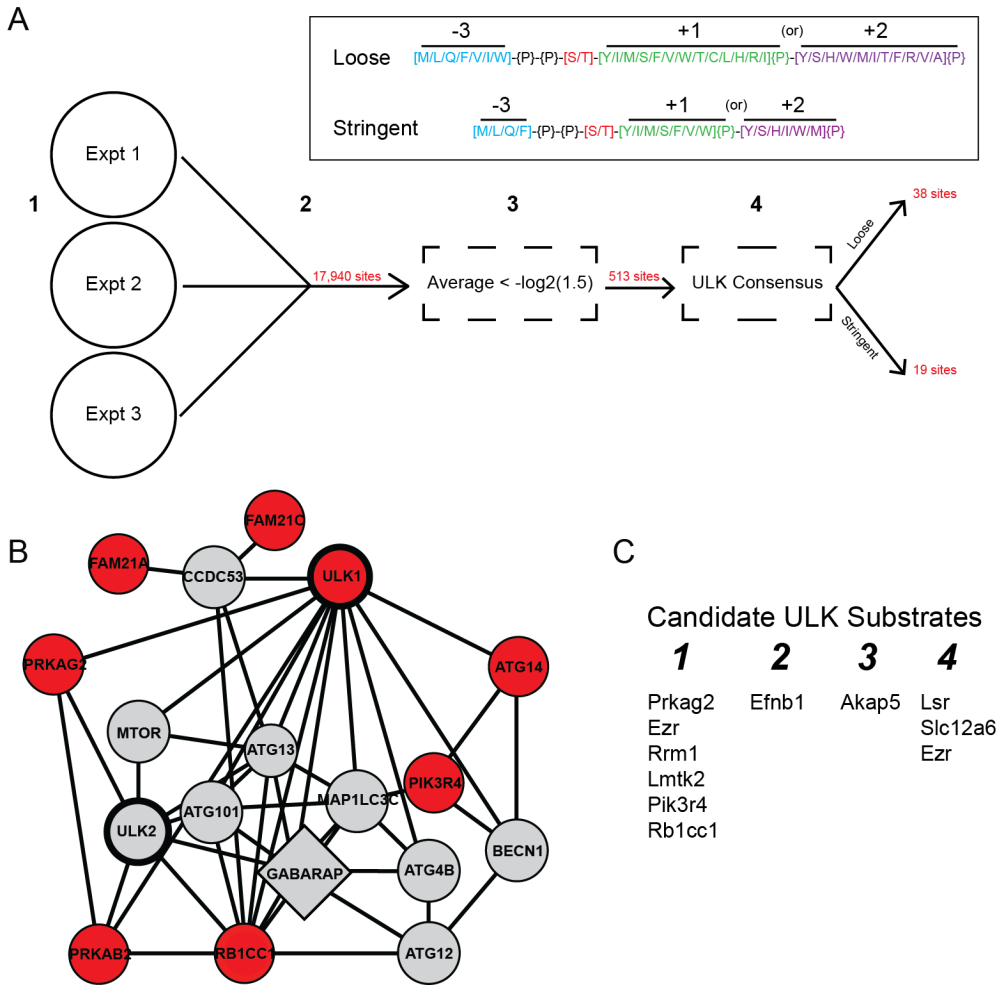

Figure 3.7 – *Fine-grained analysis of SILAC dataset yields high confidence ULK substrate shortlist.* **A** – Flow diagram indicating steps taken to triage SILAC dataset **B** – Human protein-protein interaction network based on interactions from CORUM, Bioplex and Autophagy Regulatory Network databases (Giurgiu et al., 2019; Türei et al., 2015; Stark et al., 2006). Curated network shows proteins within 2 nodes of ULK1 or ULK2 (bold). Annotated in red are proteins containing phosphopeptides depleted in the absence of Ulk1/2. Proteins that were identified in a previously published screen for ULK regulators are shown as a diamond (McKnight et al., 2012). **C** - List of ULK substrate candidates, comprised of phosphoproteins containing a potential ULK site(s) that were within two nodes of ULK1 and ULK2 (Column 1), identified in a previously published siRNA screen for autophagy regulators (McKnight et al., 2012) (Column 2) or known to directly bind a protein in this screen (Column 3), or are components of the ATG9 compartment (Judith et al., 2019) (Column 4). The analyses in Figure 3.7 were performed with the help of Stefan Boeing (Bioinformatics STP).

3.5 Discussion

The SILAC dataset offers a valuable insight into the affect loss of ULK has on the phosphoproteome. Technical and experimental repeats provide relatively comprehensive scope and allow the immediate assessment of data reproducibility within and between experiments. Focussing on proteins within two nodes of ULK1 and ULK2 revealed a number of interaction partners that bore differentially-regulated phosphosites that matched the ULK consensus motif. These included a known ULK target, Prkab2-S38. Cross-referencing with independent datasets resulted in the formation of a high-confidence list of potential substrates at residue-specific resolution. However, further validation experiments are required to confirm these sites as direct ULK substrates.

Technical limitations of SILAC -based analyses impinged on experimental design. Most notably, as detection of differentially labelled peptides occurs during MS1 (which leads to a limit on the number of labelling conditions that can be compared simultaneously due to prohibitive spectra complexity when upwards of 3 samples are used), only two samples were compared per experiment. In this instance, WT and DKO MEFs were compared with one treatment condition (2hrs starvation or Torin1). Without knowledge of phosphoproteomal status in the absence of autophagic stimuli in both cell types, protein level differences that inevitably ensue after cells adapt to genetic manipulation (in this case the removal of two highly conserved signalling kinases) can feed through as false positives that are largely indistinguishable from the targets of interest. Exacerbating this issue, whilst the WT MEFs were of a pure Black 6 background, the Ulk1/2 DKO cells were derived from a mixed Black 6/Agouti cross.

This phenomenon may be demonstrated by the reciprocal enrichment patterns observed between phosphopeptides assigned to Sorbs1 and Sorbs2 (Figure 3.2B), and is likely revealed when considering the dissimilarity between the published ULK1 motif and the consensus signature generated from the phosphopeptides depleted in the SILAC dataset (Figure 3.6B). However, it is also important to consider that, as the published motif was generated by assessing phosphorylation of peptides by ULK1 *in vitro*, it may not reflect ULK's *in vivo* substrate specificity. This consideration is particularly important when assessing the use of this motif to triage the SILAC dataset (Figure 3.7B; Table 3.1), however it likely describes ULK1's substrate biases at least partly, and was chosen in the absence of any alternative.

Intriguingly, the redistribution of SORBS2 observed upon starvation is very similar to that observed with the focal adhesion proteins Vinculin and Paxillin in MEFs (Chen et al., 2008). Both proteins translocate from focal adhesions to the cytoplasm, possibly to autophagic membranes, in a Paxillin dependent fashion, and is possible that SORBS2 also follows this pathway. Interestingly, Paxillin is an Atg1 substrate in Drosophila and autophagosome formation is inhibited when it is removed (Chen et al., 2008). It is possible that SORBS2 functions as part of an autophagic signalling hub centred around focal adhesions.

SORBS2, FAM21 and Capzb are all likely ULK kinase substrates. However, in the case of SORBS2 and possibly Capzb, current evidence does not support the sites predicted in the SILAC screen to be the sole/major phosphoacceptors downstream of ULK. It is important to consider that only *in vivo* approaches were used to validate these substrates, in which both kinase and substrate were coexpressed before measuring substrate electrophoretic mobility shift as a readout for phosphorylation. These approaches rely on the fact that phosphorylation events increase a protein's relative mass. With a molar weight of 80Da, the phosphate group itself adds little discernible mass to a polypeptide, however the strong negative charge increases a proteins effective molecular weight noticeably, resulting in an upwards band shift relative to the unphosphorylated protein. A key drawback of this approach is that band shifts are more apparent in smaller proteins than larger proteins – this in turn entails that small shifts in large proteins are indicative of multi-site phosphorylation, as in the case of FAM21 (which is perhaps unsurprising due to the repetitive nature of the extended tail). The most pronounced shift was noted with SORBS2, for which the discreet ladder of bands noted upon ULK1 WT phosphorylation was strongly indicative of multi-site phosphorylation. With this in mind, it is perhaps unsurprising that mutation of 5 single phosphorylation sites had little if any noticeable effect on total band shift.

With the exception of LSR, phosphorylation of the all putative substrates was assessed via kinase/substrate overexpression. As in this format substrate phosphorylation occurs within the cell, the approach is arguably more reliable than the profoundly non-physiological *in vitro* kinase assay. However, as overexpression of either substrate or kinase could inadvertently alter cellular signalling networks, it is impossible to validate direct substrates without additional corroborating data derived from complementary techniques. This is compounded

by both kinase and substrate being present at non-stoichiometric levels due to overexpression, meaning even direct phosphorylation could be non-physiological.

The caveats associated with *in vitro* kinase assay data are discussed in the introduction to this chapter. Nonetheless this approach is one such complementary technique that could be used to help validate SORBS2, FAM21 and Capzb as direct ULK substrates. The phosphorylation of LSR by Ulk1 was tested in this manner. LSR was included in the final SILAC shortlist as it contained at least one depleted site that matched the ULK1 consensus sequence and was identified in the ATG9 compartment. Several LSR phosphopeptides were depleted in DKO MEFs, indicative of either multisite hypophosphorylation or a difference in protein level. Whilst the *in vitro* kinase assay data did not support direct phosphorylation of LSR by ULK1, it is entirely possible that the experimental conditions were suboptimal and must be changed before phosphorylation is observed.

In the case of SORBS2, compounding the difficulty in target site identification was the dearth of reagents capable of detecting the endogenous protein by either Western blot or immunofluorescence. Furthermore, SORBS2 expression is undetectable in many tissues/cell lines, and may exhibit mosaic expression pattern in cell lines in which it can be detected, with around half of COS7 and HeLa cells being negative likely due to histone deacetylase control of transcription (Anekal et al., 2015). Combined with the limited inhibitory phenotype noted upon overexpression (Figure 3.3A), these findings make SORBS2 unattractive as a putative substrate as it is unlikely to be crucial for starvation-induced autophagy.

Alongside differences in protein level, it is entirely possible that a secondary kinase whose activity is hampered in the DKO MEFs is responsible for the phosphoproteomal alterations describes herein. The MAP kinases Erk1/2 and the downstream effector p90rsk were investigated as their consensus motifs closely match that observed in when consensus sequence enrichment was examined, however no clear difference in Erk1/2 activity was observed in WT vs DKO MEFs in either basal or starved conditions. Whilst MEFs in experiment 1 were cultured in full medium in the presence of Torin1, experiments 2 and 3 both utilised starvation as the autophagy-inducing stimulus. It is notable that the MAPK cascade is largely switched off when cells are cultured in the absence of growth factor (i.e. in EBSS), providing further evidence that Erk1/2 and p90rsk are not the major secondary kinases responsible for

the major variations in the DKO MEF phosphoproteome. Of note, SP/TP motifs are highly represented in the proteome, and these motifs are targeted by kinases across many families (e.g. mTOR, the cyclin-dependent kinases, mitogen-activated kinases and GSK3).

There are thus four potentially complementary explanations for the major phosphoproteomal alterations observed in the DKO MEFs: 1) Ulk1/2 are capable of proline-directed phosphorylation, 2) ULK phosphorylation drives substrate destabilisation and destruction, leading to an underrepresentation of detectable substrates, 3) The levels/activity of an unidentified kinase(s), not necessarily downstream of Ulk1/2, are reduced in DKO MEFs, or 4) Basal, cell line-specific proteomal changes skewed the dataset. Based on the features of the ULK consensus motif (Egan et al., 2015), but more importantly on ULK and Atg1p substrates identified to date (even taking into account confirmation bias) (Papinski and Kraft, 2016, Mercer et al., 2018), point 1 seems unlikely. Furthermore, with the exception of a mutant form of ATG16L1 found in Crohn's disease, phosphorylation by ULK is not usually associated with substrate destabilisation (Alsaadi et al., 2019). It is thus most feasible that alterations in protein level, secondary kinase activity or a mixture of the two resulted in the enriched consensus motif observed in Figure 3.6B.

With these factors in mind, a battery of bioinformatics techniques was used to extract biologically relevant insight from the SILAC dataset, resulting in the construction of a 'high-confidence' list of potential ULK substrates (Figure 3.7C). However, as the potential impact from points 2 and 3 persist, so does the chance that the list is enriched with false positives. This is exemplified by the presence of LSR in the final dataset. Assessing changes in proteome levels in parallel may have improved data quality in this regard. Importantly, the ability to assess phosphoproteomal status in basal conditions is crucial to increase the confidence with which ULK substrates are identified.

Chapter 4. Further phosphoproteomic screening and validation of candidate ULK substrates

4.1 Introduction and aims

The data presented in Chapter 3 describe a SILAC-based screen as a means for ULK substrate discovery. This approach is advantageous as it provides an unbiased and a global snapshot of comparative phosphoproteomes in the wild type and Ulk1/2 DKO MEFs, however the complexity of dataset makes analysis difficult. This problem is evidenced by the preponderance of non-specific hits and is compounded by the use of genetically distinct cell lines. Together, these data emphasise the requirement for further unbiased screens for ULK substrates. Two screening approaches will be discussed in this chapter: *in vivo* crosslinking and TMT (tandem mass tag)-based phosphoproteomics.

In vivo crosslinking

The low affinity interaction between kinase and substrate is exceedingly transient and therefore difficult to detect using existing methods of studying protein-protein association. Co-immunoprecipitation alone is capable of probing only relatively strong interaction events, and combination with chemical crosslinking does not afford the specificity required to identify substrates with any degree of confidence. The site-specific incorporation of photo-crosslinking amino acids into proteins via genetic code expansion (GCE) has arisen as a viable method to study protein-protein interaction (Chin, 2014). This system involves introducing a non-proteinogenic codon (typically the amber stop codon TAG) into a plasmid-encoded gene of interest, followed by the coexpression of this construct with a complementary tRNA and corresponding tRNA synthetase engineered to load it with a non-natural amino acid added to the growth media (Figure 4.1A). This leads to incorporation of the non-natural amino acid at the introduced amber stop codon, hence the name amber suppression.

Much of the pioneering work in GCE was performed via the introduction of tRNAs artificially aminoacylated with non-natural amino acids (Bain et al., 1992, Nowak et al., 1995, Noren et al., 1989). However the potential applications for GCE expanded greatly when the tRNA/tRNA synthetase pairs capable of facilitating this process *in vivo* were generated in the laboratory of Peter Schultz (Wang et al., 2001, Chin et al., 2002). Key to this phenomenon is the existence of

'orthogonal' pairs that, based on unique modes of tRNA recognition by the synthetase, do not cross react with endogenous counterparts (Kobayashi et al., 2003). Ergo, introduced orthogonal tRNA synthetases will only esterify non-natural amino acids to the exogenous and matching tRNAs.

Due to the early identification and characterization of archaeal amber codon-specific $tRNA^{Tyr}$-tyrosyl-tRNA synthetase pair from *Methanosarcina jannaschii*, which is orthogonal to *E. Coli* counterparts (Wang et al., 2000), tyrosine and its derivatives were heavily utilised in the development of GCE and were the first employed to incorporate unnatural amino acids in live cells (Wang et al., 2001). Initial $tRNA^{Tyr}$ sequence optimisation via genetic selection was required to generate a fully orthogonal pair and further directed evolution of the *M. jannaschii* tyrosyl tRNA synthase has resulted in a panoply of mutants able to load UAG-specific tRNAs with more than 70 non-natural amino acids (e.g. O-methyl-L-tyrosine p-acetyl-L-phenylalanine, p-iodo-L-tyrosine, p-azido-L-phenylalanine and p-benzoyl-L-phenylalanine (Brown et al., 2018, Mitra, 2013)).

These experiments were initially performed in bacteria; however, optimisation of bacterial tRNA/tRNA synthetase pairs orthogonal in both yeast and mammals allowed the first deployment of genetic code expansion in eukaryotes (Chin et al., 2003). Furthermore, the amber stop codon-encoded amino acid pyrrolyisine found only in specific archaeal and bacterial species was discovered at a similar time. $tRNA^{Pyl}$ -pyrrolysyl-tRNA synthetase pairs were first identified in the genomes of *Methanosarcina barkeri* and M. *mazei* and are ideal for GCE in both bacterial and mammalian systems (Blight et al., 2004, Srinivasan et al., 2002, Wan et al., 2014, Krzycki, 2005, Brown et al., 2018). Accordingly, *M. barkeri-/M. mazei-derived* pairs have been used extensively in mammalian cell lines and also more recently in a host of model animals including *C. elegans*, Drosophila, mice (Liu et al., 2017, Greiss and Chin, 2011, Bianco et al., 2012, Ernst et al., 2016, Brown et al., 2018).

Non-natural amino acids with photoactivatable crosslinking moieties were soon developed to study protein-protein interaction, the first chemical class being benzophenone-based probes (Chin et al., 2002). However, insertion of such bulky, hydrophobic and therefore sterically-demanding R groups into surface-facing residues is often associated with structural disruptions, with non-conservative substitutions liable to destroy binding events the

experiment is designed to capture. To combat this, GCE has been adapted to facilitate the incorporation of a number of aliphatic photocrosslinking amino acids (Yang et al., 2016b, Chou et al., 2011, Hancock et al., 2010).

One such amino acid is the diazirine-based photo-crosslinker 3'-azibutyl-*N*-carbamoyl-lysine (AbK) (Chou et al., 2011, Hancock et al., 2010, Ai et al., 2011). AbK is derived from pyrrolysine and the tRNA synthetase engineered to load it onto its corresponding tRNA (AbKRS) was generated by directed evolution of *M. barkeri* pyrrolysyl-tRNA synthetase (Ai et al., 2011). It has a long and flexible and hydrophilic R group resulting in a relatively large sampling area for the diazirine group at the terminus. This moiety consists of a carbon atom bound to two atoms of nitrogen, which are themselves double bonded (Figure 4.1B). It is inert in physiological conditions; however, photolysis following irradiation with 365nm UV light results in the release of molecular nitrogen and the formation of a highly reactive carbene radical intermediate capable of covalently inserting into nearby C-C, C-H, N-H or O-H bonds (Dubinsky et al., 2012).

Importantly, when inserted into the substrate binding site of CDK5, AbK was able to capture the over-expressed model substrate PAK1 (Ai et al., 2011), raising the possibility that this method could be used to identify novel substrates expressed at physiological levels.

TMT-based phosphoproteomics

As discussed previously, a major drawback of the SILAC approach is the restriction on the number of samples that can be compared simultaneously. This is a direct consequence of the limits on labelling conditions, with a maximum of 3 per experiment able to be included. Post-lysis isobaric labelling methods greatly expand the number of labels that can be utilized in a single experiment and thereby present a viable alternative. Labelling takes place immediately after proteolytic cleavage, using labels that covalently interact with the newly generated peptides. Compared to SILAC labelling therefore, isobaric labeling techniques require no prior label incorporation.

Two commonly used isobaric labelling methods utilise iTRAQ and TMT reagents. Whilst iTRAQ allows comparison of up to 8 samples, 10plex TMT experiments are routinely employed, with an 11plex TMT system now commercially available. Demonstrating the practical potential of isobaric labelling, multiple sets of TMT reagents have been 'hyperplexed' to achieve

simultaneous measurement of 54 samples in a single mass spectrometry run (Everley et al., 2013). Both iTRAQ and TMT labels have three distinct domains: an amine-reactive moiety that covalently interacts with NH2 groups, a reporter group of a specific mass that varies depending on the sample being labelled and a balancer group which varies depending on the reporter group mass. The specific distribution of heavy isotopes between the latter two groups yield labels with the same m/z value in MS1, which are distinguished after label fragmentation during high energy collision-induced dissociation. This allows the relative enrichment of sample peptides to be inferred from the ratios of reporter ion intensities in MS2. As labelling occurs at a relatively late stage during sample processing, post-lysis isobaric labelling is associated with increased scope for quantification biases arising due to improper handling. To help combat this, labelling efficiency and sample mixing checks are performed and samples are pooled before phosphopeptide enrichment or mass spectrometry analysis.

A more significant problem is the persistence of contaminating peptides with similar elution times and m/z values after MS2. In this instance, the reporter ion intensity assigned to a target peptide reflects the sum total of those corresponding to the target protein as well as any contaminants. As the majority of peptides in a sample are likely not to have responded to a given experimental condition, reporter ion ratios tend to approach 1 and are thus 'compressed' resulting in global underestimation of quantitative ratios (Cheng et al., 2016). While post-lysis isobaric labelling can afford similar depths of analysis as SILAC, ratio compression has been reported to impinge on quantification accuracy (Hogrebe et al., 2018, Altelaar et al., 2013). It is possible to accommodate for this via additional peptide fractionation stages to reduce sample complexity, the use of specially designed software to account for label interference and/or the inclusion of additional round of mass spectrometry on the MS2 fragments termed MS3 (Cheng et al., 2016, Savitski et al., 2013, McAlister et al., 2014, Ting et al., 2011). Despite these concerns, post-lysis isobaric labelling offers a promising solution for the issues associated with the SILAC screen.

Aims:

- Optimise *in vivo* crosslinking and TMT-based phosphoproteomics for use in identification of novel ULK substrates.
- Cross-reference any resulting data with those from the SILAC screen.
- Validate shortlisted ULK substrates

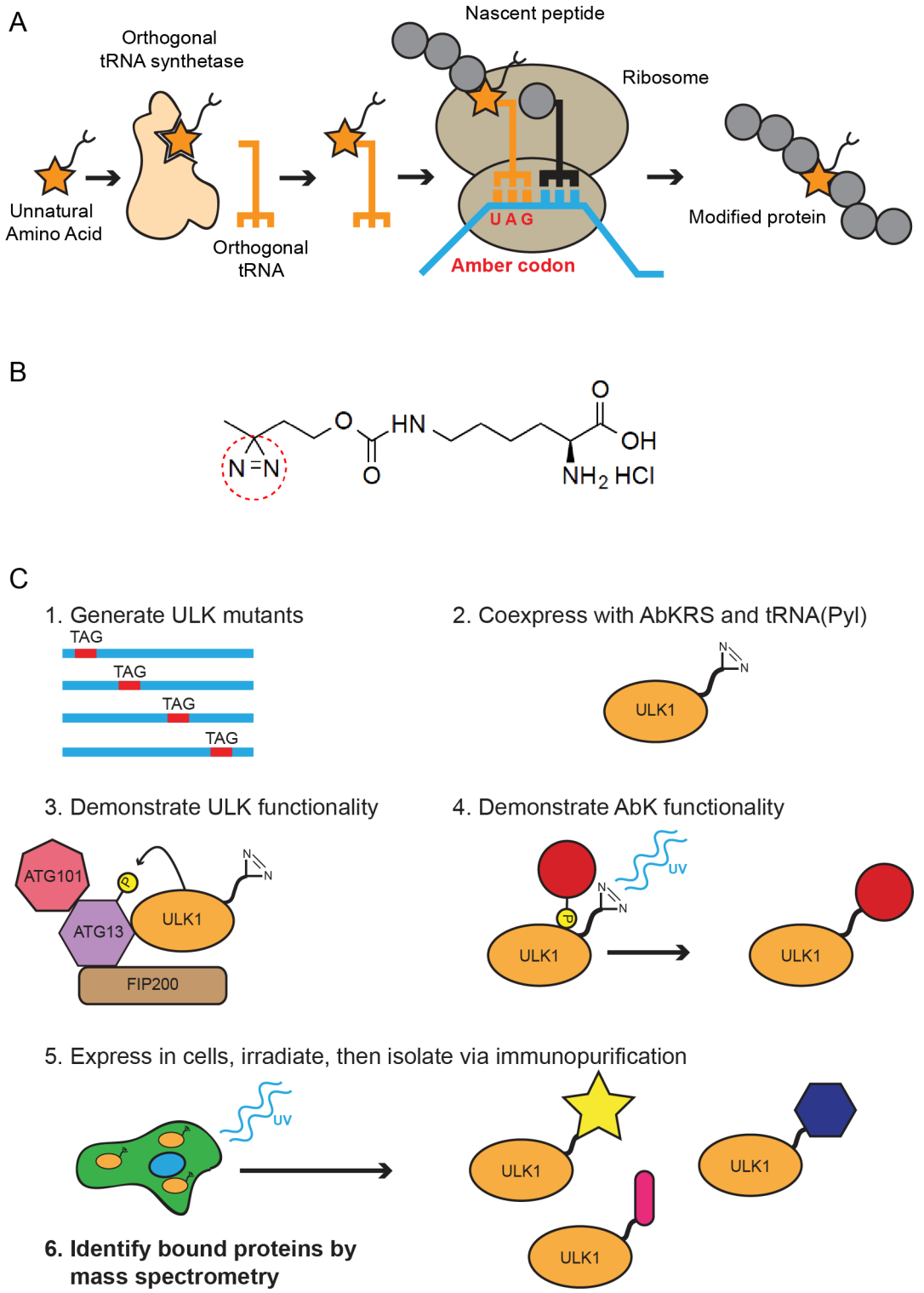

Figure 4.1 – *In vivo crosslinking screen concepts and protocol:* **A** – The mechanism of genetic code expansion is rendered schematically. **B** – Chemical structure of 3'-azibutyl-N-carbamoyl-lysine (AbK), the diazirine moiety is circled. **C** – Schematic representation of the stages involved in the crosslinking screen protocol.

4.2 *In vivo* crosslinking screen

4.2.1 Schematic overview of *in vivo* crosslinking screen

The *in vivo* crosslinking screen was designed to identify direct substrates by capturing kinase-substrate interaction events via the formation of covalent conjugates. This technique was optimised in parallel with Khalil Davis and Peter Parker (The Francis Crick Institute; unpublished data).

The *in vivo* crosslinking screen was facilitated by genetic code expansion. To capture and preserve kinase-substrate conjugates, the non-natural amino acid AbK was incorporated into the active site of ULK1. A schematic representation the crosslinking screen is shown in Figure 4.1C. Several ULK1 TAG mutants, otherwise referred to as amber mutants, were screened for expression levels, complex association, kinase activity and ability to capture overexpressed substrates before bringing forward the top candidate for use in the screen. The screen involved expression of the ULK amber mutants in cells before starvation to activate autophagy, UV irradiation to potentiate the crosslinking moiety and immunoprecipitation to isolate kinase-substrate conjugates to be identified by mass spectrometry.

4.2.2 Production and characterisation of ULK1 amber mutants

Amber stop codons were introduced into ULK1's kinase domain for AbK incorporation. Using the ULK1 kinase domain crystal structure (Lazarus et al., 2015), 6 sites were chosen that were surface accessible and close to the substrate-binding pocket (Figure 4.2A). When cultured in basal media, translation of exogenously expressed HA-ULK1 was terminated at the introduced amber stop codons. In presence of 1mM AbK the stop codon was read through and full-length HA-ULK1 bearing a non-natural amino acid at the given positions was expressed (Figure 4.2B). Assuming amber suppression efficiency was even between constructs, the protein level variability was likely due to altered stability depending on position of AbK incorporation. While all of the amber mutants were able to bind ULK complex members in coimmunoprecipitation experiments (Figure 4.2C), their activity (revealed by their capacity to autophosphorylate *in vitro*) was altered differentially (Figure 4.2D) – ranging from no observable effect (ULK1TAG186) to complete abrogation (ULK1TAG142, hitherto removed from analysis).

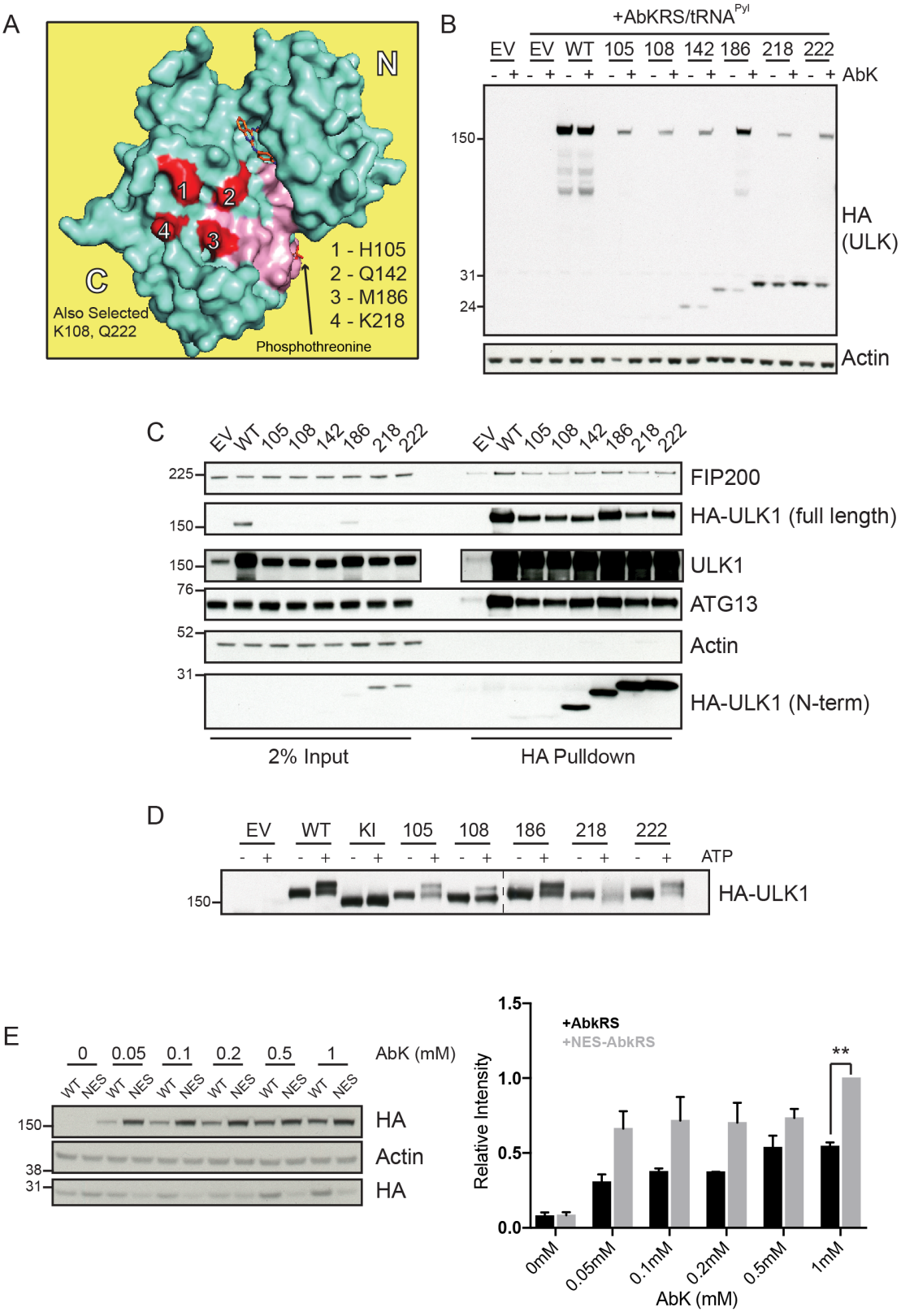
A
N
C
1
2
3
4
1 - H105
2 - Q142
3 - M186
4 - K218
Also Selected
K108, Q222
Phosphothreonine
B
+AbKRS/tRNA^Pyl
EV EV WT 105 108 142 186 218 222
AbK
150
31
24
HA
(ULK)
Actin
C
EV WT 105 108 142 186 218 222
EV WT 105 108 142 186 218 222
225
150
150
76
52
31
FIP200
HA-ULK1 (full length)
ULK1
ATG13
Actin
HA-ULK1 (N-term)
2% Input
HA Pulldown
D
EV WT KI 105 108 186 218 222
ATP
150
HA-ULK1
E
0 0.05 0.1 0.2 0.5 1
AbK (mM)
WT NES WT NES WT NES WT NES WT NES WT NES
150
38
31
HA
Actin
HA
+AbkRS
+NES-AbkRS
Relative Intensity
1.5
1.0
0.5
0.0
**
0mM
0.05mM
0.1mM
0.2mM
0.5mM
1mM
AbK (mM)

Figure 4.2 – *Production and characterisation of ULK1 amber mutants*. **A** - Crystal structure of the human ULK1 kinase domain with an ATP-competitive inhibitor from (Lazarus, 2015). The autocatalytic loop is shown in pink, with the phospho-threonine labelled. The small-molecule inhibitor docks in the ATP binding site between the N and C terminal lobes. Highlighted in red are four of the sites selected for amber mutation. They define a patch immediately adjacent to the consensus sequence binding area. PDB 4WNO, manipulated using Pymol 2.0.0. **B** - HEK293A were cotransfected with HA-ULK1 amber mutants with TAG codons at the indicated amino acid positions, AbKRS and $tRNA^{Pyl}$ before culturing in the presence or absence of 1mM AbK. WT = Wild Type, EV = Empty Vector. **C** – WT or amber mutant HA-ULK1 were expressed as before. After lysis, anti HA resin was used to isolate the exogenous protein plus bound complex members via coimmunoprecipitation. **D** - *In vitro* kinase assays using ULK amber mutants purified from HEK293A were performed in the presence or absence of ATP. **E** - Cells were cotransfected with HA-ULK1TAG222, $tRNA^{Pyl}$ and AbKRS wild type or NES mutant before culturing in media containing a range of AbK concentrations. Mean +/-SEM is shown, n=3, **<0.01

Unexpectedly, a functioning nuclear localisation signal was recently discovered in the *M. mazei* pyrrolysyl-tRNA synthetase, with nuclear exclusion shown to improve amber suppression efficiency (Nikić et al., 2016). While derived from a different archaeal species, sequence comparison revealed that AbKRS contains the same motif. To improve expression of the ULK1 amber mutants, a nuclear export signal was added to the N terminus of AbKRS (NESAbKRS), which resulted in a significant increase in amber suppression efficiency across a range of AbK concentrations (Figure 4.2E). For further validation experiments, cells were cotransfected with ULK1 mutants and NESAbKRS before culturing in 1mM AbK.

4.2.3 ULK1TAG186 bearing D165N has substrate crosslinking functionality

Having generated a set of amber mutants that display normal complex association and kinase activity, their substrate-crosslinking functionality was assessed to identify which amber mutant to use for the screen. The kinases were coexpressed with model substrates before UV irradiation followed by immunoprecipitation and analysis via Western blotting. Taking advantage of the fact that any covalent kinase substrate conjugate will survive preparation for Western blot and necessarily be larger in size than ULK alone, the appearance of ULK positive bands with molecular weights higher than full length ULK1 was used to assess crosslinking

efficiency. However, after testing a range of ULK substrates including ATG13, no kinase-substrate conjugates were detected (data not shown).

All active kinases contain an activation loop, which most often starts with the conserved Aspartate-Phenylalanine-Glycine (DFG) motif. In the active state, the invariant aspartate coordinates two Mg^{2+} ions to facilitate binding of ATP, with the DFG motif flipped 'in' relative to the inactive conformation. In the inactive 'out' state, aspartate is protonated and cannot chelate Mg^{2+}, promoting association with ADP. The tyrosine kinase Src was shown to have a 12-fold greater affinity for substrate in its inactive conformation (Foda et al., 2015). However, it was unknown whether this property applied to the serine/threonine kinase ULK1.

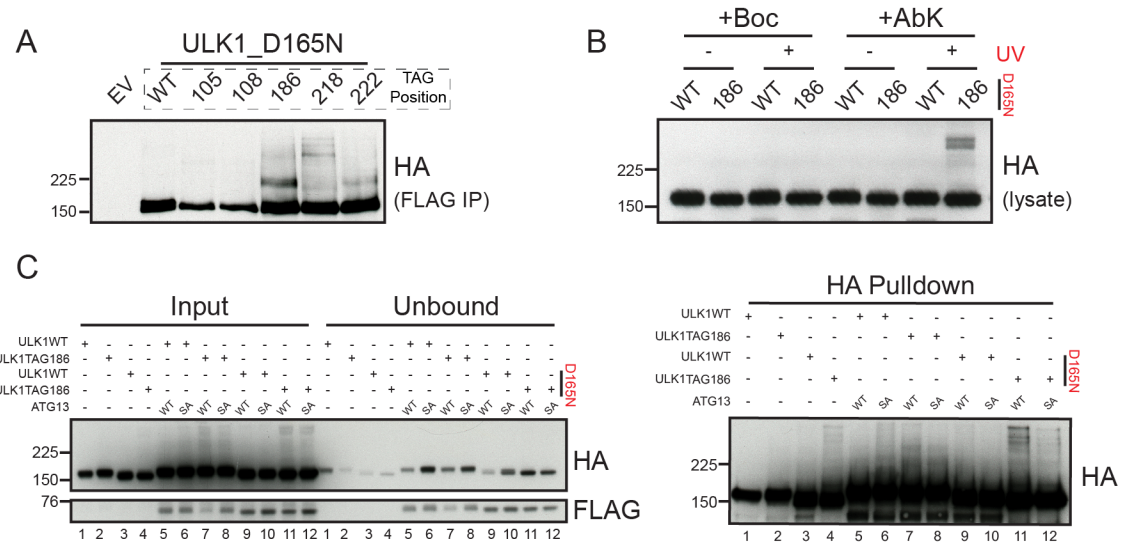

Figure 4.3 - *ULK1TAG186 bearing D165N has substrate crosslinking functionality*. **A** - HEK293A were cotransfected with HA-ULK1_D165N (which was otherwise wild type (WT) or bore TAG codons at specified amino acid positions), NESAbKRS, $tRNA^{Pyl}$ and ATG13 S355/356A -FLAG, before culturing in 1mM AbK. The cells were starved before UV irradiation to activate the diazirine moiety. Anti-FLAG immunoprecipitation (IP) was followed by Western analysis. After probing for HA, non-cross-linked ULK1 was visible at ~150kDa and the potential kinase-substrate conjugate bands at >150kDa. **B** – HEK293A were cotransfected with ATG13 S355/ 356A and either ULK1_D165N WT or TAG186 as indicated. Furthermore, cells were cotransfected with PylRS/$tRNA^{Pyl}$ and cultured in Boc-Lysine, or AbKRS/$tRNA^{Pyl}$ and cultured in AbK, resulting in 4 transfection conditions. Half of these cells were irradiated with UV immediately pre-lysis. Post-nuclear supernatant was analysed by Western blot. **C** – ULK1 WT/TAG186 containing either aspartate or asparagine at position 165 were transfected alone or cotransfected with ATG13 WT or S355/356A as indicated before HA pulldown. High molecular weight HA-positive bands present in both the 2% input (left) and pull down (right) lanes are potential kinase-substrate conjugates. n=1.

Therefore, to prolong kinase-substrate interaction time and thus boost the efficiency of substrate capture, aspartate 165 in the ULK1 DFG motif was mutated to asparagine to mimic protonation and lock ULK1 in its inactive state. To the same end the ULK target residue in ATG13 serine 355 (alongside neighbouring S356), was mutated to alanine, such that this unphosphorylatable residue might prolong interaction time in a manner similar to the pseudosubstrate mechanism of autoinhibition (Sommese et al., 2017).

After coexpression of the DFG-NFG amber mutants with ATG13 S355/356A-FLAG and irradiation followed by immunoprecipitation with anti-FLAG resin, the samples were separated by SDS PAGE and probed for HA to reveal crosslinked products. Potential kinase-substrate conjugates were detected when ULKTAG186, 218 or 222 were coexpressed (Figure 4.3A). Of these, HA-ULK1TAG186 was selected for further experiments due to its relatively high expression level (Figure 4.2B) and kinase activity (Figure 4.2D). When Boc-lysine, which is inert to UV, was incorporated in place of AbK in HA-ULKTAG186, no putative kinase-substrate conjugate bands were detected. Furthermore, in the presence of AbK, the formation of high molecular weight HA-positive bands required both HA-ULK1TAG186 expression and UV irradiation (Figure 4.3B).

To dissect the relative contributions of the D165N and S355/356A mutations, HA-ULK1 WT/TAG186 bearing aspartate or asparagine at position 165 were expressed alone, or in combination with ATG13-FLAG WT or S355/356A. Potential kinase-substrate conjugate bands were observed when ULK1TAG186_D165N was expressed alone (Figure 4.3C; *pulldown lane 4*). Coexpression of ATG13 WT appeared to promote/allow crosslinking compared to ATG13 S355/356A (Figure 1.3C; *input and pulldown lanes 11 and 12*), however crosslinking efficiency between samples expressing ULK1 alone (*pulldown lanes 1-4*) and ULK1 + ATG13 (*pulldown lanes 5-12*) were not compared due to expression level differences. Importantly, the effective molecular weight of ATG13 was increased *in vivo* in the presence of ULK1 WT/TAG186 when compared to the D165N mutants (Figure 4.3C; *unbound lanes 5-8 vs 9-12*), suggesting that substitution of methionine 186 for AbK allows kinase activity phosphorylation and does not destroy substrate accessibility or selectivity with regards to ATG13. For the screen, ULK1TAG186_D165N was coexpressed with ATG13-FLAG WT, with this condition chosen to maintain mutant ULK stability and complex stoichiometry and thus improve screen reliability.

4.2.4 Crosslinking Screen Results

Having identified expression conditions, the crosslinking screen was performed. The experiment was designed to exclude non-covalently bound proteins and to allow separation of sample proteins by size prior to mass spectrometry analysis. SILAC-labelled HEK293A were cotransfected with HA-ULK1 WT or TAG186 along with ATG13-FLAG and tRNA^{Pyl}/AbkRS before culturing in 1mM AbK to facilitate amber suppression. To remove non-covalent interactors, after the initial round of immunoprecipitation and washing, bound proteins were denatured and released from the beads via incubation in high SDS buffer. Dilution of SDS was followed by a second HA-immunoprecipitation (immunoprecipitation-recapture, IP-Re), before separation of the sample by SDS PAGE. After this, the gel was fixed and cut into horizontal slices before the protein constituents of each slice analysed by mass spectrometry. SILAC ratios were then used to quantify the relative contribution of proteins in each gel slice between WT and TAG186 ULK samples.

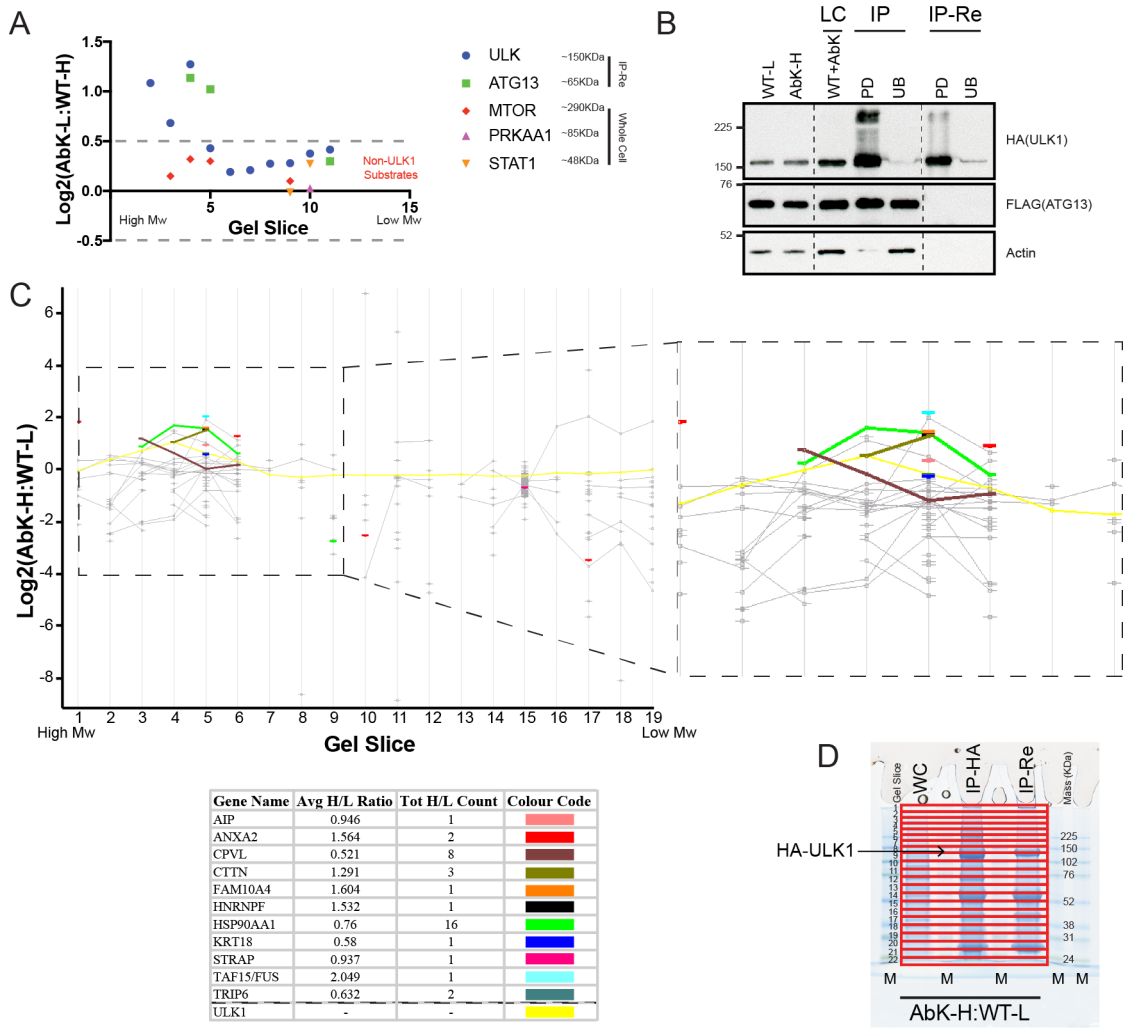

Gene Name	Avg H/L Ratio	Tot H/L Count	Colour Code
AIP	0.946	1	
ANXA2	1.564	2	
CPVL	0.521	8	
CTTN	1.291	3	
FAM10A4	1.604	1	
HNRNPF	1.532	1	
HSP90AA1	0.76	16	
KRT18	0.58	1	
STRAP	0.937	1	
TAF15/FUS	2.049	1	
TRIP6	0.632	2	
ULK1	-	-	

Figure 4.4 – *Crosslinking screen results*. **A** – Graph featuring SILAC enrichment ratios (log_2(AbK/WT), Y axis) in each gel slice (X axis) for selected proteins measured in proof of principle experiment. Proteins identified in post-nuclear supernatant (whole cell - WC) demonstrate molecular weight (Mw)-dependent separation. ULK1 and ATG13 ratios from the immunoprecipitation-recapture (IP-Re) were both indicative of AbK-dependent crosslinking. Proteins not enriched in either sample fall within the grey lines (threshold set arbitrarily at +/- log_2(0.5)) **B** – IP-Re control samples generated during production of crosslinking screen samples were analysed by Western blot. SILAC-labelled HEK293A expressing ATG13-FLAG along with wild type (WT) or mutant (AbK) ULK1 were lysed before two rounds of HA coimmunoprecipitation (IP, then IP-Re). 0.2% Loading control (LC), unbound (UB) and 1% pulldown (PD) samples from both IP and IP-Re stages were analysed. The first two lanes show protein levels and ULK1/ATG13 expression in both samples prior to mixing (WT+AbK). The absence of ATG13-FLAG or Actin in the IP-Re sample indicates that non-covalent interactors have been excluded. **C** – SILAC ratios for proteins detected in the crosslinking screen IP-Re sample. Grey points represent proteins detected in both samples in a given gel band with proteins detected in contiguous bands joined by a line. Proteins enriched in an AbK-dependent manner in high Mw bands 1-6 are coloured. The table below lists the relevant gene names, H/L ratio averaged between all bands within 1-6 in which the given protein was detected (Avg H/L Ratio) and the total number of times a SILAC ratio was calculated for each peptide between bands (Tot H/L Count). Graphs were exported from Perseus. **D** –Crosslinking screen samples were separated by SDS PAGE and the gel stained by Coomassie. The image shows the gel prior to cutting; the slices are annotated in red with slice number and relative mass in black. Data was collected for slices 1-19 only; M= Mw marker.

In a proof of principle experiment, ATG13 was enriched in high molecular weight band slices in the mutant sample, indicating that crosslinking had occurred. Supporting this indication, whilst ULK was identified along the length of the gel, ULK1TAG186 was enriched in all slices >150kDa (Figure 4.4A). Having established a workflow for which novel substrate conjugation was theoretically detectable, the experiment was scaled up 5-fold and repeated. The associated Western blots demonstrate that both immunoprecipitation steps were efficient and show the removal of coimmunoprecipitating proteins (Figure 4.4B). Again, ULK1 was identified across the length of the gel and enriched in the highest molecular weight slices in the mutant sample, indicative of successful crosslinking (Figure 4.4C/D). As full length, unconjugated ULK1 was enriched in gel slices 7 and 8 (Figure 4.4D), proteins detected in gel slices 1-6 were examined for potential kinase-substrate conjugates. Promisingly, a number of proteins were enriched in a mutant-specific manner in these slices (Figure 4.4C). Proteins possessing the following three qualities were defined as putative substrates:

1. Identified in the recaptured IP sample in bands 1-6
2. Major isoform <150kDa
3. SILAC ratio H:L >0.5 (enriched in mutant samples)

In SILAC-based quantification, H/L count reflects the number of occasions a heavy/light ratio was determined for a given peptide. It is therefore roughly equivalent to peptide count and similarly a higher the H/L counts confers greater confidence to the reported SILAC ratio (Cox and Mann, 2008, Cox et al., 2009). It was notable that of the 11 shortlisted hits, only CPVL, CTTN and HSP90AA1 had a H/L counts of 3 or more.

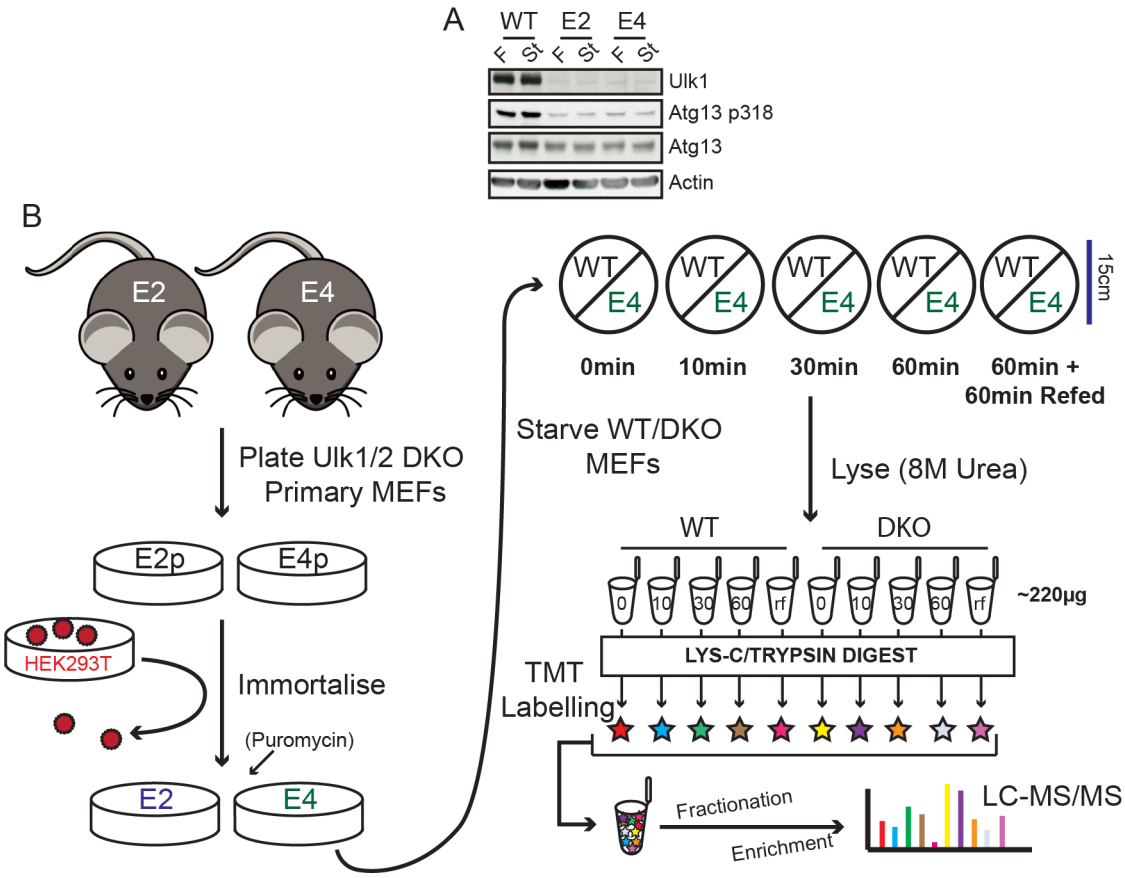

Figure 4.5 – *Generation of Ulk1/2 DKO MEF cell lines and TMT screen design*. **A** – Two primary Ulk1/2 double knockout (DKO) MEF lines were subject to SV40-mediated immortalisation. Wild type (WT) and DKO MEFs (E2 = Ulk1/2 DKO embryo 2; E4 = Ulk1/2 DKO embryo 4) were incubated in EBSS for 1 hour. Western blot analysis of the lysates revealed that ULK expression was abolished in the DKOs and Atg13 S318 phosphorylation was greatly reduced. **B** – Schematic depicting the TMT starvation time course protocol.

4.3 Starvation time-course utilising 10-plex tandem mass tag label-based mass spectrometry

4.3.1 TMT screen design

Phosphorylation events can occur very rapidly following stimulation, and a given residue may undergo several cycles of phosphorylation and dephosphorylation when cells are maintained activating signalling environment. Indeed, such dynamic phosphorylation events might be entirely missed when only one or two timepoints are analysed (Humphrey et al., 2015). Therefore, taking phosphoproteomal snapshots over a time course can provide colour to the picture of phosphorylation-dependent signalling. TMT-based phosphoproteomics offers unique advantages over SILAC-based protocols - key amongst these is the ability to perform multiplexed experiments. Therefore, this method was applied to identify quantitative changes in the phosphoproteomes of WT and Ulk1/2 DKO MEFs over a starvation time course.

As previously discussed, another potentially confounding factor affecting the SILAC dataset was the differing genetic background of WT and Ulk1/2 DKO MEFs used in the screen. To amend this, new Ulk1/2 DKO MEF lines were generated from Bl6 embryos (matching the WT cell background) via retroviral immortalisation, one of which (E4) was used in the screen (Figure 4.5A). 5x15cm dishes of each cell type (WT and DKO, 10 dishes total) were seeded to 80% confluency before starvation for 0, 10, 30 or 60 minutes. Additionally, a set of dishes starved for 60 minutes had basal media replenished for a further 60 minutes (Refed; RF). The samples were lysed before 220µg from each was digested overnight with Trypsin/Lys-C. The resulting peptides were labelled with TMT reagents before mixing in equal proportion. Phosphopeptide enrichment was assessed by mass spectrometry analysis (Figure 4.5B).

4.3.2 Overview of the starvation time course dataset

Comparison of the relative phosphopeptide enrichment in response to amino acid deprivation in both cell lines allowed for the identification of phosphorylation events that occur in both a starvation- and ULK-dependent manner. As discussed in the introduction mTOR activity is governed by nutrient availability such that in the presence of amino acids and growth factors, mTOR is mostly active and ULK mostly inactive, with the opposite scenario true when cells are

cultured in EBSS. A large number of well characterised mTOR target sites have been described as a result of its pivotal position in proliferative proline-directed phosphorylation-dependent signalling, thus providing a plentiful supply of potential positive controls. Promisingly, the dataset was replete with such examples, indicating the experiment was technically successful (Figure 4.6A, left and middle). A well-established but indirect phosphotarget downstream of mTOR and Erk1/2, the 40S ribosomal component Rps6, was dephosphorylated upon starvation (Rosner et al., 2011), with depletion reaching its lowest point after 60 minutes before returning to baseline after refeeding. A similar pattern was noted for Uvrag serine 549 (serine 550 in human UVRAG) (Munson et al., 2015, Kim et al., 2015), which is phosphorylated by lysosomally-localised pools of mTOR to promote autophagic lysosome reformation.

To identify potential ULK targets, it was important to first describe the profile of a model ULK substrate. In WT cells, phosphorylation would increase upon starvation, peaking at either 10, 30 or 60 minutes, before returning to baseline after 60 minutes refeeding. Meanwhile in DKO cells it would remain at a baseline level unresponsive to starvation, possibly being maintained at a level much lower than that observed in the WT fed condition. Promisingly the established ULK substrate Prkab2 serine 38 (Table 1.1) displayed such a profile indicating that the dataset might contain further, novel ULK substrates (Figure 4.6A, right). The prevalence of the model profile in the dataset was therefore examined. After discarding phosphopeptides that were not detected in all 10 conditions, the TMT screen yielded ~15,000 unique phosphorylation events. To describe the variation in the dataset in an unbiased manner, a global correlation cluster analysis was performed. The top ~20% most variable phosphopeptides (2926 in total) were grouped into averaged principle patterns, yielding 6 patterns present in the dataset (Figure 4.6B). Whilst cell line-specific (ULK-dependent) and starvation-dependent phosphoproteomic changes were readily apparent, the expected profile for a model ULK substrate was noticeably absent indicating that the sites of interest were poorly represented.

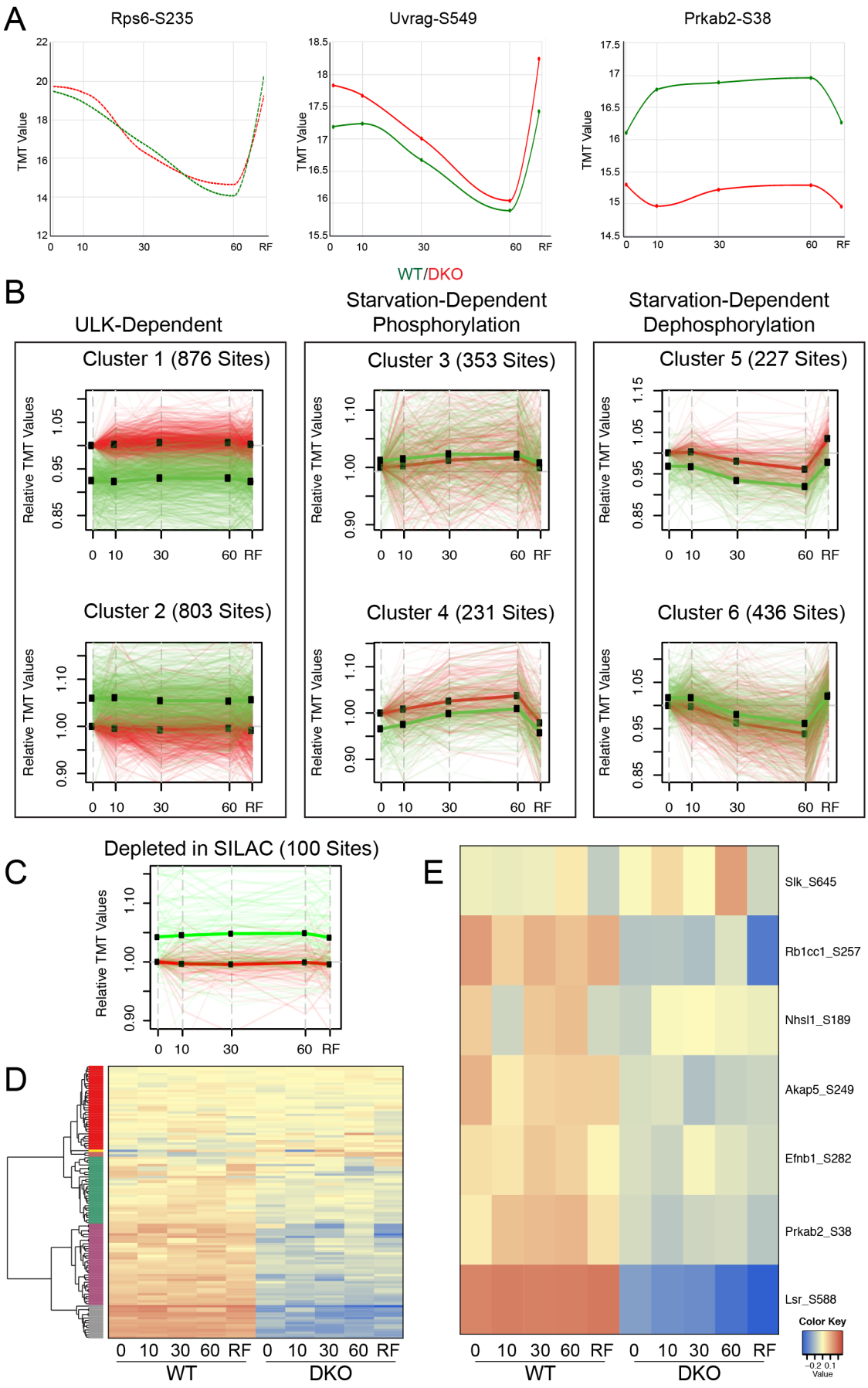
A
Rps6-S235
Uvrag-S549
Prkab2-S38
TMT Value
0 10 30 60 RF
WT/DKO
B
ULK-Dependent
Starvation-Dependent Phosphorylation
Starvation-Dependent Dephosphorylation
Cluster 1 (876 Sites)
Cluster 2 (803 Sites)
Cluster 3 (353 Sites)
Cluster 4 (231 Sites)
Cluster 5 (227 Sites)
Cluster 6 (436 Sites)
Relative TMT Values
C
Depleted in SILAC (100 Sites)
D
0 10 30 60 RF 0 10 30 60 RF
WT
DKO
E
Slk_S645
Rb1cc1_S257
Nhsl1_S189
Akap5_S249
Efnb1_S282
Prkab2_S38
Lsr_S588
Color Key
Value

Figure 4.6 – *Overview of the starvation time course dataset*. **A** – Profile plots for three model substrates are shown. In each case, log_{10} TMT enrichment (Y axis) from each of the starvation time course samples (X axis) are plotted. X axis units = minutes; RF=Refed. TMT enrichment values from wild type (WT) MEFs are plotted in green and Ulk1/2 double knockout (DKO) in red. **B** – TMT enrichment profiles corresponding to the most variable 2926 phosphopeptides were grouped based on similarity. 6 basic patterns are exhibited with the number of phosphopeptide constituents detailed above. WT values are plotted in green and DKO in red. The average profile for each pattern is depicted as a thick green or red line, with individual profiles plotted as thinner translucent lines of the same colour. For each phosphopeptide, TMT enrichment values at every timepoint were divided by DKO 0 minutes and relative values plotted on the Y axis. **C** – TMT profiles corresponding to phosphopeptides depleted in DKOs in the SILAC analysis (Appendix Table A) were plotted as in Figure 4.6B. **D** – Sites plotted in Figure 4.6D were displayed in a heat map. Columns show 10 starvation screen conditions with phosphosites populating rows (100 total). The colour of each cell represents the relative enrichment for each phosphopeptide in each condition. For each site, this was calculated by averaging TMT enrichment values across all 10 conditions, then dividing the enrichment value at each time point by the average before plotting the logarithm of this fraction to base 2. Positive log_2 values (indicating relative enrichment) are depicted in red with negative values (indicating relative depletion) in blue (see colour key in panel E). Peptides were grouped by global correlation cluster analysis - the 6 most common clusters are annotated on the left. The red cluster is populated mostly with phosphopeptides displaying little variation between cell types and time course conditions. **E** – Phosphopeptides exhibiting reproducible and sufficient depletion in the SILAC screen that corresponded with the loose ULK consensus motif (Table 3.1) were projected onto the TMT screen. 7 phosphopeptides fit these criteria and are depicted in the heat map as in Figure 4.6D, with gene name and phosphoacceptor residue annotated on the left. The analyses in Figure 4.6 were performed with the help of Stefan Boeing from the Bioinformatics STP.

As the TMT screen provided time-resolved phosphoproteomic data derived from MEFs subject to similar treatments as in the SILAC screen, a sizeable crossover in datasets was expected. The phosphorylation events identified in Appendix Table A were therefore cross-referenced with the TMT dataset. However, many of these phosphorylation events were not detected in the TMT screen, after averaging the 100 phosphopeptides identified in both screens, the resulting profile closely resembled cluster 3 from the global pattern analysis, indicating that much of the variation in the SILAC experiment was due to starvation-independent dephosphorylation or decreased protein level rather than direct loss of ULK phosphorylation (Figure 4.6C). However,

some of these sites did not demonstrate noticeable enrichment/depletion in either cell type or condition, suggesting that the correlation between experiments was not perfect. This may be due to slightly differing treatments and cell lines utilised in the experiments (Figure 4.6D). Of the SILAC top hits that matched the ULK consensus signature (Table 3.1) the majority did not respond to starvation indicating that these were not direct ULK substrates (Figure 4.6E).

4.3.3 Characterisation of ULK-independent substrate phenotypes

Despite not displaying profiles indicative of ULK-dependent phosphorylation, some of the clusters likely contained biologically interesting and potentially novel phosphorylation events. Specifically, the phosphorylation events in clusters 5 and 6 were exhibitive of ULK-independent and starvation-dependent phosphorylation, with clusters 1 and 4 showing ULK-independent and starvation-dependent dephosphorylation. Candidates displaying either pattern were selected for further analysis based on identified roles in autophagy.

ULK-independent, starvation-dependent phosphorylation

As discussed in the introduction, the VPS34 Complex II accessory component RUBICON binds UVRAG, BECN1 and VPS34 to inhibit activity by inhibiting membrane binding and kinase activity. In WT MEFs, Rubicon was phosphorylated at serine 351, with phosphorylation peaking at 10 minutes before returning to near baseline at 60 minutes starvation (Figure 4.7A). The UVRAG binding domain in RUBICON has been mapped to amino acids 300-600 (Sun et al., 2011). Therefore, despite the peak of phosphorylation being relatively modest, RUBICON was brought forward for further study. However, in cells cultured in both basal and starvation media, no clear difference in VPS34 complex coimmunoprecipitation was noted between WT, S351A or S351D forms of RUBICON-GFP (Figure 4.7B). RUBICON is a multifunctional protein and interestingly, serine 351 lies within the binding region for a second protein (14-3-3beta) (Yang et al., 2012). It is feasible that, if genuine, the starvation-dependent phosphorylation of RUBICON at serine 351 regulates interactions outside of the VPS34 complex.

ULK-independent, starvation-dependent dephosphorylation

ATG2A is membrane associated protein implicated in multiple stages of autophagosome formation. In mammals, the homolog ATG2B is believed to serve redundant functions despite significant variation in amino acid sequence (Velikkakath et al., 2012). In the screen, serine

1246 in murine Atg2a (corresponding to serine 1266 in human ATG2A) was dephosphorylated upon starvation, with maximum depletion noted at 60 minutes and basal phosphorylation restored when full media was replenished (Figure 4.7A). The phosphorylation profile for Atg2a-S1246 was similar to that of ribosomal protein S6 S235 (corcoeff = 0.88; Figure 4.6A).

To examine the phosphorylation-dependent phenotype, autophagic flux was examined in HEK293A overexpressing WT, S1266A or S1266D ATG2A. LC3-II accumulation upon 1hr starvation in the presence of Bafilomycin A1 was significantly reduced upon overexpression of WT ATG2A compared to empty vector-expressing negative controls. Interestingly, no significant reduction in LC3-II accumulation was observed in cells expressing ATG2A bearing either alanine or glutamate at position 1266, with the levels of autophagic flux in phosphomutant-expressing cells significantly higher than in WT-expressing counterparts. These data potentially implicate serine 1266 phosphorylation in the regulation of starvation-induced autophagy (Figure 4.7D).

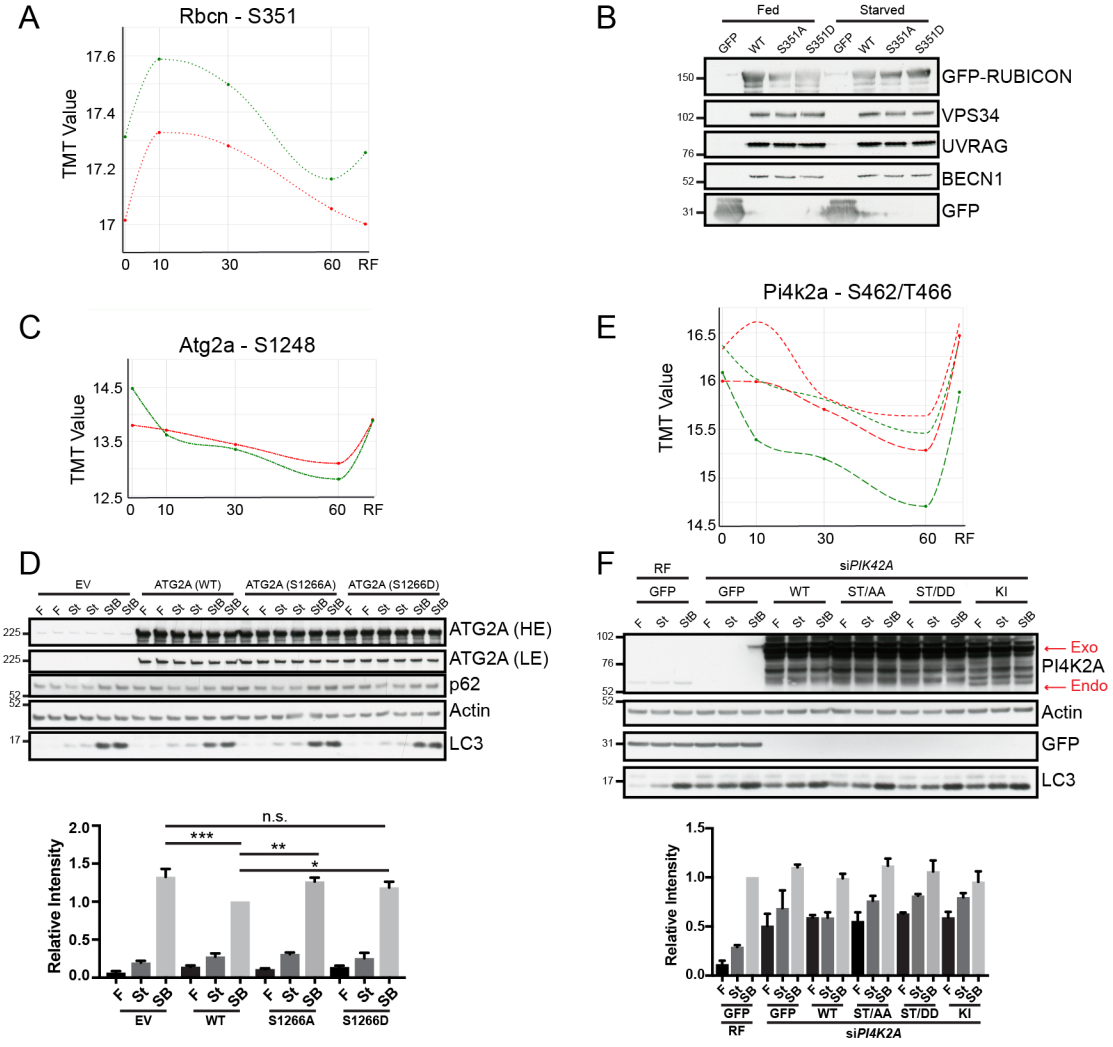

Figure 4.7 – *Characterisation of ULK-independent substrate phenotypes*. **A** – Rubicon S351 phosphorylation profiles from WT (green) and DKO (red) MEFs. Log_{10} TMT enrichment values (Y axis) from each of the starvation time course samples (X axis) are plotted (units = minutes; RF=refed). **B** – Either GFP alone or GFP-RUBICON wild type (WT), S351A or S351D were transiently overexpressed in HEK293A. Cells were starved in EBSS for 1 hour before lysis followed by GFP immunoprecipitation. Western analysis of the immunoprecipitates suggested that VPS34 complex II association was unaffected by 351 phosphorylation status. **C** – TMT profiles for Atg2A S1246. **D** –HEK293A transiently expressing WT/phosphomutant (S1266A/D) ATG2A-HA or empty vector (EV) alone were starved for 1 hour +/- Bafilomycin A1 (100nM) before lysis and Western analysis. Technical duplicate lysates were analysed on the same gel, high (HE) and low (LE) exposures for ATG2A demonstrate that expression levels of ATG2A constructs were equal, as well as revealing expression relative to endogenous. **E** – TMT profiles for Pi4k2a S462 (short dashes) and T466 (long dashes). **F** – HEK293A expressing RISC-free (RF) or si*PI4K2A* were transfected with si-resistant WT, S462A/T466A (ST/AA), S462D/T466D (ST/DD) or kinase inactive (KI) PI4K2A-GFP or GFP alone. Cells were starved for 1 hour +/- 100nM Bafilomycin A1 before lysis and western blot analysis. Positions of endogenous (endo) and exogenous (exo) PI4K2A are annotated. Data in Figures 4.6A, 4.6C and 4.6E were displayed using software generated by Stefan Boeing (Bioinformatics STP, Francis Crick Institute). Bars show n=3 mean +/- SEM. *p<0.05, **p<0.01, ***p<0.005.

PI4K2A is a lipid metabolising kinase involved in the production of PI4P from phosphatidyl-inositol. It has been shown to bind GABARAP and thus regulate autophagosome-lysosome fusion (Wang et al., 2015). Furthermore, it was recently identified as a component of the ATG9 compartment where along with the related enzyme PI4KIIIB it generates PI4P to drive autophagosome biogenesis (Judith et al., 2019). Pi4k2a was dephosphorylated at two residues at the extreme C terminus, serine 462 and threonine 466, with maximum depletion noted at 60 minutes before returning to baseline upon refeeding. Again, the profiles matched that of Rps6-S235 well (S462 corcoeff =0.922; T466 corcoeff = 0.811).

Both overexpression of kinase dead PI4K2A and siRNA knockdown block autophagic flux (Wang et al., 2015), therefore autophagic flux was again used as a readout for autophagy modulation. Overexpression of PI4K2A in HEK293A resulted in cell toxicity, therefore DNA levels were reduced until toxicity was no longer observed. Knockdown of PI4K2A resulted in inhibition of autophagic flux, evidenced by the accumulation of LC3-II in fed and starved conditions

compared to RISC-free transfected cells. Expression of WT, S462A/T466A, S462D/T466D or kinase inactive PI4K2A did not rescue the knockdown phenotype (Figure 4.7F). As these data are inconclusive, further experiment are necessitated to probe the potential role of C-terminal PI4K2A dephosphorylation in starvation-inducted autophagy.

4.3.4 Identifying ULK substrates for further study

To identify substrates that were both ULK- and starvation-dependent, three variables were chosen to describe the behaviour of phosphorylation events within the TMT dataset. In each case, two specific conditions were selected and phosphopeptide enrichment (measured via absolute TMT label enrichment) between each were compared. The comparisons selected along with a brief explanation are (Figure 4.8A):

1. **WT0mins – WT60mins**: Phosphopeptides showing an appreciable increase in phosphorylation after 60 minutes starvation were brought forward
2. **WT60mins – WT60mins(Refed)**: Phosphopeptides showing an appreciable decrease in phosphorylation when full media was replenished were brought forward
3. **WT60mins – DKO60mins**: Phosphopeptides showing an appreciable decrease in phosphorylation in Ulk1/2 DKO compared to WT MEFs at 60 minutes starvation were brought forward

Trial and error was used to establish the thresholds employed to triage the dataset and phosphopeptides were satisfying the three variables simultaneously were selected (Figure 4.8A). Whilst sorting based on these criteria was effective, the shortlisting procedure was by no means fully optimised. For example, phosphopeptides that were sufficiently depleted in the Ulk1/2 DKO mutants whilst displaying similar starvation-dependent phosphorylation (likely representing ULK-independent substrates) were present. To help combat this, a fourth variable was used to annotate the dataset – similarity to the model ULK substrate Prkab2-S38 (Figure 4.8A). Generally, a correlation coefficient of >0.8 or <-0.8 is considered significant. However, to maximise chance of potential substrate identification and considering that not all genuine ULK substrates should display the same profile as this single site, this threshold was relaxed such that peptides with a Prkab2-S38 correlation coefficient of >0.7 were brought forward.

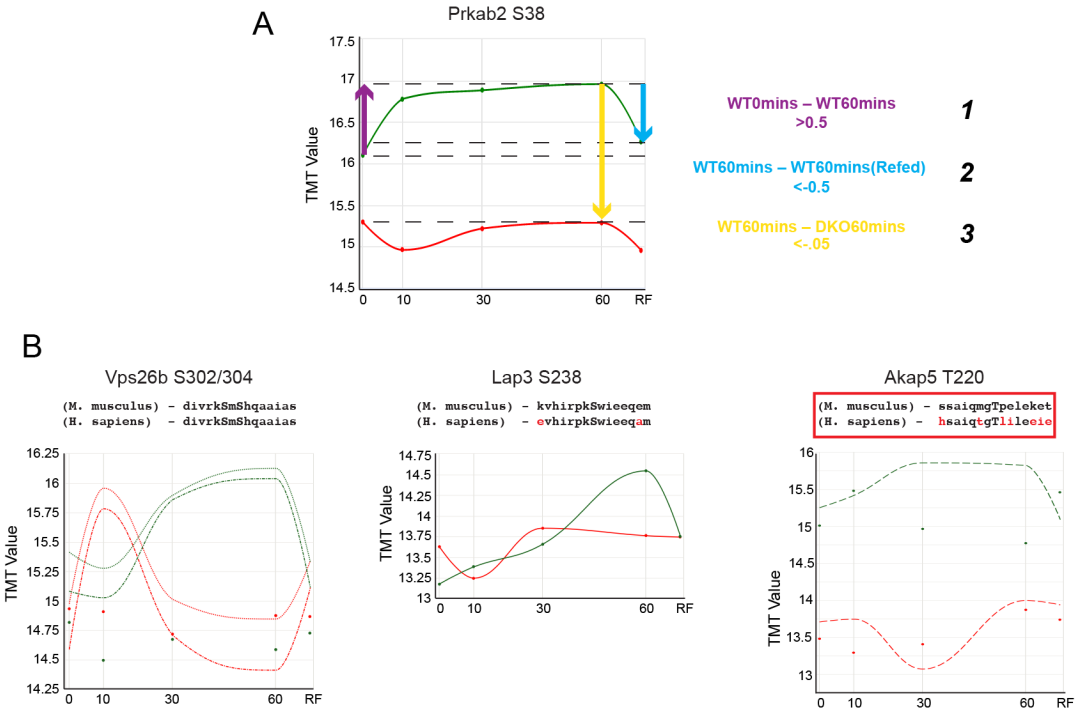

Figure 4.8 – *Identifying ULK substrates for further study*. **A** – Phosphorylation profiles Prkab2-S38. TMT enrichment values (Y axis) from each of the starvation time course samples (X axis) are plotted on a $\log_{10}$ scale with WT profile in green and DKO in red. X axis scale = minutes; RF=Refed. Arrows and colour coded descriptions describe the three variables used to triage the TMT dataset (units for thresholds = $\log_{10}$(TMT Enrichment)). **B** – Phosphorylation profiles for Vps26b S302/S304, Lap3 S238 and Akap5 T220. The relevant human/mouse sequence comparison for the residues surrounding the phosphoacceptor is shown above with mismatches in red in the human sequence. Akap5 T220 was removed from the analysis due to low sequence conservation. Data in Figure 4.8 were displayed using software developed by Stefan Boeing (Bioinformatics STP, Francis Crick Institute).

When shortlisting potential ULK substrates, precedence was given to substrates satisfying the first three variables as this was most consistent in practice. However, it is important to note that despite the range of techniques used to narrow down hits from the dataset, the unpredictable nature of phosphoproteomics meant that many of the sites matching the above criteria were found to have profiles dissimilar to the 'model substrate' scenario. The shortlist was therefore curated manually, such that phosphopeptides with non-ULK profiles (i.e. those clearly not indicative of ULK-dependent phosphorylation) were removed.

Despite the suggestion that the SILAC screen shortlist was enriched with false positives (Figure 4.6C/D), it was still a potentially rich source of ULK substrates. Supporting this notion, p150 (gene name PIK3R4), which was identified as a potential ULK1 substrate in the SILAC screen (Figure 3.7B/C), was validated as a direct substrate whilst analysis of the TMT dataset was taking place (see Chapter 5). Therefore, the SILAC and TMT datasets were cross-referenced to further increase confidence with which substrates were identified. When forming the SILAC shortlist (Figure 3.7A; Appendix Table A), phosphopeptides with a $\log_2$(DKO/WT) value when forward and reverse experiments were averaged of <-1.5 were considered potential ULK substrates. To increase the likelihood of identification in both datasets, this threshold was relaxed such that phosphopeptides with a SILAC enrichment of $\log_2$(DKO/WT) <-1 in both forward and reverse conditions were brought forward. Finally, the list of candidate ULK substrates identified in the crosslinking screen were cross-referenced with the TMT dataset. As the crosslinking screen did not provide site-specific resolution, with readout restricted to candidate proteins rather than phosphoacceptor residues, TMT enrichment values for all detected phosphopeptides from each protein were checked. From this analysis, S127 in ANXA2 emerged as a potential ULK phosphoacceptor.

Phosphopeptides displaying a poor degree of conservation in *H. sapien* homologs (those with 5 or more amino acid differences between 15mer peptides surrounding the phosphoacceptor) were removed from the analysis (Figure 4.8B). To increase the confidence with which potential ULK targets were shortlisted, phosphopeptides satisfying multiple of the selection criteria detailed above were preferentially selected for further analysis. The high confidence shortlist is shown in Table 4.1. Whilst displaying an 'ULK-dependent profile' was considered the chief qualifying characteristic for inclusion in the shortlist, three candidates identified in the SILAC shortlist (Table 3.1) but not detected in the TMT screen were also brought forward.

4.4 ULK substrate validation

4.4.1 Validating shortlisted putative substrates in peptide array format

It remained unknown whether the high-confidence list of potential substrates (Table 4.1) were directly phosphorylated by ULK. ULK1 retains its activity after purification and *in vitro* phosphorylation has been used extensively to identify and validate novel ULK substrates.

Notably, Prkab2-S38 was identified as a substrate in this manner (Löffler et al., 2011) and the ULK1 consensus motif was generated via phosphorylation of a positional scanning peptide library *in vitro* (Egan et al., 2015). Therefore, to narrow the dataset further the capacity for ULK to phosphorylate each substrate *in vitro* was assessed.

	Gene Name	Human Residue(s)	Murine Residue(s)	Profile Match	Prkab2 CorCoeff	SILAC Experiment 1	X Linking
TMT Alone	ACTG1	S33	S33	y	n	-	-
	CHEK1	S317	S317	y	y	-	-
	CTNND1	S920	S819	y	n	-	-
	LAP3	S238	S238	y	y	-	-
	MSL3	S315	S311	y	n	-	-
	NEDD4L	T302	T182	y	y	-	-
	PCM1	S110	S110	y	n	-	-
	PRKAB2	S44	S43	y	y	-	-
	RALGPS2	S289/T290	S289/T290	y*	y	-	-
	SCEL	S91	S90	y	y	-	-
	SHROOM1	S49	S49	y	n	-	-
	STAG2	S1198	S1198	y	n	-	-
	TBC1D1	S627	S621	y	n	-	-
	VAMP5	S41	S22	y	y	-	-
	VIM	T426	T426	y	n	-	-
	VPS26B	S302/S304	S302/S304	y	n	-	-
	ZNF800	S462	S460	y	y	-	-
TMT+SILAC	CARS	S307	S390	y	y	y	-
	F11R	S287	S288	y*	y	y	-
	GPRC5A	S301	S303	y	y	y	-
	NHSL1	S190	S189	y*	n	y	-
	SHROOM2	S231	S236	y	y	y	-
	SORBS2	S298/S299/S301/S302	S442/S443/S445/S446	y	y	y	-
	VILL	S234	S234	y*	y	y	-
TMT+X linking	ANXA2	S127	-	y*	n	n	y
SILAC Alone	PRKAG2	S122	S122	-	-	y	-
	SORBS2	S239	S383	-	-	y	-

Table 4.1 – *High-confidence substrate shortlist*. The gene names as well as both human and murine residue numbers for each of the putative ULK1 substrates identified in the analysis are listed. Where multiple sites in close proximity with similar profiles were identified, all were included with residues separated by a dash. The fourth column indicates whether the peptide in question matched all three TMT variables (see Figure 4.8). Asterisks represent cases where phosphopeptides matched only 2 of the previously described TMT variables, but were brought forward due to fulfilment of additional criteria (e.g. NHSL1, which had a WT0-WT60 score of 0.185 but was identified in the SILAC screen shortlist). The subversive fifth column indicates whether the phosphopeptide scored a Prkab2 correlation coefficient of >0.7. The sixth and seventh columns indicate whether ULK-dependent phosphorylation was supported in the SILAC or crosslinking screens respectively.

To minimise co-immunopurification of contaminating kinases/phosphatases, an N-terminal fragment of murine Ulk1 encoding the kinase domain and part of the intrinsically disordered region (mUlk1KI 1-427) was used. Myc-tagged mUlk1 1-427 was efficiently eluted from anti-myc (9E10)-coated protein G beads when incubated in kinase reaction buffer supplemented with 0.5mg/ml myc peptide (Figure 4.9A). Kinase activity of eluted and bead-bound mUlk1 1-427, measured by *in vitro* phosphorylation of ATG14 (Table 1.1) and p150/PIK3R4 (see Figure 3.7B/C and Chapter 5), was identical for both kinases preparations (Figure 4.9B). Having

optimised the protocol for active kinase purification, a peptide array was designed featuring peptides spanning each of the substrate residues identified in Table 4.1. A number of validated substrates were included on the array as positive controls. These were as follows:

- ATG13 – S355
- ATG14 – S29
- BECN1 – S15
- NR3C2 – S843
- PIK3R4 – S861
- PRKAB2 – S39
- ULK1 – S1042/T1046
- ULKtide (Reported in (Egan et al, 2015) the ULKtide was designed to be optimally phosphorylated by ULK1 and as such closely matches the ULK consensus signature)

Alongside wild-type peptides, a set of single phosphomutant peptides (S->A), in which the phosphoacceptor identified in the screen was mutated to alanine, was spotted. If applicable, also synthesised was a set of peptides in which all potential phosphoacceptors, in this case serine and threonine residues, were mutated to alanine (S/T->AA). Finally, for putative substrates whose surrounding sequences differed between human and mouse but not enough to be excluded, peptides encoding the mouse sequence were included (murinised). Peptides were spotted in triplicate to reduce the impact of technical errors. The peptide sequences used in the screen are detailed in Appendix Table B.

To exclude the impact of contaminating kinases, three varying Ulk1 immunoprecipitates were utilised across two experiments. In the first instance, separate peptide arrays were incubated with either wild type or kinase inactive Ulk1 eluates. Peptide phosphorylation was observed exclusively in arrays incubated with the WT kinase (Figure 4.9C). In the second experiment two arrays were again phosphorylated in parallel, this time using WT Ulk1 in the presence or absence of a small molecule inhibitor (MRT68921) (Figure 4.9D). Promisingly, the pattern of phosphorylation observed in the absence of MRT68921 was identical to the WT scenario in first experiment (compare WT arrays in Figures 4.9C and 4.9D). Peptide phosphorylation fell precipitously in the presence of MRT68921, resembling the KI scenario and supporting the notion that the observed phosphorylation was Ulk-dependent (Figure 4.9D).

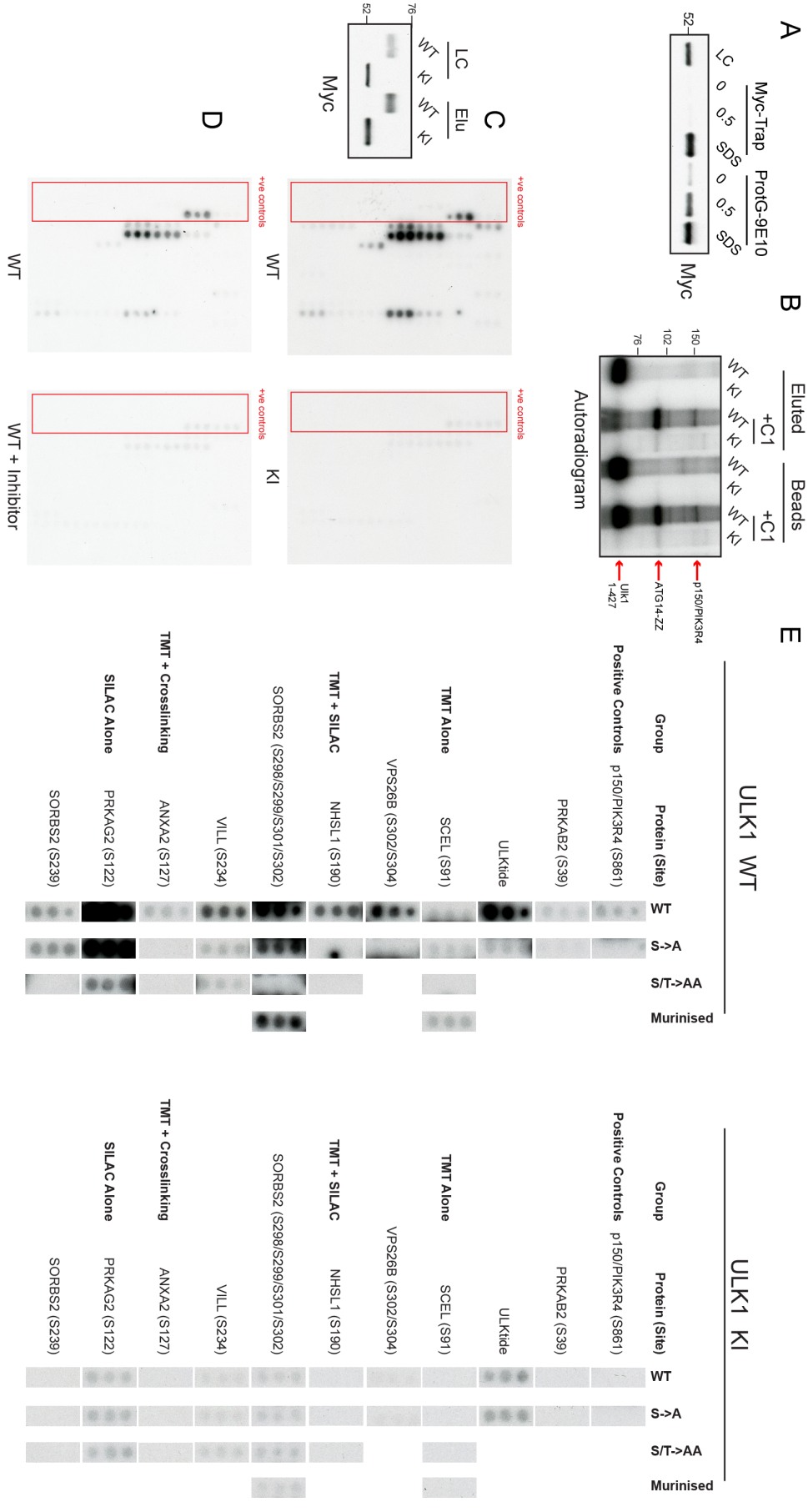
A
Myc-Trap
ProtG-9E10
LC
0
0.5
SDS
Myc
52
B
Eluted
Beads
+C1
WT
KI
Autoradiogram
150
102
76
ULK1 1-427
ATG14-ZZ
p150/PIK3R4
C
LC
Elu
Myc
76
52
D
+ve controls
WT
KI
WT + Inhibitor
E
ULK1 WT
ULK1 KI
Group
Protein (Site)
WT
S->A
S/T->AA
Murinised
Positive Controls
p150/PIK3R4 (S861)
PRKAB2 (S39)
ULKtide
TMT Alone
SCEL (S91)
VPS26B (S302/S304)
TMT + SILAC
NHSL1 (S190)
SORBS2 (S298/S299/S301/S302)
TMT + Crosslinking
VILL (S234)
ANXA2 (S127)
SILAC Alone
PRKAG2 (S122)
SORBS2 (S239)

Figure 4.9 – *Assessing Phosphorylation of Shortlisted Candidate Proteins in Peptide Array Format*. **A** – HEK293A overexpressing myc-mUlk1 1-427 kinase inactive (KI) were lysed before immunoprecipitation with nanobody- (Myc-Trap) or 9E10-coated resin. To elute the bound kinase, beads were incubated in 0 or 0.5mg/ml myc peptide, or boiled in sample buffer (SDS). The eluates alongside a 3% loading control (LC) were analysed by Western blot in which myc-mUlk1 was probed. **B** – VPS34 complex I (CI) components were overexpressed and immunopurified via ATG14-ZZ. An *in vitro* kinase assay was performed using CI as substrate for bead-bound (Beads) or eluted wild type (WT) and KI myc-mUlk1 1-427. Phosphorylation of ATG14 and p150 was detected as well as Ulk1 autophosphorylation. **C** – Peptide arrays were phosphorylated *in vitro* by WT or KI Ulk1. Loading control and elution Western blots (left) demonstrate that protein levels used in the assay were similar. Autoradiograms (right) show array phosphorylation was observed in a WT-specific manner. Positive controls are indicated by a red box. **D** – Autoradiograms from peptide arrays phosphorylated *in vitro* by WT Ulk1 in the presence or absence of an Ulk1 inhibitor (MRT68921 – 1µM). **E** – Peptides demonstrating Ulk-dependent phosphorylation in the autoradiogram from Figure 4.9C were sectioned and annotated. The same exposure was used for all sections displayed.

Annotated peptide arrays from the first experiment (WT vs KI, Figure 4.9C) are shown in Figure 4.9E. The background signal observed in the arrays incubated with ULK1 KI was likely non-specific as no decrease in phosphorylation was observed in the S/T->AA scenario, whereas this reduction was very apparent in arrays incubated with WT Ulk1 (Figure 4.9C/E).

4.4.2 Validating candidate substrates

From the peptide array data, two candidate substrates were selected for further analysis based on identified roles in autophagy. They corresponded with the reported ULK consensus to varying degrees (Figure 4.10A). ANXA2 is a multifunctional signalling adaptor implicated in membrane trafficking and actin remodelling (Grindheim et al., 2017). It has been reported to regulate ATG9A recycling through endosomes (Moreau et al., 2015), ULK1 trafficking to omegasomes (Chen et al., 2017) and phagophore assembly via ATG16L1-dependent vesicle biogenesis/homotypic fusion (Morozova et al., 2015) amongst other processes. A small pool of ANXA2 underwent an electrophoretic mobility shift upon coexpression with ULK1 WT, indicative of ULK-dependent phosphorylation *in vivo* (Figure 4.10B). In an *in vitro* kinase assay, very little if any ULK-dependent phosphorylation of ANXA2 was detected. Furthermore,

mutation of the putative ULK site to alanine (S127A) did not appear to reduce phosphorylation level, suggesting that ANXA2 is phosphorylated by ULK1 at an independent and unknown residue (Figure 4.10C).

The 15mer peptide mapping to PRKAG2 (long-form protein name 5'-AMP-activated protein kinase subunit gamma-2) was strongly phosphorylated in the screen. PRKAG2 is a regulatory subunit of the AMPK complex and is crucial for activation in response to ATP depletion. 3 PRKAG homologs exist (PRKAG1/2/3), with each containing 4 nucleotide-binding CBS (cystathionine β-synthase) domains and differing depending on expression profile and/or the presence of unstructured N-terminal domains found in PRKAG2 and PRKAG3. Mutation of the site identified in the SILAC screen (serine 122), which lies in PRKAG2's unstructured N-terminus, to alanine reduced peptide phosphorylation (see arrays in Figure 4.9C for lower exposures) but replacing all phosphoacceptors with alanine abolished phosphorylation. The peptide used in this assay contains 2 further phosphoacceptors, serine 117 and serine 124; whilst serine 122 does correspond with the ULK1 consensus motif, of the two S124 is a closer match (Figure 4.10A). It is possible that the decrease in phosphorylation noted upon mutation of serine 122 to alanine was due to decreased phosphorylation efficiency at serine 124, however this cannot be proven with current data. The final serine at position 117 is flanked by prolines at positions -3, -2 and +1 with proline at each of these sites predicted to strongly prevent phosphorylation *in vitro* (Egan et al., 2015).Furthermore, very little *in vivo* evidence supports ULK1 as a proline-directed kinase (2 of the potential ULK1 substrates residues in RAPTOR possess a proline at +1 (Dunlop et al., 2011), however proline at any position -3 to +2 relative to the phosphoacceptor and it is generally absent in these positions in *in vivo* validated substrates). It is therefore highly unlikely that phosphorylation at this site is responsible for the signal remaining after serine 122 mutation.

PRKAG1 is phosphorylated by ULK1 at three residues immediately preceding the 4th CBS domain in a region well conserved in PRKAG2 (Löffler et al., 2011). Therefore, to remove interference from independent potential phosphoacceptors, constructs encoding the full PRKAG2 tail or amino acids 1-136, both C-terminally tagged to GFP were generated. These recombinant proteins were amply phosphorylated by ULK1 in vitro, and deletion of both potential substrates (del122-124) abolished phosphorylation (Figure 4.10D). Considering the peptide array data and the ULK1 consensus motif (Egan et al., 2015), serine 124 was predicted

to be the major phosphoacceptor of the three candidates. Two phosphoantibodies were therefore raised against this epitope. Full length PRKAG2 was immunopurified before phosphorylation *in vitro* by wild type or kinase inactive Ulk1. A strong band whose size corresponded with PRKAG2 was visible in samples phosphorylated by Ulk1 WT in Western blots probed with one of these antibodies (Sera 32) (Figure 4.10E).

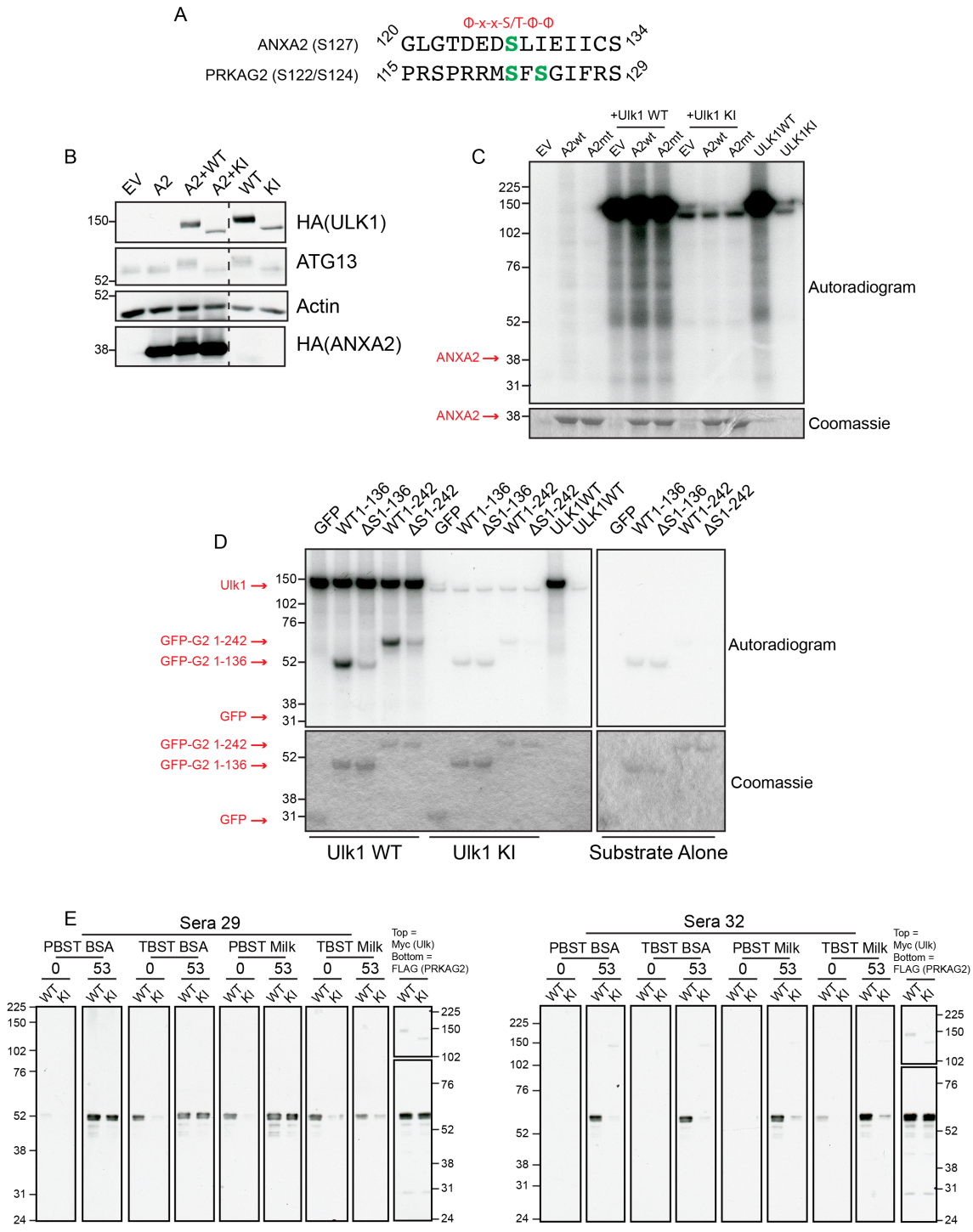

Figure 4.10 – *Validating candidate substrates.* **A** – Human ANXA2 and PRKAG2 15mer peptide sequences centred on predicted ULK1 target residues are shown. **B** – HA-ANXA2 (A2) was expressed in HEK293A alone or with ULK1 wild type (WT) or kinase inactive (KI). Cells expressing empty vector (EV) or the kinases alone were included as controls. A pool of ANXA2 underwent a mobility shift in the presence of ULK1 WT. ULK-dependent phosphorylation of the canonical substrate ATG13 was also observed in this manner. **C** – HEK293A were transfected with HA-ANXA2 WT, ANXA2 S127A (mt), Ulk1 WT, Ulk1 KI or EV. Substrates (ANXA2 WT/mt and EV) and kinases (Ulk1 WT/KI) were immunopurified before mixing as indicated for the *in vitro* kinase assay. ANXA2 incorporated very little ATP in the presence of WT Ulk1 and this was not reduced when the mutant protein was utilised. Coomassie-stained gel bands show that relative substrate levels were even. **D** – GFP alone and WT/Δ122-124 (ΔS) GFP-PRKAG2 N-terminal fragments (1-136 and 1-242) were immunopurified from HEK293A along with Ulk1 WT and Ulk1 KI. The proteins were mixed as indicated before performing an *in vitro* kinase assay. Very little phosphate incorporation was seen when no kinase or Ulk1 KI was included. The robust phosphorylation observed when both PRKAG2 tail fragments were incubated in the presence of Ulk1 WT was almost abolished in the ΔS mutants. **E** – Two rabbits were immunised with a synthesised peptide corresponding to the residues surrounding PRKAG2 S124 encoding a phosphoserine at this position. The resulting sera were used to analyse immunopurified full length PRKAG2 that had been phosphorylated *in* vitro by Ulk1 WT or Ulk1 KI. Day 0 (pre-immunisation) and Day 53 (post immunisation) sera were diluted in four buffers as indicated before immunoblot analysis. Membranes probed for FLAG and myc (right) revealed the position of PRKAG2 and Ulk respectively. Rabbit sera 32 appeared to recognise Ulk1 WT-phosphorylated PRKAG2 only. n=1.

4.5 Discussion

In Chapters 3 and 4, three ULK substrate screens along with a host of validation experiments are described. The SILAC screen had a wide scope for discovery as an unbiased swathe of the phosphoproteome was sampled. However, despite the identification and quantification of many thousands of phosphorylation events, a number of factors such as protein level differences between cell lines and the sheer complexity of the dataset impeded analysis. Furthermore, even when only genuine differentially regulated phosphorylation events were considered, insight into direct relationships between kinase and substrate was lacking.

In vivo crosslinking screen

The crosslinking screen was designed to overcome these obstacles as in principle only direct substrates should have survived sample preparation and analysis. It was performed in a different cellular background than the SILAC and TMT screens (HEK293A compared to MEFs), decreasing the likelihood of congruency between datasets but increasing the confidence with which shared hits would be identified. As the screen was designed to identify substrates proteins (as opposed to phosphoacceptor residues), it offered a unique advantage over the SILAC and TMT screens which were biased towards peptides that were easily detected by mass spectrometry.

Whilst taking inspiration from a previously published experiment in which kinase-substrate conjugation was achieved after overexpression of CDK5 along with its substrate PAK1 (designed to prove the efficacy of AbK) (Ai et al., 2011), the crosslinking screen was novel in conception. This meant that a greater degree of creativity and empiricism had to be employed during protocol development and that the impediments remained partially theoretical.
For example, it is unknown whether the activation loop mutation (D165N) locked the kinase in a confirmation amenable to substrate-binding. Furthermore, as sites selected for AbK incorporation had to be surface accessible and close to the substrate binding pocket, it was possible that the ULK mutants might possess altered substrate specificity. To combat this, 6 unique AbK mutants were initially generated, however only one was utilised in the final screen experiments. When selecting sites for incorporation, initially favoured were those that had similar chemical properties to the pyrrolysine-derivative AbK. However, this criterion proved

too restrictive and the mutant eventually used in the screen (M186TAG) potentially changed the chemical milieu of the substrate-binding surface.

The capacity for ULK1TAG186 to support ATG13 phosphorylation *in vivo* partially alleviates these concerns, however direct phosphorylation was not demonstrated and, in any case, only one substrate was examined. Importantly, arguing against altered substrate specificity, WT ULK1 was able to phosphorylate ANXA2 (a substrate identified in the screen) *in vivo* in validation experiments (Figure 4.10B). Future *in vivo* crosslinking screens should use more than 1 amber mutant to control for this potential issue. Additionally, as a selection of non-natural amino acids suitable for use in *in vivo* crosslinking are now commercially available, different candidates could be trialled. Some of these have varying functionalities, notably the photo-affinity probe reported in (Yang et al., 2016b) which transfers a chemical moiety that is identifiable during mass spectrometry and thus could be beneficial when identifying novel substrates.

During analysis of the crosslinking screen dataset, proteins whose major isoform was smaller than 150kDa that were enriched in the mutant sample in high molecular weight (>150kDa) gel slices were considered potential ULK substrates. Accordingly, proteins whose major isoform was larger than ULK were excluded from the shortlist. This step was taken to exclude false positives, however it potentially resulted in the loss of genuine ULK substrates. Furthermore, this approach did not promise absolute avoidance of false-positives as expression of larger (>150kDa) splice variants or post-translational modification, such as polyubiquitination, could shift a small protein to high molecular weight regions of an SDS PAGE gel. Supporting the latter notion, ubiquitin (UBB) was identified in gel slices 1-6, however ULK1 itself is a target for ubiquitination (see section 1.3.3) suggesting that it could be largely responsible for the presence of ubiquitin in these slices.

8 of the 11 shortlisted proteins had fewer than 2 H/L counts, a measure roughly equivalent to peptide count. Higher H/L counts confer greater confidence to the consequent SILAC ratio. The dearth of robust hits potentially indicates a need for further procedural optimisation. However, the observation that a SILAC ratio was determined for each of the top hits has a consequence that challenges this assessment whilst potentially further impinging on data reliability. As kinase-substrate conjugates should theoretically only have been detected in the

mutant (heavy) channel, the absence of WT (light) peptides should have prevented the calculation of a SILAC ratio. In this instance, it is possible that the relative enrichment of proteins in the mutant sample is the result of potentially stochastic variation from contaminating proteins.

The presence of defined high molecular weight bands in some of the optimisation screen experiments suggested that specific conjugates were being preferentially generated rather than a random sample of substrates. However, this was not apparent in the screen data, although the few proteins identified with high H/L counts, or ULK1 itself, would be the most likely candidates. One such protein was HSP90AA1, however it is tempting to consider that ULK1, a known HSP90 client (Joo et al., 2011), was somewhat destabilised by mutation of its kinase domain, increasing its affinity for the chaperone in CoIPs. Confusing this scenario is the knowledge that many of ULK1's substrates associate/coimmunoprecipitate with the kinase either directly or indirectly, such as the HSP90 cochaperone CDC37 (which was also detected in the screen, but whose enrichment in the mutant sample fell below threshold levels so was not in the shortlist).

It is notable that many of the shortlisted hits had relatively low intensity values (data not shown), suggesting that WT peptide values could have been inappropriately derived from background noise. However, bands 1-6 each contained around 25 proteins for which only a WT (light) value was measured, whilst no instances were observed in the reverse scenario (data not shown). Furthermore, when considering the plotted data in Figure 4C similar numbers of proteins in high molecular weight bands 1-6 were enriched in the WT sample as in the mutant sample. With these data in mind, a low degree of confidence was assigned to the putative substrates identified in the crosslinking dataset shortlist.

Notably, the Parker lab have utilised a related *in vivo* crosslinking procedure to identify novel substrates of PKCe (unpublished data), however whilst this protocol was developed independently it was associated with similar technical challenges. The *in vivo* crosslinking screen may present a viable method of substrate identification (supported by the ANXA2 peptide array data), however, the level of optimisation yet required, together with the relative success of the phosphoproteomic approaches, meant that at this stage the crosslinking screen was shelved in favour of the TMT screen.

TMT-based phosphoproteomics

Stemming from an increase in the number of samples that could be examined simultaneously, the TMT screen held important advantages over the SILAC screen. The ability to track phosphorylation rates over a starvation time course allowed assessment of dynamic changes in phosphorylation in both ULK positive and negative backgrounds. The presence of a positive controls (i.e. a known ULK1 target site that was progressively phosphorylated during starvation and dephosphorylated upon refeeding and mTOR sites showing the inverse pattern) suggested that the TMT dataset is likely a rich source of both starvation and ULK-dependent phosphorylation events. The TMT label enrichment profiles for 3 selected positive controls shown in Figure 4.7A provided examples for the ranges of phosphorylation/dephosphorylation to expect during interrogation of the dataset.

The identification of biologically interesting ULK-independent substrates supports the TMT screen dataset as a rich source for phosphorylation-dependent signalling during starvation generally. Starvation-dependent fluctuations in phosphorylation were detected in crucial regulators of autophagy (Rubicon, Atg2a and Pi4k2a). However, as the functional analyses pertaining to all three proteins were incomplete or inconclusive, further examination is required. The kinase(s) implicated in each phosphorylation event remain unknown, however it is important to consider signalling environment in which the cells were maintained during kinase identification. EBSS is devoid of growth factors as well as amino acids, therefore each of these substrates (indeed all of those identified in the screen) might reflect a response to growth factor removal and could be entirely independent of autophagy.

To identify ULK substrates, correlation with Prkab2-S38, as well enrichment in WT MEFs at 60 minutes starvation compared to fed (WT), refed (WT) and 60 minutes starvation (DKO) conditions, were used as criteria to interrogate the dataset. It is important to consider that any ULK-dependent sites for which phosphorylation peaked at earlier time points before returning to near baseline at 60 minutes may have been overlooked. However, by manually searching the dataset, sites bearing these or similar dynamics were not readily apparent suggesting that they were at least uncommon and it is possible that the asynchronous behaviour of the cell population precluded detection of such sites. Ratio compression may have generally reduced perceived amplitude of phosphorylation, potentially masking some genuine hits. However, this

was likely offset partially by the empirical establishment of threshold variables based on the identified positive control profiles.

When formulating the 'SILAC shortlist', conformity with the ULK consensus sequence was used to triage the dataset, such that residues containing a mismatch at positions -3 or +1/+2 were removed (Figure 3.7C; Table 3.1). Compared to the SILAC dataset, the TMT screen provided relatively firm supporting evidence of ULK-dependent phosphorylation. Therefore, considering the possibility that the published ULK consensus sequence might be inaccurate or might not reflect ULK's *in vivo* biases (Egan et al., 2015), the amino acid sequence surrounding the phosphoacceptor was not considered when generating the 'TMT shortlist' in (Table 4.1).

Many of the sites identified in the initial SILAC screen shortlist (Appendix Table A) were not detected in the TMT screen, limiting the ability to assess the accuracy SILAC shortlist. However, of the ones that were detected the majority were not responsive to starvation, potentially indicating an enrichment of false positives. With this in mind, when cross referencing with the TMT dataset, SILAC ratio thresholds were relaxed to increase the number of phosphopeptides that were picked up in both screens.

It should also be considered that pools of ULK retain activity in the presence of mTOR signalling, promoting basal and selective autophagy alongside non-canonical autophagy-independent functions (Ravenhill et al., 2019, Wang et al., 2019, Rui et al., 2015, McAlpine et al., 2013). By focussing on starvation-regulated phosphorylation events, these substrates might be overlooked as false positives. However, due to the difficulty in confidently identifying such substrates based on the design of the screen, those displaying starvation-dependence were focussed on during candidate selection.

Finally, when identifying potential phosphoacceptors, peptides with a low degree of similarity to their human homologs were removed, thus successfully identified murine-specific Ulk1 phosphotargets could have been lost at this stage. More generally, as a significant degree of manual input was exercised when formulating the putative ULK substrate shortlist it is almost certain that a number of ULK substrates remain unidentified in the dataset.

Substrate validation

The peptide array offered a medium throughput method to assess direct putative substrate phosphorylation by Ulk1 *in vitro*. Combined with the *in vivo* phosphoproteomic data, this double-pronged identification method increases the confidence with which substrates were selected. However, alongside the well-understood drawbacks associated with *in vitro* kinase assays (reduced specify due to high kinase concentration, lack of regulation by protein localisation or adaptor proteins etc.), the use of peptides and thus the absence of structural information decreased readout reliability further.

Despite these caveats, a number of potential substrates were part-validated in this manner. Notably, phosphorylation of SCEL (S91), SORBS2 (S239), SORBS2 (S298/S299/S301/S302) and PRKAG2 (S122) was only abolished when all phosphoacceptors were mutated to alanine. In each case, the additional potential phosphoacceptor(s) can be identified by isolating the other serine and threonine residues present in the peptides used in the screen. This might reflect inaccuracies during mass spectrometry annotation: the presence of serine/threonine residues in the same peptide as the genuine phosphoacceptor residue can lead to improper assignment during data processing. Alternatively, these data may demonstrate that the sites in question were false positives with phosphorylation of the array peptides an experimental artefact. Further validation is required on a substrate by substrate basis to clarify this.

The SORBS2 sites selected for analysis in the peptide array were the same as those selected for mutation in the ULK coexpression experiments detailed in Figure 3.3C. These initial findings are potentially corroborated by the peptide array data, as in both cases mutation of the specific sites did not affect phosphate incorporation, however both experiments indicate Ulk1-dependent phosphorylation at independent site(s) in SORBS2. VPS26B is a component of the heterotrimeric retromer sorting complex previously noted to regulate endosomal sorting via interaction with FAM21 (Gomez and Billadeau, 2009). Notably, 80-90% knockdown of VPS26A, a closely related homolog, had no effect on ATG9A dispersal or LC3 lipidation upon starvation in HEK293A (Orsi et al., 2012). However, as the inhibition of VPS26 activity in these experiments was potentially incomplete (due to incomplete knockdown/redundancy), and as VPS26B is reported to possess different subcellular localisation to VPS26A (Kerr et al., 2005, Bugarcic et al., 2011), it is still entirely possible that VPS26B regulates starvation-induced autophagy.

Unexpectedly, 5 of the 8 positive controls included in the analysis were not phosphorylated by Ulk1. Of the remaining three, both PRKAB2-S39 (the human equivalent of Prkab2-S38) and p150/PIK3R4-S861 appeared to be phosphorylated with much reduced efficiency compared to the ULKtide (Egan et al., 2015). Closely matching the consensus motif, this peptide was designed to be optimally phosphorylated by ULK1. As discussed previously, the ULK1 consensus motif itself was calculated by measuring the capacity for ULK1 to phosphorylate a positional scanning peptide library. It therefore reflects ULK's *in vitro* specificities which may well diverge from biases noted in the cell.

This raises two pertinent questions with regards to the specificity/promiscuity of ULK1 both within and outside of my analysis: 1) How closely does the ULK1 consensus motif convey its selectivity *in vivo*? And 2) Does *in vitro* phosphorylation efficiency correlate with that observed in the cell? Regarding the first question, there appears to a disparity between ULK1's *in vitro* and *in vivo* specificities based on the data demonstrated in this thesis. Of the peptides that were phosphorylated, ANXA2-S127, p150/PIK3R4-S861, VILL-S234 and VPS26B-S304 lacked a hydrophobic/glutamine at position -3, the most strongly stipulated in the motif, whilst NHSL1-S189, PRKAB2-S39, ULKtide and VPS26B-S302 were a match at this position. Furthermore, some peptides showing close fidelity to the ULK consensus (e.g. PIK3R4-S865, BECN1-S15) were not phosphorylated *in vitro*. Whilst the consensus motif remains a useful tool in the study of ULK kinase biology, it should be used with caution in the absence of a more nuanced understanding of ULK kinase specificity.

The second question is less tractable due to the drawbacks associated with protein/peptide-based *in vitro* kinase assays discussed previously. With these considerations in mind the peptide array results were considered as qualitative rather than quantitative when selecting proteins for further analysis.

As a point for consideration – the SILAC and TMT screens compared WT and Ulk1/2 DKO phosphoproteomes, however only Ulk1 was used to phosphorylate candidate in the peptide array screen. The vast majority of work on ULK kinases has focussed on ULK1 and dogma states that ULK1 and ULK2 are functionally redundant. Indeed, when ULK2 is included, it is often used to demonstrate that the kinase can target a given substrate *as well as* ULK1 rather than to

identify ULK2-specific substrates (Park et al., 2016). Nevertheless, it would be interesting to perform the peptide array experiment using ULK2 in the place of ULK1 as their specificities might differ.

The integration of kinase-assay data with endogenous phosphoproteomics promoted the accuracy and confidence with which substrates were identified. This approach has similarities to KALIP (kinase assay linked with phosphoproteomics), a procedure published by Xue and colleagues (Xue et al., 2012). KALIP involves the isolation of *in vivo* phosphorylated peptides before complete dephosphorylation resulting in a pool of peptides representing genuine kinase substrates. The peptide sample is then used as a substrate in a kinase reaction using a purified kinase of interest, before mass spectrometry-based identification of phosphorylated targets. In parallel, phosphoproteomes from cell lines in which the kinase is either inhibited or removed entirely are examined. Cross-referencing the *in vitro* and *in vivo* datasets allows the identification of a high-confidence shortlist of putative substrates. KALIP was used to identify a host of novel substrates of the tyrosine kinase Syk. Resulting from the requirement to purify formerly *in vivo* phosphorylated peptides for use as candidates, this approach is likely restricted to the study of tyrosine kinases due to the prohibitive number of serine/threonine phosphorylation events relative to tyrosine, which would likely limit phosphoproteomal coverage (Khoury et al., 2011, Sharma et al., 2014). However, this study demonstrates the utility of confirmatory peptide-based *in vitro* kinase assays to complement phosphoproteomal datasets.

Conventional *in vitro* kinase data supported the direct phosphorylation of PRKAG2 by ULK1, with the specific residue likely identified by phosphoantibody. Expressed in around 20 tissues, PRKAG2 contains an unstructured N-terminal tail which modulates nuclear localisation (Cao et al., 2017), localisation to Z-disks/T-tubules in cardiomyocytes (Pinter et al., 2013) and ERK/p38 MAP Kinase binding. It is truncated in two positions to yield three PRKAG2 isoforms with varying N-terminal tail lengths (Pinter et al., 2013).

Much of the focus on PRKAG2 centres around the implication of over-activating mutations in autosomal dominant hypertrophic cardiomyopathy (Pöyhönen et al., 2015). The vast majority of identified pathogenic mutations are found in the structured C terminal region that is conserved between PRKAG homologs and is implicated in nucleotide binding. However, one

disease-causing mutation – G100S – lies well within the unstructured N-terminal tail and is within 25 amino acids of the ULK substrate residue (Zhang et al., 2013a). These data underscore the importance of the N-terminal tail for AMPK regulation and in human disease, highlighting phosphorylation by ULK as an avenue for further study.

Identified in the final shortlist of putative substrates from the SILAC screen, p150 was initially selected for further study due to its crucial role in stabilisation of the class III lipid kinase VPS34 complex and thereby its proximity to ULK during starvation-induced autophagy. Due to the early identification of p150 as an ULK substrate, many of the initial validation experiments were performed alongside the TMT, *in vivo* crosslinking and peptide array screens. The final chapter will therefore cover both the validation of p150 as an ULK phosphotarget along with characterisation of the phosphorylation-dependent phenotype.

Chapter 5. Validation and characterisation of the novel ULK substrate p150

5.1 Introduction and aims

The pseudokinase p150 (gene name *PIK3R4*) is best characterised as a scaffolding component of VPS34 complexes I and II, for which it is crucial for complex stability, localisation and activity (Stjepanovic et al., 2017, Stack et al., 1993). It possesses a high degree of structural, functional and sequence and conservation with the yeast homolog Vps15p (Rostislavleva et al., 2015, Baskaran et al., 2014) and its ablation in yeast (Herman et al., 1991b), Drosophila (Lindmo et al., 2008, Anding and Baehrecke, 2015) and mice (Nemazanyy et al., 2013) destabilises the VPS34 complex limiting both endosomal sorting and autophagy *in vivo*. Emphasising its importance, p150 removal is associated with embryonic lethality in both Drosophila and in mice (Nemazanyy et al., 2013, Lindmo et al., 2008). Despite these insights, p150 is by far the least studied component of the VPS34 complex.

Much of the pioneering work on p150 was performed in the early 1990's by Scott Emr and colleagues. Vps15p was identified as a regulator of vacuolar protein sorting in yeast (Kihara et al., 2001, Herman et al., 1991a). In a series of seminal papers, Vps15p was characterised as a myristoylated, membrane-bound protein that interacts with Vps34p and is crucial in facilitating its localisation, stability and activity (Herman et al., 1991b, Herman et al., 1991a, Stack et al., 1993, Stack and Emr, 1994, Stack et al., 1995). Furthermore, it was reported to be a serine/threonine kinase based on sequence similarity with other kinases reported at the time (Herman et al., 1991a). Supporting this notion, Vps15p was shown to undergo autophosphorylation in a manganese-dependent manner (Stack and Emr, 1994). Mutation of key catalytic residues in the N-terminal suspected kinase domain blocked autophosphorylation, carboxy peptidase Y sorting (a key phenotype of vacuolar protein sorting mutants) and Vps34p (yeast homolog of VPS34) binding, with mutant yeast largely phenocopying Vps15p or Vps34p deletion strains (Stack et al., 1993, Stack et al., 1995).

When p150 was identified in humans, several aspects of its biology (myristoylation and VPS34 binding for example) were found to be conserved. Furthermore, whilst p150-VPS34 immunoprecipitates were incapable of autophosphorylation, *in vitro* phosphorylation of

generic substrates, also in a manganese-dependent manner, was observed (Panaretou et al., 1997). However, the subsequent dearth of validated p150 substrates drew its identification as an active kinase into question. Both yeast Vps15p and human p150 lack residues crucial for kinase activity (Backer, 2008). Moreover, the impact of contaminating kinases from the initial *in vitro* kinase assays used to demonstrate Vps15p kinase activity cannot be ruled out (this also applies for Vps34p, which in the same study was shown to show phosphorylate phosphatidylinositol, serine, threonine and tyrosine *in vitro*, the latter three again in a manganese-dependent manner (Stack and Emr, 1994)). Consequently, p150 is now widely considered to be a pseudokinase.

As discussed in Chapter 1, recent structural studies have shed light on the function of p150 within the VPS34 complex. First to be published was a 28-Å single particle negative stain structure of human complex I (Baskaran et al., 2014). This initially contextualised some of the previously reported binding events elucidated between single domains of the core complex components. In this publication, both VPS34 complexes I and II were discovered to have a 'Y'-shaped conformation in which p150 spanned both arms bridging the other elements of the complex components (see an approximation of this structure in Introduction Figure 1.7).

When assessing global conformational changes in VPS34 complex I, a pivot point between the HEAT and WD40 domains of p150 was identified, indicating that the unstructured linker region connecting these domains is implicated in complex flexibility. Furthermore, VPS34's kinase domain, which appears to make intimate associations with the p150 pseudokinase domain in a favoured conformation, was found to be highly flexible (Baskaran et al., 2014). Based on this finding, a further investigation established that the p150 pseudokinase domain physically anchors the VPS34 lipid kinase resulting in inhibition of lipid kinase activity whilst inducing significant conformational changes in p150. These data implicate p150 as the 'master allosteric switch' in the VPS34 complex, potentially translating signals from the regulatory left arm by binding and inhibiting the VPS34 catalytic domain (Stjepanovic et al., 2017, Baskaran et al., 2014).

A crystal structure of yeast Vps34p complex II (4.4 Å) confirmed the gross structure reported by Baskaran and colleagues (Rostislavleva et al., 2015). Each structured domain of Vps15p is implicated in complex member binding, with p150's C-terminal WD40 domain alone physically

associating with all other complex components. Vps15p was shown to make extensive contacts with Vps34p, particularly between the Vps34p C2 and Vps15p HEAT domains at the base of the 'Y'. Furthermore, intimate associations between a host of elements important for Vps34p kinase activity with Vps15p's pseudokinase domain were detected. This study also provided indications that conformational changes at the base of the complex could facilitate complex flexibility, going on to suggest that this was important in allowing 'opening' of the complex arms allowing adaption to membranes of varying curvature. In context of the human complex, this could suggest that the previously described pivot point in the HEAT-WD40 linker of p150, a region is not conserved between yeast and mammals, is implicated in the functional regulation of complex flexibility.

Despite recent advances in understanding, p150 remains the most understudied component of the VPS34 complex. However, its identification as a potential ULK substrate offers an exciting new insight into p150 biology. ULK substrate residues have been identified in ATG14, VPS34 and BECN1, and the mechanistic consequence of these phosphorylation events vary. The characterisation of an ULK-p150 signalling axis could unveil a novel facet of this elusive but crucial protein.

Aims:

- Validate p150 as an ULK substrate
- Characterise the phenotypic consequences of phosphorylation by ULK

5.2 Validation of p150 as a novel ULK substrate

5.2.1 Identification of ULK phosphorylation sites in p150

P150 contains an N-terminal pseudokinase domain followed by 4 tandem HEAT repeats, which are joined via an unstructured linker to a C-terminal WD40 domain (Baskaran et al., 2014). Two potential ULK substrate residues were identified in the SILAC screen (Table 1.1), serine 861 and 865. Both match the ULK consensus sequence to some extent and lie in a stretch of well conserved residues (Figure 5.1A and B).

As discussed in Chapter 4, mass spectrometry-based substrate screens are hampered by incomplete phosphoproteomal coverage. This is caused in part by the relative paucity of most phosphorylation events, evidenced recently in a large-scale HeLa phosphoproteomic screen, in which 11% (4963 out of 49193) of the unique phosphopeptides detected were found to represent 80% of the cumulative phosphopeptide signal detected (Sharma et al., 2014). However, technical issues such as the ability of a given peptide to be detected, dependent on peptide length (i.e. spacing of proteolytic cleavage sites) and amino acid constituents, also decrease coverage.

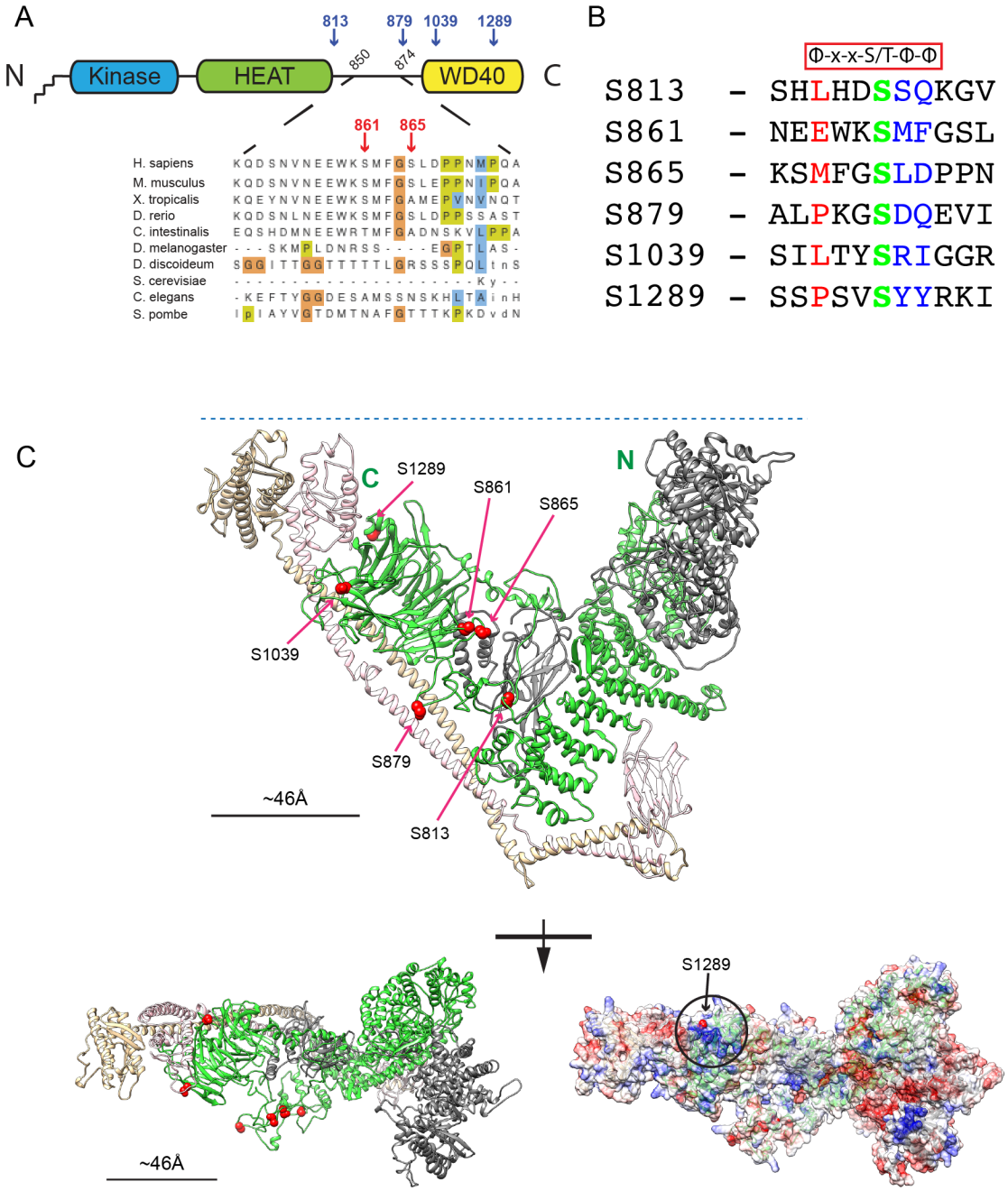

Figure 5.1 –*p150 is a potential substrate of ULK*. **A** – Schematic representation of p150, depicting three structured modules (kinase, HEAT and WD40 domains) and the N-terminal myristate moiety. The two putative ULK substrate residues identified in the SILAC screen are shown in red and those identified upon Ulk1 and p150 coexpression in blue. A sequence alignment shows that the region containing the putative ULK sites (serine 861 and serine 865) is highly conserved (alignment made using Proviz alignment tool (Jehl, 2016), residues annotated following Clustal X default colour scheme to convey evolutionary conservation (Larkin, 2007)). **B** – Alignment of sequences spanning 6 potential ULK substrate residues in human p150. A simplified version of the ULK consensus motif, stipulating hydrophobics at position -3, +1 and +2 relative to the phosphoacceptor is shown above. In the sequence alignment, these positions are highlighted in red (-3) and blue (+1/+2) with the phosphoacceptor in green. **C** –Human VPS34 complex II homology model depicting p150 (green), VPS34 (grey), BECN1 (beige) and UVRAG (pink). Putative ULK1 substrates are depicted as spheres. Scale = ~46Å. (Top) VPS34 complex II standard view, blue dotted line represents the membrane. p150's N and C termini are labelled. (Bottom) Rotated 90 degrees on horizontal axis towards point of view. Charge of surface-facing residues is visualised in right hand structure, S1289 is highlighted. Positively charged residues are in blue and negatively charged residues in red. Model generated by R. Williams Ph.D. (LMB, Cambridge), manipulated using Chimera 1.13.1 (Pettersen et al., 2004).

Protein coverage can be improved by reducing sample heterogeneity via target protein purification prior to analysis. Therefore, to corroborate the screen results, p150 coexpressed with either myc-Ulk1 WT or myc-Ulk1 KI was immunoprecipitation before analysis by mass spectrometry. Based on relative enrichment in WT and KI-coexpressing samples, 4 further phosphoacceptors were identified in p150: serines 813, 879, 1039 and 1289 (Figure 5.1A). These matched the ULK consensus motif to varying degrees (Figure 5.1B). Notably, as the peptide covering serine 861 and serine 865 went undetected in both phosphorylated and non-phosphorylated forms, these data neither corroborate nor contradict the initial screen data.

Using the crystal structure of yeast Vps34p complex II as the template, a homology model of human VPS34 complex II was generated (Figure 5.1C). When the putative ULK substrate residues were mapped onto this model, five of the six putative phosphorylation sites occupied the same face of the macromolecule with the 6th (S1289) on the opposite side. This raises the possibility that phosphorylation might create a clustered patch of acidic residues, amplifying the local negative charge relative to that introduced by a single phosphorylation event.

Promisingly all 6 residues were surface-facing and 5 of the 6 sites (excluding S1039, which mapped to the WD2 region of the WD40 domain) were in intrinsically disordered regions, favouring kinase phosphorylation. Notably, these regions, predicted to be disordered based on primary sequence, were not conserved in S. *cerevisiae* Vps15. All six are distant to the lipid kinase domain of VPS34, suggesting that any potential modulation of kinase activity would be allosteric. As serine 1289 was positioned in a patch of basic residues, deposition of an acidic phosphate group would result in a local switch in charge (Figure 5.1C) (Pettersen et al., 2004).

5.2.2 Identification of ULK phosphorylation sites in p150

To validate the data shown in Figure 5.1, p150 C-terminally tagged with ZZ (a synthetic protein derived from the Fc region-binding 'B' domain of Protein A (Chen et al., 2006)) was coexpressed with Ulk1 and Ulk2. Despite its relatively large molecular weight (150kDa), a noticeable shift in electrophoretic mobility was noted upon coexpression with Ulk1 WT and Ulk2 WT (Figure 5.2A). However, no band shift was observed upon coexpression with inactive forms of each kinase, suggesting that p150 is subject to multi-site phosphorylation *in vivo* in an ULK-dependent manner.

As it was unknown whether this band shift occurs due to direct phosphorylation, *in vitro* phosphorylation of untagged p150 by Ulk1 was assessed. Wild type Ulk1 has approximately the same effective Mw as p150, so bead-bound Ulk1 1-427 was again used as in Figure 4.9A. As the majority of cellular p150 is associated with VPS34 (Kim et al., 2013), untagged p150, VPS34 and BECN1 were coexpressed with ATG14-ZZ, via which VPS34 complex I was coimmunoprecipitated as the substrate (Figure 5.2B). The resulting autoradiogram indicated that ATG14-ZZ, a known ULK target, was strongly phosphorylated in these conditions. A further phosphoprotein was detectable only in the presence of both Ulk1 and VPS34 complex I, which was confirmed to be p150 by Western blot.

To examine whether ULK specifically phosphorylates p150 incorporated into complex I or II, VPS34 complex I and II was enriched as above (with UVRAG-ZZ expressed in place of ATG14-ZZ for Complex II). The two immunoisolates were phosphorylated *in vitro* by WT or KI Ulk1 1-427 (Figure 5.2C). WT Ulk1 phosphorylated p150 incorporated into both VPS34 complex I and

complex II with comparable efficiently, indicating that association with either BECN1-ATG14 or BECN1-UVRAG subcomplexes allows *in vitro* ULK phosphorylation. ATG14 was directly phosphorylated by Ulk1 as before. Unexpectedly however, UVRAG was also phosphorylated in these conditions, potentially identifying it as an additional novel ULK substrate.

Finally, this format was used to assess which if any of the 6 putative substrate residues were phosphorylated by ULK *in vitro*. P150-ZZ bearing serine to alanine mutations at each of the 6 potential sites alone or in combination were expressed before immunoprecipitation and phosphorylation by Ulk1 1-427 WT. Wild type p150 was phosphorylated in the presence of Ulk1 and this was abolished upon mutation of all 6 putative sites (6SA), with a similar reduction observed when the sites identified in the SILAC screen alone were mutated (2SA). By examining phosphorylation of the single putative substrate residues, serine 861 emerged as the major phosphoacceptor in these conditions.

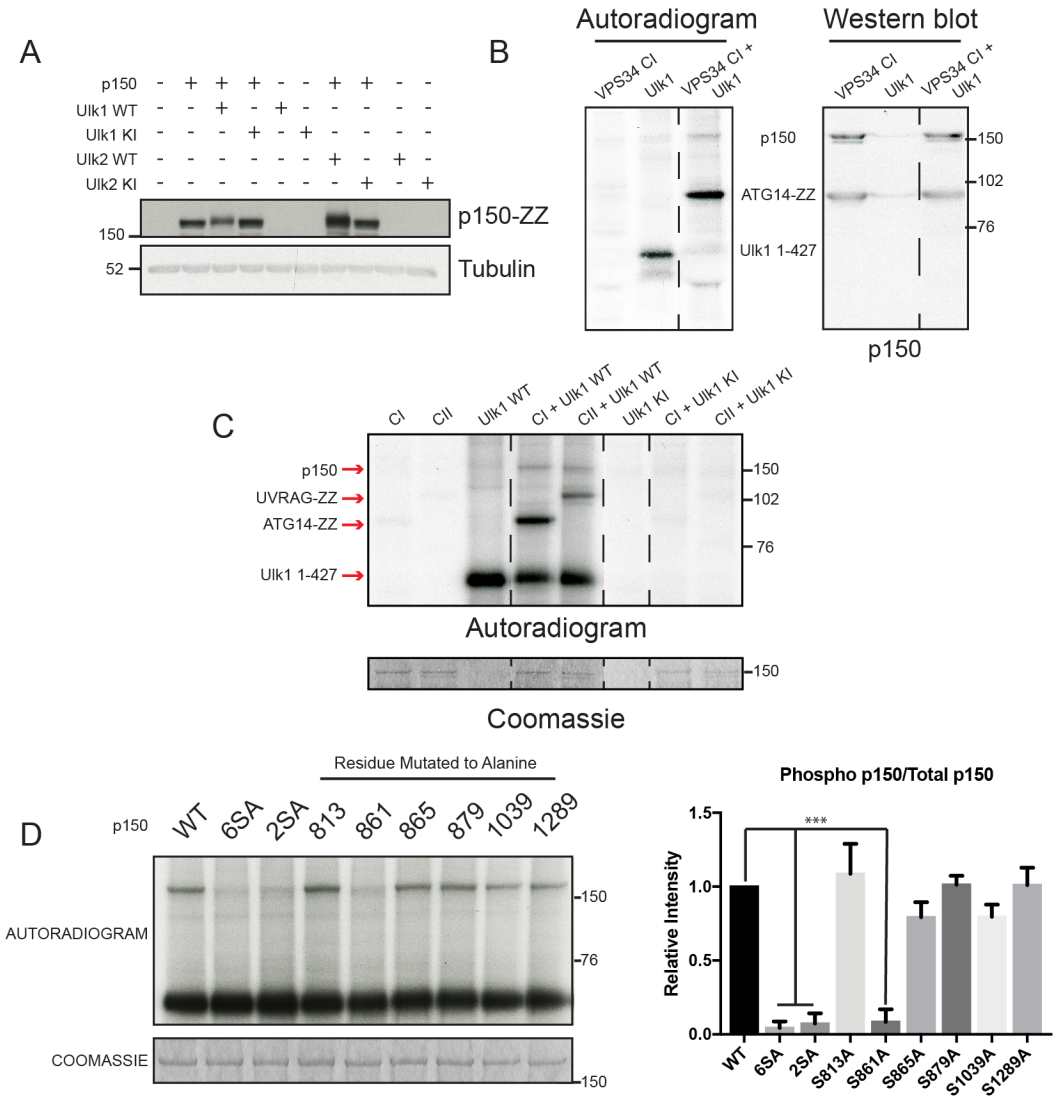

Figure 5.2 – *Identification of ULK phosphorylation sites in p150*. **A** – Coexpression of p150-ZZ with Ulk1 and Ulk2 wild type (WT) results in an electrophoretic mobility shift of p150-ZZ after immunoblotting. No band shift is noted upon coexpression of the inactive kinases (KI). **B** – Immunoprecipitated VPS34 complex I and Ulk1 1-427 were mixed as indicated for in vitro kinase assays with [γ-^{32}P]ATP. Phosphoproteins were resolved by SDS PAGE and transferred onto PVDF membrane before visualisation by autoradiography. The same membrane was then probed with antibodies for p150. Phosphoproteins at ~150kDa and ~90kDa corresponding to p150 and ATG14-ZZ respectively are visible. ATG14 was detected by immunoblot due to the intrinsic ability of the ZZ group to bind antibodies. **C** – VPS34 complex I (CI) or VPS34 complex II (CII) were purified alongside WT and KI Ulk1 1-427. Immunoprecipitated proteins were mixed as indicated and *in vitro* kinase assays performed before separation by SDS PAGE. The position of Ulk1 1-472, ATG14-ZZ, UVRAG-ZZ and p150 are annotated on the autoradiogram. No phosphorylation was noted in the presence of Ulk1 1-427 KI. The Coomassie stained gel (below) reveals that p150 levels were even in assay. Dashed lines indicate where blots were cropped for presentation. **D** – p150 bearing serine to alanine mutations at all putative sites (6SA), those identified in the SILAC screen (2SA) or each site singly were immunopurified before *in vitro* phosphorylation by Ulk1 1-427. Quantification shows mean +/- SEM, n=3, ***p<0.0005.

5.2.3 Validation of p150 serine 861 phosphoantibody

Data described in Chapter 4 suggest that ULK's *in vivo* and *in vitro* specificities might differ. Therefore, despite not being phosphorylated *in vitro*, the remaining 5 putative phosphoserines were not discounted as potential substrates. Conversely, it remained to be established whether ULK1 phosphorylates p150 S861 *in vivo*. Whilst data from the SILAC screen supported this notion as relative serine 861 dephosphorylation was observed in cells lacking ULK1 and ULK2 (DKOs, see Appendix Table A), p150 serine 861 phosphoantibodies were developed to use as tools to further validate this phosphorylation event.

3 rabbits were immunised with 15mer phosphopeptides centred on serine 861 in human p150 over a 77-day period (6 injections, one every two weeks beginning from day 0 before exsanguination on day 77). Sera extracted after exsanguination were examined for their ability to recognise p150 phospho-serine 861. To generate a sample enriched for this epitope, cells

expressing empty vector or p150-HA were subject to starvation to activate ULK. The cells were then lysed before immunoprecipitation of p150. The p150 expressing samples (both lysate and immunoprecipitate) were split into two and one half of each was dephosphorylated via treatment with λ phosphatase. During the primary antibody binding-stage, one set of the negative controls (EV and p150+λ, loading control/pulldown) and experimental samples (p150-λ, loading control/pulldown) were incubated in the presence of 2μg/ml non-phosphorylated p150 S861 peptide (peptide competition – PC), such that any antibodies recognising the non-phosphorylated peptide were neutralised. In this experiment two sera, STO344 and STO345, appeared able to detect p150 upon immunopurification. However, p150 detection was unaffected by λ phosphatase treatment and was abolished by peptide competition, indicating that the majority of antibodies in the sera recognised the unphosphorylated epitope (Figure 5.3A).

Therefore, affinity purification was performed to enrich the pool of specific phosphoantibodies potentially present in the sera. To test the affinity purified sera, empty vector/VPS34 complex I immunoprecipitates were prepared as before. The pulldown samples were phosphorylated by Ulk1 1-427 WT *in vitro* as in Figure 5.2B and C, with one half dephosphorylated by λ phosphatase treatment. For each affinity-purified antibody (STO344 and STO345) two sets of the four samples (EV-λ, EV+λ, C1-λ, C1+λ) were analysed by Western blot. Again, one set was incubated in the presence of non-phosphorylated peptide (+PC) during primary antibody incubation.

In the resulting Western blot, the intense band at ~90kDa represents ATG14-ZZ, appearing due to the capacity for the ZZ tag to bind both primary and secondary antibodies non-specifically (Figure 5.3B). In the absence of peptide competition both antibodies recognised p150 and antibody binding was increased with λ phosphatase treatment suggesting that, despite affinity purification, the major pool recognised non-phosphorylated p150 S861. In the presence of peptide competition however, affinity purified STO344 only recognised p150 prior to λ phosphatase treatment, thus demonstrating its efficacy as a p150 serine 861 phosphoantibody. These conditions were replicated below when using the antibody to probe ULK-dependent p150 phosphorylation *in vivo*.

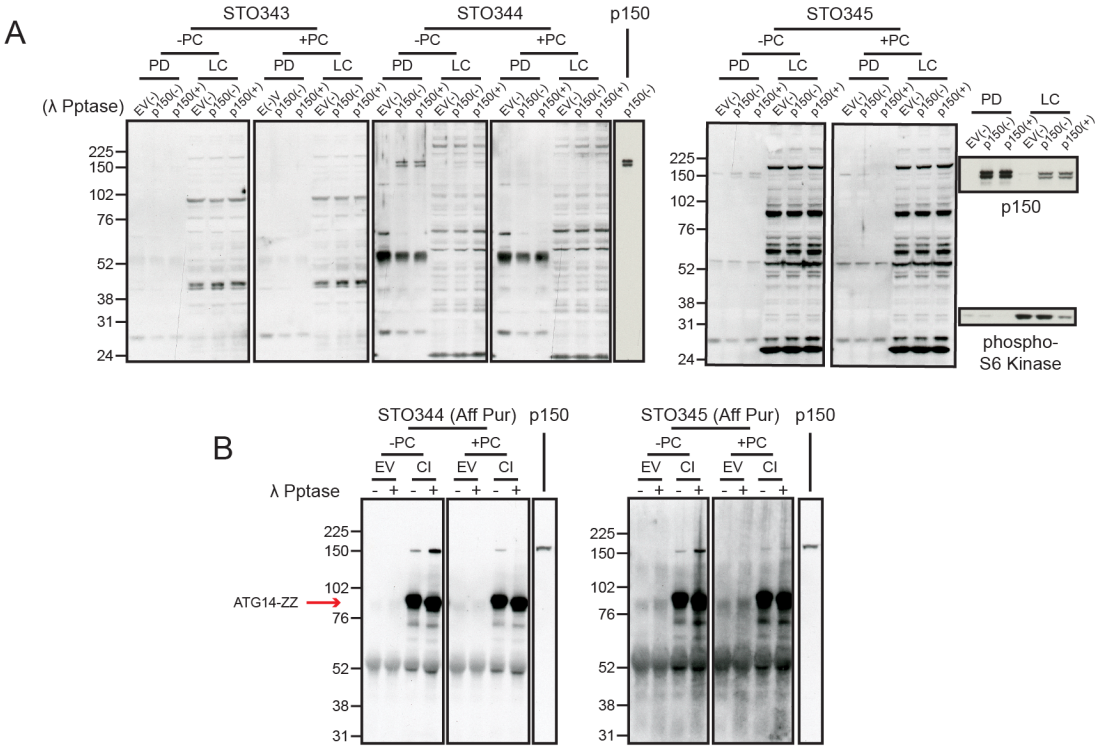

Figure 5.3 – *Validation of p150 serine 861 phosphoantibody.* **A** – HEK293A overexpressing either empty vector (EV) or p150-HA were starved for 1 hour in EBSS before immunopurification. Loading control (LC) or pull down (PD) samples were dephosphorylated via λ phosphatase treatment before analysis by Western blot. Three phosphoantibody sera were tested, each in the presence or absence of non-phosphorylated p150 S861 peptide (+/- peptide competition, PC). p150 was probed on each blot (right) revealing a doublet ~150kDa. Probing for phospho-S6 kinase reveals λ phosphatase efficiency (bottom right). **B** – EV or VPS34 complex I components were overexpressed in HEK293A before subjecting immunoprecipitates to λ phosphatase treatment. Immunoblotting with affinity purified (Aff Pur) phosphoantibodies in the presence or absence of peptide competition identified a pool of p150 serine 861 phosphoantibodies in affinity purified STO344.

5.2.4 ULK phosphorylates p150 at serine 861 *in vivo*

Having validated an antibody specific for p150 phosphorylated at serine 861 (p150 pS861), it was used to probe *in vivo* phosphorylation by ULK. The four components of VPS34 complex I (Figure 5.4A) or VPS34 complex II (Figure 5.4B) were coexpressed in HEK293A along with Ulk1 1-427 WT or KI. Prior to cell lysis, cells were starved for 1 hour in EBSS in the presence/absence of a small molecule inhibitor of ULK1 kinase activity (MRT68921, 1μM). After lysis, p150 was

coimmunoprecipitated via either ATG14-ZZ or UVRAG-ZZ and the samples separated by SDS PAGE before Western analysis.

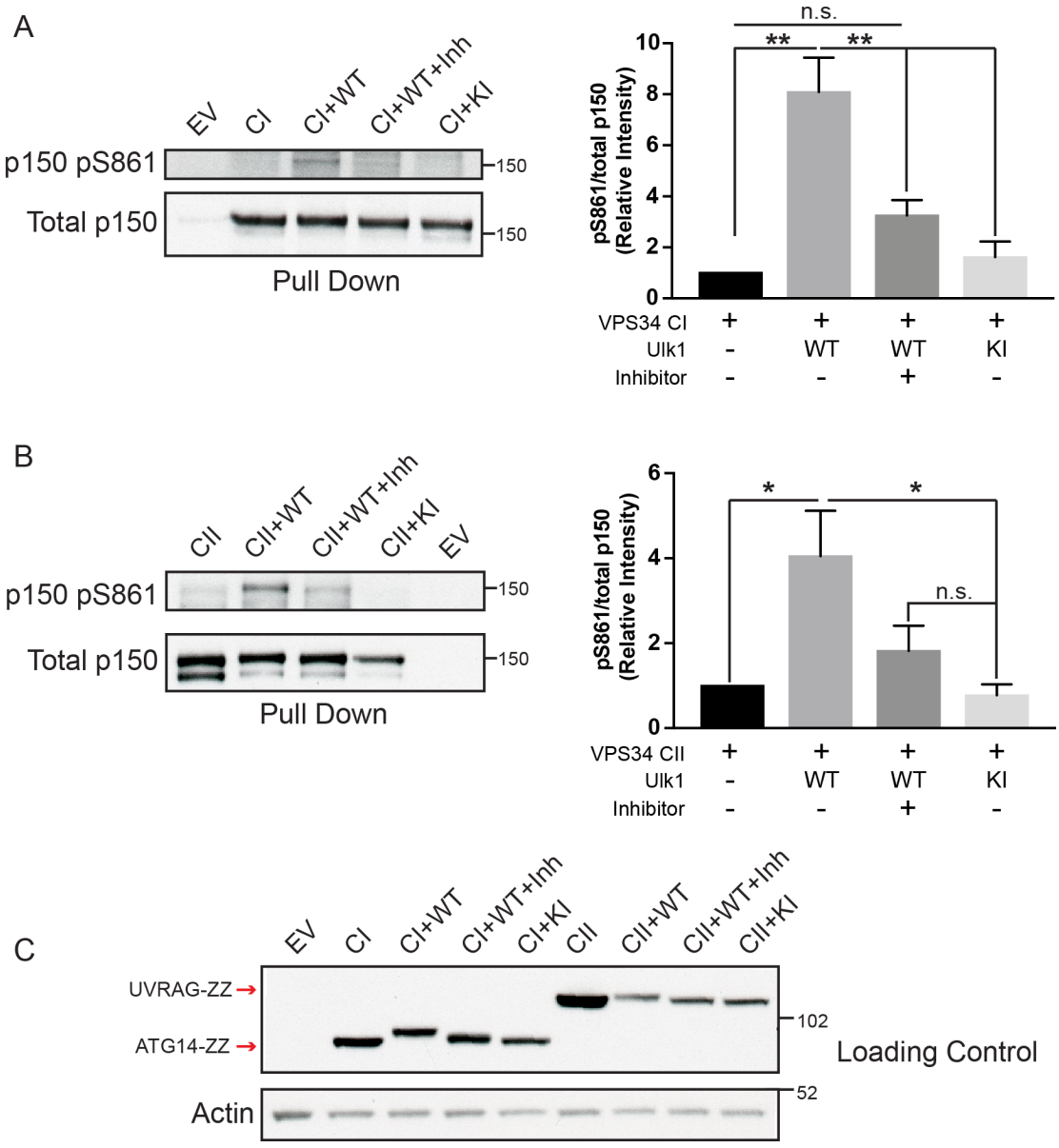

Figure 5.4 – *ULK1 phosphorylates p150 at serine 861 in vivo.* VPS34 complex I (**A**) or II (**B**) were overexpressed in HEK293A along with wild type (WT) or kinase inactive (KI) myc-Ulk1 1-427. Cells were starved for 1 hours prior to lysis in the presence (+Inh) or absence of MRT68921. VPS34 complexes were immunopurified via their ZZ-tagged unique components, before Western analysis using antibody staining conditions optimised in Figure 5.3. Anti-p150 sera were utilised to visualise total p150. Quantification of phospho-serine 861/total p150 from three independent repeats reflect mean +/-SEM, * $p<0.05$, ** $p<0.01$, n.s.= not significant. **C** – Loading control samples from a representative experiment were analysed by Western blot. Electrophoretic mobility shifts in UVRAG and ATG14 (visualised using 2° antibodies alone) indicate Ulk1-dependent phosphorylation *in vivo*.

By comparing pS861 p150 signal to the total protein, phosphorylation was almost undetectable when either VPS34 complex I or II was expressed alone. A large (8-fold for CI, 4-fold for CII) increase in phosphorylation was noted upon coexpression with Ulk1 1-427 WT, which was greatly diminished in the presence of MRT68921 and abolished when Ulk1 1-427 KI was overexpressed (Figure 5.4A and B). Taken together, the data expounded so far indicate that ULK1 is able to access and phosphorylate VPS34 complex I- and II-incorporated p150 at serine 861 both *in vitro* and *in vivo* (although they do not exclude the possibility that p150 is phosphorylated prior to complex incorporation *in vivo*). To check the efficiency of MRT68291, input samples from representative experiments displayed in Figure 5.4A and B were analysed by Western blot (Figure 5.4C). A mass shift in both ATG14 and UVRAG was observed upon overexpression of Ulk1 WT and incubation with MRT68291 lead to stepwise reduction in ATG14/UVRAG relative mass with no shift from baseline noted upon coexpression of ULK1 KI. These data demonstrate the efficiency of MRT68291 and provide complementary *in vivo* evidence of ULK-dependent UVRAG phosphorylation.

5.3 Ablation of p150 in HEK293A

5.3.1 Transient knockdown of p150 reduces autophagic flux

Removal of p150 in multiple cell/tissue types destabilises the VPS34 complex, resulting in the blockage of autophagic flux (Nemazanyy et al., 2013). To confirm the requirement of p150 for complex stability and therefore autophagy in HEK293A with the aim of supporting a functional role for phosphorylation by ULK1, p150 was knocked down, before re-expression using constructs encoding siRNA-resistant p150-HA. Knockdown of p150 (si*PIK3R4*) resulted in an accumulation of LC3-II in both fed and starved conditions as well as a decrease in cells subject to starvation in the presence of Bafilomycin A1, indicating that autophagic flux was blocked. However, p150 reexpression did not rescue autophagic flux (Figure 5.5A). Of note overexpression of p150 in cells expressing RISC-free siRNA did not modulate LC3-II levels.

The remaining capacity for LC3-II lipidation indicated that the trace amounts of p150 present were able to sustain VPS34 activity. Furthermore, the failure of p150 reintroduction to rescue flux was likely compounded by uneven expression of p150 within the cell population. Acute

knockdown and rescue was therefore deemed unsuitable for assessment of the p150 phosphorylation-dependent phenotype.

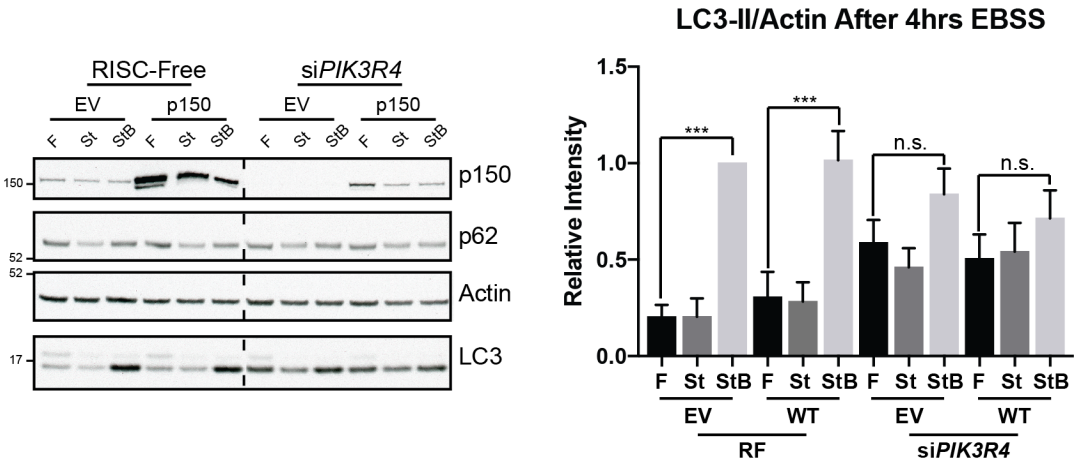

Figure 5.5 – *Transient knockdown of p150 reduces autophagic flux*. HEK293A were knocked down with RISC-free or si*PIK3R4* siRNA, before expression of empty vector (EV) or si-resistant p150. 4 hours treatment with basal media (Fed, F), EBSS (St) or EBSS + Bafilomycin A1 (100nM) (StB) preceded lysis and Western blot analysis. LC3-II/Actin was used to measure autophagic flux. The graph shows mean and SEM from three independent repeats; n.s. = not significant; ***p<0.005.

5.3.2 Positions of guide RNAs for Cas9 targeting of p150

The CRISPR (clustered regularly interspaced short palindromic repeats)-Cas9 system constitutes the type-II prokaryotic adaptive immune system and has been co-opted to facilitate targeted genome editing in eukaryotes. Cas9 is a sequence-specifiable exonuclease, which by binding RNA molecules termed CRISPR RNA (crRNA - complementary to the DNA to be targeted) and trans-activating CRISPR RNA (tracrRNA - promotes crRNA maturation and acts as a Cas9 scaffold), is targeted to complementary DNA polynucleotides leading to generation of double strand breaks. This type of lesion must be repaired by non-homologous end joining, a low-fidelity process that often leads to the introduction of indel mutations, which can result in frame shifts when Cas9 is targeted to an open reading frame. Modification of all alleles in this manner can therefore be used to knock out whatever gene is targeted. By using modified enzymes and guides, CRISPR-based technologies can also be used to induce specified insertions of genetic information, as well as to promote transcriptional activation/inhibition of specified loci (Shalem et al., 2015).

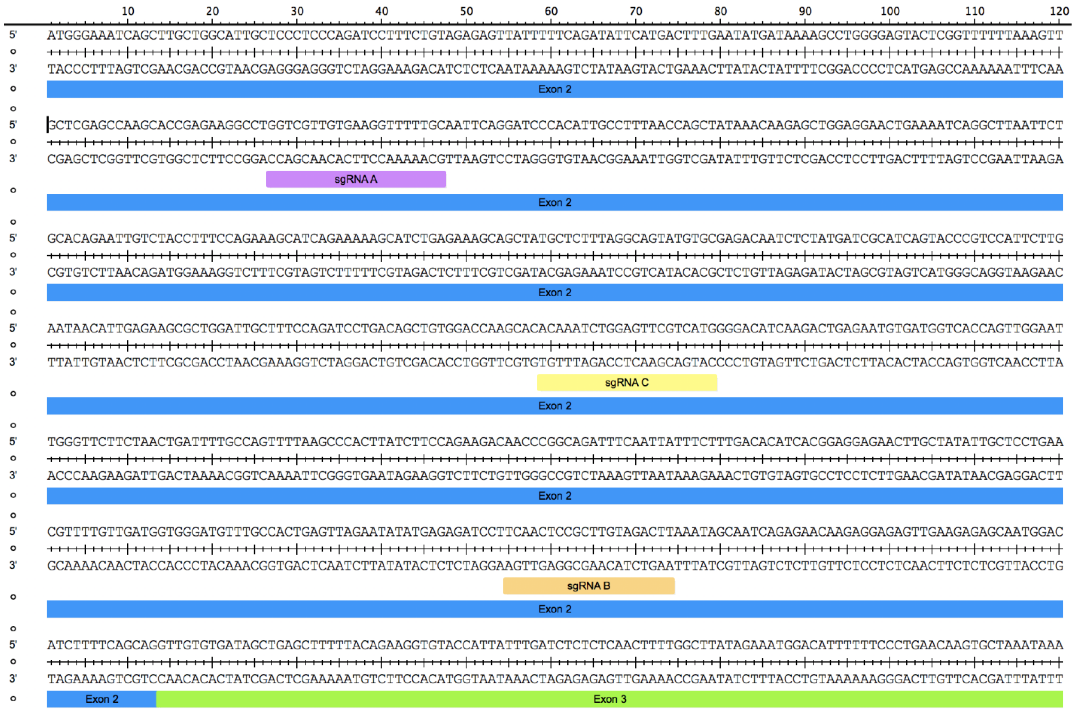

Figure 5.6 – *Positions of guide RNAs for Cas9 targeting of PIK3R4*. ORF sequence of *PIK3R4* (protein name p150) is shown with exons 2 and 3 annotated. The positions of single guide RNA A, B and C (sgRNA A-C) are annotated. Graphic was created using SeqBuilder (DNAstar).

When harnessing the CRISPR-Cas9 system for genome editing, the aforementioned crRNA and tracrRNA can be combined into a single RNA polynucleotide – the single guide RNA (sgRNA). Methods of Cas9/sgRNA delivery vary depending on experimental constraints and range from direct ribonucleoprotein delivery (Seki and Rutz, 2018) to transfection of sgRNA into cells stably-expressing Cas9 nuclease. Owing to versatility however, one of the most common methods is the transfection of a single plasmid encoding both the sequence-specific sgRNA as well as Cas9 (typically from Streptococcus *pyogenes*).

CRISPR-Cas9 genome editing was therefore utilised to knock out p150 from HEK293A. To maximise the chance of generating p150 knockouts, three sgRNAs were designed targeting three regions of exon 2, the first to code for protein. The regions of homology for each sgRNA (termed sgRNA A, B and C) are shown in Figure 5.6.

5.4 Characterisation of p150 CRISPR clones

5.4.1 Validation of p150 CRISPR clones

Around 25 clonal colonies were expanded and examined for each of the three sgRNA utilised for CRISPR, alongside 10 control clones (which were transfected with Cas9 in the absence of sgRNA), with 87 clones were examined in total. After assessing levels via Western blot, 7 clones displayed reduced p150 expression (Figure 5. 7A). 6 of the 7 were derived from sgRNA A (sgA)-transfected cells and 1 from those transfected with sgRNA C (sgC). Importantly, low level p150 expression was detectable in all 7 clones, indicating that p150 is vital for viability in HEK293A. p150 knockdown was associated with the consequent depletion of VPS34, BECN1 and ATG14. Accumulation of autophagy marker proteins p62 and LC3-I/II was observed in the sgA-derived clones, however this did not occur in sgC-H8. A small relative increase in molecular weight was observed in ATG14 in a subset of cells lacking p150, with p150 depletion appearing to correlate with an increase in the relative mass of ATG14.

As VPS34 functions in both the initiation and maturation stages of autophagy, the distribution of WIPI2 after amino acid deprivation was assessed in the CRISPR KO clones (Figure 5.7B). WIPI2 localised to punctate structures upon 1hr starvation in HEK293A, control CRISPR clones and sgA-A11, however, the size and number of WIPI2 puncta appeared to be reduced in sgC-H8. In sgA-B3, sgA-D6 and sgA-D11, the redistribution of WIPI2 to puncta was greatly reduced. Furthermore, accumulation of large cytoplasmic vacuoles that excluded WIPI2 was apparent. Concurrent with the VPS34 complex destabilisation phenotype, these were likely the 'large empty vacuoles or vacuoles filled with smaller vesicles and undigested electron-dense material' likely of endolysosomal origin described after treatment with small molecule VPS34 inhibitors or complete removal of Vp34 (Dyczynski et al., 2018, Compton et al., 2016, Jaber et al., 2012). Notably, whilst the presence of small vacuoles was persistent, the proportion of cells containing very large (>~5μm) vacuoles appeared to decrease as the cells were passaged (undocumented observation).

The significant depletion in p150 expression coupled with VPS34 complex destabilisation and the inhibition of autophagic flux suggested that the CRISPR clones were effective knockouts (KOs) as they phenocopied previously described p150 knockout clones (Nemazanyy et al., 2013). However, based on the lack of vacuolation, the ability to redistribute WIPI2 upon starvation, the comparatively modest accumulation of LC3 and the remaining level of p150, sgA-A11 was not deemed an effective knockout clone. This also applied to sgC-H8 as, despite the comparable reduction in p150 levels compared to effective KOs, no accumulation of LC3 or p62 was observed in these clones indicating they were competent for autophagic flux. Notably, the ATG14 band shift present in sgA-B3, sgA-D6 and sgA-D11 was not observed in these clones.

As p150 knockdown alone was an insufficient indicator of the effective KO phenotype, genotypic analysis was performed to explain the phenotypic variation. ~120 base pair regions centred on each the sgA or sgC target sites were amplified via genomic PCR before TOPO cloning followed by Sanger sequencing. The alleles detected, their discovery frequency and the consequent effect on amino acid sequence assuming protein expression is detailed in Figure 5.7C. Between 2 and 5 alleles were detected in each clonal cell line, with every clone retaining at least one WT *PIK3R4* allele.

To further characterise the effective KO phenotype, the distribution of p150 in the CRISPR clones was examined by immunofluorescence. sgA-D11 was selected for this and further characterisation experiments due to genotypic/phenotypic similarities with the other effective KOs. p150 is believed to be an obligate VPS34 binding partner and both proteins contain domains that promote endomembrane docking (see Introduction section 1.3.4). However, in 2016, Soetzel et al., reported that p150 regulates ciliogenesis by binding GM130 at the Golgi independently of VPS34. Supporting their hypothesis, GM130 was shown to coimmunoprecipitate with p150 but not VPS34 and, utilising an antibody recognising the endogenous protein (NBP1-30463, Novus), p150 was shown to colocalise strongly with the Golgi markers GM130 and GMAP210 by immunofluorescence (Stoetzel et al., 2016).

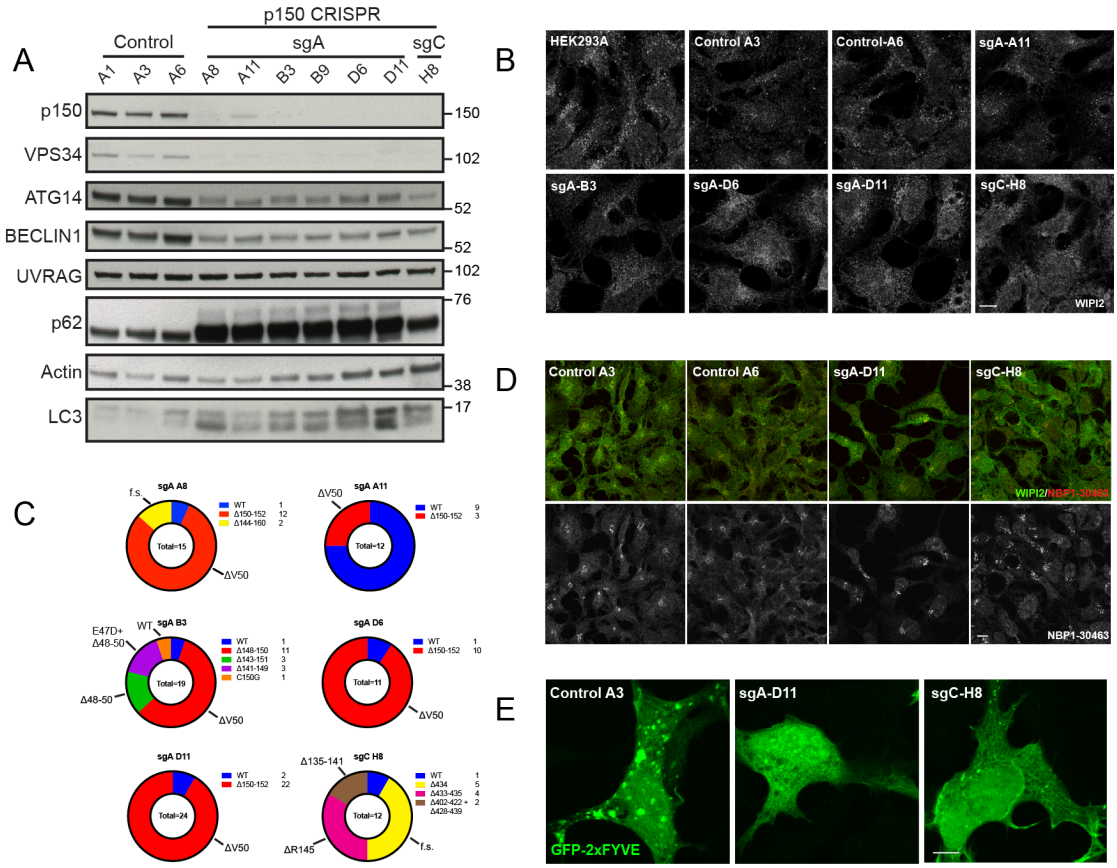

Figure 5.7 – *Validation of p150 CRISPR clones*. **A** – 7 p150 knockdown and 3 control clones were examined by Western blot. VPS34 complex I component depletion alongside accumulation of p62 and LC3 was observed in effective knockout (KO) clones. **B** – p150 KO and control clones were starved for 1 hour before fixation and immunofluorescence analysis. WIPI2 puncta formation was greatly reduced in effective KOs. Scale bar = 10µm. **C** – Genotypic analysis results from 6 p150 CRISPR clones shown in Figure A are summarised. Each pie chart reveals the relative occurrence of p150 alleles detected in each clone, with absolute numbers included alongside the nature of the mutation in the key. The consequent phenotypes are annotated on the outside of each chart (f.s. = frame shift), with the total number of TOPO clones sequenced included in the centre. **D** – As indicated, HEK293A and p150 CRISPR/control clones were starved for 1 hour before fixation and visualisation of WIPI2 and p150 (NBP1-30463). Whilst WIPI2 puncta and cytoplasmic p150 staining were greatly reduced in p150 CRISPR KO clones, the NBP1-30463 signal, potentially revealing the Golgi, was unaffected. Scale bar = 10µm. **E** – p150 CRISPR/control clones overexpressing GFP-2xFYVE were imaged by immunofluorescence. Punctate FYVE distribution was abolished in sgA-D11 and reduced in sgC-H8. Scale bar = 5µm; n=1.

To test the distribution of p150 in the CRISPR clones, control (HEK293A and Control A3) as well as p150 effective KO (sgA-D11) and knockdown (KD) (sgC-H8) cells were starved for 1hr in EBSS before fixation and costaining with WIPI2 and NBP1-30463. The same pattern of vacuolation and WIPI2 puncta formation as in Figure 5.7B was observed. NBP1-30463 strongly stained a juxtanuclear tubular compartment resembling the Golgi in control cells, closely resembling that reported by Stoetzel and colleagues (Stoetzel et al., 2016), whilst also displaying a diffuse background staining. In p150 effective KO (sgA-D11) and KD (sgC-H8) cells the Golgi signal was unaffected whilst the diffuse 'background' staining was noticeably reduced (Figure 5.7D). Assuming the cytoplasmic NBP1-30463 staining is specific, these data indicate that p150 displays a diffuse localisation in HEK293A and is not noticeably redistributed in effective KO/KDs. However, these data indicate that the NBP1-30463 Golgi staining is likely non-specific. Alternatively, although unlikely these data may indicate that the pool of p150 remaining in the effective knockouts localises almost entirely to the Golgi.

Finally, global PI3P levels were assessed by expression of GFP-2xFYVE. The FYVE finger domain is found in several PI3P-binding proteins in both the autophagy (e.g. DFCP1) and endosomal trafficking (e.g. EEA1) pathways with the domain from the ESCRT-0 component HGS routinely used to assess PI3P distribution in the cell. PI3P displayed a punctate localisation in Control A3 cells which was abolished in sgA-D11 and greatly reduced in sgC-H8 (Figure 5.7E). Together these data suggest that clones sgA-A8, sgA-B3, sgA-D6 and sgA-D11 are effective p150 KOs.

5.4.2 Autophagy in p150 effective knockouts

A series of experiments were performed to characterise the effective p150 KO phenotype. Firstly, autophagic flux was assessed (Figure 5.8A). In control clones, low levels of LC3-II were detected in Fed/Starved conditions with a large accumulation observed in the presence of Bafilomycin A1 indicating a high degree of LC3-II turnover (autophagic flux) upon starvation. This was not affected by p150 overexpression. A marked basal accumulation of p62 as well as both LC3-I and LC3-II was observed in sgA-D11 compared to controls. Excepting a small decrease in LC3-I, p62 and LC3 levels were not modulated upon starvation +/-Bafilomycin A1 indicating a block in autophagic flux. Reexpression of p150 for 48 hours completely rescued the autophagic flux phenotype. Autophagic flux in sgC-H8 was unaffected, indicating it contained a small but functionally sufficient pool of p150.

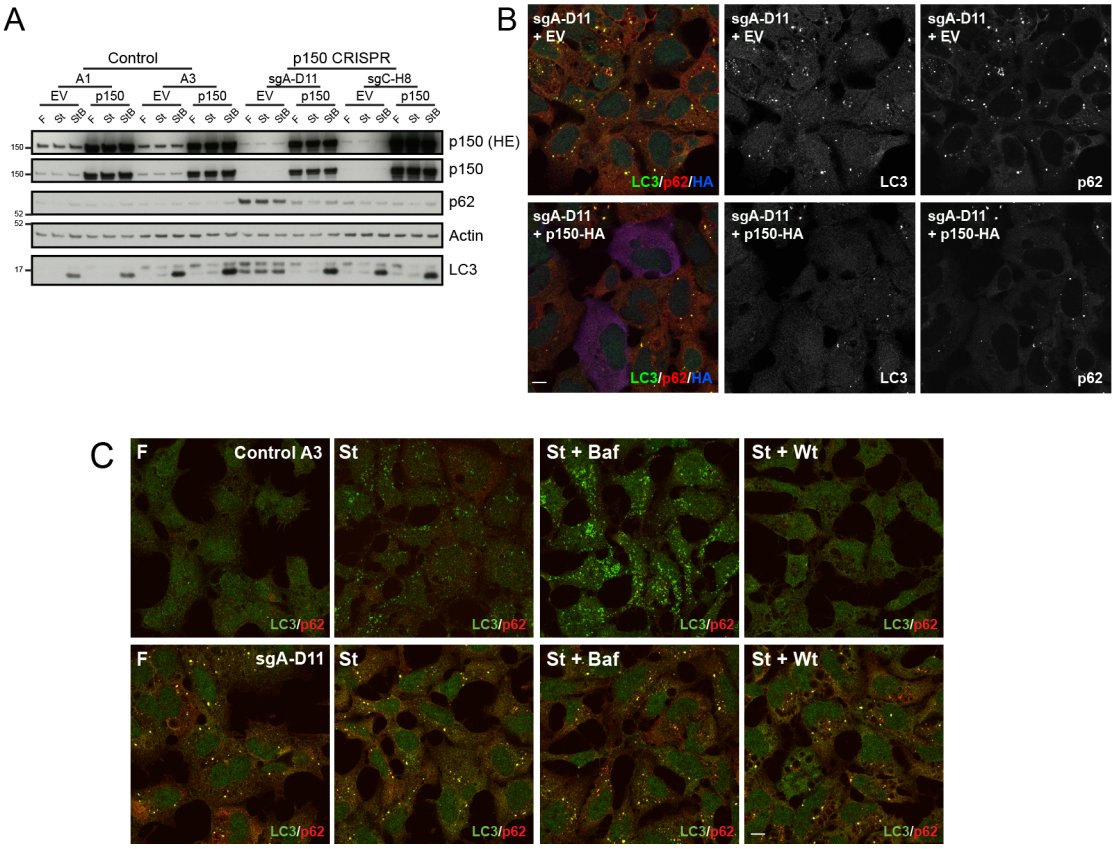

Figure 5.8 – *Examining autophagy in p150 effective knockouts*. **A** – p150 CRISPR or control cell lines were transfected with empty vector (EV) or p150-HA before starvation +/- Bafilomycin A1 (100nM). The sgA-D11 effective KO phenotype (accumulation of p62 and LC3 and the lack of detectable autophagic flux) was rescued upon p150 reexpression and not observed in sgC-H8 p150 knockdown cells. **B** – Distribution of LC3 (green) and p62 (red) was examined in sgA-D11 expressing empty vector (EV) or p150-HA (blue). Reexpression of p150 rescued accumulation of both LC3 and p62. **C** – p150 CRISPR and control clones were treated with EBSS alongside Bafilomycin A1 (100nM) or Wortmannin (100nM) before fixation and visualisation of LC3 (green) and p62 (red). sgA-D11 LC3/p62 bodies form independently of starvation and are resistant to Bafilomycin A1 and Wortmannin. RG channels were artificially brightened for illustration in 'Control A3 – St' panel; n=1. Scale bars = 10µm.

In Drosophila, p150 removal results in the aggregation of the p62 homolog Ref2p (Lindmo et al., 2008) and Vps34 ablation in MEFs leads to the accumulation of GFP-LC3 in large membrane-free aggregates (Jaber et al., 2012). As Western blot data indicated that p62 and LC3 accumulate basally in the p150 KO clones and were likely not functioning in autophagy, the distribution of both proteins was assessed by immunofluorescence. In basal conditions,

LC3 and p62 accumulated in large structures with a similar appearance to those reported previously (Nemazanyy et al., 2013, Lindmo et al., 2008) (Figure 5.8B), which were cleared by reexpression of p150.

These data indicate that the p62/LC3 bodies may represent non-autophagic protein aggregates resulting from chronic loss of p150 activity. Supporting this notion, the redistribution of LC3/p62 into these relatively large cytoplasmic structures was unaffected upon 1hr starvation in preliminary data (Figure 5.8C). Moreover, marker distribution was similarly unaffected in cells starved in the presence of Bafilomycin A1 (which greatly increased the numbers of autophagosomes in the control scenario) or Wortmannin (which otherwise abolished LC3 puncta accumulation). Finally, alongside a general increase in p62 levels corroborating Western blot data, the ratio of p62 to LC3 appeared to be much higher in the sgA-D11 structures compared to the autophagosomes detected in the Control A3 cells.

5.4.3 Endolysosomal compartments in p150 effective knockouts

Based on the increased level of vacuolation observed in cells treated with EBSS and Wortmannin (100nM) in Figure 5.8C, it was noted that sgA-D11 appeared to show increased sensitivity to VPS34 inhibitors compared to control clones. VPS34 complex II activity is crucial for maintaining endolysosomal compartment identity, in part by generating PI3P on early endosomes to promote recruitment of the FYVE domain-containing EEA1. Therefore, the distribution of EEA1 was assessed in control and p150 effective KO cell lines. EEA1 marked punctate structures in control cells and a subset of the vacuoles induced upon Wortmannin treatment were EEA1-positive. In sgA-D11 cells relative to controls, the EEA1 compartment was partially vacuolated in basal conditions and extensively vacuolated in the presence of Wortmannin (Figure 5.9A). These data potentially indicate a reduction or abolishment of functionally active VPS34 present in sgA-D11. Supporting the latter case, functional lipid kinases sensitive to Wortmannin (200nM) were detected in a p150 KO MEF line (Nemazanyy et al., 2013).

Alongside the EEA1 compartment, LAMP1 positive late endolysosomal compartments were also partially vacuolated in basal conditions in p150 effective KOs (Figure 5.9B). Corroborating observations from Vps34 KO MEFs (Jaber et al., 2012) and VPS34 knockdown U-251

glioblastoma cells (Johnson et al., 2006), they remained Lysotracker positive, likely representing late endosomes retaining capacity to fuse with lysosomes but not for inward vesicle nucleation previously described (Johnson et al., 2006). Very little LC3 and LAMP1 colocalisation was observed in sgA-D11, indicating that the LC3 structures has not undergone fusion with lysosomes. Often, LAMP1 signal intensity appeared to be increased in sgA-D11 compared to controls. These data potentially corroborate Nemazanyy et al, 2013, who demonstrate increased lysosomal mass in effective p150 KO cells.

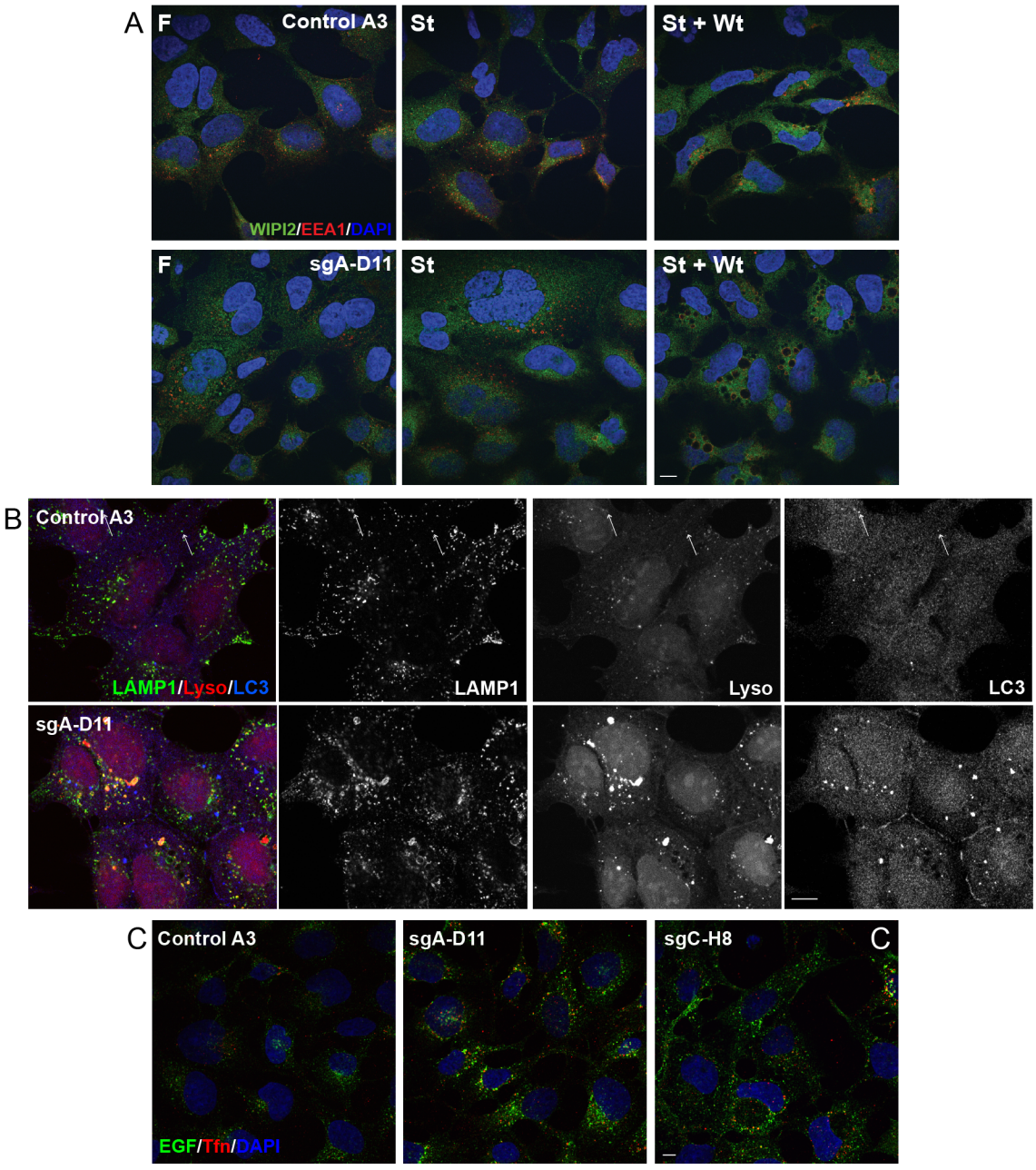

Figure 5.9 – *Examining endolysosomal compartment appearance in p150 effective knockouts*. **A** – p150 knockout (KO) or control cell lines were starved for 1 hour +/-100nM Wortmannin before fixation and visualisation of EEA1 (red) and WIPI2 (green) by immunofluorescence. Alongside abolition of starvation-induced WIPI2 puncta formation, sgA-D11 exhibited basally vacuolated early endosomal compartments with vacuolation greatly enhanced by the presence of Wortmannin compared to control cells. **B** – Control A3 and sgA-D11 p150 effective KOs were incubated with Lysotracker before fixation and visualisation of LAMP1 (green), Lysotracker (red) and LC3 (blue) by immunofluorescence. White arrows in Control A3 panels indicate areas of LAMP1, LC3 and Lysotracker colocalisation. The LAMP1 compartment, which was partly vacuolated in p150 effective KOs, still colocalised with Lysotracker but not with LC3. **C** – Control A3, effective KO (sgA-D11) and knockdown (sgC-H8) were incubated with fluorescently tagged EGF (green) and Tfn (red) for 60 minutes before fixation. In both sgA-D11 and sgC-H8, both ligands accumulated in enlarged endolysosomal compartments. Scale bars = 10µm.

Together, these data demonstrated that sgA-D11 (presumed to be representative of sgA-A8, sgA-B3 and sgA-D6) possesses a phenotype similar to those reported upon deletion of p150 or VPS34 in other experimental scenarios. This included the redistribution of autophagy markers, occurring consequently with a blockage of autophagic flux, and the vacuolation of endolysosomal compartments. Based on the latter observation, it was tested whether endolysosomal sorting was dysregulated in the p150 effective KOs.

The intracellular trafficking of EGF, Tfn and their receptors is well understood and their distribution is commonly used to assess endolysosomal functionality. Both ligands engage their cognate receptors at the plasma membrane, before internalisation into clathrin coated pits and delivery to the early endosome. Here, transferrin releases its bound iron before being trafficked to recycling endosomes for redelivery to the cell surface (Mayle et al., 2012). A population of active, dimeric EGF receptor (EGFR) disengages from the ligand in the early endosome and shuttles back to the plasma membrane in monomeric form. However, sustained ligand binding results in temporary ubiquitination and ESCRT-dependent recruitment into lumenal vesicles as early endosomes mature into late endosomes (Madshus and Stang, 2009). This is followed by terminal fusion with the lysosome leading to degradation of both ligand and receptor.

P150 KO and CRISPR control cells were pre-incubated with serum-free media to ensure maximal presentation of receptors at the plasma membrane, followed by incubation with media dually supplemented with fluorescently-tagged EGF and Tfn. Fixation was followed by immunofluorescence to reveal their intracellular localisation. EGF and to a lesser extent Tfn accumulated in enlarged compartments in both sgA-D11 and sgC-H8 relative to control (Figure 5.9C). These data partially corroborate those reported by Jaber and colleagues, who identified no aberrations in Tfn recycling in Vps34-deficient MEFs but a decrease in EGFR degradation upon ligand exposure (Jaber et al., 2016), indicating that endolysosomal trafficking was partially impeded upon CRISPR-based removal of endogenous p150.

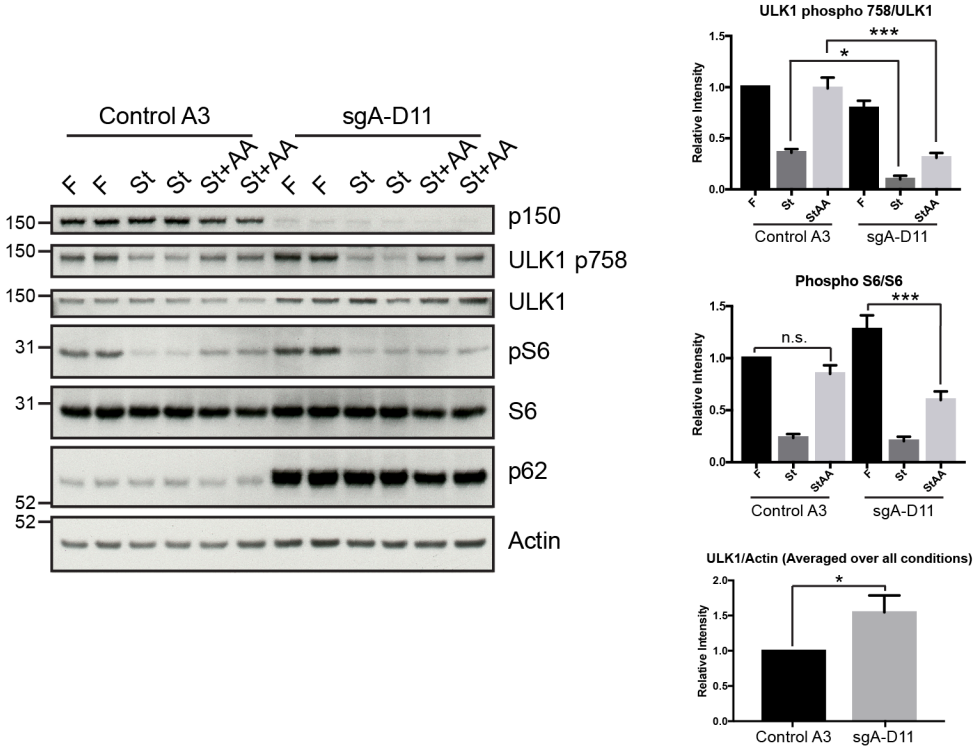

Figure 5.10 – *Differential regulation of autophagic signalling complexes in p150 KO clones*. Control A3 and sgA-D11 p150 effective KO cell lines were cultured in serum-free media for 24 hours to restrict mTOR activation to amino acid influx only. Before lysis, cells were cultured either in basal (Fed, F) or starvation media for 2 hours. Starved cells were either lysed directly (St), or had serum-free media replenished for 30mins to reactivate mTOR before lysis (St+AA). Western blotting was used to analyse ULK1 p758/ULK and phosho-S6/S6 to reveal mTOR activity in cell populations. As ULK1 levels did not appear to vary upon starvation/amino acid replenishment, the average expression across all conditions was calculated for each cell line and compared. Quantifications show mean +/- SEM, n=5 with technical duplicates, *p<0.05, ***p<0.001, n.s. = not significant.

5.4.4 Differential regulation of autophagic signalling complexes in p150 KO clones

The VPS34 complex has been implicated in the regulation of mTOR activation at the lysosomal surface in the presence of amino acids (Yoon et al., 2016). In a previously described p150 KO MEF line, no clear impact on nutrient-dependent mTOR signalling was noted, however mTOR reactivation upon introduction of growth factors was marginally slowed (Nemazanyy et al., 2013). In disagreement with the former finding and instead corroborating findings on Vps34 knockout MEFs (Jaber et al., 2012), mTOR reactivation upon amino acid stimulation was decreased in sgA-D11 (Figure 5.10). Notably however, although quantified data is lacking in (Jaber et al., 2012), the inhibition of mTOR activation appeared to be less in the p150 effective KOs. This might be due to a pool of functionally active VPS34 remaining in sgA-D11 cells discussed earlier, or indeed intrinsic differences between HEK293A and MEFs. Unexpectedly, ULK1 accumulation was detected in sgA-D11. When 5 experiments were averaged, ULK1 levels were ~50% higher in sgA-D11 than CRISPR controls.

5.4.5 p150 ablation does not affect mitophagy in HEK293A

The selective clearance of mitochondria by the autophagic machinery, termed mitophagy, is crucial for the maintenance of mitochondrial homeostasis. Mitophagy is facilitated by a suite of autophagic kinases such as ULK and TBK1, as well as signalling adaptors that link mitochondria to autophagosomal membranes, such as p62, NBR1, NDP52, NIX, BNIP3, FUNDC1 and OPTN (Yoo and Jung, 2018). Due to similarities between the targeted cargoes, there is extensive crossover between the quality control process of mitophagy and xenophagy – the rapid autophagic clearance of bacterial pathogens (Singh et al., 2018, Ravenhill et al., 2019, Vargas et al., 2019).

Of the multiple pathways by which mitophagy can be induced, PINK1/Parkin-dependent mitophagy is the best characterised due to the implication of the proteins in neurodegenerative disorders. The mitochondrial serine/threonine kinase PINK1 drives mitophagy by promoting translocation of the E3 ubiquitin ligase Parkin to depolarised mitochondria. In basal conditions, PINK1 constitutively translocates to the mitochondrial matrix where it is cleaved by the resident protease PARL, thus supressing its activity. Upon depolarisation, translocase of the outer membrane (TOM)-dependent transport is blocked

allowing PINK1 accumulation on the outer mitochondrial membrane (OMM). Here it phosphorylates ubiquitin at serine 65, creating a binding site for the Parkin, which is itself phosphorylated by PINK1 (also at serine 65, in Parkin's ubiquitin-like region), leading to activation at the OMM (Kazlauskaite et al., 2014b, Kazlauskaite et al., 2014a, McWilliams et al., 2018). Ubiquitination of mitochondrial substrates promotes feed-forward amplification, which can be reversed via proteasomal removal of ubiquitinated proteins, cleavage of polyubiquitin chains or by sequestration of damaged membranes into mitochondria-derived vesicles (Truban et al., 2017). Once the ubiquitination of OMM proteins breaches threshold levels, the aforementioned mitophagic signalling kinases and adaptors are engaged to trigger formation of autophagosomes *in situ* (Vargas et al., 2019).

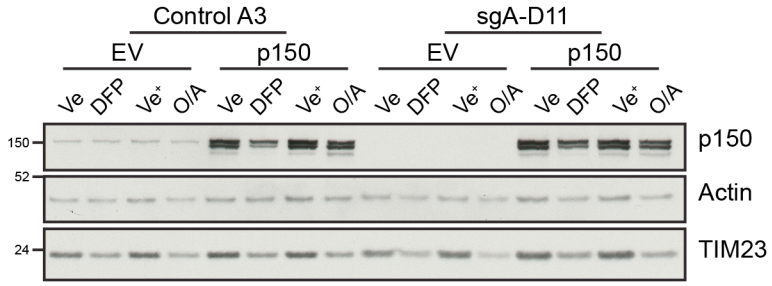

Figure 5.11 – *p150 ablation does not affect mitophagy in HEK293A.* CRISPR control and p150 effective KO cell lines were transfected with empty vector (EV) or p150-HA before treatment with DFP (1mM, 18 hours), Oligomycin + Antimycin (O/A - both 1mM, 12hrs) or vehicle (Ve). In the case of O/A-treated cells, Vehicle-treated cells were maintained in full media with an equivalent volume of DMSO (Ve+). Cells lysates were analysed by Western blot. TIM23 turnover, used to measure the progression of mitophagy, was not affected by p150 removal or overexpression. n=2.

Importantly, the physiological relevance of the PINK1/Parkin system has been drawn into question in recent years. This is partly due to the non-physiological conditions regularly employed in its study. For example, Parkin is frequently overexpressed despite being maintained at low levels endogenously. Furthermore, to drive prompt and efficient mitophagy, cells are often exposed to mitochondrial uncouplers (such as CCCP) or inhibitors of mitochondrial respiration (typically antimycin A, which blocks electron transport chain via cytochrome C reductase inhibition and oligomycin which directly inhibits ATP synthase), which both promote mitochondrial depolarisation (Von Stockum et al., 2016, Baudot et al., 2015). Of the two classes of inhibitor, antimycin A and oligomycin, which are typically used in

combination, are considered to be more physiologically relevant due to increased specificity leading to decreased toxicity (Georgakopoulos et al., 2017).

Consequently, the study of PINK1/Parkin-independent mitophagy has seen increased interest in recent years. Of note, FUNDC1, BNIP3 and NIX all recruit LC3B and GABARAP directly in response to hypoxia in a PINK1/Parkin-independent manner (Rikka et al., 2011, von Stockum et al., 2018). Furthermore, additional E3 ligases have been implicated in mitophagy such as MUL1, which acts via ubiquitination of mitofusin in Drosophila (Yun et al., 2014) whilst also promoting ULK1 recruitment during selenite-induced mitophagy in HeLa cells (Li et al., 2015a). Alongside selenite and hypoxia, other stimuli for PINK1/Parkin-independent mitophagy exist. The iron chelation Deferiprone (DFP) was i-dentified in a chemical screen for mitophagy inducers and shown to induce mitophagy in cells lacking PINK1 or Parkin (Allen et al., 2013).

To assess the role of p150 in mitophagy, CRISPR knockout and control cell lines expressing either empty vector or p150 WT were treated with DFP (1mM, 18hrs) or Oligomycin + Antimycin A (both 1mM, 12hrs). Mitophagy rates were measured via degradation of TIM23, a component of the translocase of the inner membrane complex. TIM23 was chosen as its location shields it from proteasomal degradation, therefore implicating mitophagy in its turnover. Both treatments lead to a ~50% reduction in TIM23 levels, however modulation of p150 levels via ablation or overexpression did not noticeably affect mitophagy rate (Figure 5.11).

5.5 Phosphorylation- and valine 50-dependent phenotypes of p150 *in vivo*

5.5.1 Assessing Consequence of ULK phosphorylation and loss of V50 via transient overexpression

Some of the effective KO CRISPR clones (sgA-B3, sgA-D6 and sgA-D11) were then used as tools to assess whether p150 phosphorylation regulates autophagy. Rescue with total phosphomutant p150 was examined in the first instance to test the maximal potential autophagy phenotype engendered by dephosphorylation of ULK target sites. p150 with all six of the putative ULK substrate sites substituted with alanine (6SA) was expressed in control and

p150 knockout CRISPR clones before amino acid starvation in the presence of 100nM Bafilomycin A1 for 1 hour. In this condition, no accumulation of LC3-II was observed in sgA-D11 transfected with EV. Lipidation was rescued by p150 WT reexpression and to a lesser extent by that of p150 6SA (Figure 5.12A). When identically transfected cells were subject to immunofluorescence analysis, quantification of WIPI2 puncta number in cells starved for 1 hour revealed a similar reduction in 6SA-expressing cells relative to WT (Figure 5.12B). LC3 aggregate clearance, observed in ~70% of cells, was found to be a more reliable marker for rescue than HA positivity.

At this stage, it was unknown whether the effective KO phenotype resulted from a reduction in p150 levels, the dominant-negative effect of the endogenous ATP-binding site mutations, or a combination of the two mechanisms. However, as a similar level of p150 expression was detectable in the four effective KO cell lines as well as in sgC-H8 which retained autophagic flux (see Figure 5.7A), it was likely that the nature of the introduced mutations drove the observed phenotype. Interestingly, when the effective KO mutant alleles were translated, excluding the frame shift detected in sgA-A8, all lacked valine 50 alone or alongside other mutations. Valine 50 occupies a highly conserved position in p150's predicted ATP binding site (Sigrist et al., 2013). Interestingly, the non-conformity of this site with that of bona fide kinases, specifically in the N-terminal G-x-G-x-x-G motif, has been used to condemn p150 to shameful pseudokinase ignominy (Backer, 2008). Furthermore, the major evidence supporting p150 kinase activity stems from the observed *in vitro* autophosphorylation of yeast Vps15p, which confirms with the motif in even fewer positions (Figure 5.12C). The question therefore arose as to whether ATP-binding is important for p150's functionality and whether its interference is implicated in the effective KO phenotype.

Control A3 and sgA-D11 were transfected with constructs encoding WT or ΔV50 p150-HA for 48 hours before treatment with EBSS + 100nM Bafilomycin A1 for 1 hour. Compared to WT, expression of p150 ΔV50 did not rescue VPS34 stability, p62 accumulation (indeed, p62 accumulation appeared to increase in cells overexpressing the ΔV50 mutant) or LC3 lipidation (Figure 5.12D). These data indicate that loss of valine 50 renders p150 non-functional in autophagy. If true, it is therefore likely that if expressed the WT p150 remaining in the CRISPR clones is insufficient to fully compensate for the range of p150-dependent functions, resulting in the effective knockout phenotype.

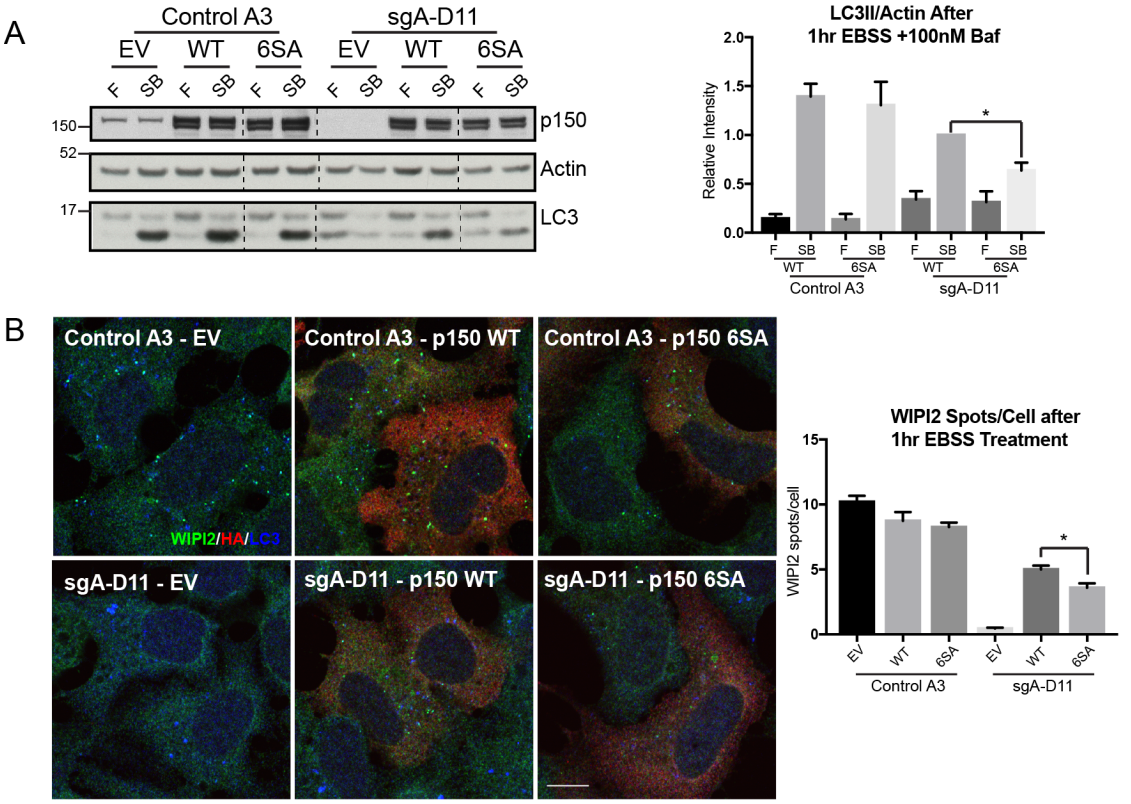

C

ATP-Binding Site (Prosite #PS00107)

[LIV]-G-{P}-G-{P}-[FYWMGSTNH]-[SGA]-{PW}-[LIVCAT]-{PD}-x-[GSTACLIVMFY]-x(5,18)-[LIVMFYWCSTAR]-[AIVP]-[LIVMFAGCKR]-K

p150 (Human)

G–x–G–x–x–G *V50*

L–G–S–T–R–F–F–K–V–A–R–A–K–H–R–E–G–L–V–V–V–K

Vps15p (S. *cerevisiae*)

G–x–G–x–x–G *I51*

L–N–S–S–R–F–L–K–T–C–K–A–L–D–P–N–G–E–I–V–I–K

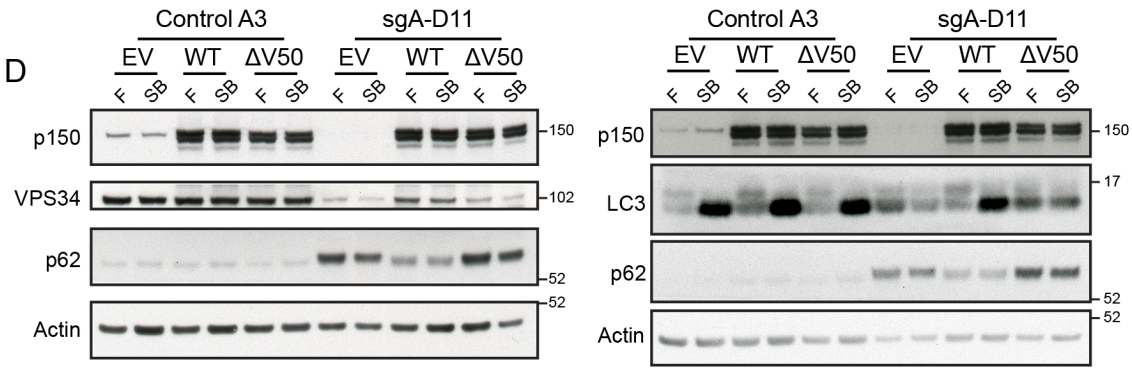

Figure 5.12 – *Assessing Consequence of ULK phosphorylation and loss of V50 via transient overexpression*. **A** – Empty vector (EV), wild type (WT) or total phosphomutant (6SA) p150-HA were expressed in Control A3 or sgA-D11 p150 effective KOs. Cells were starved for 1 hour in the presence of Bafilomycin A1 (100nM). EV-transfected sgA-D11 were not competent for LC3 lipidation upon starvation. 6SA-expressing sgA-D11 accumulated significantly less LC3-II than cells rescued with p150 WT. Dashed lines indicate where blots were cropped for presentation. **B** – Identically transfected and cells were starved for 1 hour then fixed and prepared for immunofluorescence. Fewer WIPI2 (green) puncta were generated in cells transfected with 6SA than WT p150. Resolution of putative LC3 (blue) aggregates was a better predictor of rescue than HA (red) expression. Scale bar 10µm. For A and B, quantification shows mean +/- SEM, n=3, *p<0.05. **C** – ATP binding site motif from ExPASy Prosite (#PS00107) (Sigrist, 2013). Tolerated residues are listed alone or in [square brackets] when there are multiple, 'x' indicates that any residue is permitted and 'x(5,18)' indicates that any stretch of amino acids for 5-18 positions is accepted. When specific residues are not permitted at a given position, they are included in {braces}. Below this motif, the predicted ATP-binding sites in p150 (positions 32-53) and Vps15p (positions 33-54) are shown with conforming sites in green, non-conforming sites in red and 'x' sites in grey. Regions discussed in the text are annotated. **D** – p150-HA WT or ΔV50 transfected CRISPR clones were subject to starvation in the presence of Bafilomycin A1 (100nM) for 1 hour. VPS34 destabilisation (left) and LC3 lipidation (right) as well as p62 accumulation were rescued upon overexpression of WT but not ΔV50 p150.

5.5.2 Assessing consequence of ULK phosphorylation and loss of V50 in stably rescued CRISPR clones

Based on the cell to cell variations in rescue efficiency (see Figures 5.8B and 5.12B), as well as variability between experiments, stably rescued effective KOs were generated. Focussing first on the *in vitro*-validated ULK substrate residue as well as valine 50, lentiviral transfer plasmids encoding either EGFP alone or p150 WT, S861A, S861E or ΔV50 were produced. Each of the lentiviral transfer plasmids also encoded puromycin N-acetyl-transferase (conferring resistance to puromycin) and, in the case of the p150-expressing constructs, EGFP immediately following the PIK3R4 ORF (connected via an internal ribosome entry site).

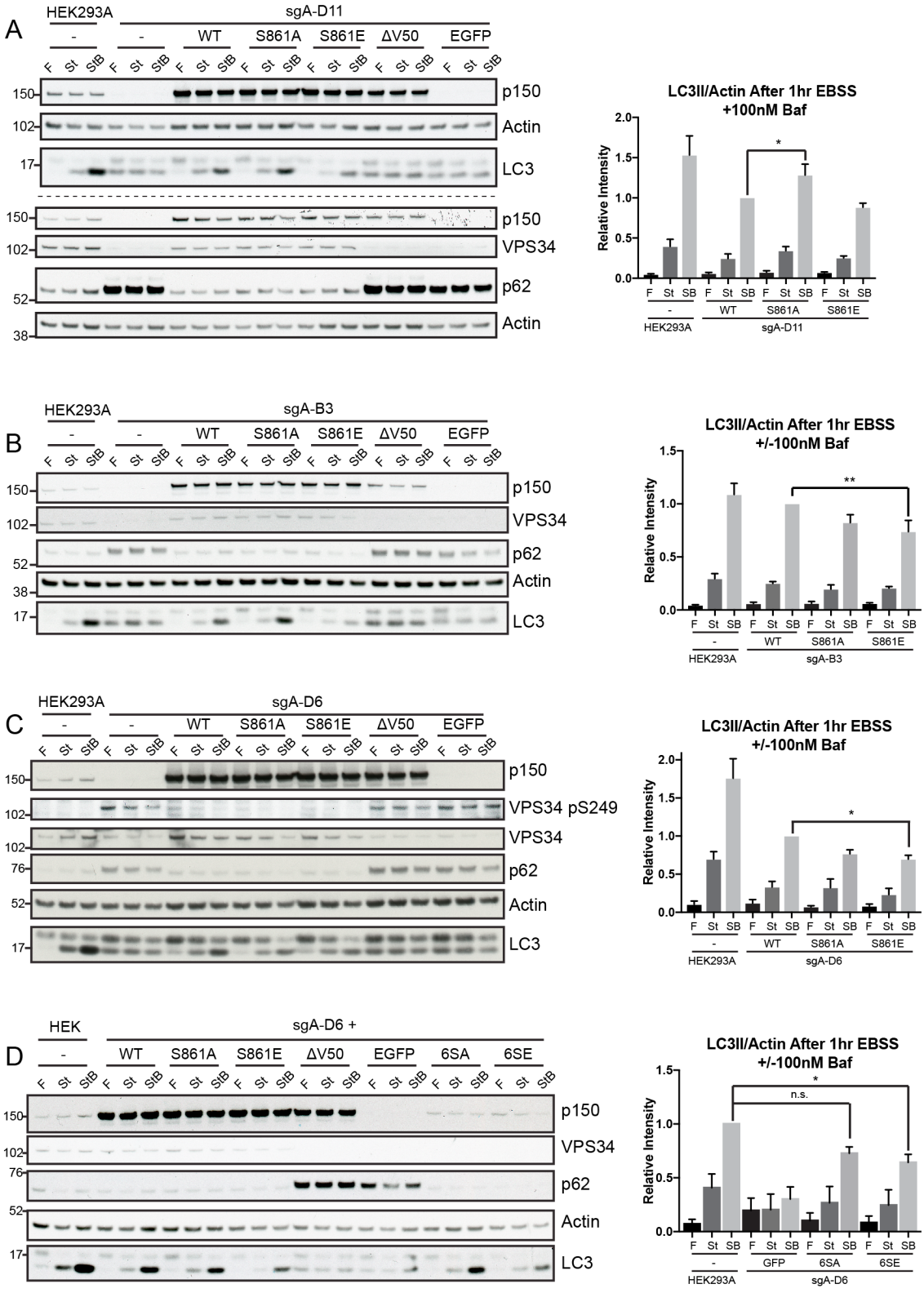
A
HEK293A
sgA-D11
-
-
WT
S861A
S861E
ΔV50
EGFP
F St StB
150
102
17
p150
Actin
LC3
150
102
p150
VPS34
52
p62
38
Actin
LC3II/Actin After 1hr EBSS
+100nM Baf
Relative Intensity
2.0
1.5
1.0
0.5
0.0
*
F St SB
-
WT
S861A
S861E
HEK293A
sgA-D11
B
HEK293A
sgA-B3
p150
VPS34
p62
Actin
LC3
LC3II/Actin After 1hr EBSS
+/-100nM Baf
**
sgA-B3
C
HEK293A
sgA-D6
p150
VPS34 pS249
VPS34
p62
Actin
LC3
76
LC3II/Actin After 1hr EBSS
+/-100nM Baf
sgA-D6
D
HEK
sgA-D6 +
-
WT
S861A
S861E
ΔV50
EGFP
6SA
6SE
p150
VPS34
p62
Actin
LC3
LC3II/Actin After 1hr EBSS
+/-100nM Baf
n.s.
GFP
6SA
6SE
sgA-D6

Figure 5.13 – *Assessing Consequence of ULK phosphorylation and loss of V50 in stably rescued CRISPR clones*. sgA-D11(**A**), sgA-B3 (**B**) or sgA-D6 (**C**) were lentivirally transduced with bicistronic constructs encoding p150 wild type (WT), S861A, S861E or ΔV50 followed by IRES-linked EGFP or EGFP alone. Stably rescued cells along with HEK293A and non-transduced CRISPR clones were starved for one hour +/- Bafilomycin A1 (100nM) to assess autophagic flux after which cells were lysed and analysed by Western blot. The dashed line in 5.13A indicates that the blots are distinct and originate from independent repeats. In sgA-D11, S861A expression correlated with increased in autophagic flux as measured by accumulation of LC3-II upon starvation + Bafilomycin A1 (StB). Autophagic flux was decreased in S861E-expressing cells relative to WT in sgA-B3 and -D6. Quantifications represent mean +/- SEM, n=5(A), n=4(B/C) with technical duplicates, *p<0.05. **D** – sgA-D6 lentivirally rescued with constructs encoding total serine to alanine/glutamate p150 phosphomutants (6SA/6SE) were subject to autophagic flux assays as before. Western blot analysis revealed that autophagic flux was significantly reduced in effective KO cells expressing p150 6SE relative to unmodified HEK293A. Quantifications represent mean +/- SEM, n=3 with technical duplicates, *p<0.05.

Three of the four effective knockouts (sgA-D11, -B3 and -D6) were transduced with lentiviruses encoding each of the 5 transfer plasmids. After time was allowed for viral integration, the pools were sorted via FACS such that cells with the lowest EGFP signal were isolated. First to be transduced was sgA-D11. In this instance, single cell clones were generated at first, however pools of stably rescued clones were used in phenotypic assays. For all three sets of rescued CRISPR clones, the lowest EGFP expressing cells were pooled and used in consequent experiments.

Stably rescued effective knockouts as well as non-transduced negative controls and unmodified HEK293A were subject to autophagic flux analysis. Cells were starved of amino acids for 1 hour in the presence or absence of Bafilomycin A1 before lysis, protein separation by SDS PAGE and analysis by Western blot. Confirming initial phenotypic data as well as those attained from transiently-transfected clones (Figures 5.7 and 5.12), chronic removal of p150 resulted in accumulation of both p62 and LC3-I/II alongside VPS34 destabilisation. No rescue was observed in cells overexpressing p150 ΔV50 or EGFP alone and in contrast with Figure 5.12D, p150 ΔV50 overexpression did not result in further accumulation of p62 in any of the clones tested.

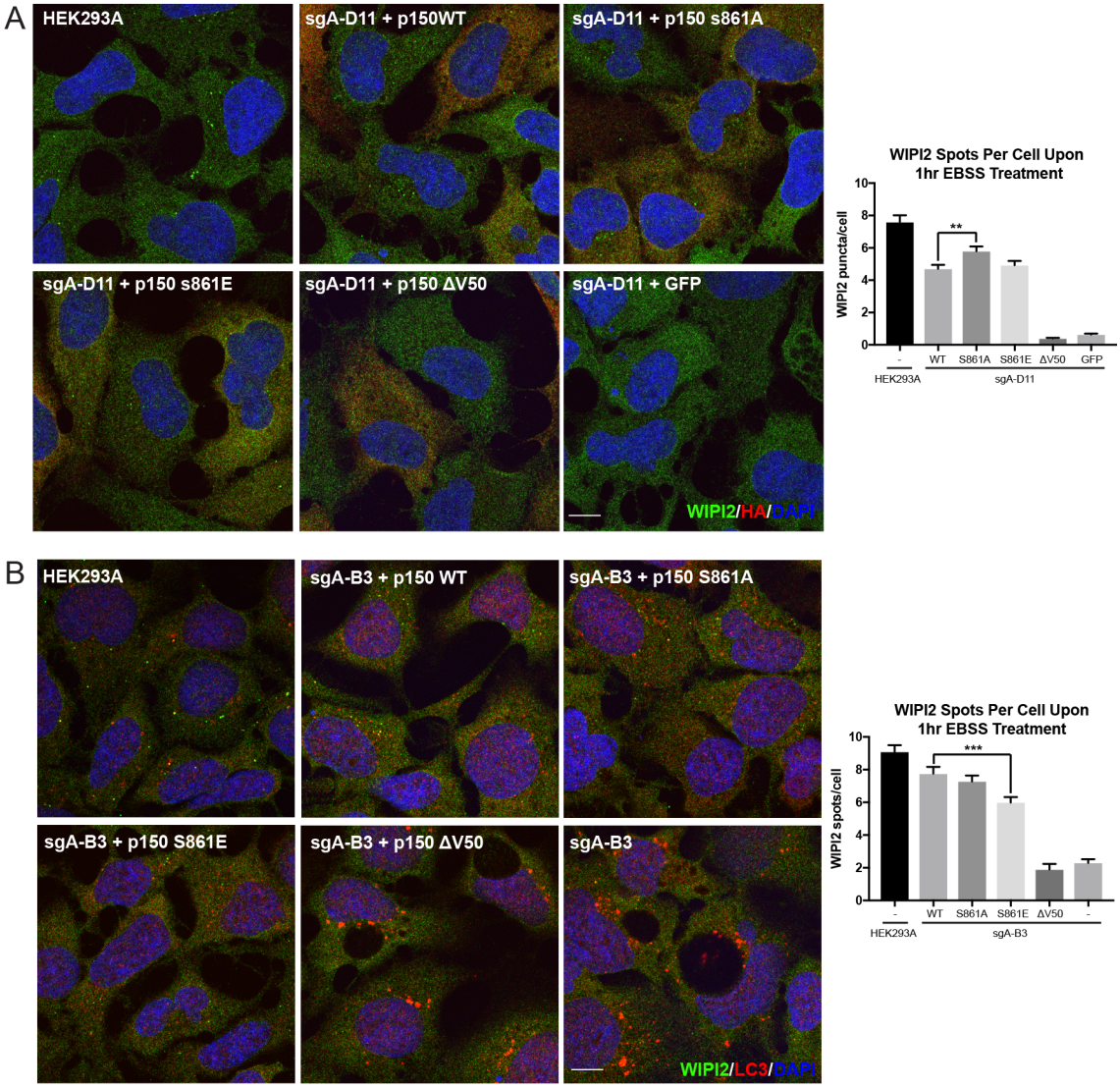

Figure 5.14 – *Assessing Consequence of ULK phosphorylation and loss of V50 in stably rescued CRISPR clones by immunofluorescence*. Stably rescued sgA-D11(**A**) and sgA-B3 (**B**) were starved for 1 hour before fixation and preparation for immunofluorescence. WIPI2 (green) and DAPI (blue) were visualised along with HA-p150 (Red, in **A**) and LC3 (Red, in **B**). Quantification of WIPI2 puncta revealed a significant increase in S861A-rescued sgA-D11 relative to WT, whilst S861E-rescued sgA-B3 exhibited significantly fewer puncta than WT counterparts. Quantifications represent mean +/- SEM, ***p<0.005, **p<0.01. n=5(A); n=4(B). Scale bar = 10µm.

WT, S861A and S861E p150 rescued the effective KO phenotype in each clonal background. Between the three sets of cell lines however, two S861-dependent phenotypes emerged. sgA-D11 stably-rescued with p150 S861A displayed a ~29% increase in LC3-II accumulation upon

starvation + Bafilomycin A1 compared to WT, with a small (~12%) but non-significant decrease observed in cells transfected with p150 S861E (Figure 5.13A). However, in sgA–B3 and –D6, rescue with S861A lead to a small reduction in LC3-II accumulation (~18% for sgA-B3, ~23% for sgA-D6) with a more pronounced reduction in S861E-rescued clones (~26% for sgA-B3, ~31% for sgA-D6) (Figure 5.13B and C).

Several ULK substrate residues have been identified within components of the VPS34 complex. It was therefore examined whether the phosphorylation of one of these, VPS34 serine 249, by ULK1 was affected by p150 serine 861 phosphorylation status. No starvation-dependent increase in VPS34 phosphoserine 249 was detected by this approach in either HEK293A or rescued sgA-D6, potentially indicating the requirement of further optimisation. Unexpectedly however, VPS34 phosphoserine 249 was enriched in non-rescued cell lines. This is especially apparent given the relative reduction of VPS34 levels in these cell lines (Figure 5.13C).

When rescuing the sgA-D6, lentiviruses were produced encoding p150 in which all putative ULK1 substrate residues were mutated to either alanine (6SA) or glutamate (6SE). Possibly due to low viral titre, transduction efficiency was relatively poor in cells rescued with these mutants, with disparity in p150 expression remaining apparent even after FACS sorting. To enrich for high expressing cells whilst removing those that had escaped transduction, 6SA/6SE-expressing cells were subjected to puromycin selection, however very little cell death was apparent indicating that the majority if not all of the cells had been transduced (with the puromycin resistance gene at minimum). These cells were also subjected to an autophagic flux assay as before. Whilst the average expression level for p150 6SA/6SE was much lower than for the other p150 constructs, it was in the same range as unmodified HEK293A. Therefore, data from samples displaying comparable levels of p150 expression (HEK293A, sgA-D6 + EGFP, 6SA and 6SE) were quantified (Figure 5.13D). Expression of both p150 6SA and 6SE rescued LC3 and p62-dependent phenotypes with the accumulation of LC3-II upon starvation in the presence of Bafilomycin A1 slightly reduced in the 6SE cells compared to 6SA. Although not quantified, the improved rescue compared to WT was likely due to the near-stoichiometric expression of p150.

5.5.3 Assessing consequence of ULK phosphorylation and loss of V50 in stably rescued CRISPR clones by immunofluorescence

Due to the difficulties in teasing apart VPS34 complex I- and complex II-dependent phenotypes based on autophagic flux data alone, the redistribution of WIPI2 upon starvation, a strictly complex I-dependent process, was assessed via immunofluorescence. Stably rescued sgA-D11 and sgA-B3 were incubated with EBSS for 1 hour before fixation. In the representative experiments selected for presentation, WIPI2 and HA were visualised for sgA-D11 (Figure 5.14A) with WIPI2 and LC3 visualised for sgA-B3 (Figure 5.14B). As expected, non-rescued clones exhibited LC3 aggregation, vacuolation and a great reduction in WIPI2 puncta formation. In both sgA-D11 and sgA-B3-derived cell lines, as expected expression of p150 resulted in clearance of likely LC3 aggregates and a resolution of the chronic vacuolation symptomatic of p150 loss. Quantification of WIPI2 puncta number again revealed suboptimal rescue efficiency compared to HEK293A (compare with Figures 5.13A and B). WIPI2 puncta in appeared smaller in rescued cells compared to HEK293A. Furthermore, the same two patterns described in the previous figure again emerged. Compared to WT, S861A-rescued sgA-D11 displaying a significant increase in puncta number and with fewer puncta were detected in sgA-B3 rescued with S861E. Together, these indicate that the S861-dependent phenotype was in part due to differential regulation of VPS34 complex I activity.

5.5.4 Assessing complex II-dependent VPS34 activity in effective KO cells

Having uncovered potential evidence of S861-dependent regulation of VPS34 complex I activity, the regulation of VPS34 complex II activity by serine 861 phosphorylation was assessed. As previously discussed, upon ligand stimulation EGFR traffics from the plasma membrane to endosomes before delivery to lysosomes via maturation or fusion, resulting in receptor degradation. As VPS34 complex II is crucial in maintaining the identity and functionality of both early/late endosomes and lysosomes, EGFR degradation was used to assay VPS34 complex II activity in rescued CRISPR KO clones.

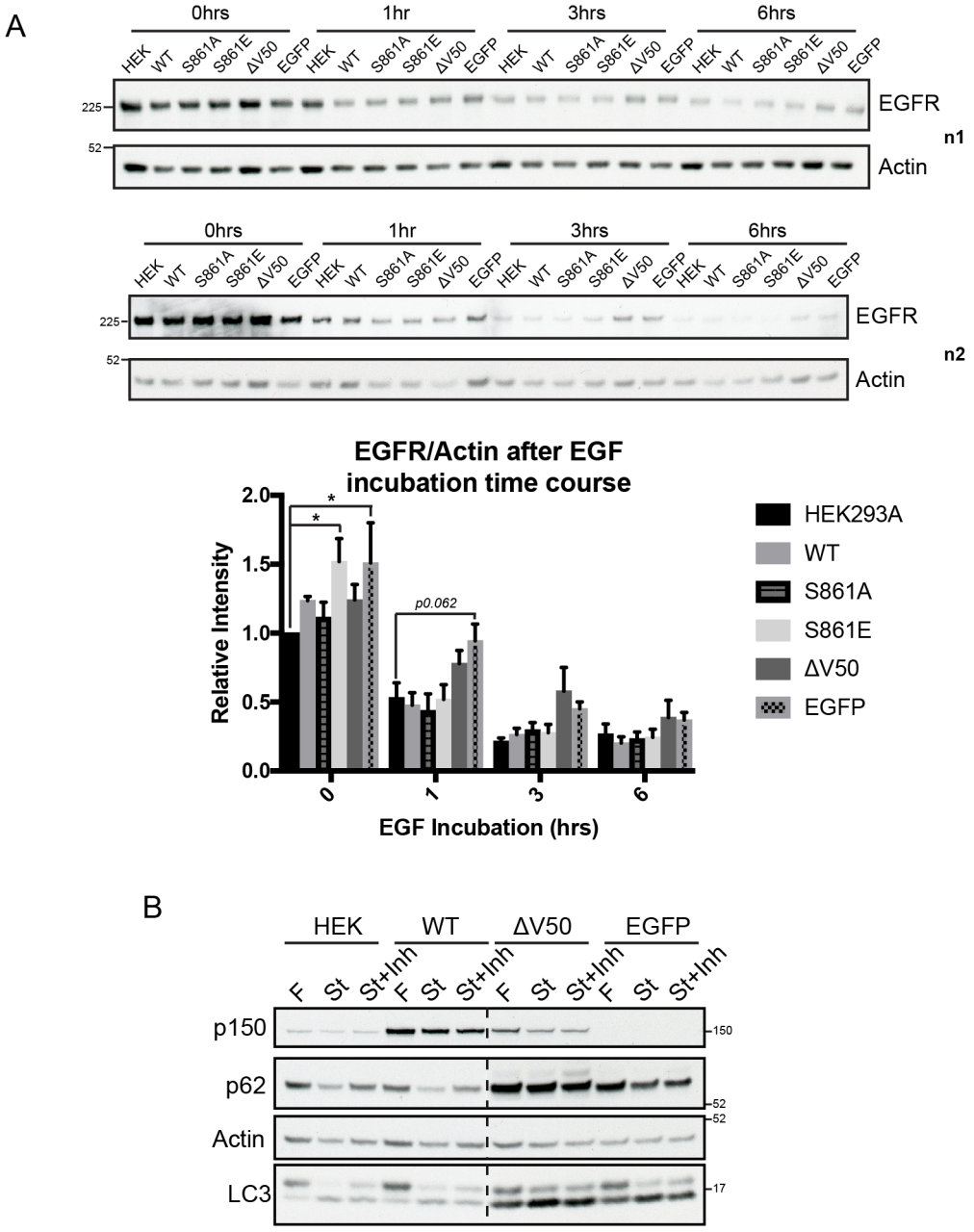

Figure 5.15 – *Assessing complex-II dependent contribution to VPS34 activity in rescued effective KO cells*. **A** – HEK293A along with sgA-D11 stably expressing p150 WT, S861A, S861E, ΔV50 or EGFP alone were preincubated in serum free media before culturing in media supplemented with 100ng/ml EGF for a 6-hour time course. Cells were lysed after 0, 1, 3 or 6 hours in EGF-containing media and analysed by Western blot. 2 independent repeats are shown. Quantifications represent mean +/- SEM, n=5, *p<0.05. **B** – HEK293A along with sgA-D11 stably expressing p150-WT, -ΔV50 or EGFP alone were cultured in EBSS for 6 hours in the presence or absence of the Vps34 inhibitor IN1 (Inh - 1μM). Dashed lines indicate where blots were cropped for presentation. LC3 lipidation was used as a readout for autophagy initiation. n=2.

Stably rescued sgA-D11 were incubated in media supplemented with EGF for 0, 1, 3 and 6 hours before lysis and Western blot analysis (Figure 5.15A). At steady state, EGFR levels were elevated in non-rescued (EGFP alone) sgA-D11. EGFR levels remained >40% higher than WT at 1, 3 and 6 hours for both ΔV50 and EGFP-expressing cells indicating that the rate of degradation was inhibited. In basal conditions, a 50% increase in EGFR was noted in p150 S861E-rescued cells compared to those rescued with p150 WT. However, as this difference was not observed at any other time points, the reliability of this finding was questioned. Due in part to the minimal impact on EGFR degradation noted in non-rescued sgA-D11, these data do not rule out the contribution of S861 to regulation of VPS34 complex II activity.

VPS34 ablation in MEFs has been shown to entirely inhibit EGFR degradation after stimulation with EGF for 3 hours (Jaber et al., 2016). Therefore, alongside the increased sensitivity to Wortmannin observed in sgA-D11 (Figure 5.8C) these data indicate that a degree of VPS34 activity remains in the p150 effective KOs. With the likelihood of trace levels of VPS34 activity remaining, the question remained as to which stage of autophagy was blocked to yield the observed phenotype. The preliminary observation of a slight reduction in LC3-I levels after 1hr starvation in effective KO cells (Figure 5.8A) suggested that autophagy initiation might persist in the effective KOs, albeit at a reduced rate. To test whether this was indeed the case and more importantly whether it was VPS34-dependent, stably-rescued sgA-D11 were subject to prolonged starvation to amplify any LC3-dependent readout, in the presence or absence of the small molecule inhibitor of VPS34, IN1 (Bago et al., 2014). This was chosen due to its increased VPS34 specificity relative to Wortmannin, which can modulate the activity of other PI3P-metabolising enzymes at low concentrations (Nemazanyy et al., 2013, Johnson et al., 2006).

In HEK293As or sgA-D11 reconstituted with p150 WT, 6hrs starvation lead to a noted depletion in p62 as well as an increase in LC3 lipidation. p62 degradation was reversed in the presence of IN1 and LC3 lipidation was slightly reduced (identifiable by the increased intensity of LC3-I) (Figure 5.15B). In the non-rescued cells, although unclear for EGFP-expressing cells in the displayed blot, p62 levels appeared to be unaffected by starvation. LC3 lipidation was clearly detectable after starvation and appeared to be somewhat reduced in the presence of the inhibitor. As IN1 treatment did not completely reverse LC3 lipidation in the control scenario and as the accumulation of LC3-II upon starvation was slight, these data do not rule out the contribution of VPS34-independnent/non-canonical autophagy in sgA-D11. However, these

data indicate that the effective knockouts retain some capacity for VPS34-dependent autophagy initiation.

5.6 Phosphorylation- and valine 50-dependent phenotypes of p150 *in vitro*

5.6.1 Biochemical analysis of ULK phosphorylation and loss of V50

Thus far, novel functionalities for 2 p150 residues have been described. Serine 861 is phosphorylated by ULK1 *in vivo*/*in vitro* and reconstituting effective KOs with phosphomutant p150 leads to a reduction in both autophagic flux and omegasome number; valine 50 lies in p150's ATP binding site and deletion of this residue renders p150 non-functional, compromising its ability to rescue both autophagic flux and VPS34 stability.

To examine the mechanism of these phenotypes, ZZ-tagged p150 WT, S861A, S861E and 6SA (Figure 5.16A) or p150 WT and ΔV50 (Figure 5.16B) were coexpressed separately with untagged VPS34. Cell lysis was followed by coimmunoprecipitation of VPS34 complex components via p150. Mutation of serine 861 alone did not affect VPS34 complex component binding, however this was expected due to the position of this residue on a likely-flexible linker with no implication in complex member binding thus far. Interestingly, whilst p150 6SA bound complex I components ATG14 and NRBF2 with comparable efficiency to WT, the binding affinity for both VPS34 and UVRAG was increased (Figure 5.16A). Removal of valine 50 did not affect VPS34 binding significantly, however a large reduction in UVRAG, ATG14 and NRBF2 association was observed (Figure 5.16B). These results indicate that dephosphorylation of the 6 ULK target residues primes p150 for complex II association, whilst valine 50 deletion destabilises the tetrameric VPS34 complexes I and II leaving the VPS34-p150 subcomplex unaffected. Interestingly, p150 ΔV50 separated as a doublet (Figure 5.16B), with the appearance of a lower molecular weight but ZZ-positive band suggesting that valine 50 deletion might promote N-terminal truncation of p150.

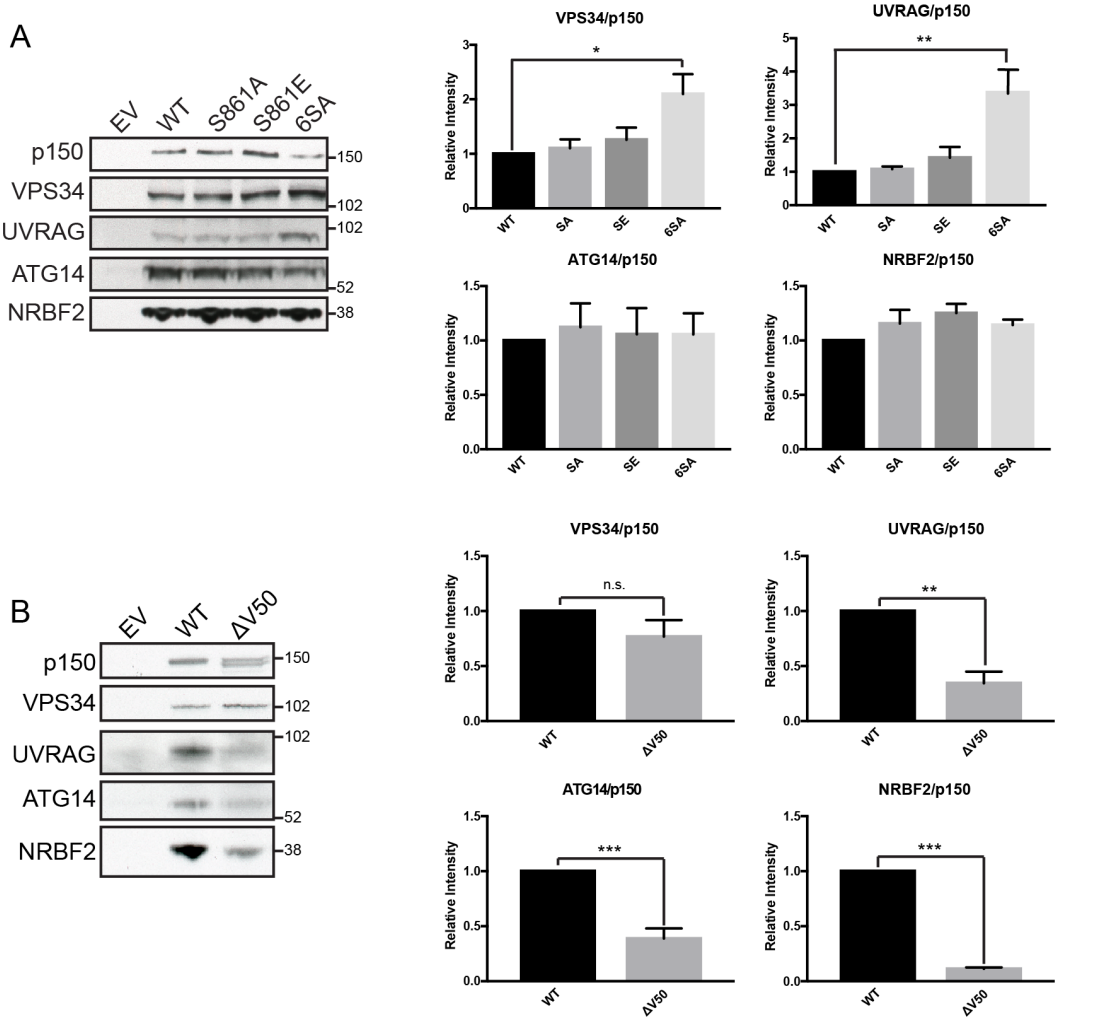
A
EV
WT
S861A
S861E
6SA
p150
VPS34
UVRAG
ATG14
NRBF2
150
102
102
52
38
VPS34/p150
UVRAG/p150
ATG14/p150
NRBF2/p150
Relative Intensity
WT
SA
SE
6SA
B
EV
WT
ΔV50
n.s.
**
***
C
FYCO
VPS34 S249
VPS34 S249pS
p150 S1289
p150 S1289pS
p150 Y1290pY
p150 S1289pS Y1290pY
LC3A
LC3B
LC3C
GABARAP
GABARAP L1
GABARAP L2
GST
1281
1304
GSTSSPSVSYYRKIIEGTEVVQEI
0
+3
D
GFP
RAB5WT
RAB5Q79L
RAB7WT
RAB7Q67L
EV
p150
ponc
E
RAB5WT
RAB7WT
GFP
S861A
S861E

Figure 5.16 – *Biochemical analysis of ULK phosphorylation and loss of V50*. **A** – HEK293A coexpressing VPS34 along with empty vector (EV) or with wild type (WT), S861A, S861E or 6SA p150 were starved for 30 minutes before lysis and p150 immunoprecipitation. Western blot analysis was used to assess coimmunoprecipitation of VPS34 complex I and II core components. Quantification of 4 independent repeats revealed that association with UVRAG and VPS34 was significantly increased with 6SA p150 compared to WT. **B** – VPS34 was coexpressed with p150 WT or ΔV50, or with EV, before immunopurification of p150. Quantification of 3 independent repeats revealed that UVRAG, NRBF2 and ATG14 binding was significantly decreased with ΔV50 p150 compared to WT. Quantifications represent mean +/- SEM, *p<0.05, **p<0.01, ***p<0.005, n.s. not significant. **C** – Peptides encoding variations of the amino acid sequence surrounding the putative LIR adjacent to serine 1289 in human p150 were arrayed in triplicate. WT (non-phosphorylated) peptides were arrayed along with those encoding either phospho-serine 1289 or -tyrosine 1290 both alone or together (green and red arrows respectively in human p150, right). LIR motifs from FYCO1 and VPS34 were included as positive controls. Arrays were incubated with GST-tagged Atg8p homologs or GST alone before immunoblotting for GST. Y1290 phosphorylation promoted binding of all Atg8p homologs except LC3A and LC3B. **D** – GFP-tagged WT and constitutively active (QL) mutants of RAB5 and RAB7 were coexpressed with either EV or p150-HA as indicated. GFP alone was included as a negative control. Cells were lysed and GFP immunopurified. Western analysis of the immunoprecipitates revealed that similar p150 binding was detectable for all of the RAB mutants. n=1. **E** – GFP-tagged RAB5/RAB7 or GFP alone were overexpressed in sgA-D11 stably expressing p150 WT, S861A or S861E. Lysis followed by GFP immunopurification and Western blot analysis revealed little difference in binding between p150 mutants and either RAB5 or RAB7. n=2. For both **D** and **E**, ponceau staining reveals GFP/GFP-RAB levels in immunoprecipitates.

Having investigated binding to VPS34 complex core components, accessory protein binding was examined. Recently, several functional LIRs were annotated in VPS34 complex components (Birgisdottir et al., 2019). Lying immediately adjacent to the VPS34's C2 domain which was implicated in membrane binding previously (Backer, 2008), residues 250-253 were shown to comprise a GABARAP-specific LIR. Interestingly, LC3C, GABARAP and GABARAPL1 binding to the VPS34 LIR is greatly increased upon phosphorylation of serine 249 – a known ULK1 substrate residue (Birgisdottir et al., 2019, Egan et al., 2015). As phosphorylation-dependent regulation has been described for multiple LIRs (Birgisdottir et al., 2013), it was examined whether any of the 6 ULK substrates corresponded with predicted LIRs.

The primary amino acid sequence for p150 was submitted into the iLIR prediction server (Kalvari et al., 2014, Jacomin et al., 2016). 20 candidate LIRs were detected, 3 of which spanned or were adjacent to a putative ULK substrate residues (see Appendix Table C for full details). These were as follows: LIR1 (S861-866; position -2 to +3), LIR2 (S1036-1041; position -2 to +3) and LIR3 (1289-1294; position -2 to +3). To analyse phosphorylation-dependent LC3/GABARAP binding at the three predicted LIR motifs, 24mer peptides centred on each of the predicted LIRs were synthesised. Phosphomutant peptides were also synthesised, encoding glutamate at the predicted ULK site in combination with selected phosphoacceptor residues N terminal or C terminal to the LIR in various permutations. These were predicted based on the stipulations reported by Wirth and colleagues (Wirth et al., 2019). For example, in the case of LIR1, both S861E and S865E were tested, as well as S861/865E, S853/S861E and S853/861/865E. Furthermore, a duplicate set of peptides were synthesised bearing phosphoserine in place of glutamate at the putative ULK substrate sites. The full list of the peptides used in the assay are detailed in Appendix Table D.

The peptides were immobilised in array format. Also included were three additional 24mer peptides containing control LIRs: residues 250-253 from VPS34, residues 250-253 from VPS34 bearing glutamate/phosphoserine at position 249 and residues 1280-1283 from the PI3P-, RAB5- and LC3-binding transport adaptor FYCO1 (encoding a strong LIR with a specificity for LC3A and LC3B (Olsvik et al., 2015)). GST-tagged Atg8p homologs purified from *E. coli* were used to perform a peptide array overlay assay, which was probed with antibodies specific to GST.

Of the three LIRs examined, only LIR3 (S1289-1294) bound Atg8p homologs in these conditions with no GST signal detected when LIR1 and LIR2 peptides were arrayed (data not shown). Of note, the serine-glutamate and serine-phosphoserine peptide array results were effectively identical, supporting the veracity of the findings. The data shown in Figure 5.16C were derived from the phosphoserine-containing peptide arrays. Amongst the positive controls, as expected FYCO1 bound all Atg8p homologs whilst exhibiting the greatest binding affinity for LC3A and LC3B (the LC3A signal is reduced due to bleaching). WT VPS34 bound GABARAP, GABARAPL1 and GABARAPL2 and phosphorylation of serine 249 greatly increased binding to all Atg8p homologs. P150 LIR 3 appeared to bind GABARAP-like proteins (GABARAP, GABARAPL1, GABARAPL2 and LC3C). Binding efficiency was increased ~3 fold by phosphorylation of tyrosine

1290, included due to its annotation in a global phosphoproteomic screen (Dephoure et al., 2008), but did not appear to be modulated by S1289 phosphorylation status (Figure 5.16C).

Finally, binding of p150 phosphomutants to small GTPases RAB5 and RAB7 was assessed. Association of these proteins with p150 promotes VPS34 complex cycling between early and late endosomes (Stein et al., 2003, Murray et al., 2002). RAB5 association was found to be GTP-dependent and p150 domain analysis demonstrated the requirement of WD40 and HEAT domains (encompassing all 6 putative ULK substrate residues). p150 was previously shown to interact more strongly with nucleotide-free RAB7 (N125I) than its WT, or constitutively active/inactive forms (Stein et al., 2003).

Based on previous findings identifying RAB nucleotide status as a regulatory factor in p150 association, p150 binding to both WT and constitutively active RABs was tested. HEK293A transiently expressing p150 WT or empty vector (EV) were cotransfected with GFP, RAB5WT-GFP, RAB5Q79L-GFP, RAB7WT-GFP or RAB7Q67L-GFP before lysis and GFP immunopurification. However, whilst variable RAB/p150 coexpression levels coupled with non-specific binding of p150 and untagged GFP meant the data derived from p150-overexpressing cells was likely unreliable, a noted increase in endogenous p150 immunoprecipitation was noted for each RAB form tested (Figure 5.16D).

Having established conditions for p150-RAB coimmunoprecipitation, binding to serine 861 phosphomutants was tested. Based on the lack of apparent differences in binding affinity between WT and constitutively active forms, WT RAB5 and RAB7 were utilised alone to simplify the experiment. To control p150 levels, stably-expressing sgA-D11 was used thus avoiding transient p150 expression (Figure 5.16E). p150 coimmunoprecipitation with both RAB5 and RAB7 was again noted. However, p150 binding efficiency was not affected by installation of phosphomutant residues at position 861, suggesting that phosphorylation of this residue is not implicated in RAB binding.

Notably excluded from this analysis due to construct unavailability was RAB7N125I. It remains possible that nucleotide-free RAB7 may bind p150 in a serine 861 phosphorylation-dependent manner.

5.6.2 Identification of a p150 phosphomutant interactome

Serine 861 phosphorylation status appeared to be dispensable in Atg8p homolog-binding, as well as that of the core VPS34 complex components and both RAB5 and RAB7. Therefore, to understand the mechanism by which serine 861 phosphorylation functions, mass spectrometry was used to identify p150 binding partners in an unbiased manner.

To this end, a triple-label SILAC experiment was performed using ZZ-tagged p150 WT, S861A and S861E as bait proteins. HEK293A that had undergone full metabolic incorporation of light, medium or heavy isotopically-labelled amino acids were cotransfected with constructs encoding each form of p150 alongside the remaining four VPS34 complex I/II components (VPS34, BECN1, ATG14 and UVRAG) in 10cm dish format. Of the 27 possible labelling permutations, three were selected (Figure 5.17A) to control for variation introduced by the labelling procedure.

Considering that S861 was phosphorylated in an ULK-dependent manner and that multiple ULK-dependent phosphorylation sites might be required to favour accessory protein-binding, the cells were starved for 30 minutes before lysis. To enrich for p150 and its bound proteins, bead-bound p150-ZZ was subject to a low stringency washing procedure such that efficient coimmunoprecipitation of overexpressed VPS34, BECN1, ATG14, UVRAG and endogenous NRBF2 via p150-ZZ was attainable. To remove contaminating immunoglobulins, the ZZ tag was removed from p150 via TEV (tobacco etch virus) cleavage at a site immediately following p150's C-terminus (+TEV sample). The remaining beads were washed before preparation for Western blot analysis to test TEV cleavage efficiency (Ig). To prevent interference during protein detection, GST-TEV was removed from the sample via incubation with glutathione resin (-TEV), with the resulting sample analysed by mass spectrometry.

Samples taken at each stage of the purification process were examined by Western blot (Figure 5.17B). Despite initial appearances to the contrary, p150 was enriched in the final sample (-TEV; the signal for p150 in the input and Ig lanes were artificially boosted due to the ability of the ZZ tag to bind both primary and secondary antibodies non-specifically). This is reflected in the relative enrichment of VPS34 in +TEV and –TEV samples. Compared to expression levels in neat lysate, ATG14 was poorly enriched and was depleted further after

TEV removal. These findings were reflected in the mass spectrometry intensity values (Figure 5.17C). As the absolute overexpression levels of UVRAG and ATG14 were unknown, no biological bias for complex I versus complex II formation could be inferred, however the intensity values suggest the sample was enriched for complex II over complex I.

A

	Mix 1	Mix 2	Mix 3
Light	WT	S861E	S861A
Medium	S861A	WT	S861E
Heavy	S861E	S861A	WT

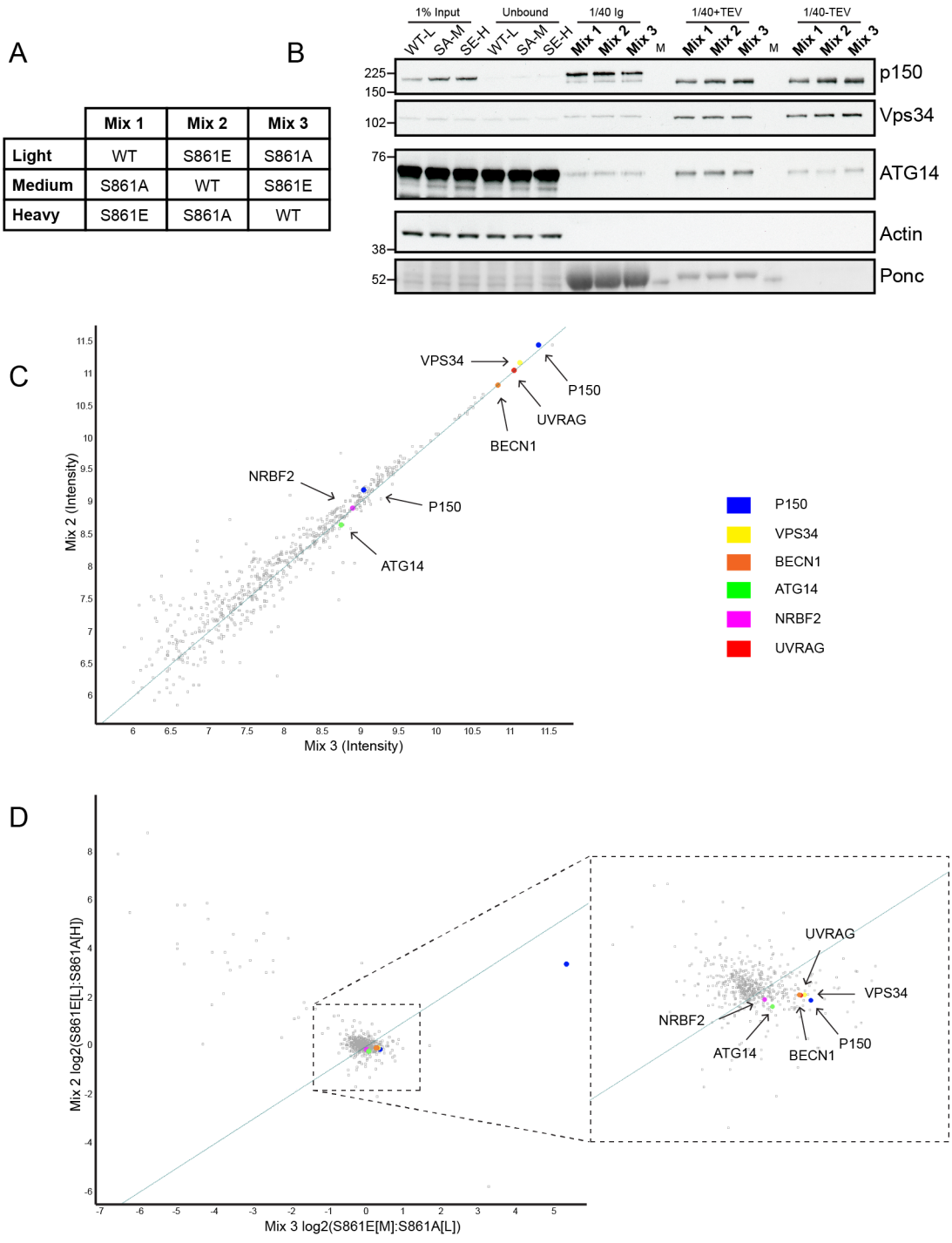

Figure 5.17 – *Identification of a p150 phosphomutant interactome.* **A** – SILAC mixing table detailing the labelling conditions and plasmids transfected for each mix. **B** – Controls generated during production of mutant p150 immunoprecipitates were analysed by Western blot. 1% input and unbound samples were analysed for mix 1 only. After washing and TEV cleavage, the beads used for the initial immunopurification were washed and boiled in 2X sample buffer. $1/40^{th}$ of this sample was loaded for mixes 1, 2 and 3, revealing the amount of p150 that was not cleaved by TEV. Aliquots of the TEV-cleaved/in-solution p150 amounting to $1/40^{th}$ of the total sample before (+TEV) and after incubation with glutathione resin (-TEV) were retained an analysed by Western blot, with the -TEV samples analysed by mass spectrometry. Ponceau staining (Ponc) revealed that the majority of both heavy chain IgG and TEV-GST (both ~52kDa) were removed successfully. **C** – Overall intensities from mixes 2 (Y axis) and 3 (X axis) are plotted on a $\log_{10}$ scale. Grey points represent proteins detected in the analysis. VPS34 core complex components are colour coded. p150 was the most highly enriched followed by VPS34, UVRAG, BECN1 and ATG14. ATG14, which was depleted upon TEV removal, was enriched to a similar extent as endogenous NRBF2. An X=Y line is plotted in blue; correlation with this line shows that protein levels are similar between mixes. **D** – Log_2(S861E/S861A) SILAC ratios are plotted from representative mixes 2 and 3. The highly enriched outlier corresponding to p150 represents the peptide encoding glutamate at position 861, indicating the experiment was a technical success. In the magnification, no noticeable skewing of data points can be observed in either direction along the X=Y line, showing the lack of proteins reproducibly enriched in either S861E or S861A samples.

Of note, the p150 mass shift after ZZ cleavage was clearly detectable, with both bands (cleaved + uncleaved) visible in Ig samples. The cause of the unexpected small mass shift in VPS34 observed upon coimmunoprecipitation (compare input to Ig lanes) was unknown.

Despite successful purification and detection of VPS34 core complex proteins from samples reconstituted with p150 WT, S861A and S861E, no differential binding of accessory proteins was detectable by mass spectrometry. A representative comparison of S861A vs S861E SILAC ratios is shown in Figure 5.17D. Plotting ratios from mixes 2 (Y axis) and 3 (X axis) revealed that as expected the core complex members were not enriched in either sample. However, an absence of coimmunoprecipitating proteins with reproducibly positive or negative SILAC ratios was noted when all mixes were compared.

Furthermore, the observation that the SILAC ratios for VPS34 complex components were slightly skewed relative to the majority of data points suggested that most of the proteins detected did not directly coimmunoprecipitate with p150 and were therefore non-specific. It is likely that this skewing was due to overexpression level differences pre-lysis. Of note, the proteins enriched in the light channel in both mixes (skewed toward the top left-hand side of the scatter plot, perpendicular to the blue X=Y line) were identified as immunoglobulins derived from the Ig beads used to immunopurify p150-ZZ.

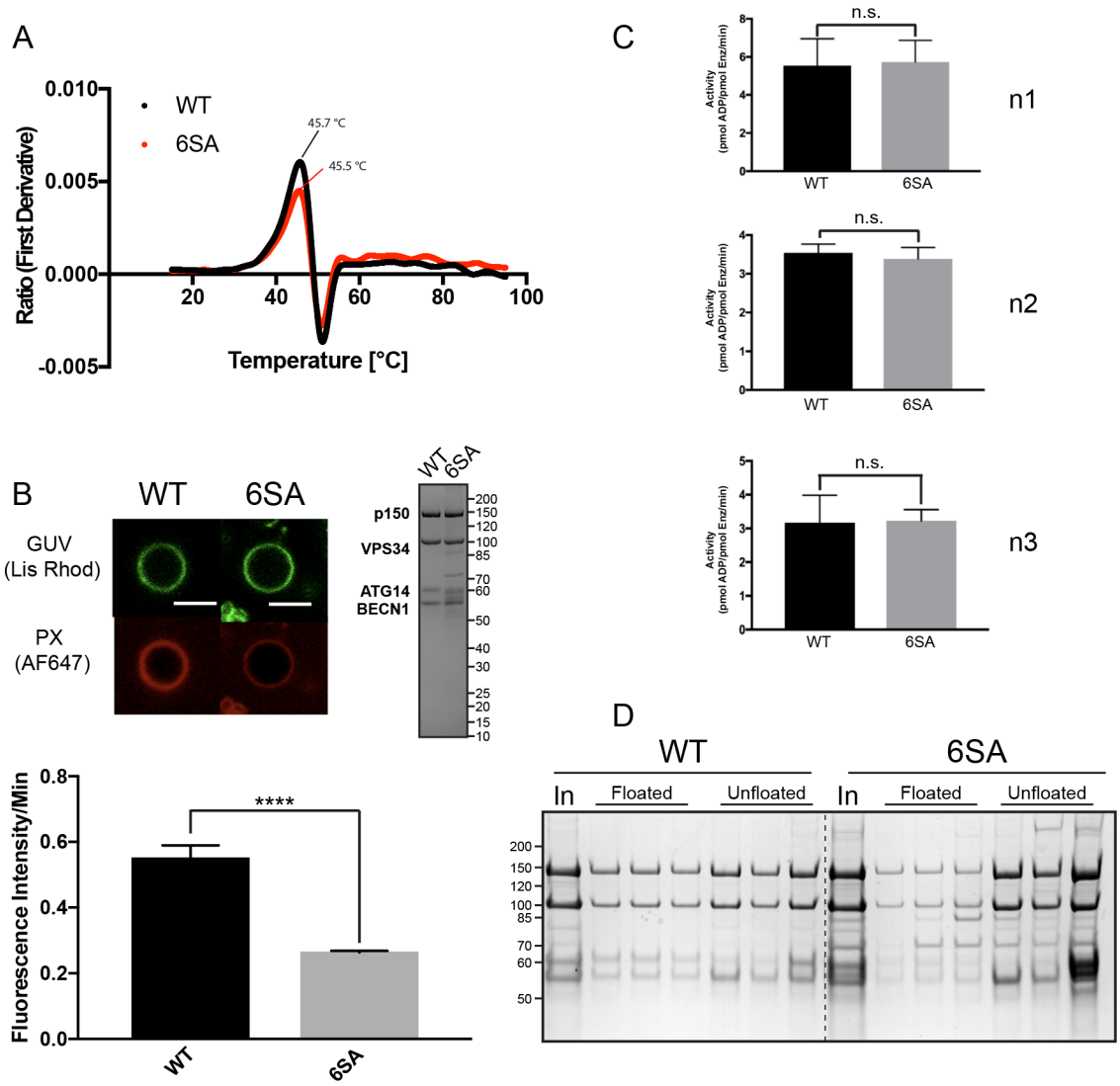

Figure 5.18 *The effect of p150 phosphorylation on the reconstituted VPS34 complex.* **A** – Thermal stability assay with VPS34 complex I incorporating p150 WT (black) or p150 6SA (red). Prometheus (nanoTEMPER) was used to make measurements. The ratio of tryptophan emission at 330 and 350nm (Y axis) is plotted against temperature (units=°C, X axis) to describe protein unfolding. Threshold melting temperatures are annotated on the graph. **B** – The *in vitro* lipid kinase activities of WT- and 6SA-reconstituted complex I on GUVs (giant unilamellar vesicles) were assessed. GUVs of the following lipid constitution (18% Liver PI, 10% DOPS, 17% DOPE, 55% DOPC) were phosphorylated *in vitro* by differentially constituted VPS34 complex I. VPS34 and p150 Coomassie staining intensity was used to assess protein concentration and roughly equal amounts of protein were used in each assay. Confocal imaging was used to measure PI3P production via recruitment of PX-AlexaFluor647 to GUVs – a representative image is displayed with Lisamine Rhodamine-PE (Avanti 810850P) used to reveal GUV membranes (green) and p40PX domain labelled with AlexaFluor647 as the PI3P probe (red). The experiment was performed three times with representative data from one of the repeats presented. Quantification reveals the slope (reaction rate) measured in the exponential phase of each kinase reaction. 44 (WT) and 50 (6SA) GUVs were measured. Scale bar = 5µm, **** = <p.0.0001. **C** - *In vitro* lipid kinase activities of WT- and 6SA-incorporated VPS34 complex I on 100nm SUVs were assessed using the ADP-Glo kinase assay (Promega V6930). SUVs were generated with identical lipid constitution as in panel B. No difference in activity was detected between p150 WT and 6SA, n.s. = not significant. **D** – Liposome floatation of VPS34 complex I containing either WT or 6SA p150 was assessed. Protein and liposomes were incubated together before separation on a sucrose gradient. The fractions containing liposome-bound (floated) and -unbound (unfloated) VPS34 complex I were separated by SDS PAGE. 6SA-containing complex I (right hand blot) bound liposomes with slightly reduced efficiency compared to WT (left hand blot). In = input; n=2.

5.6.3 The effect of p150 phosphorylation on the reconstituted VPS34 complex

The data in the following two sections were generated by Yohei Ohashi PhD and Shirley Tremel in the laboratory of Roger Williams PhD. As SILAC based protein interaction partner analysis proved uninformative, the direct impact of ULK phosphorylation on VPS34 complex functionality was assessed. To achieve this, either p150-ZZ WT or 6SA were expressed in Expi239f cells alongside the core components of VPS34 complex I. Immunoglobulin affinity chromatography was followed by gel filtration to generate purified samples of VPS34 complex I reconstituted with either WT or phosphomutant p150.

Incorporation of p150 6SA did not affect VPS34 complex I melting temperature in thermal stability assays, suggesting that blocking ULK phosphorylation was not detrimental to complex I stability (Figure 5.18A). Despite this, a ~50% decrease in PI3P production on giant unilamellar vesicles (GUVs) was observed in *in vitro* lipid kinase assays (Figure 5.18B). When the relative *in vitro* activities on small unilamellar vesicles (SUVs) were assessed, no mutant-dependent difference on kinase activity was detected (Figure 5.18C). However, liposome floatation assays revealed a small reduction in SUV binding in complexes containing p150 6SA compared to WT (Figure 5.18D). Notably, additional protein species were detected in p150 6SA-reconstitued samples compared to those containing WT p150 (see Figures 5.18B and D). These might represent novel phosphorylation-regulated binding partners; however, they are likely to represent molecular chaperones. It is unknown what bearing these proteins had on the observed results.

5.6.4 The effect of valine 50 deletion in p150 on the reconstituted VPS34 complex

The same assays were performed to characterise ΔV50-containing VPS34 complex *in vitro*. After incorporating p150 ΔV50, VPS34 complex I did not survive gel filtration and therefore could not be reconstituted in this manner, likely due to decreased complex stability. Supporting this hypothesis, whilst complex II could be purified, incorporation of mutant p150 was associated with a 2.8°C drop in melting temperature (Figure 5.19A). When protein samples were separated by SDS PAGE a decrease in relative mass was observed in p150 ΔV50. Given that the ZZ tag used for immunopurification was positioned C-terminally, this again is suggestive of N-terminal truncation of ΔV50 p150 (compare to Figure 5.16B). Interestingly, this was not observed in previous overexpression experiments (see Figures 5.12, 5.13 and 5.15), but only upon p150 ΔV50 purification (Figure 5.16B). VPS34 *in vitro* lipid kinase activity was abolished on GUVs (Figure 5.19B) and greatly reduced on SUVs (Figure 5.19C). However, no difference in SUVs binding was observed (Figure 5.19D).

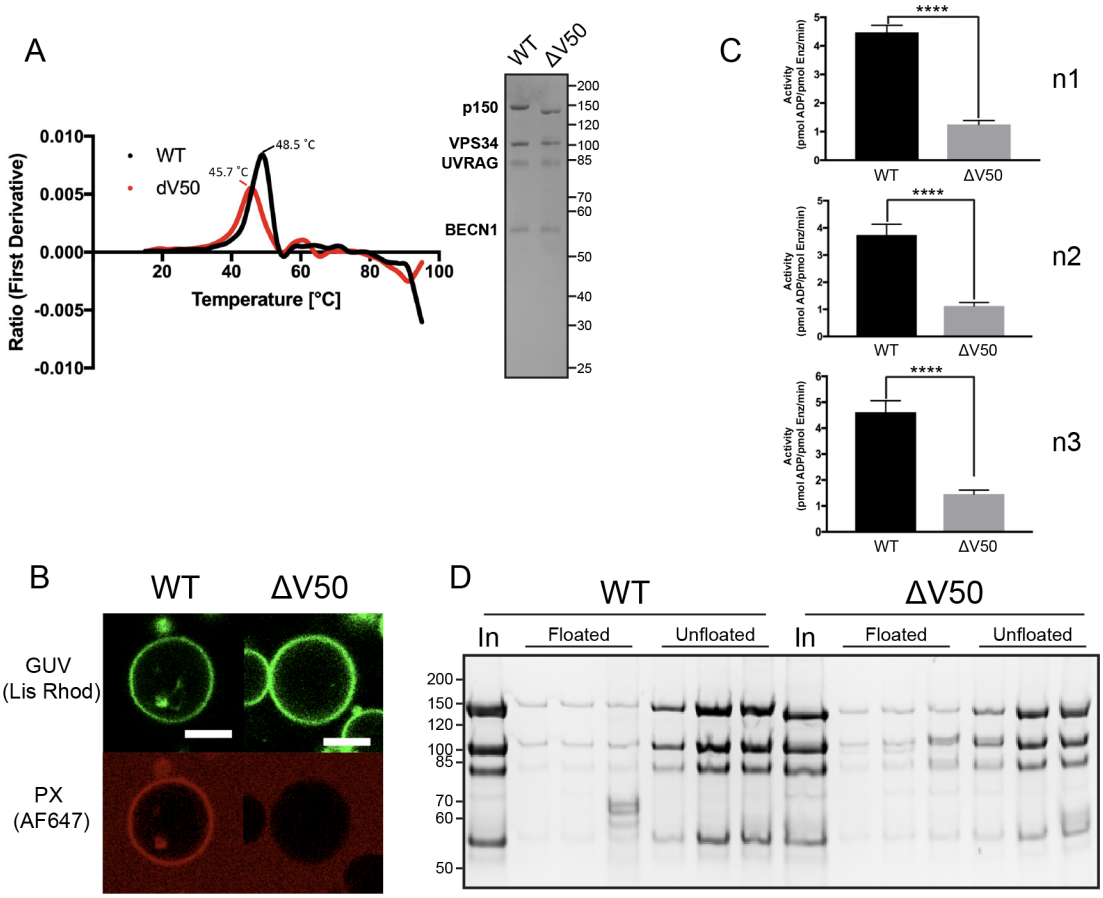

Figure 5.19 – *The effect of valine 50 deletion in p150 on the reconstituted VPS34 complex* **A** –Thermal stability assay of VPS34 complex II reconstituted with p150 WT (black) or p150 ΔV50 (red). Prometheus (nanoTEMPER) was used to make measurements. Threshold melting temperatures are annotated on the graph. (Right) Coomassie-stained SDS PAGE gel showing relative protein levels used in assayed samples. **B** - The *in vitro* lipid kinase activities of WT- and ΔV50-reconstituted complex II on GUVs (giant unilamellar vesicles) was assessed via confocal imaging. The experiment was repeated three times, representative images of single GUVs are shown. PI3P probe (red) enrichment on GUVs (green) observed in WT reactions was abolished with ΔV50-incorporated VPS34 complex II indicating loss of lipid kinase activity. Scale bar = 5µm. **C** - Lipid kinase activity of WT- and ΔV50-incorporated VPS34 complex II was assessed on 100nm SUVs via ADP-glo kinase assay (Promega V6930). In three independent experiments, SUV phosphorylation was greatly reduced. **** = <p.0.0001. **D -** Incorporation of p150 ΔV50 into VPS34 complex II does not affect SUV binding as measured by liposome floatation assay. In = input; n=2.

5.7 Discussion

The data presented here validate p150 as a novel substrate of ULK1. Building on the initial indications from the SILAC screen (Chapter 3), I was able to confirm the ULK-dependent phosphorylation of p150 serine 861 *in vivo* and *in vitro*. Additionally, the phosphorylation of 4 further residues upon ULK1 overexpression was observed. CRISPR-Cas9 gene editing was used to target the first coding exon of *PIK3R4*, yielding the first human-derived p150 effective knockout cell lines reported. Four effective KOs were generated, with each retaining trace amounts of p150 and at least one unmodified allele. Chance generation of a 5th knockdown cell line that did not exhibit an effective KO phenotype, sgC-H8, was instrumental in revealing the contribution of valine 50 deletion to the KO phenotype. Reconstitution of effective KO cells with phosphomutant p150 revealed that constitutive phosphorylation of serine 861 impinges on autophagic flux and omegasome formation, potentially revealing a novel ULK-p150 signalling axis implicated in the negative regulation of autophagy. Finally, biochemical analyses dissected the relative contributions of the putative substrate residues and valine 50 to VPS34 complex stability, membrane binding and kinase activity.

Validating p150 as an ULK phosphotarget

In total, 6 potential ULK target sites were identified in p150. Amongst these, only serine 861 was phosphorylated by Ulk1 *in vitro*, rationalising its selection for further study in stable rescue experiments. However, based on the peptide array data described in Chapter 4 highlighting the potential incongruence between ULK1's *in vitro* and *in vivo* biases, and also considering that these sites may not have been kinase accessible *in vitro*, the 5 remaining candidates remained in contention. Assuming its accuracy, 3 of the 5 potential phosphoserines (S813, S865 and S1039) arguably matched published ULK1 consensus motif with greater fidelity than serine 861. Moreover, all 6 phosphoacceptors were serine residues (Egan et al., 2015).

Supporting multisite phosphorylation by ULK, serine 813 (Zhou et al., 2013), serine 861 (Wu et al., 2009), serine 865 (Oppermann et al., 2009) and serine 1289 (Dephoure et al., 2008) have been reported as phosphoacceptors in endogenous p150. Of course, serine 865 phosphorylation was downregulated in Ulk1/2 DKOs (i.e. in the SILAC screen), however as residues 861 and 865 likely partitioned onto the same peptide it is possible that the sites were

mis-assigned during data analysis. Serine 1289 is positioned next to the identified phosphoacceptor tyrosine 1290, indicating that the amino acid stretch is accessible to kinases. Importantly, a band shift in p150-ZZ was noted upon coexpression with Ulk1 and Ulk2. As the unphosphorylated protein had a relative mass of ~170kDa, it is very likely that the shift was caused by multisite phosphorylation. Of note, whilst significant *in vitro* ULK phosphorylation of the ZZ tag or indeed any other residues in p150 can be ruled out based on the data presented herein, they can cannot be ruled out *in vivo*. Comparison of p150-WT and p150-6SA phosphorylation upon coexpression with ULK1 would be informative to this end.

The identification of target sites via kinase-substrate overexpression alone carries a reliability penalty. Chiefly, direct kinase phosphorylation cannot confidently be inferred and hyperstoichiometric expression of kinase and substrate reduces the physiological insight that can be drawn from such experiments. These concerns compounded when truncated proteins are utilised (e.g. Ulk1 1-427) that are relieved from potential regulatory information imposed by the removed domains. The *in vivo* validation experiments utilising the serine 861 phosphoantibody (STO344) suffer from these drawbacks and hence should be considered alongside supporting evidence when being used to validate p150 as a genuine ULK substrate. Accordingly, it cannot confidently be concluded that p150 is phosphorylated more efficiently when incorporated into complex I rather than complex II based on these data alone.

Phosphorylation of endogenous p150 at S861 could not be detected using STO344. If ULK1 was only able to phosphorylate complex-incorporated p150 upon starvation (when the ULK and VPS34 complex I colocalise at membranes), the low proportion of total cellular p150 incorporated into VPS34 complex I (Kim et al., 2013) combined with the potential sub-stoichiometric phosphorylation of complex-associated p150 by ULK might result in only a fraction of p150 being phosphorylated at serine 861. These factors are compounded by the low titre of the antibody or the poor antigenicity of the epitope (as evidenced by the requisite optimisation stages detailed in Figure 5.3).

A notable issue hindering a more complete understanding of the ULK-p150 signalling axis is lack of data supporting the starvation-dependence of serine 861 phosphorylation. Whilst the SILAC dataset provides evidence for endogenous ULK-dependent serine 861 phosphorylation, the necessary omission of a ‘fed’ condition means starvation-dependence cannot be inferred.

Unfortunately, serine 861 phosphorylation was not picked up in the TMT screen designed to remedy this issue, though considering its lack of detection in targeted mass spectrometry analyses described in section 5.2.1, it is likely that this was due to poor detection capacity for the peptide. Identification of the stimulus for ULK-dependent phosphorylation of serine 861 will be of importance in understanding its physiological function.

In the process of identifying p150 as an ULK substrate, ULK-dependent phosphorylation of UVRAG both *in vitro* and *in vivo* was observed. This is particularly interesting as some of UVRAG's varied roles in autophagy are known to be regulated by phosphorylation. Taking place on late endosomal compartments, the starvation-dependent phosphorylation of serine 498 in UVRAG by mTOR prevents association with both the VPS34 and HOPS complexes, negatively regulating autophagosomal/endosomal maturation (Kim et al., 2015, Liang et al., 2008). Phosphorylation at serines 550/571, also by mTOR, promotes lipid kinase activity of a separate pool of VPS34 to foster autolysosomal reformation (Munson et al., 2015). Intriguingly, both UVRAG and ULK1 are implicated in the regulation of ATG9A trafficking (He et al., 2013, Orsi et al., 2012) and, outside of autophagy, in the regulation of ER-Golgi traffic (He et al., 2013, Joo et al., 2016, Gan et al., 2017). Further research is required to identify the specific residues in UVRAG that are targeted by ULK; promisingly of the manifold UVRAG phosphoacceptor residues identified in the literature, many correspond well with the ULK1 consensus signature (see https://www.phosphosite.org/) (Hornbeck et al., 2015).

As ULK1 phosphorylation has been demonstrated in all other core VPS34 complex components (VPS34, BECN1, and ATG14, along with the accessory proteins NRBF2 and AMBRA1 – see Table 1.1), the identification of p150 and UVRAG as ULK phosphotargets provide novel facets to the growing story of ULK-dependent regulation of the VPS34 complex.

Characterising p150 effective knockouts

To study p150 biology, CRISPR-Cas9 was used to deplete endogenous p150 from HEK293A. p150 was knocked down in several clonal cell lines to a similar level, however only a subset of these were considered effective knockouts based on their autophagy phenotype.

Deletion of valine 50 in the majority of p150 alleles appeared to mark out effective KOs. However, as all effective KOs retained at least one allele encoding WT p150, it remains

unknown whether mutant p150 was expressed. The sgA effective knockouts displayed an almost complete loss of WIPI2 puncta and LC3 lipidation upon starvation. However, VPS34-dependent LC3 lipidation was observed when the duration of amino acid deprivation was increased, potentially indicating that complex I-dependent autophagy initiation was allowed to proceed albeit at a reduced rate. On the other hand, the observation that EGFR degradation was only slightly reduced in sgA-D11 suggested that sufficient VPS34 complex II activity remained. Coupled with this insight, the high degree of LAMP1 and Lysotracker colocalisation in effective KOs suggests that perturbation of lysosomal functionality was not a key driver of in the effective KO phenotype.

Intriguingly, sgA-A11, which generated WIPI2 puncta upon starvation and for which 75% of alleles detected were WT with the remaining 25% ΔV50, accumulated LC3 and p62. sgA-A11 were not classified as effective KOs due to their intermediate phenotype, however this might suggest that the p62/LC3 aggregation is the most sensitive readout for autophagic flux inhibition. Alternatively, as sgC-H8 displayed reduced numbers of WIPI2 puncta that were smaller in size without accumulating p62/LC3, this could also indicate that the WIPI2 and p62/LC3 phenotypes occur independently of each other, with the former phenotype responding to p150 expression level and the latter to valine 50 deletion. As to the manner by which p62 and LC3 aggregate, the reduction in autophagic flux upon p150 depletion, (which in turn may also lead to a reduction in proteasomal turnover (Korolchuk et al., 2009)) would likely lead to the accumulation of p62. Together with its propensity for recruitment for polyubiquitinated protein aggregates (Bjørkøy et al., 2005), the capacity for p62 self-oligomerisation/aggregation (which usually promotes autophagic clearance of bound cargo (Lee et al., 2017, Itakura and Mizushima, 2011, Zhang et al., 2018) would likely make chronic p62 aggregation inevitable. In fact, as p62 ubiquitination was reported to promote aggregate clearance (Lee et al., 2017), it is therefore likely that the high Mw p62+ve laddering observed by Western blot reflects the accumulation of ubiquitinated p62. These data are supported by the recent observation that LC3-I is recruited to ubiquitinated aggregates in autophagy deficient cells in a p62-depenedent manner positively correlating with p62 expression level (Runwal et al., 2019).

Together, these data indicate that a global downregulation in VPS34 signalling resulted in the disruption of multiple PI3P-dependent pathways, from loss of omegasome formation to

dysregulated endosomal traffic leading to the stalling of autophagy. However, there is an apparent conflict between the data evidencing the persistence of VPS34 signalling in effective KOs and the FYVE probe data, which suggested an abolition of PI3P in sgA-D11. Importantly, functional pools of PI3P exist below the detection threshold for this probe. This is due to the low binding affinity displayed by FYVE domain, important in maintaining the transience of PI3P signalling *in vivo* (Lemmon, 2003, Backer, 2008). Furthermore, whilst some VPS34 activity likely remains in effective KOs, Vps34-independent autophagy has been observed in MEFs and neurones (Devereaux et al., 2013, Zhou et al., 2010). Indeed, class II PI3Ks have been shown to supply up to ~20% of the total pool of autophagic PI3P in MEFs (Devereaux et al., 2013).

p150 has never been ablated in any cell lines of human origin. Amongst mammals, two cell lines have been described, both from a MEF background. Nemazanyy et al used cre-lox recombination to remove the first coding exon of PIK3R4, yielding embryos expressing p150 lacking the pseudokinase domain. Similarly to p150 ΔV50, this truncation mutant does not associate with Vps34 complex components and its expression in place of WT resulted in a global reduction in PI3P levels. However, whilst p62 and LC3 bodies accumulated in p150 KO MEFs, their colocalisation with LAMP1 lead to the authors conclusion that they were stalled autolysosomes (Nemazanyy et al., 2013). Whilst ubiquitous deletion of p150 resulted in embryonic lethality, skeletal muscle-, liver- and telencephalon-specific deletion mouse lines have been generated (Gstrein et al., 2018, Nemazanyy et al., 2013, Nemazanyy et al., 2015). In each tissue, deletion of p150 lead to endolysosomal vacuolation as well was accumulation of p62/LC3+ve bodies and resulted in various pathological phenotypes.

Gstrein and colleagues describe Marble (*Mbe/Mbe*) mutant mice, in which full length p150 was knocked down to a degree similar to that observed in the sgA effective KOs (Gstrein et al., 2018). These mice exhibited defects in neuronal migration resulting in hippocampal dysfunction and consequent deficits in working spatial memory. Similar to the sgA effective KOs, Vps34 and Becn1 levels were reduced in Marble MEFs. By demonstrating no alteration in transcript level, the authors implicate post-translational downregulation of Vps34 complex components (Gstrein et al., 2018). Corroborating the data presented in Chapter 5, *Mbe/Mbe* MEFs exhibited reduced EGFR degradation whilst lysosome acidification was unaffected, potentially indicating that traffic to lysosomes was inhibited rather than lysosomal function itself.

The similarity between the p150 mutant phenotype and that observed on Vps34 ablation (notably increased LC3 aggregation/endosomal vacuolation and reduced mTOR reactivation rates/EGFR degradation (Johnson et al., 2006, Devereaux et al., 2013, Jaber et al., 2012)) suggests that the p150 effective KO phenotype results primarily from destabilisation of the VPS34 complex. However, whilst subtle differences in phenotype do exist (such as the detection of WIPI1/LC3 puncta, persistent autophagic flux and the destabilisation of UVRAG 10 days after Vps34 deletion in MEFs (Devereaux et al., 2013)), as loss of VPS34 destabilises p150 and vice versa, it is difficult or often incorrect, to attempt to identify phenotypes specific to either protein.

The above comparisons justify classification of the sgA CRISPR KO clones as effective KOs. However, the accumulation of ULK1 in sgA-D11 was an unexpected and novel finding. ULK stability is tightly regulated by pre- and post- translational mechanisms (Nazio et al., 2016, Liu et al., 2016, Allavena et al., 2016). When the small ATG14 mass shift observed in effective KOs (Figure 5.7A) and the accumulation of VPS34 phosphoS249 in sgA-D6 are interpreted alongside the accumulation of ULK1, a potential narrative emerges. It could be conceived that ULK expression is upregulated upon loss of p150, potentially to compensate for the blockage of autophagic flux, leading to the increased basal phosphorylation of ULK substrates. This phenotype is similar to that observed in the LC3A/LC3B/LC3C triple knockout HeLa cell line (Nguyen et al., 2016), which were shown to upregulate phosphorylation at ATG14 serine 29 and BECN1 serine 30, two ULK1 substrate sites, in a starvation-independent manner (Grunwald et al., 2019). Of note, the accumulation of ULK1 and of VPS34 phosphoS249 was observed in separate clones. It therefore remains to be shown whether this phenotype is found in all effective KOs or clone-specific.

Identification of V50 as a crucial residue in p150's kinase domain

As discussed above, comparing genotypes and phenotypes of the sgA clones and sgC-H8 allowed for the identification of valine 50 as a crucial residue for p150's biological functionality, which was supported by the inability of p150 ΔV50 overexpression to rescue the effective KO phenotype. Amino acid sequence analysis revealed that valine 50 occupies a crucial position in p150's predicted ATP binding site. As p150 ΔV50 overexpression did not rescue VPS34 destabilisation and as VPS34 complex II reconstituted with mutant p150 was

unstable and lipid kinase inactive, this suggests that proper folding or potentially kinase activity is crucial for p150 to function properly.

These data corroborate (Stack et al., 1995), who report that rendering the activation loop of *S. cerevisiae* Vps15p non-functional (via D165R or E200R mutations) blocks interaction with Vps34p. Confusingly however, whilst valine 50 deletion did lead to the destabilisation of VPS34 complex I and II during reconstitution (albeit to differing degrees), p150 ΔV50 was able to immunoprecipitate normally with VPS34, with only a small but non-significant decrease in binding detected. Interestingly, an earlier publication from the same group potentially corroborates this as Vps15p E200R was first found to be competent for Vps34p association (Stack et al., 1993). When the findings presented in Chapter 5 are considered together, it appears that incorporation into the full tetra/pentameric VPS34 complex but not the VPS34-p150 subcomplex is hampered upon valine 50 deletion, with subcomplex formation insufficient to stabilise VPS34 expression *in vivo*.

Based on primary sequence alone, deletion of valine 50 need not destroy p150's predicted ATP binding site. Instead an acceptable leucine is shifted into position 50 and the stretch for which any amino acid is tolerated is shortened from 6 to 5 amino acids, potentially within acceptable bounds. This suggests that the mutation destabilises the protein. Also supportive of this was the probable N-terminal cleavage observed when p150 ΔV50 was immunopurified (compare molecular weight of p150 WT vs ΔV50 before (Figure 5.12D, Figure 5.13) or after (Figure 5.16B, Figure 5.19A) immunoprecipitation). This finding has additional consequences regarding data interpretation, as it is possible that the mutant phenotypes characterised *in vivo* and *in vitro* correspond to different proteins so are not entirely complementary.

Substitution mutations are likely less deleterious with regards to overall protein folding than indels, therefore the downstream phenotypes are easier to interpret. Again in yeast, both Vps15p E200R and a myristoylation site mutant (G2A) were reported to bind membranes normally during subcellular fractionation (Stack et al., 1993). Assuming the mass shift observed in VPS34 complex II-associated p150 ΔV50 reflected an N terminal truncation (which would remove the myristoylation site whilst likely disrupting pseudokinase domain structure), these insights are corroborated by the finding that this mutant was able to associate with SUVs normally.

Taken together, these data offer intriguing insights into the function of p150's pseudokinase domain. As discussed in the introduction, this module directly associates with VPS34's lipid kinase domain and undergoes conformational change upon dissociation – a crucial requisite for PI3K activity (Stjepanovic et al., 2017, Rostislavleva et al., 2015). A properly folded p150 pseudokinase domain is therefore likely important for VPS34 regulation. The question remains however as to the mechanism of the ΔV50 phenotype, namely whether it stems from domain destabilisation alone or via inhibition of ATP binding. In one of the initial reports characterising Vps15p, a number of established kinase-inactivating mutations were installed, most of which resulted in its biological inactivation. Interestingly, one such mutation, K54D, is positioned at the very C terminus of the Vps15p ATP binding domain. This led in the 95% missorting of CPY with the mutant protein also defective for *in vivo* phosphorylation, together suggesting biological inactivation (Herman et al., 1991b) and supporting the existence of a functional ATP-binding site that is required for protein function.

Consequently, it is crucial to identify whether p150 binds ATP. If this were established, close examination might allow characterisation of p150 as an active kinase or as a molecular switch (Taylor and Kornev, 2011), binding ATP to facilitate conformational change as part of a signalling cascade.

Characterising Phosphomutant Phenotype

To assess the consequence of p150 phosphorylation by ULK, three effective KO clones were rescued with p150 bearing serine to alanine or serine to glutamate mutations at position 861. These cell lines were subject autophagy and endosomal trafficking assays to probe the consequence of phosphorylation *in vivo*. Importantly, as installation of phosphomutant residues locks the exogenous protein's phosphorylation status in a non-physiological manner, any phenotype that requires cycles of phosphorylation and dephosphorylation may go undetected. Furthermore, the function of a given phosphorylation site might only become apparent in the correct signalling milieu. Indeed, multiple phosphorylation sites spread across multiple proteins may be required to drive a given phenotype. To this end, one effective KO cell line was also rescued with total phosphomutant forms of p150 (6SA and 6SE). However, as similar patterns in the relative autophagic flux rescue efficiency were noted between single (S861A vs S861E) and total (6SA vs 6SE) phosphomutant-rescued cells, it is tempting to

speculate that serine 861 is the driver behind the observed autophagy phenotype. Compared to levels measured in unmodified HEK293A, WT p150 reexpression in all three sets of clones incompletely rescued both autophagic flux and WIPI2 puncta generation. Notably, 6SA- and 6SE-rescued sgA-D6, which expressed p150 at a close to endogenous level, displayed an almost full rescue of LC3 lipidation. It is possible that hyper-stoichiometric expression of p150 hampered VPS34 complex activity via a proportional increase in non-functional subcomplex formation.

Despite some variability between cell lines, a serine 861-dependent phenotype for both autophagic flux and WIPI2 puncta formation repeatedly emerged. Excluding an apparent basal accumulation in S861E-rescued sgA-D11, no change in EGFR degradation was noted in cell lines rescued with phosphomutant compared to WT p150. Combined with the WIPI2 puncta data, it could therefore be concluded that the variation in autophagic flux rescue efficiency was due to complex I-dependent autophagy initiation in phosphomutant-rescued samples. However, as EGFR degradation was only partially impaired in effective KO clones, it is likely that any alterations in VPS34 complex II activity were not detected in this assay due to the small window of detection for differential regulation. More sensitive VPS34 complex II activity assays are therefore required before such conclusions are made.

Based on the localisation of serine 861 in a disordered linker region and on the equal phosphomutant p150 expression levels *in vivo*, it is unlikely that this phenotype resulted from protein destabilisation. Made attractive by the clustering of target sites on one face of the complex and despite the inconclusive SILAC-based interaction partner analysis, ULK-dependent regulation of binding partner association remains a potential mechanism for the observed phenotype. Intriguingly and to this end, when hydrogen-deuterium exchange was used to map NRBF2 association in mammals, protein binding was found to increase exposure of two regions of p150 to solvent – the kinase domain (amino acids 101-122 and 265-278) and the HEAT-WD40 linker (amino acids 864-881). It is unknown why this conformational change occurs, however as the latter region contains 2 putative ULK substrates, and as NRBF2 is also phosphorylated by ULK (Ma et al., 2017b), it is tempting to speculate that ULK-dependent p150 phosphorylation plays some role in NRBF2 binding. Inclusion of p150 6SE in future coimmunoprecipitation assays would be informative in this respect.

Two putative ULK substrate sites were located in p150's WD40 domain. These were of particular interest as this domain interacts directly with all other complex components in yeast Vps34p complex II (Baskaran et al., 2014). Interestingly, L1224R in p150 was recently implicated in a recessive neurodegenerative disorder (Gstrein et al., 2018). L1224 sits within WD repeat 5 in the WD40 domain, and its mutation leads to the post-translational downregulation of p150 levels resulting in a mild effective KO phenotype in dermal fibroblasts. Serine 1039 is positioned within WD repeat 2, however mutation of this residue to alanine or glutamate did not appear to result in protein destabilisation. The same was true for serine 1289, located in a loop between WD6 and WD7 and whose phosphorylation may result in a local switch in electrostatic charge. S1289-1294 was shown to comprise a weak LIR, with binding affinity increased by Y1290 phosphorylation. Whilst S1289 phosphorylation had no effect on LIR binding *in vitro*, it is possible due to their close proximity that S1289 phosphorylation status controls that of Y1290, thereby regulating LIR binding indirectly.

Insights from *in vitro* reconstitution of VPS34 complex I

Generated by Yohei Ohashi PhD and Shirley Tremel, the *in vitro* reconstitution experiments were performed as a result of a collaboration with Roger Williams PhD (LMB, Cambridge).

In sgA-D11, the first clone to be examined, an increase in autophagic flux was noted in cells rescued with p150 S861A. Therefore, this mutation became the focus for *in vitro* reconstitution experiments with the total phosphomutant (6SA) analysed first to maximise any potential dephosphorylation-dependent phenotype. Analysis of VPS34 complexes I and II incorporating S861A, S861E and 6SE p150 would provide a more comprehensive understanding as to the mechanism by which ULK regulates VPS34 activity via p150 phosphorylation.

VPS34 complex I incorporating p150 6SA displayed a ~50% decrease in GUV phosphorylation and slightly reduced binding to SUVs, although no difference in kinase activity was noted on these highly curved vesicles. It is important to consider the *in vivo* implications of these findings. The composition of GUVs/SUVs utilised in Chapter 5 included the most prominent lipids found in the ER with the exclusion of minor lipid species such as lyso-glycerophospholipids, ceramides and sterols (Jacquemyn et al., 2017, Fouillen et al., 2018). With regards to membrane curvature, SUVs (~20-100nm) are considered to be equivalent of

ER-exit sites/ERGIC that supply lipids during autophagy initiation (Graef et al., 2013, Ge et al., 2014) or of the tips of growing phagophores (Suzuki et al., 2013, Obara et al., 2008); regions in which VPS34 complex I-dependent PI3P production is heavily implicated in progression of autophagosomal biogenesis (Brier et al., 2019). GUVs (~1-20µm) are much larger in diameter and therefore have lower membrane curvature. Larger GUVs have curvatures similar to the plasma membrane with smaller counterparts similar to large lysosomes/autophagosomes (Baba et al., 1997). These data therefore suggest that p150 phosphorylation by ULK1 might be required for VPS34 complex I activity on larger early autophagic membranes, such as the sides of expanding phagophores.

The data generated using VPS34 complexes reconstituted with p150 6SA appear to contrast with *in vivo* rescue data. Whereas non-phosphorylatable p150 reduced VPS34 lipid kinase/membrane association *in vitro*, p150 6SA efficiently rescued autophagic flux in effective KO clones. It is possible that the efficient rescue of autophagy by p150 6SA demonstrates that physiological targeting of SUV-like membranes is sufficient to rescue autophagy in the chosen experimental conditions. These data underscore the importance in testing more phosphomutant complexes *in vitro* and VPS34 functionalities *in vivo*.

Conclusions

Multiple components of the VPS34 complex are substrates of ULK1. Where the specific residue has been identified and function classified, most phosphorylation events are associated with an increase in VPS34 activity and the promotion of autophagy. Three such sites, ATG14 S29, BECN1 S15 and BECN1 S30, occupy the same region at the base of the complex, with implications in ER-association and BCL2-binding (Russell et al., 2013, Park et al., 2016, Park et al., 2018, Baskaran et al., 2014). The 6 p150 sites are all located distally to this region and, whilst the effect on lipid kinase activity remains to be established, phosphorylation appears to inhibit rather than promote autophagy. It is therefore likely that these phosphorylation events are part separate of ULK-dependent regulatory mechanisms controlling VPS34 complex activity.

The negative regulation of autophagy via p150 phosphorylation might suggest that ULK is implicated in the fine tuning of the autophagic response, acting as a handbrake on runaway VPS34 activation. Similarly, it is possible that ULK phosphorylation might reinforce the overall

downregulation of VPS34 activity noted upon starvation. As discussed in section 1.3.4, this starvation response is dictated by VPS34's binding partners, with ATG14-bound VPS34 conversely activated on amino acid starvation and both ATG14- and UVRAG-bound VPS34 activated upon glucose starvation (Kim et al., 2013, Russell et al., 2013). Therefore, ULK might target only non-autophagic pools of p150, in which case the stably-rescued clones would be unsuitable to detect the physiological phenotype. In this regard, immunoprecipitation using the serine 861 phosphoantibody in fed and starved conditions before assessing the relative enrichment of complex components might prove insightful.

With this contention in mind, information regarding the localisation of the p150 phosphomutants is lacking from this thesis. The serine 861 phosphoantibody was unsuitable for immunofluorescence and both endogenous and exogenous p150 appear to have a diffuse cytoplasmic distribution. Assessment of phosphomutant p150 localisation (e.g. by subcellular fractionation) could identify whether a specific pool of p150 is targeted and more generally show how phosphorylation results in the observed autophagy phenotype.

Assuming all 6 phosphorylation sites are genuine, ULK-dependent phosphorylation would significantly alter the chemical properties of the HEAT-WD40 linker region. In addition to the conformational change noted upon NRBF2 association, as discussed in the section 5.1 this region has potential implications in complex flexibility which in turn may govern the ability of the VPS34 complex to dock to and target membranes of varying curvature (Baskaran et al., 2014, Rostislavleva et al., 2015). Regulation of VPS34 complex flexibility via p150 phosphorylation is therefore an intriguing mechanism by which ULK might govern PI3P-dependent autophagy. Alongside the need for more extensive reconstitution studies as noted above, further information as to the timing as well as the stimuli for the phosphorylation events described in this thesis must be sought to confirm these speculations.

Chapter 6. Discussion

In this thesis, I have sought to illuminate the mechanisms by which ULK regulates starvation induced autophagy. I have principally explored this by analysing changes to the MEF phosphoproteome that occur upon dual ablation of Ulk1 and Ulk2, however additional insight was provided by the *in vivo* crosslinking screen, which was novel in conception. Analysis of the screen datasets and consequent validation of the selected candidates has led to the identification of several putative ULK substrates. Numerous likely ULK-regulated phosphoacceptors were identified in Fip200 (see Figure 3.2 and Appendix Table A), however as these were not brought forward for validation they remain exciting potential candidates. Substrates that were validated include those for which no phosphoacceptor residue has been identified (CAPZB, FAM21 and UVRAG) and those for which a phosphoacceptor-containing region has been mapped to within 15 amino acids (ANXA2, NHSL1, SCEL, SORBS2, VPS26B, VILL, PRKAG2 and p150). Amongst these, exact sites have been identified for ANXA2 (serine 127 – although *in vitro* phosphorylation of this residue could not be detected when the whole protein was used as a substrate), NHSL1 (serine 189), VILL (serine 234), VPS26B (serine 302 and/or serine 304), PRKAG2 (serine 124 – possibly also serine 122) and p150 (serine 861). The latter two substrates (PRKAG2 and p150) were more thoroughly validated than the other candidates and can be considered the 'top hits' from the analysis.

In PRKAG2 and p150, I have identified key regulators of energy homeostasis and autophagic lipid signalling as direct ULK substrates. Whilst the function of PRKAG2 was not explored, phosphorylation of p150 at serine 861 appears to inhibit autophagy, unexpectedly pointing towards an ULK-dependent negative feedback loop. Full exposition of the mechanisms by which each phosphorylation event is regulated, as well as of their functional consequences, is likely to reveal novel ULK-regulated signalling axes that control starvation-induced autophagy.

Interestingly, some of the proteins identified as substrates are reported to possess restricted tissue expression. These include SCEL and VILL, which are both expressed highly in the colon but are absent in many tissues (Uhlén et al., 2015) and SORBS2 which as previously discussed is not detected in many cell/tissue types (Anekal et al., 2015). These proteins may be expressed in MEFs either endogenously or as a side effect of immortalisation, however their detection in this assay hints at a complex web of tissue-specific functionalities for ULK. As

discussed in Chapter 1, a growing number of non-autophagic functions of the ULK kinases have been identified (such as its role in stress granule disassembly which was also shown to be cell type-specific (Wang et al., 2019)). Due to the candidates selected as well as the phenotypic assays employed, these would likely have been missed in this investigation, however it is entirely possible that some of the aforementioned phosphorylation events function outside of autophagy, highlighting exciting avenues for further discovery.

In Chapter 4, I demonstrated that the 'ULKtide' was phosphorylated efficiently in peptide array format, whilst the majority of established ULK substrates included were not, even those that appear to match the consensus sequence (Figure 4.9E; Appendix Table B). Alongside highlighting the potential incongruence between phosphorylation specificity *in vitro* and *in vivo*, (which was discussed previously at length and is well appreciated), these data indicate that ULK1 consensus motif incompletely captures substrate specificity. It was generated by analysing the *in vitro* phosphorylation of a positional scanning peptide library as previously noted. In this approach, peptides with fixed residues at each position (from -5 to +4) relative to the phosphoserine/phosphothreonine, were phosphorylated by ULK1 *in vitro*. Importantly, the remaining sites were constituted of an equimolar mix of amino acids and therefore no specific combinations were analysed.

In this thesis, I have uncovered evidence of interdependence between residues surrounding the phosphoacceptor. This becomes apparent when considering serine 124 in PRKAG2's unstructured N-terminal domain, which I have shown is likely targeted by ULK1 *in vitro* and *in vivo*. Glycine at position +1 (amino acid number 125) likely allows phosphorylation at a similar efficiency to the ULKtide (compare the signal for PRKAG2 S122 S->A with ULKtide WT in Figure 4.9E), though according to the positional scanning peptide library data presented by Egan and colleagues, this generally leads to a relatively strong inhibition of phosphorylation (Egan et al., 2015). Furthermore, p150 is phosphorylated at serine 861 which possesses an inhibitory glutamate at position -3, and not at serine 865 which has a highly-conducive methionine here (along with an aspartate at +2 which, while inhibitory, is present in many ULK1 substrates) (Figure 5.2; Figure 5.4) (Egan et al., 2015). The same pattern of phosphorylation is noted in peptide format (Figure 4.9E), indicating that this is not due concealment of the substrate due to protein folding or binding partner interaction but reflects specificities encoded in the linear amino acid sequence. Together, these data suggest that the contribution of specific amino

acids surrounding the phosphoacceptor to ULK1 targeting is context dependent. This interdependence highlights that whilst the ULK consensus motif is a useful tool, close fidelity should not be considered a prerequisite when identifying novel ULK substrates.

Of the hundreds of thousands of phosphorylation events known to occur, it is highly likely that some serve no mechanistic function at all, or are phosphorylated errantly (despite the constitutive phosphatase activity believed to counteract their build-up (Ubersax and Ferrell Jr, 2007)). Furthermore, it is possible that the mechanistic significance of a given phosphorylation event only becomes apparent in the presence of specific stimuli, or as alluded to earlier in an unknown process or in another cell type. Alternatively, many stages of phosphorylation-dependent signal transduction require multisite phosphorylation before a downstream effect can be engendered. This could involve multiple kinases and/or substrates, or indeed one kinase phosphorylating one substrate at multiple sites, as is required for phagophore expansion driven by Atg1p phosphorylation of Atg9p (Papinski et al., 2014).

With these concepts in mind, the drawbacks of phosphoproteomic data become clear. If any of the cases noted above are true of the bona fide ULK substrate sites identified in the phosphoproteomic screens reported here, even ones in key autophagy proteins, their mutation might have no detectable impact on starvation-induced autophagy (this might further explain why no function has been identified for a large portion of the ULK1 substrates identified to date (Table 1.1)). However, the SILAC and TMT datasets remain valuable tools for the study of ULK biology. Whilst not discussed in this thesis, multiple gene ontology groups were significantly enriched in phosphoproteins that were depleted in ULK1/2 DKOs. It will be interesting to correlate these insights with ULK-dependent disease phenotypes, such as those reported in double/single knockout animals (Lechauve et al., 2019, Kundu et al., 2008, Wang et al., 2019, Lee and Tournier, 2011, Cheong et al., 2014, Li et al., 2016a), alongside using them to infer regulatory events in autophagy. More importantly, the utility of the SILAC and TMT datasets is supported by the identification of a host of promising candidate ULK substrates, especially p150, which has been revealed as an actively regulated component of the autophagic machinery rather than an enigmatic scaffolding subunit.

Chapter 7. Appendix

Appendix Table A –*Phosphopeptides reproducibly depleted in Ulk1$^{-/-}$/Ulk2$^{-/-}$ MEFs.* Sites detected in both forward and reverse labelling conditions with an average $\log_2$(DKO/WT) value of <-1.5 from at least one experiment are listed, with those displaying label-dependent enrichment (with $\log_2$(WT/WT) scores above 0.5 or below -0.5) in any of the three control conditions excluded. MGI Symbol lists murine gene names as listed in the Mouse Genome Informatics database (http://www.informatics.jax.org/). Uniprot identification codes are followed by the specific target sites identified. The amino acid identities at positions -3 to +2 relative to the phosphoacceptor residues (position 0 shown in bold and red) are given, along with the average of the forward and reverse $\log_2$(DKO/WT) scores in experiments 1, 2 and 3. A '+' in the 'Loose' or 'String.' (stringent) columns indicates whether the given site matches the published ULK consensus motif as rendered in Figure 3.7A (Egan et al., 2015).

MGI Symbol	Uniprot ID	Target Site	-3	-2	-1	0	1	2	Mean Expt 1	Mean Expt 2	Mean Expt 3	Loose	String.
3110082I17Rik	G5E8F7	S180	S	G	G	**S**	P	G	0.163	0.033	-1.682		
A2AG58	A2AG58	S210	R	R	G	**S**	E	D	0.1745	-1.783	0		
Ablim1	E9Q1E8	S355	R	T	L	**S**	P	T	-1.3185	-1.253	-2.7165		
Ablim1	E9Q1E8	S359	P	T	P	**S**	A	E	-0.749	-1.6815	-1.054		
Ablim1	E9Q1E8	S376	R	S	T	**S**	Q	G	-0.8235	-0.8695	-2.933		
Ablim1	E9Q1E8	T353	S	P	R	**T**	L	S	-0.818	-1.562	0		
Ablim1	E9Q1E8	T357	L	S	P	**T**	P	S	-1.3085	-1.67	-0.9605		
Acap3	Q3UH98	S383	R	T	A	**S**	P	S	-1.5525	0	0		
Adam10	O35598	T720	L	P	G	**T**	L	K	-1.158	-1.68	0		
Add1	E9Q1K3	T358	S	P	G	**T**	P	A	0	0	-2.1905		
Add2	Q9QYB8	S11	E	A	A	**S**	P	P	-2.078	0	1.0115		
Add3	Q9QYB5	S64	I	L	Q	**S**	P	A	-1.672	0	0		
Adgre5	E9QJS7	S799	F	N	S	**S**	T	T	-1.261	0	-1.7085	+	
Adgre5	E9QJS7	T803	T	T	G	**T**	G	T	0	0	-1.625		
Adra2a	Q3URE6	S362	A	S	G	**S**	G	H	0	-1.874	0		
Adrm1	Q9JKV1	S15	V	P	G	**S**	R	G	-2.1545	0	0		
Afap1l2	Q5DTU0	S119	K	I	E	**S**	P	E	-3.2015	0	0		
Afap1l2	Q5DTU0	S344	R	K	K	**S**	T	S	-3.4595	-1.157	0		

Afap1l2	Q5DTU0	S414	H	L	Y	S	F	R	-3.5325	0	0		
Aff1	E9Q921	S195	P	L	I	S	S	L	-1.947	0	0		
Ahnak	E9Q616	S2980	K	G	P	S	L	D	-1.7795	-1.1945	0		
Ahnak	E9Q616	S2985	D	I	K	S	P	K	-1.7545	-1.2205	0		
Ahnak	E9Q616	S4905	V	D	I	S	S	P	-1.5445	-1.096	0		
Ahnak2	F7DBB3	S1526	E	S	F	S	P	E	-1.652	0	0		
Aif1l	A2ATN1	S133	A	N	E	S	S	P	-1.9035	-0.36	0		
Aif1l	A2ATN1	S134	N	E	S	S	P	K	-1.9875	-0.36	0		
Aim1	E9PVP1	T20	Q	K	S	T	D	S	-0.9805	-2.035	0	+	+
Aim1	E9PVP1	S115	A	V	P	S	S	P	-1.504	-2.2685	1.4405		
Aim1	E9PVP1	S116	V	P	S	S	P	G	-1.4855	-2.0985	1.4405		
Aim1	E9PVP1	S128	A	K	E	S	P	P	-2.8795	0	0		
Aim1	E9PVP1	S19	S	Q	K	S	T	D	-1.7555	-2.2575	0		
Aim1	E9PVP1	S22	S	T	D	S	P	G	-1.01	-2.322	0		
Aim1	E9PVP1	S507	G	E	A	S	P	P	-1.487	-1.938	0		
Aim1	E9PVP1	S587	P	D	T	S	P	K	-1.028	-2.577	0		
Aim1	E9PVP1	S95	P	D	R	S	K	P	-1.94	0	0		
Aim1	E9PVP1	S950	N	V	G	S	V	D	-1.635	0	0		
Aim1	E9PVP1	S969	P	G	H	S	F	S	-1.581	0	-0.1615		
Aim1	E9PVP1	S99	K	P	L	S	P	T	-1.923	0	0		
Aim1	E9PVP1	T586	A	P	D	T	S	P	-0.7415	-2.3815	0		
Aim1	E9PVP1	T655	S	P	L	T	P	T	-1.6465	-1.798	0		
Akap13	E9Q474	T1911	S	H	S	T	D	S	-2.212	0.3815	0		
Akap5	H3BIV5	S249	Q	R	A	S	L	L	-3.344	-0.7035	0	+	
Akap5	H3BIV5	S149	T	E	D	S	G	Y	-2.5085	0	0		
Akap5	H3BIV5	S29	V	A	A	S	P	Q	-3.168	-1.773	0		
Akap5	H3BIV5	T227	Q	M	G	T	P	E	-2.1885	-0.9725	0		
Aldh1a1	P24549	S2	_	_	M	S	S	P	-2.718	-2.797	0		
Aldh1a1	P24549	S3	_	M	S	S	P	A	-2.722	-2.7565	0		
Ano1	F6R6E1	S146	A	L	L	S	K	R	-1.6755	0	0		
Arhgef1	E9PUF7	S831	P	R	P	S	P	S	-2.057	0.631	0		
Arhgef12	F8VQN6	S190	R	I	T	S	P	V	-1.564	0	0		
Arhgef16	Q3U5C8	S111	R	H	Q	S	F	G	-2.32	0	0		
Arhgef16	Q3U5C8	S212	H	K	G	S	F	K	-2.73	0	0		
Arhgef26	D3YYY8	S112	R	P	K	S	P	L	-1.9265	0	0		
Arhgef26	D3YYY8	S22	R	R	R	S	T	P	-2.0465	0	0		
Arhgef26	D3YYY8	S221	R	L	P	S	Q	G	-2.5035	0	0		
Arhgef26	D3YYY8	S390	D	I	D	S	D	E	-2.597	0	0		
Arntl	Q3UHZ2	S42	R	K	G	S	A	T	0.498	-1.7765	0		
Arntl	Q3UHZ2	T44	G	S	A	T	D	Y	0.336	-1.727	0		
Arvcf	P98203	S914	T	L	G	S	D	S	-2.446	0	0		
Asap2	Q6A074	S716	L	D	E	S	D	D	-1.508	-1.1245	0		
Atg14	Q8CDJ3	S9	G	K	G	S	W	T	-1.539	0	0		

Baiap2l1	Q9DBJ3	S421	R	S	I	S	T	V	-1.5905	-1.284	0		
Bcam	Q9R069	S590	P	E	L	S	H	S	-2.1675	0	0		
Bcl3	Q9Z2F6	S39	R	P	A	S	P	E	1.559	-1.6805	2.413		
Bcl9l	Q67FY2	S88	N	Q	I	S	P	S	0	-2.056	-0.421		
Bicd1	Q5DTM3	S610	P	P	S	S	P	V	-1.6305	0	0		
Brat1	E9QLK3	S730	R	A	S	S	P	R	0.09	0.108	-1.5355		
Cactin	A1L013	T151	S	P	G	T	A	T	-1.623	0.025	-0.458		
Cactin	A1L013	T153	G	T	A	T	L	A	-1.599	0	0		
Cald1	E9QA15	T525	D	K	V	T	S	P	-0.033	-2.556	-0.4375		
Camsap1	A2AHC3	S553	S	P	P	S	P	Q	0.1315	-4.164	0		
Cap2	Q9CYT6	S300	Q	I	R	S	P	T	-2.164	-0.8825	0		
Cap2	Q9CYT6	S311	S	P	T	S	P	K	-2.15	-0.817	-0.8895		
Cars	Q3UXN3	S390	L	S	I	S	A	D	-3.7135	0	0		
Cbx5	Q61686	S93	R	K	S	S	F	S	-0.252	-1.571	-0.3075		
Cd34	Q543B6	S343	P	G	A	S	P	E	1.414	2.54	-3.448		
Cdc42ep4	A2A6Q1	S165	G	P	H	S	P	D	-1.8065	0	0		
Cenpe	Q6RT24	S815	R	R	G	S	D	G	-1.255	-1.69	0		
Cep152	Q69ZV8	T1615	R	H	T	T	L	R	-2.5785	0.3395	0		
Cgn	D3YUW7	S130	L	I	R	S	Q	S	-2.523	0	0	+	+
Cgn	D3YUW7	S444	L	K	H	S	Q	S	-2.832	0	0	+	+
Cgn	D3YUW7	S269	V	L	Q	S	F	E	-2.2625	0	0	+	
Cgn	D3YUW7	S135	S	Q	A	S	L	T	-2.4175	0	0		
Cgn	D3YUW7	S446	H	S	Q	S	P	D	-2.637	-0.6795	0		
Cgn	D3YUW7	S91	A	L	S	S	D	S	-2.555	0	0		
Cgn	D3YUW7	T137	A	S	L	T	G	L	-1.67	0	0		
Champ1	Q8K327	S434	P	S	S	S	P	D	-2.398	-0.157	0		
Chn2	Q3V2R3	S181	R	K	A	S	V	S	-3.441	0	0		
Cobll1	E9QPU9	S1044	A	E	T	S	P	P	-1.6185	-0.6155	0		
Cobll1	E9QPU9	S1060	A	E	T	S	P	P	-1.9405	-1.3635	0		
Cobll1	E9QPU9	S521	S	V	K	S	P	D	-2.262	0	0		
Cobll1	E9QPU9	S770	V	P	L	S	P	V	-1.397	-1.694	0		
Cobll1	E9QPU9	S897	T	L	S	S	P	T	-1.538	-0.817	0		
Cobll1	E9QPU9	T1043	R	A	E	T	S	P	-1.611	0	0		
Crip2	Q4FJU3	S104	R	K	T	S	G	P	-2.1395	0	0		
Ctnnb1	Q02248	S675	K	R	L	S	V	E	-1.547	-1.53	0		
Ctnnd1	E9Q8Z4	S858	S	S	H	S	Y	D	-1.153	-1.6235	0.3525		
Ctnnd1	E9Q8Z4	Y859	S	H	S	Y	D	D	-1.211	-1.8465	0.074		
Cux1	H3BJQ9	S1469	R	R	P	S	S	L	-0.7065	-1.5965	0		
Cxxc5	Q91WA4	S79	R	P	L	S	H	Y	-1.9745	0	0		
Cyp1b1	Q64429	S282	H	R	E	S	L	V	0	-1.8355	0.9855		
D8Ertd82e	E9QLH9	S704	M	N	K	S	S	S	-1.6845	0	0	+	+
D8Ertd82e	E9QLH9	S802	R	A	A	S	S	P	-1.553	0	0		
D8Ertd82e	E9QLH9	S803	A	A	S	S	P	D	-1.591	0	0		

D8Ertd82e	E9QLH9	T208	R	P	C	T	S	P	-1.7505	0	0		
Daam2	Q80U19	S704	E	L	G	S	T	E	-2.403	0	-0.6745		
Dennd5b	A2RSQ0	S690	L	R	Q	S	S	E	-1.9725	0.345	0.0555	+	+
Dennd5b	A2RSQ0	S833	R	R	K	S	D	S	-2.072	-1.3695	-1.353		
Dennd5b	A2RSQ0	S835	K	S	D	S	G	V	-2.0755	-0.6455	0		
Dlc1	D5M8I5	S540	S	E	D	S	D	E	-1.6975	-0.83	0.447		
Dnmt1	P13864	S146	D	T	L	S	V	E	-0.1215	-1.684	0		
Dsp	E9Q557	S2221	R	S	M	S	F	Q	-5.817	0	0		
Dsp	E9Q557	S2827	G	L	P	S	P	Y	-2.488	0	0		
Dsp	E9Q557	S2832	Y	N	M	S	A	P	-2.165	0	0		
Dsp	E9Q557	S2836	A	P	G	S	R	S	-2.3265	0	0		
Efnb1	P52795	S282	L	S	L	S	T	L	-3.484	-0.2955	0	+	
Efnb1	P52795	S280	A	A	L	S	L	S	-3.3215	-0.2955	0		
Efnb1	P52795	T283	S	L	S	T	L	A	-3.364	-0.2955	0		
Eftud2	Q6A0E3	Y17	F	G	N	Y	I	G	0	-1.7085	0		
Eif3j2	Q66JS6	S16	A	G	D	S	D	S	3.9545	0	-1.5565		
Eif3j2	Q66JS6	S18	D	S	D	S	W	D	2.099	0	-1.8435		
Eif4ebp1	Q60876	T44	L	F	S	T	T	P	0.6405	0	-1.5675		
Eif4g3	E9QNX3	S1134	A	L	T	S	R	G	-1.9635	0	0		
Eif4g3	E9QNX3	S278	R	T	S	S	P	T	-1.9155	-1.6335	2.3055		
Eif4g3	E9QNX3	S292	S	L	P	S	P	M	-1.7165	0	0		
Eif6	O55135	S239	M	R	D	S	L	I	-0.7535	-1.6305	-0.381	+	+
Elac2	Q3U0M8	S797	Q	A	D	S	P	E	-1.5805	-0.6755	-0.489		
Elmo1	F8WIL9	S358	S	S	G	S	M	E	-2.852	0	0		
Emg1	O35130	T24	D	W	E	T	T	P	-0.5215	0	-4.0075		
Emg1	O35130	T25	W	E	T	T	P	P	-0.436	0	-4.0075		
Ep400	Q8CHI8	S164	C	S	N	S	P	T	-3.426	0	0		
Epb41l4a	P52963	S464	A	H	N	S	G	E	-1.8915	0	0		
Epha2	Q03145	S893	P	R	V	S	I	R	-1.2685	-1.788	0		
Ephb3	P54754	S790	Y	T	S	S	L	G	-1.5145	0	0		
Epn2	Q8CHU3	S199	Y	H	G	S	T	S	-1.5655	0	0		
Epn2	Q8CHU3	Y196	P	A	S	Y	H	G	-1.6445	-0.2105	0		
Eya4	Q8BY78	S338	N	N	P	S	P	P	-1.771	-0.4155	-1.1605		
Ezh2	Q6AXH7	S359	N	N	S	S	R	P	-1.8045	-0.1015	0		
Ezr	P26040	T533	Q	L	L	T	L	S	-1.8615	0	0	+	+
F11r	O88792	S285	S	Q	P	S	T	R	-1.3975	-1.1655	-2.2205		
Fam122b	G1UD78	S115	T	P	V	S	P	A	-0.8495	-2.0395	0		
Fam122b	G1UD78	T112	I	D	F	T	P	V	-0.2495	-2.0395	0		
Fam21	Q6PGL7	S533	G	L	F	S	D	E	-1.557	-1.052	-0.393		
Fam21	Q6PGL7	S533	G	L	F	S	D	E	-1.557	-1.052	-0.393		
Fam21	Q6PGL7	S723	L	L	F	S	D	E	-1.7335	-2.2125	-0.7955		
Fam63b	Q6PDI6	S63	D	P	T	S	P	S	-1.7325	0	0		
Fam64a	Q8BFY7	S156	L	R	L	S	G	Q	-3.1545	0	0		

Fcho2	Q3UQN2	S487	R	P	F	S	P	P	-1.297	-1.9985	0.165		
Flna	Q8BTM8	T1739	F	Q	V	T	A	L	0	-1.8155	0		
Flt4	P35917	S1296	P	E	G	S	F	S	-1.5645	0	0		
Flt4	P35917	S1298	G	S	F	S	C	K	-1.6815	0	0		
Flt4	P35917	S953	A	E	K	S	P	E	-1.952	0	0		
Flt4	P35917	T945	K	R	D	T	F	N	-2.064	0	0		
Flt4	P35917	Y949	F	N	P	Y	A	E	-2.0145	0	0		
Fn1	G5E8B8	S2475	R	D	D	S	R	E	0.6985	-1.677	0.226		
Foxa2	G5E8P5	S229	V	P	R	S	P	D	-2.9905	0	0		
Foxa2	G5E8P5	S316	S	S	A	S	P	C	-2.563	-2.7445	0		
Foxa2	G5E8P5	S444	L	D	A	S	P	L	-2.9365	0.0245	0		
Frmd4b	Q920B0	S629	R	K	S	S	I	N	-2.2655	-1.0345	0		
Frmd4b	Q920B0	S676	N	A	Y	S	S	S	-3.515	-2.2345	0		
Frmd4b	Q920B0	S779	N	S	G	S	M	P	-2.1975	0.0235	0		
Frmd4b	Q920B0	S857	Y	S	R	S	F	H	-2.06	0	0		
Frmd4b	Q920B0	S916	Q	G	H	S	P	Q	-3.116	0	0		
Fzd6	Q542J1	S519	I	S	E	S	R	R	-2.7855	0	0	+	
Fzd6	Q542J1	S517	D	P	I	S	E	S	-2.4185	0	0		
Gabbr1	Q9WV18	T875	T	M	K	T	G	S	0	0.1975	-2.4385		
Gap43	P06837	S96	P	A	T	S	P	K	-2.001	0	0		
Gata4	E9PXW9	S109	P	R	F	S	F	P	-2.01	0	0		
Gata4	E9PXW9	S406	L	K	L	S	P	Q	-3.6525	0	0		
Glcci1	Q8K3I9	S98	P	S	P	S	S	P	-1.898	0	0		
Glcci1	E9QKK4	S99	P	S	P	S	S	P	-1.898	0	0		
Gm7964	D3YWG1	S216	I	S	E	S	P	I	-0.234	-0.2015	-1.6155		
Gng10	Q9CXP8	S6	S	G	A	S	V	S	0	-2.6145	-0.1865		
Gpr126	Q6F3F9	S1134	L	S	S	S	S	I	-2.1855	0	0	+	+
Gpr126	Q6F3F9	S1132	K	S	L	S	S	S	-1.721	-1.1155	0		
Gpr126	Q6F3F9	S1135	S	S	S	S	I	G	-1.8565	-1.1155	0		
Gpr126	Q6F3F9	S1138	S	I	G	S	N	S	-1.858	0	0		
Gprc5a	G5E8C3	S303	R	A	Y	S	Q	E	-1.93	-1.916	0		
Gprc5a	G5E8C3	S344	A	P	A	S	P	Y	-2.029	-2.2495	0		
Heg1	E9Q7X6	S1275	E	N	G	S	T	K	-2.705	0	0		
Helb	G5E835	T992	D	V	D	T	D	E	-0.265	-1.521	0		
Hid1	Q8R1F6	S593	R	T	G	S	Q	E	-1.426	-1.6575	3.764		
Hid1	Q8R1F6	S673	S	N	A	S	A	S	-1.5135	0	-1.2395		
Hoxb6	A2AA00	S214	S	Q	L	S	A	E	0	0	-2.3955		
Hspb1	P14602	S13	L	L	R	S	P	S	-0.6225	-1.528	0.196		
Huwe1	A2AFQ0	S1903	P	R	G	S	G	T	0	-3.271	0		
Ildr2	E9Q9U5	S594	A	G	A	S	E	G	-2.4915	0	0		
Ilf3	Q9Z1X4	S382	E	E	K	S	P	S	0.0825	-2.0905	1.5625		
Ilf3	Q9Z1X4	S384	K	S	P	S	K	K	0.1565	-2.222	2.389		
Inadl	A2ADL9	S482	R	A	G	S	P	K	-1.5945	-1.5545	0		

Iqsec2	E9QAD8	S1158	R	R	N	S	V	G	-1.837	0	0		
Isyna1	Q9JHU9	S524	V	A	T	S	P	L	-0.8775	-1.744	0		
Isyna1	Q9JHU9	T523	V	V	A	T	S	P	-2.8095	-2.1635	0		
Kank2	Q8BX02	S532	R	V	L	S	P	A	-1.5555	-0.8825	-0.2275		
Kcnh2	O35219	S1140	R	R	L	S	L	P	-3.851	-0.8735	0		
Kdm2b	Q6P1G2	S1004	P	S	A	S	P	P	0.173	0.334	-2.258		
Kiaa1671	Q8BRV5	S166	I	S	H	S	L	R	-1.726	0	0	+	
Kiaa1671	Q8BRV5	S205	R	D	E	S	D	E	-1.768	-1.0865	0.437		
Kiaa1671	Q8BRV5	S259	Q	P	K	S	P	K	-1.695	0	0		
Kiaa1671	Q8BRV5	S288	E	E	C	S	P	Q	-1.568	0	0		
Kiaa1671	Q8BRV5	S302	K	R	Q	S	L	Y	-1.6655	-1.616	0.491		
Kif11	Q6P9P6	S988	E	L	V	S	P	E	-1.282	-1.883	0		
Klf3	Q545J5	S78	A	G	G	S	P	S	-0.3245	0.0125	-1.8055		
Larp1	Q6ZQ58	S298	D	E	T	S	S	V	0.0395	-1.984	0		
Larp1	Q6ZQ58	S302	S	V	K	S	D	G	0.108	-1.757	-0.072		
Limch1	D3YU59	S719	K	P	K	S	P	E	1.528	0	-3.1795		
Limd2	B1AR88	S30	R	S	K	S	F	S	0.591	0.217	-1.5815		
Llgl2	Q3TJ91	S1022	C	R	L	S	N	G	-1.512	-1.065	0		
Lmtk2	Q3TYD6	S656	L	S	S	S	L	D	-1.8535	0	0.112	+	
Lmtk2	Q3TYD6	S654	A	I	L	S	S	S	-1.851	0	0.112		
Lsr	Q99KG5	S588	L	A	L	S	R	E	-4.166	-2.7475	0	+	
Lsr	Q99KG5	S308	R	T	S	S	V	G	-3.8405	-2.6015	0		
Lsr	Q99KG5	S436	R	A	R	S	V	D	-2.058	-2.379	0		
Lsr	Q99KG5	S471	P	P	R	S	R	S	-2.356	0	0		
Lsr	Q99KG5	S473	R	S	R	S	R	D	-3.5265	0	0		
Lsr	Q99KG5	S591	S	R	E	S	L	V	-4.166	-2.7475	0		
Macf1	E9QA63	S2823	R	K	I	S	V	E	-1.5075	0	0		
Mal2	Q2KHK7	S2	_	_	M	S	A	G	-2.6845	0	0		
Map1b	P14873	T527	Q	V	P	T	P	P	-1.2985	-1.6125	0		
Map1b	P14873	Y1405	E	S	P	Y	E	D	-2.3775	0.2925	0		
Map3k11	Q80XI6	S743	R	T	V	S	P	P	-1.5565	0	0		
Mapk4	Q6P5G0	S382	R	A	G	S	T	P	-2.3145	0	0		
Mapk4	Q6P5G0	T383	A	G	S	T	P	L	-2.5025	0	0		
Mapkbp1	Q921Q9	S411	L	A	R	S	I	S	4.1855	0	-1.953	+	+
Mapkbp1	Q921Q9	S413	R	S	I	S	V	G	2.643	0	-2.11		
Marcks	P26645	S124	A	S	A	S	S	T	-0.532	-0.298	-1.5505		
Marcks	P26645	S141	S	P	S	S	E	T	0.378	0.028	-1.543		
Marcks	P26645	S27	V	A	S	S	P	S	-0.999	-1.211	-1.529		
Mavs	A2ANC9	S384	P	N	S	S	I	R	0	0	-1.939		
Mcc	E9PWI3	S293	S	E	L	S	Q	S	-1.5325	-0.126	-0.7165		
Mcc	E9PWI3	S359	C	S	L	S	V	A	-2.1425	0	0		
Mcc	E9PWI3	S374	T	T	A	S	E	H	-1.5935	-1.273	0		
Mcm3	P25206	S668	K	K	A	S	E	D	0.3425	0.6755	-2.1975		

Med13l	E9QLJ3	S495	F	D	N	S	D	E	-3.9025	-0.9095	0		
Met	F8VQL0	S964	D	L	G	S	E	L	-1.949	0	0		
Met	F8VQL0	S988	R	S	V	S	P	T	-2.549	-1.233	0		
Met	F8VQL0	S995	E	M	V	S	N	E	-2.129	0	0		
Mfsd6	D3Z183	T11	A	I	L	T	D	D	-2.415	0	0		
Mical2	H9KUZ1	S518	R	R	E	S	D	I	-1.7555	-0.7195	0		
Mkl1	D3YUI2	S492	P	P	V	S	P	T	-0.4735	-0.4165	-1.806		
Mkl1	D3YUI2	T488	T	G	S	T	P	P	-0.4735	-0.4165	-1.8645		
Mllt4	E9Q9C3	S1282	V	T	R	S	Q	E	0.3245	0	-1.883		
Mllt4	E9Q9C3	S1726	Q	V	L	S	P	D	-1.5775	0	0		
Mpp2	B1AQF9	S121	P	P	P	S	P	G	-1.6245	-0.255	0		
Mpp2	B1AQF9	S314	G	S	L	S	G	K	-1.82	0	0		
Mpp2	B1AQF9	T117	T	Y	E	T	P	P	-1.678	-0.372	0		
Mprip	Q5SWZ5	S2245	N	I	R	S	K	S	-1.8205	0	0		
Mprip	Q5SWZ5	S2247	R	S	K	S	L	K	-1.991	0	-0.4375		
Mrm3	Q5ND52	S42	R	V	L	S	P	S	-1.5905	0	-0.348		
Mtor	Q9JLN9	S1166	L	D	Q	S	P	E	0.7745	-1.536	-0.159		
Mtss1	Q6ZQB7	S289	T	P	P	S	S	P	-2.248	0	0		
Mtss1	Q6ZQB7	S290	P	P	S	S	P	S	-2.4995	0	0		
Mtss1	Q6ZQB7	T286	S	Y	Q	T	P	P	-2.4245	0	0		
Mtus1	Q5HZI1	S1164	K	R	L	S	M	E	-1.5585	0	0		
Myrf	Q3UR85	S294	R	A	P	S	P	P	-2.9625	0	0		
Myrf	Q3UR85	S714	R	L	D	S	L	K	-3.002	0	0		
Nav1	Q8CH77	S1824	S	T	A	S	P	P	-1.548	-0.683	0		
Nav1	Q8CH77	S651	R	K	T	S	L	D	-1.594	0	0		
Nav1	Q8CH77	T650	G	R	K	T	S	L	-1.5165	-0.9485	0		
Nbeal2	B2RXS1	T1862	A	P	M	T	P	T	-1.8445	0	0		
Ncam1	E9QB01	S774	K	D	E	S	K	E	-1.6515	0	0		
Ncapd2	E9QPT2	S589	S	K	D	S	P	S	-0.43	-1.5625	0		
Nedd4l	Q3TQK9	T287	V	T	D	T	V	A	-1.657	-0.6595	0.4465	+	
Nedd4l	Q3TQK9	S369	R	S	L	S	S	P	-1.326	-1.668	0.586		
Nedd4l	Q3TQK9	T372	S	S	P	T	V	T	0	-1.7515	0		
Neo1	P97798	S1225	P	R	N	S	Q	D	-1.596	-0.8595	0		
Neo1	P97798	S1245	R	R	N	S	Y	R	-1.5355	-1	0		
Neo1	P97798	S1254	S	E	D	S	M	S	-1.597	-1.908	0		
Nes	Q6P5H2	S977	M	V	R	S	L	E	-2.303	-2.825	0	+	
Nes	Q6P5H2	S169	A	H	A	S	P	I	-1.5535	-1.883	0.1875		
Nes	Q6P5H2	S565	C	N	S	S	I	E	-1.2175	-1.7125	0		
Nes	Q6P5H2	S575	T	V	K	S	P	E	-1.087	-1.589	0		
Nes	Q6P5H2	S816	S	Q	E	S	L	K	-1.3375	-1.9255	0		
Nes	Q6P5H2	S819	S	L	K	S	P	E	-1.3815	-1.9075	0		
Nfia	B1AUB7	S287	E	M	D	S	P	G	-1.94	-0.9245	0.3135		
Nfia	B1AUB7	S335	S	S	P	S	P	S	-1.6285	0	0		

Nfia	B1AUB7	T372	H	F	P	T	S	P	-1.8405	0	0		
Nfkbib	Q60778	S346	Q	P	P	S	P	A	-1.0105	-1.6055	0		
Nfrkb	Q6PIJ4	S298	R	K	G	S	L	A	-0.4155	-1.786	0		
Nhsl1	E0CYL9	S189	L	R	R	S	L	I	-1.59	0	0	+	+
Nhsl1	Q8CAF4	S1459	S	S	C	S	P	N	-1.8135	0	0		
Nifk	Q91VE6	S270	R	R	K	S	Q	V	-0.081	-1.5195	-0.465		
Nop2	E9QN31	S68	P	N	K	S	P	G	-0.5615	-1.8435	0		
Oxr1	E9Q0A7	S197	S	S	T	S	E	E	2.4725	2.2625	-2.2175		
Oxr1	E9Q0A7	S59	R	P	P	S	P	A	0.992	1.246	-2.428		
Oxr1	E9Q0A7	T483	D	S	E	T	E	V	1.564	-1.9425	0		
Pag1	A6H659	S292	K	R	F	S	S	L	-3.1695	0	0		
Pag1	A6H659	S293	R	F	S	S	L	S	-2.6845	0	0		
Pak3	A3KGC0	S4	M	S	D	S	L	D	-1.5535	0	-0.5285	+	
Pak3	A3KGC0	S186	P	P	V	S	E	E	-0.249	-0.1195	-1.8305		
Palm2	A2APJ5	S74	S	S	L	S	P	D	-0.31	-0.4355	-1.8065		
Pard3b	Q9CSB4	S990	R	P	L	S	P	D	-1.5505	0	0		
Pard6b	Q9JK83	S10	H	G	A	S	S	G	-0.7965	-1.542	0		
Pdcd4	Q61823	S313	R	K	D	S	V	W	-1.6775	0	0		
Pde3b	Q61409	S273	R	R	R	S	S	C	-2.6605	0	0		
Pde3b	Q61409	S274	R	R	S	S	C	V	-2.728	0	0		
Pde3b	Q61409	S296	R	R	P	S	L	P	-4.254	-1.4665	0		
Pde3b	Q61409	S411	G	R	T	S	F	P	-3.981	0	0		
Pde3b	Q61409	S421	R	R	S	S	G	A	-4.6225	0	-2.1805		
Pde3b	Q61409	S424	S	G	A	S	S	L	-2.3285	0	0		
Pde3b	Q61409	S474	R	S	S	S	V	S	-4.2915	-2.029	0		
Pde3b	Q61409	T410	S	G	R	T	S	F	-4.334	0	0		
Pdha1	P35486	Y301	G	V	S	Y	R	T	-2.179	0	-0.2965		
Pdlim5	Q8CI51	S322	S	G	A	S	P	L	-2.8915	-1.5955	0		
Pdlim5	Q8CI51	S332	G	P	E	S	P	G	-3.541	-3.75	-0.594		
Pdzrn3	Q69ZS0	S775	L	E	I	S	P	D	-2.7845	-1.255	0.4475		
Peak1	Q69Z38	T571	T	S	P	T	A	T	-1.6165	0.0865	0		
Peak1	Q69Z38	T896	T	K	P	T	S	P	-0.4535	-1.6855	-0.2385		
Peg3	Q3URU2	S14	D	M	N	S	D	D	-3.215	0	0		
Peg3	Q3URU2	S71	R	D	L	S	L	P	-3.3245	0	0		
Phldb1	D3Z0X5	S553	T	G	A	S	P	R	0.491	0.445	-1.6455		
Pik3r4	Q8VD65	S865	M	F	G	S	L	E	-3.109	0	0	+	
Pik3r4	Q8VD65	S861	E	W	K	S	M	F	-3.02	0	0		
Pkp1	P97350	S156	A	S	R	S	E	P	-4.074	0	0		
Pkp2	Q3TIY5	S135	S	Q	K	S	V	E	-1.684	0	0		
Pkp2	Q3TIY5	S155	P	D	S	S	P	E	-1.9085	0	0		
Pkp2	Q3TIY5	S235	S	A	G	S	L	L	-1.648	-0.6975	0		
Pkp2	Q3TIY5	T181	G	R	L	T	L	P	-1.814	-0.9015	0		
Plcd3	Q8K2J0	S492	R	I	L	S	D	R	-1.899	-1.386	0		

Plekha6	Q7TQG1	S448	R	R	L	S	L	Q	-2.846	0	0		
Plekha6	Q7TQG1	S901	R	T	K	S	P	A	-2.7495	0	0		
Plekha6	Q7TQG1	S992	R	H	R	S	I	H	-2.412	0	0		
Plekha6	Q7TQG1	S999	V	D	I	S	N	L	-2.6995	0	0		
Plekhg3	Q4VAC9	S1158	S	P	L	S	P	F	-1.6215	0	0		
Pom121	Q3U425	S83	A	L	S	S	F	V	-0.886	-0.3405	-1.5365		
Ppfibp1	B2KFS4	S538	S	P	P	S	P	D	0.378	-3.155	-0.138		
Ppl	Q9R269	S1656	L	R	R	S	I	V	-1.5745	-0.908	0	+	+
Ppp1r12b	A6H644	S833	R	L	E	S	G	G	-2.107	0	0.2145		
Ppp1r9a	H3BJD6	S199	E	A	V	S	P	T	-2.415	0	0		
Prkab2	Q6PAM0	S38	M	V	G	S	T	D	-3.3515	-1.788	1.5325	+	
Prkag2	Q3U4D5	S122	R	R	M	S	F	S	-3.0315	0	0		
Proser2	Q8C5R2	S220	E	A	L	S	P	T	-3.266	0	0		
Proser2	Q8C5R2	S223	S	P	T	S	P	S	-1.9755	0	0		
Prrg4	Q3TLN5	S202	H	S	V	S	P	P	-1.641	0	0		
Ptprb	B2RU80	S1667	R	P	L	S	V	H	-5.5795	-2.782	0		
Ptprm	E9Q9S6	S845	R	S	V	S	S	P	-1.658	0	0		
Ptprm	E9Q9S6	S849	S	P	S	S	F	T	-1.648	0	0		
Pwwp2b	E9Q9M8	S214	G	P	D	S	E	H	-1.568	-0.668	0		
Q9D8L0	Q9D8L0	S32	P	T	L	S	I	L	-0.687	-2.786	0		
Q9D8L0	Q9D8L0	T30	P	R	P	T	L	S	-3.0405	-2.3755	0		
Rab38	Q5FW76	S187	L	L	E	S	I	E	-2.96	0	0	+	+
Rab3b	A2A7Z6	S199	M	S	D	S	M	D	-2.302	-2.562	0	+	+
Rab3ip	Q68EF0	S147	R	L	R	S	P	S	-1.7735	0	0		
Ralgapa2	E9Q4R6	S373	R	R	L	S	N	S	-2.4645	0	0		
Ralgps2	Q9ERD6	S293	T	P	R	S	A	A	-2.3365	-2.1355	0		
Ralgps2	Q9ERD6	S296	S	A	A	S	R	E	-2.6465	-2.1525	0		
Ralgps2	Q9ERD6	S315	G	R	K	S	S	A	-2.9475	0	0		
Ralgps2	Q9ERD6	S316	R	K	S	S	A	A	-2.8545	-0.2065	0		
Ralgps2	Q9ERD6	S336	T	P	P	S	P	R	-2.3595	0.1645	0		
Ralgps2	Q9ERD6	T368	K	S	A	T	F	P	-1.089	-1.7965	0		
Rb1cc1	Q9ESK9	S257	L	V	T	S	F	H	-2.2625	0	-2.3545	+	+
Rb1cc1	Q9ESK9	S237	M	K	R	S	T	E	-4.278	-3.551	-3.29	+	
Rb1cc1	Q9ESK9	S643	V	S	T	S	Q	A	-2.1815	0	0	+	
Rb1cc1	Q9ESK9	T238	K	R	S	T	E	L	-4.226	-3.402	-2.451		
Rbm14	Q8C2Q3	S618	R	R	L	S	E	S	-0.0345	-1.728	-0.0575		
Rbm14	Q8C2Q3	S620	L	S	E	S	Q	L	0	-1.7705	0		
Rbm34	B2RUP0	S19	R	R	Q	S	S	G	-0.339	-1.5445	0.0795		
Rbsn	Q80Y56	S214	T	H	T	S	P	S	-0.7645	-1.536	0		
Reep2	Q8VCD6	S152	R	S	F	S	M	Q	-2.0985	-1.3135	0		
Rem2	E9Q4D5	S27	R	Q	A	S	P	L	-1.223	-2.5895	0		
Rem2	E9Q4D5	S295	P	E	P	S	S	P	-3.0555	-1.533	0		
Rem2	E9Q4D5	S296	E	P	S	S	P	D	-3.287	-2.724	0		

Rem2	E9Q4D5	S334	R	S	R	S	C	H	-3.208	0	0		
Rem2	E9Q4D5	S69	R	R	G	S	M	P	-3.246	-0.9715	0		
Rhpn2	Q497Z4	S642	S	F	L	S	W	G	-2.3915	0	0		
Rhpn2	Q497Z4	S654	K	S	A	S	T	L	-2.472	-1.862	0		
Riok3	Q3TC66	S8	G	V	S	S	P	E	-1.699	0	0		
Rps9	Q6ZWN5	S160	I	D	F	S	L	R	-1.5225	0	0	+	
Rrm1	P07742	S780	M	V	C	S	L	E	-1.771	0	0	+	
Rtn4	Q99P72	S766	E	R	L	S	A	S	0.439	-0.014	-1.75		
Rtn4	Q99P72	S768	L	S	A	S	P	Q	0.962	0.0335	-1.747		
Scd2	P13011	S37	F	E	K	S	S	H	-1.6255	0	0	+	+
Scd2	P13011	S38	E	K	S	S	H	H	-1.638	0	0		
Scel	E9PYR5	S264	R	A	Q	S	L	E	-3.106	0	0		
Scel	Q14DU0	S343	R	G	K	S	L	D	-3.804	-1.286	0		
Scnm1	Q8K136	S141	P	S	V	S	S	P	-1.8455	0	0		
Scnm1	Q8K136	S182	A	P	M	S	P	T	1.5915	-3.4825	0		
Senp3	Q9EP97	S163	N	H	L	S	P	Q	-1.549	-1.0605	-0.182		
Sept10	Q8C650	S13	H	P	R	S	L	S	-0.359	-1.8625	0		
Sept11	Q8C1B7	S9	G	R	P	S	N	E	0.409	0.053	-1.673		
Shroom2	A7TU71	S1047	T	S	R	S	P	S	-1.6535	0	0		
Shroom2	A7TU71	S1049	R	S	P	S	P	Q	-1.6535	0	0		
Shroom2	A7TU71	S1171	S	C	S	S	P	P	-1.7225	-0.84	-2.0245		
Shroom2	A7TU71	S798	K	S	Y	S	E	P	-1.366	-1.5035	0		
Shroom2	A7TU71	S935	R	Y	H	S	A	D	-2.196	0	0		
Shroom2	A7TU71	S959	R	S	R	S	S	P	-2.031	-1.073	-0.443		
Shroom2	A7TU71	S960	S	R	S	S	P	S	-1.991	0	0		
Shroom2	A7TU71	Y966	T	D	H	Y	S	Q	-1.967	0	0		
Shroom3	E9QMY5	S1390	S	P	R	S	P	E	-2.6495	0	0		
Shroom3	E9QMY5	S1409	K	R	T	S	L	P	-3.4425	0	0		
Shroom3	E9QMY5	S244	K	S	T	S	S	I	-2.6245	0	0		
Shroom3	E9QMY5	S439	P	E	R	S	P	E	-2.345	-0.6525	0		
Shroom3	E9QMY5	S443	P	E	N	S	P	P	-2.5535	0.58	0		
Shroom3	E9QMY5	S663	A	F	S	S	L	Q	-2.57	0	0		
Shroom3	E9QMY5	S675	R	R	Q	S	N	V	-3.0795	-2.7035	0		
Shroom3	E9QMY5	S888	R	S	Q	S	T	F	-1.915	0	0		
Shroom3	E9QMY5	S969	G	M	R	S	P	E	-2.047	0	0		
Sipa1l1	Q8C0T5	S1687	R	P	L	S	A	A	-1.565	0	0		
Sipa1l1	Q8C0T5	S1692	A	S	N	S	D	Q	-1.8745	0	0		
Slc12a6	A2AGJ6	T977	L	R	L	T	S	I	-1.9605	0	0	+	+
Slc12a6	A2AGJ6	S21	G	P	L	S	P	E	-3.1905	-1.393	0		
Slc12a6	A2AGJ6	S978	R	L	T	S	I	G	-1.772	-0.5935	0		
Slc12a6	A2AGJ6	S981	S	I	G	S	D	E	-2.4055	-2.074	0		
Slc1a6	B2RQX4	S3	_	M	S	S	H	G	2.688	0	-1.522		
Slc38a1	Q8K2P7	S52	S	R	R	S	L	T	-1.42	-1.896	0		

Slc38a1	Q8K2P7	T54	R	S	L	T	N	S	-1.517	-0.8655	0		
Slc38a3	Q9DCP2	S53	K	S	P	S	K	E	-2.2725	0	0		
Slc39a6	Q8C145	S489	Q	L	S	S	N	E	-0.002	-1.5685	0		
Slc9a3r1	P70441	S273	E	P	A	S	E	S	-1.9655	-1.3515	-0.4485		
Slc9a3r1	P70441	S275	A	S	E	S	P	R	-1.894	-1.445	-0.4485		
Slc9a3r1	P70441	S285	R	S	A	S	S	D	-1.918	-1.5365	-0.89		
Slc9a3r1	P70441	S289	S	D	T	S	E	E	-1.5275	0	0		
Slc9a3r1	P70441	S294	E	L	N	S	Q	D	-1.8165	-1.868	-0.2765		
Slc9a3r1	P70441	T288	S	S	D	T	S	E	0.7825	-1.543	0		
Slc9a7	Q8BLV3	S546	E	E	L	S	E	E	-2.3165	0	0		
Slk	O54988	S645	V	S	E	S	N	S	-0.0515	0	-1.877	+	
Slk	O54988	S340	K	R	A	S	S	D	-2.2505	0	0		
Slk	O54988	S647	E	S	N	S	I	E	0.116	0.211	-2.2625		
Smim1	P0C8K7	S3	_	M	Q	S	Q	E	-1.723	0	0		
Smpd3	Q9JJY3	S299	S	R	E	S	L	V	-1.575	0	0		
Smpd3	Q9JJY3	S326	Y	K	T	S	V	V	0	-2.072	-1.182		
Snap23	Q9D3L3	S20	T	D	E	S	L	E	-1.7215	-0.3325	0		
Sntb1	Q99L88	S218	P	P	E	S	P	R	-2.8665	0	0		
Sntb1	Q99L88	T213	G	W	E	T	P	P	-2.6225	0	0		
Sorbs2	B2RXQ9	S383	I	D	R	S	L	E	-3.4975	-2.923	0	+	
Sorbs2	B2RXQ9	S231	K	S	H	S	D	N	-2.075	0	0		
Sorbs2	D3Z080	S27	R	V	Q	S	S	P	-3.6985	-4.456	-4.2625		
Sorbs2	D3Z080	S28	V	Q	S	S	P	N	-4.5355	-2.9425	-3.607		
Sorbs2	B2RXQ9	S299	P	R	P	S	A	P	-5.0025	-3.979	-2.473		
Sorbs2	B2RXQ9	S304	P	D	L	S	P	T	-4.106	-2.117	-1.7535		
Sorbs2	E9Q8K9	S316	Y	Q	S	S	I	D	-4.408	-0.781	-0.557		
Sorbs2	B2RXQ9	S320	K	P	L	S	V	S	-3.045	-2.844	0		
Sorbs2	B2RXQ9	S322	L	S	V	S	P	S	-3.92	-4.007	0		
Sorbs2	B2RXQ9	S324	V	S	P	S	T	D	-3.5475	-1.5755	0		
Sorbs2	B2RXQ9	S330	G	L	R	S	P	S	-2.9895	-2.9565	0		
Sorbs2	B2RXQ9	S332	R	S	P	S	P	P	-3.1295	-3.2145	-1.07		
Sorbs2	D3Z080	S345	P	R	P	S	A	P	-5.0025	-3.3825	-2.473		
Sorbs2	D3Z080	S350	P	D	L	S	P	T	-3.778	-2.624	-2.2675		
Sorbs2	B2RXQ9	S390	P	S	S	S	A	S	-3.9395	-1.3395	0		
Sorbs2	B2RXQ9	S403	R	R	K	S	E	P	-4.4495	-4.628	-3.8335		
Sorbs2	B2RXQ9	S422	S	R	T	S	P	G	-4.3685	-4.693	-2.5625		
Sorbs2	B2RXQ9	S442	F	I	S	S	S	P	-4.1485	-3.506	-2.402		
Sorbs2	B2RXQ9	S443	I	S	S	S	P	S	-4.263	-3.416	-1.007		
Sorbs2	B2RXQ9	S445	S	S	P	S	S	P	-2.256	-1.4165	-2.672		
Sorbs2	B2RXQ9	S446	S	P	S	S	P	S	-5.1525	-4.1015	-2.6435		
Sorbs2	B2RXQ9	S448	S	S	P	S	R	A	-1.501	-2.5195	-1.405		
Sorbs2	B2RXQ9	S634	H	S	Y	S	S	D	-4.4915	-3.3925	-3.0985		
Sorbs2	B2RXQ9	S635	S	Y	S	S	D	R	-1.5315	-1.9715	-1.307		

Sorbs2	B2RXQ9	S7	G	R	E	S	Q	S	-2.595	0	0		
Sorbs2	B2RXQ9	S86	R	P	F	S	P	S	-2.6725	0	0		
Sorbs2	B2RXQ9	S9	E	S	Q	S	P	D	-2.4355	0	0		
Sorbs2	B2RXQ9	T325	S	P	S	T	D	G	-3.6645	-0.991	-0.46		
Sorbs2	D3Z080	T352	L	S	P	T	R	P	-1.9425	-3.165	-3.1895		
Sorbs2	B2RXQ9	T421	S	S	R	T	S	P	-4.3685	-2.805	-2.5625		
Sort1	Q6PHU5	S791	H	R	Y	S	V	L	-2.627	0	0		
Ssh1	Q76I79	S1028	S	G	K	S	A	P	-3.841	0	0		
Ssh1	Q76I79	S516	R	R	L	S	D	P	-3.7895	-3.035	0		
Stim2	B7ZN44	S94	R	R	A	S	G	S	-0.4575	-1.5235	-0.9695		
Stim2	B7ZN44	S96	A	S	G	S	A	G	-0.029	-1.5155	-0.441		
Stk26	A2AD85	S4	M	A	H	S	P	V	-2.546	0	0		
Ston2	E9PXP7	S270	S	T	G	S	F	K	-2.9505	0	0		
Ston2	E9PXP7	S278	R	P	K	S	T	L	-2.148	0	0		
Strn	O55106	S227	L	T	D	S	A	S	-2.364	0	0	+	+
Sytl2	Q99N50	S317	K	E	F	S	L	E	-1.558	0	0		
Sytl2	Q99N50	S400	S	S	P	S	D	S	-1.967	0	0		
Sytl2	Q99N50	S493	E	E	H	S	P	V	-1.6755	0	0		
Sytl2	E9QKS6	S511	P	S	K	S	L	E	-1.92	-1.4875	0		
Sytl2	E9QKS6	S638	K	Q	P	S	Q	V	-1.7125	0	0		
Sytl2	E9QKS6	T632	R	R	D	T	L	E	-1.908	0	0		
Tanc1	B9EJ77	S1429	A	N	D	S	D	N	-1.5645	0	0		
Tanc1	B9EJ77	S267	D	N	C	S	P	V	-1.8425	-1.143	0		
Tanc1	B9EJ77	S310	R	P	N	S	V	A	-1.85	0	0		
Tanc1	B9EJ77	S434	A	S	S	S	P	S	-2.0895	-1.2845	0		
Tanc1	B9EJ77	S436	S	S	P	S	L	S	-1.926	-0.759	0		
Tanc1	B9EJ77	S455	P	L	L	S	P	S	-1.631	-1.8025	-0.287		
Tbc1d22a	Q8R5A6	T148	E	S	H	T	P	C	-1.5145	0	0.2205		
Tmem51	A2AC36	T230	E	P	L	T	P	P	-1.787	0	0		
Tmx2	Q9D710	S209	Y	K	V	S	T	S	-3.006	0	0		
Tnfaip3	Q3U695	S550	R	S	K	S	D	P	-1.034	-1.5635	0		
Tns1	E9Q0S6	S1067	E	A	T	S	P	R	-1.734	0	0		
Tns1	E9Q0S6	S156	V	S	P	S	I	Q	-1.247	-1.518	0		
Tns1	E9Q0S6	S163	Q	P	Q	S	Q	P	-1.6525	0	0		
Tns1	E9Q0S6	S167	Q	P	T	S	L	S	-1.646	0	0		
Tns1	E9Q0S6	S545	K	K	D	S	L	N	-1.562	-1.611	0		
Tns1	E9Q0S6	S604	A	A	L	S	P	Q	-1.053	-1.7525	1.791		
Tns1	E9Q0S6	S754	P	S	Y	S	A	Q	0	-1.7485	0		
Tns3	Q5SSZ5	S844	F	P	V	S	P	E	-1.8395	0	0		
Tns3	Q5SSZ5	T445	K	D	M	T	D	M	0	-0.537	-2.2905		
Tor1aip1	Q921T2	T169	R	P	V	T	S	Q	0.3025	1.589	-2.0005		
Tp53bp1	P70399	S423	P	T	V	S	P	Q	3.768	2.8525	-1.96		
Tuft1	O08970	S378	K	P	P	S	P	K	-2.8035	0	0		

Ulk1	Q3UFT4	S465	I	R	R	S	G	S	-4.0505	0	0	+	
Ulk1	Q3UFT4	S561	R	L	H	S	A	P	-4.4565	-2.9765	0		
Ulk1	Q3UFT4	S628	I	L	G	S	P	T	-2.59	-1.9	-1.381		
Ulk1	Q3UFT4	S643	K	T	P	S	S	Q	-4.2595	-3.647	-2.1115		
Ulk1	Q3UFT4	T468	S	G	S	T	S	P	-2.3705	0	0		
Ulk1	Q3UFT4	T641	F	P	K	T	P	S	-3.1275	0	-1.051		
Ulk1	Q3UFT4	T665	R	N	R	T	L	P	-4.3	-2.178	0		
Usp8	A2AI52	T696	P	D	I	T	Q	A	-3.031	0	0		
Vamp5	Q5M9K2	S48	L	D	M	S	S	A	-1.74	0	0	+	+
Vamp5	Q5M9K2	S41	E	Q	R	S	D	Q	-2.3475	0	0		
Vill	G5E8C6	S766	S	Q	D	S	P	E	-1.522	0	0		
Wdr11	G5E8J3	S711	S	M	G	S	I	T	-1.804	0	-0.3985		
Zc3h13	B9EHN9	S355	R	T	P	S	P	S	-0.157	-1.675	0		
Zc3hc1	Q80YV2	S406	R	L	C	S	S	S	-0.531	-3.052	0		
Zdhhc2	A0JP44	S332	E	S	Q	S	H	L	-2.134	-0.962	0		
Zfp462	B1AWL2	S2158	R	N	K	S	R	V	-1.933	-1.092	0		
Zfp462	B1AWL2	S2161	S	R	V	S	P	V	-1.8605	-1.9185	0		
Zfp462	B1AWL2	S681	L	D	L	S	P	V	-1.4695	-1.814	0		
Zfpm1	O35615	S681	G	S	Q	S	P	G	-1.3475	-1.6835	0		
Zfpm1	O35615	S925	A	P	R	S	P	S	-2.1615	-2.0465	0		
Zfpm1	O35615	S927	R	S	P	S	P	A	-1.941	-0.9275	0		
Zfpm1	O35615	T666	G	T	T	T	P	E	-2.304	2.5245	0		

Appendix Table B – *Peptides synthesised for peptide array-based ULK1 in vitro kinase assay.* Peptides spanning putative ULK substrates were immobilised in array format in triplicate as described in section 4.4.1. They are grouped depending on the screens from which substrates were identified, with positive controls also listed. In 'Name' column, protein name is followed by phosphoacceptor residue and number, along with encoded mutation. S/T-AA indicates that all serine and threonine residues changed to alanine (i.e. total phosphomutant). 'ULKtide_S' refers to optimal peptide substrate from (Egan et al., 2015) with serine in central position; 'ULKtide_A' encodes an alanine in the central position and is therefore non-phosphorylatable. Where 'murinised' peptides were used, the specific mutations are listed alongside the gene name. In 'Sequence' column, putative phosphoacceptor position is shown in bold. Murinised VILL S234 was excluded from analysis due to technical error.

Positive Controls

Name	Sequence
ATG13_S355	EDTETVSN**S**SEGRAS
ATG13_S355A	EDTETVSN**A**SEGRAS
ATG14_S29	PLARDLVD**S**VDDAEG
ATG14_S29A	PLARDLVD**A**VDDAEG
BECN1_S15	SNNSTMQV**S**FVCQRC
BECN1_S15A	SNNSTMQV**A**FVCQRC
NR3C2_S843	FNEEKMHQ**S**AMYELC
NR3C2_S843A	FNEEKMHQ**A**AMYELC
P150_S861	SNVNEEWK**S**MFGSLD
P150_S861A	SNVNEEWK**A**MFGSLD
PRKAB2_S39	HKIMVG**ST**DDP**S**VFSLPDS
PRKAB2_S39A	HKIMVG**AT**DDP**S**VFSLPDS
ULK1_S1042_T1046	CIERRL**S**ALL**T**GICA
ULK1_S1042A_T1046A	CIERRL**A**ALL**A**GICA

ULKtide_S	YANWLAA**S**IYLDGKKK
ULKtide_A	YANWLAA**A**IYLDGKKK

TMT Alone

Name	Sequence
ACTG1_S33	DAPRAVFP**S**IVGRPR
ACTG1_S33A	DAPRAVFP**A**IVGRPR
CHEK1_S317	EENVKYSS**S**QPEPRT
CHEK1_S317A	EENVKYSS**A**QPEPRT
CHEK1_S/T-AA	EENVKYAA**A**QPEPRA
CHEK1_S317_N311T/Y314F	EETVKFSS**S**QPEPRT
CTNND1_S920	DHNRTLDR**S**GDLGDM
CTNND1_S920A	DHNRTLDR**A**GDLGDM
CTNND1_S/T-AA	DHNRALDR**A**GDLGDM
LAP3_S238	TEVHIRPK**S**WIEEQA
LAP3_S238A	TEVHIRPK**A**WIEEQA
LAP3_S/T-AA	AEVHIRPK**A**WIEEQA
MSL3_S315	RSQEELSP**S**PPLLNP
MSL3_S315A	RSQEELSP**A**PPLLNP
MSL3_S/T-AA	RAQEELAP**A**PPLLNP
NEDD4L_T302	PPASPGSR**T**SPQELS
NEDD4L_T302A	PPASPGSR**A**SPQELS
NEDD4L_S/T-AA	PPAAPGAR**A**APQELA
NEDD4L_T302_G299V	PPASPVSR**T**SPQELS
PCM1_S110	KLKQRINF**S**DLDQRS
PCM1_S110A	KLKQRINF**A**DLDQRS
PCM1_S/T-AA	KLKQRINF**A**DLDQRA
RALGPS2_S289/T290	SLKIEPG**TS**TPRSAA
RALGPS2_S289/T290A	SLKIEPG**AA**TPRSAA
RALGPS2_S/T-AA	ALKIEPG**AA**APRAAA

SCEL_S91	KATISRYS**S**DDTLDR
SCEL_S91A	KATISRYS**A**DDTLDR
SCEL_S/T-AA	KAAIARYA**A**DDALDR
SCEL_S91_S90R/D92E/T93M	KATISRYR**S**EDMLDR
SHROOM1_S49	GGPEPRTQ**S**PGTDLL
SHROOM1_S49A	GGPEPRTQ**A**PGTDLL
SHROOM1_S/T-AA	GGPEPRAQ**A**PGADLL
SHROOM1_S49_Q48P	GGPEPRTP**S**PGTDLL
STAG2_S1198	QHAIRRGT**S**LMEDDE
STAG2_S1198A	QHAIRRGT**A**LMEDDE
STAG2_S/T-AA	QHAIRRGA**A**LMEDDE
TBC1D1_S627	QRKLMRYH**S**VSTETP
TBC1D1_S627A	QRKLMRYH**A**VSTETP
TBC1D1_S/T-AA	QRKLMRYH**A**VAAEAP
VAMP5_S41	KLAELQQR**S**DQLLDM
VAMP5_S41A	KLAELQQR**A**DQLLDM
VAMP5_S41_Q38E	KLAELEQR**S**DQLLDM
VIM_T426	FSSLNLRE**T**NLDSLP
VIM_T426A	FSSLNLRE**A**NLDSLP
VIM_S/T-AA	FAALNLRE**A**NLDALP
VPS26B_S302/304	RKGDIVRK**S**M**S**HQAA
VPS26B_S302/304A	RKGDIVRK**A**M**A**HQAA
ZNF800_S462	DSESPKST**S**PSAAGG
ZNF800_S462A	DSESPKST**A**PSAAGG
ZNF800_S/T-AA	DAEAPKAA**A**PAAAGG

TMT + SILAC

Name	Sequence
CARS_S307	EGEGDLSI**S**ADRLSE
CARS_S307A	EGEGDLSI**A**ADRLSE

CARS_S/T-AA	EGEGDLAI**A**ADRLAE
F11R_S287	IYSQPSAR**S**EGEFKQ
F11R_S287A	IYSQPSAR**A**EGEFKQ
F11R_S/T-AA	IYAQPAAR**A**EGEFKQ
F11R_S287_A285T	IYSQPSTR**S**EGEFKQ
GPRC5A_S301	YGVENRAY**S**QEEITQ
GPRC5A_S301A	YGVENRAY**A**QEEITQ
GPRC5A_S/T-AA	YGVENRAY**A**QEEIAQ
NHSL1_S190	DRQASLRR**S**LIYTDT
NHSL1_S190A	DRQASLRR**A**LIYTDT
NHSL1_S/T-AA	DRQAALRR**A**LIYADA
SHROOM2_S231	TLSKADTS**S**AENILY
SHROOM2_S231A	TLSKADTS**A**AENILY
SHROOM2_S/T-AA	ALAKADAA**A**AENILY
SHROOM2_S231_S225P/T229A/A232T	TLPKADAS**S**TENILY
SORBS2_S298/299/301/302	LTKSFTS**SS**P**SS**PSRAKGG
SORBS2_ S298/299/301/302A	LTKSFTS**AA**P**AA**PSRAKGG
SORBS2_S298/299/301/302A_S/T-AA	LAKAFAA**AA**P**AA**PARAKGG
SORBS2_S298/299/301/302_T296I/L291F	FTKSFIS**SS**P**SS**PSRAKGG
VILL_S234	AVLGRRVG**S**LRAATP
VILL_S234A	AVLGRRVG**A**LRAATP
VILL_S/T-AA	AVLGRRVG**A**LRAAAP

TMT + Crosslinking

Name	Sequence
ANXA2_S127	KGLGTDED**S**LIEIIC
ANXA2_S127A	KGLGTDED**A**LIEIIC
ANXA2_S/T-AA	KGLGADED**A**LIEIIC

SILAC Alone

Name	Sequence
PRKAG2_S122	PPRSPRRM**S**FSGIFR
PRKAG2_S122A	PPRSPRRM**A**FSGIFR
PRKAG2_S/T-AA	PPRAPRRM**A**FAGIFR
SORBS2_S239	LYQSSIDR**S**LERPMS
SORBS2_S239A	LYQSSIDR**A**LERPMS
SORBS2_S239A_S/T-AA	LYQAAIDR**A**LERPMA

Appendix Table C – *Bioinformatic prediction of LIRs in human p150*. The amino acid sequence for p150 was entered into the iLIR prediction server (Kalvari et al., 2014, Jacomin et al., 2016) and 19 potential LIRs (LC3-interacting regions) were predicted. LIRs satisfying the minimal core-LIR ([**WFY**]-x-x-[**ILV**]) are listed as WxxL motifs,

whereas those matching the extended LIR motif ([ADEFGLPRSK][DEGMSTV][**WFY**] [DEILQTV][ADEFHIKLMPSTV][**ILV**]) are listed as 'xLIR' motifs. The start and end amino acid positions, LIR sequence and associated PSSM (position-specific scoring matrix) score are included. Putative LIRs matching the xLIR motif more closely have a higher PSSM score. The 'Anchor' column indicates whether a predicted LIR overlaps by >3 amino acids with an intrinsically disordered region predicted to undergo a disorder to order transition upon protein binding, indicative of a functional LIR.

MOTIF	START	END	LIR sequence	PSSM score	Anchor
WxxL	671	676	IRYGAV	1 (3.6e+00)	No
WxxL	1265	1270	IRFWDL	1 (3.6e+00)	Yes
WxxL	1153	1158	QCWLCI	10 (2.0e-01)	No
xLIR	628	633	EEFVIV	13 (7.9e-02)	No
WxxL	35	40	TRFFKV	2 (2.6e+00)	No
WxxL	314	319	NAFPEI	3 (1.9e+00)	No
WxxL	740	745	SLFRHL	4 (1.4e+00)	No
WxxL	1112	1117	LAYATV	4 (1.4e+00)	No
WxxL	18	23	SYFSDI	5 (1.0e+00)	No
WxxL	1289	1294	SYYRKI	5 (1.0e+00)	No
WxxL	109	114	NLYDRI	6 (7.4e-01)	No
WxxL	128	133	IAFQIL	6 (7.4e-01)	No
WxxL	596	601	AFFDSI	6 (7.4e-01)	No
WxxL	690	695	DVYCKL	6 (7.4e-01)	No
WxxL	494	499	LRFLEL	7 (5.3e-01)	No
WxxL	861	866	SMFGSL	7 (5.3e-01)	No
WxxL	1036	1041	LTYSRI	7 (5.3e-01)	No
WxxL	157	162	TSWNWV	9 (2.8e-01)	No
WxxL	1054	1059	SHYLAI	9 (2.8e-01)	No

Appendix Table D - *Peptide identities in array-based p150 LIR binding assay.* Peptides encoding 3 putative LIRs flanking or spanning ULK target sites in p150 were immobilised in array format. Also included were peptides encoding control LIRs (LC3-interacting region) from VPS34 (amino acids 240-263) and FYCO1 (amino acids 1270-

1293). Wild type (WT) 24mer peptide were included alongside various phosphomutants, specific mutations are described in the name column. Predicted LIR positions 0 and +3 are highlighted in blue with mutated residues in green. P150 sites were selected for mutation based on biases displayed by LC3/GABARAPs for acidic R groups N- or C-terminal to the LIR, described by (Wirth et al., 2019). Phosphorylated amino acids are depicted in bold and red. Two sets of arrays were synthesised. In A, putative ULK sites were mutated to glutamate whereas in B they were switched to phosphoserine.

A

Controls

Name	Sequence
VPS34_WT	GDESSPILTSFELVKVPDPQMSME
VPS34_S249E	GDESSPILTEFELVKVPDPQMSME
FYCO1_WT	TDYRPPDDAVFDIITDEELCQIQE

S861/S865

Name	Sequence
P150_S861/S865_WT	SNVNEEWKSMFGSLDPPNMPQALP
P150_S861/S865_S861E	SNVNEEWKEMFGSLDPPNMPQALP
P150_S861/S865_S865E	SNVNEEWKSMFGELDPPNMPQALP
P150_S861/S865_S8615/865E	SNVNEEWKEMFGELDPPNMPQALP
P150_S861/S865_S853/861E	ENVNEEWKEMFGSLDPPNMPQALP
P150_S861/S865_861/865E_S853	ENVNEEWKEMFGELDPPNMPQALP

S1039

Name	Sequence
P150_S1039_WT	KTTTTRSILTYSRIGGRVKTLTFC
P150_S1039_S1039E	KTTTTRSILTYERIGGRVKTLTFC
P150_S1039_T1037E	KTTTTRSILEYSRIGGRVKTLTFC
P150_S1039_T1039E/S1037E	KTTTTRSILEYERIGGRVKTLTFC
P150_S1039_S1039E/S1034E	KTTTTREILTYERIGGRVKTLTFC
P150_S1039_T1039E/S1031E	KTTTERSILTYERIGGRVKTLTFC

P150_S1039_T1039E/S1030E	KTTETRSILTYERIGGRVKTLTFC
P150_S1039_T1039E/S1029E	KTETTRSILTYERIGGRVKTLTFC
P150_S1039_T1039E/S1028E	KETTTRSILTYERIGGRVKTLTFC

S1289

Name	Sequence
P150_S1289_WT	GSTSSPSVSYYRKIIEGTEVVQEI
P150_S1289_S1289E	GSTSSPSVEYYRKIIEGTEVVQEI
P150_S1289_Y1290pY	GSTSSPSVSYYRKIIEGTEVVQEI
P150_S1289_S1289E/T1298E	GSTSSPSVEYYRKIIEGEEVVQEI
P150_S1289_S1289E_Y1290pY	GSTSSPSVEYYRKIIEGTEVVQEI
P150_S1289_S1289E/S1287E	GSTSSPEVEYYRKIIEGTEVVQEI
P150_S1289_S1289E/S1285E	GSTSEPSVEYYRKIIEGTEVVQEI
P150_S1289_S1289E/S1284E	GSTESPSVEYYRKIIEGTEVVQEI
P150_S1289_S1289E/T1283E	GSESSPSVEYYRKIIEGTEVVQEI
P150_S1289_S1289E/S1282E	GETSSPSVEYYRKIIEGTEVVQEI

B

Controls

Name	Sequence
VPS34_WT	GDESSPILTSFELVKVPDPQMSME
VPS34_S249pS	GDESSPILTSFELVKVPDPQMSME
FYCO1_WT	TDYRPPDDAVFDIITDEELCQIQE

S861/S865

Name	Sequence
P150_S861/S865_WT	SNVNEEWKSMFGSLDPPNMPQALP
P150_S861/S865_S861pS	SNVNEEWKSMFGSLDPPNMPQALP
P150_S861/S865_S865pS	SNVNEEWKSMFGSLDPPNMPQALP
P150_S861/S865_S8615/865pS	SNVNEEWKSMFGSLDPPNMPQALP
P150_S861/S865_861pS_S853E	ENVNEEWKSMFGSLDPPNMPQALP
P150_S861/S865_S861/865pS_S853E	ENVNEEWKSMFGSLDPPNMPQALP

S1039

Name	Sequence

P150_S1039_WT	KTTTTRSILTYSRIGGRVKTLTFC
P150_S1039_S1039pS	KTTTTRSILTYSRIGGRVKTLTFC
P150_S1039_T1037E	KTTTTRSILEYSRIGGRVKTLTFC
P150_S1039_S1039pS_T1037E	KTTTTRSILEYSRIGGRVKTLTFC
P150_S1039_S1039pS_S1034E	KTTTTREILTYSRIGGRVKTLTFC
P150_S1039_S1039pS_T1031E	KTTTERSILTYSRIGGRVKTLTFC
P150_S1039_S1039pS_T1030E	KTTETRSILTYSRIGGRVKTLTFC
P150_S1039_S1039pS_T1029E	KTETTRSILTYSRIGGRVKTLTFC
P150_S1039_S1039pS_T1028E	KETTTRSILTYSRIGGRVKTLTFC

S1289

Name	Sequence
P150_S1289_WT	GSTSSPSVSYYRKIIEGTEVVQEI
P150_S1289_S1289pS	GSTSSPSVSYYRKIIEGTEVVQEI
P150_S1289_Y1290pY	GSTSSPSVSYYRKIIEGTEVVQEI
P150_S1289_S1289pS_T1298E	GSTSSPSVSYYRKIIEGEEVVQEI
P150_S1289_S1289pS_Y1290pY	GSTSSPSVSYYRKIIEGTEVVQEI
P150_S1289_S1289pS_S1287E	GSTSSPEVSYYRKIIEGTEVVQEI
P150_S1289_S1289pS_S1285E	GSTSEPSVSYYRKIIEGTEVVQEI
P150_S1289_S1289pS_S1284E	GSTESPSVSYYRKIIEGTEVVQEI
P150_S1289_S1289pS_T1283E	GSESSPSVSYYRKIIEGTEVVQEI
P150_S1289_S1289pS_S1282E	GETSSPSVSYYRKIIEGTEVVQEI

Reference List

AGROTIS, A., PENGO, N., BURDEN, J. J. & KETTELER, R. 2019a. Redundancy of human ATG4 protease isoforms in autophagy and LC3/GABARAP processing revealed in cells. *Autophagy,* 15**,** 976-997.

AGROTIS, A., VON CHAMIER, L., OLIVER, H., KISO, K., SINGH, T. & KETTELER, R. 2019b. Human ATG4 autophagy proteases counteract attachment of ubiquitin-like LC3/GABARAP proteins to other cellular proteins. *Journal of Biological Chemistry*.

AI, H.-W., SHEN, W., SAGI, A., CHEN, P. R. & SCHULTZ, P. G. 2011. Probing Protein–Protein Interactions with a Genetically Encoded Photo-crosslinking Amino Acid. *ChemBioChem,* 12**,** 1854-1857.

ALBANESI, J., WANG, H., SUN, H.-Q., LEVINE, B. & YIN, H. 2015. GABARAP-mediated targeting of PI4K2A/PI4KIIα to autophagosomes regulates PtdIns4P-dependent autophagosome-lysosome fusion. *Autophagy,* 11**,** 2127-2129.

ALEMU, E. A., LAMARK, T., TORGERSEN, K. M., BIRGISDOTTIR, A. B., LARSEN, K. B., JAIN, A., OLSVIK, H., ØVERVATN, A., KIRKIN, V. & JOHANSEN, T. 2012. ATG8 Family Proteins Act as Scaffolds for Assembly of the ULK Complex: SEQUENCE REQUIREMENTS FOR LC3-INTERACTING REGION (LIR) MOTIFS. *The Journal of Biological Chemistry,* 287**,** 39275-39290.

ALERS, S., LÖFFLER, A. S., PAASCH, F., DIETERLE, A. M., KEPPELER, H., LAUBER, K., CAMPBELL, D. G., FEHRENBACHER, B., SCHALLER, M., WESSELBORG, S. & STORK, B. 2011. Atg13 and FIP200 act independently of Ulk1 and Ulk2 in autophagy induction. *Autophagy,* 7**,** 1424-1433.

ALLAVENA, G., BOYD, C., OO, K. S., MAELLARO, E., ZHIVOTOVSKY, B. & KAMINSKYY, V. O. 2016. Suppressed translation and ULK1 degradation as potential mechanisms of autophagy limitation under prolonged starvation. *Autophagy,* 12**,** 2085-2097.

ALLEN, G. F. G., TOTH, R., JAMES, J. & GANLEY, I. G. 2013. Loss of iron triggers PINK1/Parkin-independent mitophagy. *EMBO reports,* 14**,** 1127-1135.

ALSAADI, R. M., LOSIER, T. T., TIAN, W., JACKSON, A., GUO, Z., RUBINSZTEIN, D. C. & RUSSELL, R. C. 2019. ULK1-mediated phosphorylation of ATG16L1 promotes xenophagy, but destabilizes the ATG16L1 Crohn's mutant. *EMBO reports,* 20**,** e46885.

ALTELAAR, A. F. M., FRESE, C. K., PREISINGER, C., HENNRICH, M. L., SCHRAM, A. W., TIMMERS, H. T. M., HECK, A. J. R. & MOHAMMED, S. 2013. Benchmarking stable isotope labeling based quantitative proteomics. *Journal of Proteomics,* 88**,** 14-26.

ANDING, A. L. & BAEHRECKE, E. H. 2015. Vps15 is required for stress induced and developmentally triggered autophagy and salivary gland protein secretion in Drosophila. *Cell death and differentiation,* 22**,** 457-464.

ANEKAL, P. V., YONG, J. & MANSER, E. 2015. Arg kinase-binding protein 2 (ArgBP2) interaction with α-actinin and actin stress fibers inhibits cell migration. *The Journal of biological chemistry,* 290**,** 2112-2125.

ANTONIOLI, M., ALBIERO, F., NAZIO, F., VESCOVO, T., PERDOMO, ARIEL B., CORAZZARI, M., MARSELLA, C., PISELLI, P., GRETZMEIER, C., DENGJEL, J., CECCONI, F., PIACENTINI, M. & FIMIA, GIAN M. 2014. AMBRA1 Interplay with Cullin E3 Ubiquitin Ligases Regulates Autophagy Dynamics. *Developmental Cell,* 31**,** 734-746.

ANWAR, T., LIU, X., SUNTIO, T., MARJAMÄKI, A., BIAZIK, J., CHAN, E. Y. W., VARJOSALO, M. & ESKELINEN, E.-L. 2019. ER-Targeted Beclin 1 Supports Autophagosome Biogenesis in the Absence of ULK1 and ULK2 Kinases. *Cells,* 8**,** 475.

ARIAS, E., KOGA, H., DIAZ, A., MOCHOLI, E., PATEL, B. & CUERVO, A. M. 2015. Lysosomal mTORC2/PHLPP1/Akt Regulate Chaperone-Mediated Autophagy. *Mol Cell,* 59**,** 270-84.

ARSTILA, A. U. A. T., B.F. 1968. Studies on Cellular autophagocytosis. *Amer J Pathol,* 53**,** 687 - 733.

ASHKENAZI, A., BENTO, C. F., RICKETTS, T., VICINANZA, M., SIDDIQI, F., PAVEL, M., SQUITIERI, F., HARDENBERG, M. C., IMARISIO, S., MENZIES, F. M. & RUBINSZTEIN, D. C. 2017. Polyglutamine tracts regulate beclin 1-dependent autophagy. *Nature,* 545**,** 108-111.

AXE, E. L., WALKER, S. A., MANIFAVA, M., CHANDRA, P., RODERICK, H. L., HABERMANN, A., GRIFFITHS, G. & KTISTAKIS, N. T. 2008. Autophagosome formation from membrane compartments enriched in phosphatidylinositol 3-phosphate and dynamically connected to the endoplasmic reticulum. *J Cell Biol,* 182**,** 685-701.

BABA, M., OSUMI, M., SCOTT, S. V., KLIONSKY, D. J. & OHSUMI, Y. 1997. Two distinct pathways for targeting proteins from the cytoplasm to the vacuole/lysosome. *The Journal of cell biology,* 139**,** 1687-1695.

BACH, M., LARANCE, M., JAMES, D. E. & RAMM, G. 2011. The serine/threonine kinase ULK1 is a target of multiple phosphorylation events. *Biochemical Journal,* 440**,** 283.

BACKER, JONATHAN M. 2008. The regulation and function of Class III PI3Ks: novel roles for Vps34. *Biochemical Journal,* 410**,** 1.

BACKER, JONATHAN M. 2016. The intricate regulation and complex functions of the Class III phosphoinositide 3-kinase Vps34. *Biochemical Journal,* 473**,** 2251.

BAGO, R., MALIK, N., MUNSON, M. J., PRESCOTT, A. R., DAVIES, P., SOMMER, E., SHPIRO, N., WARD, R., CROSS, D., GANLEY, I. G. & ALESSI, D. R. 2014. Characterization of VPS34-IN1, a selective inhibitor of Vps34, reveals that the phosphatidylinositol 3-phosphate-binding SGK3 protein kinase is a downstream target of class III phosphoinositide 3-kinase. *The Biochemical journal,* 463**,** 413-427.

BAIN, J. D., SWITZER, C., CHAMBERLIN, R. & BENNER, S. A. 1992. Ribosome-mediated incorporation of a non-standard amino acid into a peptide through expansion of the genetic code. *Nature,* 356**,** 537-539.

BAKER, R. W. & HUGHSON, F. M. 2016. Chaperoning SNARE assembly and disassembly. *Nature Reviews Molecular Cell Biology,* 17**,** 465.

BALDERHAAR, H. J. K. & UNGERMANN, C. 2013. CORVET and HOPS tethering complexes – coordinators of endosome and lysosome fusion. *Journal of Cell Science,* 126**,** 1307.

BANDYOPADHYAY, U., KAUSHIK, S., VARTICOVSKI, L. & CUERVO, A. M. 2008. The chaperone-mediated autophagy receptor organizes in dynamic protein complexes at the lysosomal membrane. *Molecular and cellular biology,* 28**,** 5747-5763.

BANDYOPADHYAY, U., SRIDHAR, S., KAUSHIK, S., KIFFIN, R. & CUERVO, A. M. 2010. Identification of regulators of chaperone-mediated autophagy. *Molecular cell,* 39**,** 535-547.

BAR-PELED, L., CHANTRANUPONG, L., CHERNIACK, A. D., CHEN, W. W., OTTINA, K. A., GRABINER, B. C., SPEAR, E. D., CARTER, S. L., MEYERSON, M. & SABATINI, D. M. 2013. A Tumor suppressor complex with GAP activity for the Rag GTPases that signal amino acid sufficiency to mTORC1. *Science (New York, N.Y.),* 340**,** 1100-1106.

BAR-PELED, L., SCHWEITZER, L. D., ZONCU, R. & SABATINI, D. M. 2012. Ragulator is a GEF for the rag GTPases that signal amino acid levels to mTORC1. *Cell,* 150**,** 1196-1208.

BASKARAN, S., CARLSON, L. A., STJEPANOVIC, G., YOUNG, L. N., KIM DO, J., GROB, P., STANLEY, R. E., NOGALES, E. & HURLEY, J. H. 2014. Architecture and dynamics of the autophagic phosphatidylinositol 3-kinase complex. *Elife,* 3.

BAUDOT, A. D., HALLER, M., MRSCHTIK, M., TAIT, S. W. G. & RYAN, K. M. 2015. Using enhanced-mitophagy to measure autophagic flux. *Methods (San Diego, Calif.),* 75**,** 105-111.

BEHRENDS, C., SOWA, M. E., GYGI, S. P. & HARPER, J. W. 2010. Network organization of the human autophagy system. *Nature,* 466**,** 68-76.

BHARADWAJ, R., CUNNINGHAM, K. M., ZHANG, K. & LLOYD, T. E. 2016. FIG4 regulates lysosome membrane homeostasis independent of phosphatase function. *Human molecular genetics,* 25**,** 681-692.

BIANCO, A., TOWNSLEY, F. M., GREISS, S., LANG, K. & CHIN, J. W. 2012. Expanding the genetic code of Drosophila melanogaster. *Nature Chemical Biology,* 8**,** 748.

BIAZIK, J., YLA-ANTTILA, P., VIHINEN, H., JOKITALO, E. & ESKELINEN, E. L. 2015. Ultrastructural relationship of the phagophore with surrounding organelles. *Autophagy,* 11**,** 439-51.

BIRGISDOTTIR, Å. B., LAMARK, T. & JOHANSEN, T. 2013. The LIR motif – crucial for selective autophagy. *Journal of Cell Science,* 126**,** 3237.

BIRGISDOTTIR, Å. B., MOUILLERON, S., BHUJABAL, Z., WIRTH, M., SJØTTEM, E., EVJEN, G., ZHANG, W., LEE, R., O'REILLY, N., TOOZE, S. A., LAMARK, T. & JOHANSEN, T. 2019. Members of the autophagy class III phosphatidylinositol 3-kinase complex I interact with GABARAP and GABARAPL1 via LIR motifs. *Autophagy,* 15**,** 1333-1355.

BJØRKØY, G., LAMARK, T., BRECH, A., OUTZEN, H., PERANDER, M., OVERVATN, A., STENMARK, H. & JOHANSEN, T. 2005. p62/SQSTM1 forms protein aggregates degraded by autophagy and has a protective effect on huntingtin-induced cell death. *The Journal of cell biology,* 171**,** 603-614.

BLIGHT, S. K., LARUE, R. C., MAHAPATRA, A., LONGSTAFF, D. G., CHANG, E., ZHAO, G., KANG, P. T., GREEN-CHURCH, K. B., CHAN, M. K. & KRZYCKI, J. A. 2004. Direct charging of tRNACUA with pyrrolysine in vitro and in vivo. *Nature,* 431**,** 333-335.

BODEMANN, B. O., ORVEDAHL, A., CHENG, T., RAM, R. R., OU, Y. H., FORMSTECHER, E., MAITI, M., HAZELETT, C. C., WAUSON, E. M., BALAKIREVA, M., CAMONIS, J. H., YEAMAN, C., LEVINE, B. & WHITE, M. A. 2011. RalB and the exocyst mediate the cellular starvation response by direct activation of autophagosome assembly. *Cell,* 144**,** 253-67.

BOZIC, M., VAN DEN BEKEROM, L., MILNE, B. A., GOODMAN, N., ROBERSTON, L., PRESCOTT, A. R., MACARTNEY, T. J., DAWE, N. & MCEWAN, D. G. 2019. A conserved ATG2-GABARAP interaction is critical for phagophore closure. *bioRxiv***,** 624627.

BRENNER, S. 1974. The genetics of Caenorhabditis elegans. *Genetics,* 77**,** 71-94.

BRIER, L. W., GE, L., STJEPANOVIC, G., THELEN, A. M., HURLEY, J. H. & SCHEKMAN, R. 2019. Regulation of LC3 lipidation by the autophagy-specific class III phosphatidylinositol-3 kinase complex. *Molecular Biology of the Cell,* 30**,** 1098-1107.

BROWN, W., LIU, J. & DEITERS, A. 2018. Genetic Code Expansion in Animals. *ACS Chemical Biology,* 13**,** 2375-2386.

BUGARCIC, A., ZHE, Y., KERR, M. C., GRIFFIN, J., COLLINS, B. M. & TEASDALE, R. D. 2011. Vps26A and Vps26B Subunits Define Distinct Retromer Complexes. *Traffic,* 12**,** 1759-1773.

BUSSE, RICARDA A., SCACIOC, A., KRICK, R., PÉREZ-LARA, Á., THUMM, M. & KÜHNEL, K. 2015. Characterization of PROPPIN-Phosphoinositide Binding and Role of Loop 6CD in PROPPIN-Membrane Binding. *Biophysical Journal,* 108**,** 2223-2234.

BYFIELD, M. P., MURRAY, J. T. & BACKER, J. M. 2005. hVps34 Is a Nutrient-regulated Lipid Kinase Required for Activation of p70 S6 Kinase. *Journal of Biological Chemistry,* 280**,** 33076-33082.

CAO, Y., BOJJIREDDY, N., KIM, M., LI, T., ZHAI, P., NAGARAJAN, N., SADOSHIMA, J., PALMITER, R. D. & TIAN, R. 2017. Activation of gamma2-AMPK Suppresses Ribosome Biogenesis and Protects Against Myocardial Ischemia/Reperfusion Injury. *Circ Res,* 121**,** 1182-1191.

CARLOS MARTÍN ZOPPINO, F., DAMIÁN MILITELLO, R., SLAVIN, I., ÁLVAREZ, C. & COLOMBO, M. I. 2010. Autophagosome Formation Depends on the Small GTPase Rab1 and Functional ER Exit Sites. *Traffic,* 11**,** 1246-1261.

CARROLL, B. & DUNLOP, E. A. 2017. The lysosome: a crucial hub for AMPK and mTORC1 signalling. *Biochemical Journal,* 474**,** 1453.

CARROLL, B., MOHD-NAIM, N., MAXIMIANO, F., FRASA, M. A., MCCORMACK, J., FINELLI, M., THORESEN, S. B., PERDIOS, L., DAIGAKU, R., FRANCIS, R. E., FUTTER, C., DIKIC, I. & BRAGA, V. M. M. 2013. The TBC/RabGAP Armus coordinates Rac1 and Rab7 functions during autophagy. *Developmental cell,* 25**,** 15-28.

CEBOLLERO, E., VAN DER VAART, A., ZHAO, M., RIETER, E., KLIONSKY, DANIEL J., HELMS, J. B. & REGGIORI, F. 2012. Phosphatidylinositol-3-Phosphate Clearance Plays a Key Role in Autophagosome Completion. *Current Biology,* 22**,** 1545-1553.

CESTRA, G., TOOMRE, D., CHANG, S. & DE CAMILLI, P. 2005. The Abl/Arg substrate ArgBP2/nArgBP2 coordinates the function of multiple regulatory mechanisms converging on the actin cytoskeleton. *Proceedings of the National Academy of Sciences of the United States of America,* 102**,** 1731-1736.

CHAN, E. Y., LONGATTI, A., MCKNIGHT, N. C. & TOOZE, S. A. 2009. Kinase-inactivated ULK proteins inhibit autophagy via their conserved C-terminal domains using an Atg13-independent mechanism. *Mol Cell Biol,* 29**,** 157-71.

CHAN, E. Y. W., KIR, S. & TOOZE, S. A. 2007. siRNA screening of the kinome identifies ULK1 as a multi-domain modulator of autophagy. *J. Biol. Chem.,* 282**,** 25464-25474.

CHANG, C., YOUNG, L. N., MORRIS, K. L., VON BÜLOW, S., SCHÖNEBERG, J., YAMAMOTO-IMOTO, H., OE, Y., YAMAMOTO, K., NAKAMURA, S., STJEPANOVIC, G., HUMMER, G., YOSHIMORI, T. & HURLEY, J. H. 2019. Bidirectional Control of Autophagy by BECN1 BARA Domain Dynamics. *Molecular Cell,* 73**,** 339-353.e6.

CHANOCA, A., KOVINICH, N., BURKEL, B., STECHA, S., BOHORQUEZ-RESTREPO, A., UEDA, T., ELICEIRI, K. W., GROTEWOLD, E. & OTEGUI, M. S. 2015. Anthocyanin Vacuolar Inclusions Form by a Microautophagy Mechanism. *The Plant cell,* 27**,** 2545-2559.

CHEN, C., HUANG, Q.-L., JIANG, S.-H., PAN, X. & HUA, Z.-C. 2006. Immobilized protein ZZ, an affinity tool for immunoglobulin isolation and immunological experimentation. *Biotechnology and Applied Biochemistry,* 45**,** 87-92.

CHEN, D., FAN, W., LU, Y., DING, X., CHEN, S. & ZHONG, Q. 2012. A mammalian autophagosome maturation mechanism mediated by TECPR1 and the Atg12-Atg5 conjugate. *Molecular cell,* 45**,** 629-641.

CHEN, G. C., LEE, J. Y., TANG, H. W., DEBNATH, J., THOMAS, S. M. & SETTLEMAN, J. 2008. Genetic interactions between Drosophila melanogaster Atg1 and paxillin reveal a role for paxillin in autophagosome formation. *Autophagy,* 4**,** 37-45.

CHEN, H.-K., JI, Z.-S., DODSON, S. E., MIRANDA, R. D., ROSENBLUM, C. I., REYNOLDS, I. J., FREEDMAN, S. B., WEISGRABER, K. H., HUANG, Y. & MAHLEY, R. W. 2011. Apolipoprotein E4 domain interaction mediates

detrimental effects on mitochondria and is a potential therapeutic target for Alzheimer disease. *The Journal of biological chemistry,* 286**,** 5215-5221.
CHEN, S., WANG, C., YEO, S., LIANG, C.-C., OKAMOTO, T., SUN, S., WEN, J. & GUAN, J.-L. 2016. Distinct roles of autophagy-dependent and -independent functions of FIP200 revealed by generation and analysis of a mutant knock-in mouse model. *Genes & Development,* 30**,** 856-869.
CHEN, X., BARTON, L. F., CHI, Y., CLURMAN, B. E. & ROBERTS, J. M. 2007. Ubiquitin-independent degradation of cell-cycle inhibitors by the REGgamma proteasome. *Molecular cell,* 26**,** 843-852.
CHEN, Y.-D., FANG, Y.-T., CHANG, C.-P., LIN, C.-F., HSU, L.-J., WU, S.-R., CHIU, Y.-C., ANDERSON, R. & LIN, Y.-S. 2017. S100A10 Regulates ULK1 Localization to ER–Mitochondria Contact Sites in IFN-γ-Triggered Autophagy. *Journal of Molecular Biology,* 429**,** 142-157.
CHENG, J., FUJITA, A., YAMAMOTO, H., TATEMATSU, T., KAKUTA, S., OBARA, K., OHSUMI, Y. & FUJIMOTO, T. 2014. Yeast and mammalian autophagosomes exhibit distinct phosphatidylinositol 3-phosphate asymmetries. *Nature Communications,* 5**,** 3207.
CHENG, L., PISITKUN, T., KNEPPER, M. A. & HOFFERT, J. D. 2016. Peptide Labeling Using Isobaric Tagging Reagents for Quantitative Phosphoproteomics. *Methods in molecular biology (Clifton, N.J.),* 1355**,** 53-70.
CHEONG, H., WU, J., GONZALES, L. K., GUTTENTAG, S. H., THOMPSON, C. B. & LINDSTEN, T. 2014. Analysis of a lung defect in autophagy-deficient mouse strains. *Autophagy,* 10**,** 45-56.
CHEUNG, P. C., SALT, I. P., DAVIES, S. P., HARDIE, D. G. & CARLING, D. 2000. Characterization of AMP-activated protein kinase gamma-subunit isoforms and their role in AMP binding. *Biochem J,* 346 Pt 3**,** 659-69.
CHIN, J. W. 2014. Expanding and Reprogramming the Genetic Code of Cells and Animals. *Annual Review of Biochemistry,* 83**,** 379-408.
CHIN, J. W., CROPP, T. A., ANDERSON, J. C., MUKHERJI, M., ZHANG, Z. & SCHULTZ, P. G. 2003. An Expanded Eukaryotic Genetic Code. *Science,* 301**,** 964.
CHIN, J. W., MARTIN, A. B., KING, D. S., WANG, L. & SCHULTZ, P. G. 2002. Addition of a photocrosslinking amino acid to the genetic code of Escherichia coli. *Proceedings of the National Academy of Sciences,* 99**,** 11020.
CHOU, C., UPRETY, R., DAVIS, L., W. CHIN, J. & DEITERS, A. 2011. Genetically encoding an aliphatic diazirine for protein photocrosslinking. *Chem. Sci.,* 2**,** 480-483.
CHOWDHURY, S., OTOMO, C., LEITNER, A., OHASHI, K., AEBERSOLD, R., LANDER, G. C. & OTOMO, T. 2018. Insights into autophagosome biogenesis from structural and biochemical analyses of the ATG2A-WIPI4 complex. *Proceedings of the National Academy of Sciences of the United States of America,* 115**,** E9792-E9801.
CHRISTOFORIDIS, S., MIACZYNSKA, M., ASHMAN, K., WILM, M., ZHAO, L., YIP, S.-C., WATERFIELD, M. D., BACKER, J. M. & ZERIAL, M. 1999. Phosphatidylinositol-3-OH kinases are Rab5 effectors. *Nature Cell Biology,* 1**,** 249-252.
CLARK, S. L., JR. 1957. Cellular Differentiation in the kidneys of newborn mice studies with the electron microscope. *J. Cell Biol.,* 3**,** 349-362.
COLLINS, G. A. & GOLDBERG, A. L. 2017. The Logic of the 26S Proteasome. *Cell,* 169**,** 792-806.
COMPTON, L. M., IKONOMOV, O. C., SBRISSA, D., GARG, P. & SHISHEVA, A. 2016. Active vacuolar H+ ATPase and functional cycle of Rab5 are required for

the vacuolation defect triggered by PtdIns(3,5)P2 loss under PIKfyve or Vps34 deficiency. *American Journal of Physiology-Cell Physiology,* 311**,** C366-C377.
COX, J. & MANN, M. 2008. MaxQuant enables high peptide identification rates, individualized p.p.b.-range mass accuracies and proteome-wide protein quantification. *Nature Biotechnology,* 26**,** 1367.
COX, J., MATIC, I., HILGER, M., NAGARAJ, N., SELBACH, M., OLSEN, J. V. & MANN, M. 2009. A practical guide to the MaxQuant computational platform for SILAC-based quantitative proteomics. *Nature Protocols,* 4**,** 698.
CROTZER, V. L. & BLUM, J. S. 2009. Autophagy and its role in MHC-mediated antigen presentation. *Journal of immunology (Baltimore, Md. : 1950),* 182**,** 3335-3341.
CUERVO, A. M., KNECHT, E., TERLECKY, S. R. & DICE, J. F. 1995. Activation of a selective pathway of lysosomal proteolysis in rat liver by prolonged starvation. *Am J Physiol,* 269**,** C1200-8.
CUNNINGHAM, C. N., BAUGHMAN, J. M., PHU, L., TEA, J. S., YU, C., COONS, M., KIRKPATRICK, D. S., BINGOL, B. & CORN, J. E. 2015. USP30 and parkin homeostatically regulate atypical ubiquitin chains on mitochondria. *Nature Cell Biology,* 17**,** 160.
DASKALAKI, I., GKIKAS, I. & TAVERNARAKIS, N. 2018. Hypoxia and Selective Autophagy in Cancer Development and Therapy. *Frontiers in Cell and Developmental Biology,* 6.
DAVIES, A. K., ITZHAK, D. N., EDGAR, J. R., ARCHULETA, T. L., HIRST, J., JACKSON, L. P., ROBINSON, M. S. & BORNER, G. H. H. 2018. AP-4 vesicles contribute to spatial control of autophagy via RUSC-dependent peripheral delivery of ATG9A. *Nature communications,* 9**,** 3958-3958.
DAVIS, S., WANG, J., ZHU, M., STAHMER, K., LAKSHMINARAYAN, R., GHASSEMIAN, M., JIANG, Y., MILLER, E. A. & FERRO-NOVICK, S. 2016. Sec24 phosphorylation regulates autophagosome abundance during nutrient deprivation. *eLife,* 5**,** e21167.
DE DUVE, C. 1963. The lysosome. *Sci Am,* 208**,** 64-72.
DE DUVE, C., PRESSMAN, B. C., GIANETTO, R., WATTIAUX, R. & APPELMANS, F. 1955. Tissue fractionation studies. 6. Intracellular distribution patterns of enzymes in rat-liver tissue. *Biochem J,* 60**,** 604-17.
DE LA BALLINA, L. R., MUNSON, M. J. & SIMONSEN, A. 2019. Lipids and Lipid-Binding Proteins in Selective Autophagy. *Journal of Molecular Biology*.
DENG, Z., PURTELL, K., LACHANCE, V., WOLD, M. S., CHEN, S. & YUE, Z. 2017. Autophagy Receptors and Neurodegenerative Diseases. *Trends in Cell Biology,* 27**,** 491-504.
DEPHOURE, N., ZHOU, C., VILLÉN, J., BEAUSOLEIL, S. A., BAKALARSKI, C. E., ELLEDGE, S. J. & GYGI, S. P. 2008. A quantitative atlas of mitotic phosphorylation. *Proceedings of the National Academy of Sciences of the United States of America,* 105**,** 10762-10767.
DESAI, C., GARRIGA, G., MCLNTIRE, S. L. & HORVITZ, H. R. 1988. A genetic pathway for the development of the Caenorhabditis elegans HSN motor neurons. *Nature,* 336**,** 638-646.
DEVEREAUX, K., DALL'ARMI, C., ALCAZAR-ROMAN, A., OGASAWARA, Y., ZHOU, X., WANG, F., YAMAMOTO, A., DE CAMILLI, P. & DI PAOLO, G. 2013. Regulation of mammalian autophagy by class II and III PI 3-kinases through PI3P synthesis. *PloS one,* 8**,** e76405-e76405.
DI BARTOLOMEO, S., CORAZZARI, M., NAZIO, F., OLIVERIO, S., LISI, G., ANTONIOLI, M., PAGLIARINI, V., MATTEONI, S., FUOCO, C., GIUNTA, L., AMELIO, M., NARDACCI, R., ROMAGNOLI, A., PIACENTINI, M., CECCONI, F. & FIMIA, G. M. 2010. The dynamic interaction of AMBRA1 with the dynein

motor complex regulates mammalian autophagy. *The Journal of Cell Biology,* 191**,** 155.

DI RIENZO, M., ANTONIOLI, M., FUSCO, C., LIU, Y., MARI, M., ORHON, I., REFOLO, G., GERMANI, F., CORAZZARI, M., ROMAGNOLI, A., CICCOSANTI, F., MANDRIANI, B., PELLICO, M. T., DE LA TORRE, R., DING, H., DENTICE, M., NERI, M., FERLINI, A., REGGIORI, F., KULESZ-MARTIN, M., PIACENTINI, M., MERLA, G. & FIMIA, G. M. 2019. Autophagy induction in atrophic muscle cells requires ULK1 activation by TRIM32 through unanchored K63-linked polyubiquitin chains. *Science advances,* 5**,** eaau8857-eaau8857.

DIAO, J., LIU, R., RONG, Y., ZHAO, M., ZHANG, J., LAI, Y., ZHOU, Q., WILZ, L. M., LI, J., VIVONA, S., PFUETZNER, R. A., BRUNGER, A. T. & ZHONG, Q. 2015. ATG14 promotes membrane tethering and fusion of autophagosomes to endolysosomes. *Nature,* 520**,** 563-566.

DITE, T. A., LING, N. X. Y., SCOTT, J. W., HOQUE, A., GALIC, S., PARKER, B. L., NGOEI, K. R. W., LANGENDORF, C. G., O'BRIEN, M. T., KUNDU, M., VIOLLET, B., STEINBERG, G. R., SAKAMOTO, K., KEMP, B. E. & OAKHILL, J. S. 2017. The autophagy initiator ULK1 sensitizes AMPK to allosteric drugs. *Nature Communications,* 8**,** 571.

DOOLEY, H. C., RAZI, M., POLSON, H. E., GIRARDIN, S. E., WILSON, M. I. & TOOZE, S. A. 2014. WIPI2 links LC3 conjugation with PI3P, autophagosome formation, and pathogen clearance by recruiting Atg12-5-16L1. *Mol Cell,* 55**,** 238-52.

DORSEY, F. C., ROSE, K. L., COENEN, S., PRATER, S. M., CAVETT, V., CLEVELAND, J. L. & CALDWELL-BUSBY, J. 2009. Mapping the Phosphorylation Sites of Ulk1. *Journal of Proteome Research,* 8**,** 5253-5263.

DRIESSE, S., BERLETH, N., FRIESEN, O., LÖFFLER, A. S., BÖHLER, P., HIEKE, N., STUHLDREIER, F., PETER, C., SCHINK, K. O., SCHULTZ, S. W., STENMARK, H., HOLLAND, P., SIMONSEN, A., WESSELBORG, S. & STORK, B. 2015. Deubiquitinase inhibition by WP1130 leads to ULK1 aggregation and blockade of autophagy. *Autophagy,* 11**,** 1458-1470.

DU, W., SU, QIAN P., CHEN, Y., ZHU, Y., JIANG, D., RONG, Y., ZHANG, S., ZHANG, Y., REN, H., ZHANG, C., WANG, X., GAO, N., WANG, Y., SUN, L., SUN, Y. & YU, L. 2016. Kinesin 1 Drives Autolysosome Tubulation. *Developmental Cell,* 37**,** 326-336.

DUBINSKY, L., KROM, B. P. & MEIJLER, M. M. 2012. Diazirine based photoaffinity labeling. *Bioorganic & Medicinal Chemistry,* 20**,** 554-570.

DUKE, E. M., RAZI, M., WESTON, A., GUTTMANN, P., WERNER, S., HENZLER, K., SCHNEIDER, G., TOOZE, S. A. & COLLINSON, L. M. 2014. Imaging endosomes and autophagosomes in whole mammalian cells using correlative cryo-fluorescence and cryo-soft X-ray microscopy (cryo-CLXM). *Ultramicroscopy,* 143**,** 77-87.

DUNLOP, E. A., HUNT, D. K., ACOSTA-JAQUEZ, H. A., FINGAR, D. C. & TEE, A. R. 2011. ULK1 inhibits mTORC1 signaling, promotes multisite Raptor phosphorylation and hinders substrate binding. *Autophagy,* 7**,** 737-747.

DUNLOP, E. A., SEIFAN, S., CLAESSENS, T., BEHRENDS, C., KAMPS, M. A. F., ROZYCKA, E., KEMP, A. J., NOOKALA, R. K., BLENIS, J., COULL, B. J., MURRAY, J. T., VAN STEENSEL, M. A. M., WILKINSON, S. & TEE, A. R. 2014. FLCN, a novel autophagy component, interacts with GABARAP and is regulated by ULK1 phosphorylation. *Autophagy,* 10**,** 1749-1760.

DUPONT, N., NASCIMBENI, A. C., MOREL, E. & CODOGNO, P. 2017. Chapter One - Molecular Mechanisms of Noncanonical Autophagy. *In:* GALLUZZI, L. (ed.) *International Review of Cell and Molecular Biology.* Academic Press.

DWANE, L., GALLAGHER, W. M., NÍ CHONGHAILE, T. & O'CONNOR, D. P. 2017. The Emerging Role of Non-traditional Ubiquitination in Oncogenic Pathways. *The Journal of biological chemistry,* 292**,** 3543-3551.

DYCZYNSKI, M., YU, Y., OTROCKA, M., PARPAL, S., BRAGA, T., HENLEY, A. B., ZAZZI, H., LERNER, M., WENNERBERG, K., VIKLUND, J., MARTINSSON, J., GRANDÉR, D., DE MILITO, A. & POKROVSKAJA TAMM, K. 2018. Targeting autophagy by small molecule inhibitors of vacuolar protein sorting 34 (Vps34) improves the sensitivity of breast cancer cells to Sunitinib. *Cancer Letters,* 435**,** 32-43.

EGAN, D. F., CHUN, M. G., VAMOS, M., ZOU, H., RONG, J., MILLER, C. J., LOU, H. J., RAVEENDRA-PANICKAR, D., YANG, C. C., SHEFFLER, D. J., TERIETE, P., ASARA, J. M., TURK, B. E., COSFORD, N. D. & SHAW, R. J. 2015. Small Molecule Inhibition of the Autophagy Kinase ULK1 and Identification of ULK1 Substrates. *Mol Cell,* 59**,** 285-97.

EGAN, D. F., SHACKELFORD, D. B., MIHAYLOVA, M. M., GELINO, S., KOHNZ, R. A., MAIR, W., VASQUEZ, D. S., JOSHI, A., GWINN, D. M., TAYLOR, R., ASARA, J. M., FITZPATRICK, J., DILLIN, A., VIOLLET, B., KUNDU, M., HANSEN, M. & SHAW, R. J. 2011. Phosphorylation of ULK1 (hATG1) by AMP-Activated Protein Kinase Connects Energy Sensing to Mitophagy. *Science,* 331**,** 456-461.

ENDICOTT, J. A., NOBLE, M. E. & JOHNSON, L. N. 2012. The structural basis for control of eukaryotic protein kinases. *Annu Rev Biochem,* 81**,** 587-613.

ERNST, R. J., KROGAGER, T. P., MAYWOOD, E. S., ZANCHI, R., BERÁNEK, V., ELLIOTT, T. S., BARRY, N. P., HASTINGS, M. H. & CHIN, J. W. 2016. Genetic code expansion in the mouse brain. *Nature Chemical Biology,* 12**,** 776.

ESKELINEN, E.-L., REGGIORI, F., BABA, M., KOVÁCS, A. L. & SEGLEN, P. O. 2011. Seeing is believing: The impact of electron microscopy on autophagy research. *Autophagy,* 7**,** 935-956.

EVERLEY, R. A., KUNZ, R. C., MCALLISTER, F. E. & GYGI, S. P. 2013. Increasing Throughput in Targeted Proteomics Assays: 54-Plex Quantitation in a Single Mass Spectrometry Run. *Analytical Chemistry,* 85**,** 5340-5346.

FAN, W., NASSIRI, A. & ZHONG, Q. 2011. Autophagosome targeting and membrane curvature sensing by Barkor/Atg14(L). *Proceedings of the National Academy of Sciences,* 108**,** 7769-7774.

FARG, M. A., SUNDARAMOORTHY, V., SULTANA, J. M., YANG, S., ATKINSON, R. A. K., LEVINA, V., HALLORAN, M. A., GLEESON, P. A., BLAIR, I. P., SOO, K. Y., KING, A. E. & ATKIN, J. D. 2014. C9ORF72, implicated in amytrophic lateral sclerosis and frontotemporal dementia, regulates endosomal trafficking. *Human molecular genetics,* 23**,** 3579-3595.

FASS, E., SHVETS, E., DEGANI, I., HIRSCHBERG, K. & ELAZAR, Z. 2006. Microtubules support production of starvation-induced autophagosomes but not their targeting and fusion with lysosomes. *J. Biol. Chem.,* 281**,** 36303-36316.

FERNÁNDEZ-BUSNADIEGO, R., SAHEKI, Y. & DE CAMILLI, P. 2015. Three-dimensional architecture of extended synaptotagmin-mediated endoplasmic reticulum-plasma membrane contact sites. *Proceedings of the National Academy of Sciences of the United States of America,* 112**,** E2004-E2013.

FERREIRA, J. V., SOARES, A. R., RAMALHO, J. S., PEREIRA, P. & GIRAO, H. 2015. K63 linked ubiquitin chain formation is a signal for HIF1A degradation by Chaperone-Mediated Autophagy. *Scientific reports,* 5**,** 10210-10210.

FILIMONENKO, M., STUFFERS, S., RAIBORG, C., YAMAMOTO, A., MALERØD, L., FISHER, E. M. C., ISAACS, A., BRECH, A., STENMARK, H. & SIMONSEN, A. 2007. Functional multivesicular bodies are required for autophagic clearance of

protein aggregates associated with neurodegenerative disease. *The Journal of cell biology,* 179**,** 485-500.
FODA, Z. H., SHAN, Y., KIM, E. T., SHAW, D. E. & SEELIGER, M. A. 2015. A dynamically coupled allosteric network underlies binding cooperativity in Src kinase. *Nature communications,* 6**,** 5939-5939.
FOUILLEN, L., MANETA-PEYRET, L. & MOREAU, P. 2018. ER Membrane Lipid Composition and Metabolism: Lipidomic Analysis.
FU, M. M., NIRSCHL, J. J. & HOLZBAUR, E. L. 2014. LC3 binding to the scaffolding protein JIP1 regulates processive dynein-driven transport of autophagosomes. *Dev Cell,* 29**,** 577-90.
FUJIKAKE, N., SHIN, M. & SHIMIZU, S. 2018. Association Between Autophagy and Neurodegenerative Diseases. *Frontiers in neuroscience,* 12**,** 255-255.
FUJIOKA, Y., SUZUKI, S. W., YAMAMOTO, H., KONDO-KAKUTA, C., KIMURA, Y., HIRANO, H., AKADA, R., INAGAKI, F., OHSUMI, Y. & NODA, N. N. 2014. Structural basis of starvation-induced assembly of the autophagy initiation complex. *Nature Structural &Amp; Molecular Biology,* 21**,** 513.
FUJITA, N., HAYASHI-NISHINO, M., FUKUMOTO, H., OMORI, H., YAMAMOTO, A., NODA, T. & YOSHIMORI, T. 2008a. An Atg4B Mutant Hampers the Lipidation of LC3 Paralogues and Causes Defects in Autophagosome Closure. *Mol. Biol. Cell,* 19**,** 4651-4659.
FUJITA, N., ITOH, T., OMORI, H., FUKUDA, M., NODA, T. & YOSHIMORI, T. 2008b. The Atg16L Complex Specifies the Site of LC3 Lipidation for Membrane Biogenesis in Autophagy. *Mol. Biol. Cell,* 19**,** 2092-2100.
FUJITA, N., MORITA, E., ITOH, T., TANAKA, A., NAKAOKA, M., OSADA, Y., UMEMOTO, T., SAITOH, T., NAKATOGAWA, H., KOBAYASHI, S., HARAGUCHI, T., GUAN, J.-L., IWAI, K., TOKUNAGA, F., SAITO, K., ISHIBASHI, K., AKIRA, S., FUKUDA, M., NODA, T. & YOSHIMORI, T. 2013. Recruitment of the autophagic machinery to endosomes during infection is mediated by ubiquitin. *The Journal of Cell Biology,* 203**,** 115.
FUJIWARA, N., USUI, T., OHAMA, T. & SATO, K. 2016. Regulation of Beclin 1 Protein Phosphorylation and Autophagy by Protein Phosphatase 2A (PP2A) and Death-associated Protein Kinase 3 (DAPK3). *The Journal of Biological Chemistry,* 291**,** 10858-10866.
FURUSE, M., ODA, Y., HIGASHI, T., IWAMOTO, N. & MASUDA, S. 2012. Lipolysis-stimulated lipoprotein receptor: a novel membrane protein of tricellular tight junctions. *Annals of the New York Academy of Sciences,* 1257**,** 54-58.
GALLUZZI, L., PIETROCOLA, F., BRAVO-SAN PEDRO, J. M., AMARAVADI, R. K., BAEHRECKE, E. H., CECCONI, F., CODOGNO, P., DEBNATH, J., GEWIRTZ, D. A., KARANTZA, V., KIMMELMAN, A., KUMAR, S., LEVINE, B., MAIURI, M. C., MARTIN, S. J., PENNINGER, J., PIACENTINI, M., RUBINSZTEIN, D. C., SIMON, H.-U., SIMONSEN, A., THORBURN, A. M., VELASCO, G., RYAN, K. M. & KROEMER, G. 2015. Autophagy in malignant transformation and cancer progression. *The EMBO journal,* 34**,** 856-880.
GAMMOH, N., FLOREY, O., OVERHOLTZER, M. & JIANG, X. 2013. Interaction between FIP200 and ATG16L1 distinguishes ULK1 complex-dependent and -independent autophagy. *Nat Struct Mol Biol,* 20**,** 144-9.
GAN, W., ZHANG, C., SIU, K. Y., SATOH, A., TANNER, J. A. & YU, S. 2017. ULK1 phosphorylates Sec23A and mediates autophagy-induced inhibition of ER-to-Golgi traffic. *BMC Cell Biology,* 18**,** 22.
GANLEY, I. G., LAM, D. H., WANG, J., DING, X., CHEN, S. & JIANG, X. 2009. ULK1·ATG13·FIP200 Complex Mediates mTOR Signaling and Is Essential for Autophagy. *The Journal of Biological Chemistry,* 284**,** 12297-12305.

GAO, J., LANGEMEYER, L., KÜMMEL, D., REGGIORI, F. & UNGERMANN, C. 2018. Molecular mechanism to target the endosomal Mon1-Ccz1 GEF complex to the pre-autophagosomal structure. *eLife,* 7**,** e31145.

GARCÍA, I. A., MARTINEZ, H. E. & ALVAREZ, C. 2011. Rab1b regulates COPI and COPII dynamics in mammalian cells. *Cellular logistics,* 1**,** 159-163.

GAROFALO, T., MATARRESE, P., MANGANELLI, V., MARCONI, M., TINARI, A., GAMBARDELLA, L., FAGGIONI, A., MISASI, R., SORICE, M. & MALORNI, W. 2016. Evidence for the involvement of lipid rafts localized at the ER-mitochondria associated membranes in autophagosome formation. *Autophagy,* 12**,** 917-935.

GE, L., MELVILLE, D., ZHANG, M. & SCHEKMAN, R. 2013. The ER-Golgi intermediate compartment is a key membrane source for the LC3 lipidation step of autophagosome biogenesis. *Elife,* 2**,** e00947.

GE, L., ZHANG, M. & SCHEKMAN, R. 2014. Phosphatidylinositol 3-kinase and COPII generate LC3 lipidation vesicles from the ER-Golgi intermediate compartment. *Elife,* 3**,** e04135.

GENG, J., NAIR, U., YASUMURA-YORIMITSU, K. & KLIONSKY, D. J. 2010. Post-Golgi Sec Proteins Are Required for Autophagy in Saccharomyces cerevisiae. *Mol Biol Cell,* 21**,** 2257-2269.

GEORGAKOPOULOS, N. D., WELLS, G. & CAMPANELLA, M. 2017. The pharmacological regulation of cellular mitophagy. *Nature Chemical Biology,* 13**,** 136.

GILLOOLY, D. J., MORROW, I. C., LINDSAY, M., GOULD, R., BRYANT, N. J., GAULLIER, J.-M., PARTON, R. G. & STENMARK, H. 2000. Localization of phosphatidylinositol 3-phosphate in yeast and mammalian cells. *The EMBO Journal,* 19**,** 4577-4588.

GIURGIU, M., REINHARD, J., BRAUNER, B., DUNGER-KALTENBACH, I., FOBO, G., FRISHMAN, G., MONTRONE, C. & RUEPP, A. 2019. CORUM: the comprehensive resource of mammalian protein complexes-2019. *Nucleic acids research,* 47**,** D559-D563.

GOMEZ, T. S. & BILLADEAU, D. D. 2009. A FAM21-containing WASH complex regulates retromer-dependent sorting. *Developmental cell,* 17**,** 699-711.

GÓMEZ-SÁNCHEZ, R., ROSE, J., GUIMARÃES, R., MARI, M., PAPINSKI, D., RIETER, E., GEERTS, W. J., HARDENBERG, R., KRAFT, C., UNGERMANN, C. & REGGIORI, F. 2018. Atg9 establishes Atg2-dependent contact sites between the endoplasmic reticulum and phagophores. *The Journal of Cell Biology,* 217**,** 2743.

GOWANS, G. J., HAWLEY, S. A., ROSS, F. A. & HARDIE, D. G. 2013. AMP is a true physiological regulator of AMP-activated protein kinase by both allosteric activation and enhancing net phosphorylation. *Cell metabolism,* 18**,** 556-566.

GRAEF, M., FRIEDMAN, J. R., GRAHAM, C., BABU, M. & NUNNARI, J. 2013. ER exit sites are physical and functional core autophagosome biogenesis components. *Molecular Biology of the Cell,* 24**,** 2918-2931.

GREISS, S. & CHIN, J. W. 2011. Expanding the Genetic Code of an Animal. *Journal of the American Chemical Society,* 133**,** 14196-14199.

GRINDHEIM, A. K., SARASTE, J. & VEDELER, A. 2017. Protein phosphorylation and its role in the regulation of Annexin A2 function. *Biochimica et Biophysica Acta (BBA) - General Subjects,* 1861**,** 2515-2529.

GRUMATI, P. & DIKIC, I. 2018. Ubiquitin signaling and autophagy. *Journal of Biological Chemistry,* 293**,** 5404-5413.

GRUNWALD, D. S., OTTO, N. M., PARK, J.-M., SONG, D. & KIM, D.-H. 2019. GABARAPs and LC3s have opposite roles in regulating ULK1 for autophagy induction. *Autophagy***,** 1-15.

GSTREIN, T., EDWARDS, A., PŘISTOUPILOVÁ, A., LECA, I., BREUSS, M., PILAT-CAROTTA, S., HANSEN, A. H., TRIPATHY, R., TRAUNBAUER, A. K., HOCHSTOEGER, T., ROSOKLIJA, G., REPIC, M., LANDLER, L., STRÁNECKÝ, V., DÜRNBERGER, G., KEANE, T. M., ZUBER, J., ADAMS, D. J., FLINT, J., HONZIK, T., GUT, M., BELTRAN, S., MECHTLER, K., SHERR, E., KMOCH, S., GUT, I. & KEAYS, D. A. 2018. Mutations in Vps15 perturb neuronal migration in mice and are associated with neurodevelopmental disease in humans. *Nature Neuroscience,* 21**,** 207-217.

GUAN, J., STROMHAUG, P. E., GEORGE, M. D., HABIBZADEGAH-TARI, P., BEVAN, A., DUNN, W. A., JR. & KLIONSKY, D. J. 2001. Cvt18/Gsa12 is required for cytoplasm-to-vacuole transport, pexophagy, and autophagy in Saccharomyces cerevisiae and Pichia pastoris. *Molecular biology of the cell,* 12**,** 3821-3838.

GUTIERREZ, M. G., MUNAFO, D. B., BERON, W. & COLOMBO, M. I. 2004. Rab7 is required for the normal progression of the autophagic pathway in mammalian cells. *J Cell Sci,* 117**,** 2687-2697.

GWINN, D. M., SHACKELFORD, D. B., EGAN, D. F., MIHAYLOVA, M. M., MERY, A., VASQUEZ, D. S., TURK, B. E. & SHAW, R. J. 2008. AMPK phosphorylation of raptor mediates a metabolic checkpoint. *Molecular cell,* 30**,** 214-226.

HAILEY, D. W., RAMBOLD, A. S., SATPUTE-KRISHNAN, P., MITRA, K., SOUGRAT, R., KIM, P. K. & LIPPINCOTT-SCHWARTZ, J. 2010. Mitochondria Supply Membranes for Autophagosome Biogenesis during Starvation. *Cell,* 141**,** 656-667.

HAMASAKI, M., FURUTA, N., MATSUDA, A., NEZU, A., YAMAMOTO, A., FUJITA, N., OOMORI, H., NODA, T., HARAGUCHI, T., HIRAOKA, Y., AMANO, A. & YOSHIMORI, T. 2013. Autophagosomes form at ER-mitochondria contact sites. *Nature,* 495**,** 389-393.

HAN, S. H., KORM, S., HAN, Y. G., CHOI, S.-Y., KIM, S.-H., CHUNG, H. J., PARK, K., KIM, J.-Y., MYUNG, K., LEE, J.-Y., KIM, H. & KIM, D.-W. 2019. GCA links TRAF6-ULK1-dependent autophagy activation in resistant chronic myeloid leukemia. *Autophagy***,** 1-15.

HANCOCK, S. M., UPRETY, R., DEITERS, A. & CHIN, J. W. 2010. Expanding the Genetic Code of Yeast for Incorporation of Diverse Unnatural Amino Acids via a Pyrrolysyl-tRNA Synthetase/tRNA Pair. *Journal of the American Chemical Society,* 132**,** 14819-14824.

HANSEN, M., RUBINSZTEIN, D. C. & WALKER, D. W. 2018. Autophagy as a promoter of longevity: insights from model organisms. *Nature reviews. Molecular cell biology,* 19**,** 579-593.

HARA, T., NAKAMURA, K., MATSUI, M., YAMAMOTO, A., NAKAHARA, Y., SUZUKI-MIGISHIMA, R., YOKOYAMA, M., MISHIMA, K., SAITO, I., OKANO, H. & MIZUSHIMA, N. 2006. Suppression of basal autophagy in neural cells causes neurodegenerative disease in mice. *Nature,* 441**,** 885-889.

HARA, T., TAKAMURA, A., KISHI, C., IEMURA, S.-I., NATSUME, T., GUAN, J.-L. & MIZUSHIMA, N. 2008. FIP200, a ULK-interacting protein, is required for autophagosome formation in mammalian cells. *The Journal of Cell Biology,* 181**,** 497-510.

HARDING, T. M., MORANO, K. A., SCOTT, S. V. & KLIONSKY, D. J. 1995. Isolation and characterization of yeast mutants in the cytoplasm to vacuole protein targeting pathway. *J Cell Biol,* 131**,** 591-602.

HARWOOD, F. C., KLEIN GELTINK, R. I., O'HARA, B. P., CARDONE, M., JANKE, L., FINKELSTEIN, D., ENTIN, I., PAUL, L., HOUGHTON, P. J. & GROSVELD, G. C. 2018. ETV7 is an essential component of a rapamycin-insensitive mTOR complex in cancer. *Science advances,* 4**,** eaar3938-eaar3938.

HASEGAWA, J., IWAMOTO, R., OTOMO, T., NEZU, A., HAMASAKI, M. & YOSHIMORI, T. 2016. Autophagosome-lysosome fusion in neurons requires INPP5E, a protein associated with Joubert syndrome. *The EMBO journal,* 35**,** 1853-1867.

HAWLEY, S. A., BOUDEAU, J., REID, J. L., MUSTARD, K. J., UDD, L., MÄKELÄ, T. P., ALESSI, D. R. & HARDIE, D. G. 2003. Complexes between the LKB1 tumor suppressor, STRAD alpha/beta and MO25 alpha/beta are upstream kinases in the AMP-activated protein kinase cascade. *Journal of biology,* 2**,** 28-28.

HAWLEY, S. A., ROSS, F. A., CHEVTZOFF, C., GREEN, K. A., EVANS, A., FOGARTY, S., TOWLER, M. C., BROWN, L. J., OGUNBAYO, O. A., EVANS, A. M. & HARDIE, D. G. 2010. Use of cells expressing gamma subunit variants to identify diverse mechanisms of AMPK activation. *Cell metabolism,* 11**,** 554-565.

HAYASHI-NISHINO, M., FUJITA, N., NODA, T., YAMAGUCHI, A., YOSHIMORI, T. & YAMAMOTO, A. 2009. A subdomain of the endoplasmic reticulum forms a cradle for autophagosome formation. *Nat Cell Biol,* 11**,** 1433-7.

HE, C., SONG, H., YORIMITSU, T., MONASTYRSKA, I., YEN, W. L., LEGAKIS, J. E. & KLIONSKY, D. J. 2006. Recruitment of Atg9 to the preautophagosomal structure by Atg11 is essential for selective autophagy in budding yeast. *J Cell Biol,* 175**,** 925-35.

HE, S., NI, D., MA, B., LEE, J.-H., ZHANG, T., GHOZALLI, I., PIROOZ, S. D., ZHAO, Z., BHARATHAM, N., LI, B., OH, S., LEE, W.-H., TAKAHASHI, Y., WANG, H.-G., MINASSIAN, A., FENG, P., DERETIC, V., PEPPERKOK, R., TAGAYA, M., YOON, H. S. & LIANG, C. 2013. PtdIns(3)P-bound UVRAG coordinates Golgi-ER retrograde and Atg9 transport by differential interactions with the ER tether and the beclin 1 complex. *Nature cell biology,* 15**,** 1206-1219.

HE, Y., SHE, H., ZHANG, T., XU, H., CHENG, L., YEPES, M., ZHAO, Y. & MAO, Z. 2018. p38 MAPK inhibits autophagy and promotes microglial inflammatory responses by phosphorylating ULK1. *The Journal of Cell Biology,* 217**,** 315.

HEDGECOCK, E. M., CULOTTI, J. G., THOMSON, J. N. & PERKINS, L. A. 1985. Axonal guidance mutants of Caenorhabditis elegans identified by filling sensory neurons with fluorescein dyes. *Developmental Biology,* 111**,** 158-170.

HERMAN, P. K. & EMR, S. D. 1990. Characterization of VPS34, a gene required for vacuolar protein sorting and vacuole segregation in Saccharomyces cerevisiae. *Mol. Cell. Biol.,* 10**,** 6742-6754.

HERMAN, P. K., STACK, J. H., DEMODENA, J. A. & EMR, S. D. 1991a. A novel protein kinase homolog essential for protein sorting to the yeast lysosome-like vacuole. *Cell,* 64**,** 425-437.

HERMAN, P. K., STACK, J. H. & EMR, S. D. 1991b. A genetic and structural analysis of the yeast Vps15 protein kinase: evidence for a direct role of Vps15p in vacuolar protein delivery. *The EMBO journal,* 10**,** 4049-4060.

HERSHKO, A. & CIECHANOVER, A. 1998. THE UBIQUITIN SYSTEM. *Annual Review of Biochemistry,* 67**,** 425-479.

HIEKE, N., LÖFFLER, A. S., KAIZUKA, T., BERLETH, N., BÖHLER, P., DRIESSE, S., STUHLDREIER, F., FRIESEN, O., ASSANI, K., SCHMITZ, K., PETER, C., DIEDRICH, B., DENGJEL, J., HOLLAND, P., SIMONSEN, A., WESSELBORG, S., MIZUSHIMA, N. & STORK, B. 2015. Expression of a ULK1/2 binding-deficient ATG13 variant can partially restore autophagic activity in ATG13-deficient cells. *Autophagy,* 11**,** 1471-1483.

HILL, S. M., WROBEL, L. & RUBINSZTEIN, D. C. 2019. Post-translational modifications of Beclin 1 provide multiple strategies for autophagy regulation. *Cell Death & Differentiation,* 26**,** 617-629.

HO, W. Y., TAI, Y. K., CHANG, J.-C., LIANG, J., TYAN, S.-H., CHEN, S., GUAN, J.-L., ZHOU, H., SHEN, H.-M., KOO, E. & LING, S.-C. 2019. The ALS-FTD-linked gene product, C9orf72, regulates neuronal morphogenesis via autophagy. *Autophagy,* 15**,** 827-842.

HOGREBE, A., VON STECHOW, L., BEKKER-JENSEN, D. B., WEINERT, B. T., KELSTRUP, C. D. & OLSEN, J. V. 2018. Benchmarking common quantification strategies for large-scale phosphoproteomics. *Nature Communications,* 9**,** 1045.

HOLLAND, P., KNÆVELSRUD, H., SØRENG, K., MATHAI, B. J., LYSTAD, A. H., PANKIV, S., BJØRNDAL, G. T., SCHULTZ, S. W., LOBERT, V. H., CHAN, R. B., ZHOU, B., LIESTØL, K., CARLSSON, S. R., MELIA, T. J., DI PAOLO, G. & SIMONSEN, A. 2016. HS1BP3 negatively regulates autophagy by modulation of phosphatidic acid levels. *Nature communications,* 7**,** 13889-13889.

HORNBECK, P. V., ZHANG, B., MURRAY, B., KORNHAUSER, J. M., LATHAM, V. & SKRZYPEK, E. 2015. PhosphoSitePlus, 2014: mutations, PTMs and recalibrations. *Nucleic acids research,* 43**,** D512-D520.

HOSOKAWA, N., HARA, T., KAIZUKA, T., KISHI, C., TAKAMURA, A., MIURA, Y., IEMURA, S.-I., NATSUME, T., TAKEHANA, K., YAMADA, N., GUAN, J.-L., OSHIRO, N. & MIZUSHIMA, N. 2009a. Nutrient-dependent mTORC1 Association with the ULK1–Atg13–FIP200 Complex Required for Autophagy. *Molecular Biology of the Cell,* 20**,** 1981-1991.

HOSOKAWA, N., SASAKI, T., IEMURA, S.-I., NATSUME, T., HARA, T. & MIZUSHIMA, N. 2009b. Atg101, a novel mammalian autophagy protein interacting with Atg13. *Autophagy,* 5**,** 973-979.

HUMPHREY, S. J., AZIMIFAR, S. B. & MANN, M. 2015. High-throughput phosphoproteomics reveals in vivo insulin signaling dynamics. *Nature Biotechnology,* 33**,** 990.

HURLEY, J. H. & HANSON, P. I. 2010. Membrane budding and scission by the ESCRT machinery: it's all in the neck. *Nature reviews. Molecular cell biology,* 11**,** 556-566.

HUTTLIN, E. L., BRUCKNER, R. J., PAULO, J. A., CANNON, J. R., TING, L., BALTIER, K., COLBY, G., GEBREAB, F., GYGI, M. P., PARZEN, H., SZPYT, J., TAM, S., ZARRAGA, G., PONTANO-VAITES, L., SWARUP, S., WHITE, A. E., SCHWEPPE, D. K., RAD, R., ERICKSON, B. K., OBAR, R. A., GURUHARSHA, K. G., LI, K., ARTAVANIS-TSAKONAS, S., GYGI, S. P. & HARPER, J. W. 2017. Architecture of the human interactome defines protein communities and disease networks. *Nature,* 545**,** 505-509.

HWANG, S.-H., BANG, S., KANG, K. S., KANG, D. & CHUNG, J. 2019. ULK1 negatively regulates Wnt signaling by phosphorylating Dishevelled. *Biochemical and Biophysical Research Communications,* 508**,** 308-313.

INOKI, K., ZHU, T. & GUAN, K.-L. 2003. TSC2 Mediates Cellular Energy Response to Control Cell Growth and Survival. *Cell,* 115**,** 577-590.

ITAKURA, E., KISHI, C., INOUE, K. & MIZUSHIMA, N. 2008. Beclin 1 Forms Two Distinct Phosphatidylinositol 3-Kinase Complexes with Mammalian Atg14 and UVRAG. *Molecular Biology of the Cell,* 19**,** 5360-5372.

ITAKURA, E., KISHI-ITAKURA, C. & MIZUSHIMA, N. 2012. The hairpin-type tail-anchored SNARE syntaxin 17 targets to autophagosomes for fusion with endosomes/lysosomes. *Cell,* 151**,** 1256-69.

ITAKURA, E. & MIZUSHIMA, N. 2010. Characterization of autophagosome formation site by a hierarchical analysis of mammalian Atg proteins. *Autophagy,* 6**,** 764-776.

ITAKURA, E. & MIZUSHIMA, N. 2011. p62 Targeting to the autophagosome formation site requires self-oligomerization but not LC3 binding. *The Journal of cell biology,* 192**,** 17-27.

ITZHAK, D. N., TYANOVA, S., COX, J. & BORNER, G. H. H. 2016. Global, quantitative and dynamic mapping of protein subcellular localization. *eLife,* 5**,** e16950.

IVANKOVIC, D., LÓPEZ-DOMÉNECH, G., DREW, J., TOOZE, S. A. & KITTLER, J. T. 2017. AP-4 mediated ATG9A sorting underlies axonal and autophagosome biogenesis defects in a mouse model of AP-4 deficiency syndrome. *bioRxiv***,** 235101.

JABER, N., DOU, Z., CHEN, J.-S., CATANZARO, J., JIANG, Y.-P., BALLOU, L. M., SELINGER, E., OUYANG, X., LIN, R. Z., ZHANG, J. & ZONG, W.-X. 2012. Class III PI3K Vps34 plays an essential role in autophagy and in heart and liver function. *Proceedings of the National Academy of Sciences,* 109**,** 2003-2008.

JABER, N., MOHD-NAIM, N., WANG, Z., DELEON, J. L., KIM, S., ZHONG, H., SHESHADRI, N., DOU, Z., EDINGER, A. L., DU, G., BRAGA, V. M. & ZONG, W. X. 2016. Vps34 regulates Rab7 and late endocytic trafficking through recruitment of the GTPase-activating protein Armus. *J Cell Sci,* 129**,** 4424-4435.

JACOMIN, A.-C., SAMAVEDAM, S., PROMPONAS, V. & NEZIS, I. P. 2016. iLIR database: A web resource for LIR motif-containing proteins in eukaryotes. *Autophagy,* 12**,** 1945-1953.

JACQUEMYN, J., CASCALHO, A. & GOODCHILD, R. E. 2017. The ins and outs of endoplasmic reticulum-controlled lipid biosynthesis. *EMBO reports,* 18**,** 1905-1921.

JANG, M., PARK, R., KIM, H., NAMKOONG, S., JO, D., HUH, Y. H., JANG, I.-S., LEE, J. I. & PARK, J. 2018. AMPK contributes to autophagosome maturation and lysosomal fusion. *Scientific Reports,* 8**,** 12637.

JAO, C. C., RAGUSA, M. J., STANLEY, R. E. & HURLEY, J. H. 2013. A HORMA domain in Atg13 mediates PI 3-kinase recruitment in autophagy. *Proceedings of the National Academy of Sciences,* 110**,** 5486-5491.

JARNUCZAK, A. F., LEE, D. C., LAWLESS, C., HOLMAN, S. W., EYERS, C. E. & HUBBARD, S. J. 2016. Analysis of Intrinsic Peptide Detectability via Integrated Label-Free and SRM-Based Absolute Quantitative Proteomics. *J Proteome Res,* 15**,** 2945-59.

JEAN, S. & KIGER, A. A. 2014. Classes of phosphoinositide 3-kinases at a glance. *Journal of cell science,* 127**,** 923-928.

JEHL, P., MANGUY, J., SHIELDS, D. C., HIGGINS, D. G. & DAVEY, N. E. 2016. ProViz-a web-based visualization tool to investigate the functional and evolutionary features of protein sequences. *Nucleic acids research,* 44**,** W11-W15.

JEONG, Y.-T., SIMONESCHI, D., KEEGAN, S., MELVILLE, D., ADLER, N. S., SARAF, A., FLORENS, L., WASHBURN, M. P., CAVASOTTO, C. N., FENYÖ, D., CUERVO, A. M., ROSSI, M. & PAGANO, M. 2018. The ULK1-FBXW5-SEC23B nexus controls autophagy. *eLife,* 7**,** e42253.

JI, C. H. & KWON, Y. T. 2017. Crosstalk and Interplay between the Ubiquitin-Proteasome System and Autophagy. *Molecules and cells,* 40**,** 441-449.

JIA, D., S GOMEZ, T., METLAGEL, Z., UMETANI, J., OTWINOWSKI, Z., K ROSEN, M. & D BILLADEAU, D. 2010. WASH and WAVE actin regulators of the Wiskott–Aldrich syndrome protein (WASP) family are controlled by analogous structurally related complexes. *Proceedings of the National Academy of Sciences of the United States of America,* 107**,** 10442-7.

JIANG, P., NISHIMURA, T., SAKAMAKI, Y., ITAKURA, E., HATTA, T., NATSUME, T. & MIZUSHIMA, N. 2014. The HOPS complex mediates autophagosome–

lysosome fusion through interaction with syntaxin 17. *Molecular Biology of the Cell,* 25**,** 1327-1337.

JIAO, H., SU, G. Q., DONG, W., ZHANG, L., XIE, W., YAO, L. M., CHEN, P., WANG, Z. X., LIOU, Y. C. & YOU, H. 2015. Chaperone-like protein p32 regulates ULK1 stability and autophagy. *Cell Death and Differentiation,* 22**,** 1812-1823.

JOACHIM, J., JEFFERIES, HAROLD B., RAZI, M., FRITH, D., SNIJDERS, AMBROSIUS P., CHAKRAVARTY, P., JUDITH, D. & TOOZE, SHARON A. 2015. Activation of ULK Kinase and Autophagy by GABARAP Trafficking from the Centrosome Is Regulated by WAC and GM130. *Molecular Cell,* 60**,** 899-913.

JOHNSON, E. E., OVERMEYER, J. H., GUNNING, W. T. & MALTESE, W. A. 2006. Gene silencing reveals a specific function of hVps34 phosphatidylinositol 3-kinase in late versus early endosomes. *Journal of Cell Science,* 119**,** 1219.

JOO, J. H., DORSEY, F. C., JOSHI, A., HENNESSY-WALTERS, K. M., ROSE, K. L., MCCASTLAIN, K., ZHANG, J., IYENGAR, R., JUNG, C.-H., SUEN, D.-F., STEEVES, M. A., YANG, C.-Y., PRATER, S. M., KIM, D.-H., THOMPSON, C. B., YOULE, R., NEY, P. A., CLEVELAND, J. L. & KUNDU, M. 2011. Hsp90-Cdc37 chaperone complex regulates Ulk1- and Atg13-mediated mitophagy. *Molecular cell,* 43**,** 572-585.

JOO, J. H., WANG, B., FRANKEL, E., GE, L., XU, L., IYENGAR, R., LI-HARMS, X., WRIGHT, C., SHAW, T. I., LINDSTEN, T., GREEN, D. R., PENG, J., HENDERSHOT, L. M., KILIC, F., SZE, J. Y., AUDHYA, A. & KUNDU, M. 2016. Noncanonical Role of ULK/ATG1 in ER-to-Golgi Trafficking Is Essential for Cellular Homeostasis. *Molecular cell,* 62**,** 491-506.

JORDENS, I., FERNANDEZ-BORJA, M., MARSMAN, M., DUSSELJEE, S., JANSSEN, L., CALAFAT, J., JANSSEN, H., WUBBOLTS, R. & NEEFJES, J. 2001. The Rab7 effector protein RILP controls lysosomal transport by inducing the recruitment of dynein-dynactin motors. *Current Biology,* 11**,** 1680-1685.

JUDITH, D., JEFFERIES, H. B. J., BOEING, S., FRITH, D., SNIJDERS, A. P. & TOOZE, S. A. 2019. ATG9A shapes the forming autophagosome through Arfaptin 2 and phosphatidylinositol 4-kinase IIIbeta. *J Cell Biol*.

JUNG, C. H., JUN, C. B., RO, S.-H., KIM, Y.-M., OTTO, N. M., CAO, J., KUNDU, M. & KIM, D.-H. 2009. ULK-Atg13-FIP200 Complexes Mediate mTOR Signaling to the Autophagy Machinery. *Molecular Biology of the Cell,* 20**,** 1992-2003.

JUNG, J., NAYAK, A., SCHAEFFER, V., STARZETZ, T., KIRSCH, A. K., MÜLLER, S., DIKIC, I., MITTELBRONN, M. & BEHRENDS, C. 2017. Multiplex image-based autophagy RNAi screening identifies SMCR8 as ULK1 kinase activity and gene expression regulator. *eLife,* 6**,** e23063.

KALVARI, I., TSOMPANIS, S., MULAKKAL, N. C., OSGOOD, R., JOHANSEN, T., NEZIS, I. P. & PROMPONAS, V. J. 2014. iLIR: A web resource for prediction of Atg8-family interacting proteins. *Autophagy,* 10**,** 913-925.

KAMADA, Y., YOSHINO, K.-I., KONDO, C., KAWAMATA, T., OSHIRO, N., YONEZAWA, K. & OHSUMI, Y. 2010. Tor Directly Controls the Atg1 Kinase Complex To Regulate Autophagy. *Mol. Cell. Biol.,* 30**,** 1049-1058.

KARANASIOS, E., STAPLETON, E., MANIFAVA, M., KAIZUKA, T., MIZUSHIMA, N., WALKER, S. A. & KTISTAKIS, N. T. 2013. Dynamic association of the ULK1 complex with omegasomes during autophagy induction. *Journal of Cell Science,* 126**,** 5224.

KARANASIOS, E., WALKER, S. A., OKKENHAUG, H., MANIFAVA, M., HUMMEL, E., ZIMMERMANN, H., AHMED, Q., DOMART, M.-C., COLLINSON, L. & KTISTAKIS, N. T. 2016. Autophagy initiation by ULK complex assembly on ER tubulovesicular regions marked by ATG9 vesicles. *Nature Communications* 7**,** 12420.

KAST, D. J. & DOMINGUEZ, R. 2017. The Cytoskeleton-Autophagy Connection. *Current biology : CB,* 27**,** R318-R326.

KAUFFMAN, K. J., YU, S., JIN, J., MUGO, B., NGUYEN, N., O'BRIEN, A., NAG, S., LYSTAD, A. H. & MELIA, T. J. 2018. Delipidation of mammalian Atg8-family proteins by each of the four ATG4 proteases. *Autophagy,* 14**,** 992-1010.

KAUSHIK, S. & CUERVO, A. M. 2018. The coming of age of chaperone-mediated autophagy. *Nature reviews. Molecular cell biology,* 19**,** 365-381.

KAZLAUSKAITE, A., KELLY, V., JOHNSON, C., BAILLIE, C., HASTIE, C. J., PEGGIE, M., MACARTNEY, T., WOODROOF, H. I., ALESSI, D. R., PEDRIOLI, P. G. A. & MUQIT, M. M. K. 2014a. Phosphorylation of Parkin at Serine65 is essential for activation: elaboration of a Miro1 substrate-based assay of Parkin E3 ligase activity. *Open biology,* 4**,** 130213-130213.

KAZLAUSKAITE, A., KONDAPALLI, C., GOURLAY, R., CAMPBELL, D. G., RITORTO, M. S., HOFMANN, K., ALESSI, D. R., KNEBEL, A., TROST, M. & MUQIT, M. M. K. 2014b. Parkin is activated by PINK1-dependent phosphorylation of ubiquitin at Ser65. *The Biochemical journal,* 460**,** 127-139.

KERR, M. C., BENNETTS, J. S., SIMPSON, F., THOMAS, E. C., FLEGG, C., GLEESON, P. A., WICKING, C. & TEASDALE, R. D. 2005. A Novel Mammalian Retromer Component, Vps26B. *Traffic,* 6**,** 991-1001.

KHOURY, G. A., BALIBAN, R. C. & FLOUDAS, C. A. 2011. Proteome-wide post-translational modification statistics: frequency analysis and curation of the swiss-prot database. *Sci Rep,* 1.

KIEL, J. A. K. W., RECHINGER, K. B., VAN DER KLEI, I. J., SALOMONS, F. A., TITORENKO, V. I. & VEENHUIS, M. 1999. The Hansenula polymorpha PDD1 gene product, essential for the selective degradation of peroxisomes, is a homologue of Saccharomyces cerevisiae Vps34p. *Yeast,* 15**,** 741-754.

KIHARA, A., NODA, T., ISHIHARA, N. & OHSUMI, Y. 2001. Two Distinct Vps34 Phosphatidylinositol 3-Kinase Complexes Function in Autophagy and Carboxypeptidase Y Sorting in Saccharomyces cerevisiae. *J Cell Biol,* 152**,** 519-530.

KIM, B.-W., JIN, Y., KIM, J., KIM, J. H., JUNG, J., KANG, S., KIM, I. Y., KIM, J., CHEONG, H. & SONG, H. K. 2018a. The C-terminal region of ATG101 bridges ULK1 and PtdIns3K complex in autophagy initiation. *Autophagy,* 14**,** 2104-2116.

KIM, J., KIM, Y. C., FANG, C., RUSSELL, R. C., KIM, J. H., FAN, W., LIU, R., ZHONG, Q. & GUAN, K.-L. 2013. Differential regulation of distinct Vps34 complexes by AMPK in nutrient stress and autophagy. *Cell,* 152**,** 290-303.

KIM, J., KUNDU, M., VIOLLET, B. & GUAN, K.-L. 2011. AMPK and mTOR regulate autophagy through direct phosphorylation of Ulk1. *Nat Cell Biol,* 13**,** 132-141.

KIM, J. H., LEE, C., LEE, M., WANG, H., KIM, K., PARK, S. J., YOON, I., JANG, J., ZHAO, H., KIM, H. K., KWON, N. H., JEONG, S. J., YOO, H. C., KIM, J. H., YANG, J. S., LEE, M. Y., LEE, C. W., YUN, J., OH, S. J., KANG, J. S., MARTINIS, S. A., HWANG, K. Y., GUO, M., HAN, G., HAN, J. M. & KIM, S. 2017. Control of leucine-dependent mTORC1 pathway through chemical intervention of leucyl-tRNA synthetase and RagD interaction. *Nature communications,* 8**,** 732-732.

KIM, J. H., SEO, D., KIM, S.-J., CHOI, D. W., PARK, J. S., HA, J., CHOI, J., LEE, J.-H., JUNG, S. M., SEO, K.-W., LEE, E.-W., LEE, Y. S., CHEONG, H., CHOI, C. Y. & PARK, S. H. 2018b. The deubiquitinating enzyme USP20 stabilizes ULK1 and promotes autophagy initiation. *EMBO reports,* 19**,** e44378.

KIM, Y.-M., JUNG, CHANG H., SEO, M., KIM, EUN K., PARK, J.-M., BAE, SUN S. & KIM, D.-H. 2015. mTORC1 Phosphorylates UVRAG to Negatively Regulate Autophagosome and Endosome Maturation. *Molecular Cell,* 57**,** 207-218.

KIMURA, S., NODA, T. & YOSHIMORI, T. 2008. Dynein-dependent Movement of Autophagosomes Mediates Efficient Encounters with Lysosomes. *Cell Structure and Function,* 33**,** 109-122.

KIMURA, T., JAIN, A., CHOI, S. W., MANDELL, M. A., SCHRODER, K., JOHANSEN, T. & DERETIC, V. 2015. TRIM-mediated precision autophagy targets cytoplasmic regulators of innate immunity. *The Journal of Cell Biology,* 210**,** 973.

KIRISAKO, T., ICHIMURA, Y., OKADA, H., KABEYA, Y., MIZUSHIMA, N., YOSHIMORI, T., OHSUMI, M., TAKAO, T., NODA, T. & OHSUMI, Y. 2000. The reversible modification regulates the membrane-binding state of Apg8/Aut7 essential for autophagy and the cytoplasm to vacuole targeting pathway. *The Journal of cell biology,* 151**,** 263-276.

KIRKIN, V., MCEWAN, D. G., NOVAK, I. & DIKIC, I. 2009. A Role for Ubiquitin in Selective Autophagy. *Molecular Cell,* 34**,** 259-269.

KISHI-ITAKURA, C., KOYAMA-HONDA, I., ITAKURA, E. & MIZUSHIMA, N. 2014. Ultrastructural analysis of autophagosome organization using mammalian autophagy-deficient cells. *Journal of Cell Science,* 127**,** 4089-4102.

KLIONSKY, D. J., ELAZAR, Z., SEGLEN, P. O. & RUBINSZTEIN, D. C. 2008. Does bafilomycin A1 block the fusion of autophagosomes with lysosomes? *Autophagy,* 4**,** 849-950.

KNÆVELSRUD, H., SØRENG, K., RAIBORG, C., HÅBERG, K., RASMUSON, F., BRECH, A., LIESTØL, K., RUSTEN, T. E., STENMARK, H., NEUFELD, T. P., CARLSSON, S. R. & SIMONSEN, A. 2013. Membrane remodeling by the PX-BAR protein SNX18 promotes autophagosome formation. *The Journal of cell biology,* 202**,** 331-349.

KNORR, R. L., LIPOWSKY, R. & DIMOVA, R. 2015. Autophagosome closure requires membrane scission. *Autophagy,* 11**,** 2134-2137.

KOBAYASHI, T., NUREKI, O., ISHITANI, R., YAREMCHUK, A., TUKALO, M., CUSACK, S., SAKAMOTO, K. & YOKOYAMA, S. 2003. Structural basis for orthogonal tRNA specificities of tyrosyl-tRNA synthetases for genetic code expansion. *Nature Structural & Molecular Biology,* 10**,** 425-432.

KOGA, H., MARTINEZ-VICENTE, M., MACIAN, F., VERKHUSHA, V. V. & CUERVO, A. M. 2011. A photoconvertible fluorescent reporter to track chaperone-mediated autophagy. *Nature communications,* 2**,** 386-386.

KOMANDER, D. & RAPE, M. 2012. The ubiquitin code. *Annu Rev Biochem,* 81**,** 203-29.

KOMATSU, M., WAGURI, S., CHIBA, T., MURATA, S., IWATA, J.-I., TANIDA, I., UENO, T., KOIKE, M., UCHIYAMA, Y., KOMINAMI, E. & TANAKA, K. 2006. Loss of autophagy in the central nervous system causes neurodegeneration in mice. *Nature,* 441**,** 880-884.

KONNO, H., KONNO, K. & BARBER, G. N. 2013. Cyclic Di Nucleotides Trigger ULK1 (ATG1) Phosphorylation of STING to Prevent Sustained Innate Immune Signaling. *Cell,* 155**,** 688-698.

KOROLCHUK, V. I., MANSILLA, A., MENZIES, F. M. & RUBINSZTEIN, D. C. 2009. Autophagy inhibition compromises degradation of ubiquitin-proteasome pathway substrates. *Molecular cell,* 33**,** 517-527.

KRAFT, C., KIJANSKA, M., KALIE, E., SIERGIEJUK, E., LEE, S. S., SEMPLICIO, G., STOFFEL, I., BREZOVICH, A., VERMA, M., HANSMANN, I., AMMERER, G., HOFMANN, K., TOOZE, S. & PETER, M. 2012. Binding of the Atg1/ULK1 kinase to the ubiquitin-like protein Atg8 regulates autophagy. *EMBO J,* 31**,** 3691-703.

KRIEGENBURG, F., BAS, L., GAO, J., UNGERMANN, C. & KRAFT, C. 2019. The multi-functional SNARE protein Ykt6 in autophagosomal fusion processes. *Cell cycle (Georgetown, Tex.),* 18**,** 639-651.

KRZYCKI, J. A. 2005. The direct genetic encoding of pyrrolysine. *Current Opinion in Microbiology,* 8**,** 706-712.

KUMAR, S., GU, Y., ABUDU, Y. P., BRUUN, J.-A., JAIN, A., FARZAM, F., MUDD, M., ANONSEN, J. H., RUSTEN, T. E., KASOF, G., KTISTAKIS, N., LIDKE, K. A., JOHANSEN, T. & DERETIC, V. 2019. Phosphorylation of Syntaxin 17 by TBK1 Controls Autophagy Initiation. *Developmental Cell,* 49**,** 130-144.e6.

KUMAR, S., JAIN, A., FARZAM, F., YUE, J., GU, Y., CHOI, S. W., MUDD, M. H., CLAUDE-TAUPIN, A., WESTER, M. J., LIDKE, K. A., RUSTEN, T. E. & DERETIC, V. 2018. Mechanism of Stx17 recruitment to autophagosomes via IRGM and mammalian Atg8 proteins. *Journal of Cell Biology,* in press.

KUNDU, M., LINDSTEN, T., YANG, C.-Y., WU, J., ZHAO, F., ZHANG, J., SELAK, M. A., NEY, P. A. & THOMPSON, C. B. 2008. Ulk1 plays a critical role in the autophagic clearance of mitochondria and ribosomes during reticulocyte maturation. *Blood,* 112**,** 1493-1502.

KUROYANAGI, H., YAN, J., SEKI, N., YAMANOUCHI, Y., SUZUKI, Y.-I., TAKANO, T., MURAMATSU, M.-A. & SHIRASAWA, T. 1998. Human ULK1, a Novel Serine/Threonine Kinase Related to UNC-51 Kinase ofCaenorhabditis elegans:cDNA Cloning, Expression, and Chromosomal Assignment. *Genomics,* 51**,** 76-85.

LAKER, R. C., DRAKE, J. C., WILSON, R. J., LIRA, V. A., LEWELLEN, B. M., RYALL, K. A., FISHER, C. C., ZHANG, M., SAUCERMAN, J. J., GOODYEAR, L. J., KUNDU, M. & YAN, Z. 2017. Ampk phosphorylation of Ulk1 is required for targeting of mitochondria to lysosomes in exercise-induced mitophagy. *Nature Communications,* 8**,** 548.

LAMB, C. A., NUHLEN, S., JUDITH, D., FRITH, D., SNIJDERS, A. P., BEHRENDS, C. & TOOZE, S. A. 2016. TBC1D14 regulates autophagy via the TRAPP complex and ATG9 traffic. *EMBO J,* 35**,** 281-301.

LAMB, C. A., YOSHIMORI, T. & TOOZE, S. A. 2013. The autophagosome: origins unknown, biogenesis complex. *Nat Rev Mol Cell Biol,* 14**,** 759-74.

LANDAJUELA, A., HERVÁS, JAVIER H., ANTÓN, Z., MONTES, L. R., GIL, D., VALLE, M., RODRIGUEZ, J. F., GOÑI, FELIX M. & ALONSO, A. 2016. Lipid Geometry and Bilayer Curvature Modulate LC3/GABARAP-Mediated Model Autophagosomal Elongation. *Biophysical Journal,* 110**,** 411-422.

LAPLANTE, M. & SABATINI, D. M. 2009. mTOR signaling at a glance. *Journal of Cell Science,* 122**,** 3589.

LAPLANTE, M. & SABATINI, D. M. 2013. Regulation of mTORC1 and its impact on gene expression at a glance. *Journal of cell science,* 126**,** 1713-1719.

LARKIN, M. A., BLACKSHIELDS, G., BROWN, N. P., CHENNA, R., MCGETTIGAN, P. A., MCWILLIAM, H., VALENTIN, F., WALLACE, I. M., WILM, A., LOPEZ, R., THOMPSON, J. D., GIBSON, T. J. & HIGGINS, D. G. 2007. Clustal W and Clustal X version 2.0. *Bioinformatics,* 23**,** 2947-2948.

LAW, F., SEO, J. H., WANG, Z., DELEON, J. L., BOLIS, Y., BROWN, A., ZONG, W. X., DU, G. & ROCHELEAU, C. E. 2017. The VPS34 PI3K negatively regulates RAB-5 during endosome maturation. *J Cell Sci,* 130**,** 2007-2017.

LAZARUS, M. B., NOVOTNY, C. J. & SHOKAT, K. M. 2015. Structure of the human autophagy initiating kinase ULK1 in complex with potent inhibitors. *ACS Chem Biol,* 10**,** 257-61.

LECHAUVE, C., KEITH, J., KHANDROS, E., FOWLER, S., MAYBERRY, K., FREIWAN, A., THOM, C. S., DELBINI, P., ROMERO, E. B., ZHANG, J., MOTTA, I., TILLMAN, H., CAPPELLINI, M. D., KUNDU, M. & WEISS, M. J.

2019. The autophagy-activating kinase ULK1 mediates clearance of free α-globin in β-thalassemia. *Science Translational Medicine,* 11**,** eaav4881.
LEE, E. J. & TOURNIER, C. 2011. The requirement of uncoordinated 51-like kinase 1 (ULK1) and ULK2 in the regulation of autophagy. *Autophagy,* 7**,** 689-95.
LEE, J.-Y., KOGA, H., KAWAGUCHI, Y., TANG, W., WONG, E., GAO, Y.-S., PANDEY, U. B., KAUSHIK, S., TRESSE, E., LU, J., TAYLOR, J. P., CUERVO, A. M. & YAO, T.-P. 2010a. HDAC6 controls autophagosome maturation essential for ubiquitin-selective quality-control autophagy. *The EMBO Journal,* 29**,** 969-980.
LEE, J. W., PARK, S., TAKAHASHI, Y. & WANG, H.-G. 2010b. The Association of AMPK with ULK1 Regulates Autophagy. *PLoS ONE,* 5**,** e15394.
LEE, Y., CHOU, T.-F., PITTMAN, S., L. KEITH, A., RAZANI, B. & WEIHL, C. 2017. Keap1/Cullin3 Modulates p62/SQSTM1 Activity via UBA Domain Ubiquitination. *Cell Reports,* 20**,** 1994.
LEMASTERS, J. J. 2014. Variants of mitochondrial autophagy: Types 1 and 2 mitophagy and micromitophagy (Type 3). *Redox Biology,* 2**,** 749-754.
LEMMON, M. A. 2003. Phosphoinositide Recognition Domains. *Traffic,* 4**,** 201-213.
LEMMON, M. A. 2007. Pleckstrin homology (PH) domains and phosphoinositides. *Biochemical Society symposium***,** 81-93.
LEVINE, B. & KROEMER, G. 2019. Biological Functions of Autophagy Genes: A Disease Perspective. *Cell,* 176**,** 11-42.
LI, J., QI, W., CHEN, G., FENG, D., LIU, J., MA, B., ZHOU, C., MU, C., ZHANG, W., CHEN, Q. & ZHU, Y. 2015a. Mitochondrial outer-membrane E3 ligase MUL1 ubiquitinates ULK1 and regulates selenite-induced mitophagy. *Autophagy,* 11**,** 1216-1229.
LI, L., FANG, R., LIU, B., SHI, H., WANG, Y., ZHANG, W., ZHANG, X. & YE, L. 2015b. Deacetylation of tumor-suppressor MST1 in Hippo pathway induces its degradation through HBXIP-elevated HDAC6 in promotion of breast cancer growth. *Oncogene,* 35**,** 4048.
LI, R., YUAN, F., FU, W., ZHANG, L., ZHANG, N., WANG, Y., MA, K., LI, X., WANG, L., ZHU, W.-G. & ZHAO, Y. 2017. Serine/Threonine Kinase Unc-51-like Kinase-1 (Ulk1) Phosphorylates the Co-chaperone Cell Division Cycle Protein 37 (Cdc37) and Thereby Disrupts the Stability of Cdc37 Client Proteins. *Journal of Biological Chemistry,* 292**,** 2830-2841.
LI, T. Y., LIN, S.-Y. & LIN, S.-C. 2013a. Mechanism and Physiological Significance of Growth Factor-Related Autophagy. *Physiology,* 28**,** 423-431.
LI, TERYTTY Y., SUN, Y., LIANG, Y., LIU, Q., SHI, Y., ZHANG, C.-S., ZHANG, C., SONG, L., ZHANG, P., ZHANG, X., LI, X., CHEN, T., HUANG, H.-Y., HE, X., WANG, Y., WU, Y.-Q., CHEN, S., JIANG, M., CHEN, C., XIE, C., YANG, JAMES Y., LIN, Y., ZHAO, S., YE, Z., LIN, S.-Y., CHIU, DANIEL T.-Y. & LIN, S.-C. 2016a. ULK1/2 Constitute a Bifurcate Node Controlling Glucose Metabolic Fluxes in Addition to Autophagy. *Molecular Cell,* 62**,** 359-370.
LI, X., RYDZEWSKI, N., HIDER, A., ZHANG, X., YANG, J., WANG, W., GAO, Q., CHENG, X. & XU, H. 2016b. A molecular mechanism to regulate lysosome motility for lysosome positioning and tubulation. *Nature cell biology,* 18**,** 404-417.
LI, Y., ZHAO, Y., HU, J., XIAO, J., QU, L., WANG, Z., MA, D. & CHEN, Y. 2013b. A novel ER-localized transmembrane protein, EMC6, interacts with RAB5A and regulates cell autophagy. *Autophagy,* 9**,** 150-163.
LIANG, C., LEE, J.-S., INN, K.-S., GACK, M. U., LI, Q., ROBERTS, E. A., VERGNE, I., DERETIC, V., FENG, P., AKAZAWA, C. & JUNG, J. U. 2008. Beclin1-binding UVRAG targets the class C Vps complex to coordinate autophagosome maturation and endocytic trafficking. *Nat Cell Biol,* 10**,** 776-787.

LIM, J., LACHENMAYER, M. L., WU, S., LIU, W., KUNDU, M., WANG, R., KOMATSU, M., OH, Y. J., ZHAO, Y. & YUE, Z. 2015. Proteotoxic Stress Induces Phosphorylation of p62/SQSTM1 by ULK1 to Regulate Selective Autophagic Clearance of Protein Aggregates. *PLoS Genet,* 11**,** e1004987.

LIN, M. G., SCHÖNEBERG, J., DAVIES, C. W., REN, X. & HURLEY, J. H. 2018. The dynamic Atg13-free conformation of the Atg1 EAT domain is required for phagophore expansion. *Molecular biology of the cell,* 29**,** 1228-1237.

LIN, S.-Y., LI, T. Y., LIU, Q., ZHANG, C., LI, X., CHEN, Y., ZHANG, S.-M., LIAN, G., LIU, Q., RUAN, K., WANG, Z., ZHANG, C.-S., CHIEN, K.-Y., WU, J., LI, Q., HAN, J. & LIN, S.-C. 2012. GSK3-TIP60-ULK1 Signaling Pathway Links Growth Factor Deprivation to Autophagy. *Science,* 336**,** 477.

LINDMO, K., BRECH, A., FINLEY, K. D., GAUMER, S., CONTAMINE, D., RUSTEN, T. E. & STENMARK, H. 2008. The PI 3-kinase regulator Vps15 is required for autophagic clearance of protein aggregates. *Autophagy,* 4**,** 500-506.

LIU, C.-C., LIN, Y.-C., CHEN, Y.-H., CHEN, C.-M., PANG, L.-Y., CHEN, H.-A., WU, P.-R., LIN, M.-Y., JIANG, S.-T., TSAI, T.-F. & CHEN, R.-H. 2016. Cul3-KLHL20 Ubiquitin Ligase Governs the Turnover of ULK1 and VPS34 Complexes to Control Autophagy Termination. *Molecular Cell,* 61**,** 84-97.

LIU, J., HEMPHILL, J., SAMANTA, S., TSANG, M. & DEITERS, A. 2017. Genetic Code Expansion in Zebrafish Embryos and Its Application to Optical Control of Cell Signaling. *Journal of the American Chemical Society,* 139**,** 9100-9103.

LIU, J., XIA, H., KIM, M., XU, L., LI, Y., ZHANG, L., CAI, Y., NORBERG, H. V., ZHANG, T., FURUYA, T., JIN, M., ZHU, Z., WANG, H., YU, J., LI, Y., HAO, Y., CHOI, A., KE, H., MA, D. & YUAN, J. 2011. Beclin1 controls the levels of p53 by regulating the deubiquitination activity of USP10 and USP13. *Cell,* 147**,** 223-234.

LÖFFLER, A. S., ALERS, S., DIETERLE, A. M., KEPPELER, H., FRANZ-WACHTEL, M., KUNDU, M., CAMPBELL, D. G., WESSELBORG, S., ALESSI, D. R. & STORK, B. 2011. Ulk1-mediated phosphorylation of AMPK constitutes a negative regulatory feedback loop. *Autophagy,* 7**,** 696-706.

LONG, X., LIN, Y., ORTIZ-VEGA, S., YONEZAWA, K. & AVRUCH, J. 2005. Rheb Binds and Regulates the mTOR Kinase. *Current Biology,* 15**,** 702-713.

LONGATTI, A., LAMB, C. A., RAZI, M., YOSHIMURA, S.-I., BARR, F. A. & TOOZE, S. A. 2012. TBC1D14 regulates autophagosome formation via Rab11- and ULK1-positive recycling endosomes. *The Journal of Cell Biology,* 197**,** 659-675.

LU, H., XIAO, J., KE, C., NI, X., XIU, R., TIAN, Q., PAN, H., ZOU, L., WANG, F., MA, T., JI, X., YUAN, P., LIU, L., ZHANG, J., JIA, W., DUAN, Q. & ZHU, F. 2019. TOPK inhibits autophagy by phosphorylating ULK1 and promotes glioma resistance to TMZ. *Cell death & disease,* 10**,** 583-583.

LU, J., HE, L., BEHRENDS, C., ARAKI, M., ARAKI, K., WANG, Q. J., CATANZARO, J. M., FRIEDMAN, S. L., ZONG, W.-X., FIEL, M. I., LI, M. & YUE, Z. 2014. NRBF2 Regulates Autophagy and Prevents Liver Injury by Modulating Atg14L-Linked Phosphatidylinositol-3 Kinase III Activity. *Nature communications,* 5**,** 3920-3920.

LYSTAD, A. H., CARLSSON, S. R., DE LA BALLINA, L. R., KAUFFMAN, K. J., NAG, S., YOSHIMORI, T., MELIA, T. J. & SIMONSEN, A. 2019. Distinct functions of ATG16L1 isoforms in membrane binding and LC3B lipidation in autophagy-related processes. *Nature Cell Biology,* 21**,** 372-383.

M DONG, L., WILSON, C., WARDELL, M., SIMMONS, T., W MAHLEY, R., H WEISGRABER, K. & AGARD, D. A. 1994. Human apolipoprotein E. Role of arginine 61 in mediating the lipoprotein preferences of the E3 and E4 isoforms. *The Journal of biological chemistry,* 269**,** 22358-65.

MA, B., CAO, W., LI, W., GAO, C., QI, Z., ZHAO, Y., DU, J., XUE, H., PENG, J., WEN, J., CHEN, H., NING, Y., HUANG, L., ZHANG, H., GAO, X., YU, L. & CHEN, Y.-G. 2014. Dapper1 promotes autophagy by enhancing the Beclin1-Vps34-Atg14L complex formation. *Cell Research,* 24**,** 912-924.

MA, M., LIU, J.-J., LI, Y., HUANG, Y., TA, N., CHEN, Y., FU, H., YE, M.-D., DING, Y., HUANG, W., WANG, J., DONG, M.-Q., YU, L. & WANG, H.-W. 2017a. Cryo-EM structure and biochemical analysis reveal the basis of the functional difference between human PI3KC3-C1 and -C2. *Cell research,* 27**,** 989-1001.

MA, X., ZHANG, S., HE, L., RONG, Y., BRIER, L. W., SUN, Q., LIU, R., FAN, W., CHEN, S., YUE, Z., KIM, J., GUAN, K.-L., LI, D. & ZHONG, Q. 2017b. MTORC1-mediated NRBF2 phosphorylation functions as a switch for the class III PtdIns3K and autophagy. *Autophagy,* 13**,** 592-607.

MA, Y., GALLUZZI, L., ZITVOGEL, L. & KROEMER, G. 2013. Autophagy and Cellular Immune Responses. *Immunity,* 39**,** 211-227.

MACK, H. I. D., ZHENG, B., ASARA, J. M. & THOMAS, S. M. 2012. AMPK-dependent phosphorylation of ULK1 regulates ATG9 localization. *Autophagy,* 8**,** 1197-1214.

MADSHUS, I. H. & STANG, E. 2009. Internalization and intracellular sorting of the EGF receptor: a model for understanding the mechanisms of receptor trafficking. *Journal of Cell Science,* 122**,** 3433.

MAEDA, S., OTOMO, C. & OTOMO, T. 2019. The autophagic membrane tether ATG2A transfers lipids between membranes. *eLife,* 8**,** e45777.

MANDELL, M. A., KIMURA, T., JAIN, A., JOHANSEN, T. & DERETIC, V. 2014. TRIM proteins regulate autophagy: TRIM5 is a selective autophagy receptor mediating HIV-1 restriction. *Autophagy,* 10**,** 2387-2388.

MANIL-SÉGALEN, M., LEFEBVRE, C., JENZER, C., TRICHET, M., BOULOGNE, C., SATIAT-JEUNEMAITRE, B. & LEGOUIS, R. 2014. The C. elegans LC3 Acts Downstream of GABARAP to Degrade Autophagosomes by Interacting with the HOPS Subunit VPS39. *Developmental Cell,* 28**,** 43-55.

MARI, M., GRIFFITH, J., RIETER, E., KRISHNAPPA, L., KLIONSKY, D. J. & REGGIORI, F. 2010. An Atg9-containing compartment that functions in the early steps of autophagosome biogenesis. *J Cell Biol,* 190**,** 1005-22.

MARSH, B. J., MASTRONARDE, D. N., BUTTLE, K. F., HOWELL, K. E. & MCINTOSH, J. R. 2001. Organellar relationships in the Golgi region of the pancreatic beta cell line, HIT-T15, visualized by high resolution electron tomography. *Proceedings of the National Academy of Sciences,* 98**,** 2399.

MARTIN, K. R., CELANO, S. L., SOLITRO, A. R., GUNAYDIN, H., SCOTT, M., O'HAGAN, R. C., SHUMWAY, S. D., FULLER, P. & MACKEIGAN, J. P. 2018. A Potent and Selective ULK1 Inhibitor Suppresses Autophagy and Sensitizes Cancer Cells to Nutrient Stress. *iScience,* 8**,** 74-84.

MATSCHEKO, N., MAYRHOFER, P., RAO, Y., BEIER, V. & WOLLERT, T. 2019. Atg11 tethers Atg9 vesicles to initiate selective autophagy. *PLOS Biology,* 17**,** e3000377.

MATSUI, T., JIANG, P., NAKANO, S., SAKAMAKI, Y., YAMAMOTO, H. & MIZUSHIMA, N. 2018. Autophagosomal YKT6 is required for fusion with lysosomes independently of syntaxin 17. *The Journal of cell biology,* 217**,** 2633-2645.

MATSUNAGA, K., MORITA, E., SAITOH, T., AKIRA, S., KTISTAKIS, N. T., IZUMI, T., NODA, T. & YOSHIMORI, T. 2010. Autophagy requires endoplasmic reticulum targeting of the PI3-kinase complex via Atg14L. *The Journal of Cell Biology,* 190**,** 511.

MATSUURA, A., TSUKADA, M., WADA, Y. & OHSUMI, Y. 1997. Apg1p, a novel protein kinase required for the autophagic process in Saccharomyces cerevisiae. *Gene,* 192**,** 245-50.

MATTERA, R., PARK, S. Y., DE PACE, R., GUARDIA, C. M. & BONIFACINO, J. S. 2017. AP-4 mediates export of ATG9A from the trans-Golgi network to promote autophagosome formation. *Proc Natl Acad Sci U S A,* 114**,** E10697-E10706.

MAUTHE, M., ORHON, I., ROCCHI, C., ZHOU, X., LUHR, M., HIJLKEMA, K.-J., COPPES, R. P., ENGEDAL, N., MARI, M. & REGGIORI, F. 2018. Chloroquine inhibits autophagic flux by decreasing autophagosome-lysosome fusion. *Autophagy,* 14**,** 1435-1455.

MAUVEZIN, C., NAGY, P., JUHÁSZ, G. & NEUFELD, T. P. 2015. Autophagosome-lysosome fusion is independent of V-ATPase-mediated acidification. *Nature communications,* 6**,** 7007-7007.

MAYLE, K. M., LE, A. M. & KAMEI, D. T. 2012. The intracellular trafficking pathway of transferrin. *Biochimica et biophysica acta,* 1820**,** 264-281.

MCALISTER, G. C., NUSINOW, D. P., JEDRYCHOWSKI, M. P., WÜHR, M., HUTTLIN, E. L., ERICKSON, B. K., RAD, R., HAAS, W. & GYGI, S. P. 2014. MultiNotch MS3 enables accurate, sensitive, and multiplexed detection of differential expression across cancer cell line proteomes. *Analytical chemistry,* 86**,** 7150-7158.

MCALPINE, F., WILLIAMSON, L., TOOZE, S. A. & CHAN, E. Y. W. 2013. Regulation of nutrient-sensitive autophagy by uncoordinated-51 like kinases 1 and 2. *Autophagy,* 9**,** 361-373.

MCBRIDE, A., GHILAGABER, S., NIKOLAEV, A. & HARDIE, D. G. 2009. The glycogen-binding domain on the AMPK beta subunit allows the kinase to act as a glycogen sensor. *Cell metabolism,* 9**,** 23-34.

MCEWAN, D. G., POPOVIC, D., GUBAS, A., TERAWAKI, S., SUZUKI, H., STADEL, D., COXON, F. P., MIRANDA DE STEGMANN, D., BHOGARAJU, S., MADDI, K., KIRCHOF, A., GATTI, E., HELFRICH, M. H., WAKATSUKI, S., BEHRENDS, C., PIERRE, P. & DIKIC, I. 2015. PLEKHM1 regulates autophagosome-lysosome fusion through HOPS complex and LC3/GABARAP proteins. *Mol Cell,* 57**,** 39-54.

MCINTIRE, S. L., GARRIGA, G., WHITE, J., JACOBSON, D. & ROBERT HORVITZ, H. 1992. Genes necessary for directed axonal elongation or fasciculation in C. elegans. *Neuron,* 8**,** 307-322.

MCKNIGHT, N. C., JEFFERIES, H. B., ALEMU, E. A., SAUNDERS, R. E., HOWELL, M., JOHANSEN, T. & TOOZE, S. A. 2012. Genome-wide siRNA screen reveals amino acid starvation-induced autophagy requires SCOC and WAC. *EMBO J,* 31**,** 1931-46.

MCLELLAND, G.-L., LEE, S. A., MCBRIDE, H. M. & FON, E. A. 2016. Syntaxin-17 delivers PINK1/parkin-dependent mitochondrial vesicles to the endolysosomal system. *The Journal of Cell Biology,* 214**,** 275.

MCWILLIAMS, T. G., BARINI, E., POHJOLAN-PIRHONEN, R., BROOKS, S. P., SINGH, F., BUREL, S., BALK, K., KUMAR, A., MONTAVA-GARRIGA, L., PRESCOTT, A. R., HASSOUN, S. M., MOUTON-LIGER, F., BALL, G., HILLS, R., KNEBEL, A., ULUSOY, A., DI MONTE, D. A., TAMJAR, J., ANTICO, O., FEARS, K., SMITH, L., BRAMBILLA, R., PALIN, E., VALORI, M., EEROLA-RAUTIO, J., TIENARI, P., CORTI, O., DUNNETT, S. B., GANLEY, I. G., SUOMALAINEN, A. & MUQIT, M. M. K. 2018. Phosphorylation of Parkin at serine 65 is essential for its activation in vivo. *Open biology,* 8**,** 180108.

MENG, J. & FERGUSON, S. M. 2018. GATOR1-dependent recruitment of FLCN–FNIP to lysosomes coordinates Rag GTPase heterodimer nucleotide status in response to amino acids. *The Journal of Cell Biology,* 217**,** 2765.

MENON, S., DIBBLE, C. C., TALBOTT, G., HOXHAJ, G., VALVEZAN, A. J., TAKAHASHI, H., CANTLEY, L. C. & MANNING, B. D. 2014. Spatial control of the TSC complex integrates insulin and nutrient regulation of mTORC1 at the lysosome. *Cell,* 156**,** 771-785.

MERCER, C. A., KALIAPPAN, A. & DENNIS, P. B. 2009. A novel, human Atg13 binding protein, Atg101, interacts with ULK1 and is essential for macroautophagy. *Autophagy,* 5**,** 649-662.

MERCER, T. J., GUBAS, A. & TOOZE, S. A. 2018. A molecular perspective of mammalian autophagosome biogenesis. *The Journal of biological chemistry,* 293**,** 5386-5395.

METAXAKIS, A., PLOUMI, C. & TAVERNARAKIS, N. 2018. Autophagy in Age-Associated Neurodegeneration. *Cells,* 7**,** 37.

METLAGEL, Z., OTOMO, C., TAKAESU, G. & OTOMO, T. 2013. Structural basis of ATG3 recognition by the autophagic ubiquitin-like protein ATG12. *Proceedings of the National Academy of Sciences of the United States of America,* 110**,** 18844-18849.

MI, N., CHEN, Y., WANG, S., CHEN, M., ZHAO, M., YANG, G., MA, M., SU, Q., LUO, S., SHI, J., XU, J., GUO, Q., GAO, N., SUN, Y., CHEN, Z. & YU, L. 2015. CapZ regulates autophagosomal membrane shaping by promoting actin assembly inside the isolation membrane. *Nat Cell Biol,* 17**,** 1112-23.

MICHAUD, M., MARTINS, I., SUKKURWALA, A. Q., ADJEMIAN, S., MA, Y., PELLEGATTI, P., SHEN, S., KEPP, O., SCOAZEC, M., MIGNOT, G., RELLO-VARONA, S., TAILLER, M., MENGER, L., VACCHELLI, E., GALLUZZI, L., GHIRINGHELLI, F., DI VIRGILIO, F., ZITVOGEL, L. & KROEMER, G. 2011. Autophagy-Dependent Anticancer Immune Responses Induced by Chemotherapeutic Agents in Mice. *Science,* 334**,** 1573.

MITRA, N. 2013. Incorporating Unnatural Amino Acids into Recombinant Proteins in Living Cells. *Materials and Methods,* 3.

MIZUSHIMA, N., KUMA, A., KOBAYASHI, Y., YAMAMOTO, A., MATSUBAE, M., TAKAO, T., NATSUME, T., OHSUMI, Y. & YOSHIMORI, T. 2003. Mouse Apg16L, a novel WD-repeat protein, targets to the autophagic isolation membrane with the Apg12-Apg5 conjugate. *J Cell Sci,* 116**,** 1679-1688.

MIZUSHIMA, N., NODA, T., YOSHIMORI, T., TANAKA, Y., ISHII, T., GEORGE, M. D., KLIONSKY, D. J., OHSUMI, M. & OHSUMI, Y. 1998. A protein conjugation system essential for autophagy. *Nature,* 395**,** 395-8.

MIZUSHIMA, N., YAMAMOTO, A., HATANO, M., KOBAYASHI, Y., KABEYA, Y., SUZUKI, K., TOKUHISA, T., OHSUMI, Y. & YOSHIMORI, T. 2001. Dissection of autophagosome formation using Apg5-deficient mouse embryonic stem cells. *J Cell Biol,* 152**,** 657-68.

MOCHIZUKI, H., TODA, H., ANDO, M., KURUSU, M., TOMODA, T. & FURUKUBO-TOKUNAGA, K. 2011. Unc-51/ATG1 controls axonal and dendritic development via kinesin-mediated vesicle transport in the Drosophila brain. *PloS one,* 6**,** e19632-e19632.

MOLEJON, M. I., ROPOLO, A., RE, A. L., BOGGIO, V. & VACCARO, M. I. 2013. The VMP1-Beclin 1 interaction regulates autophagy induction. *Scientific Reports,* 3**,** 1055.

MOREAU, K., GHISLAT, G., HOCHFELD, W., RENNA, M., ZAVODSZKY, E., RUNWAL, G., PURI, C., LEE, S., SIDDIQI, F., MENZIES, F. M., RAVIKUMAR, B. & RUBINSZTEIN, D. C. 2015. Transcriptional regulation of Annexin A2 promotes starvation-induced autophagy. *Nature Communications,* 6**,** 8045.

MOREAU, K., RAVIKUMAR, B., RENNA, M., PURI, C. & RUBINSZTEIN, DAVID C. 2011. Autophagosome Precursor Maturation Requires Homotypic Fusion. *Cell,* 146**,** 303-317.

MOREL, E., PARTON, R. G. & GRUENBERG, J. 2009. Annexin A2-Dependent Polymerization of Actin Mediates Endosome Biogenesis. *Developmental Cell,* 16**,** 445-457.

MOROZOVA, K., CLEMENT, C. C., KAUSHIK, S., STILLER, B., ARIAS, E., AHMAD, A., RAUCH, J. N., CHATTERJEE, V., MELIS, C., SCHARF, B., GESTWICKI, J. E., CUERVO, A.-M., ZUIDERWEG, E. R. P. & SANTAMBROGIO, L. 2016. Structural and Biological Interaction of hsc-70 Protein with Phosphatidylserine in Endosomal Microautophagy. *The Journal of biological chemistry,* 291**,** 18096-18106.

MOROZOVA, K., SIDHAR, S., ZOLLA, V., CLEMENT, C. C., SCHARF, B., VERZANI, Z., DIAZ, A., LAROCCA, J. N., HAJJAR, K. A., CUERVO, A. M. & SANTAMBROGIO, L. 2015. Annexin A2 promotes phagophore assembly by enhancing Atg16L+ vesicle biogenesis and homotypic fusion. *Nature Communications,* 6**,** 5856.

MUNSON, M. J., ALLEN, G. F. G., TOTH, R., CAMPBELL, D. G., LUCOCQ, J. M. & GANLEY, I. G. 2015. mTOR activates the VPS34–UVRAG complex to regulate autolysosomal tubulation and cell survival. *The EMBO Journal,* 34**,** 2272-2290.

MUNSON, M. J. & GANLEY, I. G. 2016. Determination of Cellular Phosphatidylinositol-3-phosphate (PI3P) Levels Using a Fluorescently Labelled Selective PI3P Binding Domain (PX). *Bio-protocol,* 6**,** e1903.

MURAKAWA, T., OKAMOTO, K., OMIYA, S., TANEIKE, M., YAMAGUCHI, O. & OTSU, K. 2019. A Mammalian Mitophagy Receptor, Bcl2-L-13, Recruits the ULK1 Complex to Induce Mitophagy. *Cell reports,* 26**,** 338-345.e6.

MURRAY, J. T., PANARETOU, C., STENMARK, H., MIACZYNSKA, M. & BACKER, J. M. 2002. Role of Rab5 in the recruitment of hVps34/p150 to the early endosome. *Traffic,* 3**,** 416-27.

NAIR, U., JOTWANI, A., GENG, J., GAMMOH, N., RICHERSON, D., YEN, W.-L., GRIFFITH, J., NAG, S., WANG, K., MOSS, T., BABA, M., MCNEW, J. A., JIANG, X., REGGIORI, F., MELIA, T. J. & KLIONSKY, D. J. 2011. SNARE proteins are required for macroautophagy. *Cell,* 146**,** 290-302.

NAIR, U., YEN, W.-L., MARI, M., CAO, Y., XIE, Z., BABA, M., REGGIORI, F. & KLIONSKY, D. J. 2012. A role for Atg8-PE deconjugation in autophagosome biogenesis. *Autophagy,* 8**,** 780-793.

NAKATOGAWA, H. 2013. Two ubiquitin-like conjugation systems that mediate membrane formation during autophagy. *Essays In Biochemistry,* 55**,** 39.

NAKATOGAWA, H., ICHIMURA, Y. & OHSUMI, Y. 2007. Atg8, a Ubiquitin-like Protein Required for Autophagosome Formation, Mediates Membrane Tethering and Hemifusion. *Cell,* 130**,** 165-178.

NAKATOGAWA, H., ISHII, J., ASAI, E. & OHSUMI, Y. 2012. Atg4 recycles inappropriately lipidated Atg8 to promote autophagosome biogenesis. *Autophagy,* 8**,** 177-186.

NAKATOGAWA, H., SUZUKI, K., KAMADA, Y. & OHSUMI, Y. 2009. Dynamics and diversity in autophagy mechanisms: lessons from yeast. *Nature Reviews Molecular Cell Biology,* 10**,** 458.

NASCIMBENI, A. C., GIORDANO, F., DUPONT, N., GRASSO, D., VACCARO, M. I., CODOGNO, P. & MOREL, E. 2017. ER-plasma membrane contact sites contribute to autophagosome biogenesis by regulation of local PI3P synthesis. *The EMBO journal,* 36**,** 2018-2033.

NATH, S., DANCOURT, J., SHTEYN, V., PUENTE, G., FONG, W. M., NAG, S., BEWERSDORF, J., YAMAMOTO, A., ANTONNY, B. & MELIA, T. J. 2014. Lipidation of the LC3/GABARAP family of autophagy proteins relies on a membrane-curvature-sensing domain in Atg3. *Nat Cell Biol,* 16**,** 415-24.

NAZIO, F., CARINCI, M., VALACCA, C., BIELLI, P., STRAPPAZZON, F., ANTONIOLI, M., CICCOSANTI, F., RODOLFO, C., CAMPELLO, S., FIMIA, G. M., SETTE, C., BONALDO, P. & CECCONI, F. 2016. Fine-tuning of ULK1 mRNA and protein levels is required for autophagy oscillation. *The Journal of Cell Biology*.

NAZIO, F., STRAPPAZZON, F., ANTONIOLI, M., BIELLI, P., CIANFANELLI, V., BORDI, M., GRETZMEIER, C., DENGJEL, J., PIACENTINI, M., FIMIA, G. M. & CECCONI, F. 2013. mTOR inhibits autophagy by controlling ULK1 ubiquitylation, self-association and function through AMBRA1 and TRAF6. *Nat Cell Biol,* 15**,** 406-416.

NEMAZANYY, I., BLAAUW, B., PAOLINI, C., CAILLAUD, C., PROTASI, F., MUELLER, A., PROIKAS-CEZANNE, T., RUSSELL, R. C., GUAN, K.-L., NISHINO, I., SANDRI, M., PENDE, M. & PANASYUK, G. 2013. Defects of Vps15 in skeletal muscles lead to autophagic vacuolar myopathy and lysosomal disease. *EMBO Molecular Medicine,* 5**,** 870-890.

NEMAZANYY, I., MONTAGNAC, G., RUSSELL, R. C., MORZYGLOD, L., BURNOL, A.-F., GUAN, K.-L., PENDE, M. & PANASYUK, G. 2015. Class III PI3K regulates organismal glucose homeostasis by providing negative feedback on hepatic insulin signalling. *Nature communications,* 6**,** 8283-8283.

NGUYEN, T. N., PADMAN, B. S., USHER, J., OORSCHOT, V., RAMM, G. & LAZAROU, M. 2016. Atg8 family LC3/GABARAP proteins are crucial for autophagosome–lysosome fusion but not autophagosome formation during PINK1/Parkin mitophagy and starvation. *J Cell Biol,* 215**,** 857-874.

NIE, T., YANG, S., MA, H., ZHANG, L., LU, F., TAO, K., WANG, R., YANG, R., HUANG, L., MAO, Z. & YANG, Q. 2016. Regulation of ER stress-induced autophagy by GSK3β-TIP60-ULK1 pathway. *Cell Death &Amp; Disease,* 7**,** e2563.

NIKIĆ, I., ESTRADA GIRONA, G., KANG, J. H., PACI, G., MIKHALEVA, S., KOEHLER, C., SHYMANSKA, N. V., VENTURA SANTOS, C., SPITZ, D. & LEMKE, E. A. 2016. Debugging Eukaryotic Genetic Code Expansion for Site-Specific Click-PAINT Super-Resolution Microscopy. *Angewandte Chemie (International ed. in English),* 55**,** 16172-16176.

NISHIDA, Y., ARAKAWA, S., FUJITANI, K., YAMAGUCHI, H., MIZUTA, T., KANASEKI, T., KOMATSU, M., OTSU, K., TSUJIMOTO, Y. & SHIMIZU, S. 2009. Discovery of Atg5/Atg7-independent alternative macroautophagy. *Nature,* 461**,** 654.

NISHIMURA, T., KAIZUKA, T., CADWELL, K., SAHANI, M. H., SAITOH, T., AKIRA, S., VIRGIN, H. W. & MIZUSHIMA, N. 2013. FIP200 regulates targeting of Atg16L1 to the isolation membrane. *EMBO reports,* 14**,** 284-291.

NODA, N. N., OHSUMI, Y. & INAGAKI, F. 2009. ATG systems from the protein structural point of view. *Chem Rev,* 109**,** 1587-98.

NOREN, C. J., ANTHONY-CAHILL, S. J., GRIFFITH, M. C. & SCHULTZ, P. G. 1989. A general method for site-specific incorporation of unnatural amino acids into proteins. *Science,* 244**,** 182.

NOVIKOFF, A. B. 1959. The proximal tubule cell in experimental hydronephrosis. *The Journal of biophysical and biochemical cytology,* 6**,** 136-138.

NOWAK, M. W., KEARNEY, P. C., SAMPSON, SAKS, M. E., LABARCA, C. G., SILVERMAN, S. K., ZHONG, W., THORSON, J., ABELSON, J. N., DAVIDSON, N. & ET, A. 1995. Nicotinic receptor binding site probed with unnatural amino acid incorporation in intact cells. *Science,* 268**,** 439.

NWADIKE, C., WILLIAMSON, L. E., GALLAGHER, L. E., GUAN, J.-L. & CHAN, E. Y. W. 2018. AMPK Inhibits ULK1-Dependent Autophagosome Formation and Lysosomal Acidification via Distinct Mechanisms. *Molecular and Cellular Biology,* 38**,** e00023-18.

OBARA, K., SEKITO, T., NIIMI, K. & OHSUMI, Y. 2008. The Atg18-Atg2 complex is recruited to autophagic membranes via phosphatidylinositol 3-phosphate and exerts an essential function. *J Biol Chem,* 283**,** 23972-80.

OBARA, K., SEKITO, T. & OHSUMI, Y. 2006. Assortment of phosphatidylinositol 3-kinase complexes--Atg14p directs association of complex I to the pre-autophagosomal structure in Saccharomyces cerevisiae. *Molecular biology of the cell,* 17**,** 1527-1539.

OGURA, K., WICKY, C., MAGNENAT, L., TOBLER, H., MORI, I., MULLER, F. & OHSHIMA, Y. 1994a. Caenorhabditis elegans unc-51 gene required for axonal elongation encodes a novel serine/threonine kinase. *Genes Dev,* 8**,** 2389-400.

OGURA, K.-I. & GOSHIMA, Y. 2006. The autophagy-related kinase UNC-51 and its binding partner UNC-14 regulate the subcellular localization of the Netrin receptor UNC-5 in <em>Caenorhabditis elegans</em&gt. *Development,* 133**,** 3441.

OGURA, K.-I., OKADA, T., MITANI, S., GENGYO-ANDO, K., BAILLIE, D. L., KOHARA, Y. & GOSHIMA, Y. 2010. Protein phosphatase 2A cooperates with the autophagy-related kinase UNC-51 to regulate axon guidance in <em>Caenorhabditis elegans</em&gt. *Development,* 137**,** 1657.

OGURA, K. I., WICKY COLLAUD, C., MAGNENAT, L., TOBLER, H., MORI, I., MÜLLER, F. & OHSHIMA, Y. 1994b. Caenorhabditis elegans unc-51 gene required for axonal elongation encodes a novel serine/threonine kinase. *Genes & development,* 8**,** 2389-400.

OHASHI, Y. & MUNRO, S. 2010. Membrane Delivery to the Yeast Autophagosome from the Golgi-Endosomal System. *Mol. Biol. Cell,* 21**,** 3998-4008.

OHASHI, Y., SOLER, N., GARCÍA ORTEGÓN, M., ZHANG, L., KIRSTEN, M. L., PERISIC, O., MASSON, G. R., BURKE, J. E., JAKOBI, A. J., APOSTOLAKIS, A. A., JOHNSON, C. M., OHASHI, M., KTISTAKIS, N. T., SACHSE, C. & WILLIAMS, R. L. 2016. Characterization of Atg38 and NRBF2, a fifth subunit of the autophagic Vps34/PIK3C3 complex. *Autophagy,* 12**,** 2129-2144.

OHASHI, Y., TREMEL, S. & WILLIAMS, R. L. 2019. VPS34 complexes from a structural perspective. *Journal of lipid research,* 60**,** 229-241.

OHSUMI, Y. 2014. Historical landmarks of autophagy research. *Cell research,* 24**,** 9-23.

OKU, M., NISHIMURA, T., HATTORI, T., ANO, Y., YAMASHITA, S.-I. & SAKAI, Y. 2006. Role of Vac8 in Formation of the Vacuolar Sequestering Membrane during Micropexophagy. *Autophagy,* 2**,** 272-279.

OKU, M. & SAKAI, Y. 2018. Three Distinct Types of Microautophagy Based on Membrane Dynamics and Molecular Machineries. *BioEssays,* 40**,** 1800008.

OLSVIK, H. L., LAMARK, T., TAKAGI, K., LARSEN, K. B., EVJEN, G., ØVERVATN, A., MIZUSHIMA, T. & JOHANSEN, T. 2015. FYCO1 Contains a C-terminally Extended, LC3A/B-preferring LC3-interacting Region (LIR) Motif Required for Efficient Maturation of Autophagosomes during Basal Autophagy. *The Journal of biological chemistry,* 290**,** 29361-29374.

ONG, S. E., BLAGOEV, B., KRATCHMAROVA, I., KRISTENSEN, D. B., STEEN, H., PANDEY, A. & MANN, M. 2002. Stable isotope labeling by amino acids in cell culture, SILAC, as a simple and accurate approach to expression proteomics. *Mol Cell Proteomics,* 1**,** 376-86.

OPPERMANN, F. S., GNAD, F., OLSEN, J. V., HORNBERGER, R., GREFF, Z., KÉRI, G., MANN, M. & DAUB, H. 2009. Large-scale proteomics analysis of the human kinome. *Molecular & cellular proteomics : MCP,* 8**,** 1751-1764.

ORSI, A., RAZI, M., DOOLEY, H. C., ROBINSON, D., WESTON, A. E., COLLINSON, L. M. & TOOZE, S. A. 2012. Dynamic and transient interactions of Atg9 with

autophagosomes, but not membrane integration, are required for autophagy. *Mol Biol Cell,* 23**,** 1860-73.

OSAWA, T., KOTANI, T., KAWAOKA, T., HIRATA, E., SUZUKI, K., NAKATOGAWA, H., OHSUMI, Y. & NODA, N. N. 2019. Atg2 mediates direct lipid transfer between membranes for autophagosome formation. *Nature Structural & Molecular Biology,* 26**,** 281-288.

OSHIMA, R., HASEGAWA, T., TAMAI, K., SUGENO, N., YOSHIDA, S., KOBAYASHI, J., KIKUCHI, A., BABA, T., FUTATSUGI, A., SATO, I., SATOH, K., TAKEDA, A., AOKI, M. & TANAKA, N. 2016. ESCRT-0 dysfunction compromises autophagic degradation of protein aggregates and facilitates ER stress-mediated neurodegeneration via apoptotic and necroptotic pathways. *Scientific Reports,* 6**,** 24997.

OTTO, G. P., WU, M. Y., KAZGAN, N., ANDERSON, O. R. & KESSIN, R. H. 2004. Dictyostelium Macroautophagy Mutants Vary in the Severity of Their Developmental Defects. *Journal of Biological Chemistry,* 279**,** 15621-15629.

OUYANG, L., ZHANG, L., ZHANG, S., YAO, D., ZHAO, Y., WANG, G., FU, L., LEI, P. & LIU, B. 2018. Small-Molecule Activator of UNC-51-Like Kinase 1 (ULK1) That Induces Cytoprotective Autophagy for Parkinson's Disease Treatment. *Journal of Medicinal Chemistry,* 61**,** 2776-2792.

PANARETOU, C., DOMIN, J., COCKCROFT, S. & WATERFIELD, M. D. 1997. Characterization of p150, an Adaptor Protein for the Human Phosphatidylinositol (PtdIns) 3-Kinase: SUBSTRATE PRESENTATION BY PHOSPHATIDYLINOSITOL TRANSFER PROTEIN TO THE p150·;PtdIns 3-KINASE COMPLEX. *Journal of Biological Chemistry,* 272**,** 2477-2485.

PANKIV, S., ALEMU, E. A., BRECH, A., BRUUN, J.-A., LAMARK, T., OVERVATN, A., BJORKOY, G. & JOHANSEN, T. 2010. FYCO1 is a Rab7 effector that binds to LC3 and PI3P to mediate microtubule plus end-directed vesicle transport. *J. Cell Biol.,* 188**,** 253-269.

PAPINSKI, D. & KRAFT, C. 2016. Regulation of Autophagy By Signaling Through the Atg1/ULK1 Complex. *Journal of Molecular Biology,* 428**,** 1725-1741.

PAPINSKI, D., SCHUSCHNIG, M., REITER, W., WILHELM, L., BARNES, C. A., MAIOLICA, A., HANSMANN, I., PFAFFENWIMMER, T., KIJANSKA, M., STOFFEL, I., LEE, S. S., BREZOVICH, A., LOU, J. H., TURK, B. E., AEBERSOLD, R., AMMERER, G., PETER, M. & KRAFT, C. 2014. Early steps in autophagy depend on direct phosphorylation of Atg9 by the Atg1 kinase. *Molecular cell,* 53**,** 471-483.

PAQUETTE, M., EL-HOUJEIRI, L. & PAUSE, A. 2018. mTOR Pathways in Cancer and Autophagy. *Cancers,* 10**,** 18.

PARK, J.-M., JUNG, C. H., SEO, M., OTTO, N. M., GRUNWALD, D., KIM, K. H., MORIARITY, B., KIM, Y.-M., STARKER, C., NHO, R. S., VOYTAS, D. & KIM, D.-H. 2016. The ULK1 complex mediates MTORC1 signaling to the autophagy initiation machinery via binding and phosphorylating ATG14. *Autophagy,* 12**,** 547-564.

PARK, J.-M., SEO, M., JUNG, C. H., GRUNWALD, D., STONE, M., OTTO, N. M., TOSO, E., AHN, Y., KYBA, M., GRIFFIN, T. J., HIGGINS, L. & KIM, D.-H. 2018. ULK1 phosphorylates Ser30 of BECN1 in association with ATG14 to stimulate autophagy induction. *Autophagy,* 14**,** 584-597.

PAVEL, M., RENNA, M., PARK, S. J., MENZIES, F. M., RICKETTS, T., FÜLLGRABE, J., ASHKENAZI, A., FRAKE, R. A., LOMBARTE, A. C., BENTO, C. F., FRANZE, K. & RUBINSZTEIN, D. C. 2018. Contact inhibition controls cell survival and proliferation via YAP/TAZ-autophagy axis. *Nature communications,* 9**,** 2961-2961.

PENGO, N., AGROTIS, A., PRAK, K., JONES, J. & KETTELER, R. 2017. A reversible phospho-switch mediated by ULK1 regulates the activity of autophagy protease ATG4B. *Nature Communications,* 8**,** 294.

PETHERICK, K. J., CONWAY, O. J., MPAMHANGA, C., OSBORNE, S. A., KAMAL, A., SAXTY, B. & GANLEY, I. G. 2015. Pharmacological inhibition of ULK1 kinase blocks mammalian target of rapamycin (mTOR)-dependent autophagy. *J Biol Chem,* 290**,** 28726.

PETTERSEN, E. F., GODDARD, T. D., HUANG, C. C., COUCH, G. S., GREENBLATT, D. M., MENG, E. C. & FERRIN, T. E. 2004. UCSF Chimera—A visualization system for exploratory research and analysis. *Journal of Computational Chemistry,* 25**,** 1605-1612.

PHILLIPS, M. J. & VOELTZ, G. K. 2015. Structure and function of ER membrane contact sites with other organelles. *Nature Reviews Molecular Cell Biology,* 17**,** 69.

PINTER, K., GRIGNANI, R. T., WATKINS, H. & REDWOOD, C. 2013. Localisation of AMPK γ subunits in cardiac and skeletal muscles. *Journal of muscle research and cell motility,* 34**,** 369-378.

PONOMARENKO, E. A., POVERENNAYA, E. V., ILGISONIS, E. V., PYATNITSKIY, M. A., KOPYLOV, A. T., ZGODA, V. G., LISITSA, A. V. & ARCHAKOV, A. I. 2016. The Size of the Human Proteome: The Width and Depth. *Int J Anal Chem,* 2016**,** 7436849.

PÖYHÖNEN, P., HIIPPALA, A., OLLILA, L., KAASALAINEN, T., HÄNNINEN, H., HELIÖ, T., TALLILA, J., VASILESCU, C., KIVISTÖ, S., OJALA, T. & HOLMSTRÖM, M. 2015. Cardiovascular magnetic resonance findings in patients with PRKAG2 gene mutations. *Journal of cardiovascular magnetic resonance : official journal of the Society for Cardiovascular Magnetic Resonance,* 17**,** 89-89.

PRYOR, P. R., MULLOCK, B. M., BRIGHT, N. A., LINDSAY, M. R., GRAY, S. R., RICHARDSON, S. C., STEWART, A., JAMES, D. E., PIPER, R. C. & LUZIO, J. P. 2004. Combinatorial SNARE complexes with VAMP7 or VAMP8 define different late endocytic fusion events. *EMBO Rep,* 5**,** 590-5.

PUENTE, C., HENDRICKSON, R. C. & JIANG, X. 2016. Nutrient-Regulated Phosphorylation of ATG13 Inhibits Starvation-Induced Autophagy. *Journal of Biological Chemistry,* 291**,** 6026-6035.

PURI, C., VICINANZA, M., ASHKENAZI, A., GRATIAN, M. J., ZHANG, Q., BENTO, C. F., RENNA, M., MENZIES, F. M. & RUBINSZTEIN, D. C. 2018. The RAB11A-Positive Compartment Is a Primary Platform for Autophagosome Assembly Mediated by WIPI2 Recognition of PI3P-RAB11A. *Developmental cell,* 45**,** 114-131.e8.

PYO, J.-O., YOO, S.-M., AHN, H.-H., NAH, J., HONG, S.-H., KAM, T.-I., JUNG, S. & JUNG, Y.-K. 2013. Overexpression of Atg5 in mice activates autophagy and extends lifespan. *Nature communications,* 4**,** 2300-2300.

PYO, K. E., KIM, C. R., LEE, M., KIM, J. S., KIM, K. I. & BAEK, S. H. 2018. ULK1 O-GlcNAcylation Is Crucial for Activating VPS34 via ATG14L during Autophagy Initiation. *Cell Rep,* 25**,** 2878-2890 e4.

QI, S., KIM, D. J., STJEPANOVIC, G. & HURLEY, J. H. 2015. Structure of the Human Atg13-Atg101 HORMA Heterodimer: an Interaction Hub within the ULK1 Complex. *Structure (London, England : 1993),* 23**,** 1848-1857.

RAGUSA, MICHAEL J., STANLEY, ROBIN E. & HURLEY, JAMES H. 2012. Architecture of the Atg17 Complex as a Scaffold for Autophagosome Biogenesis. *Cell,* 151**,** 1501-1512.

RAIMONDI, M., CESSELLI, D., DI LORETO, C., LA MARRA, F., SCHNEIDER, C. & DEMARCHI, F. 2019. USP1 (ubiquitin specific peptidase 1) targets ULK1 and

regulates its cellular compartmentalization and autophagy. *Autophagy,* 15**,** 613-630.

RAJAMOHAN, F., REYES, A. R., FRISBIE, R. K., HOTH, L. R., SAHASRABUDHE, P., MAGYAR, R., LANDRO, J. A., WITHKA, J. M., CASPERS, N. L., CALABRESE, M. F., WARD, J. & KURUMBAIL, R. G. 2016. Probing the enzyme kinetics, allosteric modulation and activation of alpha1- and alpha2-subunit-containing AMP-activated protein kinase (AMPK) heterotrimeric complexes by pharmacological and physiological activators. *Biochem J,* 473**,** 581-92.

RAJESH, S., BAGO, R., ODINTSOVA, E., MURATOV, G., BALDWIN, G., SRIDHAR, P., RAJESH, S., OVERDUIN, M. & BERDITCHEVSKI, F. 2011. Binding to Syntenin-1 Protein Defines a New Mode of Ubiquitin-based Interactions Regulated by Phosphorylation. *Journal of Biological Chemistry,* 286**,** 39606-39614.

RAN, F. A., HSU, P. D., WRIGHT, J., AGARWALA, V., SCOTT, D. A. & ZHANG, F. 2013. Genome engineering using the CRISPR-Cas9 system. *Nature protocols,* 8**,** 2281-2308.

RAO, Y., PERNA, M. G., HOFMANN, B., BEIER, V. & WOLLERT, T. 2016. The Atg1–kinase complex tethers Atg9-vesicles to initiate autophagy. *Nature Communications,* 7**,** 10338.

RAVENHILL, B. J., BOYLE, K. B., VON MUHLINEN, N., ELLISON, C. J., MASSON, G. R., OTTEN, E. G., FOEGLEIN, A., WILLIAMS, R. & RANDOW, F. 2019. The Cargo Receptor NDP52 Initiates Selective Autophagy by Recruiting the ULK Complex to Cytosol-Invading Bacteria. *Molecular Cell*.

RAVIKUMAR, B., MOREAU, K., JAHREISS, L., PURI, C. & RUBINSZTEIN, D. C. 2010. Plasma membrane contributes to the formation of pre-autophagosomal structures. *Nat Cell Biol,* advance online publication**,** 747-57.

RAZI, M., CHAN, E. Y. & TOOZE, S. A. 2009. Early endosomes and endosomal coatomer are required for autophagy. *J Cell Biol,* 185**,** 305-21.

REGGIORI, F., TUCKER, K. A., STROMHAUG, P. E. & KLIONSKY, D. J. 2004. The Atg1-Atg13 Complex Regulates Atg9 and Atg23 Retrieval Transport from the Pre-Autophagosomal Structure. *Developmental Cell,* 6**,** 79-90.

RIETER, E., VINKE, F., BAKULA, D., CEBOLLERO, E., UNGERMANN, C., PROIKAS-CEZANNE, T. & REGGIORI, F. 2013. Atg18 function in autophagy is regulated by specific sites within its β-propeller. *Journal of Cell Science,* 126**,** 593.

RIKKA, S., QUINSAY, M. N., THOMAS, R. L., KUBLI, D. A., ZHANG, X., MURPHY, A. N. & GUSTAFSSON, Å. B. 2011. Bnip3 impairs mitochondrial bioenergetics and stimulates mitochondrial turnover. *Cell death and differentiation,* 18**,** 721-731.

RILEY, B. E., KAISER, S. E., SHALER, T. A., NG, A. C. Y., HARA, T., HIPP, M. S., LAGE, K., XAVIER, R. J., RYU, K.-Y., TAGUCHI, K., YAMAMOTO, M., TANAKA, K., MIZUSHIMA, N., KOMATSU, M. & KOPITO, R. R. 2010. Ubiquitin accumulation in autophagy-deficient mice is dependent on the Nrf2-mediated stress response pathway: a potential role for protein aggregation in autophagic substrate selection. *The Journal of cell biology,* 191**,** 537-552.

RO, S.-H., JUNG, C. H., HAHN, W. S., XU, X., KIM, Y.-M., YUN, Y. S., PARK, J.-M., KIM, K. H., SEO, M., HA, T.-Y., ARRIAGA, E. A., BERNLOHR, D. A. & KIM, D.-H. 2013. Distinct functions of Ulk1 and Ulk2 in the regulation of lipid metabolism in adipocytes. *Autophagy,* 9**,** 2103-2114.

RO, S.-H., SEMPLE, I. A., PARK, H., PARK, H., PARK, H.-W., KIM, M., KIM, J. S. & LEE, J. H. 2014. Sestrin2 Promotes Unc-51-like Kinase 1 (ULK1)-Mediated Phosphorylation of p62/sequestosome-1. *The FEBS journal,* 281**,** 3816-3827.

RONG, Y., LIU, M., MA, L., DU, W., ZHANG, H., TIAN, Y., CAO, Z., LI, Y., REN, H., ZHANG, C., LI, L., CHEN, S., XI, J. & YU, L. 2012. Clathrin and

phosphatidylinositol-4,5-bisphosphate regulate autophagic lysosome reformation. *Nat Cell Biol,* 14**,** 924-34.
ROSNER, M., FUCHS, C., DOLZNIG, H. & HENGSTSCHLÄGER, M. 2011. Different cytoplasmic/nuclear distribution of S6 protein phosphorylated at S240/244 and S235/236. *Amino acids,* 40**,** 595-600.
ROSS, C. A. & POIRIER, M. A. 2004. Protein aggregation and neurodegenerative disease. *Nature Medicine,* 10**,** S10.
ROSS, F. A., JENSEN, T. E. & HARDIE, D. G. 2016. Differential regulation by AMP and ADP of AMPK complexes containing different gamma subunit isoforms. *Biochem J,* 473**,** 189-99.
ROSTISLAVLEVA, K., SOLER, N., OHASHI, Y., ZHANG, L., PARDON, E., BURKE, J. E., MASSON, G. R., JOHNSON, C., STEYAERT, J., KTISTAKIS, N. T. & WILLIAMS, R. L. 2015. Structure and flexibility of the endosomal Vps34 complex reveals the basis of its function on membranes. *Science (New York, N.Y.),* 350**,** aac7365-aac7365.
ROTTY, J. D., WU, C. & BEAR, J. E. 2012. New insights into the regulation and cellular functions of the ARP2/3 complex. *Nature Reviews Molecular Cell Biology,* 14**,** 7.
ROUT, A. K., STRUB, M.-P., PISZCZEK, G. & TJANDRA, N. 2014. Structure of transmembrane domain of lysosome-associated membrane protein type 2a (LAMP-2A) reveals key features for substrate specificity in chaperone-mediated autophagy. *The Journal of biological chemistry,* 289**,** 35111-35123.
RUAN, H.-B., MA, Y., TORRES, S., ZHANG, B., FERIOD, C., HECK, R. M., QIAN, K., FU, M., LI, X., NATHANSON, M. H., BENNETT, A. M., NIE, Y., EHRLICH, B. E. & YANG, X. 2017. Calcium-dependent O-GlcNAc signaling drives liver autophagy in adaptation to starvation. *Genes & development,* 31**,** 1655-1665.
RUBIN, G. M., YANDELL, M. D., WORTMAN, J. R., GABOR MIKLOS, G. L., NELSON, C. R., HARIHARAN, I. K., FORTINI, M. E., LI, P. W., APWEILER, R., FLEISCHMANN, W., CHERRY, J. M., HENIKOFF, S., SKUPSKI, M. P., MISRA, S., ASHBURNER, M., BIRNEY, E., BOGUSKI, M. S., BRODY, T., BROKSTEIN, P., CELNIKER, S. E., CHERVITZ, S. A., COATES, D., CRAVCHIK, A., GABRIELIAN, A., GALLE, R. F., GELBART, W. M., GEORGE, R. A., GOLDSTEIN, L. S., GONG, F., GUAN, P., HARRIS, N. L., HAY, B. A., HOSKINS, R. A., LI, J., LI, Z., HYNES, R. O., JONES, S. J., KUEHL, P. M., LEMAITRE, B., LITTLETON, J. T., MORRISON, D. K., MUNGALL, C., O'FARRELL, P. H., PICKERAL, O. K., SHUE, C., VOSSHALL, L. B., ZHANG, J., ZHAO, Q., ZHENG, X. H. & LEWIS, S. 2000. Comparative genomics of the eukaryotes. *Science,* 287**,** 2204-15.
RUI, Y.-N., XU, Z., PATEL, B., CHEN, Z., CHEN, D., TITO, A., DAVID, G., SUN, Y., STIMMING, E. F., BELLEN, H. J., CUERVO, A. M. & ZHANG, S. 2015. Huntingtin functions as a scaffold for selective macroautophagy. *Nat Cell Biol,* 17**,** 262-275.
RUNWAL, G., STAMATAKOU, E., SIDDIQI, F. H., PURI, C., ZHU, Y. & RUBINSZTEIN, D. C. 2019. LC3-positive structures are prominent in autophagy-deficient cells. *Scientific Reports,* 9**,** 10147.
RUSSELL, R. C., TIAN, Y., YUAN, H., PARK, H. W., CHANG, Y.-Y., KIM, J., KIM, H., NEUFELD, T. P., DILLIN, A. & GUAN, K.-L. 2013. ULK1 induces autophagy by phosphorylating Beclin-1 and activating Vps34 lipid kinase. *Nature cell biology,* 15**,** 741-750.
RUSTEN, T. E. & STENMARK, H. 2009. How do ESCRT proteins control autophagy? *Journal of Cell Science,* 122**,** 2179.
RUSTEN, T. E., VACCARI, T., LINDMO, K., RODAHL, L. M. W., NEZIS, I. P., SEM-JACOBSEN, C., WENDLER, F., VINCENT, J.-P., BRECH, A., BILDER, D. &

STENMARK, H. 2007. ESCRTs and Fab1 Regulate Distinct Steps of Autophagy. *Current Biology,* 17**,** 1817-1825.
SADRE-BAZZAZ, K., WHITBY, F. G., ROBINSON, H., FORMOSA, T. & HILL, C. P. 2010. Structure of a Blm10 complex reveals common mechanisms for proteasome binding and gate opening. *Molecular cell,* 37**,** 728-735.
SAHU, R., KAUSHIK, S., CLEMENT, C. C., CANNIZZO, E. S., SCHARF, B., FOLLENZI, A., POTOLICCHIO, I., NIEVES, E., CUERVO, A. M. & SANTAMBROGIO, L. 2011. Microautophagy of Cytosolic Proteins by Late Endosomes. *Developmental Cell,* 20**,** 131-139.
SAITO, T., NAH, J., OKA, S.-I., MUKAI, R., MONDEN, Y., MAEJIMA, Y., IKEDA, Y., SCIARRETTA, S., LIU, T., LI, H., BALJINNYAM, E., FRAIDENRAICH, D., FRITZKY, L., ZHAI, P., ICHINOSE, S., ISOBE, M., HSU, C.-P., KUNDU, M. & SADOSHIMA, J. 2019. An alternative mitophagy pathway mediated by Rab9 protects the heart against ischemia. *The Journal of Clinical Investigation,* 129**,** 802-819.
SAITOH, T., FUJITA, N., HAYASHI, T., TAKAHARA, K., SATOH, T., LEE, H., MATSUNAGA, K., KAGEYAMA, S., OMORI, H., NODA, T., YAMAMOTO, N., KAWAI, T., ISHII, K., TAKEUCHI, O., YOSHIMORI, T. & AKIRA, S. 2009. Atg9a controls dsDNA-driven dynamic translocation of STING and the innate immune response. *Proceedings of the National Academy of Sciences of the United States of America,* 106**,** 20842-20846.
SAKOH-NAKATOGAWA, M., MATOBA, K., ASAI, E., KIRISAKO, H., ISHII, J., NODA, N. N., INAGAKI, F., NAKATOGAWA, H. & OHSUMI, Y. 2013. Atg12–Atg5 conjugate enhances E2 activity of Atg3 by rearranging its catalytic site. *Nature Structural &Amp; Molecular Biology,* 20**,** 433.
SANCAK, Y., BAR-PELED, L., ZONCU, R., MARKHARD, A. L., NADA, S. & SABATINI, D. M. 2010. Ragulator-Rag complex targets mTORC1 to the lysosomal surface and is necessary for its activation by amino acids. *Cell,* 141**,** 290-303.
SANCAK, Y., PETERSON, T. R., SHAUL, Y. D., LINDQUIST, R. A., THOREEN, C. C., BAR-PELED, L. & SABATINI, D. M. 2008. The Rag GTPases Bind Raptor and Mediate Amino Acid Signaling to mTORC1. *Science,* 320**,** 1496-1501.
SÁNCHEZ-WANDELMER, J., KRIEGENBURG, F., ROHRINGER, S., SCHUSCHNIG, M., GÓMEZ-SÁNCHEZ, R., ZENS, B., ABREU, S., HARDENBERG, R., HOLLENSTEIN, D., GAO, J., UNGERMANN, C., MARTENS, S., KRAFT, C. & REGGIORI, F. 2017. Atg4 proteolytic activity can be inhibited by Atg1 phosphorylation. *Nature communications,* 8**,** 295-295.
SAVITSKI, M., MATHIESON, T., ZINN, N., SWEETMAN, G., DOCE, C., BECHER, I., PACHL, F., KUSTER, B. & BANTSCHEFF, M. 2013. Measuring and Managing Ratio Compression for Accurate iTRAQ/TMT Quantification. *Journal of proteome research,* 12.
SCHAFER, D. A., KORSHUNOVA, Y. O., SCHROER, T. A. & COOPER, J. A. 1994. Differential localization and sequence analysis of capping protein beta-subunit isoforms of vertebrates. *The Journal of cell biology,* 127**,** 453-465.
SCHU, P. V., TAKEGAWA, K., FRY, M. J., STACK, J. H., WATERFIELD, M. D. & EMR, S. D. 1993. Phosphatidylinositol 3-kinase encoded by yeast VPS34 gene essential for protein sorting. *Science,* 260**,** 88.
SCHUCK, S., GALLAGHER, C. M. & WALTER, P. 2014. ER-phagy mediates selective degradation of endoplasmic reticulum independently of the core autophagy machinery. *Journal of cell science,* 127**,** 4078-4088.
SEKI, A. & RUTZ, S. 2018. Optimized RNP transfection for highly efficient CRISPR/Cas9-mediated gene knockout in primary T cells. *The Journal of experimental medicine,* 215**,** 985-997.

SELLIER, C., CAMPANARI, M. L., JULIE CORBIER, C., GAUCHEROT, A., KOLB‐CHEYNEL, I., OULAD‐ABDELGHANI, M., RUFFENACH, F., PAGE, A., CIURA, S., KABASHI, E. & CHARLET‐BERGUERAND, N. 2016. Loss of C9ORF72 impairs autophagy and synergizes with polyQ Ataxin‐2 to induce motor neuron dysfunction and cell death. *The EMBO Journal,* 35**,** 1276-1297.

SHALEM, O., SANJANA, N. E. & ZHANG, F. 2015. High-throughput functional genomics using CRISPR-Cas9. *Nature reviews. Genetics,* 16**,** 299-311.

SHANG, L., CHEN, S., DU, F., LI, S., ZHAO, L. & WANG, X. 2011. Nutrient starvation elicits an acute autophagic response mediated by Ulk1 dephosphorylation and its subsequent dissociation from AMPK. *Proceedings of the National Academy of Sciences,* 108**,** 4788-4793.

SHARIFI, M. N., MOWERS, E. E., DRAKE, L. E., COLLIER, C., CHEN, H., ZAMORA, M., MUI, S. & MACLEOD, K. F. 2016. Autophagy Promotes Focal Adhesion Disassembly and Cell Motility of Metastatic Tumor Cells through the Direct Interaction of Paxillin with LC3. *Cell reports,* 15**,** 1660-1672.

SHARMA, K., D'SOUZA, ROCHELLE C. J., TYANOVA, S., SCHAAB, C., WIŚNIEWSKI, JACEK R., COX, J. & MANN, M. 2014. Ultradeep Human Phosphoproteome Reveals a Distinct Regulatory Nature of Tyr and Ser/Thr-Based Signaling. *Cell Reports,* 8**,** 1583-1594.

SHI, C.-S. & KEHRL, J. H. 2010. Traf6 and A20 differentially regulate TLR4-induced autophagy by affecting the ubiquitination of Beclin 1. *Autophagy,* 6**,** 986-987.

SHIBATA, S., ISHIZAWA, K., WANG, Q., XU, N., FUJITA, T., UCHIDA, S. & LIFTON, R. P. 2018. ULK1 Phosphorylates and Regulates Mineralocorticoid Receptor. *Cell Reports,* 24**,** 569-576.

SHIMA, T., KIRISAKO, H. & NAKATOGAWA, H. 2019. COPII vesicles contribute to autophagosomal membranes. *The Journal of Cell Biology,* 218**,** 1503.

SHIN, S. H., LEE, E. J., CHUN, J., HYUN, S. & KANG, S. S. 2015. ULK2 Ser 1027 Phosphorylation by PKA Regulates Its Nuclear Localization Occurring through Karyopherin Beta 2 Recognition of a PY-NLS Motif. *PLoS One,* 10**,** e0127784.

SIDDIQUI, S. S. 1990. Mutations affecting axonal growth and guidance of motor neurons and mechanosensory neurons in the nematode Caenorhabditis elegans. *Neuroscience Research Supplements,* 13**,** S171-S190.

SIGRIST, C. J. A., DE CASTRO, E., CERUTTI, L., CUCHE, B. A., HULO, N., BRIDGE, A., BOUGUELERET, L. & XENARIOS, I. 2013. New and continuing developments at PROSITE. *Nucleic acids research,* 41**,** D344-D347.

SINGH, A., KENDALL, S. L. & CAMPANELLA, M. 2018. Common Traits Spark the Mitophagy/Xenophagy Interplay. *Frontiers in Physiology,* 9.

SMITH, R. E. & FARQUHAR, M. G. 1966. Lysosome function in the regulation of the secretory process in cells of the anterior pituitary gland. *J. Cell Bio.,* 31**,** 319-347.

SOMMESE, R. F., RITT, M., SWANSON, C. J. & SIVARAMAKRISHNAN, S. 2017. The Role of Regulatory Domains in Maintaining Autoinhibition in the Multidomain Kinase PKCα. *The Journal of biological chemistry,* 292**,** 2873-2880.

SØRENG, K., MUNSON, M. J., LAMB, C. A., BJØRNDAL, G. T., PANKIV, S., CARLSSON, S. R., TOOZE, S. A. & SIMONSEN, A. 2018a. SNX18 regulates ATG9A trafficking from recycling endosomes by recruiting Dynamin‐2. *EMBO reports*.

SØRENG, K., NEUFELD, T. P. & SIMONSEN, A. 2018b. Chapter One - Membrane Trafficking in Autophagy. *In:* GALLUZZI, L. (ed.) *International Review of Cell and Molecular Biology.* Academic Press.

SOU, Y.-S., WAGURI, S., IWATA, J.-I., UENO, T., FUJIMURA, T., HARA, T., SAWADA, N., YAMADA, A., MIZUSHIMA, N., UCHIYAMA, Y., KOMINAMI, E.,

TANAKA, K. & KOMATSU, M. 2008. The Atg8 Conjugation System Is Indispensable for Proper Development of Autophagic Isolation Membranes in Mice. *Mol. Biol. Cell,* 19**,** 4762-4775.

SOU, Y. S., TANIDA, I., KOMATSU, M., UENO, T. & KOMINAMI, E. 2006. Phosphatidylserine in addition to phosphatidylethanolamine is an in vitro target of the mammalian Atg8 modifiers, LC3, GABARAP, and GATE-16. *J Biol Chem,* 281**,** 3017-24.

SRIDHAR, S., PATEL, B., APHKHAZAVA, D., MACIAN, F., SANTAMBROGIO, L., SHIELDS, D. & CUERVO, A. M. 2013. The lipid kinase PI4KIIIβ preserves lysosomal identity. *The EMBO journal,* 32**,** 324-339.

SRINIVASAN, G., JAMES, C. M. & KRZYCKI, J. A. 2002. Pyrrolysine Encoded by UAG in Archaea: Charging of a UAG-Decoding Specialized tRNA. *Science,* 296**,** 1459.

STACK, J. H., DEWALD, D. B., TAKEGAWA, K. & EMR, S. D. 1995. Vesicle-mediated protein transport: regulatory interactions between the Vps15 protein kinase and the Vps34 PtdIns 3-kinase essential for protein sorting to the vacuole in yeast. *The Journal of cell biology,* 129**,** 321-334.

STACK, J. H. & EMR, S. D. 1994. Vps34p required for yeast vacuolar protein sorting is a multiple specificity kinase that exhibits both protein kinase and phosphatidylinositol-specific PI 3-kinase activities. *Journal of Biological Chemistry,* 269**,** 31552-62.

STACK, J. H., HERMAN, P. K., SCHU, P. V. & EMR, S. D. 1993. A membrane-associated complex containing the Vps15 protein kinase and the Vps34 PI 3-kinase is essential for protein sorting to the yeast lysosome-like vacuole. *The EMBO journal,* 12**,** 2195-2204.

STARK, C., BREITKREUTZ, B.-J., REGULY, T., BOUCHER, L., BREITKREUTZ, A. & TYERS, M. 2006. BioGRID: a general repository for interaction datasets. *Nucleic acids research,* 34**,** D535-D539.

STARLING, G. P., YIP, Y. Y., SANGER, A., MORTON, P. E., EDEN, E. R. & DODDING, M. P. 2016. Folliculin directs the formation of a Rab34-RILP complex to control the nutrient-dependent dynamic distribution of lysosomes. *EMBO reports,* 17**,** 823-841.

STEIN, M. P., FENG, Y., COOPER, K. L., WELFORD, A. M. & WANDINGER-NESS, A. 2003. Human VPS34 and p150 are Rab7 interacting partners. *Traffic,* 4**,** 754-71.

STEPHAN, J. S., YEH, Y.-Y., RAMACHANDRAN, V., DEMINOFF, S. J. & HERMAN, P. K. 2009. The Tor and PKA signaling pathways independently target the Atg1/Atg13 protein kinase complex to control autophagy. *Proceedings of the National Academy of Sciences of the United States of America,* 106**,** 17049-17054.

STJEPANOVIC, G., BASKARAN, S., LIN, M. G. & HURLEY, J. H. 2017. Vps34 Kinase Domain Dynamics Regulate the Autophagic PI 3-Kinase Complex. *Molecular Cell,* 67**,** 528-534.

STJEPANOVIC, G., DAVIES, C. W., STANLEY, R. E., RAGUSA, M. J., KIM DO, J. & HURLEY, J. H. 2014. Assembly and dynamics of the autophagy-initiating Atg1 complex. *Proc Natl Acad Sci U S A,* 111**,** 12793-8.

STOETZEL, C., BÄR, S., DE CRAENE, J.-O., SCHEIDECKER, S., ETARD, C., CHICHER, J., RECK, J. R., PERRAULT, I., GEOFFROY, V., CHENNEN, K., STRÄHLE, U., HAMMANN, P., FRIANT, S. & DOLLFUS, H. 2016. A mutation in VPS15 (PIK3R4) causes a ciliopathy and affects IFT20 release from the cis-Golgi. *Nature Communications,* 7**,** 13586.

SU, H., YANG, F., WANG, Q., SHEN, Q., HUANG, J., PENG, C., ZHANG, Y., WAN, W., WONG, C. C. L., SUN, Q., WANG, F., ZHOU, T. & LIU, W. 2017. VPS34

Acetylation Controls Its Lipid Kinase Activity and the Initiation of Canonical and Non-canonical Autophagy. *Molecular Cell,* 67**,** 907-921.e7.

SUN, Q., WESTPHAL, W., WONG, K. N., TAN, I. & ZHONG, Q. 2010. Rubicon controls endosome maturation as a Rab7 effector. *Proceedings of the National Academy of Sciences of the United States of America,* 107**,** 19338-19343.

SUN, Q., ZHANG, J., FAN, W., WONG, K. N., DING, X., CHEN, S. & ZHONG, Q. 2011. The RUN domain of rubicon is important for hVps34 binding, lipid kinase inhibition, and autophagy suppression. *The Journal of biological chemistry,* 286**,** 185-191.

SUN, T., LI, X., ZHANG, P., CHEN, W.-D., ZHANG, H.-L., LI, D.-D., DENG, R., QIAN, X.-J., JIAO, L., JI, J., LI, Y.-T., WU, R.-Y., YU, Y., FENG, G.-K. & ZHU, X.-F. 2015. Acetylation of Beclin 1 inhibits autophagosome maturation and promotes tumour growth. *Nature communications,* 6**,** 7215-7215.

SUN, Y., LI, T. Y., SONG, L., ZHANG, C., LI, J., LIN, Z.-Z., LIN, S.-C. & LIN, S.-Y. 2018. Liver-specific deficiency of unc-51 like kinase 1 and 2 protects mice from acetaminophen-induced liver injury. *Hepatology,* 67**,** 2397-2413.

SUZUKI, K., AKIOKA, M., KONDO-KAKUTA, C., YAMAMOTO, H. & OHSUMI, Y. 2013. Fine mapping of autophagy-related proteins during autophagosome formation in Saccharomyces cerevisiae. *Journal of Cell Science,* 126**,** 2534-2544.

SUZUKI, K., KUBOTA, Y., SEKITO, T. & OHSUMI, Y. 2007. Hierarchy of Atg proteins in pre-autophagosomal structure organization. *Genes to Cells,* 12**,** 209-218.

SUZUKI, S. W., YAMAMOTO, H., OIKAWA, Y., KONDO-KAKUTA, C., KIMURA, Y., HIRANO, H. & OHSUMI, Y. 2015. Atg13 HORMA domain recruits Atg9 vesicles during autophagosome formation. *Proceedings of the National Academy of Sciences,* 112**,** 3350-3355.

TAKAHASHI, Y., HE, H., TANG, Z., HATTORI, T., LIU, Y., YOUNG, M. M., SERFASS, J. M., CHEN, L., GEBRU, M., CHEN, C., WILLS, C. A., ATKINSON, J. M., CHEN, H., ABRAHAM, T. & WANG, H.-G. 2018. An autophagy assay reveals the ESCRT-III component CHMP2A as a regulator of phagophore closure. *Nature Communications,* 9**,** 2855.

TAKAMURA, A., KOMATSU, M., HARA, T., SAKAMOTO, A., KISHI, C., WAGURI, S., EISHI, Y., HINO, O., TANAKA, K. & MIZUSHIMA, N. 2011. Autophagy-deficient mice develop multiple liver tumors. *Genes & development,* 25**,** 795-800.

TAN, D., CAI, Y., WANG, J., ZHANG, J., MENON, S., CHOU, H.-T., FERRO-NOVICK, S., REINISCH, K. M. & WALZ, T. 2013. The EM structure of the TRAPPIII complex leads to the identification of a requirement for COPII vesicles on the macroautophagy pathway. *Proceedings of the National Academy of Sciences of the United States of America,* 110**,** 19432-19437.

TAN, X., THAPA, N., LIAO, Y., CHOI, S. & ANDERSON, R. A. 2016. PtdIns(4,5)P2 signaling regulates ATG14 and autophagy. *Proceedings of the National Academy of Sciences,* 113**,** 10896-10901.

TANAKA, K. 2009. The proteasome: overview of structure and functions. *Proceedings of the Japan Academy. Series B, Physical and biological sciences,* 85**,** 12-36.

TANG, F., HU, P., YANG, Z., XUE, C., GONG, J., SUN, S., SHI, L., ZHANG, S., LI, Z., YANG, C., ZHANG, J. & XIE, C. 2017a. SBI0206965, a novel inhibitor of Ulk1, suppresses non-small cell lung cancer cell growth by modulating both autophagy and apoptosis pathways. *Oncology Reports,* 37.

TANG, H. W., WANG, Y. B., WANG, S. L., WU, M. H., LIN, S. Y. & CHEN, G. C. 2011. Atg1-mediated myosin II activation regulates autophagosome formation during starvation-induced autophagy. *EMBO J,* 30**,** 636-51.

TANG, Z., TAKAHASHI, Y., CHEN, C., LIU, Y., HE, H., TSOTAKOS, N., SERFASS, J. M., GEBRU, M. T., CHEN, H., YOUNG, M. M. & WANG, H.-G. 2017b. Atg2A/B

deficiency switches cytoprotective autophagy to non-canonical caspase-8 activation and apoptosis. *Cell death and differentiation,* 24**,** 2127-2138.

TANG, Z., TAKAHASHI, Y., HE, H., HATTORI, T., CHEN, C., LIANG, X., CHEN, H., YOUNG, M. M. & WANG, H.-G. 2019. TOM40 Targets Atg2 to Mitochondria-Associated ER Membranes for Phagophore Expansion. *Cell reports,* 28**,** 1744-1757.e5.

TAYLOR, R. P., PARKER, G. J., HAZEL, M. W., SOESANTO, Y., FULLER, W., YAZZIE, M. J. & MCCLAIN, D. A. 2008. Glucose Deprivation Stimulates O-GlcNAc Modification of Proteins through Up-regulation of O-Linked N-Acetylglucosaminyltransferase. *Journal of Biological Chemistry,* 283**,** 6050-6057.

TAYLOR, S. S. & KORNEV, A. P. 2011. Protein kinases: evolution of dynamic regulatory proteins. *Trends in biochemical sciences,* 36**,** 65-77.

TEKIRDAG, K. & CUERVO, A. M. 2018. Chaperone-mediated autophagy and endosomal microautophagy: Joint by a chaperone. *J Biol Chem,* 293**,** 5414-5424.

THUMM, M., EGNER, R., KOCH, B., SCHLUMPBERGER, M., STRAUB, M., VEENHUIS, M. & WOLF, D. H. 1994. Isolation of autophagocytosis mutants of Saccharomyces cerevisiae. *FEBS Lett,* 349**,** 275-80.

TIAN, W., LI, W., CHEN, Y., YAN, Z., HUANG, X., ZHUANG, H., ZHONG, W., CHEN, Y., WU, W., LIN, C., CHEN, H., HOU, X., ZHANG, L., SUI, S., ZHAO, B., HU, Z., LI, L. & FENG, D. 2015. Phosphorylation of ULK1 by AMPK regulates translocation of ULK1 to mitochondria and mitophagy. *FEBS Letters,* 589**,** 1847-1854.

TING, L., RAD, R., GYGI, S. P. & HAAS, W. 2011. MS3 eliminates ratio distortion in isobaric multiplexed quantitative proteomics. *Nature methods,* 8**,** 937-940.

TODA, H., MOCHIZUKI, H., FLORES, R., 3RD, JOSOWITZ, R., KRASIEVA, T. B., LAMORTE, V. J., SUZUKI, E., GINDHART, J. G., FURUKUBO-TOKUNAGA, K. & TOMODA, T. 2008. UNC-51/ATG1 kinase regulates axonal transport by mediating motor-cargo assembly. *Genes Dev,* 22**,** 3292-307.

TOMODA, T., BHATT, R. S., KUROYANAGI, H., SHIRASAWA, T. & HATTEN, M. E. 1999. A Mouse Serine/Threonine Kinase Homologous to C. elegans UNC51 Functions in Parallel Fiber Formation of Cerebellar Granule Neurons. *Neuron,* 24**,** 833-846.

TOOZE, J., HOLLINSHEAD, M., LUDWIG, T., HOWELL, K., HOFLACK, B. & KERN, H. 1990. In exocrine pancreas, the basolateral endocytic pathway converges with the autophagic pathway immediately after the early endosome. *J Cell Biol,* 111**,** 329-45.

TOOZE, S. A., NEW, M., VAN ACKER, T., SAKAMAKI, J.-I., JIANG, M., SAUNDERS, R. E., LONG, J., WANG, V. M. Y., BEHRENS, A., SUDHAKAR, P., KORCSMAROS, T., RYAN, K. M., HOWELL, M., CERVEIRA, J. & JEFFERIES, H. B. J. 2019. MDH1 and MPP7 regulate autophagy in pancreatic ductal adenocarcinoma. *Cancer Research***,** canres.2553.2018.

TORGGLER, R., PAPINSKI, D., BRACH, T., BAS, L., SCHUSCHNIG, M., PFAFFENWIMMER, T., ROHRINGER, S., MATZHOLD, T., SCHWEIDA, D., BREZOVICH, A. & KRAFT, C. 2016. Two Independent Pathways within Selective Autophagy Converge to Activate Atg1 Kinase at the Vacuole. *Molecular Cell,* 64**,** 221-235.

TORII, S., YOSHIDA, T., ARAKAWA, S., HONDA, S., NAKANISHI, A. & SHIMIZU, S. 2016. Identification of PPM1D as an essential Ulk1 phosphatase for genotoxic stress‐induced autophagy. *EMBO reports,* 17**,** 1552.

TRUBAN, D., HOU, X., CAULFIELD, T. R., FIESEL, F. C. & SPRINGER, W. 2017. PINK1, Parkin, and Mitochondrial Quality Control: What can we Learn about Parkinson's Disease Pathobiology? *Journal of Parkinson's disease,* 7**,** 13-29.

TSUBOYAMA, K., KOYAMA-HONDA, I., SAKAMAKI, Y., KOIKE, M., MORISHITA, H. & MIZUSHIMA, N. 2016. The ATG conjugation systems are important for degradation of the inner autophagosomal membrane. *Science,* 354**,** 1036-1041.

TSUKADA, M. & OHSUMI, Y. 1993. Isolation and characterization of autophagy-defective mutants of Saccharomyces cerevisiae. *FEBS Lett,* 333**,** 169-74.

TSUN, Z.-Y., BAR-PELED, L., CHANTRANUPONG, L., ZONCU, R., WANG, T., KIM, C., SPOONER, E. & SABATINI, D. M. 2013. The folliculin tumor suppressor is a GAP for the RagC/D GTPases that signal amino acid levels to mTORC1. *Molecular cell,* 52**,** 495-505.

TURCO, E., FRACCHIOLLA, D. & MARTENS, S. 2019a. Recruitment and Activation of the ULK1/Atg1 Kinase Complex in Selective Autophagy. *Journal of Molecular Biology*.

TURCO, E., WITT, M., ABERT, C., BOCK-BIERBAUM, T., SU, M.-Y., TRAPANNONE, R., SZTACHO, M., DANIELI, A., SHI, X., ZAFFAGNINI, G., GAMPER, A., SCHUSCHNIG, M., FRACCHIOLLA, D., BERNKLAU, D., ROMANOV, J., HARTL, M., HURLEY, J. H., DAUMKE, O. & MARTENS, S. 2019b. FIP200 Claw Domain Binding to p62 Promotes Autophagosome Formation at Ubiquitin Condensates. *Molecular Cell,* 74**,** 330-346.e11.

TÜREI, D., FÖLDVÁRI-NAGY, L., FAZEKAS, D., MÓDOS, D., KUBISCH, J., KADLECSIK, T., DEMETER, A., LENTI, K., CSERMELY, P., VELLAI, T. & KORCSMÁROS, T. 2015. Autophagy Regulatory Network - a systems-level bioinformatics resource for studying the mechanism and regulation of autophagy. *Autophagy,* 11**,** 155-165.

UBERSAX, J. A. & FERRELL JR, J. E. 2007. Mechanisms of specificity in protein phosphorylation. *Nature Reviews Molecular Cell Biology,* 8**,** 530.

UEMURA, T., YAMAMOTO, M., KAMETAKA, A., SOU, Y.-S., YABASHI, A., YAMADA, A., ANNOH, H., KAMETAKA, S., KOMATSU, M. & WAGURI, S. 2014. A Cluster of Thin Tubular Structures Mediates Transformation of the Endoplasmic Reticulum to Autophagic Isolation Membrane. *Molecular and Cellular Biology,* 34**,** 1695-1706.

UGOLINO, J., JI, Y. J., CONCHINA, K., CHU, J., NIRUJOGI, R. S., PANDEY, A., BRADY, N. R., HAMACHER-BRADY, A. & WANG, J. 2016. Loss of C9orf72 Enhances Autophagic Activity via Deregulated mTOR and TFEB Signaling. *PLoS Genetics,* 12**,** e1006443.

UHLÉN, M., FAGERBERG, L., HALLSTRÖM, B. M., LINDSKOG, C., OKSVOLD, P., MARDINOGLU, A., SIVERTSSON, Å., KAMPF, C., SJÖSTEDT, E., ASPLUND, A., OLSSON, I., EDLUND, K., LUNDBERG, E., NAVANI, S., SZIGYARTO, C. A.-K., ODEBERG, J., DJUREINOVIC, D., TAKANEN, J. O., HOBER, S., ALM, T., EDQVIST, P.-H., BERLING, H., TEGEL, H., MULDER, J., ROCKBERG, J., NILSSON, P., SCHWENK, J. M., HAMSTEN, M., VON FEILITZEN, K., FORSBERG, M., PERSSON, L., JOHANSSON, F., ZWAHLEN, M., VON HEIJNE, G., NIELSEN, J. & PONTÉN, F. 2015. Tissue-based map of the human proteome. *Science,* 347**,** 1260419.

VAITES, L. P., PAULO, J. A., HUTTLIN, E. L. & HARPER, J. W. 2017. Systematic Analysis of Human Cells Lacking ATG8 Proteins Uncovers Roles for GABARAPs and the CCZ1/MON1 Regulator C18orf8/RMC1 in Macroautophagic and Selective Autophagic Flux. *Molecular and cellular biology,* 38**,** e00392-17.

VALDOR, R., MOCHOLI, E., BOTBOL, Y., GUERRERO-ROS, I., CHANDRA, D., KOGA, H., GRAVEKAMP, C., CUERVO, A. M. & MACIAN, F. 2014.

Chaperone-mediated autophagy regulates T cell responses through targeted degradation of negative regulators of T cell activation. *Nature immunology,* 15**,** 1046-1054.

VALVERDE, D. P., YU, S., BOGGAVARAPU, V., KUMAR, N., LEES, J. A., WALZ, T., REINISCH, K. M. & MELIA, T. J. 2019. ATG2 transports lipids to promote autophagosome biogenesis. *The Journal of Cell Biology,* 218**,** 1787.

VAN WIJK, S. J. L., FRICKE, F., HERHAUS, L., GUPTA, J., HÖTTE, K., PAMPALONI, F., GRUMATI, P., KAULICH, M., SOU, Y.-S., KOMATSU, M., GRETEN, F. R., FULDA, S., HEILEMANN, M. & DIKIC, I. 2017. Linear ubiquitination of cytosolic Salmonella Typhimurium activates NF-κB and restricts bacterial proliferation. *Nature Microbiology,* 2**,** 17066.

VARGAS, J. N. S., WANG, C., BUNKER, E., HAO, L., MARIC, D., SCHIAVO, G., RANDOW, F. & YOULE, R. J. 2019. Spatiotemporal Control of ULK1 Activation by NDP52 and TBK1 during Selective Autophagy. *Molecular Cell,* 74**,** 347-362.e6.

VELIKKAKATH, A. K., NISHIMURA, T., OITA, E., ISHIHARA, N. & MIZUSHIMA, N. 2012. Mammalian Atg2 proteins are essential for autophagosome formation and important for regulation of size and distribution of lipid droplets. *Mol Biol Cell,* 23**,** 896-909.

VERGNE, I. & DERETIC, V. 2010. The role of PI3P phosphatases in the regulation of autophagy. *FEBS letters,* 584**,** 1313-1318.

VON STOCKUM, S., MARCHESAN, E. & ZIVIANI, E. 2018. Mitochondrial quality control beyond PINK1/Parkin. *Oncotarget,* 9**,** 12550-12551.

VON STOCKUM, S., NARDIN, A., SCHREPFER, E. & ZIVIANI, E. 2016. Mitochondrial dynamics and mitophagy in Parkinson's disease: A fly point of view. *Neurobiology of Disease,* 90**,** 58-67.

WAN, W., THARP, J. M. & LIU, W. R. 2014. Pyrrolysyl-tRNA synthetase: an ordinary enzyme but an outstanding genetic code expansion tool. *Biochimica et biophysica acta,* 1844**,** 1059-1070.

WANG, B., IYENGAR, R., LI-HARMS, X., JOO, J. H., WRIGHT, C., LAVADO, A., HORNER, L., YANG, M., GUAN, J.-L., FRASE, S., GREEN, D. R., CAO, X. & KUNDU, M. 2018a. The autophagy-inducing kinases, ULK1 and ULK2, regulate axon guidance in the developing mouse forebrain via a noncanonical pathway. *Autophagy,* 14**,** 796-811.

WANG, B., MAXWELL, B. A., JOO, J. H., GWON, Y., MESSING, J., MISHRA, A., SHAW, T. I., WARD, A. L., QUAN, H., SAKURADA, S. M., PRUETT-MILLER, S. M., BERTORINI, T., VOGEL, P., KIM, H. J., PENG, J., TAYLOR, J. P. & KUNDU, M. 2019. ULK1 and ULK2 Regulate Stress Granule Disassembly Through Phosphorylation and Activation of VCP/p97. *Molecular Cell,* 74**,** 742-757.e8.

WANG, C., WANG, H., ZHANG, D., LUO, W., LIU, R., XU, D., DIAO, L., LIAO, L. & LIU, Z. 2018b. Phosphorylation of ULK1 affects autophagosome fusion and links chaperone-mediated autophagy to macroautophagy. *Nature Communications,* 9**,** 3492.

WANG, H., SUN, H.-Q., ZHU, X., ZHANG, L., ALBANESI, J., LEVINE, B. & YIN, H. 2015. GABARAPs regulate PI4P-dependent autophagosome:lysosome fusion. *Proceedings of the National Academy of Sciences,* 112**,** 7015-7020.

WANG, J., MENON, S., YAMASAKI, A., CHOU, H.-T., WALZ, T., JIANG, Y. & FERRO-NOVICK, S. 2013. Ypt1 recruits the Atg1 kinase to the preautophagosomal structure. *Proceedings of the National Academy of Sciences of the United States of America,* 110**,** 9800-9805.

WANG, L., BROCK, A., HERBERICH, B. & SCHULTZ, P. G. 2001. Expanding the Genetic Code of Escherichia coli. *Science,* 292**,** 498.

WANG, L., MAGLIERY, T. J., LIU, D. R. & SCHULTZ, P. G. 2000. A New Functional Suppressor tRNA/Aminoacyl−tRNA Synthetase Pair for the in Vivo Incorporation of Unnatural Amino Acids into Proteins. *Journal of the American Chemical Society,* 122**,** 5010-5011.

WANG, Z., MIAO, G., XUE, X., GUO, X., YUAN, C., WANG, Z., ZHANG, G., CHEN, Y., FENG, D., HU, J. & ZHANG, H. 2016. The Vici Syndrome Protein EPG5 Is a Rab7 Effector that Determines the Fusion Specificity of Autophagosomes with Late Endosomes/Lysosomes. *Molecular Cell,* 63**,** 781-795.

WEBBER, J. L. & TOOZE, S. A. 2010. Coordinated regulation of autophagy by p38alpha MAPK through mAtg9 and p38IP. *EMBO J,* 29**,** 27-40.

WEBSTER, C. P., SMITH, E. F., BAUER, C. S., MOLLER, A., HAUTBERGUE, G. M., FERRAIUOLO, L., MYSZCZYNSKA, M. A., HIGGINBOTTOM, A., WALSH, M. J., WHITWORTH, A. J., KASPAR, B. K., MEYER, K., SHAW, P. J., GRIERSON, A. J. & DE VOS, K. J. 2016. The C9orf72 protein interacts with Rab1a and the ULK1 complex to regulate initiation of autophagy. *The EMBO Journal,* 35**,** 1656-1676.

WEERASEKARA, V. K., PANEK, D. J., BROADBENT, D. G., MORTENSON, J. B., MATHIS, A. D., LOGAN, G. N., PRINCE, J. T., THOMSON, D. M., THOMPSON, J. W. & ANDERSEN, J. L. 2014. Metabolic-stress-induced rearrangement of the 14-3-3ζ interactome promotes autophagy via a ULK1- and AMPK-regulated 14-3-3ζ interaction with phosphorylated Atg9. *Molecular and cellular biology,* 34**,** 4379-4388.

WEI, Y., AN, Z., ZOU, Z., SUMPTER, R., SU, M., ZANG, X., SINHA, S., GAESTEL, M. & LEVINE, B. 2015. The stress-responsive kinases MAPKAPK2/MAPKAPK3 activate starvation-induced autophagy through Beclin 1 phosphorylation. *eLife,* 4**,** e05289.

WEIDBERG, H., SHPILKA, T., SHVETS, E., ABADA, A., SHIMRON, F. & ELAZAR, Z. 2011. LC3 and GATE-16 N Termini Mediate Membrane Fusion Processes Required for Autophagosome Biogenesis. *Developmental Cell,* 20**,** 444-454.

WEIDBERG, H., SHVETS, E., SHPILKA, T., SHIMRON, F., SHINDER, V. & ELAZAR, Z. 2010. LC3 and GATE-16/GABARAP subfamilies are both essential yet act differently in autophagosome biogenesis. *EMBO J,* 29**,** 1792-802.

WEN, X. & KLIONSKY, D. J. 2016. An overview of macroautophagy in yeast. *Journal of molecular biology,* 428**,** 1681-1699.

WHITE, E. 2016. Autophagy and p53. *Cold Spring Harbor perspectives in medicine,* 6**,** a026120-a026120.

WIJDEVEN, R. H., JANSSEN, H., NAHIDIAZAR, L., JANSSEN, L., JALINK, K., BERLIN, I. & NEEFJES, J. 2016. Cholesterol and ORP1L-mediated ER contact sites control autophagosome transport and fusion with the endocytic pathway. *Nature communications,* 7**,** 11808-11808.

WILKINSON, D. S., JARIWALA, J. S., ANDERSON, E., MITRA, K., MEISENHELDER, J., CHANG, J. T., IDEKER, T., HUNTER, T., NIZET, V., DILLIN, A. & HANSEN, M. 2015. Phosphorylation of LC3 by the Hippo kinases STK3/STK4 is essential for autophagy. *Mol Cell,* 57**,** 55-68.

WILLOWS, R., NAVARATNAM, N., LIMA, A., READ, J. & CARLING, D. 2017. Effect of different gamma-subunit isoforms on the regulation of AMPK. *Biochem J,* 474**,** 1741-1754.

WIRBEL, J., CUTILLAS, P. & SAEZ-RODRIGUEZ, J. 2018. Phosphoproteomics-Based Profiling of Kinase Activities in Cancer Cells. *Methods Mol Biol,* 1711**,** 103-132.

WIRTH, M., ZHANG, W., RAZI, M., NYONI, L., JOSHI, D., O'REILLY, N., JOHANSEN, T., TOOZE, S. A. & MOUILLERON, S. 2019. Molecular determinants regulating selective binding of autophagy adapters and receptors to ATG8 proteins. *Nature Communications,* 10**,** 2055.

WONG, C.-O., LI, R., MONTELL, C. & VENKATACHALAM, K. 2012. Drosophila TRPML is required for TORC1 activation. *Current biology : CB,* 22**,** 1616-1621.

WONG, P.-M., FENG, Y., WANG, J., SHI, R. & JIANG, X. 2015. Regulation of autophagy by coordinated action of mTORC1 and protein phosphatase 2A. *Nature Communications,* 6**,** 8048.

WU, C.-J., CAI, T., RIKOVA, K., MERBERG, D., KASIF, S. & STEFFEN, M. 2009. A predictive phosphorylation signature of lung cancer. *PloS one,* 4**,** e7994-e7994.

WU, W., TIAN, W., HU, Z., CHEN, G., HUANG, L., LI, W., ZHANG, X., XUE, P., ZHOU, C., LIU, L., ZHU, Y., ZHANG, X., LI, L., ZHANG, L., SUI, S., ZHAO, B. & FENG, D. 2014. ULK1 translocates to mitochondria and phosphorylates FUNDC1 to regulate mitophagy. *EMBO Reports,* 15**,** 566-575.

XIA, P., WANG, S., DU, Y., ZHAO, Z., SHI, L., SUN, L., HUANG, G., YE, B., LI, C., DAI, Z., HOU, N., CHENG, X., SUN, Q., LI, L., YANG, X. & FAN, Z. 2013. WASH inhibits autophagy through suppression of Beclin 1 ubiquitination. *The EMBO Journal,* 32**,** 2685-2696.

XU, D. Q., WANG, Z., WANG, C. Y., ZHANG, D. Y., WAN, H. D., ZHAO, Z. L., GU, J., ZHANG, Y. X., LI, Z. G., MAN, K. Y., PAN, Y., WANG, Z. F., KE, Z. J., LIU, Z. X., LIAO, L. J. & CHEN, Y. 2016. PAQR3 controls autophagy by integrating AMPK signaling to enhance ATG14L‐associated PI3K activity. *The EMBO Journal,* 35**,** 496-514.

XU, J., FOTOUHI, M. & MCPHERSON, P. S. 2015. Phosphorylation of the exchange factor DENND3 by ULK in response to starvation activates Rab12 and induces autophagy. *EMBO Reports,* 16**,** 709-718.

XU, J., KOZLOV, G., MCPHERSON, P. S. & GEHRING, K. 2018. A PH-like domain of the Rab12 guanine nucleotide exchange factor DENND3 binds actin and is required for autophagy. *The Journal of biological chemistry,* 293**,** 4566-4574.

XUE, L. & TAO, W. A. 2013. Current technologies to identify protein kinase substrates in high throughput. *Front Biol (Beijing),* 8**,** 216-227.

XUE, L., WANG, W.-H., ILIUK, A., HU, L., GALAN, J. A., YU, S., HANS, M., GEAHLEN, R. L. & TAO, W. A. 2012. Sensitive kinase assay linked with phosphoproteomics for identifying direct kinase substrates. *Proceedings of the National Academy of Sciences of the United States of America,* 109**,** 5615-5620.

YAMAMOTO, H., FUJIOKA, Y., SUZUKI, SHO W., NOSHIRO, D., SUZUKI, H., KONDO-KAKUTA, C., KIMURA, Y., HIRANO, H., ANDO, T., NODA, NOBUO N. & OHSUMI, Y. 2016. The Intrinsically Disordered Protein Atg13 Mediates Supramolecular Assembly of Autophagy Initiation Complexes. *Developmental Cell,* 38**,** 86-99.

YAMAMOTO, H., KAKUTA, S., WATANABE, T. M., KITAMURA, A., SEKITO, T., KONDO-KAKUTA, C., ICHIKAWA, R., KINJO, M. & OHSUMI, Y. 2012. Atg9 vesicles are an important membrane source during early steps of autophagosome formation. *J Cell Biol,* 198**,** 219-33.

YAN, J., KUROYANAGI, H., KUROIWA, A., MATSUDA, Y.-I., TOKUMITSU, H., TOMODA, T., SHIRASAWA, T. & MURAMATSU, M.-A. 1998. Identification of Mouse ULK1, a Novel Protein Kinase Structurally Related to C. elegans UNC-51. *Biochemical and Biophysical Research Communications,* 246**,** 222-227.

YAN, J., KUROYANAGI, H., TOMEMORI, T., OKAZAKI, N., ASATO, K., MATSUDA, Y.-I., SUZUKI, Y.-I., OHSHIMA, Y., MITANI, S., MASUHO, Y., SHIRASAWA, T. & MURAMATSU, M.-A. 1999. Mouse ULK2, a novel member of the UNC-51-like protein kinases: unique features of functional domains. *Oncogene,* 18**,** 5850-5859.

YAN, Y., FLINN, R. J., WU, H., SCHNUR, R. S. & BACKER, J. M. 2009. hVps15, but not Ca2+/CaM, is required for the activity and regulation of hVps34 in mammalian cells. *The Biochemical journal,* 417**,** 747-755.

YANG, C.-S., RODGERS, M., MIN, C.-K., LEE, J.-S., KINGETER, L., LEE, J.-Y., JONG, A., KRAMNIK, I., LIN, X. & JUNG, J. U. 2012. The autophagy regulator Rubicon is a feedback inhibitor of CARD9-mediated host innate immunity. *Cell host & microbe,* 11**,** 277-289.

YANG, M., LIANG, C., SWAMINATHAN, K., HERRLINGER, S., LAI, F., SHIEKHATTAR, R. & CHEN, J.-F. 2016a. A C9ORF72/SMCR8-containing complex regulates ULK1 and plays a dual role in autophagy. *Science Advances,* 2**,** e1601167.

YANG, Y., SONG, H., HE, D., ZHANG, S., DAI, S., LIN, S., MENG, R., WANG, C. & CHEN, P. R. 2016b. Genetically encoded protein photocrosslinker with a transferable mass spectrometry-identifiable label. *Nature communications,* 7**,** 12299-12299.

YEH, Y.-Y., SHAH, K. H. & HERMAN, P. K. 2011. An Atg13 protein-mediated self-association of the Atg1 protein kinase is important for the induction of autophagy. *The Journal of biological chemistry,* 286**,** 28931-28939.

YLA-ANTTILA, P., VIHINEN, H., JOKITALO, E. & ESKELINEN, E. L. 2009. 3D tomography reveals connections between the phagophore and endoplasmic reticulum. *Autophagy,* 5**,** 1180-5.

YOO, S.-M. & JUNG, Y.-K. 2018. A Molecular Approach to Mitophagy and Mitochondrial Dynamics. *Molecules and cells,* 41**,** 18-26.

YOON, M.-S., SON, K., ARAUZ, E., HAN, J. M., KIM, S. & CHEN, J. 2016. Leucyl-tRNA Synthetase Activates Vps34 in Amino Acid-Sensing mTORC1 Signaling. *Cell reports,* 16**,** 1510-1517.

YOUNG, A. R., CHAN, E. Y., HU, X. W., KOCHL, R., CRAWSHAW, S. G., HIGH, S., HAILEY, D. W., LIPPINCOTT-SCHWARTZ, J. & TOOZE, S. A. 2006. Starvation and ULK1-dependent cycling of mammalian Atg9 between the TGN and endosomes. *J Cell Sci,* 119**,** 3888-900.

YOUNG, L. N., CHO, K., LAWRENCE, R., ZONCU, R. & HURLEY, J. H. 2016. Dynamics and architecture of the NRBF2-containing phosphatidylinositol 3-kinase complex I of autophagy. *Proceedings of the National Academy of Sciences,* 113**,** 8224-8229.

YU, L., MCPHEE, C. K., ZHENG, L., MARDONES, G. A., RONG, Y., PENG, J., MI, N., ZHAO, Y., LIU, Z., WAN, F., HAILEY, D. W., OORSCHOT, V., KLUMPERMAN, J., BAEHRECKE, E. H. & LENARDO, M. J. 2010. Termination of autophagy and reformation of lysosomes regulated by mTOR. *nature,* 465**,** 942-6.

YU, Z.-Q., NI, T., HONG, B., WANG, H.-Y., JIANG, F.-J., ZOU, S., CHEN, Y., ZHENG, X.-L., KLIONSKY, D. J., LIANG, Y. & XIE, Z. 2012. Dual roles of Atg8-PE deconjugation by Atg4 in autophagy. *Autophagy,* 8**,** 883-892.

YUAN, F., JIN, X., LI, D., SONG, Y., ZHANG, N., YANG, X., WANG, L., ZHU, W.-G., TIAN, C. & ZHAO, Y. 2019. ULK1 phosphorylates Mad1 to regulate spindle assembly checkpoint. *Nucleic Acids Research,* 47**,** 8096-8110.

YUAN, H.-X., RUSSELL, R. C. & GUAN, K.-L. 2013. Regulation of PIK3C3/VPS34 complexes by MTOR in nutrient stress-induced autophagy. *Autophagy,* 9**,** 1983-1995.

YUN, J., PURI, R., YANG, H., LIZZIO, M. A., WU, C., SHENG, Z.-H. & GUO, M. 2014. MUL1 acts in parallel to the PINK1/parkin pathway in regulating mitofusin and compensates for loss of PINK1/parkin. *eLife,* 3**,** e01958-e01958.

ZAFFAGNINI, G. & MARTENS, S. 2016. Mechanisms of Selective Autophagy. *Journal of molecular biology,* 428**,** 1714-1724.

ZAVODSZKY, E., SEAMAN, M. N. J., MOREAU, K., JIMENEZ-SANCHEZ, M., BREUSEGEM, S. Y., HARBOUR, M. E. & RUBINSZTEIN, D. C. 2014. Mutation in VPS35 associated with Parkinson's disease impairs WASH complex association and inhibits autophagy. *Nature communications,* 5**,** 3828-3828.

ZHANG, B.-L., XU, R.-L., ZHANG, J., ZHAO, X.-X., WU, H., MA, L.-P., HU, J.-Q., ZHANG, J.-L., YE, Z., ZHENG, X. & QIN, Y.-W. 2013a. Identification and functional analysis of a novel PRKAG2 mutation responsible for Chinese PRKAG2 cardiac syndrome reveal an important role of non-CBS domains in regulating the AMPK pathway. *Journal of Cardiology,* 62**,** 241-248.

ZHANG, C.-S., JIANG, B., LI, M., ZHU, M., PENG, Y., ZHANG, Y.-L., WU, Y.-Q., LI, TERYTTY Y., LIANG, Y., LU, Z., LIAN, G., LIU, Q., GUO, H., YIN, Z., YE, Z., HAN, J., WU, J.-W., YIN, H., LIN, S.-Y. & LIN, S.-C. 2014. The Lysosomal v-ATPase-Ragulator Complex Is a Common Activator for AMPK and mTORC1, Acting as a Switch between Catabolism and Anabolism. *Cell Metabolism,* 20**,** 526-540.

ZHANG, D., WANG, W., SUN, X., XU, D., WANG, C., ZHANG, Q., WANG, H., LUO, W., CHEN, Y., CHEN, H. & LIU, Z. 2016a. AMPK regulates autophagy by phosphorylating BECN1 at threonine 388. *Autophagy,* 12**,** 1447-1459.

ZHANG, J., ZHOU, W., LIN, J., WEI, P., ZHANG, Y., JIN, P., CHEN, M., MAN, N. & WEN, L. 2016b. Autophagic lysosomal reformation depends on mTOR reactivation in H2O2-induced autophagy. *The International Journal of Biochemistry & Cell Biology,* 70**,** 76-81.

ZHANG, L., FU, L., ZHANG, S., ZHANG, J., ZHAO, Y., ZHENG, Y., HE, G., YANG, S., OUYANG, L. & LIU, B. 2017. Discovery of a small molecule targeting ULK1-modulated cell death of triple negative breast cancer in vitro and in vivo. *Chemical science,* 8**,** 2687-2701.

ZHANG, Y., MUN, S. R., LINARES, J. F., AHN, J., TOWERS, C. G., JI, C. H., FITZWALTER, B. E., HOLDEN, M. R., MI, W., SHI, X., MOSCAT, J., THORBURN, A., DIAZ-MECO, M. T., KWON, Y. T. & KUTATELADZE, T. G. 2018. ZZ-dependent regulation of p62/SQSTM1 in autophagy. *Nature Communications,* 9**,** 4373.

ZHANG, Y. L., GUO, H., ZHANG, C. S., LIN, S. Y., YIN, Z., PENG, Y., LUO, H., SHI, Y., LIAN, G., ZHANG, C., LI, M., YE, Z., YE, J., HAN, J., LI, P., WU, J. W. & LIN, S. C. 2013b. AMP as a low-energy charge signal autonomously initiates assembly of AXIN-AMPK-LKB1 complex for AMPK activation. *Cell Metab,* 18**,** 546-55.

ZHAO, Y., WANG, Q., QIU, G., ZHOU, S., JING, Z., WANG, J., WANG, W., CAO, J., HAN, K., CHENG, Q., SHEN, B., CHEN, Y., ZHANG, WEIPING J., MA, Y. & ZHANG, J. 2015. RACK1 Promotes Autophagy by Enhancing the Atg14L-Beclin 1-Vps34-Vps15 Complex Formation upon Phosphorylation by AMPK. *Cell Reports,* 13**,** 1407-1417.

ZHAO, Y. G., CHEN, Y., MIAO, G., ZHAO, H., QU, W., LI, D., WANG, Z., LIU, N., LI, L., CHEN, S., LIU, P., FENG, D. & ZHANG, H. 2017. The ER-Localized Transmembrane Protein EPG-3/VMP1 Regulates SERCA Activity to Control ER-Isolation Membrane Contacts for Autophagosome Formation. *Molecular Cell,* 67**,** 974-989.e6.

ZHAO, Y. G., LIU, N., MIAO, G., CHEN, Y., ZHAO, H. & ZHANG, H. 2018. The ER Contact Proteins VAPA/B Interact with Multiple Autophagy Proteins to Modulate Autophagosome Biogenesis. *Current Biology,* 28**,** 1234-1245.e4.

ZHEN, Y., SPANGENBERG, H., MUNSON, M. J., BRECH, A., SCHINK, K. O., TAN, K.-W., SØRENSEN, V., WENZEL, E. M., RADULOVIC, M., ENGEDAL, N., SIMONSEN, A., RAIBORG, C. & STENMARK, H. 2019. ESCRT-mediated phagophore sealing during mitophagy. *Autophagy***,** 1-16.

ZHENG, N. & SHABEK, N. 2017. Ubiquitin Ligases: Structure, Function, and Regulation. *Annual Review of Biochemistry,* 86**,** 129-157.

ZHONG, Y., MORRIS, D. H., JIN, L., PATEL, M. S., KARUNAKARAN, S. K., FU, Y.-J., MATUSZAK, E. A., WEISS, H. L., CHAIT, B. T. & WANG, Q. J. 2014. Nrbf2 Protein Suppresses Autophagy by Modulating Atg14L Protein-containing Beclin 1-Vps34 Complex Architecture and Reducing Intracellular Phosphatidylinositol-3 Phosphate Levels. *The Journal of Biological Chemistry,* 289**,** 26021-26037.

ZHONG, Y., WANG, Q. J., LI, X., YAN, Y., BACKER, J. M., CHAIT, B. T., HEINTZ, N. & YUE, Z. 2009. Distinct regulation of autophagic activity by Atg14L and Rubicon associated with Beclin 1-phosphatidylinositol-3-kinase complex. *Nat Cell Biol,* 11**,** 468-476.

ZHOU, C., MA, K., GAO, R., MU, C., CHEN, L., LIU, Q., LUO, Q., FENG, D., ZHU, Y. & CHEN, Q. 2017. Regulation of mATG9 trafficking by Src- and ULK1-mediated phosphorylation in basal and starvation-induced autophagy. *Cell Res,* 27**,** 184-201.

ZHOU, F., WU, Z., ZHAO, M., MURTAZINA, R., CAI, J., ZHANG, A., LI, R., SUN, D., LI, W., ZHAO, L., LI, Q., ZHU, J., CONG, X., ZHOU, Y., XIE, Z., GYURKOVSKA, V., LI, L., HUANG, X., XUE, Y., CHEN, L., XU, H., XU, H., LIANG, Y. & SEGEV, N. 2019. Rab5-dependent autophagosome closure by ESCRT. *The Journal of Cell Biology,* 218**,** 1908.

ZHOU, H., DI PALMA, S., PREISINGER, C., PENG, M., POLAT, A. N., HECK, A. J. R. & MOHAMMED, S. 2013. Toward a Comprehensive Characterization of a Human Cancer Cell Phosphoproteome. *Journal of Proteome Research,* 12**,** 260-271.

ZHOU, X., BABU, J. R., DA SILVA, S., SHU, Q., GRAEF, I. A., OLIVER, T., TOMODA, T., TANI, T., WOOTEN, M. W. & WANG, F. 2007. Unc-51-like kinase 1/2-mediated endocytic processes regulate filopodia extension and branching of sensory axons. *Proceedings of the National Academy of Sciences,* 104**,** 5842.

ZHOU, X., WANG, L., HASEGAWA, H., AMIN, P., HAN, B.-X., KANEKO, S., HE, Y. & WANG, F. 2010. Deletion of PIK3C3/Vps34 in sensory neurons causes rapid neurodegeneration by disrupting the endosomal but not the autophagic pathway. *Proceedings of the National Academy of Sciences of the United States of America,* 107**,** 9424-9429.